TECHNISCHE
UNIVERSITÄT
WIEN

Master Thesis

Investigation of cermet grades for saw blades

carried out at the

Institut für Chemische Technologien und Analytik - TU Wien
Getreidemarkt 9/164-CT
1060 Wien

under the supervision of

Ao.Univ.Prof. Dipl.-Ing. Dr. techn. Walter Lengauer
Projektass. Dipl.-Ing. Markus Fürst

by

Peter Michael Nahringbauer, BSc.
[redacted]

Abstract

Cermets are an advantageous material for cutting operations due to their beneficial properties such as high hardness, excellent wear resistance and thermal stability. In recent years, the demand for efficient and durable cutting tools like saw teeth has grown significantly in various industries. This has prompted researchers and engineers to explore the possibilities of tailoring the properties of cermet materials to increase tool life and productivity.

In this work, thirteen commercially available cermet saw teeth were analyzed in regard to their elemental and phase composition, mechanical properties and microstructure. The formulations of grades with desirable behavior e.g. a high fracture toughness were selected as basis for two sample series synthesizing cermets by classical powder metallurgy on a laboratory scale. In both series, the influence of different starting material grain sizes and pre-alloyed powders was studied. Furthermore, sintering was conducted in a vacuum and a SinterHIP furnace in Ar or N_2 with various partial pressures. Lastly, carbon was added to study the attributes of cermets and the prevention of eta phase. The mechanical properties of the samples were determined with a Vickers indenter and cermets were investigated by Light Optical Microscopy (LOM), Scanning Electron Microscopy (SEM), X-Ray Diffraction (XRD) and C, N and O analysis. Additionally, the binder phase dissolution state was characterized with XRD and magnetic saturation measurements.

Not only could the mechanical properties and microstructure of the target grades be matched, but also a wide range of hardness and fracture toughness was achieved by variation of the raw materials and the sintering conditions. As these adjustments in performance could be linked to changes in the microstructure and the binder solution state, this thesis can provide the basis for the design of cermet saw teeth prototypes with specific and optimized qualities.

Kurzfassung

Aufgrund zahlreicher vorteilhafter Eigenschaften wie einer hohen Härte, ausgezeichneten Verschleißeigenschaften und thermischer Stabilität sind Cermets ein geeignetes Material für Schneidwerkzeuge. In den letzten Jahren hat sich der Bedarf an effizienten Schneidmaterialien signifikant erhöht. Dies hat dazu geführt, dass die gezielte Entwicklung von Cermetsorten mit spezifischen Eigenschaften in den wissenschaftlichen Fokus gerückt wurde, um die Lebensdauer und Produktivität von Werkzeugen wie Sägezähnen zu erhöhen.

In dieser Arbeit wurden dreizehn handelsübliche Cermetsägezähne hinsichtlich ihrer elementaren und Phasenzusammensetzung, mechanischer Eigenschaften und Mikrostruktur untersucht. Zwei dieser Sorten wurden aufgrund ihrer vorteilhaften Eigenschaften, insbesondere einer hohen Risszähigkeit, ausgewählt und deren elementare Zusammensetzung als Basis für zwei Versuchsreihen herangezogen. Für beide Probenserien wurde der Einfluss von Ausgangspulvern mit verschiedenen Korngrößen und Legierungszuständen evaluiert. Die Sinterung erfolgte in einem Vakuumofen und einer SinterHIP Anlage in einer Ar oder N_2 Atmosphäre mit unterschiedlichen Partialdrücken. Des Weiteren wurden die Auswirkung des Kohlenstoffgehalts auf die Cermeteigenschaften und Ausbildung von eta-Phase analysiert, indem ausgewählten Pulvermischungen elementarer Kohlenstoff zugesetzt wurde. Die mechanischen Eigenschaften der gesinterten Proben wurden mit der Vickers-Methode bestimmt und die Cermets anschließend mittels Lichtmikroskopie (LOM), Rasterelektronenmikroskopie (SEM), Röntgenbeugung (XRD) und C-, N- und O-Analysen charakterisiert.

Sowohl die mechanischen Eigenschaften als auch die Mikrostruktur der Referenzsorten konnten im Labormaßstab reproduziert werden. Außerdem wurden durch die Variation der Ausgangspulver und Sinterbedingungen Härte und Risszähigkeit über einen großen Bereich modifiziert. Durch die Aufklärung der Einflussfaktoren und des Zusammenspiels aus Mikrostruktur, Binderzustand und mechanischer Eigenschaften kann diese Arbeit als Ausgangspunkt für die gezielte Fertigung von Cermetsorten mit spezifischen Anforderungen dienen.

Acknowledgements

First and foremost, I would like to thank my supervisor Walter Lengauer for his guidance, feedback and the chance to work in his research group on an interesting topic with hands-on applications.

I want to thank our project partners Steven Moseley, José-Maria Tarragó, Reinhold Wartbichler and Christa Beltz de Arancibia for their assistance and the valuable discussions during regular meetings.

Many thanks should also go to Markus Fürst for always finding time during his own PhD studies to show me the way around a powdermetallurgical lab and the university in general.

I would like to express my gratitude to my parents, Christa and Peter, for sending me on the way to my MSc a long time ago. Thank you for your support and your belief in me.

I am also grateful to my partner Alwine. Without your unconditional help and encouragement I would have stopped my studies a long time ago. Thank you for always being there for me and keeping me sane in desperate times.

Thank you Aurel, Bastian, Bernhard, Elisabeth, Ella, Eva, Felix, Felix, Irina, Johannes, Johannes, Katharina, Lena, Lisa, Moritz, Nico, Nico, Robert, Sophie, Stefan, Theresa, Tobias, Vinzent and all the other friends, visitors and colleagues for making the second floor an inspiring and pleasant work environment.

Contents

1. Introduction

Cermets are a composite material consisting of a brittle hard phase and a ductile binder phase. The name is derived from the mostly **cer**amic hard phase and the **met**allic binder. For industrial cutting tools, TiC or Ti(C,N) *fcc* hard phases and Co, Ni or Co/Ni binder phases are commonly employed. TiC-based composites were patented as early as the 1920s, industrial cutting tools are predominantly made out of hardmetals or cemented carbides with a hexagonal WC hard phase and a binder phase mainly composed of Co. Therefore, the properties of cermets are often compared to the well-established WC-Co hardmetals. Generally, cermets are harder, allowing for higher cutting speeds, but also more brittle, reducing the cutting depth or feed rate during cutting operations. In addition to their lower density, cermets show excellent chemical stability, oxidation resistance and low friction. These beneficial properties combined with further efforts to raise strength and toughness led to an increased use of cermet in the production of cutting tools [1].
While hardmetals and high-speed steel still take up the majority of the global market share by material with 50% and 20% respectively, already 5% of global cutting tools in 2018 were made of cermets. The cermet market is especially developed in Japan due to a high density of manufacturing and powder supply companies. Because both Co and W are on the list of critical raw materials in the EU, the development of alternative composite hard materials is of great interest [2].

The aim of this work is to increase the understanding of the impact of several parameters on the microstructure and properties of cermet materials, especially for circular saw teeth. To improve the targeted development of cermets with specific properties, only one parameter was changed at a time. For this, thirteen industrially available saw teeth were screened and grades with desirable characteristics were selected. Based on these grades, chemically identical cermet samples were produced and the influences of the Ti(C,N) grain size, raw powder pre-alloyed state, carbon content and different sintering parameters were studied and evaluated.

2. Theoretical background

2.1. Hard phase

2.1.1. Titanium carbonitride Ti(C,N)

The hard phase of cermets for cutting operations mainly consists of TiC or Ti(C,N) with varying C/N ratio and stoichiometry resulting from the complete miscibility of TiC and TiN as shown in fig. 1a. Therefore, the hardness of these cermets directly correlates to the hardness of the Ti(C,N) implemented. For both the micro- and nanohardness there is a significant increase when the [C]/([C]+[N]) ratio approaches pure TiC. In contrast to the WC-Co system used in hardmetals, the ternary δ-TiC_xN_{1-x} phase shows a relatively high tolerance for non-metal substoichiometry. Hence, the mechanical properties can also be adjusted utilizing sub-stoichiometric Ti(C,N) powders.

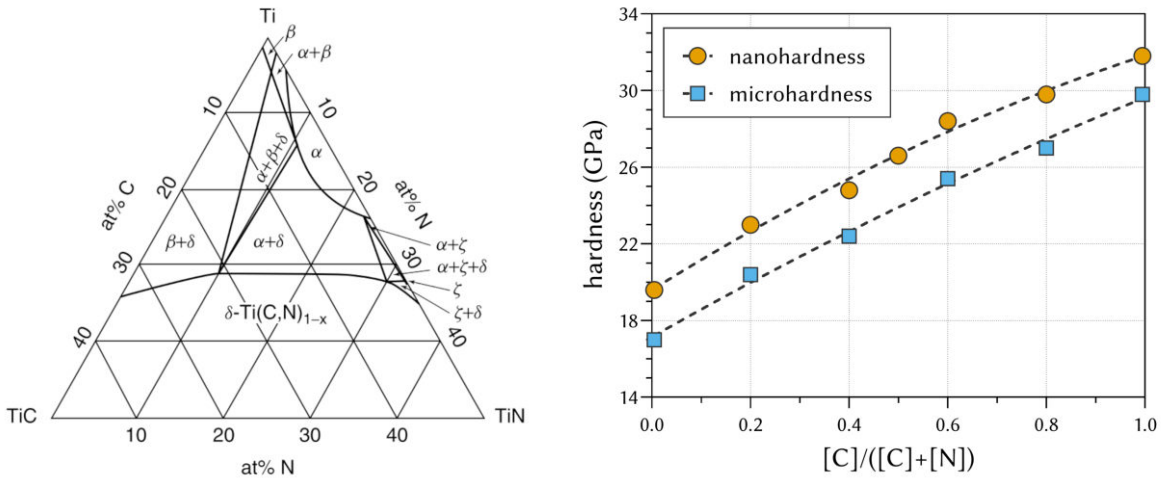

(a) (b)

Figure 1: (a) Phase diagram of the Ti-C-N system at 1200 °C [3] and (b) micro- and nanohardness of Ti(C,N) as a function of [C]/([C]+[N]) [4].

Two main synthesis routes can be distinguished for the industrial production of TiC, TiN and Ti(C,N) powders. In the carbothermal synthesis (CTS), the metal oxide TiO_2 is directly reduced by carbon at temperatures above 1200 °C in vacuum or Ar atmosphere. To arrive at carbonitrides with specific C/N ratios, N_2 gas is introduced at different partial pressures into the furnace and Ti(C,N) powders are formed [5]:

$$TiO_{2(s)} + 2\,C_{(s)} + 0.5\,N_{2(g)} \rightleftharpoons Ti(C,N)_{(s)} + 2\,CO_{(g)} \tag{1}$$

As the reaction takes place in the solid state, the shape of the resulting powders is dependent on the shape of the starting TiO_2. Hence, the round grains of the Ti(C,N) from the CTS usually remain visible in the microstructure of cermets after sintering.
In the metal route synthesis, metallic Ti is directly heated with a carbon source such as graphite

or carbohydrates. Again, N_2 might be applied to obtain Ti(C,N) [6]:

$$Ti_{(s)} + C_{(s)} + 0.5\,N_{2(g)} \rightleftharpoons Ti(C,N)_{(s)} \tag{2}$$

This process results in mostly elongated Ti(C,N) grains. Therefore, the Ti(C,N)-rich grains in the microstructure of cermets can indicate the synthesis route used in the production of the starting material.

2.1.2. Carbon content and C/N ratio

The influence of Ti(C,N) with different C/N ratios has been studied to some extent. In the work of Schwarz et al. [7], Ti(C,N)-WC-(Ta,Nb)C-Cr_3C_2-Co/Ni cermets were prepared with $TiC_{0.5}N_{0.5}$ and $TiC_{0.7}N_{0.3}$ powders. When sintered under Ar partial pressure, cermets containing $TiC_{0.7}N_{0.3}$ developed grains with a pronounced core-rim structure. Due to the higher C content (and therefore lower N content), the heavier W, Mo, Ta and Nb atoms can be incorporated in the Ti(C,N) lattice to form the bright inner rim amount the Ti(C,N)-rich dark core. The outer rim is formed during sintering when the N outgassing is inhibited by the formation of liquid phase and consists of an intermediate solid solution. When increasing the N activity during sintering by applying 10 or 100 mbar N_2 to the atmosphere, the formation of the rim phases is decreased due to the unstable Me-N bonds for W, Mo, Ta and Nb. Therefore, the Ti(C,N)-rich dark grains appear more isolated, especially for the higher N activity under 100 mbar N_2.
Contrary to the findings for $TiC_{0.7}N_{0.3}$, the higher N content of cermets using $TiC_{0.5}N_{0.5}$ led to mostly isolated Ti(C,N)-rich dark cores regardless of the sintering atmosphere. Additionally, the grains are significantly smaller because of the grain growth inhibiting effect of N.
These changes in microstructure also caused significant differences in the mechanical properties plotted in fig. 2a. The low N activity in cermets utilizing $TiC_{0.7}N_{0.3}$ powder sintered under Ar atmosphere led to the toughest samples with a fracture toughness of around 9 MPa · $m^{1/2}$. Increasing the N activity by introducing N_2 to the sintering atmosphere, a significant decrease of the fracture toughness to approximately 8.5 and 7 MPa · $m^{1/2}$ could be observed for 10 and 100 mbar N_2, respectively. At the same time, the hardness was significantly increased from approximately 1500 HV10 in Ar to 1650 HV10 in 10 mbar and 1750 HV10 in 100 mbar N_2 atmosphere.
The hardness can also be increased by the use of the N-rich $TiC_{0.5}N_{0.5}$ powder. The cermets sintered in Ar and 10 mbar (1650 and 1750 HV10 respectively) achieved a higher hardness compared to the $TiC_{0.7}N_{0.3}$ cermets. However, under 100 mbar both Ti(C,N) powders show similar hardness. For all sintering atmospheres tested, the $TiC_{0.7}N_{0.3}$-based cermets revealed a reduced fracture toughness of approximately 7 MPa · $m^{1/2}$.
Similar studies were conducted by Cutard et al. [8]. Three different Ti(C,N)-Mo_2C-(Co,Ni)-cermet formulations with varying Co and Mo_2C content were prepared with $TiC_{0.5}N_{0.5}$ and $TiC_{0.7}N_{0.3}$ powders. All samples were sintered in Ar atmosphere, hence core-rim grains were observed in the microstructure. In fig. 2b, the mechanical properties of all three formulations

show an increase in fracture toughness when the C-rich $TiC_{0.7}N_{0.3}$ powder was used. Compared to the findings of [7], the hardness varies only slightly. This is probably because the stoichiometry of the Ti(C,N) is only nominal and the difference in the powders used was not sufficient to produce a similarly significant effect. Additionally, this is apparent in the remarks on the microstructure, as no isolated Ti(C,N)-rich grains were reported and the N activity was low enough that core-rim structures could be formed with both Ti(C,N) powders.

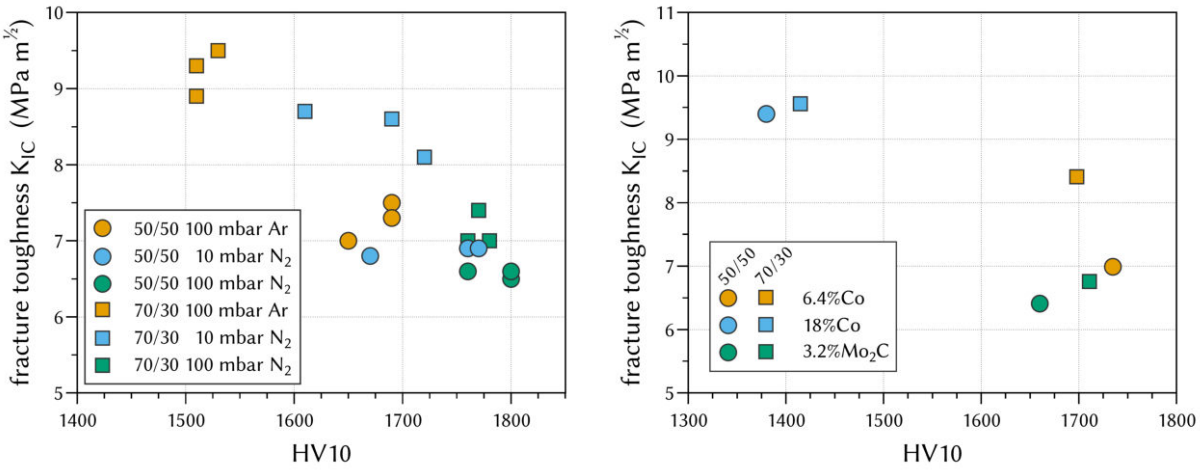

Figure 2: Mechanical properties of cermets with $TiC_{0.5}N_{0.5}$ and $TiC_{0.7}N_{0.3}$ (a) sintered in changing atmospheres [7] and (b) with different Co and Mo_2C contents [8].

2.1.3. Raw powder grain size

On the one hand, the mechanical properties of cermets can be improved by a finer average grain size according to the Hall-Petch relation. Therefore, they are directly dependent on the starting powders' grain size. On the other hand, the microstructure is influenced by the grain size of the Ti(C,N) raw powder. This is especially noticeable in the core and rim thickness of the cermets.

The influence of the initial TiC grain size on the properties of TiC-TiN-WC-Mo_2C-Ni cermets was tested by Chao et al. [9]. Samples containing submicron TiC were significantly harder and less tough compared to cermets based on 2-4 µm TiC powder. Similar results were also found by Chai et al. [10] evaluating the different properties of Ti(C,N)-Mo-Ni cermets with 0.2 and 0.5 µm average Ti(C,N) grain sizes. The formulations including finer Ti(C,N) developed a slight increase in hardness and decrease in fracture toughness. However, the difference in grain size was smaller, hence the effect is less pronounced compared to the previous study. The mechanical properties found in both studies are summarized in fig. 3a. Submicron starting powders were also utilized by Demoly et al. [11] in the preparation of two grades of Ti(C,N)-(Ta,Nb)C-WC-Cr_3C_2-Co-Ni cermets. In comparison to a coarser commercial Ti(C,N) powder, the use of submicron $TiC_{0.5}N_{0.5}$ revealed an increase in hardness for both tested compositions (see fig 3b). The fracture toughness also improved for the tested grade B while it slightly declined for grade A. The findings for grade A were later confirmed by the same authors in

a second study in 2012 [12]. Differences were also observed in the microstructure, as the submicron Ti(C,N) dissolved more readily and led to the formation of a homogeneous, thicker outer rim phase and a higher amount of inverse grains.

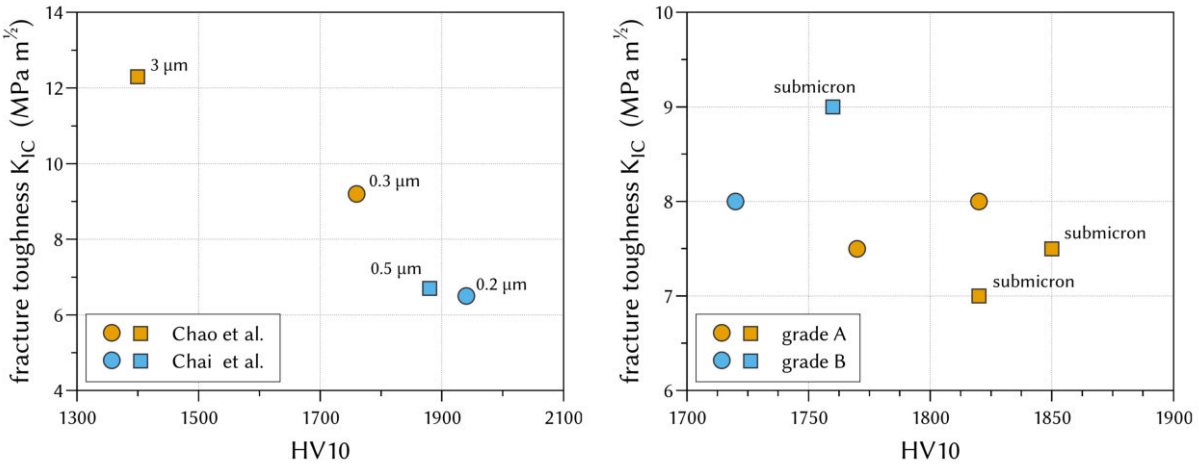

(a) (b)

Figure 3: Influence of the Ti(C,N) powder grain size on the mechanical properties of (a) TiC-TiN-WC-Mo_2C-Ni and Ti(C,N)-Mo-Ni cermets [9, 10] and (b) Ti(C,N)-(Ta,Nb)C-WC-Cr_3C_2-Co-Ni cermets [11, 12].

2.1.4. WC content

WC is commonly added to cermets to improve the sintering activity and thus the densification during the sintering process.

The effect of the WC content on TiC-TiN-WC-Co-C cermets was studied by Li et al. [13]. In their work, the amount of WC was varied between 0 and 20 wt% in steps of 5 wt%. Up to 10 wt% WC, the hardness was steeply increased with a corresponding drop in fracture toughness. Further addition of WC again improved the hardness while the fracture toughness reached a plateau at around 16 MPa · $m^{1/2}$.

Similar results were reported by Wu et al. [14] for 10 to 30 wt% WC in $TiC_{0.7}N_{0.3}$-WC-Ni cermets. Up to 25 wt% WC led to an almost linear increase in hardness and decline in toughness (see fig. 4b). The maximum tested amount (30 wt% WC) caused the formation of an extra WC phase responsible the maximum hardness and toughness of all tested cermets. Both studies reason that the WC addition led to a higher sinter activity and therefore a reduction in the mean free path of the binder phase, improving the hardness of the samples.

$TiC_{0.6}N_{0.4}$-WC-Mo_2C-Ni cermets with variable WC content between 0 and 9 wt% were prepared by Xu et al. [15]. Up to 3 wt% WC, the hardness improved and the fracture toughness declined slightly due to the formation of finer grains (fig. 5a). Further addition resulted in much tougher but softer cermets as more inverse grains were present in the microstructure. This general trend for the mechanical properties held true for two tested cooling rates. Cermets that were rapidly cooled down showed both higher hardness and toughness values in

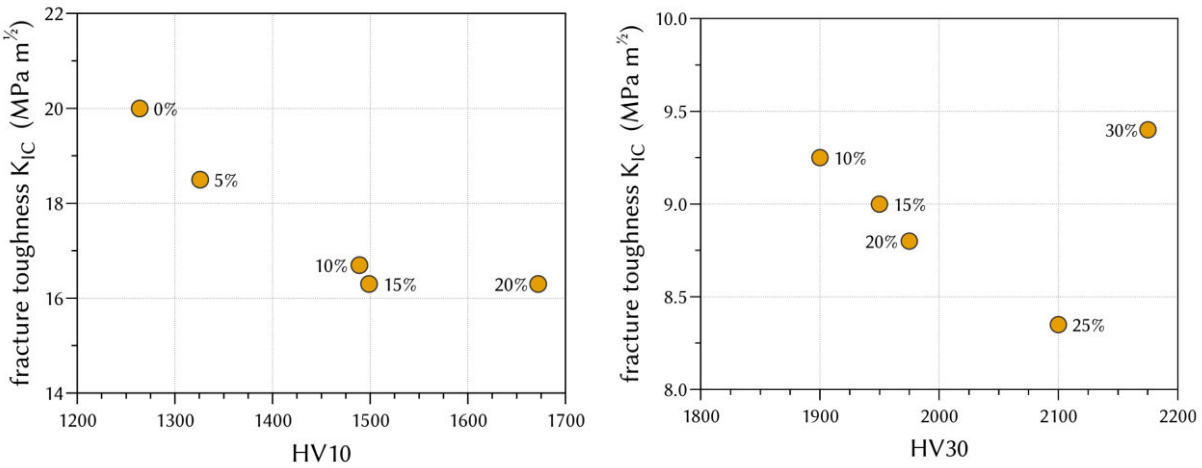

Figure 4: Mechanical properties for cermets with different amounts of WC addition (a) in TiC-TiN-WC-Co-C [13] and (b) in $TiC_{0.7}N_{0.3}$-WC-Ni cermets [14].

comparison to cermets with lower cooling rates. The rapid temperature reduction led to generally finer microstructure and a strengthening effect via the Hall-Petch relation. Furthermore, quicker cooling also suppressed the dissolution process and therefore reduced the amount of rim phase.

Zhang et al. [16] tested the same variation of WC content on very similar $TiC_{0.6}N_{0.4}$-WC-Mo_2C-Ni cermets but implemented a higher Mo and Ni content. All four samples developed the typical core-rim structure and also some inverse grains with a white core and a gray rim phase. Addition of WC led to a higher amount of inverse grains and a grain refinement by reducing the solubility of Ti(C,N) in the binder, thus grain growth was diminished. A gradual increase in WC content slightly reduced the hardness of the cermets (fig. 5b). The authors explained this the reduction of the amount of harder Ti(C,N) grains by the lower solubility when WC was added. The fracture toughness on the other hand was strongly dependent on the WC content. Up to 6 wt%, the fracture toughness increased by over 30 %. Further addition to 9 wt% WC the fracture toughness significantly drops. The authors also found that a higher WC content has negative effects on the hot temperature oxidation stability of cermets as a result of the formation of volatile tungsten oxides.

Despite using similar cermets, the increase in WC addition showed contradictory effects in comparison to the findings of [15]. This suggest that the mechanical properties of cermets also depend on the W/Mo ratio in the formulation.

2.1.5. Mo content and W/Mo ratio

In their study, Cutard et al. [8] additionally investigated the influence of the Mo content on Ti(C,N)-based cermets. The mechanical properties are summarized in fig. 6a. $TiC_{0.7}N_{0.3}$-based cermets with a pure Ni binder were almost linearly affected by a rising Mo content resulting in slightly lowered toughness and an improved hardness. The hardness of the $TiC_{0.5}N_{0.5}$-Mo_2C-Co also increased when the Mo content reached 3.2 vol%, but the fracture toughness stayed

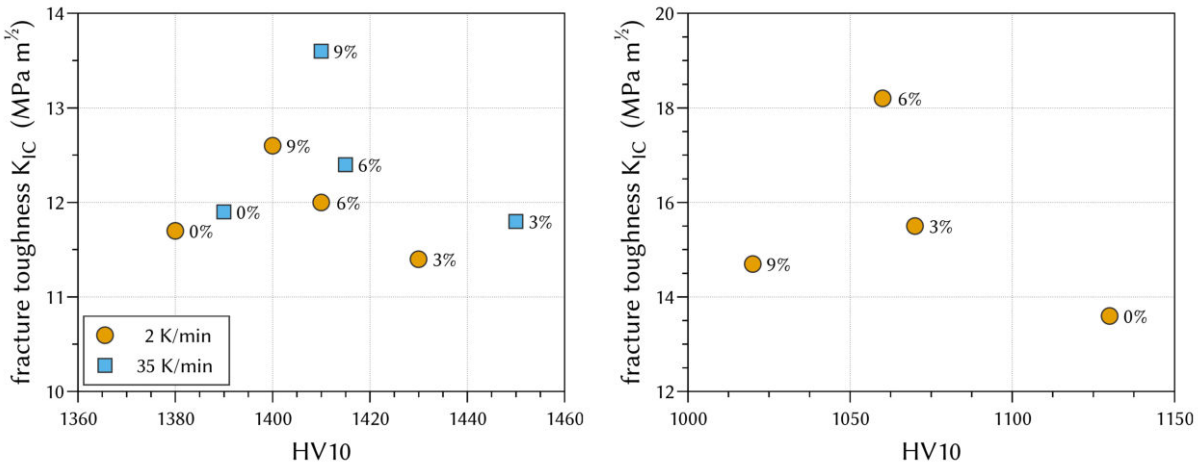

(a) (b)

Figure 5: Mechanical properties of varying WC contents in $TiC_{0.6}N_{0.4}$-WC-Mo_2C-Ni cermets (a) with 8 wt% Mo and 25 wt% Ni [15] and (b) with 12 wt% Mo and 36 wt% Ni [16].

constant. Additional Mo addition to 6.4 vol% increased the hardness again, but the fracture toughness was also improved. Elevating the Mo content from 3.2 vol% to 6.4 vol% in the third series ($TiC_{0.7}N_{0.3}$-Mo_2C-Co) provided a significant jump to higher toughness with only a minor reduction in hardness. However, the maximum amount of 18 vol% Mo lowered the fracture toughness again to similar levels as the starting 3.2 vol% with a slightly better hardness.
Schwarz et al. [7] analyzed the influence of the Mo/W ratio on Ti(C,N)-based cermets with different C/N stoichiometries. The [Mo]/([Mo]+[W]) ratio was varied between 0 and 1 in steps of 0.2. For cermets based on $TiC_{0.7}N_{0.3}$, the hardness improved almost linearly when the samples where sintered under N_2 (see fig. 6b). When Ar was used in the sintering atmosphere, the hardness stayed almost constant with increasing Mo content. Regardless of the sintering atmosphere, the fracture toughness was only marginally affected by the Mo/W ratio, with the exception of the cermet with [Mo]/([Mo]+[W]) = 0 sintered in Ar, where a significant drop in fracture toughness was observed. In conclusion, overall better properties were achieved with both W and Mo present in the cermet formulation.
Samples with the same composition but a $TiC_{0.5}N_{0.5}$ powder had a similar correlation. With increasing Mo content, the hardness of the cermets sintered in both Ar or N_2 improved, with the N_2 atmosphere showing the larger increase. On the other hand, the fracture toughness changed only within 0.5 MPa · $m^{1/2}$ and revealed no clear dependency on the Mo content.

2.1.6. Powder alloy state

Components of cermet formulations can be added as individual carbide, nitride or carbonitride powders or as a pre-alloyed powder mixtures such as (Ti,W)C or (Ti,W)(C,N). The effect of such complete solid solution phases (CSS phases) on Ti(C,N)-(Ti,W)C-WC-TaC-Mo_2C-Co/Ni cermets was studied in the publication of Kim et al. [17]. Generally, the gradual substitution of binary Ti(C,N) and WC powders by CSS led to higher amounts of coreless grains and development of larger rim phases in the microstructure. The mechanical properties of the various

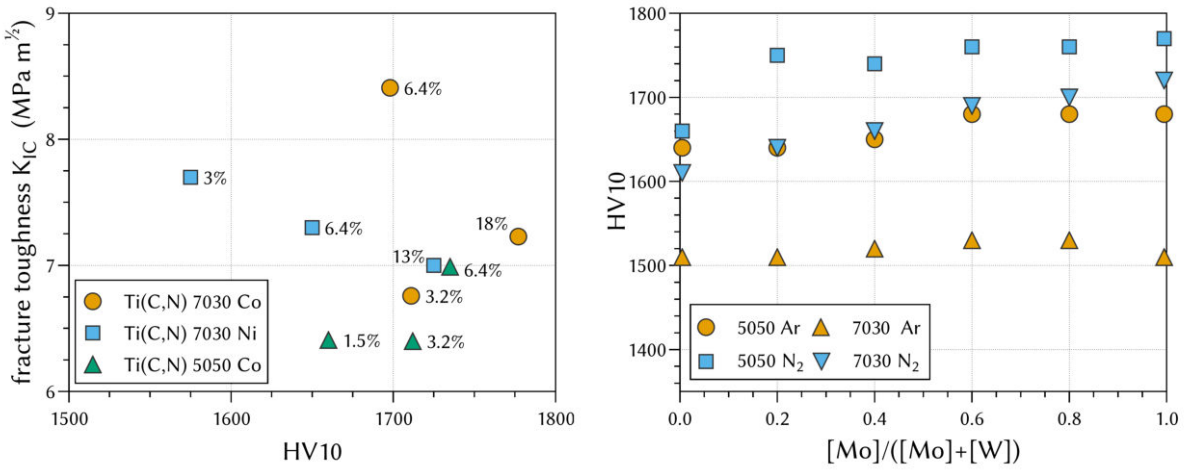

(a) (b)

Figure 6: Mechanical properties of (a) Ti(C,N)-Mo_2C-Co/Ni cermets with varying Mo content in vol% [8] and (b) hardness of Ti(C,N)-based cermets with varying Mo/([Mo]+[W]) ratio [7].

substitution grades are depicted in fig. 7a. When Ti(C,N) and WC were partially replaced by (Ti,W)C powder, the toughness of the cermets increased significantly up to 50% substitution. The hardness of the samples declined up to 10% substitution, then plateaued for 20%. Further increase to 50% CSS slightly increased the hardness again. Total substitution did not improve the mechanical properties as both the toughness and hardness dropped steeply. Therefore, the best overall mechanical properties were achieved with 50% substitution. The authors explain this behavior by the reduction Ti(C,N)-rich dark cores in the microstructure due to the CSS addition.

In two studies, Park et al. added 32% (Ti,W)C or (Ti,W)(C,N) to a Ti(C,N)-WC-Mo_2C-NbC-Co/Ni cermet [18, 19]. Additionally, the binder content was also varied. The results of their works are summarized in fig. 7b. For 12% binder content, both hardness and toughness of the commercial cermet formulation were improved by (Ti,W)(C,N) or (Ti,W)C, with the latter powder increasing the properties the most. At a higher binder content of 15%, the addition of (Ti,W)C led to a notable improvement in toughness. The hardness stayed approximately the same, while (Ti,W)(C,N) reduces the hardness with only a marginal gain in fracture toughness. For 12% binder phase, the cermets using Ti(C,N) and (Ti,W)(C,N) perform very similar while the toughness can be increased by 2 MPa · m$^{1/2}$. Generally, the substitution with (Ti,W)C led to better mechanical performance, while (Ti,W)(C,N) did not always improve the properties of the commercial target cermet. The authors attribute these improvements to the higher sinter-activity of the CSS phases resulting in a reduction of core/rim interfaces. In the (Ti,W)(C,N) cermet the thermodynamically unstable W-N bond increased the amount of dissolved elements in the binder phase, but the mechanical properties could not always be improved by this effect.

A more recent study by Lv et al. [20] compared cermets with three different powder alloy states. The first cermet only contained binary powders (TiC + TiN + WC) and showed the

lowest fracture toughness of 7.8 MPa · $m^{1/2}$. Using Ti(C,N) and WC powders, the fracture toughness improved to over 10 MPa · $m^{1/2}$, but an even higher toughness could be produced with (Ti,W)(C,N) powder. The hardness of the samples did not change significantly in this study. The increase in fracture toughness was explained by the formation of rimless grains when pre-alloyed powders were used. These rimless grains incorporated a higher concentration of dislocations and internal stress, resulting in a higher energy consumption during crack propagation. At the same time, the wear resistance at room temperature or elevated temperature was improved.

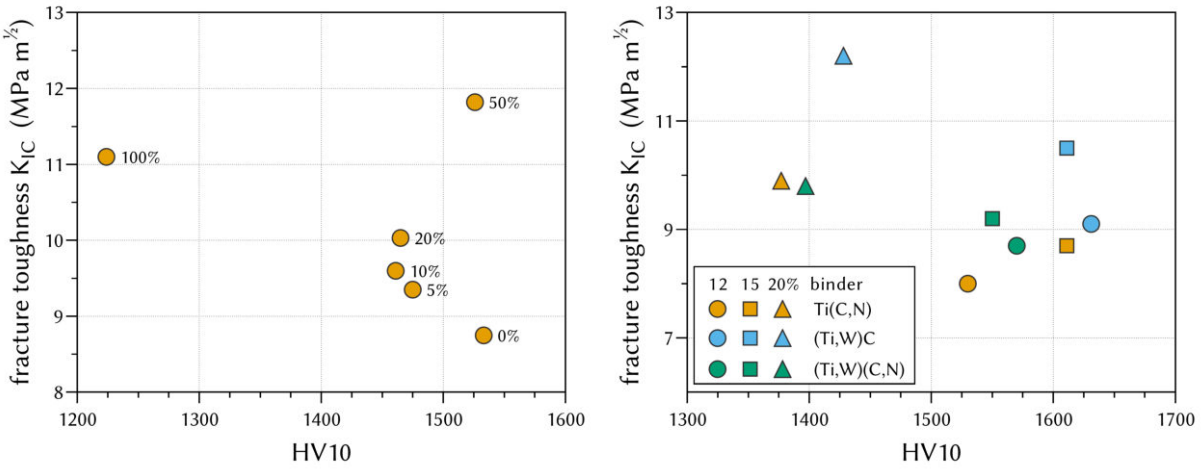

Figure 7: (a) Mechanical properties for cermets with different amount of (Ti,W)C substitution [17] and (b) cermet substituted with (Ti,W)C and (Ti,W)(C,N) with different binder content [18, 19].

Another study on the hard phase alloy state was carried out by Waldner et al. [21], comparing binary WC or Mo_2C with quarternary (Ti,W)(C,N) and (Ti,Mo)(C,N) powders, respectively. The starting formulations were adjusted to arrive at the desired molar composition and a fixed binder content of 16.4 vol%. The authors found substantially different microstructures for the pre-alloyed powders, which frequently formed inverse grains with a bright core and gray rim. Additionally, the magnetic saturation of the cermets with quarternary powders was higher than the samples containing binary carbide powders. However, these differences did not result in a clear trend for the mechanical properties as very similar behavior was found for the sample series.

2.1.7. Other carbides

In addition to Ti(C,N), WC and Mo_2C, other secondary carbides are added to the hard phase to improve certain properties of cermets. Most commonly, TaC, NbC or ternary (Ta,Nb)C is used to improve the hot hardness and thermoshock stability, which is especially important for interrupted cutting or milling applications [1]. As high temperature properties can only be tested with elaborate equipment, not much research on this topic is available. However, some studies were selected to represent the influence of those carbides on the regularly tested

mechanical properties such as hardness or fracture toughness.
Wu et al. [22] gradually replaced 0 to 7 wt% WC by TaC in Ti(C,N)-based cermets. Both hardness and fracture toughness decreased when the TaC content was increased (see fig. 8a). The authors attribute the decline in mechanical properties to the lower microhardness of TaC and a higher porosity of the finished samples. Furthermore, it was found that larger TaC contents had a grain refining effect and also led to the formation of coreless gray grains in the microstructure.
In another study, Liu et al. [23] tested the addition of 0, 5 or 10 wt% TaC to Ti(C,N)-WC-Co/Ni cermets, but kept the WC content constant. Instead, the Ti(C,N) was gradually replaced by TaC. Again, TaC in the composition appeared to have a grain refining effect on the microstructure and also increased the porosity of the tested samples. However, the hardness very slightly improved and the fracture toughness declined. The negative effects on the fracture toughness of TaC could be mitigated by the simultaneous addition of 5% Mo_2C.

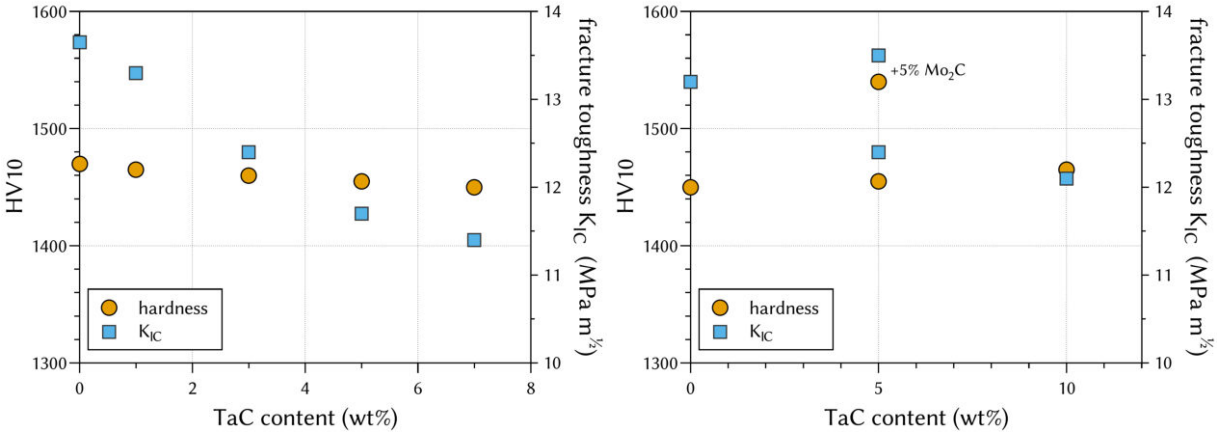

Figure 8: (a) Mechanical properties as a function of the TaC content (a) replacing WC [22] and (b) replacing Ti(C,N) [23].

The influence of the NbC content on Ti(C,N)-based cermets was recently studied by Gou et al. [24]. A NbC content of 3 wt% increased the hardness to 1900 HV, while the fracture toughness could only be improved to a lesser extend (fig. 9a). This improvement in hardness could be explained by a grain refinement effect of NbC and strengthening through the Hall-Petch relation. Also, it was found that more inverse grains were formed and also more Nb dissolved in the binder phase. The tougher inverse grains and the binder strengthening effect by dissolution of heavier elements could also be responsible for the improved mechanical properties. Further increase to 6 or 9 wt% did not provide better performance as the hardness plateaued at approximately 1800 HV and the fracture toughness even decreased to approximately 8.7 MPa · $m^{1/2}$. At the same time, the grain size was enlarged for samples with 6 and 9 wt% NbC, taking back some of the strengthening effects observed with 3 wt%. The authors also tested the cutting performance and reported lower flank wear and improved high temperature performance for the cermet with 3 wt% NbC.
Lastly, Wan et al. [25] compared the properties of $TiC_{0.7}N_{0.3}$-based cermets containing 10 wt%

WC, Mo_2C, TaC or NbC. While every secondary carbide could improve both hardness and toughness of the reference grade without any, Mo_2C and WC performed superior to TaC and NbC (see fig. 9b). The low performance of the reference grade could be explained by the high porosity (A08B04) due to the low sintering activity and wettability without secondary carbides addition, especially because a pure Ni binder was used in the formulation. Best mechanical properties were achieved by Mo_2C via a strengthening effect by grain refinement and solid solution of Mo in the binder phase.

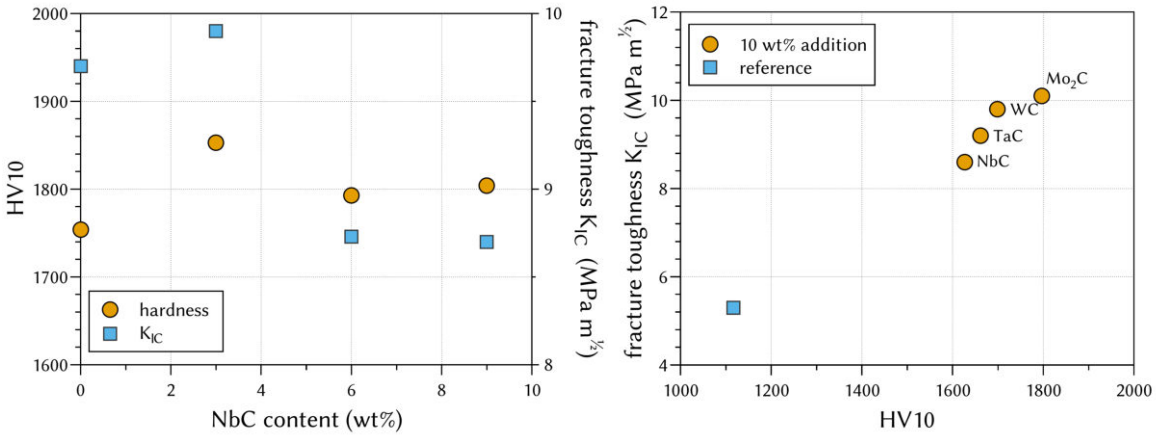

Figure 9: (a) Mechanical properties of Ti(C,N)-based cermets with (a) varying TaC content [24] and (b) comparison of the addition of Mo_2C, TaC or NbC to $TiC_{0.7}N_{0.3}$-based cermets [25].

2.2. Binder phase

2.2.1. Binder content

Due to the composite character of cermets, the properties can be adjusted by the ratio between the brittle hard phase and the ductile binder phase. Generally, higher amounts of binder phase lead to softer but tougher materials. This trend has been confirmed for both $TiC_{0.7}N_{0.3}$- and $TiC_{0.5}N_{0.5}$-based cermets by Cutard et al. [8]. Comparing the mechanical properties of the samples in fig. 10a, cermets with 6.4 wt% binder achieved the highest hardness. As can be expected from the higher N content, the $TiC_{0.5}N_{0.5}$ cermet was slightly harder and more brittle than the $TiC_{0.7}N_{0.3}$ counterpart with the same binder content. Subsequently increasing the binder content, an increase in toughness was observed for both Ti(C,N) stoichiometries up to the maximum toughness reached at 18 wt%. In fact, the cermet based on $TiC_{0.7}N_{0.3}$ was slightly harder than the N-rich $TiC_{0.5}N_{0.5}$ cermet.
Samples with higher binder content also reached higher fracture toughness values in the work of Mari et al. [26]. Further studies confirming the general trend were done by Xu et al. [27] and Park et al. [19]. The mechanical properties achieved in those three studies are summarized in fig. 10b.

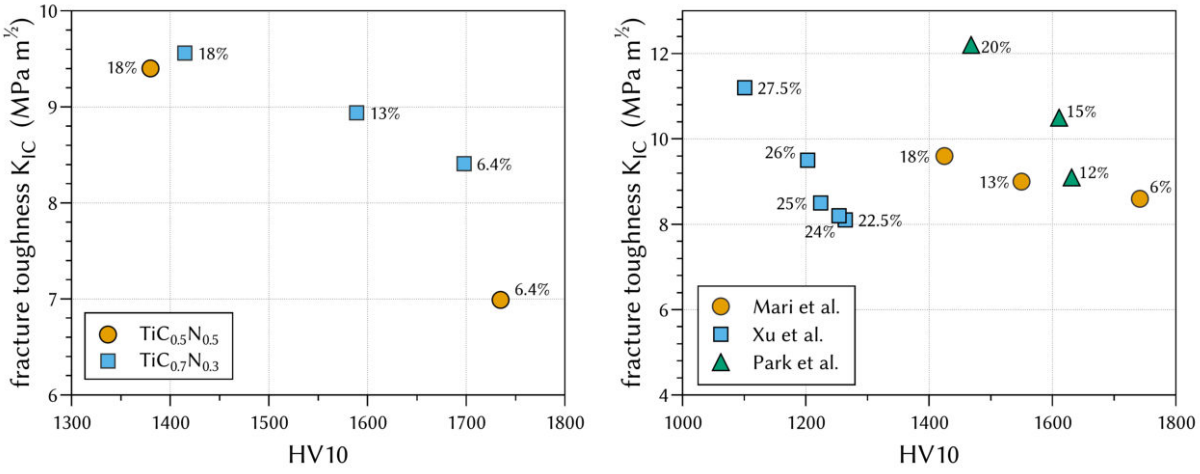

(a) (b)

Figure 10: (a) Mechanical properties as a function of the binder content in (a) $TiC_{0.7}N_{0.3}$- and $TiC_{0.5}N_{0.5}$-based cermets [8] and (b) for cermets from [26][27][19].

2.2.2. Binder composition and Ni/Co ratio

Apart from the binder content, the properties of cermets can also be influenced by the binder phase composition, for example the Ni/Co ratio. Cutard et al. [8] found that replacing the Ni by Co both hardness an fracture of cermets were improved. Another comparison between Co and Ni binders was done by Mari et al. [26]. The mechanical properties of three mixtures with either pure Co or Ni binder are shown in fig. 11a. Again, the replacement of Ni by Co led to a significant enhancement in hardness for all three tested compositions. However, the fracture toughness was only improved for the samples containing 6 wt% Mo_2C. Both the 3 wt% and the

13 wt% Mo_2C cermets performed more brittle or similar to the Ni-bound counterparts. As the Mo content directly influenced the grain size, it also affected the mean free path of the binder phase and therefore the toughness of the samples. Hence, the highest toughness levels were achieved with medium Mo contents in a Co-bound cermet.

In addition, the aforementioned study by Xu et al. [27] tested the influence of different Co/Ni ratios of the binder phase. The amount of binder phase was kept constant at 25 wt% and the composition was varied in steps of 0.2 [Co]/([Co]+[Ni]). Maximum toughness was reached with a pure Ni binder. Increasing the Co content, the fracture toughness clearly decreased towards the minimum value at pure Co binder phase. The hardness was improved up to approx. 1300 HV by medium Co contents and then slowly decreased again for higher Co amounts. Therefore, the best overall mechanical properties were achieved when both Co and Ni were present in the binder phase.

Pure Ni binder led to the finest microstructure with core-rim grains and a small amount of isolated black grains due to a relatively high solubility of Ti(C,N) in the Ni binder in comparison with pure Co. Low Co additions also led to fine grains, but for [Co]/([Co]+[Ni]) ratios between 0.4 bis 0.8, grains became coarser as less Ti(C,N) dissolved in the binder phase. Finally, thick outer rims with high contents of Mo and W formed in those cermets with pure Co binder since the heavy elements dissolved readily in the liquid Co during the sintering process.

Demoly et al. [11] compared cermets with a Co/Ni ratio of 1:1 and 2:1 containing submicron or fine Ti(C,N) powders. Cermets with higher Co contents showed lower hardness and higher toughness compared to the 1:1 Co/Ni binder samples. The influence was slightly larger for the submicron powder due to the decrease in Ti(C,N) solubility in the Ni binder.

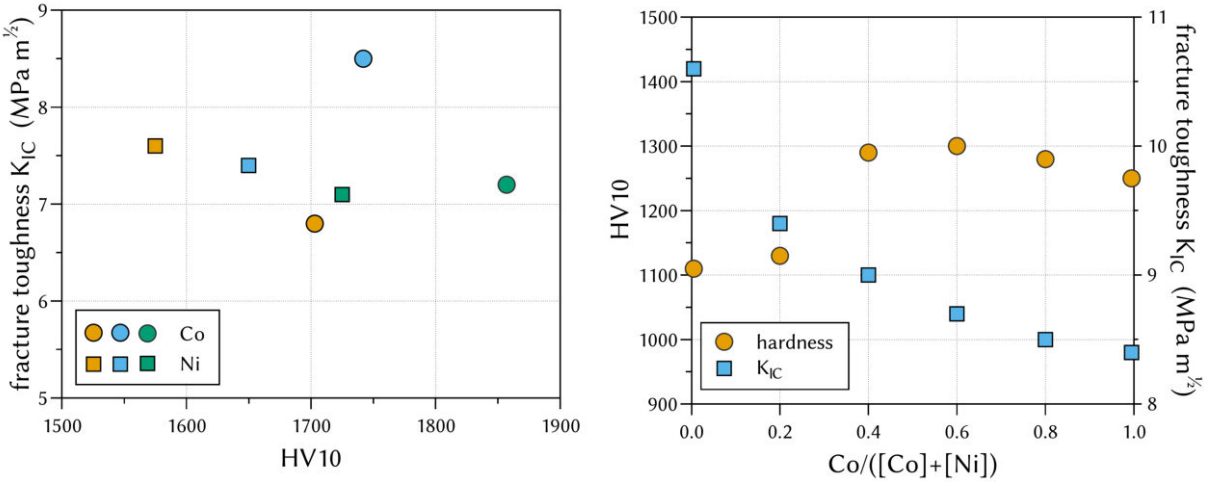

(a) (b)

Figure 11: (Mechanical properties of Ti(C,N)-based cermets with (a) Ni or Co binder [26] and (b) as a function of the Co/Ni ratio [27].

2.2.3. Binder strengthening

The binder phase of cermets can be strengthened by solid-solution hardening. One approach tested by Zhou et al. [28] was the addition of 0 to 1.5 wt% AlN to Ti(C,N)-WC-Mo_2C-Cr_3C_2-Ni cermets. With increasing AlN content, the hardness of the tested cermets reportedly improved due to the incorporation of smaller Al atoms in the binder phase lattice (fig. 12a). Additionally, the higher N content led to a thinner rim phase and a smaller average grain size. However, the maximum content of 1.5 wt% AlN caused aggregation of Ti(C,N)-rich grains and higher porosity, therefore a reduction in tensile rupture strength (TRS) was observed. Overall, best mechanical properties and abrasive wear resistance were reported with 1 wt% AlN.
The same grain refining effect was later found by Xu et al. [29] in Ti(C,N)-WC-TaC-Ni/Co cermets with 0 to 2 wt% AlN addition. Higher AlN contents resulted in higher hardness, while the fracture toughness fluctuated between 9.7 and 10.5 MPa · $m^{1/2}$ (fig. 12b). Larger Al concentrations were found near the grain-binder interfaces, leading to crack deflection and predominantly transgranular fracture mechanisms. Medium AlN contents of 1 or 1.5 wt% showed the best flank wear properties, but further increase led to higher porosities and therefore stronger edge wear.
The amount of dissolved elements in the binder phase can substantially improve the high-temperature properties of cermets. Lengauer et al. [30] studied the influence of non-metal deficiency on the binder phase dissolution state. It was found that a deficiency in the total C and N concentration leads to a significant increase in dissolved elements in the binder phase, which can also be seen in a substantial decrease in the magnetic saturation. Therefore, this interdependency of the hard phase composition and the binder phase can be used to improve the behavior of cermets.

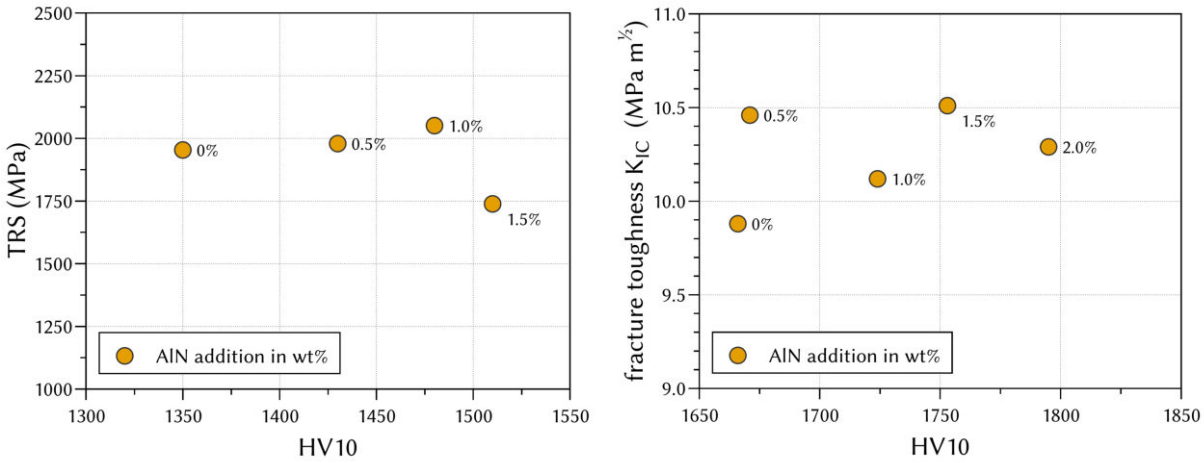

(a) (b)

Figure 12: (Mechanical properties as a function of the AlN content (a) in Ti(C,N)-WC-Mo_2C-Cr_3C_2-Ni [28] and (b) in Ti(C,N)-WC-TaC-Ni/Co cermets [29].

3. Experimental procedure

3.1. Characterisation of saw teeth

Thirteen different saw teeth grades from five manufacturers were investigated for the use as possible reference materials (see table 1). Seven grades were obtained as circular saw blades with the cermet teeth soldered onto a steel base. Thus, the individual saw teeth had to be broken out of the steel with pliers. Only larger, intact pieces without any brazing residues on them were selected for analysis. The other six saw teeth grades were available as single teeth and could be directly analyzed.
The samples were hot embedded and polished. Investigation of the porosity and microstructure was carried out using light optical microscopy (LOM) and scanning electron microscopy (SEM). The mechanical properties were evaluated with a Vickers indenter. Furthermore, the elemental composition was determined by Energy Dispersive X-Ray Spectroscopy (EDX) and X-Ray Fluorescence Spectroscopy (XRF). All methods are described in further detail in the following chapters.
Additional properties such as cutting performance or abrasion resistance of the saw blade grades were not covered by this diploma thesis. However, these findings of the project partner were taken into consideration in the selection of the target grades.

Table 1: List of investigated saw grades.

saw blades	**single teeth**
grade	grade
IA	T6
IB	N2
IC	N8
ID	Y3
M4	Y5
M5	C1
M6	

3.2. Sample preparation

3.2.1. Powder preparation

The cermet formulations of two separate sample series were based on the elemental compositions of ID and N8, respectively. For each series, the influence of two different Ti(C,N) manufacturers and four grain sizes was tested. Furthermore, the pre-alloyed state of the raw powders was varied by implementing either Ti(C,N) + WC, (Ti,W)(C,N) or (Ti,W)C. An overview of the used starting powders and their Fisher Sub Sieve Size (FSSS) grain size and chemical compositions obtained from the provided certificates of analysis is presented in table 2. Powders were weighed on an analytical scale (Mettler AE200) to 0.1 mg precision and transferred

Table 2: Specifications and grain size of used raw powders.

powder	manufacturer	FSSS (µm)	C (wt%)	N (wt%)	O (wt%)	LOT
$TiC_{0.5}N_{0.5}$	ALMT	0.88	9.89	11.53	0.44	A-22119
$TiC_{0.5}N_{0.5}$	TIAG	0.85	9.78	11.75	0.35	L46575
$TiC_{0.5}N_{0.5}$	TIAG	1.07	10.42	11.13	0.35	L46307
$TiC_{0.5}N_{0.5}$	TIAG	1.76	10.49	10.87	0.35	L79454
$TiC_{0.7}N_{0.3}$	TIAG	1.50	13.65	7.31	0.29	L79457
$TiC_{0.3}N_{0.7}$	TIAG	1.00	6.48	15.22	0.46	L79292
WC	TIAG	0.50	6.13	-	0.20	L78339
(Ti, W)(C, N)	TIAG	1.32	8.70	5.15	0.53	L79076
(Ti, W)C	TIAG	1.33	12.75	-	0.19	L78846
Mo_2C	TIAG	1.62	5.81	-	<0.30	L78162
NbC	TIAG	1.00	11.05	-	0.27	L79466
TaC	TIAG	0.78	6.28	-	0.21	L77542
ZrC	TIAG	1.62	11.41	0.08	0.29	L03062004
Co	Umicore	1.45	-	-	0.50	CoUm
Ni	Umicore	2.50	-	-	0.20	Ni255SMR
NiAl	Höganäs	-	-	-	-	3655047
C	H.C. Starck	-	-	-	-	UP030/M

into hardmetal milling drums. For the cermets based on the ID grade, 4 wt% of paraffin wax were weighed in before milling. Hardmetal balls with approximately 6 mm in diameter were added in the ratio of 1:10 and the drum was then completely filled with Cyclohexane. After closing the drums air-tight with a rubber O-ring and a hardmetal lid, the powders were milled at 120 rpm for 72 h. Excess Cyclohexane was removed with a pipette and the mixtures were sieved into large crystallizing dishes. The milling drums and the remaining hardmetal balls were rinsed with cyclohexane and the mixtures were kept at 70 °C until completely dry. Finally, the powders were sieved into plastic bottles and stored in a desiccator until pressing. Additionally, the carbon content was adjusted by adding pure carbon to some selected powder mixtures and dry mixing in a WAB Turbula mixer for 3 h. The exact powder weighing is shown in the appendix in tables 39 and 40, respectively.

3.2.2. Powder composition and sample nomenclature

An overview of the sample nomenclature and the used powders is provided in table 3. Samples were split into two major series: One series labeled with the letters 'I' for the cermets based on the composition of the ID grade and the other series designated with 'N' based on the N8 teeth. Each series was further split into three subsets titled 1,2 and 3. Samples in the N0 and I0 matched the targets' elemental composition as closely as possible using only $TiC_{0.5}N_{0.5}$ powders. These were again subdivided into the samples 0-1 and 0-2 using $TiC_{0.5}N_{0.5}$ from ALMT, Japan and Treibacher Industrie AG (TIAG), Austria, respectively.
In the sample series I1 and N1 $TiC_{0.7}N_{0.3}$ (TIAG) was added to match the C/N ratio of the target grades more closely. In this series, the grain size of the used $TiC_{0.5}N_{0.5}$ was varied. Cermets 1-1 and 1-2 used the same $TiC_{0.5}N_{0.5}$ with 0.85 µm and 0.88 µm as implemented in the samples

0-1 and 0-2, while sample 1-3 used the coarser $TiC_{0.5}N_{0.5}$ with 1.76 µm. Additionally, a cermet N1-4 was prepared with a medium Ti(C,N) grain size of 1.07 µm. To investigate the influence of pre-alloyed powders, (Ti,W)(C,N) was used in the series I2 & N2 and (Ti,W)C in I3 & N3. Furthermore, $TiC_{0.7}N_{0.3}$ was again included to match the C/N ratio. Due to time constraints, not all grades of the N series were duplicated for the I series. In total, the letters indicate the target grade, the first number the pre-alloyed state of Ti(C,N) + WC and the second number the main Ti(C,N) powder used. C-adjustments are indicated in the sample names by appending the added carbon content in wt%.

Table 3: Nomenclature of the prepared samples with main Ti(C,N), pre-alloy state and used C/N adjustment.

I & N series				
I0 & N0		**Ti(C,N)**	**pre-alloyed state**	**C/N adjustment**
I0-1	N0-1	0.88 µm $TiC_{0.5}N_{0.5}$	Ti(C,N) + WC	-
I0-2	N0-2	0.85 µm $TiC_{0.5}N_{0.5}$	Ti(C,N) + WC	-
I1 & N1		**Ti(C,N)**	**pre-alloyed state**	**C/N adjustment**
I1-1	N1-1	0.88 µm $TiC_{0.5}N_{0.5}$	Ti(C,N) + WC	$TiC_{0.7}N_{0.3}$
I1-2	N1-2	0.85 µm $TiC_{0.5}N_{0.5}$	Ti(C,N) + WC	$TiC_{0.7}N_{0.3}$
I1-3	N1-3	1.76 µm $TiC_{0.5}N_{0.5}$	Ti(C,N) + WC	$TiC_{0.7}N_{0.3}$
	N1-4	1.07 µm $TiC_{0.5}N_{0.5}$	Ti(C,N) + WC	$TiC_{0.7}N_{0.3}$
I2 & N2		**Ti(C,N)**	**pre-alloyed state**	**C/N adjustment**
I2-1	N2-1	0.88 µm $TiC_{0.5}N_{0.5}$	(Ti,W)(C,N)	$TiC_{0.3}N_{0.7}$ or $TiC_{0.7}N_{0.3}$
	N2-2	0.85 µm $TiC_{0.5}N_{0.5}$	(Ti,W)(C,N)	$TiC_{0.3}N_{0.7}$ or $TiC_{0.7}N_{0.3}$
I2-3	N2-3	1.76 µm $TiC_{0.5}N_{0.5}$	(Ti,W)(C,N)	$TiC_{0.3}N_{0.7}$ or $TiC_{0.7}N_{0.3}$
I3 & N3		**Ti(C,N)**	**pre-alloyed state**	**C/N adjustment**
I3-1	N3-1	0.88 µm $TiC_{0.5}N_{0.5}$	(Ti,W)C	$TiC_{0.3}N_{0.7}$ or $TiC_{0.7}N_{0.3}$
	N3-2	0.85 µm $TiC_{0.5}N_{0.5}$	(Ti,W)C	$TiC_{0.3}N_{0.7}$ or $TiC_{0.7}N_{0.3}$
	N3-3	1.76 µm $TiC_{0.5}N_{0.5}$	(Ti,W)C	$TiC_{0.3}N_{0.7}$ or $TiC_{0.7}N_{0.3}$

3.2.3. Pressing

Around 3 g of each powder mixture was then pressed uniaxially with approximately 80 MPa into cylinders 12.8 mm in diameter and around 6.5 mm in height using a hydraulic hand press. The sample names were engraved with the pointy tip of tweezers. The green bodies were weighed (Mettler AE200) and the dimensions were measured using a micrometer screw gauge. After pressing, the samples of both series were sintered in a SinterHIP furnace. For the N Series, dense samples could also be produced in a vacuum furnace.

3.2.4. Sintering

For the vacuum sintering, the samples were placed on an alumina plate in a graphite crucible. Sintering was carried out in a vacuum induction oven consisting of a water-cooled copper coil, radiation shields out of molybdenum and an infrared pyrometer for temperature measurement. The temperature was regulated with a control unit and the software Eurotherm iTools. As sintering atmosphere, either 5.0 purity argon, nitrogen or a mixture of both was used with different partial pressures.

The temperature profile was designed with three plateaus with a maximum temperature of 1480 °C (fig. 13). Until the first addition of gas, vacuum was applied. Four different static sintering atmospheres were applied: 100 mbar Ar, 10 mbar N_2 and two mixtures of 10 mbar N_2 + 90 mbar Ar and 50 mbar N_2 + 50 mbar (all gases 5.0 purity). Depending on the sintering atmosphere and partial pressures, the short names of the samples were appended with Ar, 10Np, 10N or 50N respectively. Before the start of the sintering program, the furnace was flushed three times with Ar or N_2. Nitrogen was added at the end of the first plateau and argon at the end of the second ramp. The temperature profile and the gas addition points were the same as in the SinterHIP cycle and are shown in fig. 13, the sintering atmospheres are summarized in tab. 4.

Table 4: Overview of the different sintering atmospheres for vacuum sintering.

name	**N_2 pressure**	**Ar pressure**
10N	10 mbar	90 mbar
50N	50 mbar	50 mbar
10Np	10 mbar	-
Ar	-	100 mbar

Additionally, samples were sintered in a SinterHIP induction furnace (FP W 1, FCT Systeme GmbH). The samples were again placed on an alumina plate and inside a graphite crucible. Temperature was measured with a thermocouple up to 850 °C and later with an infrared pyrometer. The temperature profile was the same as in the vacuum furnace for the N series sample, but the I samples had to be dewaxed and hence the temperature profile was adjusted accordingly. This was realized by a slow heating until 100 °C in 100 mbar Ar to provide enough heat transfer at low temperatures. Then the samples were slowly heated until 400 °C in 2 L/min Ar before continuing with the usual sintering profile.

Due to the setup of the furnace, the atmosphere could not be kept static as in the vacuum induction furnace. Therefore, N_2 or Ar was added after the first plateau with a flow rate of 0.2 L/min and the vacuum pump running resulting in approximately 35 mbar of partial pressure. Following the nomenclature, sample names were appended with SAr and SN, accordingly. From the beginning of the second plateau, 1 L/min Ar was added to provide approx. 100 mbar of Ar counter pressure. After reaching the maximum temperature of 1480 °C, the atmosphere was slowly equalised to 1 bar before slowly applying 60 bar of Ar over 10 min and keeping the pressure constant for the rest of the plateau. Then, the samples were cooled with 10 K/min until

reaching 850 °C, while the pressure slowly dropped due to the decreasing temperature. Lastly, the pressure was released and the samples cooled down freely. The adjusted sintering profile is shown in fig. 13.

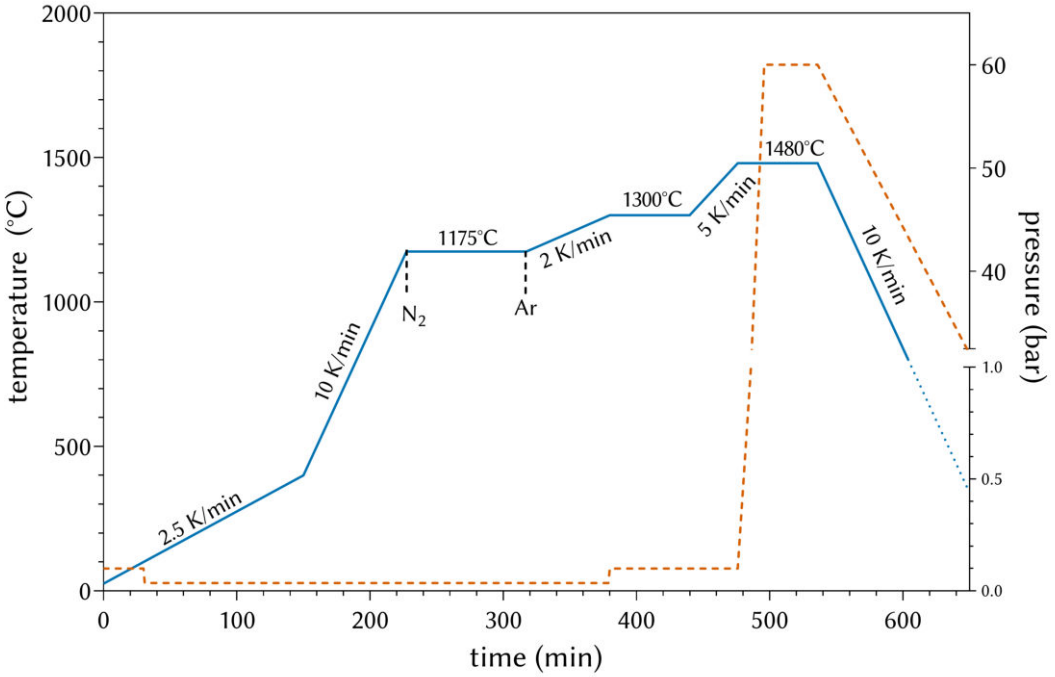

Figure 13: Temperature and pressure profile for the SinterHIP cycles including the addition points for N_2 and Ar. Temperature profile and addition points were equivalent for the vacuum sintering.

3.3. Sample characterisation

The dimensions of the cylindrical samples were measured using a micrometer gauge to ±0.001 mm precision and weighed dry as well as under water to calculate the Archimedes density (Mettler AE200). Afterwards, the samples were slowly cut in half with a circular M1D15 diamond saw blade on a Struers Accutom-10 cut-off machine. One half was hot embedded in Struers Multifast Bakelite with the rectangular cut side down.
For the reference grades, six saw teeth each were directly embedded in Bakelite and then treated the same way as the sintered samples.

3.3.1. Grinding and polishing

Grinding and polishing was both performed on a Struers RotoPol-31 polishing machine. Samples were first ground with a 120 grit grinding disk until a uniform rectangular sample surface was visible. Afterwards, samples were polished using 9 µm, 3 µm and 1 µm diamond suspensions. Between the steps, the samples were first cleaned with water and then suspended in Isopropanol in an ultrasonic bath for 5 min. The sample surface was inspected with a microscope and polishing steps were repeated if necessary. Detailed steps of the polishing procedure

are provided in tab. 5.

Table 5: Grinding and polishing steps.

step	grit	suspension	plate	force	time
grinding	120	water	MD-Piano	40 N	3 min
polishing	9 µm	DiaDuo-2 gray	MD-Allegro	35 N	15 min
polishing	3 µm	DiaDuo-2 blue	MD-Largo	30 N	10 min
polishing	1 µm	DiaDuo-2 white	MD-Dac	25 N	7 min

3.3.2. Mechanical properties

The hardness of the samples was determined with a Vickers indenter. Five indentations were made per sample or grade. For the sintered samples, the indentations were spaced out in the center of the rectangular polished surface to minimize the influence of the sample edges or other indentations. For the same reason, a maximum of two indentations was placed on a single tooth of the saw blade grades. After measuring the diagonals of each indentation, the hardness was then calculated as HV10 value using the following equation with the test force $F = 10\,\mathrm{kgf}$ and the diagonal d in m:

$$HV10 = \frac{1.8544 \cdot F}{d^2} \tag{3}$$

Additionally, the Palmqvist fracture toughness K_{IC} in $\mathrm{Mpa} \cdot \mathrm{m}^{1/2}$ was calculated using the modification of Shetty and Wright [31], where l is the sum of the crack lengths in m:

$$K_{IC} = 0.0275 \cdot \sqrt{\frac{HV \cdot F}{l}} \tag{4}$$

3.3.3. Light optical microscopy (LOM)

For the evaluation of porosity, samples were investigated at 200x magnification on an Olympus GX51 light microscope. The images were evaluated in accordance with DIN EN ISO 4499-4 standard and the porosity class estimated by comparison with the reference images [32]. Diagonals and crack lengths were measured at 200x magnification using the software Olympus Stream Motion.

3.3.4. Scanning electron microscope (SEM)

The microstructure of the samples was investigated with a FEI Quanta 200 ESEM Scanning Electron Microscope in back-scatter electron mode (BSE-SEM). Images were taken with 20 kV acceleration voltage at 5000x and 10,000x magnification. Additionally, EDX was used to estimate the elemental composition of the saw teeth.

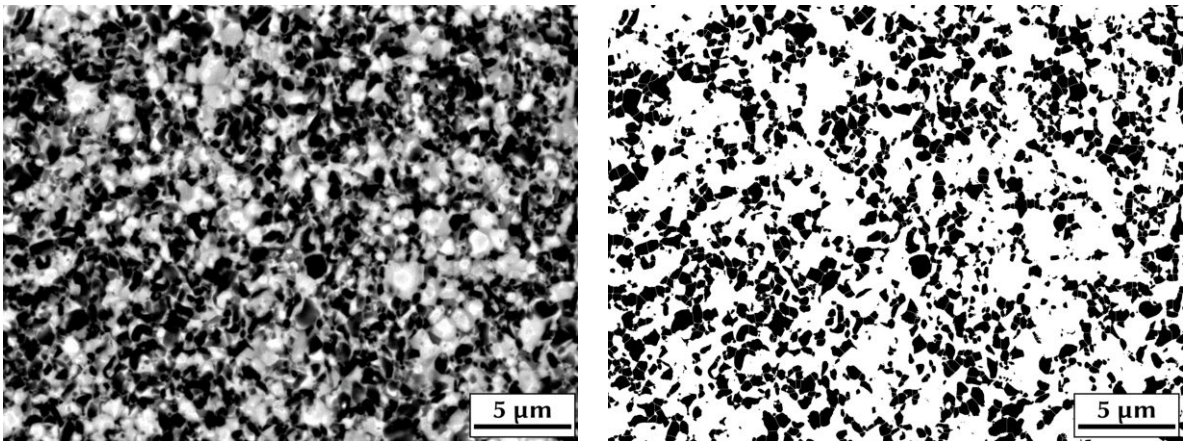

(a) BSE-SEM, 10,000x magnification. (b) BSE-SEM after image manipulation.

Figure 14: Comparison of the IA grade before and after threshold and watershed algorithms were applied.

3.3.5. Grain size distribution (GSD)

To describe the microstructure of the samples, the grain size of Ti(C,N)-rich cores and grains were both analyzed following the linear intercept method. Horizontal lines were placed over 10,000x BSE-SEM images and the length of the intercept was measured with the software ImageJ. At least 200 grains were evaluated per grade. Two different grain size distributions were calculated: One counting only the black cores or grains and the other evaluating the complete grain. Because of the strong contrast between the black Ti(C,N)-rich grains and the rest of the microstructure, this process was automated in a Python script after applying the threshold and watershed algorithms in ImageJ. An example of the image processing is shown in fig. 14. The values were sorted in 0.1 µm bins and the d_{10}, d_{50} and d_{90} values were calculated from the accumulated intercept length distribution. For a quick description of the grain size distribution, the slope between the d_{10} and d_{90} values was determined:

$$slope = \frac{90 - 10}{d_{90} - d_{10}} \tag{5}$$

3.3.6. Elemental composition and phase analysis

Approximately 2 g of each unique saw teeth grade were sent to revierlabor GmbH, Germany for elemental analysis. After borate digestion, the amount of metallic elements was determined using X-Ray Fluorescence Spectroscopy (XRF) and the C and N content by Combustion Infrared Spectroscopy and Carrier Gas Hot Extraction (CGHE), respectively. Selected mixed powders and sintered samples were submitted to TIAG, Austria to analyze the C, N and O content before and after sintering in different atmospheres.

Six saw teeth per grade were fixed closely together on a Si Wafer using paraffin wax and X-Ray Powder Diffraction (XRD) was measured in Bragg-Brentano setup on a Pan Analytical device for 2θ angles between 30 and 120°. The off-cut half of the sintered cermets was fixed in putty with the rectangular face in the middle facing up. The lattice parameter was determined

by Rietveld analysis in HighScore Plus. The hard phase was fitted as two Ti(C,N) phases [33] (H1 & H2) and the binder phase (B) with a Ni reference [34]. Possible η phase was fitted as Co_3W_3C [35].

3.3.7. Magnetic properties

The weight specific magnetic saturation M_S in $\mu Tm^3/kg$ and the coercive force H_C in kA/m of the samples were measured on a Foerster Koerzimat 1.096. For comparison of different grades, the absolute magnetic saturation was converted to relative values in reference to the pure binder phase with corresponding mass fraction of Co and Ni in equation 6 ($202\,\mu Tm^3/kg$ and $68.4\,\mu Tm^3/kg$, respectively). The total concentration of dissolved elements in the binder phase was then calculated using the estimation $c = -0.2 \cdot M_{S,\,rel.} + 21.06$ [30].
While the magnetic properties of sintered cermets could easily be measured before cutting the cylinders, the mass of the saw teeth was too low for direct measurements. Around 1 g of the grades delivered as bigger single teeth were glued together using Cyanoacrylate glue and sticky tape. The grades already brazed to finished saw blades could not be measured due to their splintering on breaking with pliers.

$$M_{S,rel.}(\%) = \frac{M_S}{2.02 \cdot x_{Co} + 0.684 \cdot x_{Ni}} \tag{6}$$

4. Results and discussion

4.1. Characterisation of commercial saw teeth

4.1.1. Elemental composition

The results of the EDX analysis are presented in table 6. Overall, the saw teeth grades show a Ti content between approximately 37 and 44 wt%, resulting in a Ti(C,N) content of around 50 wt%. The binder phase varies between 15 and 22 wt% and typical Co/Ni ratios of 1:1 or 2:1 for most of the grades. However, C1 binder phase is an exception consisting almost purely of Co. Due to the overlapping of the Mo signal, both binder content and Mo content should only be considered an estimate.
Grades IA, ID and M5 show a very similar elemental composition, indicating that in fact the same cermet teeth were used by both manufacturers. Furthermore, the single teeth grade Y3 could have been implemented in the production of the saw blade IC.

Table 6: EDX quantification of the thirteen saw teeth grades.

	elemental composition in wt%								
grade	**Ti**	**W**	**C**	**N**	**Ta**	**Nb**	**Mo**	**Co**	**Ni**
IA	39.89	14.50	8.03	7.26	9.92	0.86	0.88	9.55	9.12
IB	39.10	15.70	8.63	6.92	9.20	1.01	3.07	10.99	5.38
IC	37.16	21.19	7.98	6.77	7.37	1.13	0.04	12.39	5.98
ID	38.66	14.69	7.98	7.01	9.85	0.59	0.68	10.01	10.53
M4	40.25	18.81	9.15	6.18	3.40	1.26	5.29	8.06	7.61
M5	38.30	14.34	8.59	7.22	9.44	0.75	0.72	10.17	10.48
M6	40.47	17.68	9.13	4.93	4.84	1.55	5.15	8.29	7.96
N2	44.09	13.94	9.26	5.54	0.98	7.65	0.16	17.54	0.85
N8	37.65	15.94	10.15	6.65	0.76	4.72	2.94	13.66	7.53
T6	41.67	14.12	9.22	6.33	4.01	6.29	-	13.48	4.91
Y3	36.80	22.09	8.11	8.21	6.14	1.10	0.07	12.00	5.48
Y5	37.51	16.51	8.82	7.80	5.64	1.07	2.45	15.41	4.79
C1	42.33	12.82	9.82	8.30	0.85	8.17	-	17.20	0.51

As the EDX results imply grades IA, ID and M5 have the same composition, the more robust chemical analysis in an external laboratory was only commissioned for IA. Comparing the results in table 7, a couple of things come to notice. First, the analysis indicates that Y3 was indeed used in the IC. Furthermore, grades M6 and IA have a very similar elemental composition. However, the completely different microstructure suggest that this is the only similarity between those to grades. Also, they are the only two grades where Al and Zr could be detected. As no reference materials were available to increase the precision of the EDX measurements, the results of the external analysis by XRF and CGHE were taken as baseline for the calculations of the phases in the saw teeth and for the synthesis of cermet grades in this work.

Table 7: Elemental composition of saw teeth grades determined by XRF (metals), combustion-IR (C) and CGHE (N).

	elemental composition in wt%										
grade	**Ti**	**W**	**C**	**N**	**Ta**	**Nb**	**Mo**	**Co**	**Ni**	**Al**	**Zr**
IA	37.68	15.71	6.63	5.30	10.58	1.06	1.44	10.03	10.88	0.35	0.34
IB	37.77	17.61	7.35	4.35	9.94	1.59	4.45	11.14	5.79	-	-
IC	36.13	23.63	6.80	5.09	7.64	1.80	-	12.61	6.30	-	-
M4	38.92	18.85	8.31	4.10	4.59	2.07	6.72	8.39	8.06	-	-
M6	37.65	15.80	6.74	4.92	10.67	1.07	1.42	10.00	10.98	0.30	0.45
N2	42.13	15.75	7.73	5.72	-	10.33	-	17.55	0.79	-	-
N8	38.13	17.26	7.30	4.92	-	5.79	3.95	14.65	8.01	-	-
T6	39.82	19.46	7.66	4.74	2.79	6.97	-	14.01	4.56	-	-
Y3	35.99	23.86	6.73	5.11	7.68	1.80	-	12.73	6.09	-	-
Y5	36.15	17.98	7.04	4.72	7.84	1.76	3.40	15.77	5.34	-	-
C1	42.37	16.36	7.80	5.72	-	9.83	-	17.87	0.05	-	-

4.1.2. Mechanical properties

The hardness (HV10) and fracture toughness (K_{IC}) of the saw teeth are shown in fig. 15. For better comparability between the saw teeth and the sintered cermet samples, the scale of the axis in the plots is kept constant throughout this work. With a hardness between 1380 and 1630 HV10 and a fracture toughness between 11 MPa · $m^{1/2}$, the saw teeth grades follow the general trend of a decrease in toughness with increasing hardness. In comparison to the trend line from literature, the saw teeth show a significantly higher fracture toughness than other Ti(C,N)-based cermets.

The grades IA, ID and M5 are grouped between 1400 and 1450 HV10 at the tougher side of tested samples with a fracture toughness of around 10.5 MPa · $m^{1/2}$. With a relatively high binder content of approximately 21 wt%, a high fracture toughness can be expected.

While these three grades present similar mechanical properties, they still differ outside of the statistical range. One reason for this finding could be not only the small size, but especially the thickness of the tested teeth. Furthermore, the three grades were brazed to different saw blades and ground to their final shape. Deviations in the production of the finished saw blades could therefore have led to slightly different mechanical properties of the teeth.

Interestingly, grade M6 uses the same elemental composition and therefore the same binder content as IA, but shows a significantly higher hardness (1510 HV10) while the fracture toughness is also above the trend line at 10.4 MPa · $m^{1/2}$.

Lastly, the two grades IC and Y3 display very comparable mechanical properties, supporting the assumption that the Y3 single teeth were used in the manufacturing of the saw blade IC.

4.1.3. Magnetic properties

As the Co and Ni content of the single teeth was determined by chemical analysis (tab. 7), the relative magnetic saturation M_S could be calculated. These results and the coercive force H_C

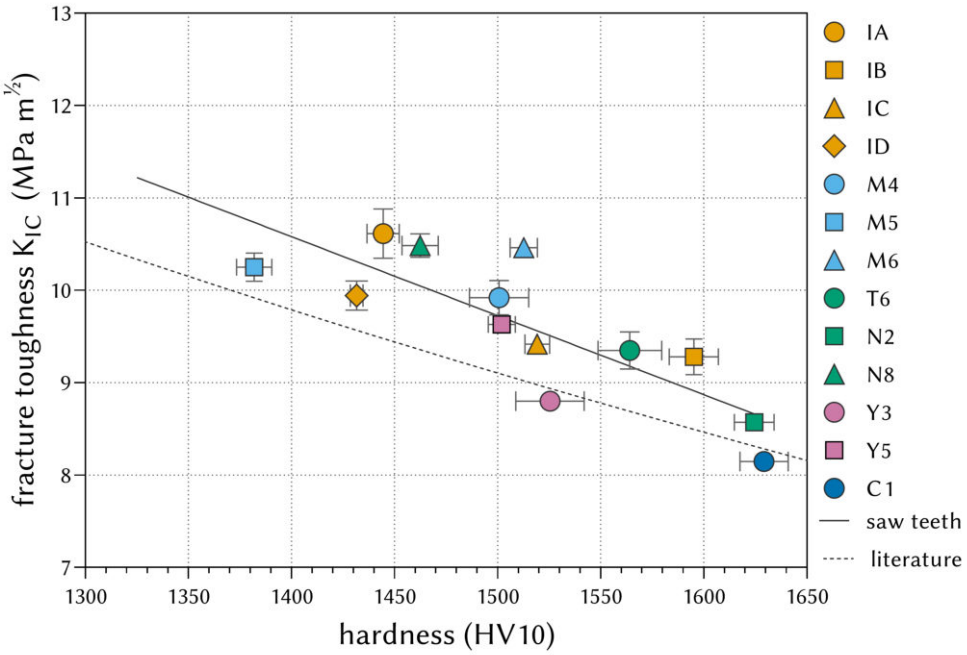

Figure 15: Hardness and fracture toughness of the thirteen saw teeth grades and trend line obtained from literature [1].

are summarized in table 8.

The magnetic saturation is reduced when paramagnetic elements such as W or Mo dissolve in the ferromagnetic Co/Ni binder [30]. Therefore, the relatively low magnetic saturation of grades T6 and Y3 can be seen as an indication for a high amount of dissolved elements in the binder, while grades N2 and C1 reach more than 60% of the magnetic saturation of pure binder phase. As can be seen in the estimation from [30], less elements dissolved in these binder phases.

Table 8: Relative magnetic saturation M_S, coercive force H_C and total concentration of dissolved elements in the binder of the single teeth grades.

grade	**M_S (%)**	**H_C (kA/m)**	**c (mol%)**
N2	60.7	10.8	8.9
N8	50.5	15.7	10.9
T6	40.2	10.8	13.0
Y3	45.5	11.6	11.9
Y5	54.8	13.8	10.1
C1	65.2	15.1	8.0

4.1.4. Phase analysis

In addition to identifying the phases in the cermets by XRD, the deviation of the lattice parameter from pure Ti(C,N) and binder can provide an estimation of the amount of dissolved elements in the binder and hard phase. The lattice parameters were calculated by Rietveld analysis and are shown in table 9. With the exception of M4, the hard phase of all grades could be fitted with tow individual Ti(C,N)-based hard phase patterns slightly different in lattice parameter. They were labelled H1 and H2, respectively. Additionally, the relative change in binder lattice parameter was calculated in reference to the pure Co/Ni-binder as determined before by the chemical analysis.

Table 9: hard phase peak form and lattice parameter (in Å) of hard phase (H1 & H2) and binder phase (B) with relative change in binder lattice parameter (B_{rel}) calculated in relation to a pure Co/Ni binder.

sample	peak form	H1	H2	B	Brel. (%)
IA	doublet	4.3359	4.2833	3.5900	1.31
IB	doublet	4.3207	4.2814	3.5974	1.51
M4	singlet	4.3104	-	3.5983	1.55
M6	doublet	4.3375	4.2836	3.5894	1.27
T6	singlet	4.3149	-	3.5995	1.56
N2	doublet	4.3286	4.2793	3.5939	1.38
N8	doublet	4.3154	4.2731	3.5876	1.23
Y3	doublet	4.3171	4.2746	3.5962	1.47
Y5	doublet	4.3176	4.2750	3.5900	1.29
C1	doublet	4.3313	4.2814	3.5921	1.33

4.1.5. Saw blade IA

The elemental composition of grade IA was based on the external chemical analysis and converted to vol% for a better comparison between grades. The overall elemental composition is listed in the left column of table 10, while the middle column shows the possible starting powders for the hard phase and binder phase. Additionally, the molar stoichiometry of the hard phase was calculated in the right column (Co or Ni were not taken into account).
Grade IA shows a relatively high binder content of 17 vol% with a Co/Ni ratio of approximately 1:1. The analysis indicates that $TiC_{0.5}N_{0.5}$ was used for the starting formulation of this cermet. The grade shows a slight non-metal deficiency and a Ta/Nb ratio of approximately 5:1. Interestingly, Al and Zr were found in the elemental analysis, with Zr probably added as ZrC. Due to the fact that the grade contains slightly more Ni than Co, the Al was most likely added as NiAl.
Fig. 16 gives an overview on the porosity, microstructure and phase composition of IA. The porosity was estimated at 200x and falls into class A04B00C00. A very fine microstructure is visible in the BSE-SEM images. Hardly any core-rim structure is observable and the black Ti(C,N)-rich grains appear mostly isolated and elongated. The absence of core-rim structure could indicate the presence of N_2 in the sintering atmosphere during production. In addition

to the relative high N activity of the $TiC_{0.5}N_{0.5}$, the elongated grains suggest a metal route as synthesis path for the Ti(C,N). Additionally, inverse grains with a bright core and a gray rim are present.

While the GSD of cores shows a narrow and uniform distribution, the grains are more spread. Due to the barely visible binder phase and grain boundaries, the second local maximum at 1.2 µm could be attributed to close grains counted as larger grains. A second local maximum at roughly double the d_{50} value is also visible in the GSD of cores, but it is much less distinct due to the higher contrast in the images.

In the XRD of grade IA, there are three distinguishable phases: Two hard phases (H) with slightly different lattice parameters and a binder phase (B). The difference in lattice parameter causes the peaks to appear as doublets for lower and as two individual shoulders for higher 2θ angles. The high amount of heavier elements such as W or Mo dissolved in the Ti(C,N) lattice results in an increase in the lattice parameter.

Cermet IA is one of the toughest grades tested with a hardness of 1440 HV and a toughness of 10.6 MPa · $m^{1/2}$. External cutting tests indicated that grades with higher toughness and a fine microstructure perform better than the harder grades. Hence, the elemental composition of IA was selected as formulation for the I samples to study different influences on the cermet performance.

Table 10: Elemental analysis and calculated phase composition, binder composition and stoichiometry of IA.

IA		**hard phase**			**stoichiometry**	
element	**wt%**		**wt%**	**vol%**		**mol**
Ti	37.68	Ti(C,N)	47.62	66.45	(C+N)/Me	0.97
W	15.71	WC	16.74	7.59		
C	6.63	TaC	11.28	5.55	**Ti(C,N)**	
N	5.30	NbC	1.19	1.09	C/Ti	0.49
Ta	10.58	Mo_2C	1.53	1.25	N/Ti	0.48
Nb	1.06	ZrC	0.38	0.41	(C+N)/Ti	0.97
Mo	1.44	**binder**			C/(C+N)	0.50
Co	10.03	Co	10.03	8.04		
Ni	10.88	Ni	10.88	8.71	**(Ta,Nb)C**	
Al	0.35	Al	0.35	0.41	Ta/Nb	5.13
Zr	0.34	binder	21.27	17.16		
sum	100.0	Co/(Co+Ni)	0.48	0.48		

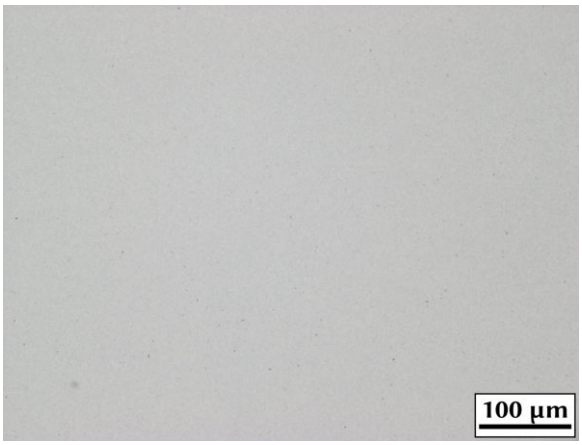

(a) LOM, 200x magnification.

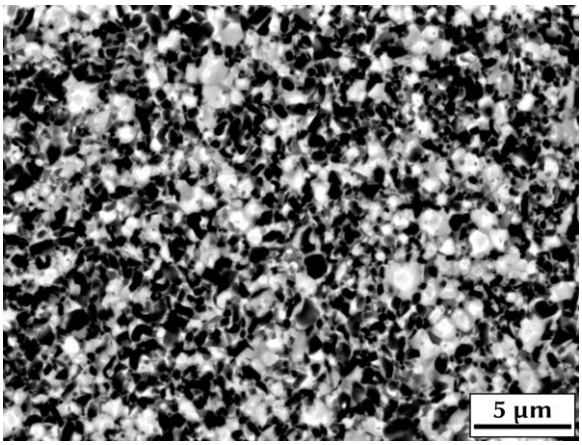

(b) BSE-SEM, 10,000x magnification.

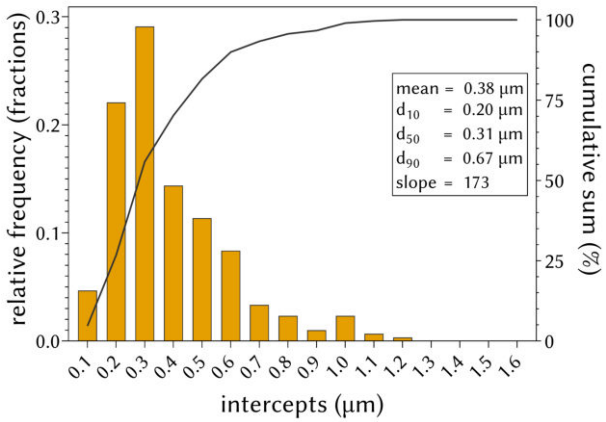

(c) GSD of cores.

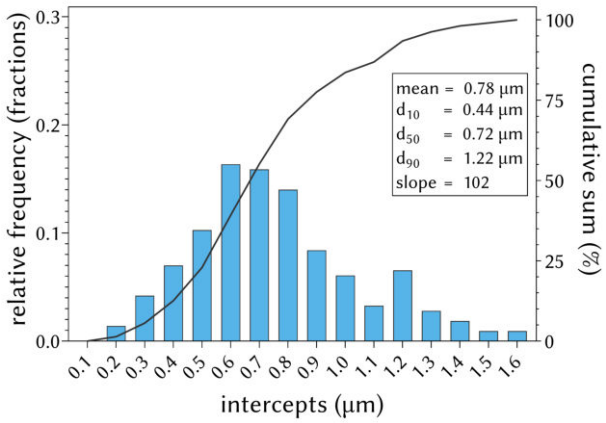

(d) GSD of grains.

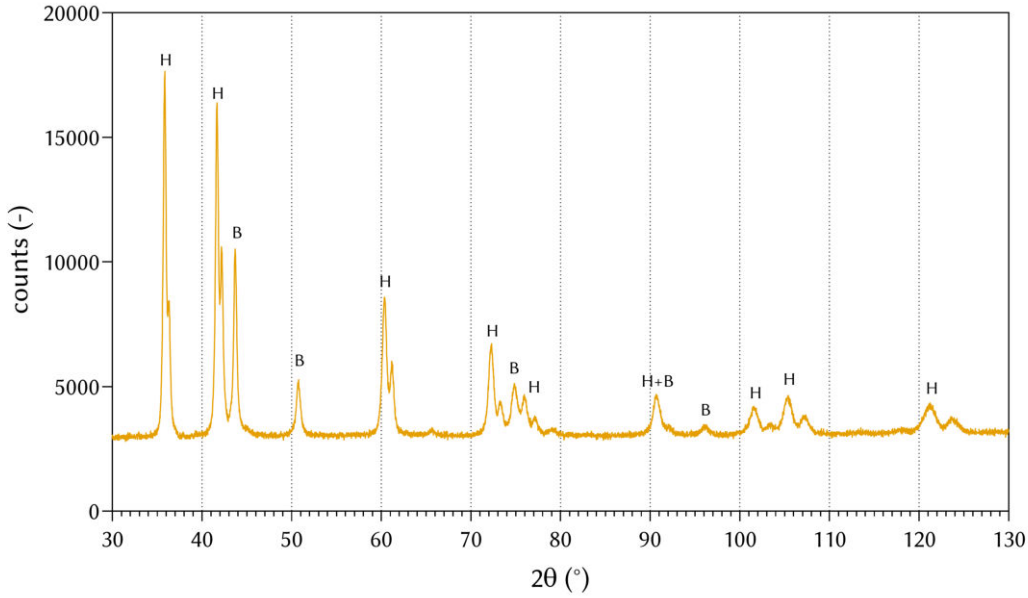

(e) XRD with hard phase (H) and binder (B) peaks identified.

Figure 16: LOM, BSE-SEM, grain size distribution and XRD of IA.

4.1.6. Saw blade IB

The elemental and phase composition of IB is shown in table 11. In contrast to IA, IB has a much lower binder content of 14 vol%, resulting in a corresponding higher hardness. Additionally, the binder phase composition differs with a Co/Ni ratio of 2:1. No Al or Zr was detected in this grade. Interestingly, the analysis reveals a much higher non-metal deficiency than IA, which can be attributed to the low N content. The data suggests that for the starting formulation $TiC_{0.6}N_{0.4}$ might have been used. Ta and Nb were added in a ratio of 3:1.
Referencing the LOM image in fig. 17, IB falls into the porosity class A08B00C00, with an unusually high A porosity for industrially sintered cermets. There are hardly any core-rim grains visible in the microstructure of IB. However, the isolated Ti(C,N)-rich grains appear rounded, indicating a carbothermal synthesis process. Compared with cermet IA, the inverse grains are finer and much easier distinguishable.
The GSD of IB shows that the cores are indeed bigger compared to IA (mean 0.50 and 0.38 µm, respectively), but the narrower distribution of grains with a mean of 0.70 µm indicates a smaller overall grain size. This could be one reason for the higher hardness due to the Hall-Petch relation.
As described for IA, there are two hard phases and one binder phase visible in the XRD pattern. Since the difference in lattice parameter is lower in IB, the H2 peaks appear as a shoulder for lower angles and more distinct as a separate peak at higher 2θ. For the binder phase, the lattice parameter of 3.5974 Å is increased by a relatively high 1.55 % compared to a pure Co/Ni binder. This indicates that compared to IA more elements dissolved in IB's binder, possibly leading to a strengthening of the binder phase and further improved hardness.
Overall, the fine grain size and the lower amount of binder phase with a high amount of dissolved elements could be responsible for the high hardness of 1600 HV10 and a fracture toughness of 9.3 MPa · $m^{1/2}$. Although these mechanical properties are above the trend line of all tested saw teeth (fig. 15), they do not meet the criteria of a high fracture toughness and therefore were not selected as basis for a sample series.

Table 11: Elemental analysis and calculated phase composition, binder composition and stoichiometry of IB.

IB		**hard phase**			**stoichiometry**	
element	**wt%**		**wt%**	**vol%**		**mol**
Ti	37.77	Ti(C,N)	47.18	67.11	(C+N)/Me	0.92
W	17.61	WC	18.76	8.53		
C	7.35	TaC	10.60	5.23	**Ti(C,N)**	
N	4.35	NbC	1.80	1.65	C/Ti	0.53
Ta	9.94	Mo_2C	4.72	3.87	N/Ti	0.39
Nb	1.59	**binder**			(C+N)/Ti	0.93
Mo	4.45	Co	11.14	8.96	C/(C+N)	0.58
Co	11.14	Ni	5.79	4.65		
Ni	5.79	Binder	16.93	13.61	**(Ta,Nb)C**	
sum	100.0	Co/(Co+Ni)	0.66	0.66	Ta/Nb	3.21

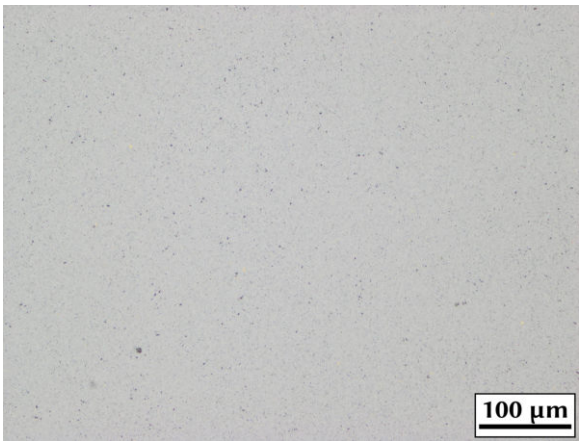

(a) LOM, 200x magnification.

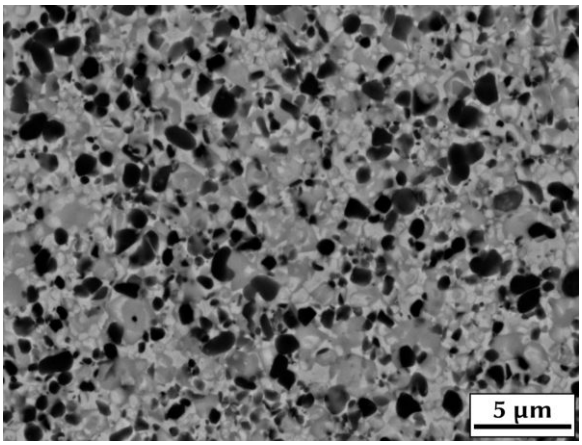

(b) BSE-SEM, 10,000x magnification.

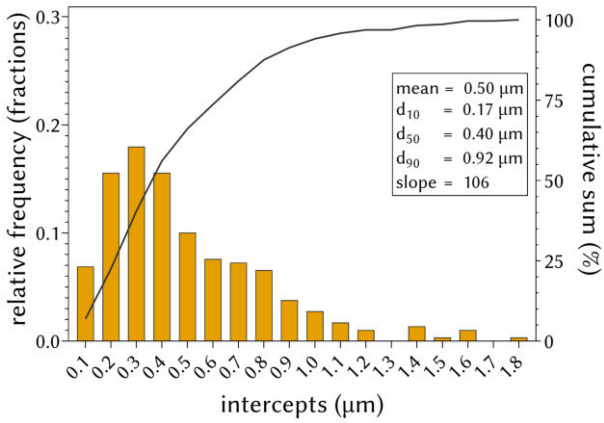

(c) GSD of cores.

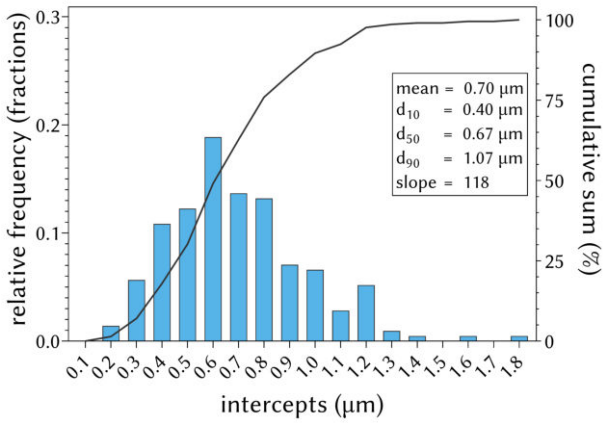

(d) GSD of grains.

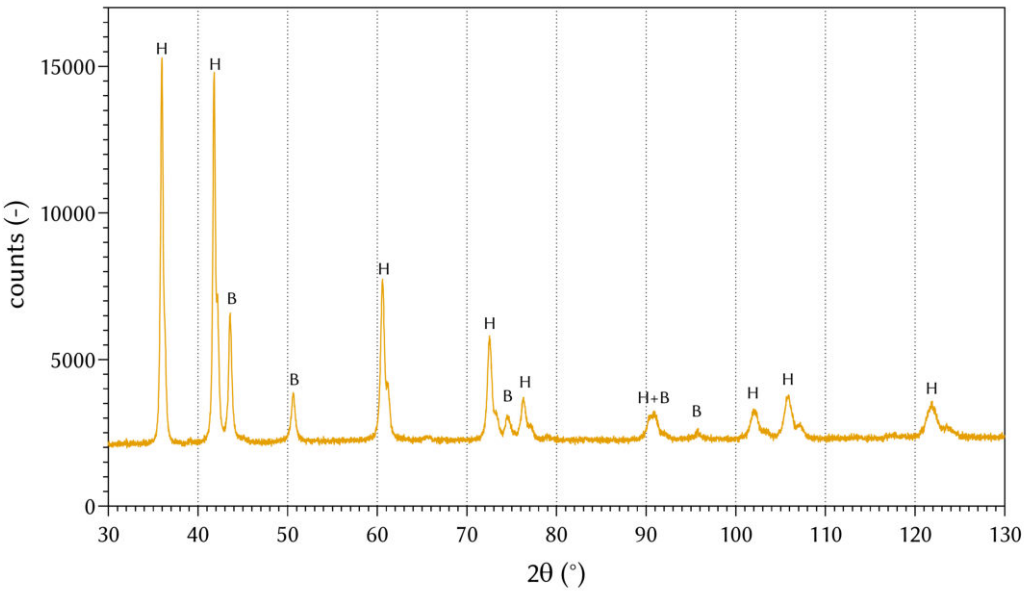

(e) XRD with hard phase (H) and binder (B) peaks identified.

Figure 17: LOM, BSE-SEM, grain size distribution and XRD of IB.

4.1.7. Saw blade IC

The phase composition of IC in table 12 shows a binder content of 16 vol% with a Co/Ni ratio of 2:1. Notably, no Mo was detected in the analysis of IC. In comparison with other I grades, IC has a relatively high WC content. The hard phase is nearly stoichiometric and $TiC_{0.5}N_{0.5}$ was probably used in the starting formulation. The Ta/Nb ratio is approximately 2:1.
Fig. 18 reveals a porosity class of A06B00C00 in the LOM image. Furthermore, the microstructure looks quite different than the other I grades. The Ti(C,N)-rich black grains are completely isolated, very fine and round. This suggests a higher N activity during sintering of the teeth and a carbothermal synthesis route for the Ti(C,N) powder. The inverse grains are homogeneously distributed between the black grains, but the brighter core is barely distinguishable from the intermediate rim phase. This could be an indication for the use of pre-alloyed powders, where the heavy elements are already evenly distributed. IC is also the first grade with a binder phase evident as a light gray phase in the microstructure.
With a mean grain size of 0.34 µm, IC has the finest Ti(C,N)-rich grains of the I grades. The GSD of cores is uniform and very narrow, as indicated by the large slope between d_{10} and d_{90}. The grains are also uniformly distributed with the exception of a local maximum at 1 µm. On the one hand, this could be caused by a bimodal grain size of added powders. On the other hand, it is approximately double the d_{50} size and could therefore be caused by counting grains that appear close together as one single grain.
Multiple results suggested that Y3 teeth were used in the manufacturing process of IC blades. Therefore, the XRD was only measured for the Y3 single teeth, as they could be easily fixed onto the Si wafer. The corresponding XRD pattern can be found in fig. 26.
The hardness and fracture toughness of IC is 1520 HV10 and 9.4 MPa · $m^{1/2}$ respectively, placing this grade in the middle range of all tested saw teeth. This is in accordance with the medium binder content and the mix of fine Ti(C,N)-rich and medium sized inverse grains in the microstructure.

Table 12: Elemental analysis and calculated phase composition, binder composition and stoichiometry of IC.

IC		**hard phase**			**stoichiometry**	
element	**wt%**		**wt%**	**vol%**		**mol**
Ti	36.13	Ti(C,N)	45.74	66.27	(C+N)/Me	0.98
W	23.63	WC	25.17	11.86		
C	6.80	TaC	8.15	4.17	**Ti(C,N)**	
N	5.09	NbC	2.03	1.93	C/Ti	0.50
Ta	7.64	Mo_2C	0.00	0.00	N/Ti	0.48
Nb	1.80	**binder**			(C+N)/Ti	0.98
Mo	0.00	Co	12.61	10.52	C/(C+N)	0.51
Co	12.61	Ni	6.30	5.25		
Ni	6.30	Binder	18.91	15.76	**(Ta,Nb)C**	
sum	100.0	Co/(Co+Ni)	0.67	0.67	Ta/Nb	2.18

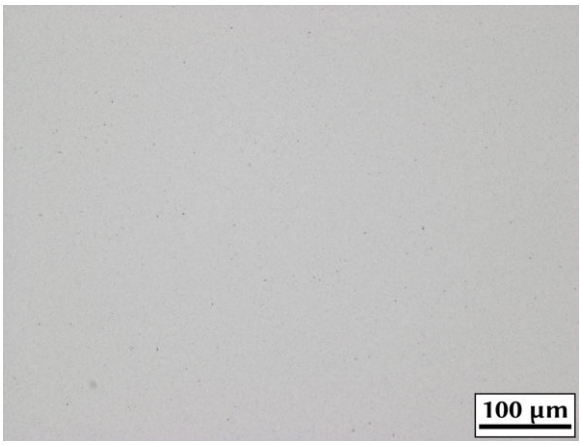

(a) LOM, 200x magnification.

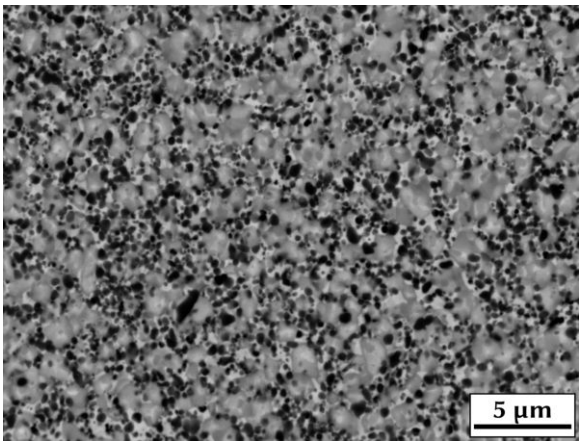

(b) BSE-SEM, 10,000x magnification.

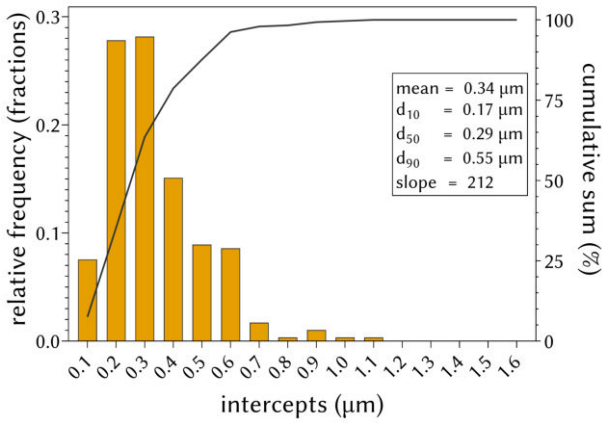

(c) GSD of cores.

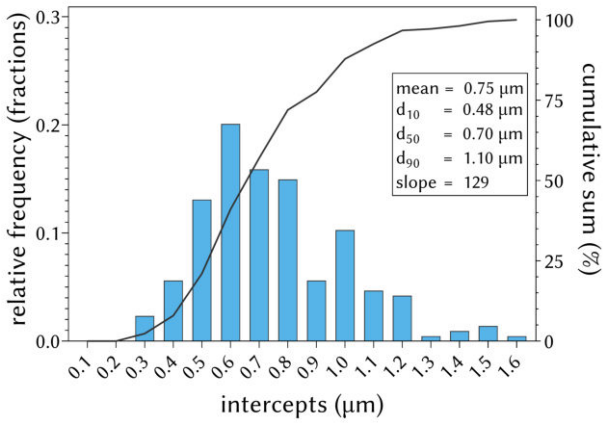

(d) GSD of grains.

Figure 18: LOM, BSE-SEM and grain size distribution of IC.

4.1.8. Saw blade ID

The elemental composition and XRD were not investigated for ID because the same teeth were most likely used on the IA, ID and M5 saw blades. Still, fig. 19 shows their porosity and microstructure to allow for comparison with the other grades.

ID has an estimated porosity of A04B00C00, making it similar to IA. In fact, the microstructure is indistinguishable from IA. The Ti(C,N)-rich black grains are isolated and elongated, the inverse grains show a bright core and gray rim, the binder phase is barely visible.

The GSDs for the black cores and the grains look very similar to IA resulting in average grain sizes of 0.36 and 0.74 µm respectively. Furthermore, the parameters used to characterize the distributions closely match the ones obtained for IA.

With a hardness of 1430 HV10 and a fracture toughness of 9.9 MPa · $m^{1/2}$, the mechanical properties are also quite comparable to IA.

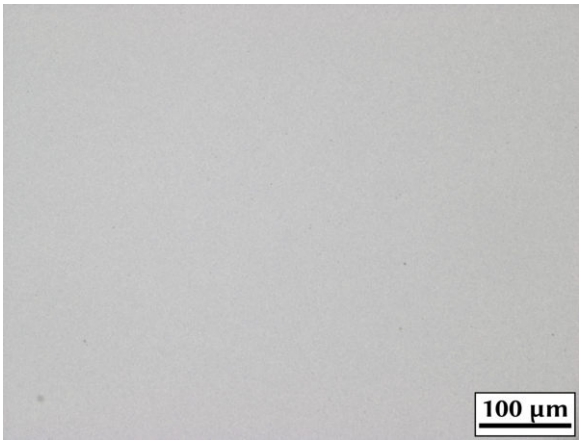

(a) LOM, 200x magnification.

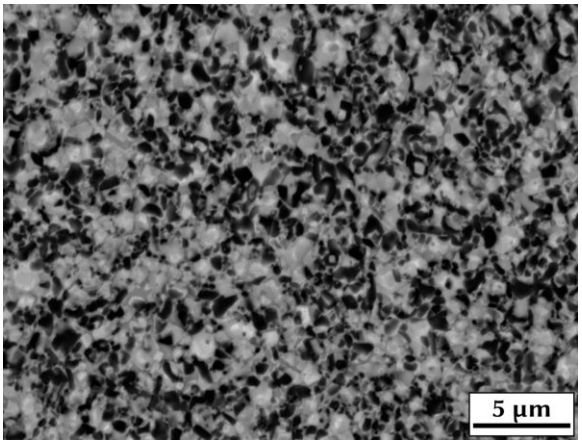

(b) BSE-SEM, 10,000x magnification.

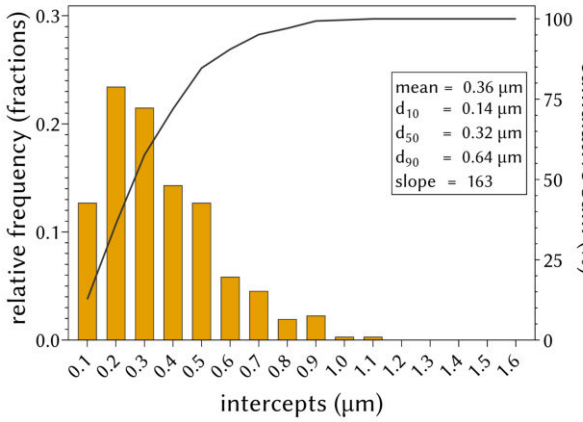

(c) GSD of cores.

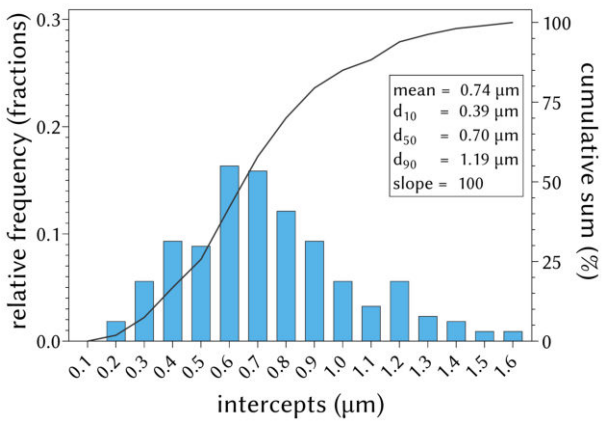

(d) GSD of grains.

Figure 19: LOM, BSE-SEM and grain size distribution of ID.

4.1.9. Saw blade M4

Table 13 presents the chemical analysis of M4 with a binder content of 13 vol% and a Ti(C,N) content of 68 vol%. Co and Ni are added in a ratio of 1:1. Also, the higher C content indicates that $TiC_{0.6}N_{0.4}$ was used in the starting formulation. This grade further shows a slight non-metal deficiency and a Ta/Nb ratio of approximately 1:1.

In fig. 20, a porosity of A06B00C00 is visible. Furthermore, the different phase composition led to a different microstructure. While all the I grades lack grains with a classic core-rim structure, nearly all Ti(C,N)-rich cores in M4 are surrounded by a gray rim of intermediate atomic weight. This can be explained by the lower N activity in the $TiC_{0.6}N_{0.4}$ and possibly also in the sintering atmosphere allowing for the formation of rim phase around the Ti(C,N) cores. The inner rim directly surrounding the cores is brighter and therefore of heavier atomic weight. However, this inner rim is only visible on bigger grains. Some grains appear to have inverse structure with a bright core, but it is unclear if these grains are truly inverse grains or just regular core-rim grains cut above the dark core. The Ti(C,N)-rich cores are elongated, indicating a metal route synthesis.

These elongated cores led to a peculiar GSD with a wide distribution and a maximum at very small intercept lengths. The orientation of the grains in relation to the intercept line influenced the obtained length. Similar effects for the GSD of grains were the different orientations led to a wide distribution with a slope of 99 as some grains were intercepted through their longer side.

In the XRD, the hard phase appears as singlets and no second hard phase with a different lattice parameter is visible. This is another indication that not many inverse grains have been formed, as a significant amount of inverse grains would be visible as doublet hard phase peaks (as was the case for IA, see fig. 16). With 3.5974 Å, the binder phase has one of the highest lattice parameters of the tested saw teeth indicating a large amount of dissolved elements in the binder. An additional peak is found at approximately 38° originating from $CaCO_3$ as filler material in the putty used to mount the sample in the sample holder.

Despite the low binder content and high amount of Ti(C,N) powder, M4 is placed in the middle range of the tested saw teeth with a hardness of 1500 HV10 and a fracture toughness of 9.9 MPa · $m^{1/2}$.

Table 13: Elemental analysis, phase composition, binder composition and stoichiometry of M4.

M4		**hard phase**			**stoichiometry**	
element	**wt%**		**wt%**	**vol%**		**mol**
Ti	38.92	Ti(C,N)	49.10	67.93	(C+N)/Me	0.95
W	18.85	WC	20.08	8.94		
C	8.31	TaC	4.89	2.36	**Ti(C,N)**	
N	4.10	NbC	2.34	2.10	C/Ti	0.62
Ta	4.59	Mo_2C	7.14	5.73	N/Ti	0.36
Nb	2.07	**binder**			(C+N)/Ti	0.98
Mo	6.72	Co	8.39	6.61	C/(C+N)	0.63
Co	8.39	Ni	8.06	6.33		
Ni	8.06	binder	16.45	12.94	**(Ta,Nb)C**	
sum	100.0	Co/(Co+Ni)	0.51	0.51	Ta/Nb	1.14

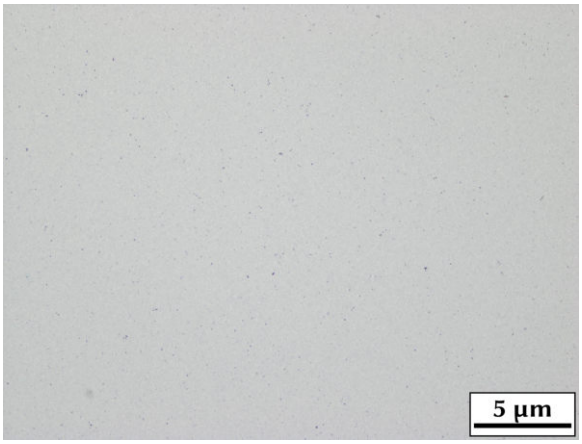

(a) LOM, 200x magnification.

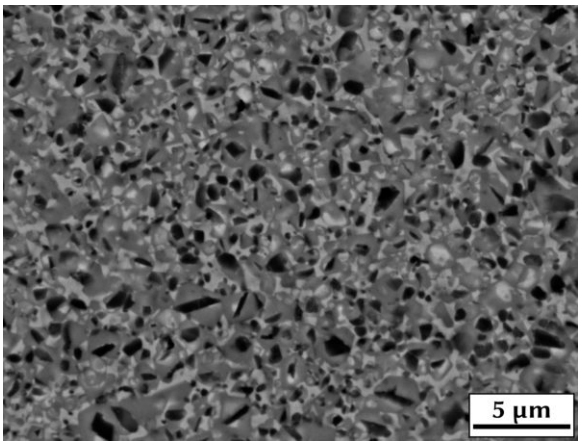

(b) BSE-SEM, 10,000x magnification.

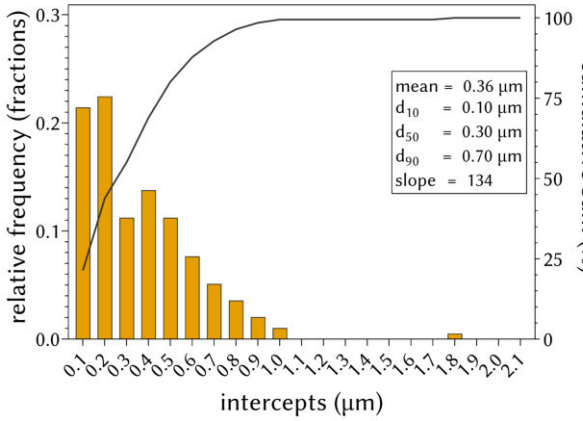

(c) GSD of cores.

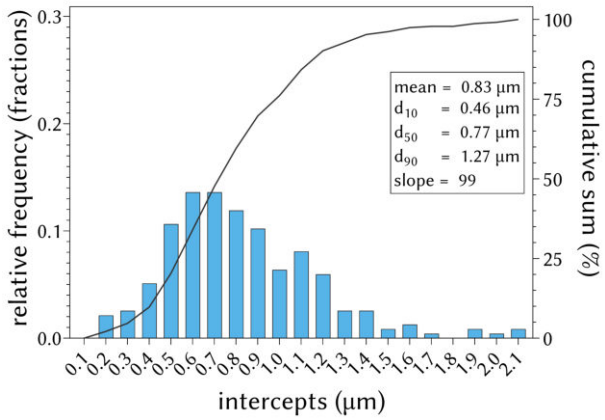

(d) GSD of grains.

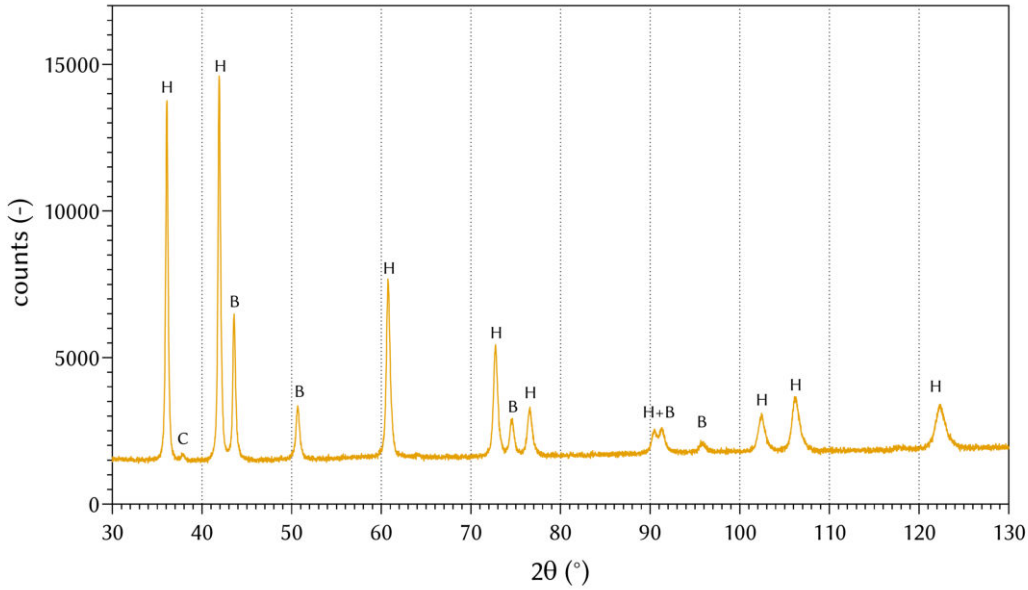

(e) XRD with hard phase (H), binder (B) and $CaCO_3$ (C) peaks identified.

Figure 20: LOM, BSE-SEM and grain size distribution of M4.

4.1.10. Saw blade M5

In fig. 21, a porosity of A04B00C00 is visible. The microstructure is again very similar to IA and ID with isolated, elongated Ti(C,N)-rich grains and inverse grains that appear fused together in the binder phase. With mean grain sizes of 0.40 µm and 0.74 µm and slopes of 153 and 120, respectively, both GSD of cores and grains closely match the results obtained for IA and ID. While the very similar microstructure and EDX quantifications strongly suggest the implementation of the same grade of teeth in the three saw blades, the achieved hardness of 1380 HV10 and fracture toughness of 10.3 MPa · $m^{1/2}$ differ from the mechanical properties of the other two grades. As mentioned before, the small sample dimensions after breaking the teeth from the saw blades and possible differences in the manufacturing of the blades themselves could have led to this discrepancy.

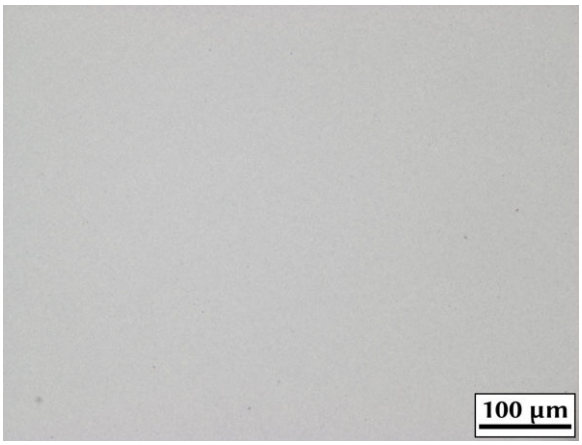

(a) LOM, 200x magnification.

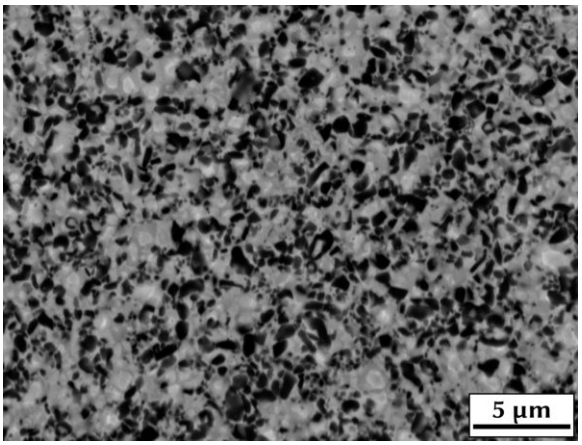

(b) BSE-SEM, 10,000x magnification.

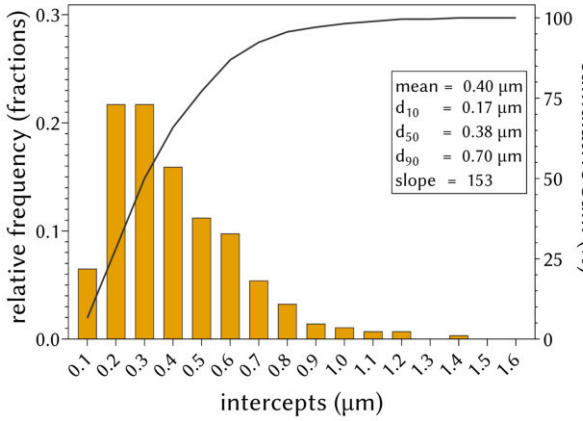

(c) GSD of cores.

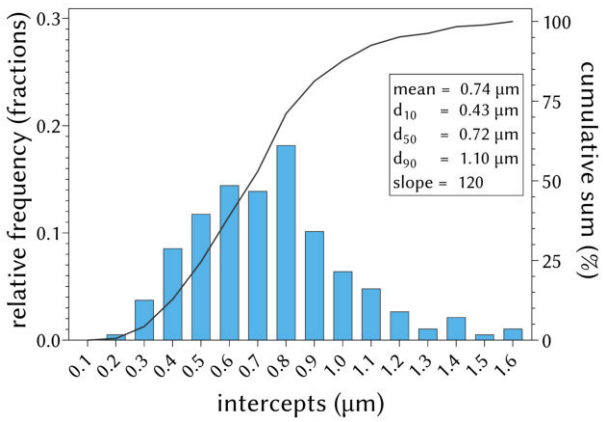

(d) GSD of grains.

Figure 21: LOM, BSE-SEM and grain size distribution of M5.

4.1.11. Saw blade M6

The phase analysis of M6 listed in table 14 closely matches the composition of IA. M6 has the same binder composition with approximately 17 vol% binder content and a Co/Ni ratio of 1:1. The grade shows the same Ta/Nb ratio of 5:1 and Zr and Al could be detected in the chemical analysis. One difference to IA is the slightly lower N content observed in M6.

Fig. 22 reveals that in fact a different saw teeth grade was used on M6. While the porosity is a comparable A06B00C00, the BSE-SEM image indicates a completely contrasting microstructure. Grains with a core-rim structure can be found in a wide variation of grain sizes. Due to the same elemental composition of the two grades, this difference in microstructure can only be caused by a lower N activity during sintering. This is indicated by a slightly higher N content in IA and a lower N content in M6, respectively.

As can be seen in the GSD, both cores and grains have a larger average grain size than IA. This can be caused by the use of a larger grain size of the starting materials and the lack of grain refining effect of nitrogen in the sintering atmosphere. Especially the grains show a very wide distribution with a slope as low as 67 between d_{10} and d_{90}.

The effects of a different sintering atmosphere are also indicated by the XRD pattern. With a lattice parameter of 3.5894 Å, the binder phase dissolved less heavier elements than IA

(3.5900 Å). Despite the presence of mostly core-rim grains, the two distinct hard phase patterns H1 and H2 are visible. This is caused by the presence of inverse grains. Furthermore, more elements dissolved in the Ti(C,N) lattice and therefore a larger lattice parameter was calculated. This observation is in contrast to the findings in the XRD of M4, where only one hard phase pattern was visible with predominantly core-rim grains in the microstructure.
The mechanical properties of M6 were tested to be 1510 HV10 and 10.5 MPa · $m^{1/2}$. Despite the lower N activity, higher hardness and a fracture toughness similar to IA were measured for M6. This is contradictory to the literature, as a higher N activity during sintering generally leads to harder samples.

Table 14: Elemental analysis and calculated phase composition, binder composition and stoichiometry of M6.

M6		**hard phase**			**stoichiometry**	
element	**wt%**		**wt%**	**Vol%**		**mol**
Ti	37.65	Ti(C,N)	47.29	66.37	(C+N)/Me	0.95
W	15.80	WC	16.83	7.62		
C	6.74	TaC	11.38	5.59	**Ti(C,N)**	
N	4.92	NbC	1.20	1.10	C/Ti	0.50
Ta	10.67	Mo_2C	1.50	1.23	N/Ti	0.45
Nb	1.07	ZrC	0.51	0.54	(C+N)/Ti	0.95
Mo	1.42	**binder**			C/(C+N)	0.53
Co	10.00	Co	10.00	8.01		
Ni	10.98	Ni	10.98	8.77	**(Ta,Nb)C**	
Al	0.30	Al	0.30	0.54	Ta/Nb	5.13
Zr	0.45	binder	21.28	17.32		
sum	100.0	Co/(Co+Ni)	0.48	0.48		

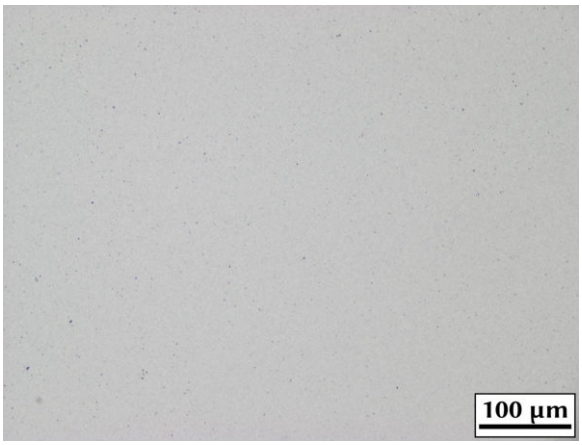

(a) LOM, 200x magnification.

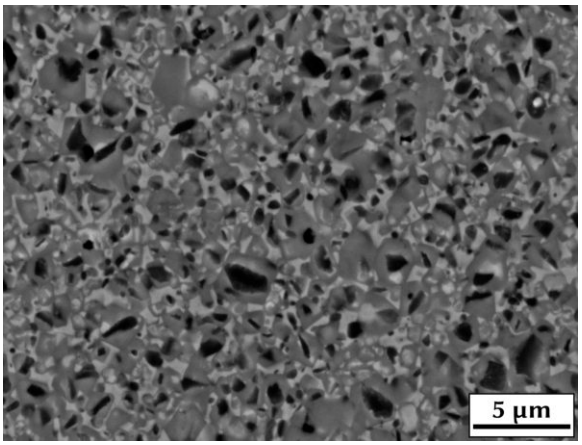

(b) BSE-SEM, 10,000x magnification.

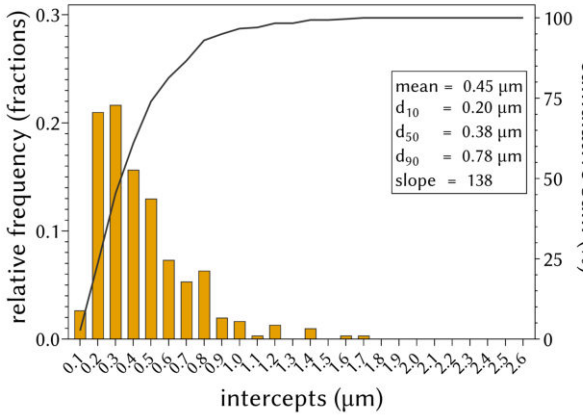

(c) GSD of cores.

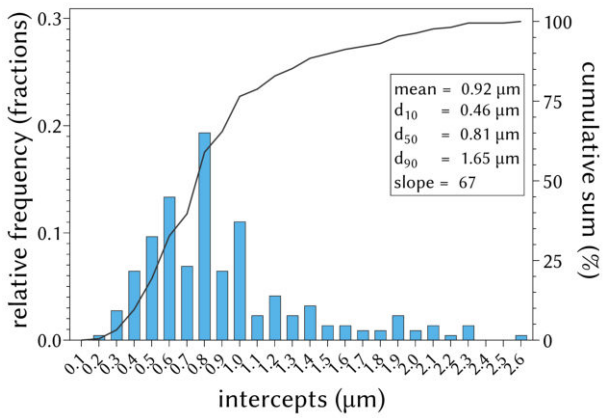

(d) GSD of grains.

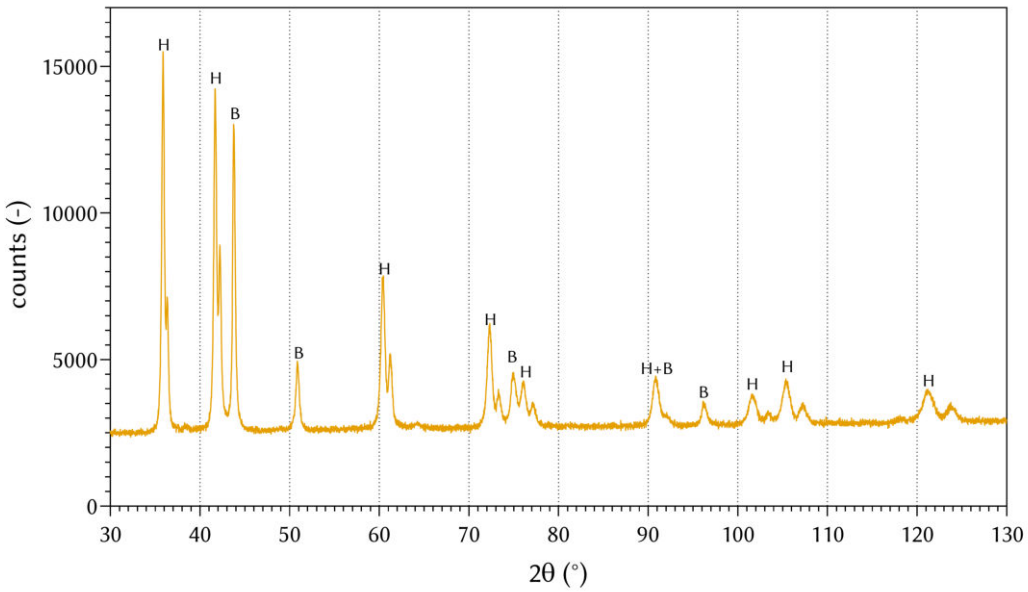

(e) XRD with hard phase (H) and binder (B) peaks identified.

Figure 22: LOM, BSE-SEM and grain size distribution of M6.

4.1.12. Cermet N2

The N2 grade was available as single teeth. The phase composition summarized in table 15 is unique and could not be matched to any teeth on the saw blades. In comparison to other grades, a relatively simple powder formulation was utilized for N2. The 14 vol% binder phase consist almost exclusively of Co. Since it is unlikely that only 0.59 vol% Ni were added in the mixture, it is likely that the N2 teeth were capped with a Ni coating for example by galvanization to improve the bonding strength with the brazing alloy. The hard phase is made up of Ti(C,N), WC and NbC. no Ta or Mo was found in the analysis. As suggested by the stoichiometry, $TiC_{0.5}N_{0.5}$ powder was probably used in the production of this grade.
Fig. 23 reveals a porosity of A02B00C00 and a distinct microstructure. Ti(C,N)-rich black grains appear both isolated and with core-rim structure. While the isolated grains are mostly round, the black cores appear more elongated and angled. This could indicate that two different Ti(C,N) powders were used in the formulation of N2. There are also inverse grains visible with a recognizable bright core. The binder phase occurs very bright and well distinguishable from the grains.
The GSD of cores indicates a quite broadened distribution of black grains lacking a clear maximum. Similarly, the grain size of overall grains is widely spread and there is a possible second local maximum at around 1.3 µm supporting the idea that two different powders were implemented in the formulation.
In the XRD of N2, two well-defined hard phase patterns are apparent already at low 2θ angles. In contrast to the high M_S compared to the other grades, the relatively high lattice parameter of the binder phase (3.5939 Å) suggests a high amount of dissolved elements.
With 1620 HV10 and 8.6 MPa $\cdot$ $m^{1/2}$, respectively, N2 has one of the highest hardness and lowest fracture toughness values of all tested grades. These mechanical properties can be explained by the low binder content of only 14 vol% and the large amount of Ti(C,N) in the composition.

Table 15: Elemental analysis and calculated phase composition, binder composition and stoichiometry of N2.

N2		**hard phase**			**stoichiometry**	
element	**wt%**		**wt%**	**Vol%**		**mol**
Ti	42.13	Ti(C,N)	53.21	69.28	(C+N)/Me	0.98
W	15.75	WC	16.78	7.08		
C	7.73	TaC	0.00	0.00	**Ti(C,N)**	
N	5.72	NbC	11.67	9.93	C/Ti	0.51
Ta	0.00	Mo_2C	0.00	0.00	N/Ti	0.46
Nb	10.33	**binder**			(C+N)/Ti	0.97
Mo	0.00	Co	17.55	13.11	C/(C+N)	0.52
Co	17.55	Ni	0.79	0.59		
Ni	0.79	binder	18.35	13.70		
sum	100.0	Co/(Co+Ni)	0.96	0.96		

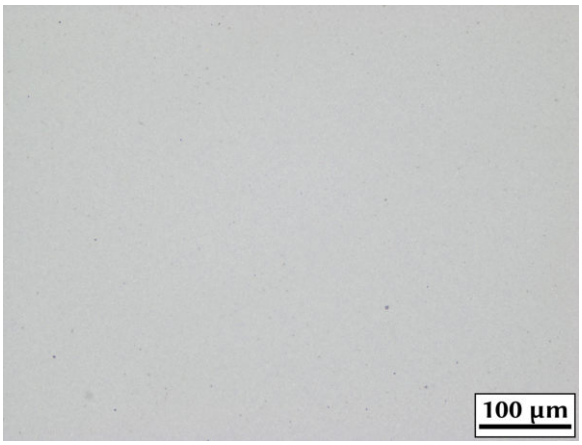

(a) LOM, 200x magnification.

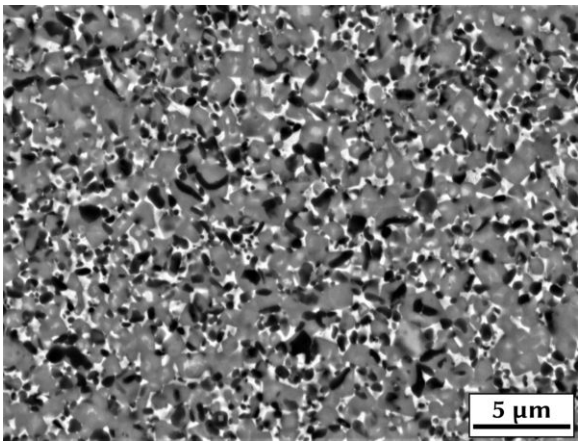

(b) BSE-SEM, 10,000x magnification.

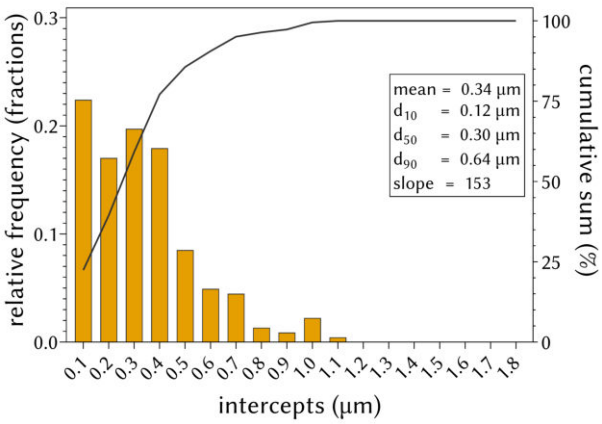

(c) GSD of cores.

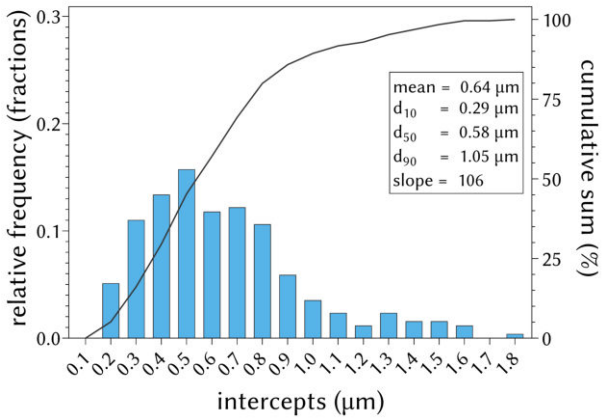

(d) GSD of grains.

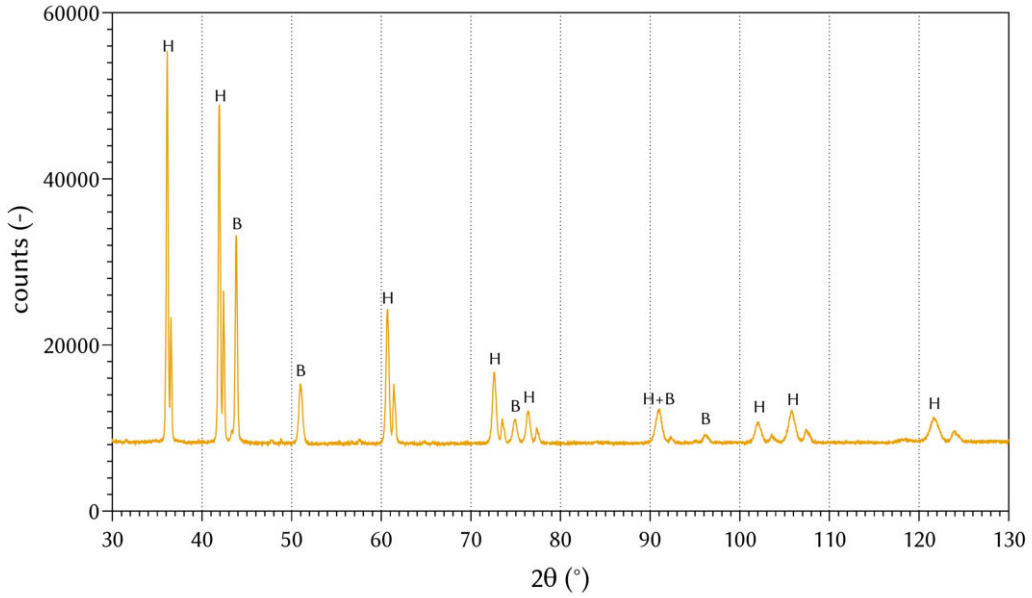

(e) XRD with hard phase (H) and binder (B) peaks identified.

Figure 23: LOM, BSE-SEM and grain size distribution of N2.

4.1.13. Cermet N8

According to the elemental composition presented in table 16, N8 has a binder content of approximately 18 vol% with a Co/Ni ratio of 2:1. The hard phase is also different with a slightly higher amount of WC and the addition of 3 vol% Mo_2C. Again, there was no Ta detectable in the analysis. N8 is slightly sub-stoichiometric and the C/N ratio lies in between $TiC_{0.5}N_{0.5}$ and $TiC_{0.6}N_{0.4}$.

Fig. 24 reveals a porosity of A06B00C00 and a fine microstructure. The majority of Ti(C,N)-rich grains appear isolated and their elongated shape points towards the metal route synthesis. Additionally, grains with inverse structure and a distinct white, heavier core are evident. The binder can be identified as a light gray phase in the microstructure.

With a mean intercept length of 0.35 µm and 0.60 µm, respectively, both the GSD of cores and grains describe a very fine microstructure. Due to the elongated shape, the distribution of grains is widened towards larger intercept lengths.

The two distinct types of grains produce two distinguishable hard phase patterns in the XRD with a lattice parameter of 4.2731 and 4.3154 Å respectively. In comparison with the other saw teeth grades, the binder phase of N8 has the lowest lattice parameter and also a relatively low M_S (see tab. 8). Hence, a low amount of dissolved elements can be assumed.

Because N8 shows desirable mechanical properties of 1480 HV10 hardness and a high fracture toughness of 10.9 MPa · $m^{1/2}$, it was selected as basis for the formulations of the N series. The fracture toughness is comparable to the IA grade, but N8 shows a slightly higher hardness.

Table 16: Elemental analysis and calculated phase composition, binder composition and stoichiometry of N8.

N8		**hard phase**			**stoichiometry**	
element	**wt%**		**wt%**	**Vol%**		**mol**
Ti	38.13	Ti(C,N)	48.22	65.26	(C+N)/Me	0.97
W	17.26	WC	18.38	8.06		
C	7.30	TaC	0.00	0.00	**Ti(C,N)**	
N	4.92	NbC	6.54	5.78	C/Ti	0.54
Ta	0.00	Mo_2C	4.20	3.32	N/Ti	0.44
Nb	5.79	**binder**			(C+N)/Ti	0.98
Mo	3.95	Co	14.65	11.37	C/(C+N)	0.55
Co	14.65	Ni	8.01	6.20		
Ni	8.01	binder	22.65	17.57		
sum	100.0	Co/(Co+Ni)	0.65	0.65		

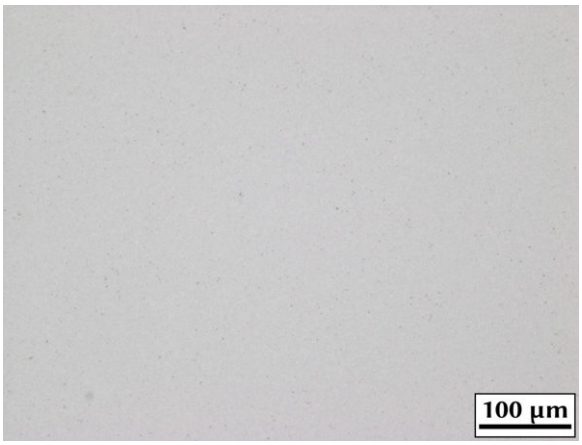

(a) LOM, 200x magnification.

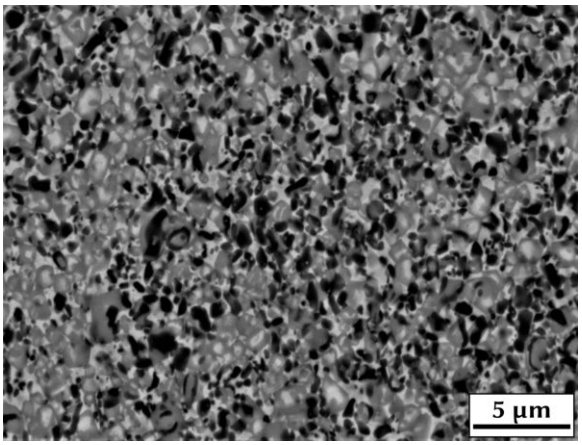

(b) BSE-SEM, 10,000x magnification.

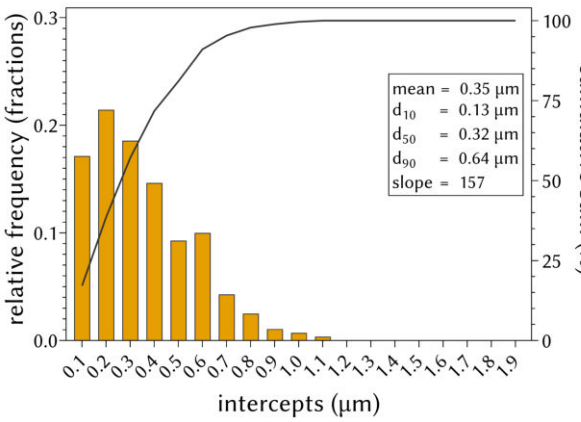

(c) GSD of cores.

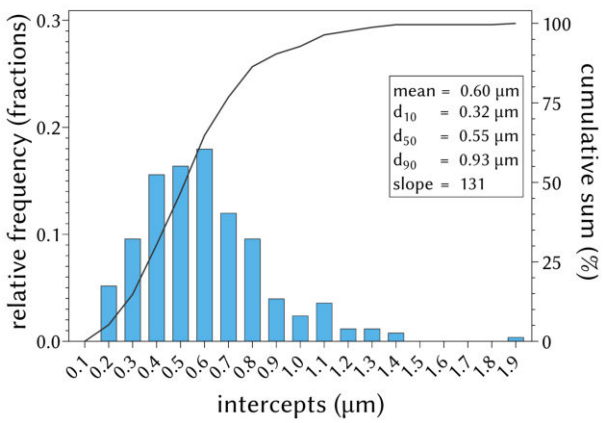

(d) GSD of grains.

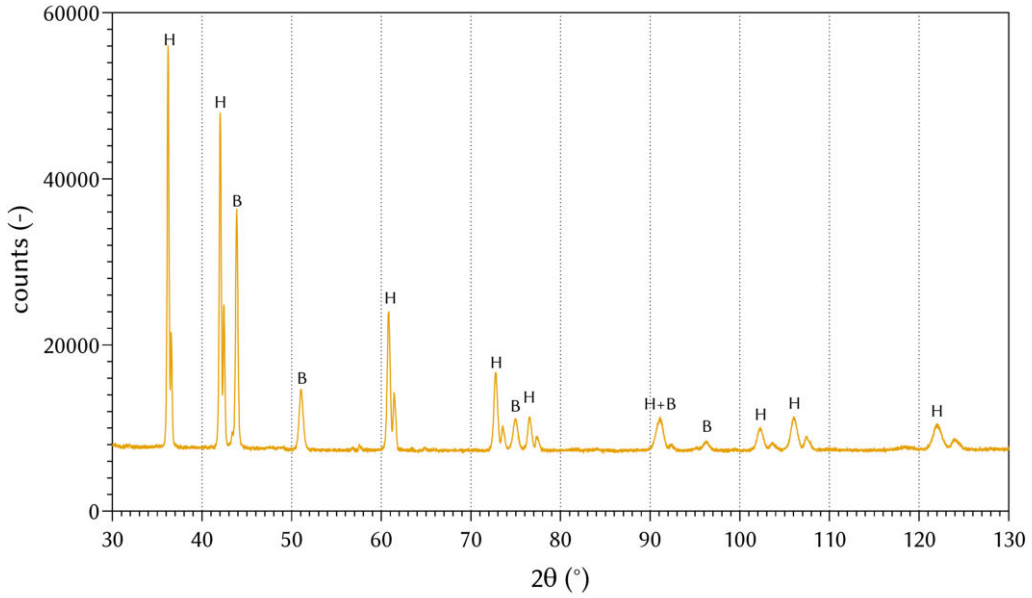

(e) XRD with hard phase (H) and binder (B) peaks identified.

Figure 24: LOM, BSE-SEM and grain size distribution of N8.

4.1.14. Cermet T6

The elemental composition of cermet T6 is listed in table 17. The 14 vol% binder phase is composed of Co and Ni in a ratio of 3:1. Similarly to the other tested grades, the hard phase consists primarily of Ti(C,N) with the addition of approximately 9 vol% WC. However, the C/N ratio is not clearly apparent from the calculation of the hard phase stoichiometry. The relatively low N content and the slight non-metal substoichiometry could indicate a high amount of N_2 outgassing during sintering. The rest of the hard phase consists of TaC and NbC added in a ratio of 1:4. Again, no Mo could be detected in the analysis.

In addition to the LOM image placing T6 in the porosity class A02B00C00, the microstructure is shown in fig. 25. While a majority of grains display a core-rim structure, most lack a distinct bright inner rim. In fact, the intermediate rim phase appears rather uniform with some of the grains showing no core at all. Overall, the microstructure indicates a low N activity in the sintering atmosphere leading to a large amount of incorporated heavier elements in the rim phase and coreless grains. Despite the relatively low binder content, the binder is visible as a distinct, bright phase in the microstructure.

Because of the wide variation of grain size and the elongated grains from the metal route synthesis of Ti(C,N) powder, the GSD shows a broad distribution. While the median grain size is comparable to other cermet grades, some large grains produce tailing towards larger intercept lengths in the GSD.

Further investigation of the phase composition with XRD reveal only one hard phase and binder phase pattern each. Even at large 2θ angles the hard phase peaks stay singlets. With 3.5995 Å, the binder phase has the largest lattice parameter of all tested saw teeth, indicating a large amount of dissolved elements in the binder. This assumption is further supported by

the lowest magnetic saturation of only 40 % relative to the pure binder composition (tab. 8). Despite the poor grain size distribution, the mechanical properties are above average with 1560 HV10 and 9.3 MPa · $m^{1/2}$. This behavior can be explained by binder phase strengthening due to the large amount of dissolved elements and the uniform intermediate rim phase.

Table 17: Elemental analysis and calculated phase composition, binder composition and stoichiometry of T6.

T6		**hard phase**			**stoichiometry**	
element	**wt%**		**wt%**	**Vol%**		**mol**
Ti	39.82	Ti(C,N)	49.86	68.16	(C+N)/Me	0.95
W	19.46	WC	20.73	9.08		
C	7.66	TaC	2.98	1.42	**Ti(C,N)**	
N	4.74	NbC	7.87	6.95	C/Ti	0.53
Ta	2.79	Mo_2C	0.00	0.00	N/Ti	0.41
Nb	6.97	**binder**			(C+N)/Ti	0.94
Mo	0.00	Co	14.01	10.87	C/(C+N)	0.57
Co	14.01	Ni	4.56	3.53		
Ni	4.56	binder	18.57	14.39	**(Ta,Nb)C**	
sum	100.0	Co/(Co+Ni)	0.75	0.76	Ta/Nb	0.21

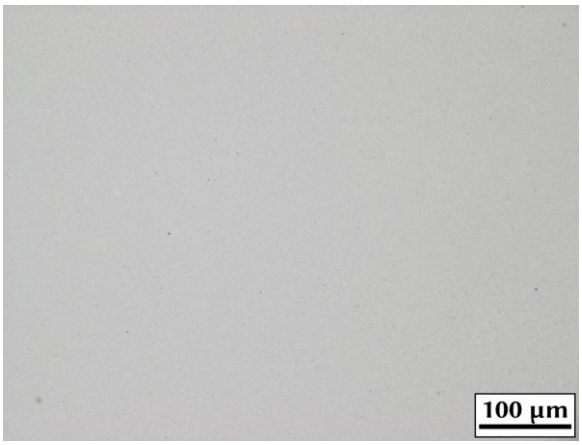

(a) LOM, 200x magnification.

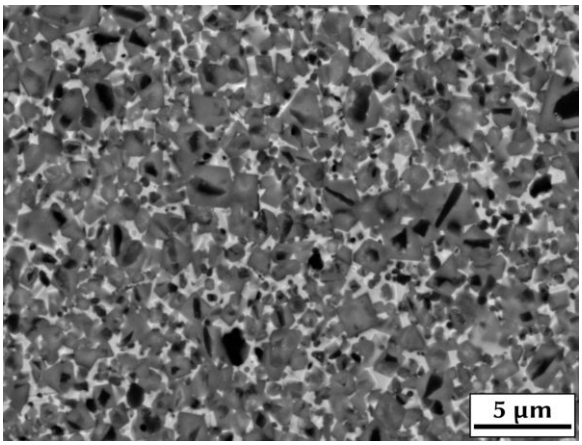

(b) BSE-SEM, 10,000x magnification.

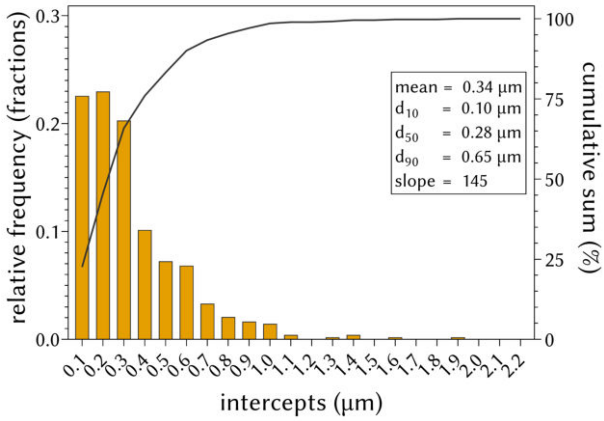

(c) GSD of cores.

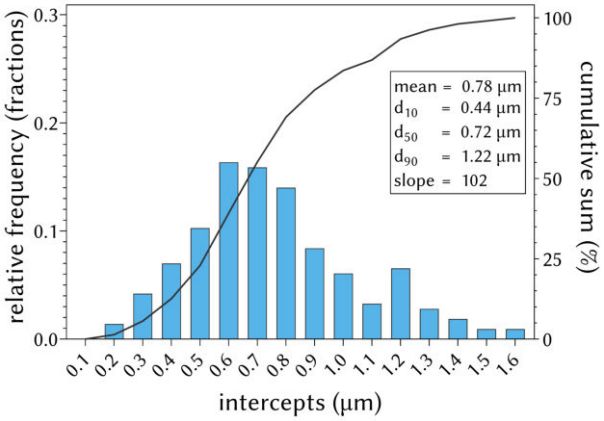

(d) GSD of grains.

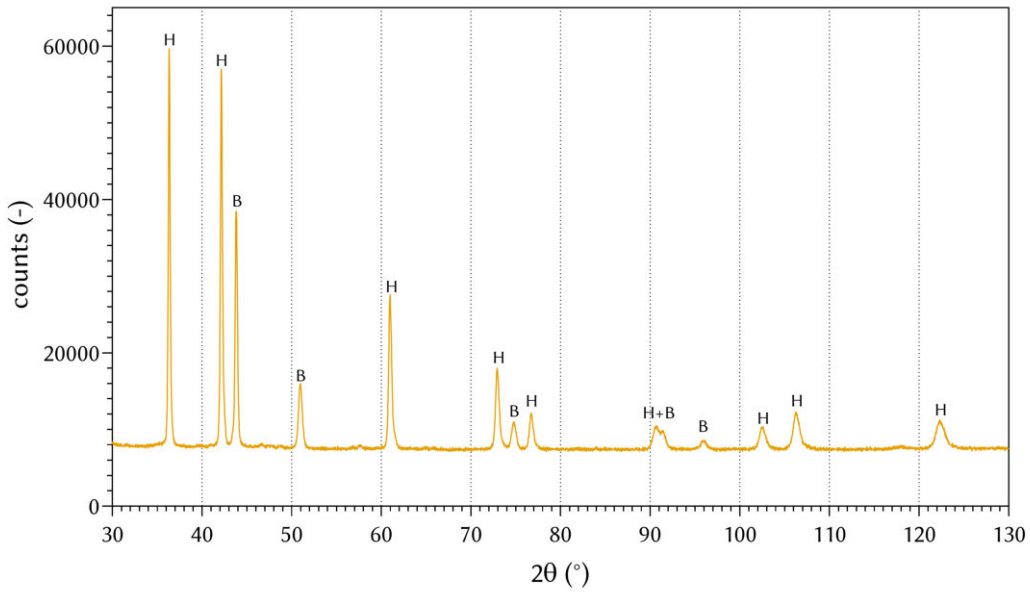

(e) XRD with hard phase (H) and binder (B) peaks identified.

Figure 25: LOM, BSE-SEM and grain size distribution of T6.

4.1.15. Cermet Y3

The elemental and phase composition of the Y3 teeth is summarized in table 18. Most importantly, the analysis shows the same elemental composition used in IC. Again, the hard phase consists of almost stoichiometric $TiC_{0.5}N_{0.5}$ with a large amount of WC added. No Mo_2C was detected, TaC and NbC is contained in the ratio of 2:1. The binder phase also matches the results of IC with a total content of 16 vol% and a Co/Ni ratio of 2:1.
In comparison with IC, Y3 falls into the slightly better porosity class of A04B00C00. To further compare the two grades, the microstructure and XRD pattern are shown in fig. 26. In the BSE-SEM image, the Ti(C,N)-rich black grains appear isolated and very round. Additionally, larger inverse grains with a bright core and a slightly darker rim are visible. The binder is distinguishable as a light gray phase. Overall, the microstructure matches the images obtained for IC, strongly suggesting the use of Y3 teeth for manufacturing of IC saw blades.
Additionally, the results of the linear intercept analysis are very similar to IC. The distribution of cores is equally narrow around a mean of 0.34 µm with a slope of 212 between d_{10} and d_{90}. Likewise, the wider distribution of grains shows matching parameters to IC.
More information on both grades can be obtained from the XRD of Y3. The hard phase is split in two distinct patterns and the doublets are already visible for low 2θ angles. Both the relatively high lattice parameter and the magnetic saturation indicate a high amount of dissolved elements in the binder (3.5962 Å and 45.5 %, respectively).
Finally, the mechanical properties of Y3 can be compared to IC. The hardness of 1530 HV10 is very similar, the fracture toughness is slightly lower at 8.8 MPa · $m^{1/2}$.

Table 18: Elemental analysis and calculated phase composition, binder composition and stoichiometry of Y3.

Y3		**hard phase**			**stoichiometry**	
element	**wt%**		**wt%**	**Vol%**		**mol**
Ti	35.99	Ti(C,N)	45.53	66.14	(C+N)/Me	0.98
W	23.86	WC	25.42	12.01		
C	6.73	TaC	8.19	4.20	**Ti(C,N)**	
N	5.11	NbC	2.04	1.94	C/Ti	0.49
Ta	7.68	Mo_2C	0.00	0.00	N/Ti	0.49
Nb	1.80	**binder**			(C+N)/Ti	0.98
Mo	0.00	Co	12.73	10.64	C/(C+N)	0.50
Co	12.73	Ni	6.09	5.07		
Ni	6.09	binder	18.82	15.72	**(Ta,Nb)C**	
sum	100.0	Co/(Co+Ni)	0.68	0.68	Ta/Nb	2.19

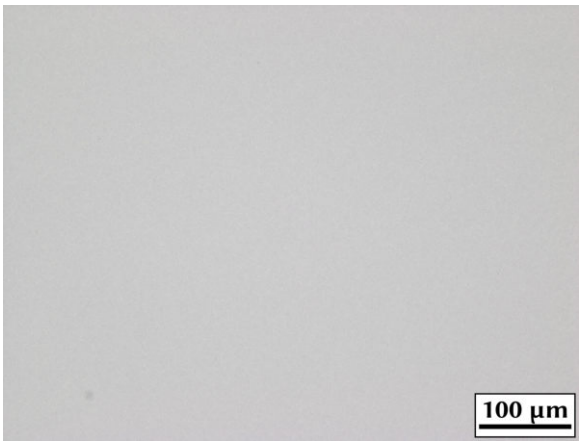

(a) LOM, 200x magnification.

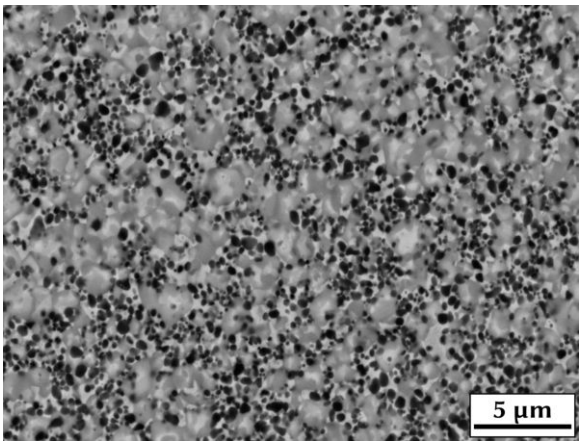

(b) BSE-SEM, 10,000x magnification.

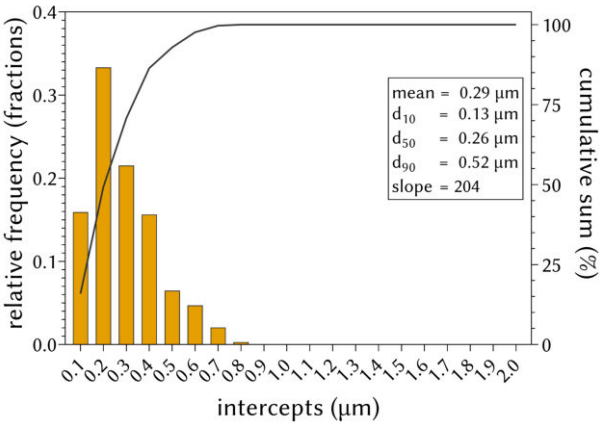

(c) GSD of cores.

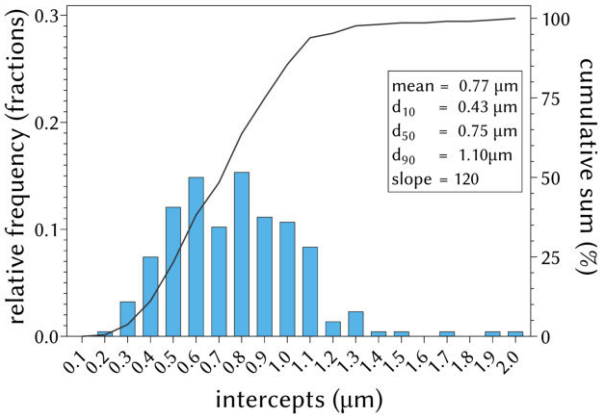

(d) GSD of grains.

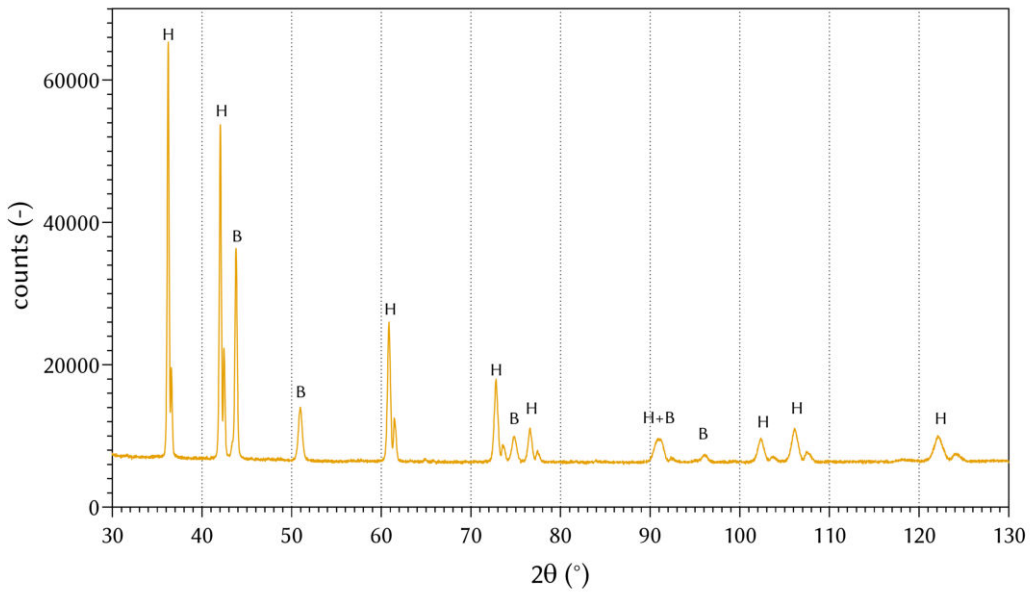

(e) XRD with hard phase (H) and binder (B) peaks identified.

Figure 26: LOM, BSE-SEM and grain size distribution of Y3.

4.1.16. Cermet Y5

With a higher binder content of 17 vol%, it can be expected that this grade is slightly softer and tougher compared to Y3 from the same manufacturer. Also, the binder consists of a Co and Ni in a ratio of 3:1. Other differences include the partial substitution of WC by 3 vol% Mo_2C. Additionally, Y5 has a higher C and lower N content.
According to the LOM image in fig. 27, Y5 falls into porosity class A02B00C00. In the BSE-SEM, the Ti(C,N)-rich grains are round and isolated, but larger than in Y3. The inverse grains present a distinct white core and intermediate gray rim structure. This could indicate the use of pre-alloyed starting materials, which could also have led to the different C/N ratio of this grade.
The GSD further highlights the differences in the microstructure. The cores have a slightly larger mean intercept length, while the overall grains show a similar GSD with a mean grain size of 0.75 µm. The presence of larger grains widened the distribution. Some of those larger intercept correspond to double the mean or median grain size, hence they could actually be multiple grains appearing as one single grain during the linear intercept method.
The XRD phase analysis reveals two distinct patterns for the hard phase. One corresponds to the Ti(C,N)-rich grains and one to the inverse grains with more dissolved elements and therefore a higher lattice parameter. For the binder phse, a lattice parameter of 3.5900 Å was measured. Hence, an intermediate amount of elements dissolved in the binder. This is also indicated by a relative magnetic saturation of 55 %.
As suspected, the lower binder content and the substitution of WC result in a slightly higher fracture toughness of 9.6 MPa · $m^{1/2}$ and a hardness of 1500 HV10. All in all, this grade performs similar to Y3/IC or other grades such as M4.

Table 19: Elemental analysis and calculated phase composition, binder composition and stoichiometry of Y5.

Y5		**hard phase**			**stoichiometry**	
element	**wt%**		**wt%**	**Vol%**		**mol**
Ti	36.15	Ti(C,N)	45.78	64.96	(C+N)/Me	0.97
W	17.98	WC	19.15	8.82		
C	7.04	TaC	8.36	4.18	**Ti(C,N)**	
N	4.72	NbC	1.98	1.84	C/Ti	0.54
Ta	7.84	Mo_2C	3.62	3.01	N/Ti	0.45
Nb	1.76	**binder**			(C+N)/Ti	0.99
Mo	3.40	Co	15.77	12.85	C/(C+N)	0.55
Co	15.77	Ni	5.34	4.34		
Ni	5.34	binder	21.11	17.19	**(Ta,Nb)C**	
sum	100.0	Co/(Co+Ni)	0.75	0.75	Ta/Nb	2.29

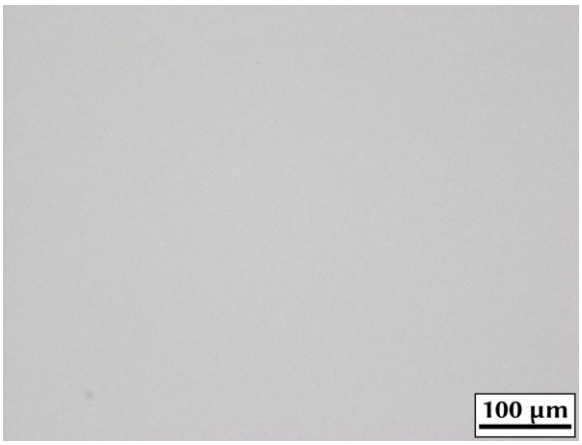

(a) LOM, 200x magnification.

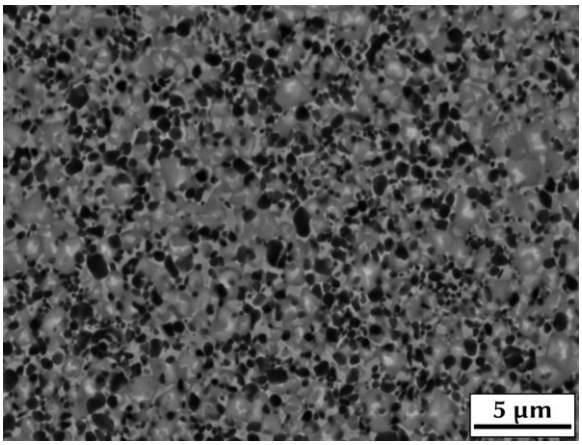

(b) BSE-SEM, 10,000x magnification.

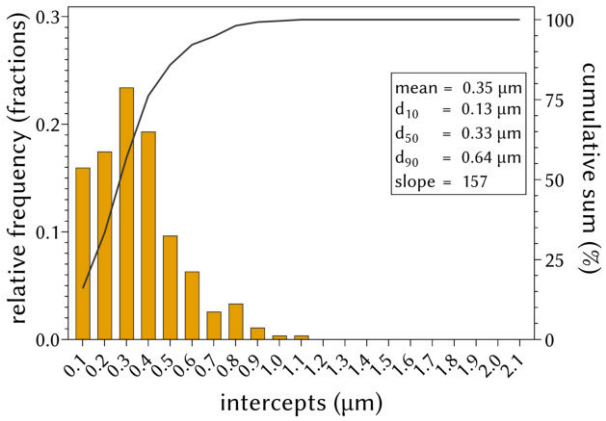

(c) GSD of cores.

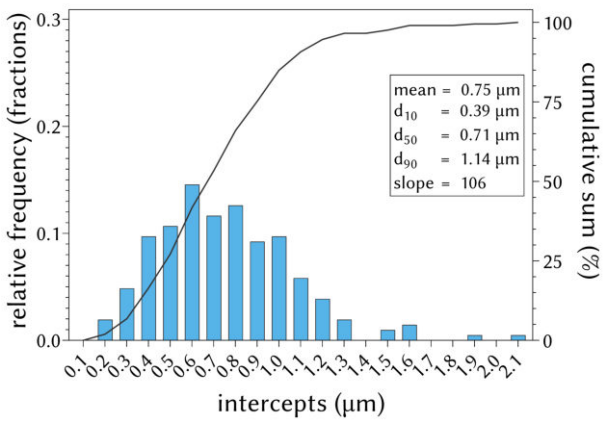

(d) GSD of grains.

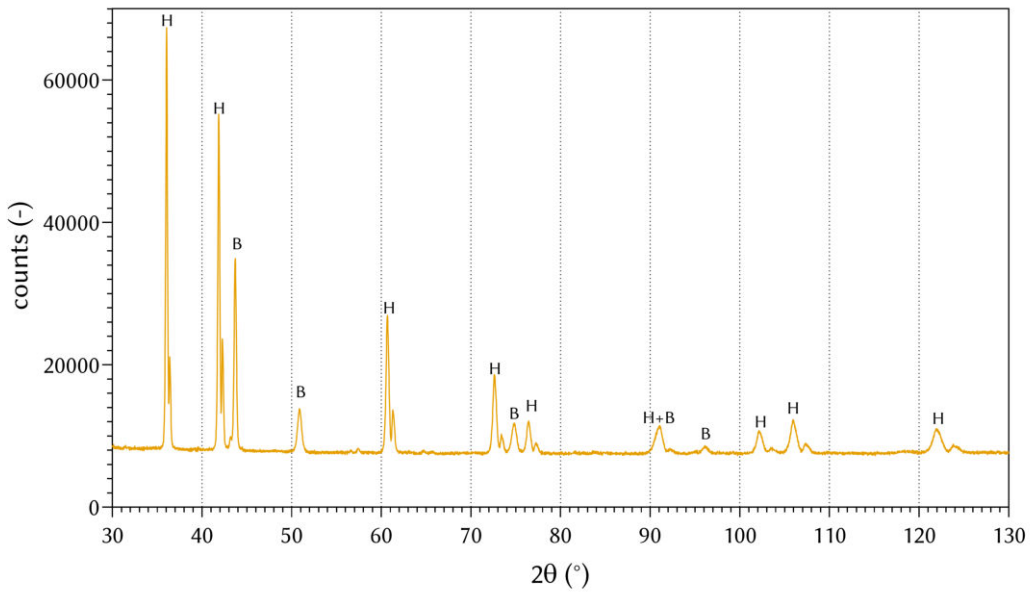

(e) XRD with hard phase (H) and binder (B) peaks identified.

Figure 27: LOM, BSE-SEM and grain size distribution of Y5.

4.1.17. Cermet C1

C1 was the last commercial saw grade tested. Notably, the results of the chemical analysis summarized in table 20 are comparable to the grade N2. The binder content is similar with 13 vol% and also mostly consists of Co with only traces of Ni being detectable. Again, it is unlikely that such small amounts of Ni were added to the formulation. Possibly, the teeth were also coated with Ni to improve the binding to the brazing (see N2). Also, the hard phase is related to N2 as neither of the two grades contains any Ta or Mo and the WC content is similar.

While the elemental composition of C1 closely resembles the formulation of N2, fig. 28 reveals some differences. Firstly, the porosity in the LOM image is slightly worse with A06B00C00. The Ti(C,N)-rich grains in the BSE-SEM also appear isolated, but these grains of C1 are much larger. The GSD of cores shows a rather wide distribution with a slope of 117 between d_{10} and d_{90}. The overall grains in the microstructure are of intermediate molecular weight with a slightly brighter core. Furthermore, the coreless grains are hard to distinguish and look melted together. Likewise, the grains had a very wide GSD with a mean and slope of 0.91 µm and 77 respectively.

In the XRD, the hard phase of C1 shows doublets similar to N2, whereas the lattice parameters are different. The same is true for the binder phase. The slightly higher lattice parameter of the hard phases and the lower lattice parameter of the binder phase indicate that more heavier elements were integrated into the hard phase of C1 and less dissolved in the binder. This is further supported by the higher relative magnetic saturation of 65 % compared to 60 % in N2. Finally, despite the differences in the microstructure and phase analysis, the mechanical properties are comparable with a hardness of 1630 HV10 and a fracture toughness of 8.1 MPa · $m^{1/2}$.

Table 20: Elemental analysis and calculated phase composition, binder composition and stoichiometry of C1.

C1		**hard phase**			**stoichiometry**	
element	**wt%**		**wt%**	**Vol%**		**mol**
Ti	42.37	Ti(C,N)	53.55	69.77	(C+N)/Me	0.98
W	16.36	WC	17.43	7.37		
C	7.80	TaC	0.00	0.00	**Ti(C,N)**	
N	5.72	NbC	11.10	9.46	C/Ti	0.51
Ta	0.00	Mo_2C	0.00	0.00	N/Ti	0.46
Nb	9.83	**binder**			(C+N)/Ti	0.98
Mo	0.00	Co	17.87	13.37	C/(C+N)	0.53
Co	17.87	Ni	0.05	0.04		
Ni	0.05	binder	17.92	13.40		
sum	100.0	Co/(Co+Ni)	1.00	1.00		

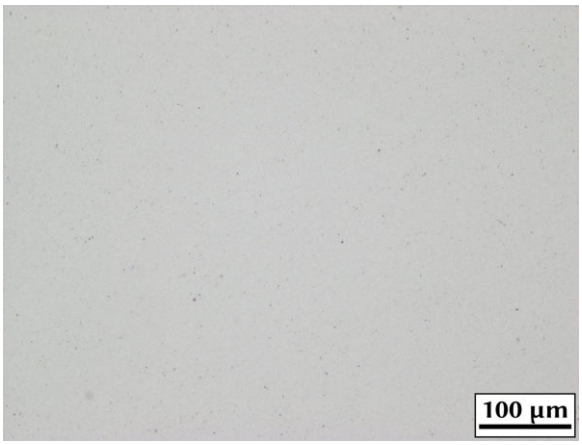

(a) LOM, 200x magnification.

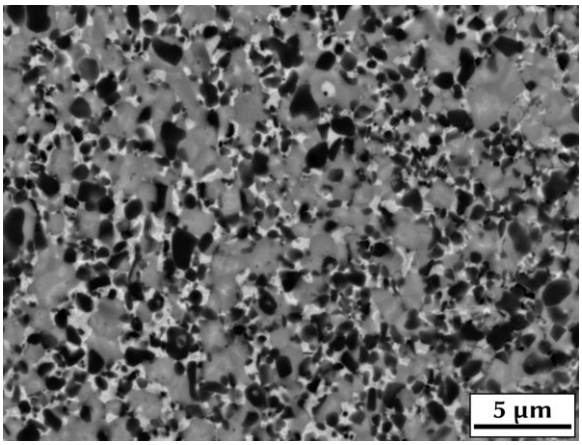

(b) BSE-SEM, 10,000x magnification.

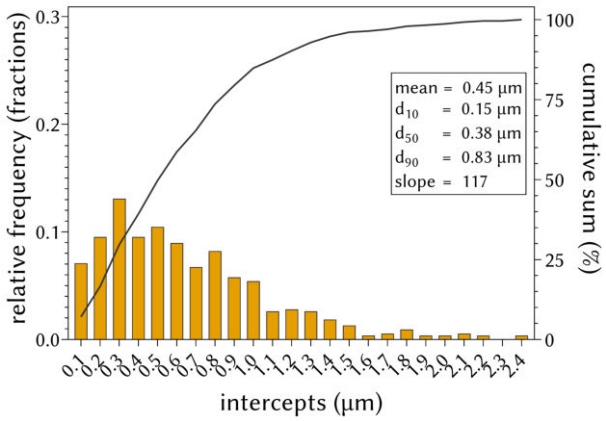

(c) GSD of cores.

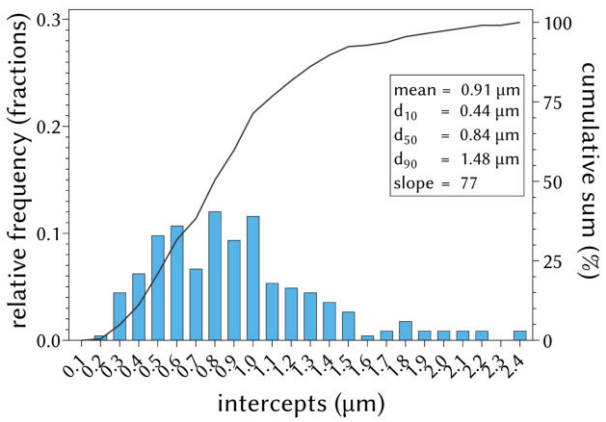

(d) GSD of grains.

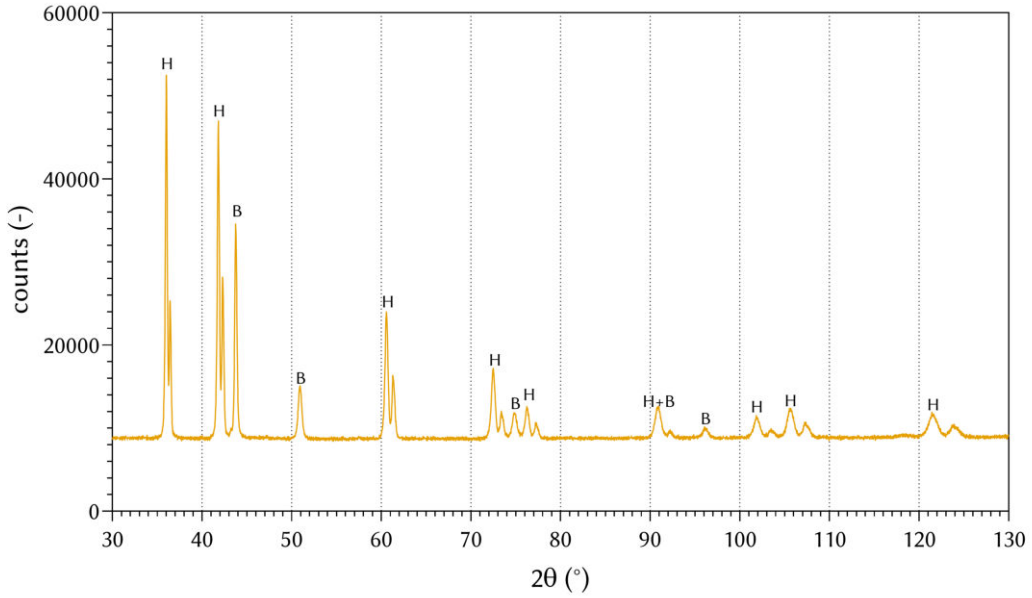

(e) XRD with hard phase (H) and binder (B) peaks identified.

Figure 28: LOM, BSE-SEM and grain size distribution of C1.

4.1.18. Analysis of cermet surface zone and brazing in saw blades

In the cooling stages of the sintering, the melted eutectic binder phase of cermets solidifies first in the interior. This process is accompanied by a phase transition and leads to a contraction of the inside of the cermet. Subsequently, the remaining liquid binder phase is squeezed out between the grains and produces so called binder capping on the surface [36]. The binder cap is visible as a metal-rich layer on the surface of the sintered pieces. While this surface layer is detrimental for some applications such as coating, it can increase the bonding strength if teeth are brazed onto saw blades [37].

The surface layer of the cermet samples was investigated by BSE-SEM and EDX analysis. A distinct binder-rich layer was found on all thirteen grades. Fig. 29 shows examples of the binder capping in IA as a finished saw blade and N2 as a grade available as single teeth. The capping of the cermets was found to be between 1 to 2 µm thick and enriched in the corresponding binder metals, e.g. Co and Ni in IA and Co in N2. This is in accordance with literature, where similar thicknesses were reported [38, 37]. The readily found capping on all grades indicates that the manufacturers intentionally took steps to increase the binding strength of the cermet teeth. These steps include a low enough cooling rate and a higher C activity at the surface than in the bulk to decrease the melting point by the formation of a eutectic [36]. For some samples, it is unclear if this surface layer was produced by binder capping mechanism or by other methods such as galvanization. This is especially likely for the grades N2 and C1, as very small amounts of Ni were found despite the use of a pure Co binder. In the elemental composition of N2, 0.79 wt% Ni was detected by dissolution and XRF analysis (see tab. 7). The average N2 tooth weighing 0.08 g, this would equal 0.0006 g or 0.71 mm^3 Ni. The shape of a single tooth can be approximated by a cuboid with the dimensions 3.9x2.0x1.6 mm. Dividing the volume of the Ni coating by the surface of the cuboid, this would equal to an estimated Ni layer with approx. 2 µm thickness. This is close to the 1.2 µm measured in fig. 29. Therefore, the layer on the surface of N2 was likely produced by galvanization and did not form during sintering.

Additionally, a second surface effect was found in the I and M grades. It can be seen that the black Ti(C,N)-rich particles are enriched near the surface of the cermet. Such graded cermets can be produced by introduction of nitrogen in the sintering atmosphere. The in-diffusion of nitrogen causes a more frequent formation of N-rich particles in the near surface area. This leads to a higher hardness of the surface and can also increase the adhesion of coatings or brazing [39].

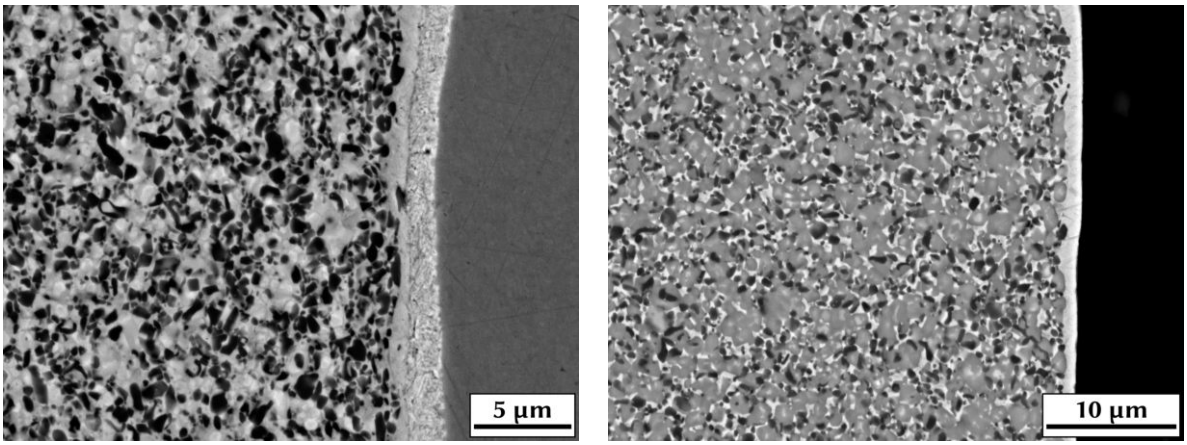

(a) approx. 1.0 µm capping, Co/Ni-rich. (b) 1.2 µm capping, Co/Ni-rich.

Figure 29: Surface-near microstructure in (a) IA and (b) N2, BSE-SEM.

4.1.19. Summary of commercial grades

The thirteen commercial saw teeth grades were successfully characterized in regards to their microstructure, elemental composition, magnetic properties and the resulting mechanical properties. The obtained data is summarized in tab. 21 and 22.
Firstly, the combination of EDX, BSE-SEM, GSD and analysis of the mechanical properties strongly suggest that the saw blades IA, ID and M5 use the same cermet teeth. Their complex hard phase is based on $TiC_{0.5}N_{0.5}$ and WC. In addition to the more commonly found secondary carbides such as Mo_2C or NbC small amounts of ZrC were added. Also, the 17 vol% binder phase contains Co and Ni in a ratio of 1:1 and was strengthened by the addition of minor amounts of Al. A relative increase in binder phase lattice parameter of 1.31 % indicates a medium amount of dissolved elements (tab. 22). The microstructure included unique elongated Ti(C,N)-rich grains that remained isolated and inverse grains with a very distinct core (see fig. 30). Additionally, all three grades have a sub-micron core and grain size with narrow distributions indicated by the relatively large slopes (see tab. 22). Overall, these properties resulted in desirable mechanical properties, especially a high fracture toughness (approx. 1440 HV10 and 10 MPa $\cdot$ $m^{1/2}$). Hence, the cermet teeth of IA, ID and M5 were selected as the target material for the I Series cermet in the next chapters.
Interestingly, the elemental composition of M6 is comparable to the results obtained for IA. However, due to the significantly different microstructure with core-rim grains and gray, coreless grains, some other cermet grade was probably used in the manufacturing of the M6 saw blade. Further differences include the slightly higher hardness, a wider GSD with a larger average grain size and less dissolved elements in the binder phase.
Secondly, the teeth used on the IC saw blade could be identified as the Y3 cermet. Both grades' were analyzed by dissolution XRF, CGHE and combustion IR and the results suggest a very similar elemental composition. Furthermore, the two grades are indistinguishable regarding their microstructure containing isolated, round Ti(C,N)-rich cores and large inverse grains. The mechanical properties are likewise similar with a hardness of approx. 1530 HV10 and a fracture toughness of approx. 9.0 MPa $\cdot$ $m^{1/2}$.

Lastly, the two hardest grades, N2 and C1 also share the same elemental composition, while some differences are apparent in the GSD and XRD analysis. C1 has larger, isolated Ti(C,N)-rich grains and less heavier elements dissolved in the binder phase. Therefore, it is not clear if they are in fact the same cermet grade or just share the same elemental composition.
In addition to the tough IA grade, grade N8 shows a very high toughness of 10.9 MPa · $m^{1/2}$. As such a high toughness can benefit the wear behavior of cutting tools, this material was selected as the second target grade. With a binder content of 18 vol%, N8 is similar to the first target grade. However, the high fracture toughness was achieved with a Co/Ni ratio of 2:1 and no strengthening effects of ZrC or Al. The microstructure in fig. 30 displays isolated, elongated Ti(C,N)-rich grains and inverse grains.

Table 21: Mechanical properties, secondary carbides, binder phase composition and microstructure of the tested commercial grades. All hard phases were based on Ti(C,N) and WC, K_{IC} in MPa · $m^{1/2}$ and binder content in vol%, IA=ID=M5, IC=Y3.

grade	HV	K_{IC}	secondary carbides	binder	microstructure
IA	1440	10.6	TaC, NbC, Mo_2C, ZrC	Co, Ni, Al (17%)	isolated Ti(C,N), inv. grains
IB	1600	9.3	TaC, NbC, Mo_2C	Co, Ni (14%)	isolated Ti(C,N), inv. grains
IC	1520	9.4	TaC,NbC	Co, Ni (16%)	isolated Ti(C,N), inv. grains
ID	1430	9.9	TaC, NbC, Mo_2C, ZrC	Co, Ni, Al (17%)	isolated Ti(C,N), inv. grains
M4	1500	9.9	TaC, NbC, Mo_2C	Co, Ni (13%)	core-rim, inverse grains
M5	1380	10.3	TaC, NbC, Mo_2C, ZrC	Co, Ni, Al (17%)	isolated Ti(C,N), inv. grains
M6	1510	10.5	TaC, NbC, Mo_2C, ZrC	Co, Ni, Al (17%)	core-rim, inverse grains
N2	1620	8.6	NbC	Co (14%)	isol. Ti(C,N), coreless grains
N8	1480	10.9	NbC, Mo_2C	Co, Ni (18%)	isolated Ti(C,N), inv. grains
T6	1560	9.3	TaC, NbC	Co, Ni (14%)	core-rim, coreless grains
Y3	1530	8.8	TaC,NbC	Co, Ni (16%)	isolated Ti(C,N), inv. grains
Y5	1500	9.6	TaC, NbC, Mo_2C	Co, Ni (17%)	isolated Ti(C,N), inv. grains
C1	1630	8.1	NbC	Co (13%)	isol. Ti(C,N), coreless grains

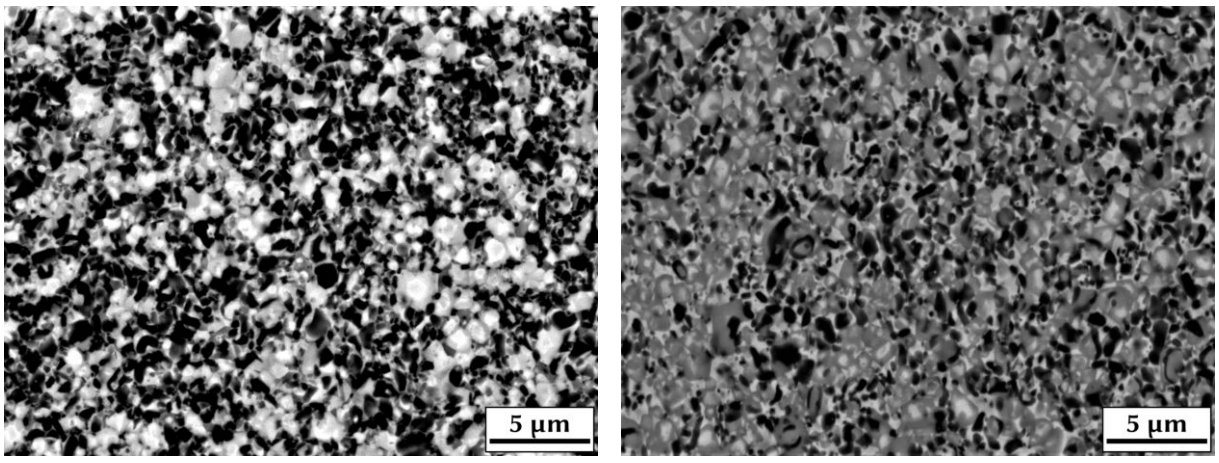

(a) IA (b) N8

Figure 30: Microstructure of the two target grades (a) IA/ID/M5 and (b) N8, BSE-SEM, 10,000x magnification.

Table 22: Grain sizes determined by linear intercept of black cores and overall grains, binder magnetic saturation and increase in lattice parameter of the tested commercial grades. IA=ID=M5, IC=Y3.

	LI - cores			**LI - grains**			**binder state**	
grade	**mean**	**d_{50}**	**slope**	**mean**	**d_{50}**	**slope**	**MS (%)**	**B_{rel} (%)**
IA	0.38	0.31	173	0.78	0.72	102	-	-
IB	0.50	0.40	106	0.70	0.67	118	-	1.51
IC	0.34	0.29	212	0.75	0.70	129	-	-
ID	0.36	0.32	163	0.74	0.70	100	-	1.31
M4	0.36	0.30	134	0.83	0.77	99	-	1.55
M5	0.40	0.38	153	0.74	0.72	120	-	-
M6	0.45	0.38	138	0.92	0.81	67	-	1.27
N2	0.34	0.30	153	0.64	0.58	105	60.7	1.38
N8	0.35	0.32	157	0.60	0.55	131	50.5	1.23
T6	0.34	0.28	145	0.81	0.75	89	40.2	1.56
Y3	0.29	0.26	204	0.77	0.75	120	45.5	1.47
Y5	0.35	0.33	157	0.75	0.71	106	54.8	1.29
C1	0.45	0.38	117	0.45	0.38	117	65.2	1.33

4.2. I series

In the second part of this work, the elemental composition of IA and N8 was used as a basis to recreate the cermets properties in the I and N series. On the one hand, the goal was to achieve a comparable microstructure and mechanical properties by standard powder metallurgical preparation on a lab scale. On the other hand, the starting powders and sintering parameters were varied to gain a deeper understanding of the influencing factors of cermet properties. For this, the two series were split into four subgroups (see chapter 3.2.2, tab. 3). The first group (I0 and N0) was based on binary starting powders and $TiC_{0.5}N_{0.5}$ powder from two different manufacturers. In the second group (I1 and N1), $TiC_{0.7}N_{0.3}$ was added to these two formulations to exactly match the targets' elemental composition. Next, in series I1 and N1 the $TiC_{0.5}N_{0.5}$ powder grain size was varied. Lastly, the influence of pre-alloyed starting materials was studied. Series I2/N2 and I3/N3 utilized (Ti,W)(C,N) and (Ti,W)C powders, respectively.
Both series were sintered in a SinterHIP furnace with Ar or N_2 atmosphere during the heating stage. For the N series cermets, additional experiments were conducted in a vacuum furnace to gain insight in the influence of different Ar or N_2 partial pressures during sintering. Due to the addition of paraffin wax, the I cermets were only sintered in the SinterHIP furnace as a dewaxing step could easily be added to the profile.

4.2.1. Porosity and dimensional change

For all I series cermets, LOM images with 100x and 200x magnification are presented in figures 65 to 86 in the appendix. Overall, the addition of paraffin wax and the use of the Sinter-HIP furnace led to dense samples. On some samples porosity classes up to A06 were determined (see table 23). Moreover, some cermets show streaks of brighter areas consisting of agglomerated binder phase. It is possible that these softer binder particles chipped out during polishing and increased the apparent porosity in some LOM images.

Table 23: Apparent porosity of sintered cermets from the I series.

	Porosity Class	
	SAr	**SN**
I0-1	A04 B00 C00	A02 B00 C00
I0-2	A06 B00 C00	A04 B00 C00
I1-1	A02 B00 C00	A02 B00 C00
I1-2	A04 B00 C00	A02 B00 C00
I1-3	A00 B00 C00	A02 B00 C00
I2-1	A04 B00 C00	A02 B00 C00
I2-3	A00 B00 C00	A02 B00 C00
I3-1	A06 B00 C00	A02 B00 C00
I0-1+0.4%C	A04 B00 C00	A04 B00 C00
I1-1+0.4%C	A06 B00 C00	A06 B00 C00
I2-1+0.4%C	A02 B00 C00	A02 B00 C00

The densification during sintering can also be estimated by considering the Archimedes density and the dimensional changes in table 24. I cermets achieved densities between 7.0 and 7.3 g/cm^3 (96 to 99 % of theoretical density 7.297 g/cm^3). Shrinkage in diameter and height was determined to be between 20 and 22 % after the sintering process. When comparing the weight loss with cermets from the N series, the dewaxing of approximately 4 % paraffin wax has to be taken into account for the I series, resulting in approximately 2 % weight loss on average.

Table 24: Archimedes density (ρ_A) in g/cm^3, shrinkage in diameter (d) and height (h) and mass loss (%) of I cermets.

		shrinkage		
sample	**ρ_A**	**d (%)**	**h (%)**	**m (%)**
I0-1_SAr	7.177	22.3	23.1	6.2
I0-1_SN	7.241	22.3	22.3	5.8
I0-2_SAr	7.113	23.3	24.1	7.0
I0-2_SN	7.137	23.5	24.2	6.9
I1-1_SAr	7.021	22.1	22.7	6.0
I1-1_SN	6.994	22.4	22.4	5.8
I1-2_SAr	7.284	23.1	23.5	6.6
I1-2_SN	7.241	23.4	23.8	6.6
I1-3_SAr	7.221	21.4	21.0	5.8
I1-3_SN	7.164	21.5	21.0	5.6
I2-1_SAr	7.216	21.5	21.5	5.5
I2-1_SN	7.120	21.6	22.0	5.3
I2-3_SAr	7.182	21.3	20.9	5.7
I2-3_SN	7.176	21.4	21.9	5.7
I3-1_SAr	7.201	21.5	21.8	5.5
I3-1_SN	6.973	21.6	21.7	5.4
I0-1+0.4%C_SAr	7.281	21.9	21.6	6.7
I0-1+0.4%C_SN	7.193	21.8	21.2	6.6
I1-1+0.4%C_SAr	7.102	21.8	21.1	6.3
I1-1+0.4%C_SN	7.034	21.8	21.0	6.2
I2-1+0.4%C_SAr	7.145	21.0	20.3	6.0
I2-1+0.4%C_SN	7.167	21.0	20.8	5.8

4.2.2. Phase analysis and magnetic properties

In the appendix, the XRD pattern of all I samples are shown in figures 65 to 86. The peak shape of the fcc phases was visually evaluated and the lattice parameters were determined by Rietveld analysis. These findings are summarized in table 25. Cermets of series I0 and I1 show two individual hard phase patterns forming doublets and therefore two lattice parameters were obtained. Regardless of sintering atmosphere, the cermets based on I2-1 and I3-1 containing pre-alloyed (Ti,W)(C,N) or (Ti,W)C show strongly overlapping patterns and therefore hard phase singlets are visible in the XRD. One exception is the I2-3 powder, where the addition of Ti(C,N) with a much larger grain size led to a higher signal strength of the second hard phase pattern.

The amount of dissolved elements in the binder can be estimated by the binder phase lattice parameter and the corresponding magnetic saturation. For better comparison, the relative increase of the lattice parameter and the magnetic saturation were compared to the pure binder phase with the same Co/Ni ratio. For the I series cermets, the binder phase lattice parameter increased between approximately 1.1 and 1.6 %. This is within the range of the tested saw teeth and and appears to be especially similar to the target grade IA with an increase of 1.3 %. This behavior also correlates with the magnetic saturation of the tested cermets: The higher the increase in lattice parameter, the lower the magnetic saturation, indicating a higher amount of dissolved elements (see fig. 31). This is also true for the C adjusted I cermets, where relatively low binder phase lattice parameters and relatively high magnetic saturation values were measured. While the general linear correlation between magnetic saturation and increase in binder lattice parameter holds true for the I series cermets, no clear trend can be seen between the SAr and SN samples. Therefore, the N_2 partial pressure in the SinterHIP has no significant influence on the binder phase dissolution state for the I cermets.

Table 25: Lattice parameters in Å, peak form and magnetic saturation of the I series cermets. Relative increase of the binder phase lattice parameter (B_{rel}), magnetic saturation (MS) in comparison to the pure Co/Ni binder and total concentration of dissolved elements in the binder (mol%).

sample	peak form	H1	H2	B	B_{rel} (%)	MS (%)	c (mol%)
I0-1_SAr	doublet	4.3259	4.2800	3.5910	1.34	47.3	11.6
I0-1_SN	doublet	4.3279	4.2862	3.5906	1.33	47.3	11.6
I0-2_SAr	doublet	4.3295	4.2800	3.5961	1.49	36.1	13.8
I0-2_SN	doublet	4.3332	4.2858	3.5994	1.58	33.2	14.4
I1-1_SAr	doublet	4.3273	4.2845	3.5928	1.39	47.5	11.6
I1-1_SN	doublet	4.3292	4.2928	3.5926	1.39	47.1	11.6
I1-2_SAr	doublet	4.3291	4.2810	3.5964	1.49	38.4	13.4
I1-2_SN	doublet	4.3300	4.2829	3.5965	1.50	36.8	13.7
I1-3_SAr	doublet	4.3314	4.2825	3.5923	1.38	44.1	12.2
I1-3_SN	doublet	4.3315	4.2834	3.5925	1.38	43.9	12.3
I2-1_SAr	singlet	4.3285		3.5945	1.44	53.7	10.3
I2-1_SN	singlet	4.3302		3.5868	1.22	54.3	10.2
I2-3_SAr	doublet	4.3243	4.2881	3.5836	1.13	55.2	10.0
I2-3_SN	doublet	4.3250	4.2774	3.5833	1.12	57.1	9.6
I3-1_SAr	singlet	4.3267		3.5894	1.30	49.3	11.2
I3-1_SN	singlet	4.3311		3.5896	1.30	50.3	11.0
I0-1+0.4%C_SAr	doublet	4.3233	4.2882	3.5826	1.10	62.0	8.7
I0-1+0.4%C_SN	doublet	4.3212	4.2818	3.5775	0.96	63.2	8.4
I1-1+0.4%C_SAr	doublet	4.3202	4.2944	3.5831	1.11	61.0	8.9
I1-1+0.4%C_SN	doublet	4.3212	4.2849	3.5784	0.99	61.7	8.7
I2-1+0.4%C_SAr	singlet	4.3239		3.5824	1.10	62.4	8.6
I2-1+0.4%C_SN	doublet	4.3224	4.2988	3.5776	0.96	64.5	8.2

4.2.3. Microstructure and grain size distribution

Certain representative figures have been selected in this chapter, while all BSE-SEM images and GSD of the I series cermets can be found in appendix A.1 in figures 65 to 86. Overall, the I cermets display a very fine microstructure with sub-micron average grain size in the BSE-SEM images (see fig. 32). Regardless of the sintering atmosphere, the black Ti(C,N) cores are mostly isolated and round. Classic core-rim structure is only present when the coarse$TiC_{0.7}N_{0.3}$ is added to the formulation. These C-rich grains are able to integrate heavier elements such as W or Mo into the lattice and therefore the inner and outer rims can be formed during sintering. The amount of inverse grains with a bright core or coreless grains which appear medium gray in BSE mode is increased for the cermets using pre-alloyed (Ti,W)C or (Ti,W)(C,N) powders. This is in accordance with findings from literature and can be explained by the more homogeneous distribution of heavier elements throughout the cermet structure [17, 19].

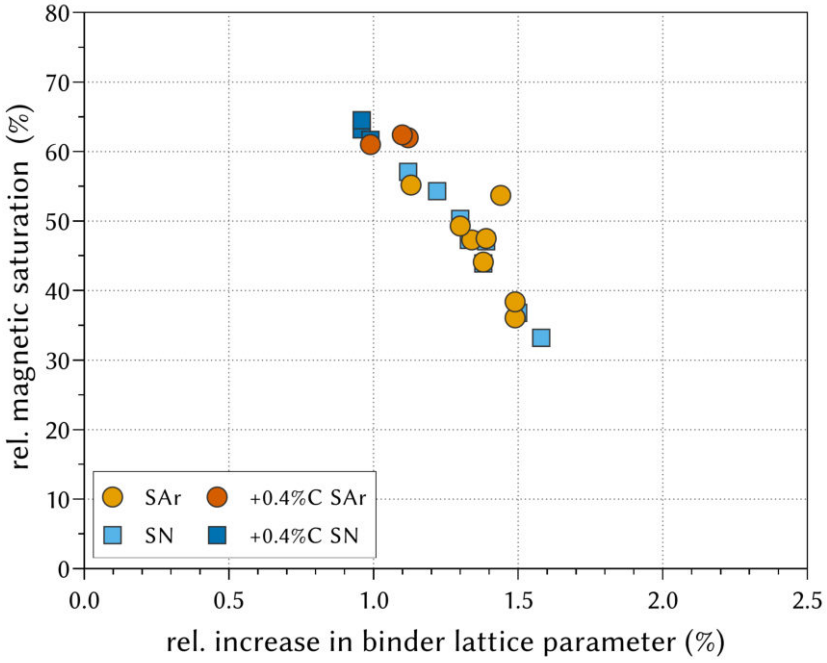

Figure 31: Correlation of relative increase in binder phase lattice parameter and magnetic saturation for the SinterHIP I series cermets.

As can be seen in fig. 32, the microstructure of IA was matched to some extend. As the target, I series cermets have a fine microstructure with mostly isolated Ti(C,N) cores and predominantly inverse or gray coreless grains. The elongated shape of the Ti(C,N)-rich grains points to a different manufacturing route for the raw powder, namely the synthesis from metallic Ti (metal route). The Ti(C,N) powder in this work was probably synthesized by carbothermal reduction of TiO_2 (CTS), causing rounder grains in the microstructure.

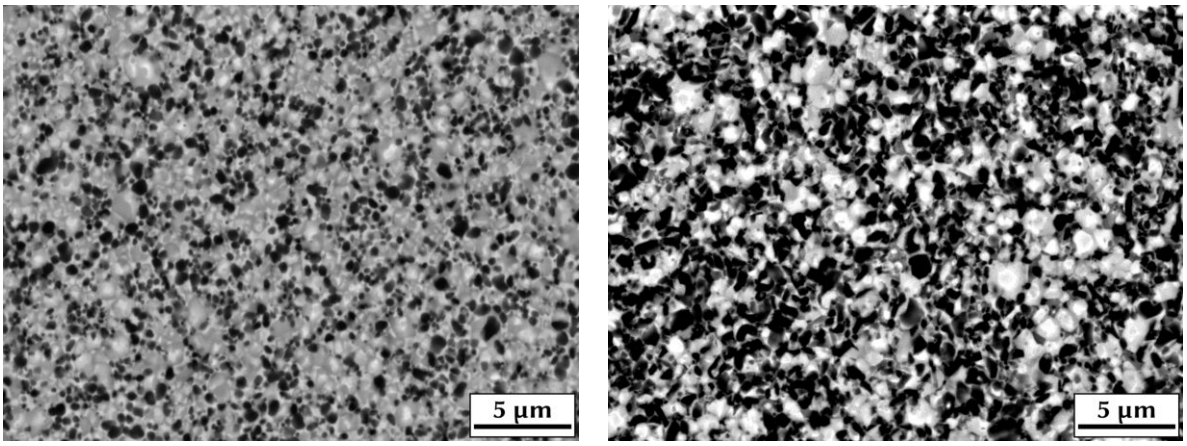

(a) I0-1_SAr, d_{50}=0.32 µm, slope=184.

(b) IA, d_{50}=0.31 µm, slope=173.

Figure 32: Microstructure of I0-1_SAr in comparison with the ID target grade, 10,000x magnification, , GSD parameters of cores.

The fine microstructure can also be seen in the parameters of the grain size distributions as estimated by the linear intercept method (table 26). With the exception of I2-3_SN, the iso-

lated Ti(C,N)-rich grains (cores) of all other grades show a smaller average grain size than the overall grains. Notably, samples sintered under nitrogen often have a very similar or even slightly increased average core size compared to samples sintered under argon. Higher nitrogen activity during sintering clearly shows a refining effect on the average grain size of the cermets. Coarser Ti(C,N) powders increase the average grain size of both cores and grains significantly, while the use of pre-alloyed powders has only a minor influence on the average grain size. However, the grain size distributions are broadened as indicated by lower slopes between d_{10} and d_{90}. Lastly, the addition of 0.4 wt% C has a minor influence on the core size but increased the grain size slightly.

Table 26: Summary of GSD parameters of the I series cermets as determined by linear intercept.

	cores			grains		
sample	**average**	**d_{50}**	**slope**	**average**	**d_{50}**	**slope**
I0-1_SAr	0.37	0.32	184	0.61	0.59	165
I0-1_SN	0.38	0.35	172	0.59	0.55	162
I0-2_SAr	0.38	0.32	162	0.49	0.46	184
I0-2_SN	0.40	0.35	162	0.47	0.45	223
I1-1_SAr	0.39	0.35	162	0.65	0.64	142
I1-1_SN	0.41	0.35	153	0.51	0.47	165
I1-2_SAr	0.36	0.32	184	0.51	0.48	212
I1-2_SN	0.34	0.32	230	0.49	0.45	172
I1-3_SAr	0.54	0.49	115	0.67	0.60	108
I1-3_SN	0.54	0.49	115	0.62	0.55	102
I2-1_SAr	0.39	0.32	153	0.70	0.65	113
I2-1_SN	0.41	0.35	138	0.53	0.49	142
I2-3_SAr	0.52	0.49	120	0.67	0.62	122
I2-3_SN	0.57	0.55	99	0.56	0.55	153
I3-1_SAr	0.53	0.46	106	0.65	0.58	126
I3-1_SN	0.57	0.55	110	0.61	0.58	120
I0-1+0.4%C_SAr	0.36	0.32	212	0.61	0.55	119
I0-1+0.4%C_SN	0.36	0.32	197	0.60	0.58	127
I1-1+0.4%C_SAr	0.38	0.35	173	0.67	0.63	97
I1-1+0.4%C_SN	0.35	0.32	197	0.63	0.59	126
I2-1+0.4%C_SAr	0.41	0.38	131	0.72	0.70	125
I2-1+0.4%C_SN	0.44	0.35	173	0.58	0.52	151

4.2.4. Mechanical properties

A comparison of the hardness and fracture toughness achieved for the I series cermets reveals two distinct groups (fig. 33). Samples based on the I0 and I1 formulations with the fine Ti(C,N) powders performed similar to the target grade of ID with I0-1 cermets being the closest. The other grades in this region show more or less similar hardness but lower fracture toughness

values.

The second group is shifted towards higher toughness values. Changing the Ti(C,N) to a coarser powder, a significantly higher fracture toughness could be obtained, whereas the hardness is slightly decreased. Grades based on pre-alloyed powders improve the fracture toughness to a similar extend while also slightly reducing the hardness.

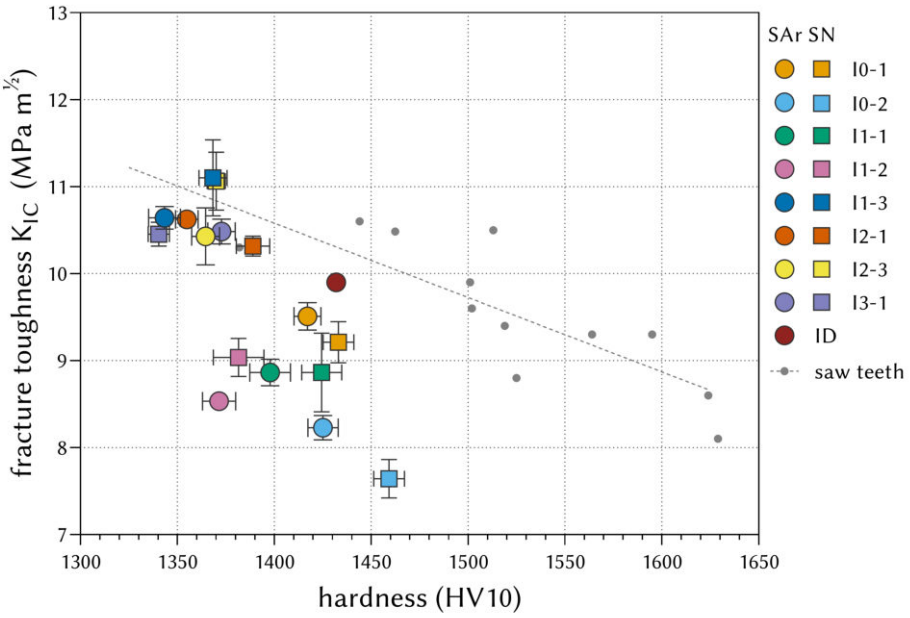

Figure 33: Hardness and fracture toughness of the I series cermets, ID target grade and the reference grades.

4.2.5. Influence of the sintering atmosphere

With the exception of the I3-1 formulation, cermets sintered under N_2 atmosphere are harder than those sintered in Ar. This is especially noteworthy as I3-1_SN has a significantly lower porosity (A02) than I3-1_SAr (A06). Cermets based on the I0-1, I0-2 and I2-1 formulations also show a decrease in fracture toughness similar to what can be expected from the slope of the trend line of the reference grades. Contrary to expectations, the other I series cermets sintered in nitrogen atmosphere show similar or even increased fracture toughness compared to those sintered in Ar. However, due to the relatively high standard errors for the fracture toughness, the sintering atmosphere during SinterHIP seems to have only a minor effect on the mechanical properties of the I series cermets. This is in contrast to the results of the N series cermets and the findings in literature. Usually, a significant increase in hardness and decrease in fracture toughness beyond the statistical error of the measurements was described [1, 7].

One reason for this behavior of the I series cermets could be the negligible influence of nitrogen on the Ti(C,N)-rich grains. In fig. 34 it is obvious, that the Ti(C,N)-rich cores are isolated and approximately the same size regardless of the sintering atmosphere. In many Ti(C,N)-based

cermets from literature, the classic core-rim grains can be formed when low N-activity was applied during sintering, while the Ti(C,N)-rich grains remain isolated when the N-activity of the gas phase is high. However, the relatively high N content in the $TiC_{0.5}N_{0.5}$ powder resulted in mostly isolated cores, even when Ar was used. Therefore, the higher N activity when switching to N_2 atmosphere did not inhibit grain growth significantly. Apart from the BSE-SEM images, this can also be observed in the average core and grain sizes: The sintering atmosphere has no obvious effect on the average core size and only a minor influence on the overall grain size.

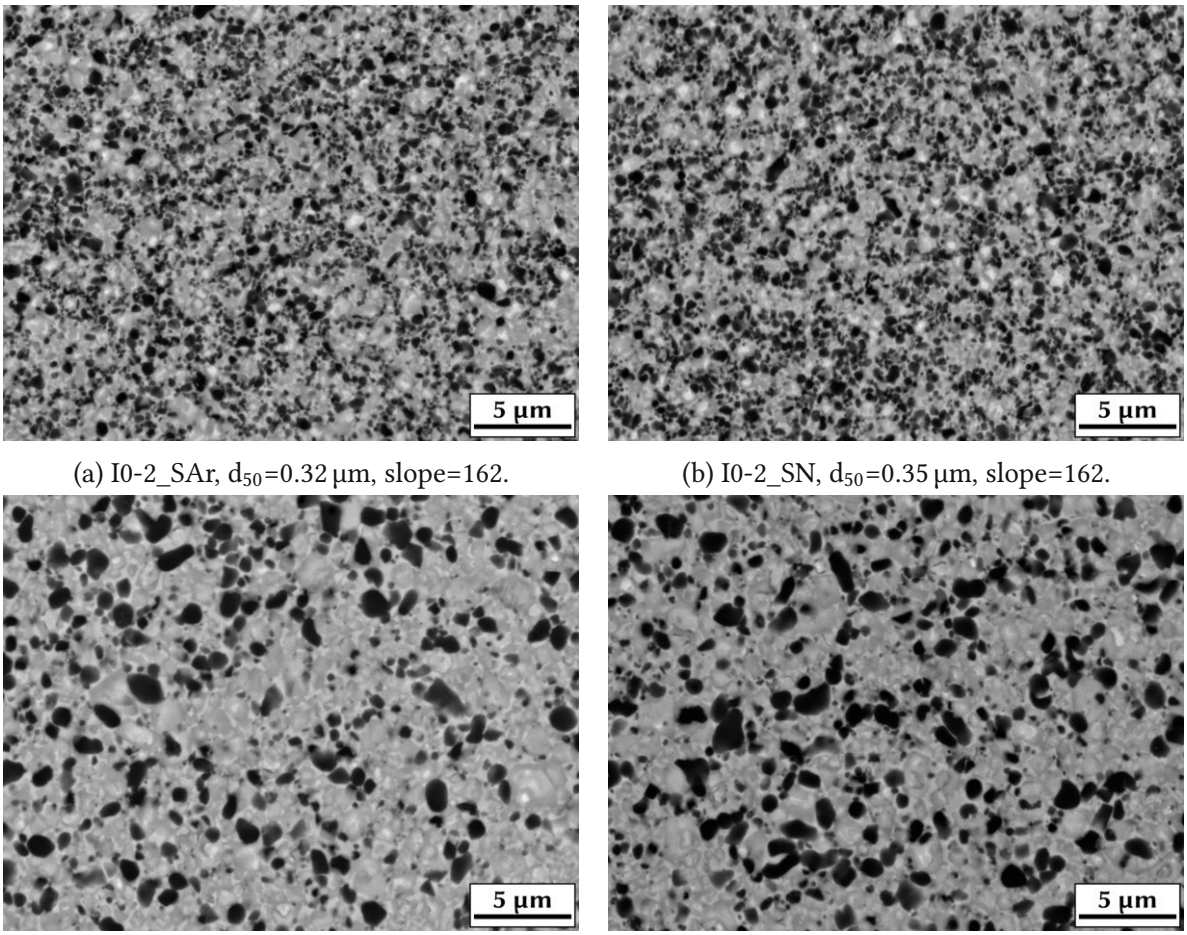

(a) I0-2_SAr, d_{50}=0.32 µm, slope=162.

(b) I0-2_SN, d_{50}=0.35 µm, slope=162.

(c) I2-3_SAr, d_{50}=0.49 µm, slope=120.

(d) I2-3_SN, d_{50}=0.55 µm, slope=99.

Figure 34: BSE-SEM images of I series cermets SinterHIPed in Ar or N_2, 10,000x magnification, GSD parameters of cores.

Lastly, the measurements of magnetic saturation and the binder phase lattice parameter are affected only marginally by the change in sintering atmosphere (tab. 25 and fig. 31). While no clear distinction can be observed between the two sintering atmospheres, some samples sintered in Ar show a slightly higher binder lattice parameter and lower magnetic saturation compared to samples sintered in N_2. This is in accordance with the results of most literature, where the higher N activity usually decreases the amount of dissolved elements in the binder due to the instability of W-N and Mo-N bonds [7]. The addition of 0.4 wt% carbon to the formulations decreases the amount of dissolved elements (as indicated by the higher magnetic saturation and lower binder phase lattice parameter) and slightly increases the difference between samples sintered under Ar or N_2. The solubility of heavier elements is reduced if the [non-metal]/[metal] ratio is decreased by the carbon addition.

4.2.6. Influence of the Ti(C,N) grain size

When using the coarser 1.76 µm Ti(C,N) in I1-3, the fracture toughness is significantly elevated both in Ar and N_2 compared to the cermets applying finer Ti(C,N) powders (I1-1 and I1-2). Larger grains tend to toughen cermets due to the higher energy required for crack propagation [1]. The BSE-SEM images in fig. 35 indeed confirm that the larger grain size of the starting powders remain visible after sintering. I1-1 and I1-2 reached average black core grain sizes of 0.39 and 0.36 µm in Ar and 0.41 and 0.34 µm in N_2, respectively, while the I1-3 cores averaged at 0.54 µm in both Ar and N_2. Therefore, the toughness increase by implementing the coarser Ti(C,N)-powder can be explained by the larger grain size in the GSD determined by linear intercept.

Furthermore, both binder lattice parameter and magnetic saturation of I1-3 are very similar to the finer cermets I1-1 and I1-2 and no obvious trend is detectable for cermets with different Ti(C,N) grain sizes. In fact, the measurements for the coarser I1-3 suggest an amount of dissolved elements between the finer I1-1 and I1-2 samples. Hence, the effect of binder strengthening by dissolution of elements and changes in the binder lattice parameter cannot be responsible for the increase in fracture toughness of I1-3.

In the I2 cermets, mostly (Ti,W)(C,N) was implemented in the formulation of the powder mixtures and Ti(C,N) was only added to reach identical C/N ratios. Hence, a less pronounced influence of the Ti(C,N) powder grain size can be expected. This is indeed confirmed by the microstructure and in the GSD parameters of cermets I2-1 and I2-3. While the average core size increases with coarser Ti(C,N) powder, the average grain size of total grains are very close for both compositions. Nevertheless, the binder phase shows a significant influence of the grain size. With the coarser Ti(C,N) powder, less elements can dissolve in the binder phase resulting in a smaller lattice parameter and a higher magnetic saturation. This can be explained by the reduction of surface area of the Ti(C,N) grains and thus a reduced dissolution of Ti in the binder when coarser powders are used.

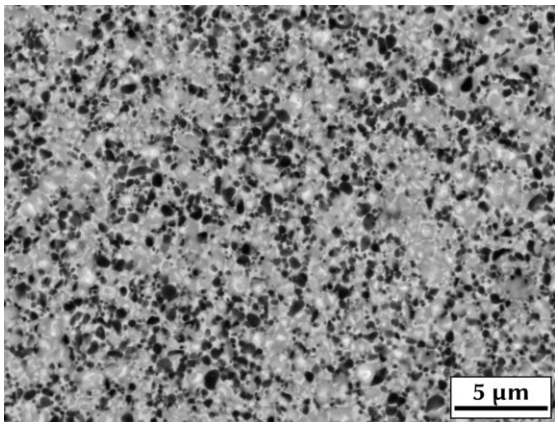

(a) I1-2_SAr, 0.85 µm Ti(C,N).

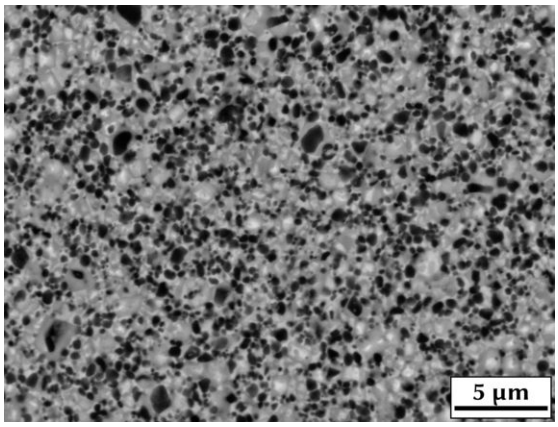

(b) I1-1_SAr, 0.88 µm Ti(C,N).

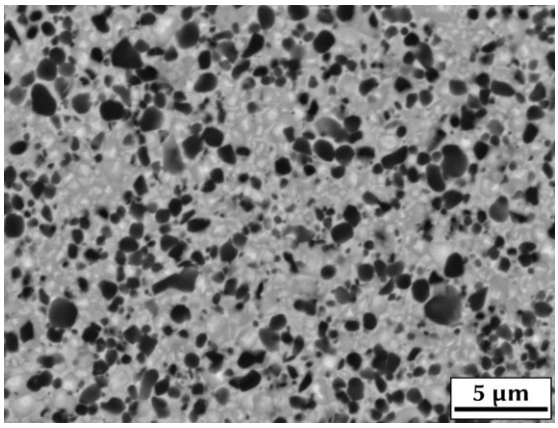

(c) I1-3_SAr, 1.76 µm Ti(C,N).

Figure 35: Influence of the Ti(C,N) powder grain size on the microstructure in I cermets, BSE-SEM images, 10,000x magnification.

4.2.7. Influence of the powder alloy state

Cermet samples based on (Ti,W)(C,N) and (Ti,W)C powders have significantly increased fracture toughness and decreased hardness compared to the Ti(C,N) + WC based cermets. The exception is I2-3 with very similar mechanical properties to the analogous I1-3 sample. This trend can be explained with the differences in the microstructure. When pre-alloyed starting materials are utilized, the formation of inverse grains with a light core and gray rim is more pronounced (see fig. 36). Additionally, pre-alloyed powders also led to a slightly larger average grain size that are especially visible in the microstructure of I2-1. This is in accordance with literature, where higher amounts of inverse and larger grains result in high toughness and a corresponding decrease in hardness [19].
Contrary to some findings in literature (e.g. Lv et al. [20] or Waldner et al. [21]), pre-alloyed powders did not increase the binder phase lattice parameter and decrease the magnetic saturation in the tested samples. In fact, I2-1 and I2-3 show a smaller lattice parameter and a higher magnetic saturation suggesting a lower amount of dissolved elements despite the unstable W-N bonds in the (Ti,W)(C,N) powder used. To a lesser extend, this was also observed for the I3-1 cermet with (Ti,W)C.

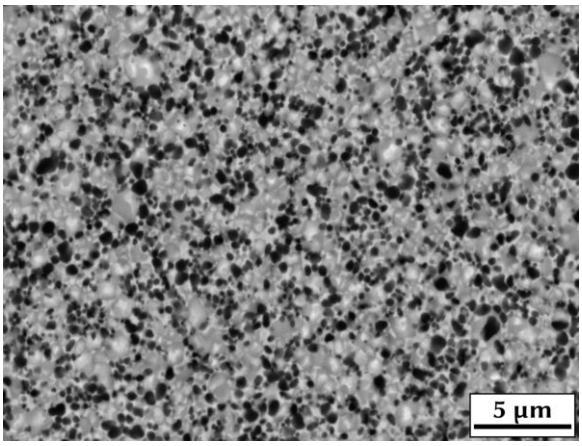

(a) I0-1_SAr, Ti(C,N) + WC.

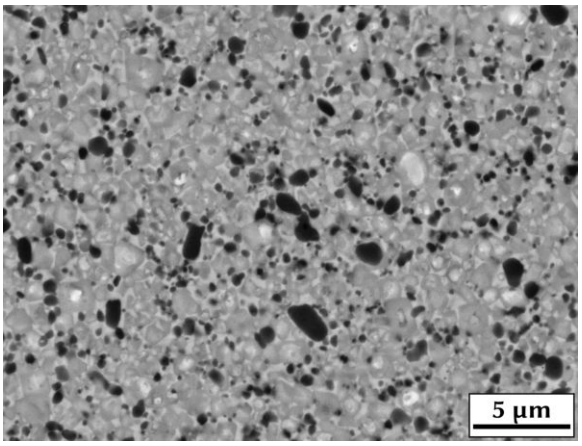

(b) I2-1_SAr, (Ti,W)(C,N).

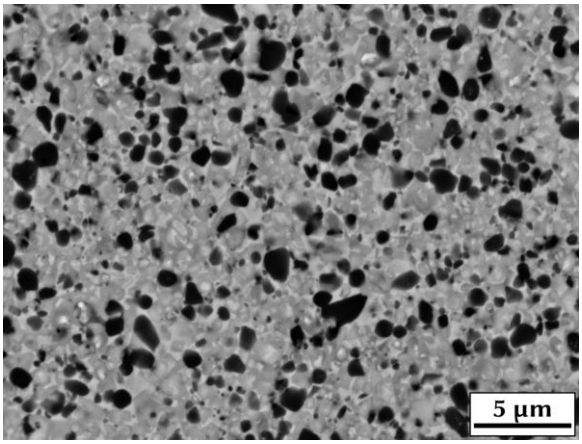

(c) I3-1_SAr, (Ti,W)C.

Figure 36: Comparison of the microstructure of I cermets with different powder alloy states, BSE-SEM images, 10,000x magnification.

4.2.8. Influence of the carbon content

Fig. 37 depicts the influence of adding 0.4 wt% C on the mechanical properties of selected I cermets. With the exception of I2-1+0.4%C_SAr, the additional carbon increased the fracture toughness and decreased the hardness of the base powders. Cermets based on I0-1+0.4%C show very similar mechanical properties sintered in Ar or N_2 and even overlap in the graph. As discussed earlier, Ar or N_2 generally have a negligible effect on the I series cermets, therefore the effect of C addition on the microstructure is shown only for samples sintered in Ar in fig. 38. For I0-1 and I1-1, the addition of C led to a lower amount of Ti(C,N)-rich isolated cores and more core-rim grains. The addition of pure C obviously changed the C/N ratio to an extend where rim phase could precipitate around the cores. The formation of the tougher rim phase and the decrease in isolated Ti(C,N) hard phase could be responsible for the higher fracture toughness. In the I2-1 formulation, the amount of dark cores increases and some core-rim grains can be identified. Due to the smaller amount of implemented Ti(C,N), the effects of C addition are less pronounced compared to I0-1 and I1-1.

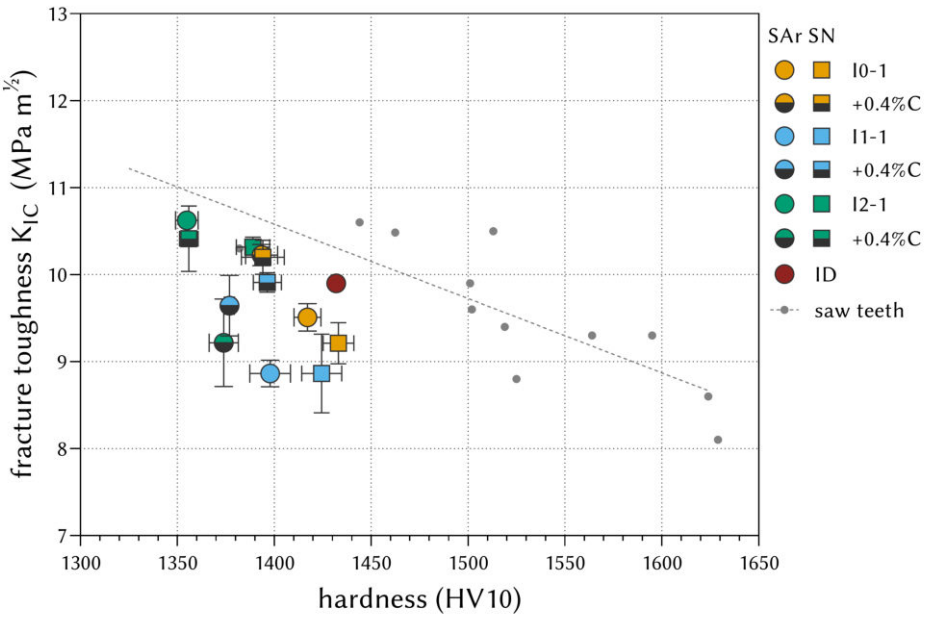

Figure 37: Hardness and fracture toughness of the I cermets with 0.4%C addition, ID target grade and the comparison grades.

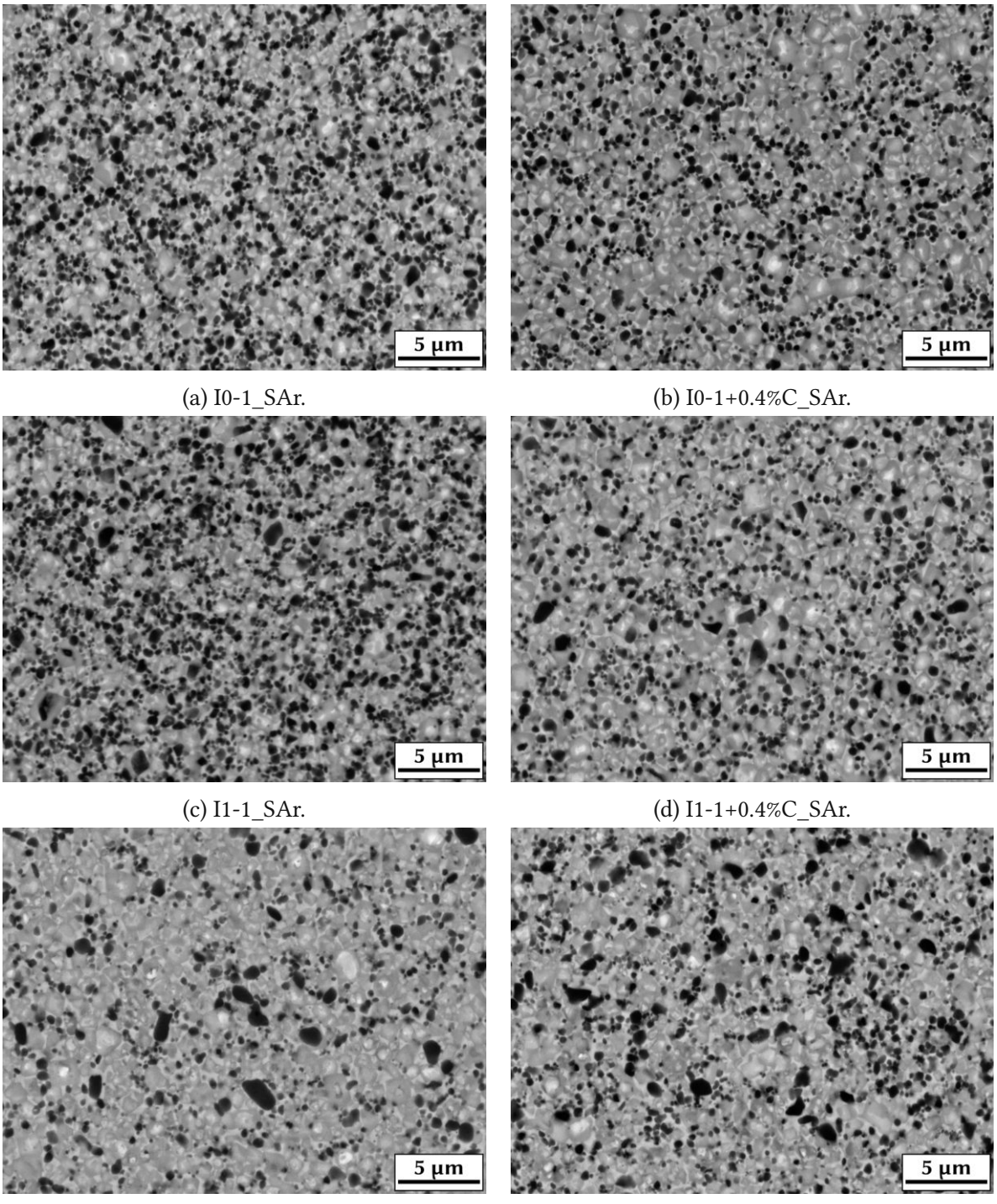

(a) I0-1_SAr. (b) I0-1+0.4%C_SAr.

(c) I1-1_SAr. (d) I1-1+0.4%C_SAr.

(e) I2-1_SAr. (f) I2-1+0.4%C_SAr.

Figure 38: Influence of 0.4 wt% C addition on the microstructure of I cermets, BSE-SEM images, 10,000x magnification.

4.3. N series - vacuum sintering

4.3.1. Porosity and dimensional change

Tab. 27 summarizes the porosity classes of the vacuum sintered N series cermets evaluated from the LOM images in fig. 87 to 121. Lowest porosity was achieved for cermets of the N series using finer Ti(C,N) powders that were sintered in 10 mbar N_2. Corresponding formulations sintered in Ar showed porosities that were of class A06 B00 C00. When coarser Ti(C,N) was used in cermets N1-3 and N1-4, the trend was the opposite: Sintering under Ar produced samples with lower porosities than sintering under N_2. For the cermets of the N2 and N3 series, a higher porosity was obtained overall, although literature suggests that pre-alloyed powders improve the sintering activity in cermets and therefore improve densification [19].

Table 27: Apparent porosity of vacuum sintered cermets from the N series.

	Porosity Class	
	Ar	**10N**
N0-1	A06 B00 C00	A02 B00 C00
N0-2	A06 B00 C00	A02 B00 C00
N1-1	A06 B00 C00	A02 B00 C00
N1-2	A06 B00 C00	A02 B00 C00
N1-3	A02 B00 C00	A08 B00 C00
N1-4	A02 B00 C00	A08 B00 C00
N2-1	A06 B00 C00	A08 B00 C00
N2-2	A08 B00 C00	A06 B00 C00
N2-3	A08 B00 C00	A08 B00 C00
N3-1	A08 B00 C00	A08 B00 C00
N3-2	A08 B00 C00	A08 B00 C00
N3-3	A08 B00 C00	A08 B00 C00

The Archimedes densities and dimensional changes of the N series cermets are listed in table 28. With densities of approximately 6.9 g/cm^3 (97 % of theoretical 7.118 g/cm^3), the densification was similar to the I cermets (95 to 99 % of theory). After sintering, the samples were approximately 20 to 21% smaller and 2-3% lighter. Weight loss above 3% could be caused by minor splintering of the surface after sintering as no paraffin wax was added to the N series formulations before pressing.

4.3.2. Phase analysis and magnetic properties

For phase analysis, the XRD pattern in figures 87 to 121 in the appendix were evaluated. Tab. 29 lists the evaluation of the peak form, hard phase lattice parameters, relative changes in the binder phase lattice parameters and magnetic saturation. Differences in the elemental composition between the N and I series cermets are also visible in these parameters. In contrast to the I series, the vacuum sintered N series cermets show a linear correlation between the increase in binder phase lattice parameter and magnetic saturation (see fig. 39). Cermets sintered under

Table 28: Archimedes density ρ_A in g/cm^3, shrinkage in diameter (d) and height (h) and mass loss (m) of vacuum sintered N series cermets.

		shrinkage					shrinkage		
sample	**ρ_A**	**d (%)**	**h (%)**	**m (%)**	**sample**	**ρ_A**	**d (%)**	**h (%)**	**m (%)**
N0-1_Ar	6.931	21.1	21.0	2.5	N0-1_10N	6.928	21.4	21.1	2.3
N0-2_Ar	6.960	21.7	21.9	2.8	N0-2_10N	6.938	22.0	21.3	2.6
N1-1_Ar	6.913	21.1	20.9	2.4	N1-1_10N	6.911	21.2	20.4	2.4
N1-2_Ar	6.893	21.4	21.4	2.6	N1-2_10N	6.905	21.5	21.2	2.6
N1-3_Ar	6.883	20.9	21.0	2.3	N1-3_10N	6.873	21.0	20.5	2.3
N1-4_Ar	6.887	20.7	20.6	2.6	N1-4_10N	6.901	20.7	20.1	2.6
N2-1_Ar	6.899	19.8	20.8	2.2	N2-1_10N	6.919	20.0	20.7	1.8
N2-2_Ar	6.915	19.8	21.2	2.4	N2-2_10N	6.930	20.1	20.4	1.9
N2-3_Ar	6.938	21.0	21.8	3.1	N2-3_10N	6.922	20.9	21.2	2.7
N3-1_Ar	6.944	21.4	21.8	1.8	N3-1_10N	6.928	21.4	21.3	3.2
N3-2_Ar	6.929	21.0	21.4	1.9	N3-2_10N	6.914	21.0	19.8	2.7
N3-3_Ar	6.932	20.2	20.2	2.7	N3-3_10N	6.924	20.2	20.1	2.3

N_2 are clearly separated from those sintered under Ar. They show the highest magnetic saturation and lowest increase in lattice parameter, therefore a low amount of dissolved elements in the binder can be assumed. Ar samples are further divided into two sub groups: N1 series and N2-1 have an intermediate amount of dissolved elements, while N0, N3 series and N2-3 dissolved the most atoms.

Similar to the I series cermets, two distinct hard phase patterns can be observed in the XRD for most samples. The lower lattice parameter is closer to pure Ti(C,N) (a=4.279 [33]) and thus to the dark cores, while the other phase with a higher lattice parameter correlates with the complex (Ti,W,Mo,...)(C,N) rim phases. The exceptions are N2 series, N3-1 and N3-2 cermets, where the patterns strongly overlap and only one lattice parameter could be determined. Again, the addition of the larger grain size of the admixed Ti(C,N) in N3-3 led to two distinguishable hard phase pattern.

Interestingly, an additional eta phase could be identified in the XRD of most N series cermets sintered under N_2. In WC-Co hardmetals, eta phases (e.g. Co_3W_3C or Co_6W_6C phases) can form due to a too low C content in the composition. Because these eta phases are hard and brittle, this is typically avoided by C addition to arrive in a very narrow C window, the two phase region in the WC-Co phase diagram. Due to the higher tolerance for non-metal deficiency in the Ti-C-N system earlier discussed in fig. 1a, eta phase is usually observed for cermets with quite low ([C]+[N])/[Me] ratio sintered in an atmosphere with low C activity such as pure Ar. Surprisingly, this eta phases could be observed for the N series samples with a [non-metal]/[metal] ratio near one (([C]+[N])/[Me] = 0.98) and sintering under various partial pressures of N_2.

Table 29: Lattice parameters in Å, peak form and relative magnetic saturation of vacuum sintered N series cermets. Relative increase of the binder phase lattice parameter (B_{rel}, magnetic saturation (MS) in comparison to the pure Co/Ni binder and total concentration of dissolved elements in the binder phase (mol%).

sample	peak form	H1	H2	B	B_{rel} (%)	MS (%)	c (mol%)
N0-1_Ar	doublet	4.3226	4.2818	3.6082	1.81	29.8	15.1
N0-1_10N	doublet	4.3284	4.2802	3.5936	1.40	57.0	9.7
N0-2_Ar	doublet	4.3213	4.2831	3.6114	1.90	18.8	17.3
N0-2_10N	doublet	4.3271	4.2803	3.5900	1.30	56.5	9.8
N1-1_Ar	doublet	4.3209	4.2828	3.6000	1.58	44.7	12.1
N1-1_10N	doublet	4.3263	4.2840	3.5888	1.26	62.7	8.5
N1-2_Ar	doublet	4.3229	4.2872	3.6011	1.69	42.2	12.6
N1-2_10N	doublet	4.3255	4.2852	3.5900	1.30	60.0	9.1
N1-3_Ar	doublet	4.3240	4.2890	3.6011	1.61	43.2	12.4
N1-3_10N	doublet	4.3267	4.2841	3.5874	1.22	61.1	8.8
N1-4_Ar	doublet	4.3249	4.2970	3.6035	1.68	39.6	13.1
N1-4_10N	doublet	4.3230	4.2823	3.5899	1.30	59.5	9.2
N2-1_Ar	singlet	4.3200	-	3.6010	1.61	46.8	11.7
N2-1_10N	singlet	4.3216	-	3.5887	1.26	67.1	7.6
N2-2_Ar	singlet	4.3173	-	3.6037	1.68	40.2	13.0
N2-2_10N	singlet	4.3208	-	3.5883	1.25	67.3	7.6
N2-3_Ar	singlet	4.3203	-	3.6164	2.04	22.8	16.5
N2-3_10N	singlet	4.3203	-	3.5904	1.31	61.3	8.8
N3-1_Ar	singlet	4.3216	-	3.6165	2.05	25.2	16.0
N3-1_10N	doublet	4.3243	4.2796	3.5910	1.33	52.9	10.5
N3-2_Ar	singlet	4.3191	-	3.6084	1.82	32.1	14.6
N3-2_10N	doublet	4.3250	4.2756	3.5910	1.33	56.7	9.7
N3-3_Ar	doublet	4.3253	4.2909	3.6061	1.75	32.7	14.5
N3-3_10N	doublet	4.3262	4.2819	3.5920	1.35	57.1	9.6

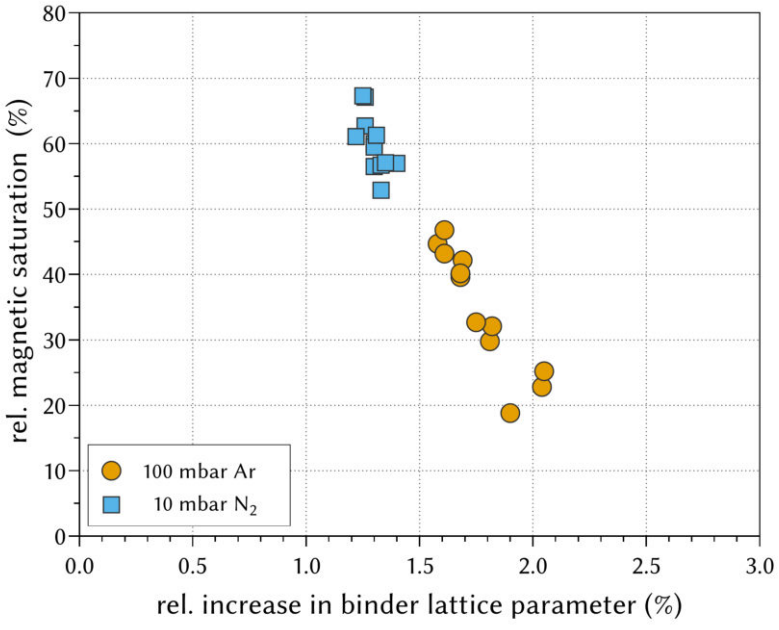

Figure 39: Correlation of relative increase in binder phase lattice parameter and magnetic saturation for the vacuum sintered N series cermets.

4.3.3. Microstructure and grain size distribution

The microstructure of the vacuum sintered N series cermets are presented in the BSE-SEM images and the corresponding grain size distributions in figures 87 to 121 in the appendix. The microstructures are also comparable to those of the I series because the same raw powders and similar sintering atmospheres were used. Ti(C,N)-rich dark grains appear mostly isolated, except when coarser $TiC_{0.7}N_{0.3}$ was added to exactly match the target's C/N ratio. Furthermore, there is a large amount of inverse grains or even coreless gray grains. In these aspects, N0-1_Ar closely resembled the microstructure of the N8 target grade. However, differences include the shape and size of the Ti(C,N)-rich dark cores. In N8, probably a coarser Ti(C,N) powder was implemented and more dark cores remained visible in the microstructure after sintering.

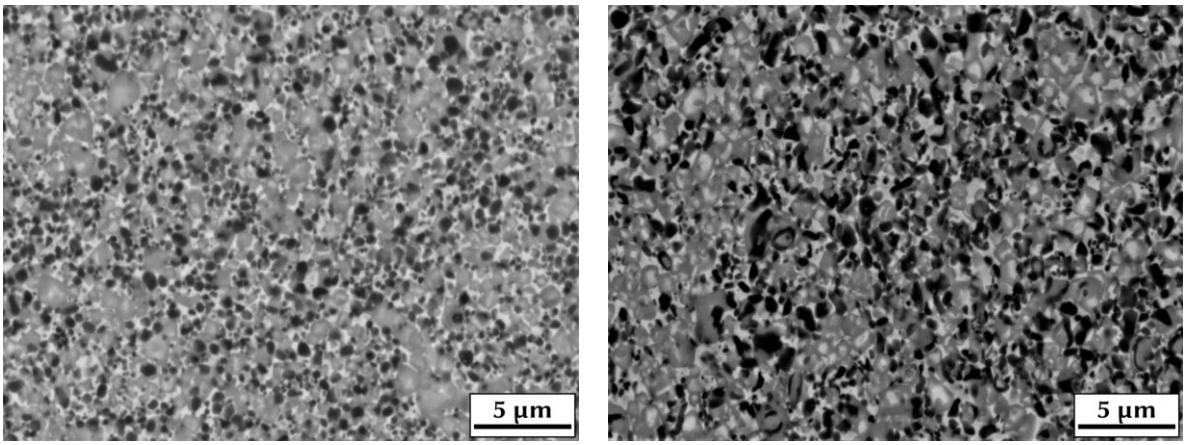

(a) N0-1_Ar. (b) N8 target grade.

Figure 40: Microstructure of N0-1_Ar in comparison with the N8 target grade, BSE-SEM, 10,000x magnification.

Average grain sizes, d_{50} and slope values for both cores and grains were gained by the linear intercept method and are summarized in table 30. As can be expected, the GSD of cores show a smaller average grain size than the overall grains. Furthermore, they are clearly influenced by the Ti(C,N) grain size used in the starting formulation. The coarsest Ti(C,N) powders also led to broader distributions, as indicated by smaller slopes between d_{10} and d_{90} values (see tab. 30). On the other hand, the grain refining effect of N_2 in the sintering atmosphere is most predominantly visible in the GSD of overall grains.

Table 30: Summary of GSD parameters of vacuum sintered N series cermets as determined by linear intercept.

	cores			grains		
sample	**average**	**d_{50}**	**slope**	**average**	**d_{50}**	**slope**
N0-1_Ar	0.43	0.35	130	0.71	0.56	109
N0-1_10N	0.36	0.32	212	0.71	0.54	99
N0-2_Ar	0.38	0.32	150	0.64	0.49	121
N0-2_10N	0.35	0.29	172	0.64	0.5	162
N1-1_Ar	0.39	0.35	153	0.79	0.57	99
N1-1_10N	0.44	0.35	120	0.75	0.56	102
N1-2_Ar	0.43	0.35	131	0.78	0.58	107
N1-2_10N	0.39	0.32	153	0.87	0.83	75
N1-3_Ar	0.54	0.49	98	0.84	0.59	84
N1-3_10N	0.51	0.43	115	0.99	0.91	84
N1-4_Ar	0.46	0.41	125	0.77	0.59	112
N1-4_10N	0.44	0.38	138	0.83	0.77	91
N2-1_Ar	0.4	0.32	138	0.77	0.71	97
N2-1_10N	0.39	0.38	162	0.84	0.8	90
N2-2_Ar	0.37	0.35	172	0.82	0.78	120
N2-2_10N	0.42	0.38	131	0.67	0.62	123
N2-3_Ar	0.54	0.46	95	0.86	0.79	97
N2-3_10N	0.53	0.43	92	1.02	0.97	86
N3-1_Ar	0.35	0.32	184	0.81	0.74	113
N3-1_10N	0.35	0.32	197	0.76	0.7	109
N3-2_Ar	0.35	0.32	197	0.76	0.72	120
N3-2_10N	0.35	0.29	184	0.87	0.79	98
N3-3_Ar	0.55	0.49	95	0.87	0.8	95
N3-3_10N	0.52	0.43	102	0.96	0.9	95

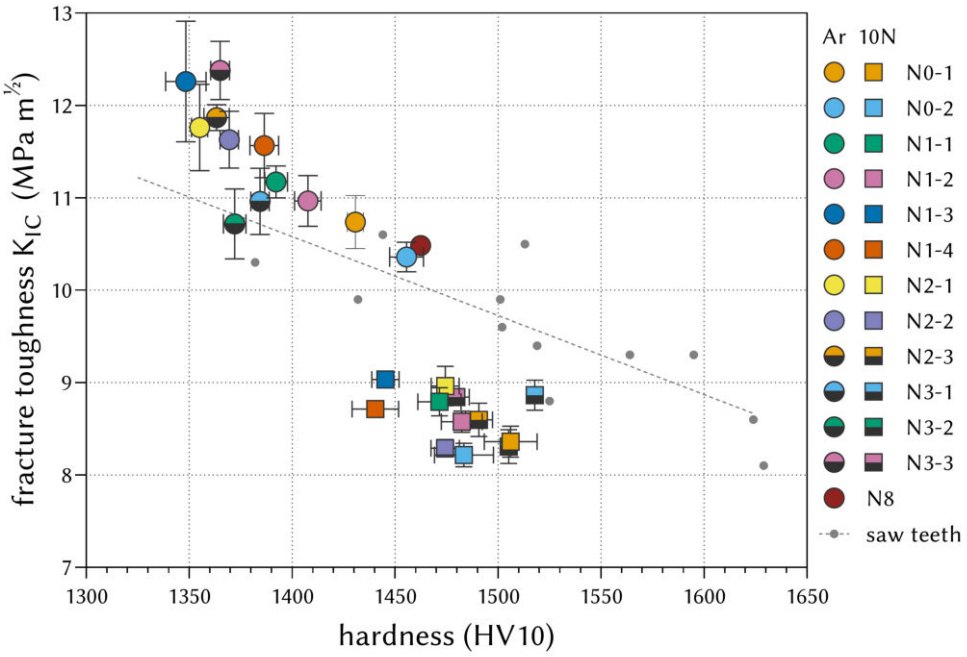

Figure 41: Hardness and fracture toughness of vacuum sintered N series, N8 target grade, saw teeth and trendline as comparison.

4.3.4. Mechanical properties

Fig. 41 provides an overview of the mechanical properties of N series cermets in comparison to all tested saw teeth (gray) and their respective trendline. All samples sintered under Ar perform similarly to the N8 target grade or reach even higher fracture toughness with a corresponding reduction in hardness. Also, nearly all Ar sintered samples perform significantly above the expected correlation between hardness and toughness as indicated by the trendline of the tested saw teeth. In contrast, all cermets with N_2 in the sintering atmosphere show a distinct drop-off in toughness and an improvement in hardness. This loss of fracture toughness is higher than expected from the general trend and is caused by the formation of brittle eta phase as confirmed by XRD measurements.

4.3.5. Influence of the sintering atmosphere

Fig. 42 compares the microstructures of two example formulations after sintering under Ar and 10 mbar N_2. Ar led to the formation of some core-rim grains, especially when C-rich Ti(C,N) was included in the formulation to balance the C/N ratio. However, most black cores still remained isolated, with inverse and coreless gray grains being present. Sintering in N_2 decreased the amount of core-rim grains and also had a grain refining effect. This grain refinement is clearly visible in the GSD of overall grains, but also led to some agglomeration of very fine Ti(C,N)-rich grains between the inverse and gray grains. In some samples, a very bright extra phase was observed in the binder, further confirming the presence of eta phase in the 10N cermets. This brittle eta phase is most likely responsible for the poor fracture toughness achieved by the cermets sintered under N_2 atmosphere.
The sintering atmosphere also clearly influenced the level of dissolved elements in the binder. In Ar, relatively high amounts of heavier elements were incorporated into the binder phase lattice, leading to higher lattice parameters and lower magnetic saturation. In addition to the larger average grain size, this incorporation of foreign atoms changes the lattice parameter and provides a strengthening effect as well as higher fracture toughness of the cermet.

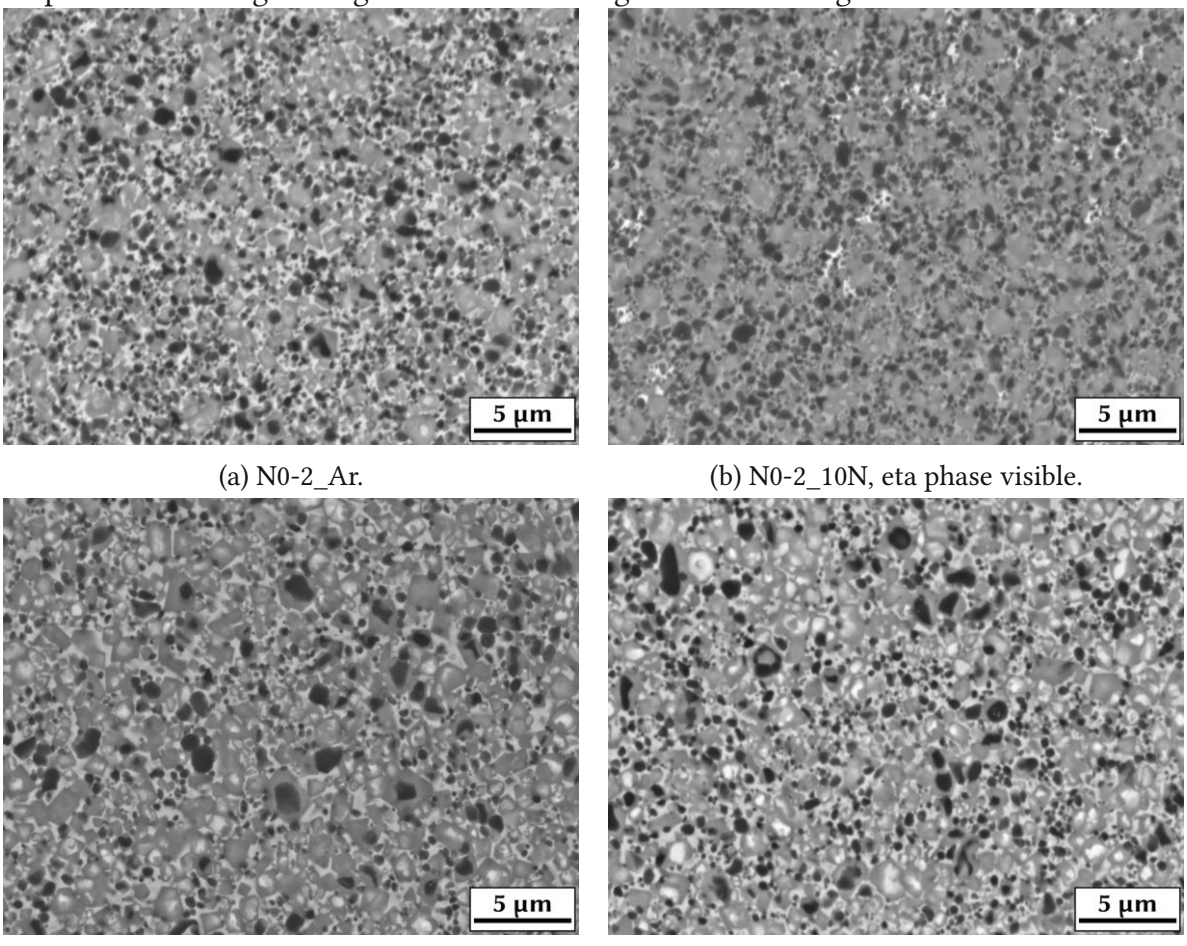

(a) N0-2_Ar. (b) N0-2_10N, eta phase visible.

(c) N2-1_Ar. (d) N2-1_10N.

Figure 42: Microstructure of vacuum sintered N series cermets as a function of the sintering atmosphere, BSE-SEM, 10,000x magnification.

4.3.6. Influence of the Ti(C,N) grain size

After sintering in Ar, the Ti(C,N)-rich dark cores in fig. 43 still show the different grain sizes used in the powder mixtures of the N1 Series cermets. Although the addition of $TiC_{0.7}N_{0.3}$ resulted in the formation of some coarse core-rim grains in all four samples, the GSD of cores and grains both reflect the increased grain size. While the bigger surface area of the finer Ti(C,N) provides more sintering activity and therefore could lead to a higher solubility of Ti in the binder, the lattice parameters and magnetic saturation reveal no conclusive trend for the N1 cermets. Therefore, the binder phase solubility is likely dominated by the integration of heavier elements such as W, Mo or Nb.

The mechanical properties of the N1 Series follows an obvious trend: An increase in the Ti(C,N) powder grain size leads to higher fracture toughness and a corresponding lower hardness. This is most likely caused by a higher energy absorbed through crack deflection by the larger grains in the microstructure together with a transgranular fracture behavior.

The average grain size of cores correlates with the Ti(C,N) grain size added even when mainly (Ti,W)(C,N) or (Ti,W)C was used as hard phase in the N2 and N3 samples. However, the overall grain size was less affected since Ti(C,N) was added in smaller amounts to obtain the desired elemental composition. Results of the binder phase analysis suggest that the coarser Ti(C,N) in N2-3 led to the largest lattice parameter and very low magnetic saturation, while the trend was reversed in the N3 series. In fact, N3-3 revealed the smallest lattice parameter and highest magnetic saturation of the subset. Hence it is possible that the high N activity in the (Ti,W)(C,N) in combination with the less sinter active coarser Ti(C,N) powder led to an increased solubility of W due to the unstable W-N bond. The thermodynamically favored W-C bonds in the N3 series could cause the Ti incorporation to be dominant in the binder strengthening mechanism.

With only minor differences in overall average grain size and despite the differences in the Ti(C,N) powders, the N2 Series cermets perform very uniformly. However, the maximum fracture toughness was still achieved by the N2-3 cermet, likely due to the binder strengthening by high amounts of dissolved elements. Similar results were accomplished for the N3 series, where the combination of pre-alloyed powders and larger average grain size in N3-3 produced the toughest cermet of all tested configurations.

As discussed earlier, sintering in N-rich atmosphere resulted in a higher brittleness due to the formation of eta phase. Hence, the influence of the grain size can hardly be judged for these cermets. However, some similarities to the Ar samples have become apparent: The powder grain size mostly affected the Ti(C,N)-rich cores in the microstructure. For the binder phase, no clear influence can be seen for the magnetic saturation or binder phase lattice parameter (see tab. 29).

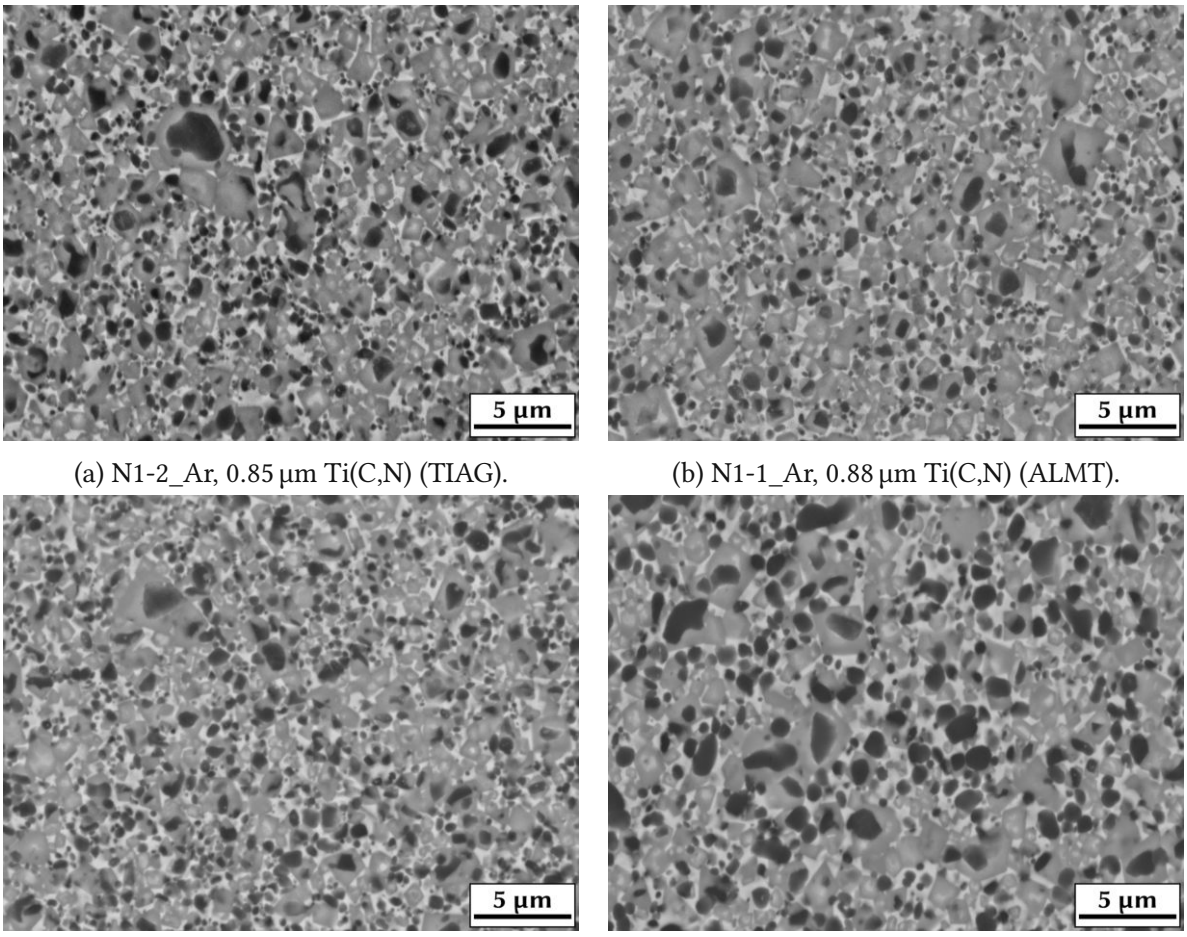

(a) N1-2_Ar, 0.85 µm Ti(C,N) (TIAG).

(b) N1-1_Ar, 0.88 µm Ti(C,N) (ALMT).

(c) N1-4_Ar, 1.07 µm Ti(C,N) (TIAG).

(d) N1-3_Ar, 1.76 µm Ti(C,N) (TIAG).

Figure 43: Microstructure of vacuum sintered N series cermets as a function of the Ti(C,N) powder grain size, BSE-SEM, 10,000x magnification.

4.3.7. Influence of the powder alloy state

Some minor differences in the microstructure can be seen for cermets with varying powder alloy states in fig. 44. When pre-alloyed powders were used, the light core of inverse grains is much more pronounced. Overall, there are less coreless, gray grains and more inverse grains. Instead of the $TiC_{0.7}N_{0.3}$ used in the other series, N-rich $TiC_{0.3}N_{0.7}$ was added to the N3 cermets containing (Ti,W)C to balance the C/N ratio. This led to more isolated Ti(C,N) grains and no core-rim grains. Furthermore, some agglomeration of dark cores is apparent. Exchanging the Ti(C,N) for (Ti,W)(C,N) in the N2 series improved the fracture toughness significantly. Most likely, this resulted from an increased amount of tough inverse grains. In the N3 series, even better toughness levels were achieved with (Ti,W)C powder. One exception is the N3-2 formulation, were actually worse mechanical properties were measured despite the binder phase analysis indicating a high amount of dissolved elements.

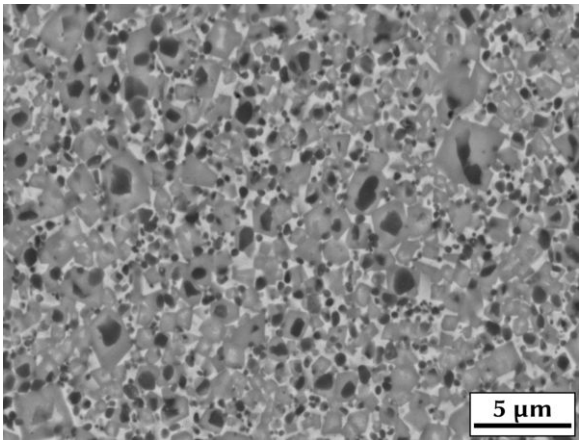

(a) N1-1_Ar, Ti(C,N) + WC.

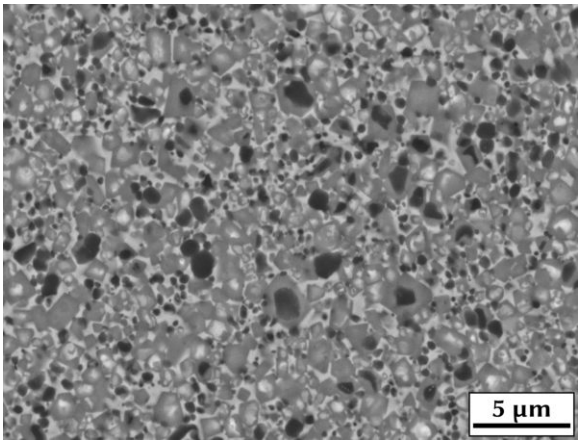

(b) N2-1_Ar, (Ti,W)(C,N).

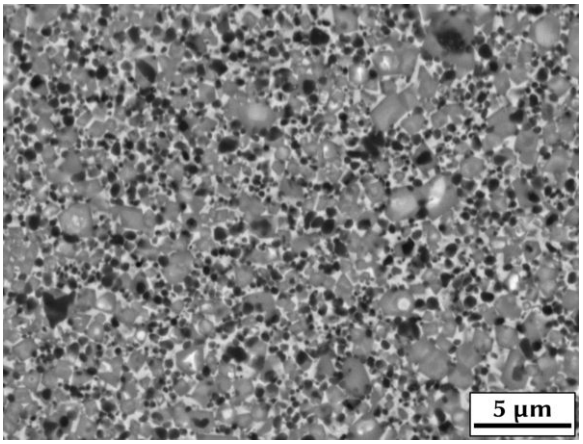

(c) N3-1_Ar, (Ti,W)C.

Figure 44: Microstructure of vacuum sintered N series cermets with different powder alloy states, BSE-SEM, 10,000x magnification.

4.3.8. Adjusted sintering atmospheres and C addition

To gain further insight into the eta phase formation, N Series samples were also sintered in an adjusted sintering atmosphere of 50 mbar N_2. Despite the possible increase in the [non metal]/[metal] ratio due to the higher N activity, the poor mechanical properties suggest the presence of brittle eta phase (see fig. 45). In fact, the cermets generally were harder and more brittle than the corresponding formulations sintered in only 10 mbar N_2. The XRD and BSE-SEM investigations (fig. 89 to 122 in the appendix) confirmed that eta phase was indeed present in all of the samples. While the hardness increase is also a result of the grain refining effect of N, optical evaluation of the microstructure suggests even more eta phase than observed in the 10N cermets. This could also be responsible for the higher apparent porosity of the 50N samples, as brittle eta phase might have broken out during the polishing process.
Because the increased N activity did not prevent the formation of eta phase, 0.1 and 0.3 wt% pure C were added to three of the powder mixtures. Additionally, the sintering atmosphere was changed to 10 mbar pure N_2 without any Ar as counter pressure. Fig. 46 shows the mechanical properties of these cermets. While the adjusted sintering profile (10Np) did improve the un-doped cermet formulations, the fracture toughness is still lower than expected from the trendline. A higher C content of 0.1 or 0.3 wt% finally improved the hardness for the formulations N0-2 and N1-2, while it mostly stayed constant for N2-2. This could be due to the higher C activity increasing the hardness of Ti(C,N) in the binary formulations of the N0 and N1 cermets (fig. 1b). On the other hand, the fracture toughness was not substantially influenced by the C content. As XRD and BSE-SEM analysis confirmed, this is again mediated by the presence of eta phase even for the samples with a substantial 0.3 wt% C addition. This suggests that the C activity is still too low when any partial pressure of N_2 is added to the sintering atmosphere during vacuum sintering.
For further investigations, the C, N and O content of some N series powder mixtures and cermets sintered in different atmospheres was analyzed. The results and the calculated molar [C+N]/[metal] and [C]/[metal] ratios can be found in tab. 31. After sintering, the approx. 2 wt% oxygen of the powder mixtures is lowered to contents between 0.1 and 0.2 wt%. This also resulted in a decrease in the carbon content as the oxygen was reduced to CO during sintering. Therefore, the [C+N]/[metal] and [C]/[metal] ratios are also lower than the ratios of the corresponding powder formulations. Comparing the influence of Ar and N_2 in the sintering atmosphere, it can be seen that the [C]/[metal] ratio is lowered the higher the partial pressure of N_2 was in the furnace. As eta phase was only formed in the samples sintered under N_2, it seems that the critical threshold is between the [C]/[metal] ratios of the Ar and 10 N cermets.

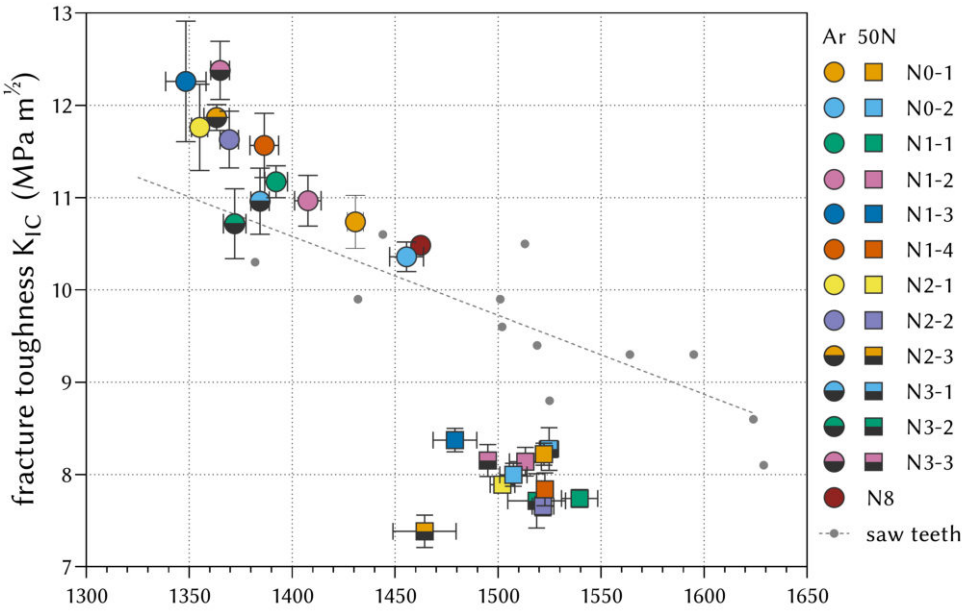

Figure 45: Hardness and fracture toughness of N series cermets sintered under 50 mbar N_2.

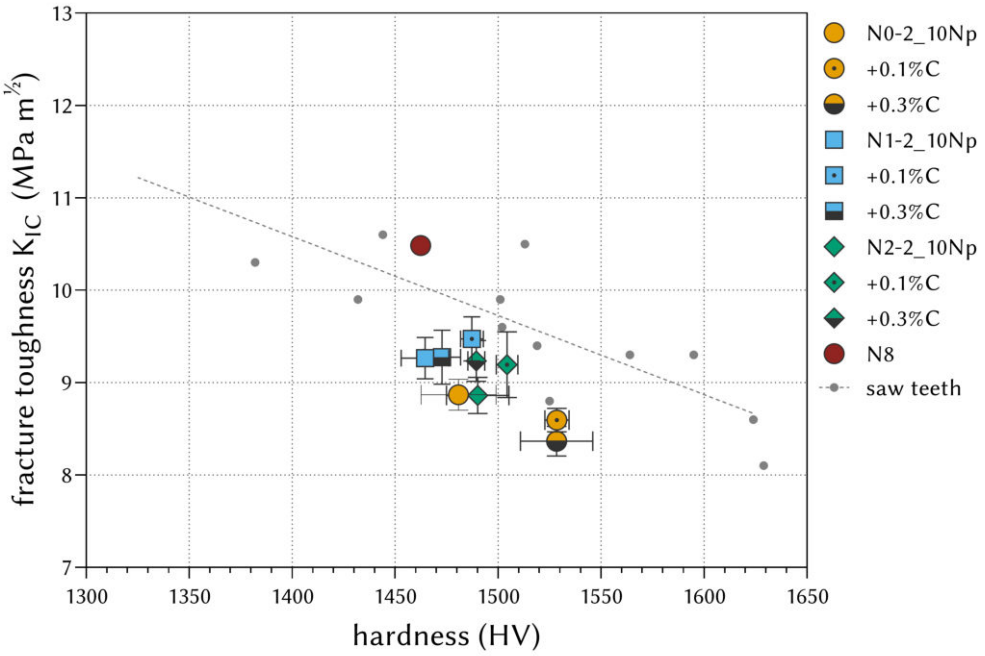

Figure 46: Hardness and fracture toughness of N series cermets with C addition and adjusted sintering atmosphere.

Table 31: Results of the C, N and O analysis of the powder mixtures and vacuum sintered N series cermets with molar ratios of the hard phase.

	content (wt%)			hard phase ratio		change (wt%)		
Probe	**C**	**N**	**O**	**[C+N]/[me]**	**[C]/[me]**	**C**	**N**	**O**
N0-1 powder	7.10	5.51	1.67	0.990	0.594			
N0-1_Ar	6.68	5.17	0.09	0.954	0.559	-0.42	-0.34	-1.58
N0-1_10N	6.58	5.44	0.07	0.941	0.551	-0.52	-0.07	-1.60
N0-2 powder	7.12	5.60	2.00	0.999	0.596			
N0-2_Ar	6.43	5.33	0.12	0.922	0.539	-0.69	-0.27	-1.88
N0-2_10N	6.28	5.63	0.11	0.931	0.526	-0.84	+0.03	-1.89
N0-2_10Np	6.25	5.56	0.29	0.923	0.524	-0.87	-0.04	-1.71
N0-2_50N	6.20	5.80	0.25	0.936	0.519	-0.92	+0.20	-1.75
N2-2 powder	7.57	4.84	1.82	0.981	0.634			
N2-2_Ar	6.93	4.88	0.22	0.930	0.580	-0.64	+0.04	-1.60
N2-2_10N	6.88	5.37	0.15	0.961	0.576	-0.69	+0.53	-1.67
N2-2_10Np	6.56	5.29	0.30	0.929	0.549	-1.01	+0.45	-1.52
N2-2_50N	6.54	5.59	0.52	0.948	0.547	-1.03	+0.75	-1.30
N3-2 powder	7.72	4.80	2.30	0.982	0.640			
N3-2_Ar	6.96	4.79	0.19	0.918	0.577	-0.76	-0.01	-2.11
N3-2_10N	6.83	5.30	0.11	0.944	0.567	-0.89	+0.50	-2.19

4.4. N series - SinterHIP

4.4.1. Porosity and dimensional changes

Porosity classes were determined from the LOM images in figures 132 to 155 and are summarized in table 32. In comparison to the vacuum sintered samples, the high pressure densification during the SinterHIP process led to lower porosity. When Ar was applied during the sintering process, the majority of cermets reached A02 porosity with the exception of N1-1 and N2-1, which showed a slightly higher A04 porosity. Under N_2 atmosphere, on the other hand, similar densities of 6.9 to 7.0 g/cm^3 or approx. 97 % of the theoretical density (7.119 g/cm^3) were achieved. Green bodies lost slightly more mass in the SinterHIP process (between 1.8 and 3.6 wt%). This could be explained by pressing faults, as many samples had lost small parts of the edge of the cylinder. However, this hardly affected the dimensional changes as measurements were taken on the bulk part of the cermets. Therefore, dimensional values similar to the vacuum sintered samples were obtained. The Archimedes density, dimensional change and weight loss of the N series SinterHIP cermets can be found in tab. 33.

4.4.2. Phase analysis and magnetic properties

The XRD patterns of the N SinterHIP cermets are presented in figures 132 to 155. The lattice parameters determined by Rietveld analysis and the magnetic saturation of the binder phase

Table 32: Apparent porosity of the N series SinterHIP cermets.

	Porosity Class	
	SAr	**SN**
N0-1	A02 B00 C00	A02 B00 C00
N0-2	A02 B00 C00	A02 B00 C00
N1-1	A04 B00 C00	A02 B00 C00
N1-2	A02 B00 C00	A04 B00 C00
N1-3	A02 B00 C00	A06 B00 C00
N1-4	A02 B00 C00	A02 B00 C00
N2-1	A04 B00 C00	A02 B00 C00
N2-2	A02 B00 C00	A02 B00 C00
N2-3	A02 B00 C00	A04 B00 C00
N3-1	A02 B00 C00	A04 B00 C00
N3-2	A02 B00 C00	A04 B00 C00
N3-3	A02 B00 C00	A06 B00 C00

are listed in tab. 34. N0 and N1 cermets exhibit two distinct hard phase patterns similar to the results of the vacuum sintered samples, while the N2 cermets with (Ti,W)(C,N) powder show only one. In contrast, the hard phase pattern could be evaluated as doublets for all N3 cermets. Despite the higher C activity in the SinterHIP furnace, eta phase was still detectable by XRD for most of the N series SN cermets.

The binder phase solution state is characterized by the relative increases in lattice parameter and magnetic saturation. Fig. 47 shows the correlation between the two values. The amount of dissolved elements in the binder is significantly reduced when N_2 is present during sintering. Magnetic saturation reached 60 to 80% for SN cermets, while for SAr the binder state it is lower and similar to the values obtained for the vacuum sintered counterparts. In comparison, the binder phases of the N0 and N3 samples incorporated the most atoms into the lattice, while the addition of C-rich Ti(C,N) or (Ti,W)(C,N) led to smaller numbers.

Table 33: Archimedes density (ρ_A) in g/cm^3, shrinkage in diameter (d) and height (h) and mass loss (%) of N series SinterHIP cermets.

		shrinkage					shrinkage	
sample	**ρ_A**	**d (%)**	**h (%)**	**m (%)**	**sample**	**ρ_A**	**d (%)**	**h (%)**	**m (%)**
N0-1_SAr	6.928	19.6	19.1	4.6	N0-1_SN	6.951	20.1	20.5	2.8
N0-2_SAr	6.938	21.2	19.3	3.2	N0-2_SN	6.957	20.9	20.9	2.7
N1-1_SAr	6.916	20.4	19.9	2.8	N1-1_SN	6.899	19.9	20.9	2.3
N1-2_SAr	6.907	20.7	18.2	3.7	N1-2_SN	6.899	20.3	18.4	2.2
N1-3_SAr	6.902	20.2	19.7	2.5	N1-3_SN	6.867	19.5	19.6	2.0
N1-4_SAr	6.917	20.9	19.3	3.6	N1-4_SN	6.896	20.5	20.8	2.3
N2-1_SAr	6.923	20.1	19.2	3.6	N2-1_SN	6.894	19.7	20.0	1.8
N2-2_SAr	6.931	20.3	16.9	2.4	N2-2_SN	6.888	20.0	19.7	2.0
N2-3_SAr	6.930	20.9	19.2	3.5	N2-3_SN	6.924	20.7	20.9	2.7
N3-1_SAr	6.937	21.4	20.7	3.6	N3-1_SN	6.907	21.1	21.1	3.2
N3-2_SAr	6.928	21.2	19.5	3.5	N3-2_SN	6.912	20.8	21.3	2.7
N3-3_SAr	6.923	19.9	19.7	3.0	N3-3_SN	6.875	19.7	20.3	2.2

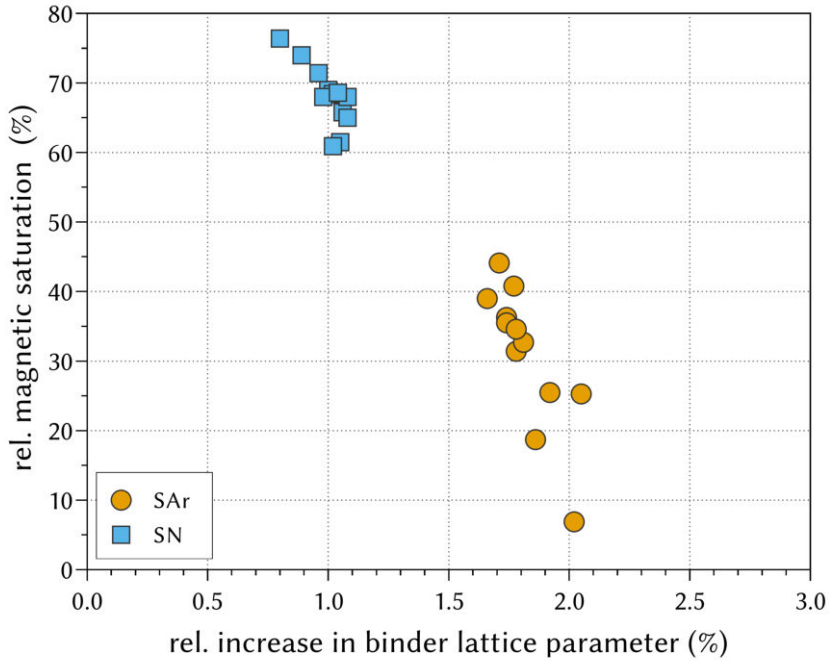

Figure 47: Correlation of relative increase in binder phase lattice parameter and magnetic saturation for the N series SinterHIP cermets.

Table 34: Lattice parameters in Å, peak form and relative magnetic saturation of N series SinterHIP cermets. Relative increase of the binder phase lattice parameter (B_{rel}, magnetic saturation (MS) in comparison to the pure Co/Ni binder and total concentration of dissolved elements in the binder phase (mol%).

sample	peak form	H1	H2	B	B_{rel} (%)	MS (%)	c (mol%)
N0-1_SAr	doublet	4.3265	4.2847	3.6098	1.86	18.7	17.3
N0-1_SN	doublet	4.3271	4.2758	3.5812	1.05	61.5	8.8
N0-2_SAr	doublet	4.3258	4.2877	3.6157	2.02	6.9	19.7
N0-2_SN	doublet	4.3267	4.2762	3.5800	1.02	60.9	8.9
N1-1_SAr	doublet	4.3251	4.3010	3.6058	1.74	36.3	13.8
N1-1_SN	doublet	4.3260	4.2824	3.5794	1.00	69.0	7.3
N1-2_SAr	doublet	4.3244	4.3049	3.6072	1.78	31.4	14.8
N1-2_SN	doublet	4.3254	4.2834	3.5817	1.06	65.8	7.9
N1-3_SAr	doublet	4.3267	4.3036	3.6028	1.66	39.0	13.3
N1-3_SN	doublet	4.3268	4.2826	3.5781	0.96	71.4	6.8
N1-4_SAr	doublet	4.3264	4.3072	3.6055	1.74	35.5	14.0
N1-4_SN	doublet	4.3264	4.2827	3.5801	1.02	68.4	7.4
N2-1_SAr	singlet	4.3207	-	3.6045	1.71	44.1	12.2
N2-1_SN	singlet	4.3229	-	3.5723	0.80	76.4	5.8
N2-2_SAr	singlet	4.3204	-	3.6069	1.77	40.8	12.9
N2-2_SN	singlet	4.3220	-	3.5754	0.89	74.0	6.3
N2-3_SAr	singlet	4.3224	-	3.6165	2.05	25.3	16.0
N2-3_SN	singlet	4.3288	-	3.5786	0.98	68	7.5
N3-1_SAr	doublet	4.3274	4.2993	3.6120	1.92	25.5	16.0
N3-1_SN	doublet	4.3271	4.2831	3.5821	1.08	65.0	8.1
N3-2_SAr	doublet	4.3282	4.3039	3.6083	1.81	32.7	14.5
N3-2_SN	doublet	4.3256	4.2838	3.5824	1.08	68.0	7.5
N3-3_SAr	doublet	4.3288	4.3040	3.6072	1.78	34.6	14.1
N3-3_SN	doublet	4.3264	4.2812	3.5809	1.04	68.6	7.3

4.4.3. Microstructure and grain size distribution

Fig. 48 compares the microstructure of N0-1_SAr with the N8 grade. Analogue to the results for the vacuum sintered samples, a very fine microstructure with mostly isolated cores and a large amount of gray, coreless rims can be observed. Therefore, there are also similarities with the N8 grade. Again, the major differences are the shape and size of the Ti(C,N)-rich dark grains, indicating a different synthesis process for the respective Ti(C,N) powders.

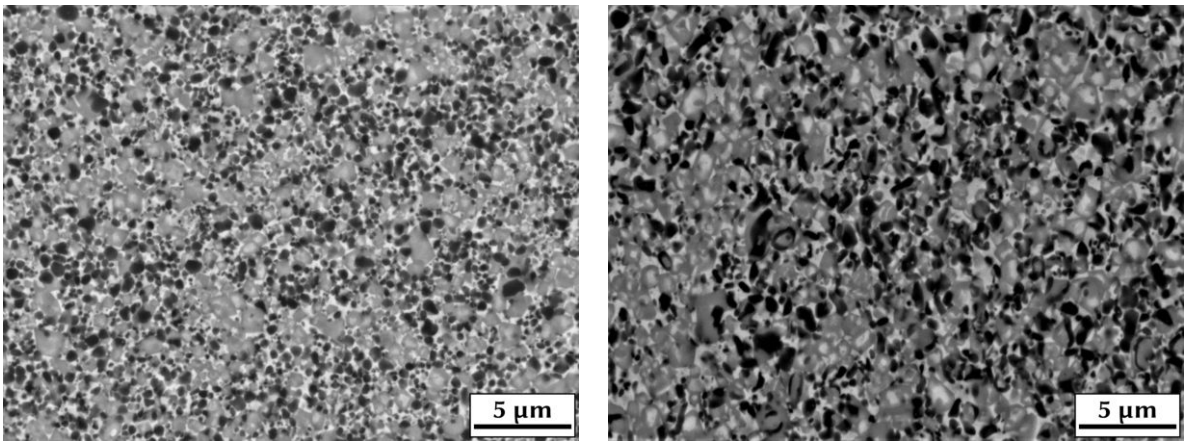

(a) N0-1_SAr, d_{50}=0.35 µm, slope=184.

(b) N8, d_{50}=0.32 µm, slope=157.

Figure 48: Microstructure of N0-1_SAr in comparison with the N8 target grade, BSE-SEM, 10,000x magnification, GSD parameters of cores.

The fine microstructure is also confirmed in the parameters of the GSD, summarized in tab. 35. On average, the grains are significantly smaller than the cores and also exhibit a narrower distribution. N0 cermets demonstrate the smallest average core and grain sizes. Addition of C-rich Ti(C,N) powder increased the average core and grain size. The different Ti(C,N) powders used in the N1 series reveal a clear trend for the cores, but the overall grain size is not greatly influenced. The same is true for the three different Ti(C,N) added to the N2 and N3 series as mostly the cores were affected by the powder grain sizes. On the other hand, the grain refining effect of N_2 in the sintering atmosphere is most obvious for the GSD of grains. While the addition of coarser Ti(C,N) in the N1 series and the implementation of pre-alloyed powders in the N2 and N3 subsets did not always improve the fracture toughness, the hardness decreased slightly in the expected manner. However, the toughest cermets were again produced with coarse Ti(C,N) powders in the grades N1-3, N2-3 and N3-3, independent of the raw material alloy state.

Table 35: Summary of GSD parameters of N SinterHIP cermets as determined by linear intercept.

	cores			grains		
sample	**average**	**d_{50}**	**slope**	**average**	**d_{50}**	**slope**
N0-1_SAr	0.37	0.35	184	0.61	0.58	132
N0-1_SN	0.35	0.32	230	0.68	0.51	105
N0-2_SAr	0.37	0.32	162	0.6	0.54	136
N0-2_SN	0.37	0.35	162	0.71	0.56	52
N1-1_SAr	0.41	0.35	145	0.81	0.67	70
N1-1_SN	0.37	0.32	172	0.83	0.63	106
N1-2_SAr	0.46	0.38	125	0.8	0.71	88
N1-2_SN	0.38	0.32	153	0.85	0.65	93
N1-3_SAr	0.5	0.46	131	0.87	0.71	89
N1-3_SN	0.54	0.46	99	0.82	0.62	110
N1-4_SAr	0.45	0.38	120	0.73	0.65	99
N1-4_SN	0.4	0.38	162	0.68	0.52	133
N2-1_SAr	0.42	0.35	145	0.93	0.84	88
N2-1_SN	0.4	0.32	145	0.76	0.56	118
N2-2_SAr	0.35	0.29	172	0.83	0.76	101
N2-2_SN	0.42	0.35	131	0.68	0.51	164
N2-3_SAr	0.51	0.41	99	0.81	0.74	99
N2-3_SN	0.52	0.46	102	0.94	0.77	90
N3-1_SAr	0.34	0.32	212	0.77	0.73	104
N3-1_SN	0.35	0.32	197	0.77	0.61	120
N3-2_SAr	0.37	0.32	153	0.83	0.72	98
N3-2_SN	0.32	0.29	212	0.82	0.64	107
N3-3_SAr	0.52	0.46	115	0.81	0.75	122
N3-3_SN	0.53	0.49	110	0.87	0.68	94

4.4.4. Mechanical properties

Considering the mechanical properties of the N series SinterHIP cermets in fig. 49, a distinct drop in fracture toughness is again noticeable for the samples sintered under N_2. However, the N0-2_SAr cermet can also be added to this particular group. This pronounced loss of fracture toughness could indicate the presence of finely dispersed, brittle eta phase. Yet, no eta phase was visible in the XRD of the sample.

In comparison with the vacuum sintered samples, the SAr cermets were slightly harder and less tough than their counterparts. Despite this minor embrittlement, they still performed closely to the expected trend line that was determined by the comparison grades. Grade N0-1_SAr reached mechanical properties closest to the N8 grade.

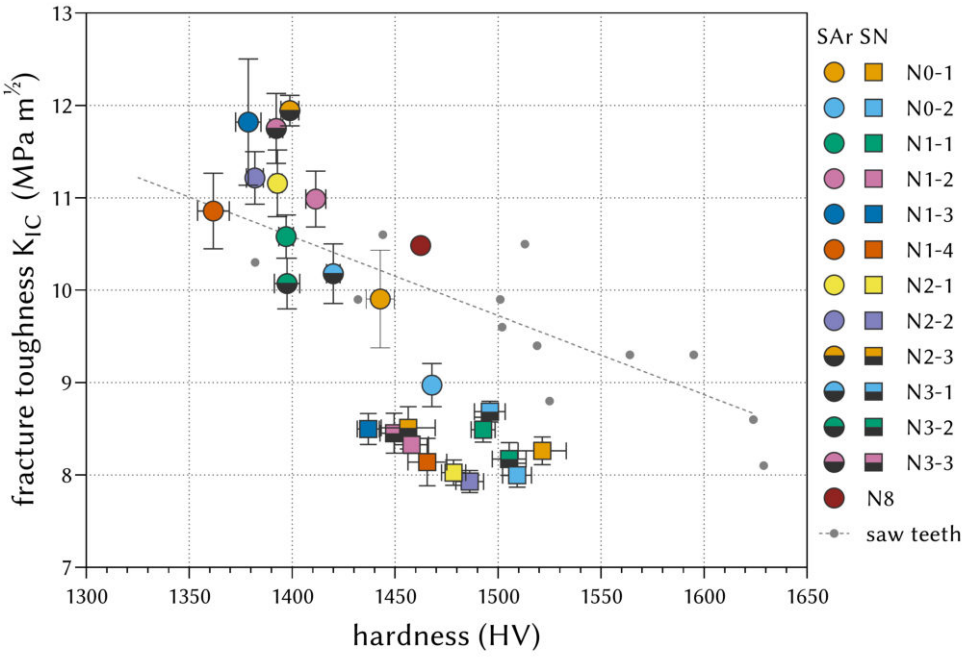

Figure 49: Hardness and fracture toughness of the N SinterHIP cermets, N8 target grade and the comparison grades.

4.4.5. Influence of the sintering atmosphere

Similarly to the vacuum sintered cermets, the features of the N series SinterHIP samples were strongly influenced by the choice of sintering atmosphere. The properties of the SN cermets were mostly dominated by the presence of eta phase that can be seen as a bright extra phase in the microstructure (fig. 50). Apart from the formation of eta phase, the increased N activity did not provide a grain refining effect on the microstructure. In fact, some of the grades even exhibit larger average grain sizes than the corresponding SAr samples. Due to the construction of the SinterHIP furnace, the N_2 activity was set as a flow rate and not a fixed pressure like in the induction furnace used for vacuum sintering. Because even N0-2_SAr shows relatively brittle properties, it is possible that the N activity was high enough for the formation of eta phase but too low for a grain refining effect.

The N activity in the SN series was sufficient to strongly influence the binder phase. While the binder of SAr samples dissolved high amounts of foreign atoms, the high magnetic saturation and low increase in binder phase lattice parameter indicate very low incorporation for the SN cermets. This is likely caused by a reduced solubility of W and Mo in the binder resulting of the thermodynamically unstable W-N and Mo-N bonds.

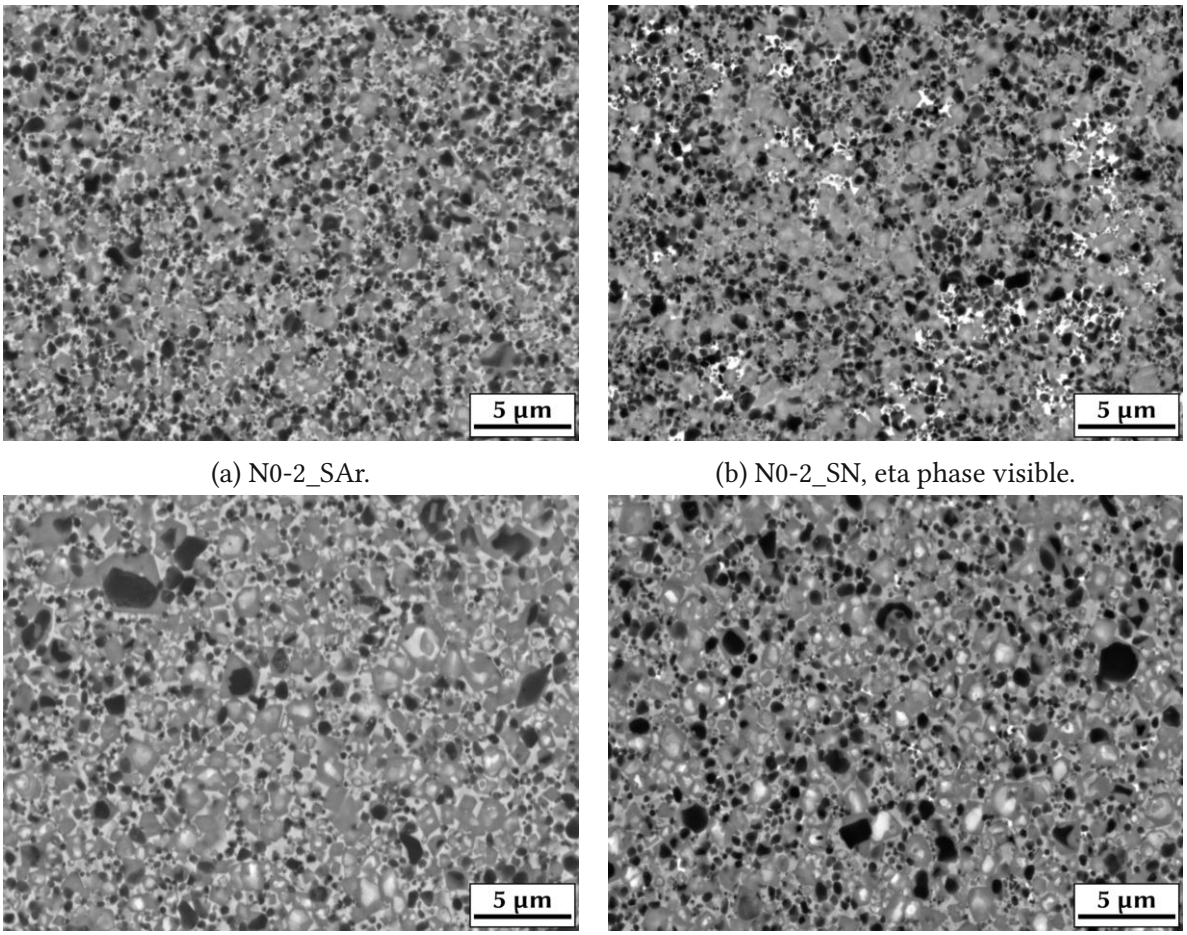

(a) N0-2_SAr. (b) N0-2_SN, eta phase visible.

(c) N2-1_SAr. (d) N2-1_SN.

Figure 50: Microstructure of vacuum sintered N SinterHIP cermets as a function of the sintering atmosphere, BSE-SEM, 10,000x magnification.

4.4.6. Influence of the Ti(C,N) grain size

Fig. 51 represents the microstructure of N1 samples with four different Ti(C,N) powder grain sizes. The addition of coarse $TiC_{0.7}N_{0.3}$ powder resulted in the formation of large core-rim grains in all four cermets. In $TiC_{0.5}N_{0.5}$ grains, the N activity was sufficiently high to prevent the formation of rim phase, therefore these grains appear isolated. Only a slight increase in grain size from N1-2 to N1-1 and N1-4 can be seen for the isolated grains, while the biggest increase is revealed looking at the N1-3 cermet. This is confirmed by the average core and grain size in tab. 35, where only a slight increase is noticeable for the three finer powders. N1-3 again shows the largest intercept lengths of this subset. Similarly, the Ti(C,N) powder grain size only had a minor influence on the binder phase state of the N1 Series. Both in Ar and N_2, the magnetic saturation and lattice parameter indicate only insignificant variances in the binder phase alloy state. The exception is N1-3_SAr, where the analysis points towards the lowest amount of dissolved elements. In combination, these effects led to a less obvious trend for the mechanical properties in comparison to the vacuum sintered samples. While the hardness decreases as a function of increasing Ti(C,N) powder grain size, the fracture toughness could only be improved for the coarsest powder in N1-3. Hence, the toughening was mostly

caused by the increased crack deflection by larger grains and the higher energy needed for crack propagation through the ceramic hard phase.
The first two cermets in the N2 and N3 series implemented similar powders in their formulation, resulting in comparable average grain sizes and binder phase properties. Consequently, performance for hardness and fracture toughness are alike as well. As seen for the Ti(C,N) + WC cermets from N1, elevated toughness was achieved with the addition of the coarser Ti(C,N) powder by the noticeable increase in average grain size. Despite the different alloy states, the mechanical properties of SinterHIPed N1-3, N2-3 and N3-3 cermet end up being very similar.

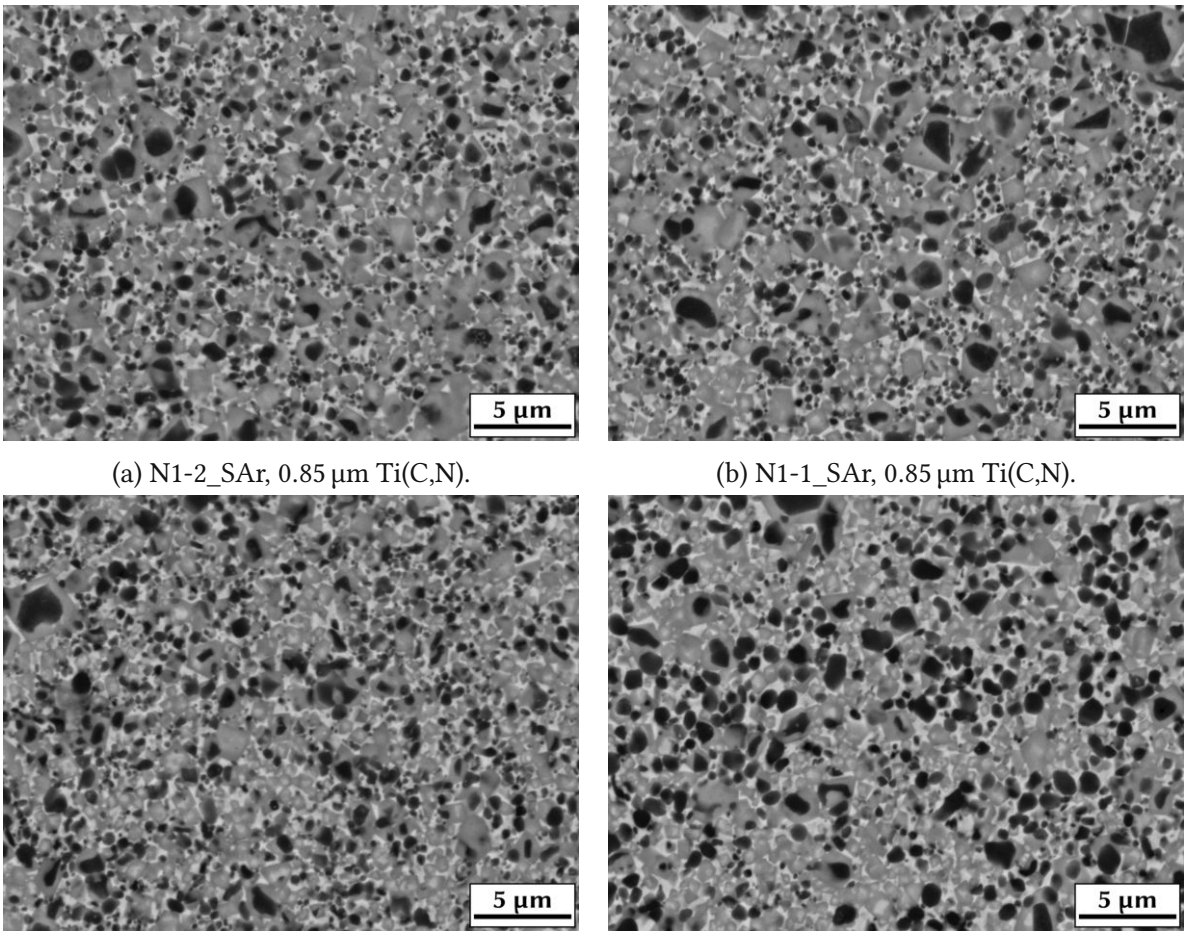

(a) N1-2_SAr, 0.85 µm Ti(C,N).

(b) N1-1_SAr, 0.85 µm Ti(C,N).

(c) N1-4_SAr, 1.07 µm Ti(C,N).

(d) N1-3_SAr, 1.76 µm Ti(C,N).

Figure 51: Microstructure of N SinterHIP cermets as a function of the Ti(C,N) powder grain size, BSE-SEM, 10,000x magnification.

4.4.7. Influence of the powder alloy state

The pre-alloyed powders in the N2 and N3 series resulted in noticeably different microstructures in the BSE-SEM images (fig. 52). The (Ti,W)(C,N) powder used in the formulation of the N2 cermets led to inverse grains with a pronounced bright core. In comparison to the binary powders used in the N1 samples the coreless grains were replaced by inverse grains. Additionally, some larger core-rim grains are still present as a result of the added coarse $TiC_{0.7}N_{0.3}$ powder to balance the C/N content. The use of (Ti,W)(C,N) also influenced the binder state of the N2 cermets, especially if coarse Ti(C,N) powder was implemented. The SinterHIPed N2-3 samples have a larger lattice parameter and lower magnetic saturation, indicating a high amount of dissolved elements in the Ni/Co binder. This can be explained by a higher sintering activity of the pre-alloyed powder, particularly as the Ti(C,N) solubility is lowered by the smaller surface area of the coarser powder.
In the N3 cermets, the lack of nitrogen in the (Ti,W)C limited the amount of admixed pre-alloyed powder in this formulation. Additionally, the C/N ratio had to be balanced with N-rich $TiC_{0.3}N_{0.7}$ powder. These changes apparently affected the microstructure, as the higher N activity in the Ti(C,N)-rich particles prevented the formation of core-rim grains. Also, the bright cores of the inverse grains are less distinct and more gray coreless grains were formed during sintering. In comparison with the formulations based on binary powders in the N1 series, the large relative increase of the binder phase lattice parameter and the low magnetic saturation indicate a higher amount of dissolved elements.
Fig. 49 reveals that higher fracture toughness could be achieved with the implementation (Ti,W)(C,N) powder in the N2 cermets. Especially the combination of coarse Ti(C,N) and CSS phases in N2-3 led to the maximum toughness levels in the SinterHIP samples. Surprisingly, (Ti,W)C did not increase the toughness for cermets using finer Ti(C,N) powder. In fact, N3-1 and N3-2 developed lower toughness and higher hardness in comparison to the corresponding N1-1 and N1-2 cermets. Nevertheless, the coarse Ti(C,N) did cause an enhanced toughness and, in the end, N3-3 performed similar to N1-3 and N2-3.

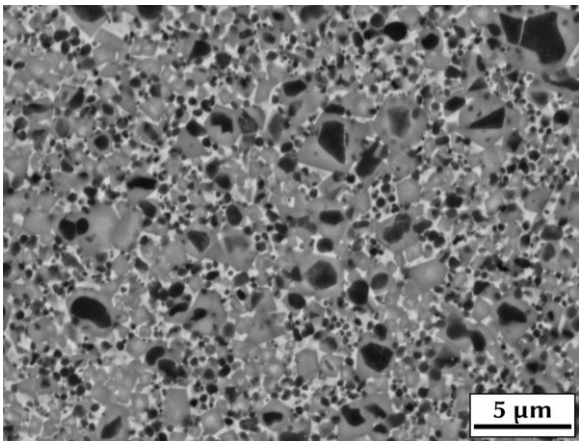

(a) N1-1_SAr, Ti(C,N) + WC.

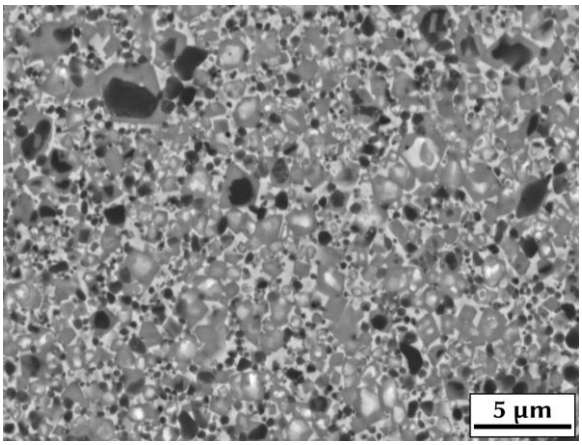

(b) N2-1_SAr, (Ti,W)(C,N).

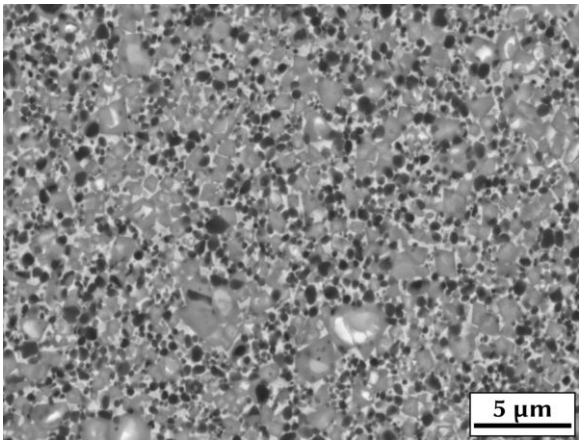

(c) N3-1_SAr, (Ti,W)C.

Figure 52: Microstructure of N SinterHIP cermets with different powder alloy states, BSE-SEM, 10,000x magnification.

4.4.8. C addition and CNO analysis

The mechanical properties of the formulations of N series cermets with 0.1 or 0.3 wt% C addition are presented in fig. 53 and 54. Under Ar atmosphere, the N0-2 cermet achieved a lower fracture toughness than expected from the trendline. Both 0.1 and 0.3 wt% significantly increased the fracture toughness and the mechanical properties were closer to the N8 target cermet. This is another indication that N0-2 indeed had a low C activity resulting in the formation of eta phase even under Ar sintering atmosphere. However, the mechanical properties of the cermets N1-2_SAr and N2-2_SAr were less affected by the C addition.

Under N_2, all three compositions developed brittle properties, which are typical for the presence of eta phase. When 0.1 wt% or more C was added, the performance drastically improved and all grades performed very similar to the N8 grade. XRD phase analysis and BSE-SEM imaging did not indicate any presence of additional phases. As discussed earlier, this was not achieved for C-doped samples by vacuum sintering in the induction furnace. This suggests that only the combination of C addition and the SinterHIP furnace was able to prevent the formation of eta phase in N_2 atmosphere.

To gain further insight into the formation of eta phase, the C, N and O contents SinterHIPed

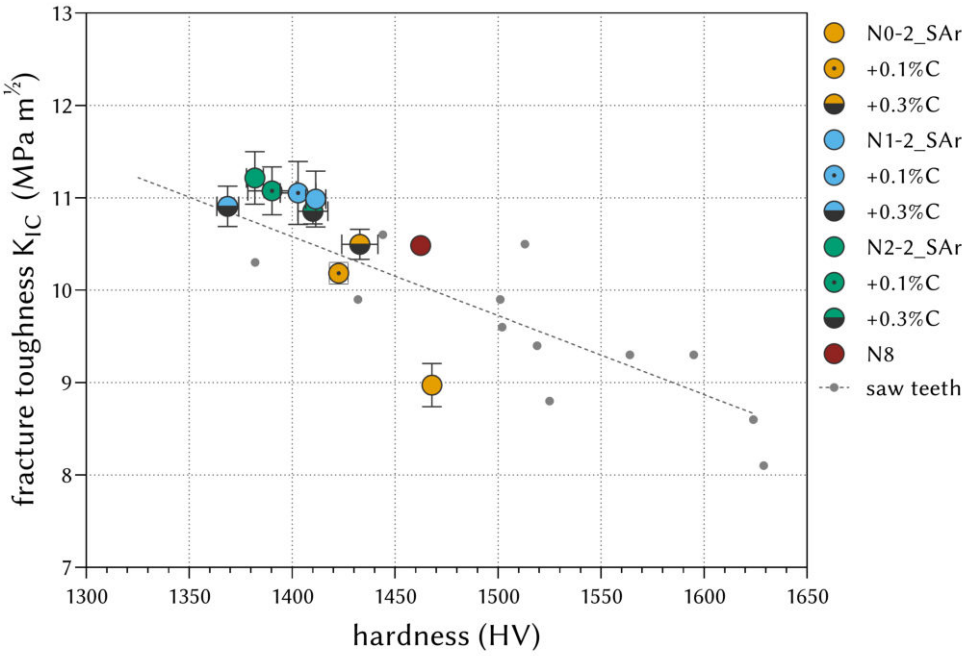

Figure 53: Mechanical properties of N series cermets with 0.1 and 0.3 wt% C sintered under Ar.

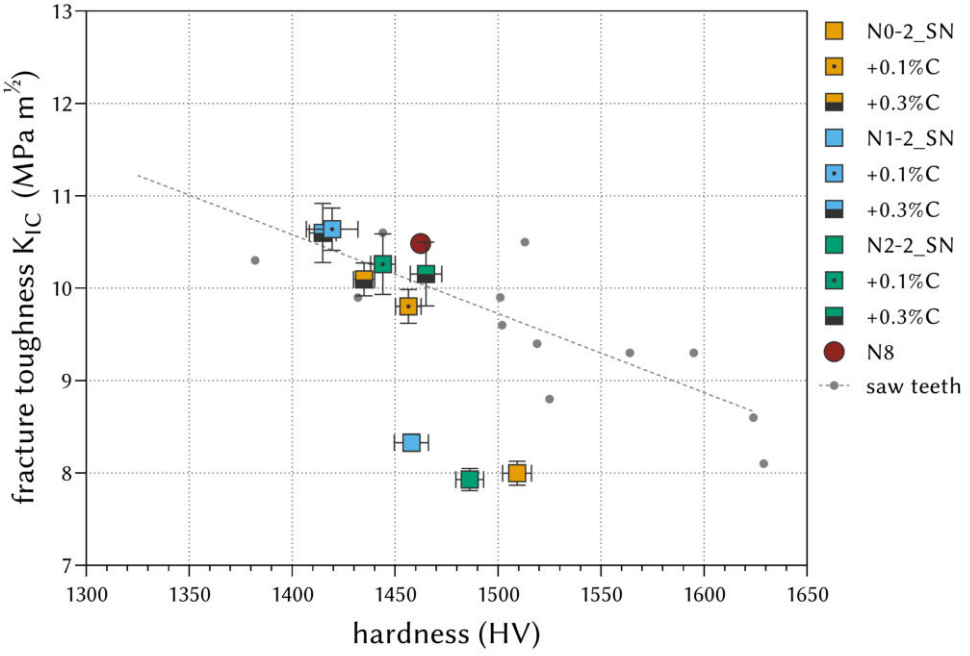

Figure 54: Mechanical properties of N series cermets with 0.1 and 0.3 wt% C sintered under N_2.

cermets were also analyzed. Tab. 36 provides an overview of the results. For the powder mixtures, relatively high oxygen contents of 1.7 to 2.3 wt% were evaluated. This is more than expected from the provided powder specification sheets and most likely a result of oxygen uptake during weighing, milling and pressing. While sintering, oxygen is removed by outgassing of CO. Therefore, both O and C contents are reduced in the sintered samples. The decrease in C content is more pronounced when N is present in the sintering atmosphere (10N, 10Np, 50N and SN samples). The higher the N partial pressure, the less C remains in the sintered cermet. Higher N activity also leads to a minor uptake of nitrogen during the sintering process. Notably, sample N0-2_SAr was the only Ar sintered cermet where eta phase was indicated by brittle mechanical properties, but no signs were found in the XRD or SEM analysis. In comparison, the C content is lower than in other grades.

Comparing the vacuum sintered Ar and SinterHIP Ar samples, there is only a minor difference in C and N contents. However, when nitrogen is introduced into the sintering atmosphere, the C and N activity of the cermets is increased. This resulted in higher [C+N]/[metal] and especially [C]/[metal] ratios of the SN samples compared with the Ar and 10N cermets. Despite this higher C content, eta phase was still clearly identified in the un-doped SN cermets by XRD and SEM analysis. Therefore, the formation of eta phase can not solely be explained by the [C]/[metal] ratio of the hard phase. As no margin of error was given in the results of the external C analysis, the uncertainty of the combustion-IR method could be one possible explanation. Furthermore, the metal content of the sintered cermets was calculated from the powder weighing and not a chemical analysis. Hence, further studies by combining the C,N and O analysis with the dissolution XRF method to better analyze the metal content of the finished cermets could be necessary.

Finally, no eta phase was found when the N series formulation was doped with C and the SinterHIP process was used. As discussed earlier, this resulted in mechanical properties similar to the N8 target grade. The C,N and O analysis of the doped and SinterHIPed N1-2 cermet in tab. 36 further shows a substantial increase in the C content, indicating that the [C]/[me] ratio still is of importance in the precipitation of eta phase.

Table 36: Results of the C, N and O analysis of the powder mixtures and vacuum sintered N series cermets with molar ratios of the hard phase.

	content (wt%)			hard phase ratio		change (wt%)		
Probe	**C**	**N**	**O**	**[C+N]/[me]**	**[C]/[me]**	**C**	**N**	**O**
N0-2 powder	7.12	5.60	2.00	0.999	0.596			
N0-2_Ar	6.43	5.33	0.12	0.922	0.539	-0.69	-0.27	-1.88
N0-2_10N	6.28	5.63	0.11	0.931	0.526	-0.84	+0.03	-1.89
N0-2_SAr	6.27	5.34	0.12	0.909	0.525	-0.85	-0.26	-1.88
N0-2_SN	6.39	5.65	0.08	0.941	0.535	-0.73	+0.05	-1.92
N2-2 powder	7.57	4.84	1.82	0.981	0.634			
N2-2_Ar	6.93	4.88	0.22	0.930	0.580	-0.64	+0.04	-1.60
N2-2_10N	6.88	5.37	0.15	0.961	0.576	-0.69	+0.53	-1.67
N2-2_SAr	6.66	4.84	0.21	0.905	0.557	-0.91	0.00	-1.61
N2-2_SN	6.95	5.33	0.22	0.964	0.582	-0.62	+0.49	-1.60
N3-2 powder	7.72	4.80	2.30	0.982	0.640			
N3-2_Ar	6.96	4.79	0.19	0.918	0.577	-0.76	-0.01	-2.11
N3-2_10N	6.83	5.30	0.11	0.944	0.567	-0.89	+0.50	-2.19
N3-2_SAr	6.92	4.82	0.15	0.917	0.574	-0.80	+0.02	-2.15
N3-2_SN	7.04	5.30	0.12	0.961	0.584	-0.68	+0.50	-2.18
N1-2+0.1%C powder	8.10	4.83	2.29	1.022	0.676			
N1-2+0.1%C_SAr	7.12	4.68	0.10	0.930	0.595	-0.98	-0.15	-2.19
N1-2+0.1%C_SN	7.06	5.40	0.10	0.976	0.590	-1.04	+0.57	-2.19

5. Summary

5.1. Characterisation of saw teeth

In this study, thirteen commercially available saw teeth were analyzed with regards to their elemental composition, binder state, microstructure and the resulting mechanical properties. One major finding of the chemical analysis was the implementation of the same elemental formulation in the saw teeth of blades IA, ID, M5 and M6. Investigations of the microstructure confirmed that the same cermets were used in the first three blades, while M6 only shares the same elemental composition. Furthermore, it was determined that the Y3 single teeth were used in the IC circular saw blade.

Tab. 37 provides an overview of the possible raw powder formulation of the saw teeth. All cermet hard phases were mostly comprised of Ti(C,N) and WC. To improve the sintering activity, some grades such as IA or N8 further contain small amounts of Mo_2C. Additionally, some variation of TaC, NbC or a mix of both was added to all compositions, likely to improve the high temperature properties of the cermets. Typical Ta/Nb ratios of 5:1 (IA, ID, M5, M6), 3:1 (IB), 2:1 (IC, Y3, Y5) or 1:1 (M4) were found, while the other compositions relied solely on the cheaper NbC. Interestingly, Zr was only detected in the formulations of IA and M6 saw blades. In literature, the addition of up to 1 wt% ZrC could increase the fracture toughness in Ti(C,N)-based cermets [40].

The binder phase content of the cermets largely influences the mechanical properties. In fig. 55, the hardness and fracture toughness are shown as a function of the binder content. An increase in the metallic binder phase clearly improved the toughness, whereas the hardness is reduced simultaneously. While a clear trend is visible for the commercial saw teeth, the hardness of the cermets differs more than expected from the variation of binder content. For example, the grades N2 and C1 are substantially harder than other grades with comparable amounts of binder phase. This is due to the high level of Ti(C,N) in the hard phase and a lower content of softer secondary carbides. Another influencing factor is the Co/Ni ratio in the metallic binder. The aforementioned grades N2 and C1 only contain very small quantities of Ni. It is possible that this stems from a Ni coating to improve the bonding strength with the brazing material. This could also have led to the higher hardness of these grades. All other binder phases contain both Co and Ni in the common ratios of 1:1 (IA, ID, M4, M5, M6), 2:1 (IB, IC, N8, Y3) or 3:1 (T6, Y5) by weight. Lastly, Al was found in the grades IA, ID, M5 and M6. The small amounts of Al were probably added in the form of NiAl powder as the ratio of Ni in these formulations is also slightly elevated in comparison to the Co content. The strengthening effect can be caused by solid solution hardening as the Al dissolves in the binder and increases the distortion of the lattice [28, 29].

Table 37: Composition and mechanical properties of the commercial saw teeth grades.

	IA	**IB**	**IC**	**ID**	**M4**	**M5**	**M6**
hard phase (wt%)							
Ti(C,N)	47.6	47.2	45.7	47.6	49.1	47.6	47.3
WC	16.7	18.8	25.2	16.7	20.1	16.7	16.8
Mo_2C	1.5	4.7	-	1.5	7.1	1.5	1.5
TaC	11.3	10.6	8.1	11.3	4.9	11.3	11.4
NbC	1.2	1.8	2.0	1.2	2.3	1.2	1.2
ZrC	0.4	-	-	0.4	-	0.4	0.5
total	78.7	83.1	81.1	78.7	83.6	78.7	78.7
binder phase (wt%)							
Co	10.0	11.1	12.6	10.0	8.4	10.0	10.0
Ni	10.9	5.8	6.3	10.9	8.1	10.9	11.0
Al	0.3	-	-	0.3	-	0.3	0.3
total	21.3	16.9	18.9	21.3	16.4	21.3	21.3
mechanical properties							
HV	1440	1600	1520	1430	1500	1380	1510
K_{IC}	10.6	9.3	9.4	9.9	9.9	10.3	10.5

	N2	**N8**	**T6**	**Y3**	**Y5**	**C1**
hard phase (wt%)						
Ti(C,N)	53.2	48.2	49.9	45.5	45.8	53.5
WC	16.8	18.4	20.7	25.4	19.1	17.4
Mo_2C	-	4.2	-	-	3.6	-
TaC	-	-	3.0	8.2	8.4	-
NbC	11.7	6.54	7.9	2.0	2.0	11.1
ZrC	-	-	-	-	-	-
total	81.7	77.3	81.4	81.2	78.9	82.1
binder phase (wt%)						
Co	17.6	14.6	14.0	12.7	15.8	17.9
Ni	0.8	8.0	4.6	6.1	5.3	0.1
Al	-	-	-	-	-	-
total	18.3	22.7	18.6	18.8	21.1	17.9
mechanical properties						
HV	1620	1480	1560	1530	1500	1630
K_{IC}	8.6	10.9	9.3	8.8	9.6	8.1

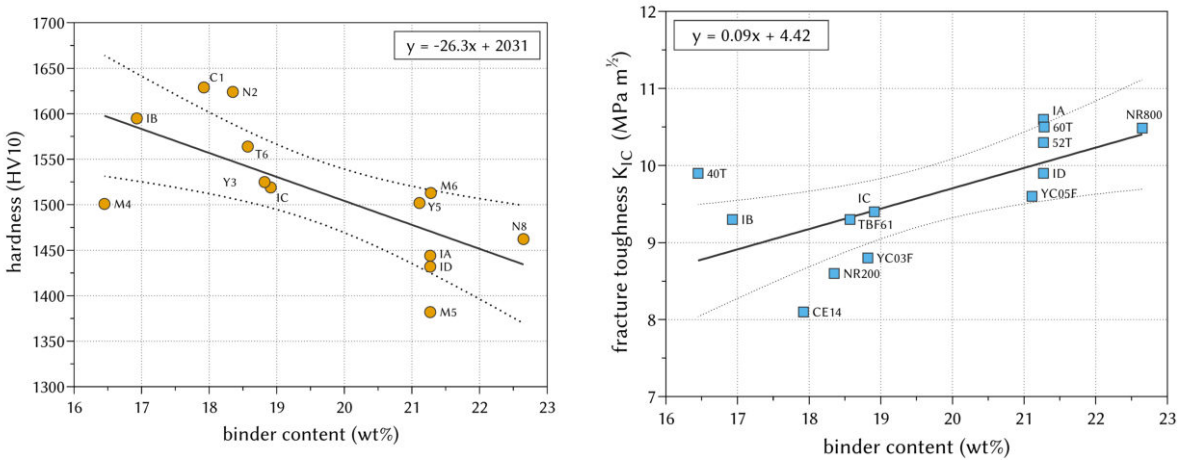

(a) (b)

Figure 55: (a) Hardness and (b) fracture toughness of saw teeth grades as a function of the binder content in wt% with linear trend line and 95 % confidence interval of the linear fit.

The differences in the elemental compositions further influence the dissolution state of the binder phase and therefore the mechanical properties. This effect can be estimated by the relative changes in binder lattice parameter and the magnetic saturation. An increasing amount of dissolved elements distorts the lattice parameter which increases the average lattice parameter. Furthermore, the foreign elements decrease the magnetic saturation of the Co/Ni binder. Tab. 38 summarizes the findings from phase analysis by XRD and magnetic measurements. For the saw blade grades, the binder phase can only be judged by the XRD analysis as the magnetic saturation could not be measured for the teeth that had to be broken out during the preparation process. The binder lattice parameter was increased the most for the grades IB, M4 and T6. All three grades perform above the trend line for the saw teeth grades and show a comparably high hardness due to a high level of dissolved elements. For T6, this is also indicated by the lowest magnetic saturation of only 40 %. Medium increases in lattice parameter were found for grades IC, Y3 and N2, but the magnetic saturation did not always correlate. Despite the increase in lattice parameter of 1.4 %, the magnetic saturation of N2 is relatively high with 61 %. Low amounts of dissolved elements were discovered for grades IA, ID, M5, N8 and Y5 with less distorted lattices and higher magnetic saturation.

Another focus of this research was the microstructure of the cermet saw teeth (fig. 57). For equivalent saw grades, e.g. IC and Y3, only one representative BSE-SEM image was selected. All grades show a very fine microstructure with average grain sizes of 1 µm or less. Only in three grades (M4, M6 and T6) classic core-rim with a dark core, bright inner rim and gray outer rim were observed. This resulted in overlapping XRD pattern for the hard phase of M4 and T6 and therefore only one lattice parameter was determined (tab. 38). Notably, the microstructure of M6 is obviously different to IA despite the same elemental composition. In the other grades, the Ti(C,N)-rich dark grains remain isolated, likely due to a higher N content preventing the precipitation of the rim phases. The heavier elements formed a separate phase consisting of

inverse grains with a bright core and an intermediate rim or gray, coreless grains. The lattice parameter differs from the Ti(C,N)-rich grains, hence two different XRD patterns can be evaluated for the hard phase of these grades. The higher lattice parameter corresponds to the higher amount of heavier elements in the inverse or coreless grains distorting the Ti(C,N) lattice.

These influencing factors result in the mechanical properties shown in fig. 56. The highest fracture toughness with a corresponding low hardness was found for the grades IA, ID, M5 and N8. This was achieved by the high binder contents of 21 wt% and 23 wt%, respectively. In IA and equivalent grades, the binder phase was additionally strengthened by the addition of Al. Therefore, toughness levels similar to N8 were achieved despite a 2 wt% lower binder content. The higher level of dissolved elements is also represented by the slightly larger binder lattice parameter. While grade M6 also reached around 10.5 $MPam^{1/2}$, it's hardness was increased by 100 HV10 due to the changed microstructure. M4, produced by the same manufacturer, performed almost equal to M6 despite the completely different elemental composition. The addition of relatively high levels of secondary carbides such as WC or Mo_2C possibly compensated the lowest binder content found for any of the grades. Additionally, the binder phase appears to be reinforced by a high amount of dissolved elements as the lattice parameter is clearly increased in reference to pure Ni/Co binder.
The hardness of the three grades IC, Y3 and Y5 was likewise measured to be around 1500 HV, but the fracture toughness was slightly lower compared to M4 or M6. This is especially interesting as the Y3 single teeth could be identified on the finished IC saw blade. Compared to Y3, the manufacturer Y replaced some WC by Mo_2C and raised the binder content by 2 wt%. Lastly, the Co/Ni ratio was changed from 2:1 to 3:1. All in all, this resulted in a minor enhancement of fracture toughness for Y5, while Y3 performed marginally harder.
Stronger variations in the mechanical properties were detected for the T6, N2 and N8 grades. As discussed earlier, N8 is a very tough cermet as a result of a large amount of binder phase and a severe substitution of Ti(C,N) by secondary carbides. The hardness of T6 was significantly improved by 100 HV as the amount of hard phase was increased by 4 wt%. Furthermore, the Co/Ni ratio was increased to 3:1. An even higher hardness with the same content of hard phase was realized by a total substitution of Ni by Co and a high content of Ti(C,N) in N2.
The grade C1 has the highest hardness of all tested saw teeth grades. With a very similar elemental composition to N2, this also is a result of the low binder content, high percentage of Ti(C,N) and a pure Co binder. The two grades show apparent differences in the microstructure, therefore it is unclear if they are in fact the same cermet.
All in all, the commercial saw grades follow the general trend of decreasing toughness for increasing hardness. The tested cermets generally developed a good ratio of mechanical properties, as most grades are positioned slightly above the trend line from literature [1]. After considering the mechanical properties, IA and N8 were selected as reference grades to recreate and study the influence of different starting materials and sintering atmospheres in the I and N Series.

Table 38: Lattice parameter of hard phase (H) and binder phase (B), relative increase in binder phase lattice parameter and magnetic saturation of the commercial saw teeth grades.

	lattice parameter					
	H1 (A)	**H2 (A)**	**B (A)**	**incr. (%)**	**MS (%)**	**c (mol%)**
IA	4.3359	4.2833	3.5900	1.31	-	-
IB	4.3207	4.2814	3.5974	1.51	-	-
IC	4.3171	4.2746	3.5962	1.47	-	-
ID	4.3359	4.2833	3.5900	1.31	-	-
M4	4.3104	-	3.5983	1.55	-	-
M5	4.3359	4.2833	3.5900	1.31	-	-
M6	4.3375	4.2836	3.5894	1.27	-	-
T6	4.3149	-	3.5995	1.56	40.2	13.0
N2	4.3286	4.2793	3.5939	1.38	60.7	8.9
N8	4.3154	4.2731	3.5876	1.23	50.5	10.9
Y3	4.3171	4.2746	3.5962	1.47	45.5	11.9
Y5	4.3176	4.2750	3.5900	1.29	54.8	10.1
C1	4.3313	4.2814	3.5921	1.33	65.2	8.0

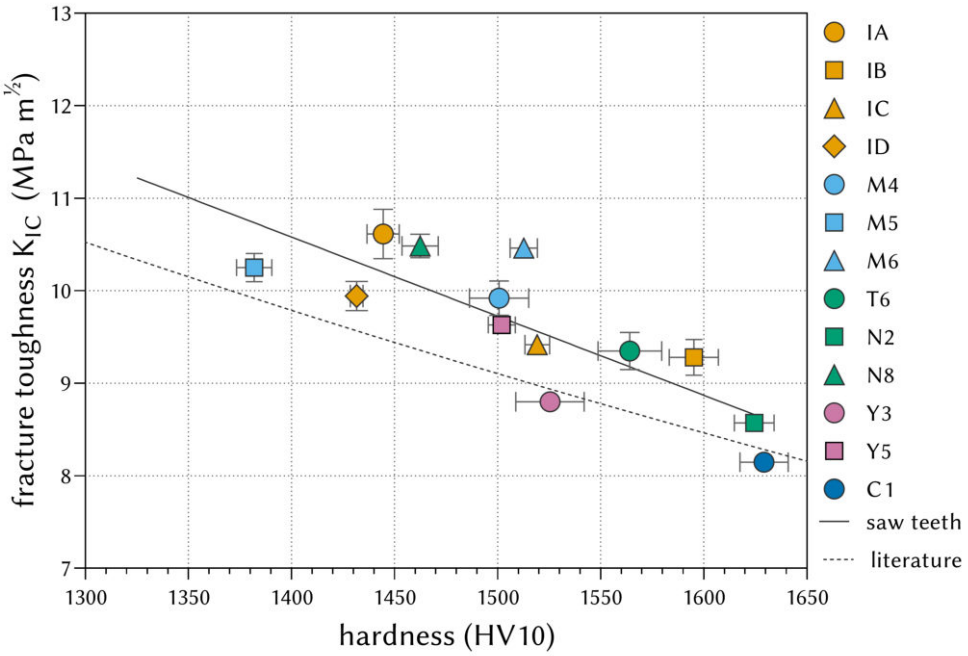

Figure 56: Mechanical properties of the commercial saw teeth grades, trendline and comparison with literature [1].

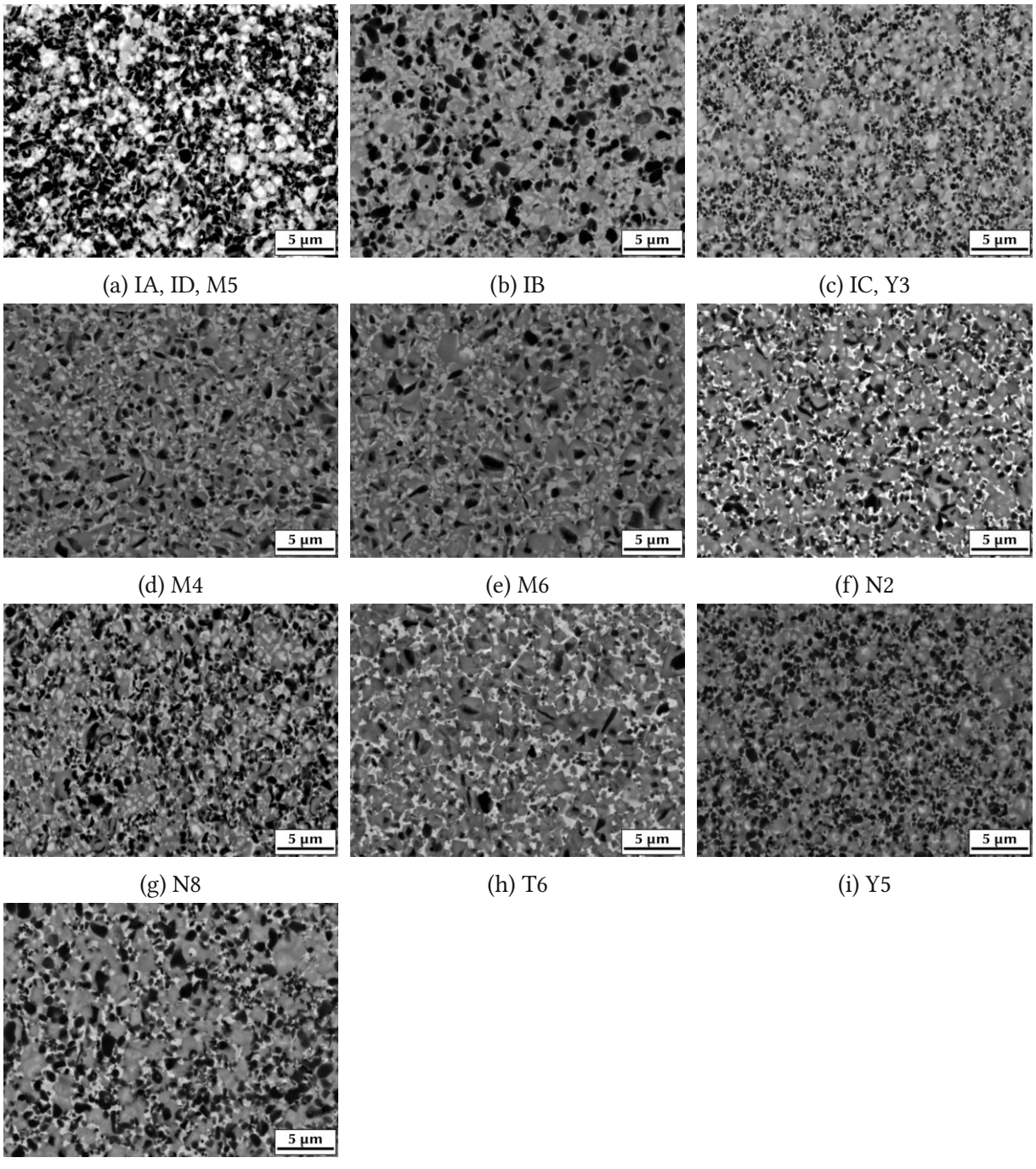

(a) IA, ID, M5 (b) IB (c) IC, Y3

(d) M4 (e) M6 (f) N2

(g) N8 (h) T6 (i) Y5

(j) C1

Figure 57: BSE-SEM images showing the microstructure of the commercial saw teeth grades, 10,000x magnification.

5.2. Recreation of reference grades

Powder formulations were calculated from the elemental analysis to match the compositions of IA and N8. After investigation of all sintered cermets, two formulations were selected from each series that matched those target grades closest in mechanical properties and microstructure (fig. 58). In the I series, cermet I0-1_SAr achieved a fracture toughness of 9.5 MPa · $m^{1/2}$ and a hardness of 1420 HV10.

Whereas the hardness of the IA, ID and M5 grades could be reached, the fracture toughness is slightly lower than the reference grades. The mean grain size of I0-1_SAr could be responsible for the lower toughness, hence the use of coarser secondary carbide powders may lead to further improvements. The mechanical properties of N8 were closely matched by cermet N0-2_Ar with 10.4 MPa · $m^{1/2}$ and 1455 HV10. Consequently, the mechanical properties of both commercial target grades could sufficiently be recreated in a laboratory scale process based on the calculations from the elemental analysis.

Comparing the microstructure of I0-1_SAr with the IA reference, the most defining features are apparent. The Ti(C,N)-rich cores are predominantly isolated and only a few core-rim grains are formed. The remaining grains developed an inverse structure with a bright core and gray rim phase. However, some differences include the contrasting shape of the black Ti(C,N) grains due to different powder synthesis routes. Also, the cores of inverse grains are brighter, indicating a change in powder alloy state of the secondary carbides. Similarly, the fine microstructure, isolated Ti(C,N) cores and inverse grains of N8 were also recreated in N0-2_Ar. Again the round shape of the Ti(C,N) grains are the major difference compared to the elongated powder from the metal route synthesis in N8.

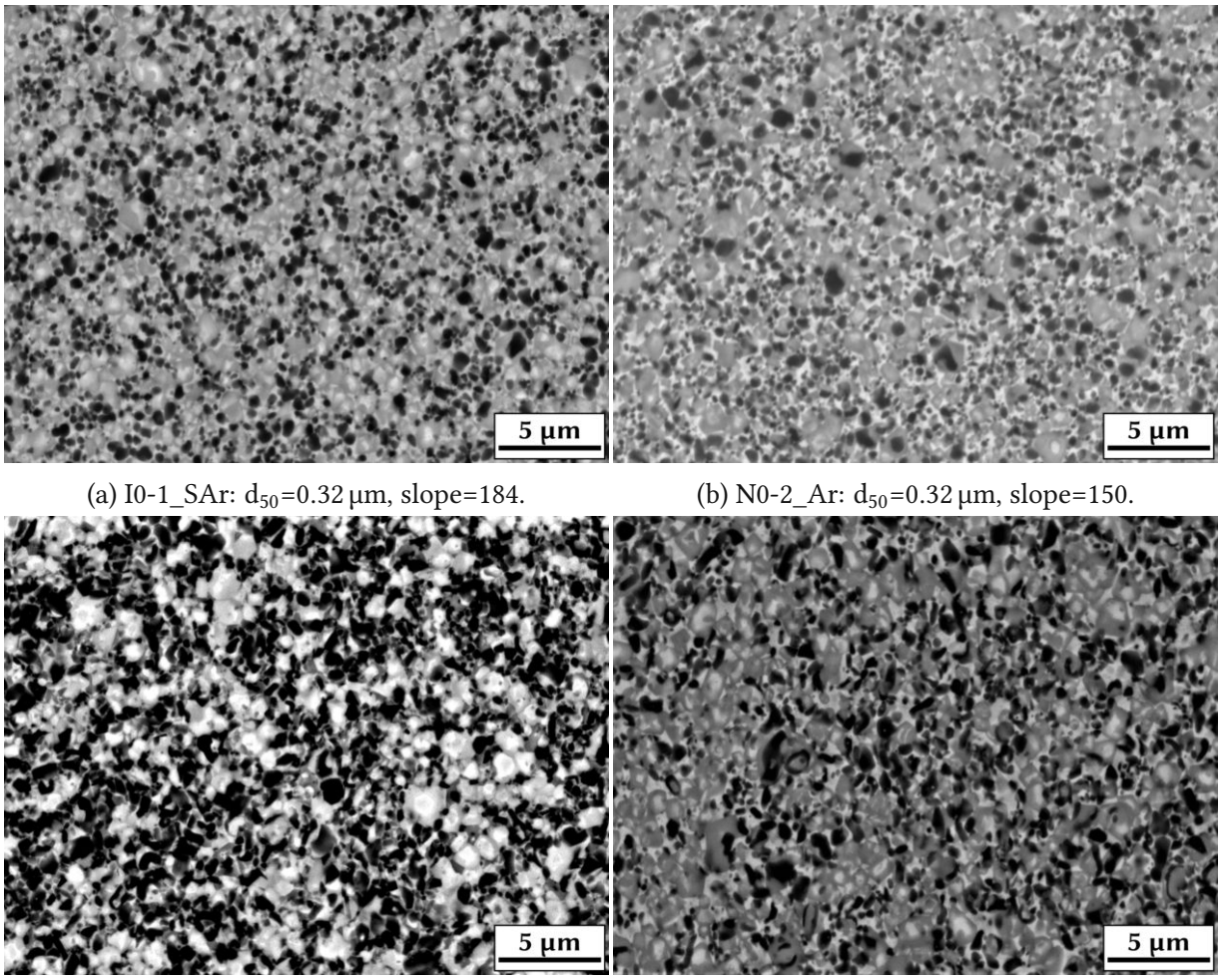

(a) I0-1_SAr: d_{50}=0.32 µm, slope=184.

(b) N0-2_Ar: d_{50}=0.32 µm, slope=150.

(c) IA: d_{50}=0.31 µm, slope=173.

(d) N8: d_{50}=0.32 µm, slope=157.

Figure 58: Comparison of microstructure and GSD parameters (cores) of I0-1_SAr and N0-2_Ar closely matching the mechanical properties of the target grades IA and N8.

5.3. Influence of the sintering atmosphere

Both I and N series cermets were sintered under Ar and atmospheres with different N_2 partial pressures. In fig. 60, the mechanical properties of the I and N cermets sintered under Ar or N_2 in the SinterHIP can be compared. Cermets of the I series are slightly harder when sintered under N_2 atmosphere. The exception is the formulation I3-1, where the opposite effect was observed. Samples I0-1, I0-2 and I2-1 are also more brittle when sintered in N_2, while the other cermets show similar toughness levels in any sintering atmosphere. Therefore, the I formulation seems to be less affected by the different N activities. This is also indicated by the very similar microstructures apparent in the BSE-SEM images comparing the SAr and SN samples (fig. 34). Only minor differences such as a slightly decreased grain size could be detected in the image analysis.

More obvious effects were attained for the cermets of the N series. With the exception of N0-2, all powder mixtures achieved similar or higher fracture toughness and hardness values when sintered under pure Ar atmosphere. A distinct drop in toughness was noticed when the atmosphere was changed to N_2. XRD phase analysis and BSE-SEM imaging revealed eta

phase for almost all samples of the N series. Hence, the strong toughness reduction and the corresponding increase in hardness can be explained by the formation of brittle eta phase.
As this extra phase usually forms in low C and N activities, a mixture of 50 mbar N_2 and 50 mbar Ar was introduced for an experimental vacuum sintering (50N). The brittleness was further increased in comparison to the 10N samples and eta phase was visible in XRD and BSE-SEM analysis. Therefore, the higher N partial pressure could not prevent the formation of the eta phase.
In the next step, 0.1 wt% or 0.3 wt% elemental C was added to three selected powder formulations (N0-2, N1-2 and N2-2). Additionally, the vacuum sintering was further adjusted to 10 mbar pure N_2. As presented in fig. 59, this did in fact improve the fracture toughness. However, the cermets were still more brittle than expected from the trendline and traces of eta phase were visible. Finally, the C-doped formulations were also sintered in the SinterHIP furnace. This combination of 0.3 wt% C addition and the higher C activity in the SinterHIP finally increased the C content of the three formulations enough to suppress the formation of eta phase. Ultimately, the mechanical properties of N8 could also be achieved with cermet N2-2+0.3%C when sintered under N_2 in the SinterHIP furnace.

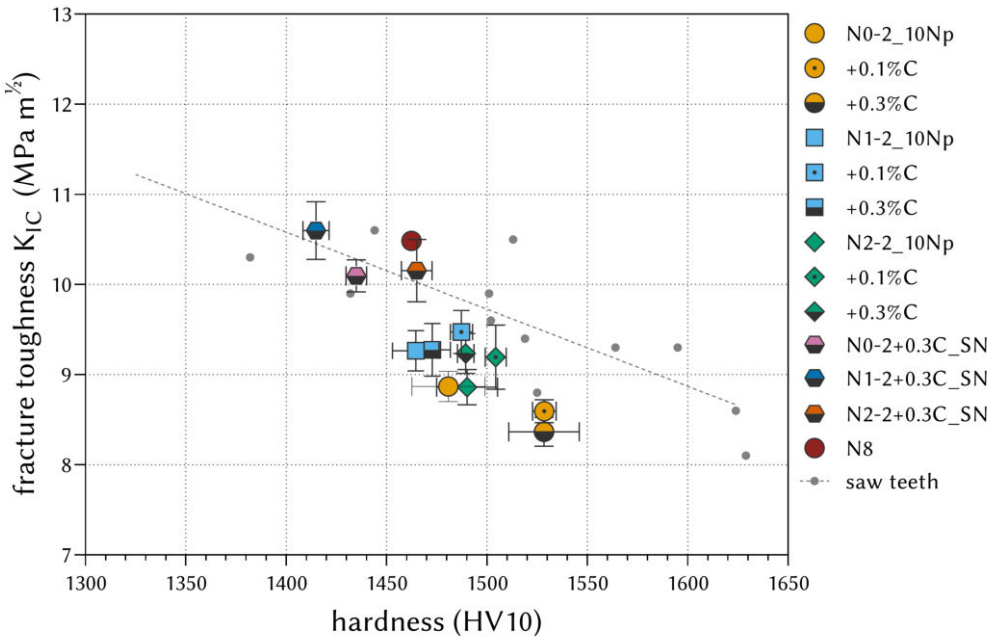

Figure 59: Hardness and fracture toughness of N series cermets with C addition in 10Np vacuum sintering and SN SinterHIP.

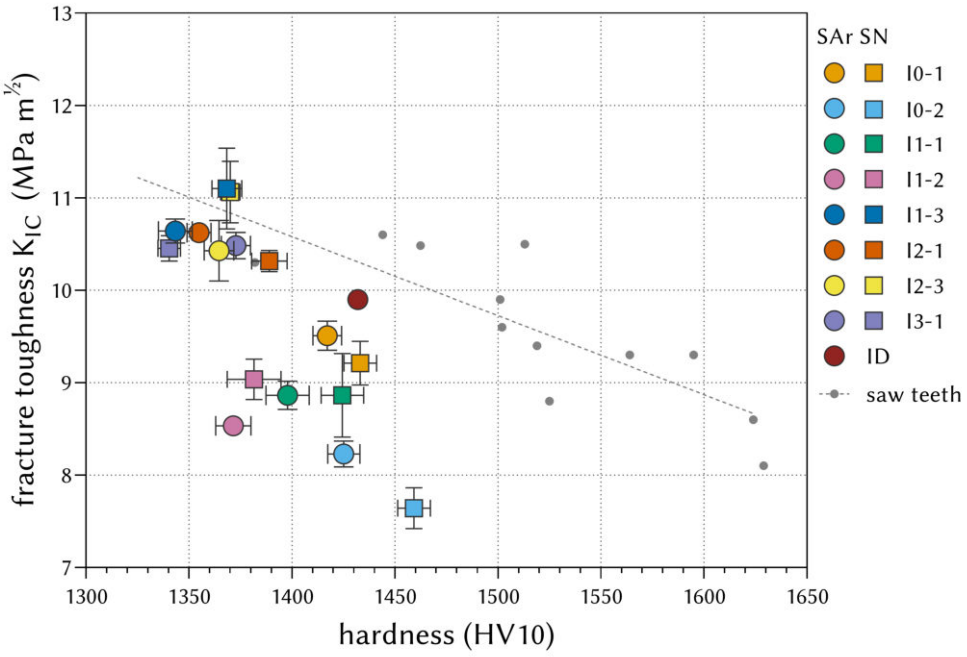

(a)

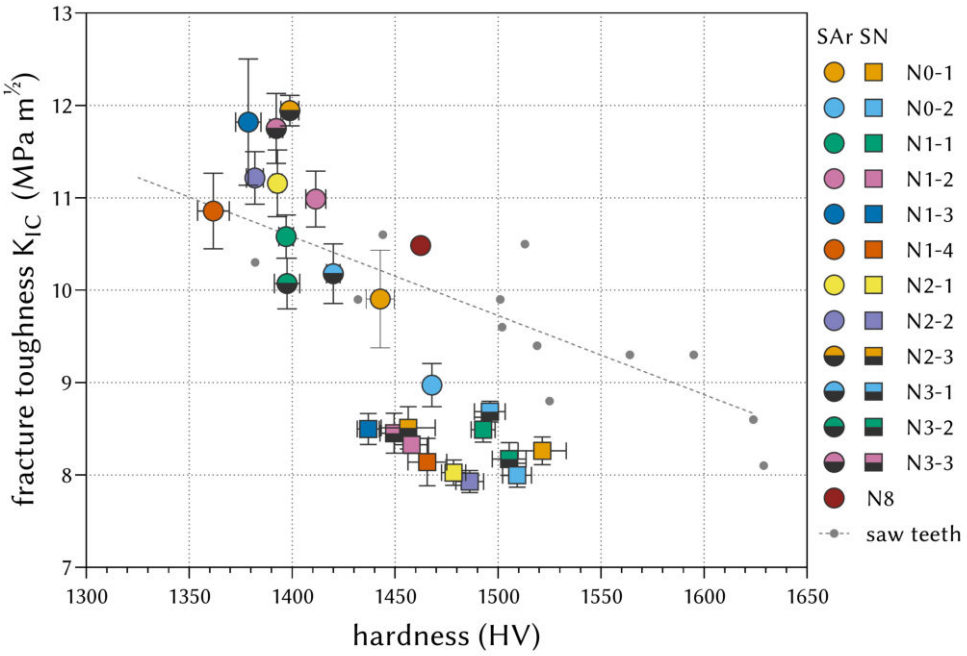

(b)

Figure 60: Hardness and fracture toughness of (a) I series and (b) N series cermets sintered under Ar and N_2 in the SinterHIP furnace.

5.4. Influence of the Ti(C,N) grain size

Ti(C,N) powders with different average grain sizes were used in the preparation of the I1 and N1 subgroup. Fig. 63 provides an overview of the resulting mechanical properties after sintering in Ar. Two cermets from the I series utilizing the finer 0.85 µm and 0.88 µm powders reached a relatively low fracture toughness of approx. 8.5 MPa · $m^{1/2}$ and a hardness just below 1400 HV10. Changing the Ti(C,N) to 1.76 µm grain size significantly improved the fracture toughness by almost 2 Mpa · $m^{1/2}$ while the hardness only decreased to approx. 1350 HV10. This leaves the sample with the coarsest Ti(C,N) with properties closer to the expected trend line for the relation between hardness and toughness.
In the N series, data from vacuum sintering and SinterHIP could be analyzed. Again, cermets with finer powders from ALMT and TIAG achieved very similar mechanical properties. However, the performance of these grades is closer to the N8 target grade. Further enhancements to the fracture toughness could be accomplished by implementing 1.07 µm Ti(C,N) for the vacuum sintered samples, while the SinterHIP cycle produced only a slightly softer cermet. Finally, the coarsest Ti(C,N) also increased the fracture toughness significantly in the N series. Cermet N1-3_Ar even reached a toughness of over 12 MPa · $m^{1/2}$.
The different grain sizes of the Ti(C,N) raw materials remain visible in BSE-SEM images after sintering (fig. 62). The average grain size of the isolated grains increases with each step and is most notable in the sample with 1.76 µm. However, some larger grains are also present in every sample as coarse $TiC_{0.7}N_{0.3}$ powder was used to balance the C/N ratio.

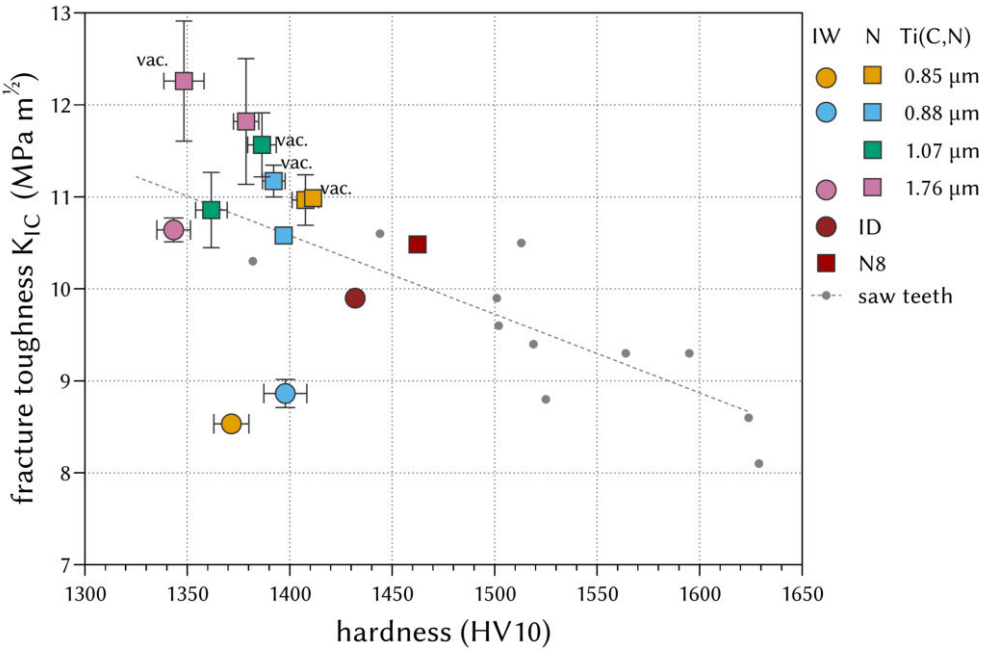

Figure 61: Hardness and fracture toughness of I and N series cermets with different Ti(C,N) grain sizes.

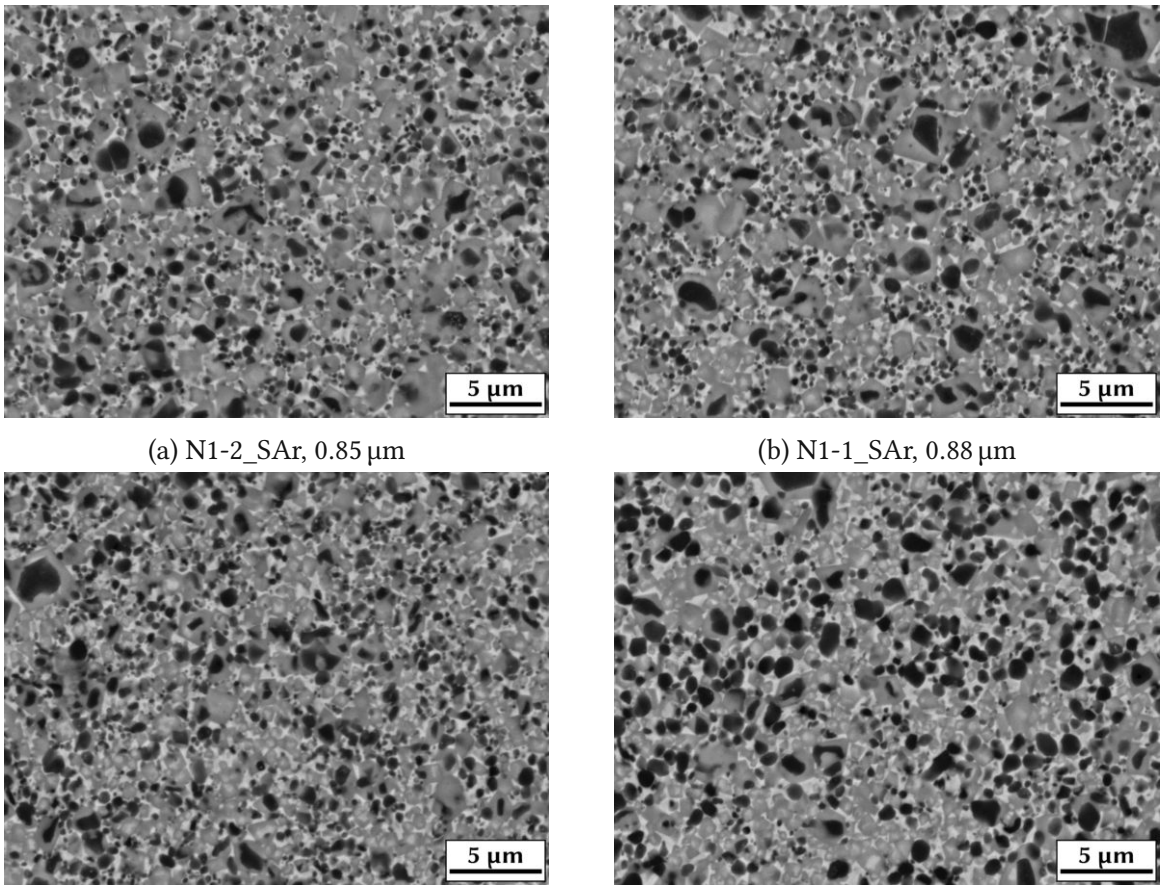

(a) N1-2_SAr, 0.85 µm (b) N1-1_SAr, 0.88 µm

(c) N1-4_SAr, 1.07 µm (d) N1-3_SAr, 1.76 µm

Figure 62: Microstructure of the N1 Series with four different Ti(C,N) powder grain sizes.

5.5. Influence of the powder alloy state

In two additional subsets, (Ti,W)(C,N) and (Ti,W)C were utilized in the powder formulation. In all samples, some Ti(C,N) was added to keep the elemental composition constant. The mechanical properties of the resulting cermets are shown in fig. 63. When the I cermets were based on pre-alloyed powders, the fracture toughness increased to a similar extent to the use of coarse Ti(C,N) powders. Both (Ti,W)(C,N) and (Ti,W)C led to a toughness around 10.5 Mpa $\cdot$ $m^{1/2}$ and hardness above 1350 HV10. When coarse Ti(C,N) was added to the (Ti,W)(C,N) cermet, the fracture toughness was not further improved. This could be explained by the small amounts added compared to the I1 series.

For the N series cermets, a similar trend was found for the cermets using (Ti,W)(C,N) powder. Toughness was enhanced by approx. 1 MPa $\cdot$ $m^{1/2}$ while the hardness slightly decreased. As the cermets in the N3 series contain relatively small amounts of (Ti,W)C to arrive at the correct C/N stoichiometry, only the sample with coarse Ti(C,N) powder gained a higher toughness. Mechanical properties similar to the N0-1 cermet were found in the samples with finer Ti(C,N). Overall, the best ratio of hardness and fracture toughness was reached in cermet N3-3_Ar with a combination of coarse Ti(C,N) and (Ti,W)C.

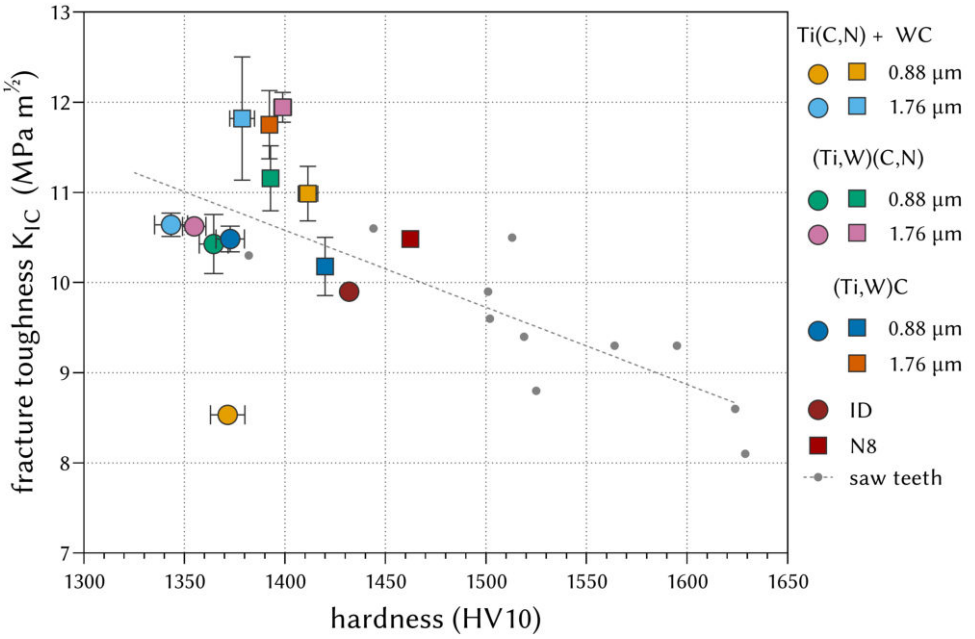

Figure 63: Hardness and fracture toughness of I (circles) and N series (squares) cermets with different pre-alloyed powders and two Ti(C,N) grain sizes.

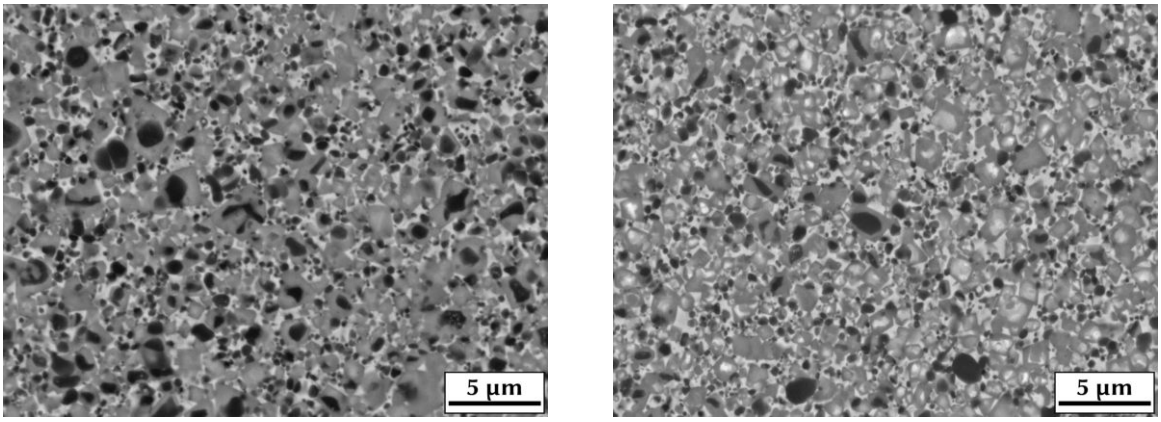

(a) N1-2_SAr, Ti(C,N) + WC.

(b) N2-2_SAr, (Ti,W)(C,N).

Figure 64: Microstructure of N series cermets with two different powder alloy states.

6. Conclusion and outlook

The investigations under laboratory settings allowed the identification of the previously described trends. Also, certain limitations were revealed. First, high temperature properties could not be assessed with the readily available laboratory equipment. Attributes such as thermal shock resistance or high temperature hardness can play an important role for interrupted cutting applications. Therefore, further research with this focus could provide important insights, especially regarding the secondary carbides TaC and NbC typically implemented to improve the mentioned high temperature properties. Secondly, elemental analysis with a high spatial resolution could improve the understanding of dissolution processes. With methods such as transmission electron microscopy, the diffusion and precipitation processes of core and rim phase formation can be studied in detail.

All in all, this thesis provides a deeper understanding of the influence factors leading to significantly tougher cermets. A high fracture toughness is especially important for cutting tool applications as it reduces wear rate and improves tool life. Therefore, the findings of this thesis can be applied to the development of cermet formulation for future saw teeth. As a possible next step, the powder mixtures of the I and N series could be sintered into saw teeth in special pressing dies and assembled to finished circular saw blades. After comparison with commercially available saw blades, results such as cutting speed, feed rate and tool life can be related to the composition and microstructure. After prototyping, the powder formulations can be further adjusted to fit the specific needs of the cermet saw teeth.

7. References

[1] W. Lengauer and F. Scagnetto. “Ti (C, N)-based cermets: Critical review of achievements and recent developments”. In: *Solid State Phenomena* 274 (2018), pp. 53–100.

[2] A. Rizzo, S. Goel, M. Luisa Grilli, R. Iglesias, L. Jaworska, V. Lapkovskis, P. Novak, B. Postolnyi, and D. Valerini. “The critical raw materials in cutting tools for machining applications: A review”. In: *Materials* 13.6 (2020), p. 1377.

[3] W. Lengauer. “Carbides: Transition-Metal Solid-State Chemistry”. In: *Encyclopedia of inorganic and bioinorganic chemistry* (2011).

[4] Q. Yang, W. Lengauer, T. Koch, M. Scheerer, and I. Smid. “Hardness and elastic properties of Ti (CxN1- x), Zr (CxN1- x) and Hf (CxN1- x)”. In: *Journal of alloys and compounds* 309.1-2 (2000), pp. L5–L9.

[5] T. Licko, V. Figusch, and J. Puchyova. “Carbothermal reduction and nitriding of TiO2”. In: *Journal of the European Ceramic Society* 5.4 (1989), pp. 257–265.

[6] A.W. Weimer. *Carbide, nitride and boride materials synthesis and processing*. Springer Science & Business Media, 2012.

[7] V. Schwarz, I. Zivadinovic, B. Lisnard, F. Traxler, R. Viala, and W. Lengauer. “Optimised properties of Ti (C, N)-based cermets by variation of the W/Mo ratio”. In: *Proc. WorldPM* (2016).

[8] T. Cutard, S. Bolognini, G. Feusier, C. Verdon, T. Viatte, and W. Benoit. “Microstructure and mechanical properties of Ti(C,N)-Mo2C-(Ni, Co) cermets as a function of their initial chemical composition”. In: *ECERS V-5th conference and exhibition of the European Ceramic Society*. Vol. 132. 1997, p–747.

[9] S. Chao, N. Liu, Y. Yuan, C. Han, Y. Xu, M. Shi, and J. Feng. “Microstructure and mechanical properties of ultrafine Ti (CN)-based cermets fabricated from nano/submicron starting powders”. In: *Ceramics International* 31.6 (2005), pp. 851–862.

[10] Y.C. Chai, H.L. Liu, C.Z. Huang, B. Zou, and H.H. Liu. “Study on influencing factors of mechanical properties of Ti (C, N)-based cermets”. In: *Key Engineering Materials*. Vol. 589. Trans Tech Publ. 2014, pp. 578–583.

[11] A. Demoly, W. Lengauer, C. Veitsch, and K. Rabitsch. “Effect of submicron Ti (C, N) on the microstructure and the mechanical properties of Ti (C, N)-based cermets”. In: *International Journal of Refractory Metals and Hard Materials* 29.6 (2011), pp. 716–723.

[12] A. Demoly, C. Veitsch, W. Lengauer, and K. Rabitsch. “Cermets based on new submicron Ti (C, N) powder: microstructural development during sintering and mechanical properties”. In: *Advances in Sintering Science and Technology II: Ceram. Trans* 232 (2012), pp. 57–69.

[13] Y. Li, N. Liu, X. Zhang, and C. Rong. “Effect of WC content on the microstructure and mechanical properties of (Ti, W)(C, N)–Co cermets”. In: *International Journal of Refractory Metals and Hard Materials* 26.1 (2008), pp. 33–40.

[14] Y. Wu, J. Xiong, Z. Guo, M. Yang, J. Chen, S. Xiong, H. Fan, and J. Luo. "Microstructure and fracture toughness of Ti (C0. 7N0. 3)-WC-Ni cermets". In: *International Journal of Refractory Metals and Hard Materials* 29.1 (2011), pp. 85–89.

[15] X. Xu, Y. Zheng, G. Zhang, Z. Ke, H. Wu, Q. Ding, and X. Lu. "Effect of WC addition and cooling rate on microstructure, magnetic and mechanical properties of Ti (C0. 6, N0. 4)-WC-Mo-Ni cermets". In: *International Journal of Refractory Metals and Hard Materials* 84 (2019), p. 105001.

[16] G.T. Zhang, Y. Zheng, Y.J. Zhao, W. Zhou, J. J. Zhang, Z. Ke, and P. Feng. "Effect of WC content on the mechanical properties and high temperature oxidation behavior of Ti (C, N)-based cermets". In: *Solid State Phenomena*. Vol. 274. Trans Tech Publ. 2018, pp. 9–19.

[17] J.W. Kim, S.Y. Ahn, and S. Kang. "Effect of the complete solid-solution phase on the microstructure of Ti (CN)-based cermet". In: *International Journal of Refractory Metals and Hard Materials* 27.2 (2009), pp. 224–228.

[18] C. Park, S. Nam, and S. Kang. "Carbide/binder interfaces in Ti (CN)–(Ti, W) C/(Ti, W)(CN)-based cermets". In: *Journal of Alloys and Compounds* 657 (2016), pp. 671–677.

[19] C. Park, S. Nam, and S. Kang. "Enhanced toughness of titanium carbonitride-based cermets by addition of (Ti, W) C carbides". In: *Materials Science and Engineering: A* 649 (2016), pp. 400–406.

[20] J. Lv, Y. Du, M. Lou, K. Xu, and K. Chang. "Enhancing mechanical properties of Ti (C, N)-based cermets via preparation with (Ti, W)(C, N) multi-component powder". In: *International Journal of Refractory Metals and Hard Materials* 108 (2022), p. 105931.

[21] C. Waldner, M. Fuerst, and W. Lengauer. "Influence of the hard-phase alloy status on the microstructure evolution and properties of Ti (C, N)-based cermets". In: *Proc. EuroPM 2020*. European Powder Metallurgy Association. 2020, p. 6.

[22] P. Wu, Y. Zheng, Y. Zhao, and H. Yu. "Effect of TaC addition on the microstructures and mechanical properties of Ti (C, N)-based cermets". In: *Materials & Design* 31.7 (2010), pp. 3537–3541.

[23] C. Liu, N. Lin, and Y.H. He. "Influence of Mo2C and TaC additions on the microstructure and mechanical properties of Ti (C, N)-based cermets". In: *Ceramics International* 42.2 (2016), pp. 3569–3574.

[24] Q. Gou, J. Xiong, Z. Guo, J. Liu, L. Yang, and X. Li. "Influence of NbC additions on microstructure and wear resistance of Ti (C, N)-based cermets bonded by CoCrFeNi high-entropy alloy". In: *International Journal of Refractory Metals and Hard Materials* 94 (2021), p. 105375.

[25] We. Wan, J. Xiong, and M. Liang. "Effects of secondary carbides on the microstructure, mechanical properties and erosive wear of Ti (C, N)-based cermets". In: *Ceramics International* 43.1 (2017), pp. 944–952.

[26] D. Mari, S. Bolognini, G. Feusier, T. Cutard, T. Viatte, and W. Benoit. "TiMoCN based cermets Part II. Microstructure and room temperature mechanical properties". In: *International Journal of Refractory Metals and Hard Materials* 21.1-2 (2003), pp. 47–53.

[27] Q. Xu, X. Ai, J. Zhao, F. Gong, J. Pang, and Y. Wang. "Effects of metal binder on the microstructure and mechanical properties of Ti (C, N)-based cermets". In: *Journal of Alloys and Compounds* 644 (2015), pp. 663–672.

[28] W. Zhou, Y. Zheng, Y. Zhao, Y. Ma, and W. Xiong. "Microstructure characterization and mechanical properties of Ti (C, N)-based cermets with AlN addition". In: *Ceramics International* 41.3 (2015), pp. 5010–5016.

[29] L.W. Xu, N. Lin, L.B. Zhao, C. Ma, Z.Y. Wang, and Y.H. He. "Improvement in wear and corrosion resistance of Ti (C, N)-based cermets via Aluminum nitride additions". In: *Vacuum* 168 (2019), p. 108849.

[30] W. Lengauer, V. Schwarz, and F. Scagnetto. "Interdependency of hard phase and binder phase composition in Ti (C, N)-based cermets". In: *Proceedings of the WorldPM* (2018), pp. 817–825.

[31] D. Shetty and I. Wright. "On estimating fracture toughness of cemented carbides from Palmqvist crack sizes". In: *Journal of materials science letters* 5.3 (1986), pp. 365–368.

[32] International Organization for Standardization. *ISO 4499-4: 2016. Hardmetals—Metallographic Determination of Microstructure—Part 4: Characterisation of Porosity, Carbon Defects and Eta-Phase Content.* 2016.

[33] P. Duwez and F. Odell. "Phase relationships in the binary systems of nitrides and carbides of zirconium, columbium, titanium, and vanadium". In: *Journal of the Electrochemical Society* 97.10 (1950), p. 299.

[34] M. Kresch, O. Delaire, R. Stevens, JYY Lin, and B. Fultz. "Neutron scattering measurements of phonons in nickel at elevated temperatures". In: *Physical Review B* 75.10 (2007), p. 104301.

[35] W. Sproul. "The Effect of the Eta Carbide Layer on the Tool Life of Titanium Carbide Coated Cemented Carbide Tools". PhD thesis. Brown University, 1975.

[36] D.S. Janisch, W. Lengauer, K. Roediger, K. Dreyer, and H. Van den Berg. "Cobalt capping: why is sintered hardmetal sometimes covered with binder?" In: *International Journal of Refractory Metals and Hard Materials* 28.3 (2010), pp. 466–471.

[37] J. Garcia, S. Englund, and F. Hagloef. "Controlling cobalt capping in sintering process of cermets". In: *International Journal of Refractory Metals and Hard Materials* 62 (2017), pp. 126–133.

[38] S. Wawrzik, A. Demoly, C. Veitsch, and W. Lengauer. "Ti (C, N)-Based Cermets: Evolution and Stability of Microstructure Within Sintering and High-Temperature/High-Pressure Annealing". In: (2011).

[39] Y. Kang and S. Kang. “The surface microstructure of TiC-(Ti, W) C-WC-Ni cermets sintered in a nitrogen atmosphere”. In: *Materials Science and Engineering: A* 527.27-28 (2010), pp. 7241–7246.

[40] X. Kang, N. Lin, Y. He, and M. Zhang. “Influence of ZrC addition on the microstructure, mechanical properties and oxidation resistance of Ti (C, N)-based cermets”. In: *Ceramics international* 44.10 (2018), pp. 11151–11159.

A. Appendix

A.1. I series

Table 39: Powder weighing of I series mixtures.

	powder weighing (wt%)							
	I0-1	**I0-2**	**I1-1**	**I1-2**	**I1-3**	**I2-1**	**I2-3**	**I3-1**
0.88 µm $TiC_{0.5}N_{0.5}$	47.69	-	45.72	-	-	21.44	-	-
0.85 µm $TiC_{0.5}N_{0.5}$	-	47.71	-	43.87	-	-	-	-
1.76 µm $TiC_{0.5}N_{0.5}$	-	-	-	-	42.65	-	17.41	-
$TiC_{0.7}N_{0.3}$	-	-	2.18	3.98	-	-	-	-
$TiC_{0.3}N_{0.7}$	-	-	-	-	-	6.45	10.51	35.20
(Ti,W)(C,N)	-	-	-	-	-	36.34	36.32	-
(Ti,W)C	-	-	-	-	-	-	-	25.25
WC	16.76	16.77	16.62	16.67	16.64	-	-	4.02
Mo_2C	1.53	1.53	1.52	1.52	1.52	1.52	1.51	1.52
TaC	11.29	11.30	11.20	11.23	11.21	11.19	11.19	11.24
NbC	1.20	1.20	1.19	1.19	1.19	1.19	1.19	1.19
ZrC	0.38	0.38	0.38	0.38	0.38	0.38	0.38	0.38
Co	10.05	10.03	10.08	10.06	10.07	10.21	10.21	10.07
Ni	10.05	10.04	10.08	10.06	10.07	10.21	10.21	10.07
NiAl	1.05	1.05	1.05	1.05	1.05	1.07	1.06	1.05

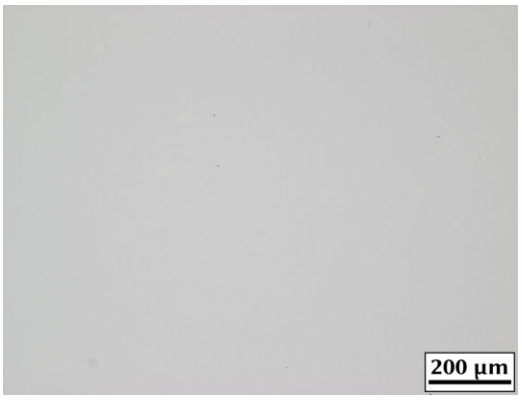

(a) LOM, 100x magnification.

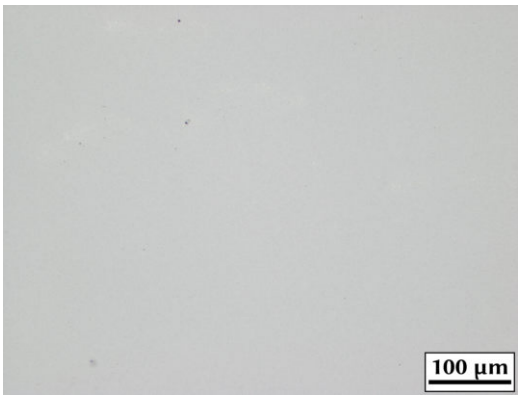

(b) LOM, 200x magnification.

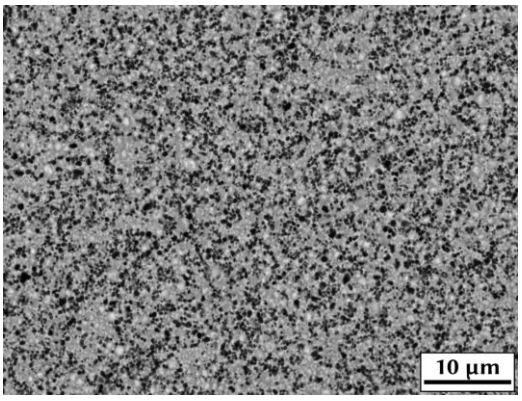

(c) BSE-SEM, 5000x magnification.

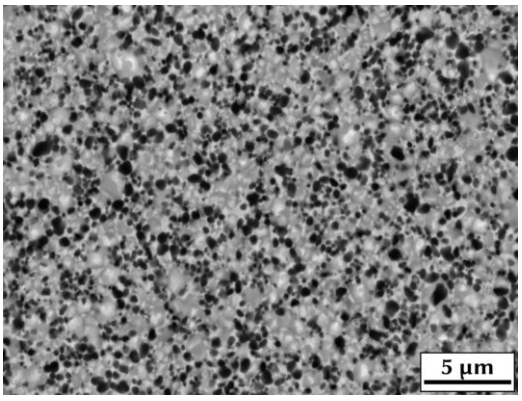

(d) BSE-SEM, 10,000x magnification.

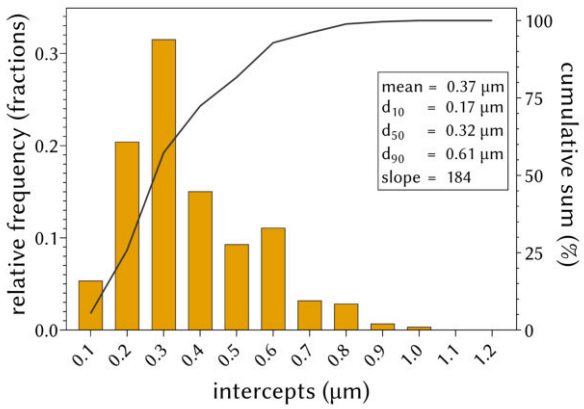

(e) GSD of cores.

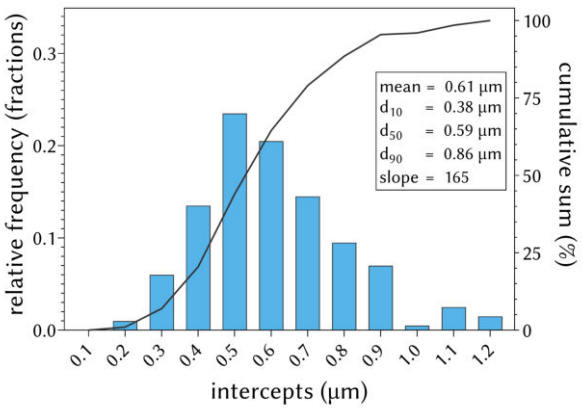

(f) GSD of grains.

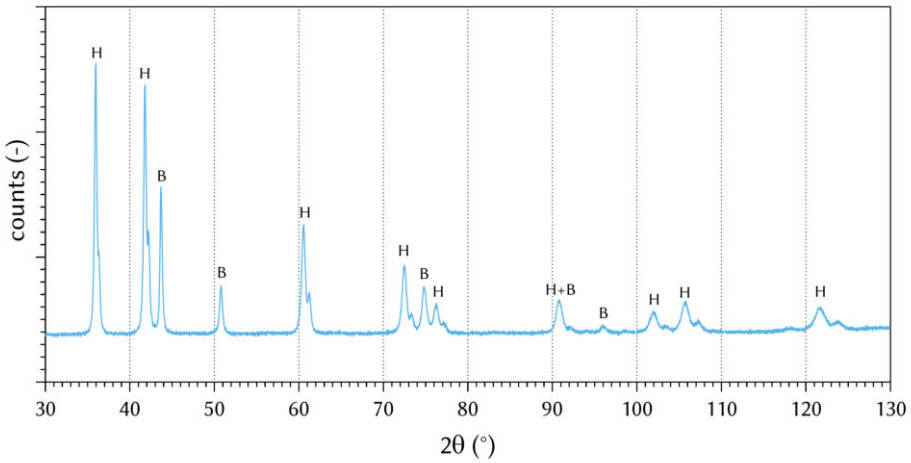

(g) XRD with hard phase (H) and binder (B) peaks identified.

Figure 65: LOM, BSE-SEM, GSD and XRD of I0-1_SAr.

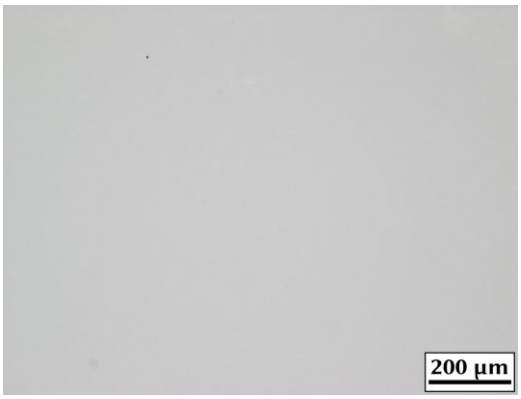

(a) LOM, 100x magnification.

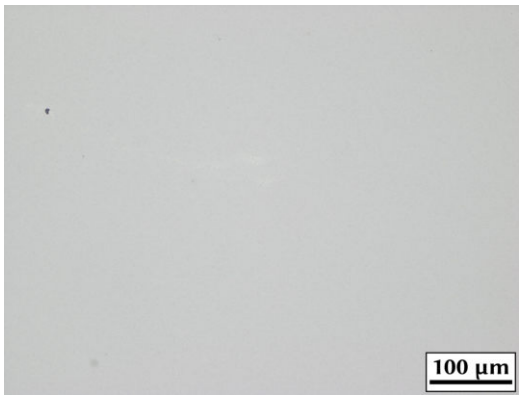

(b) LOM, 200x magnification.

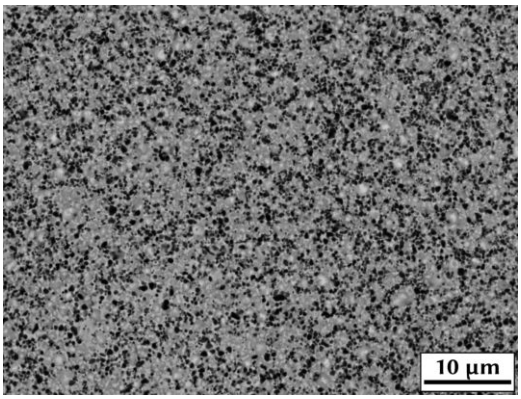

(c) BSE-SEM, 5000x magnification.

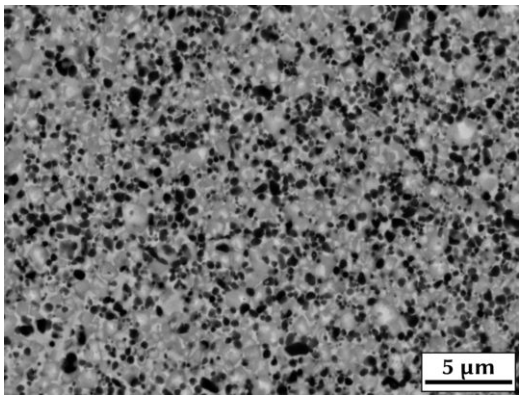

(d) BSE-SEM, 10,000x magnification.

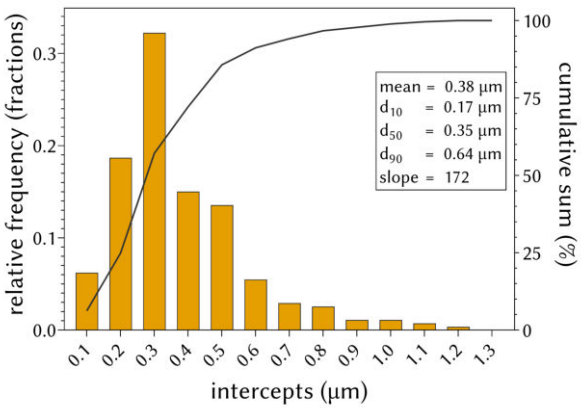

(e) GSD of cores.

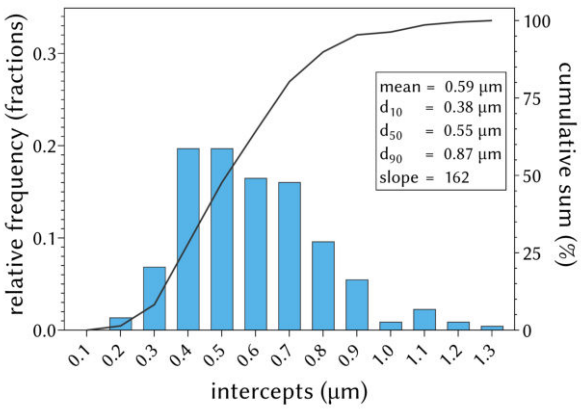

(f) GSD of grains.

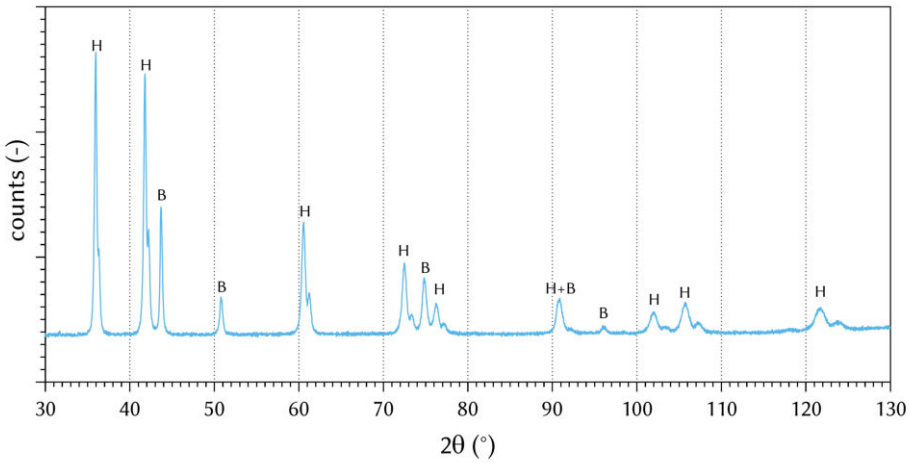

(g) XRD with hard phase (H) and binder (B) peaks identified.

Figure 66: LOM, BSE-SEM, GSD and XRD of I0-1_SN.

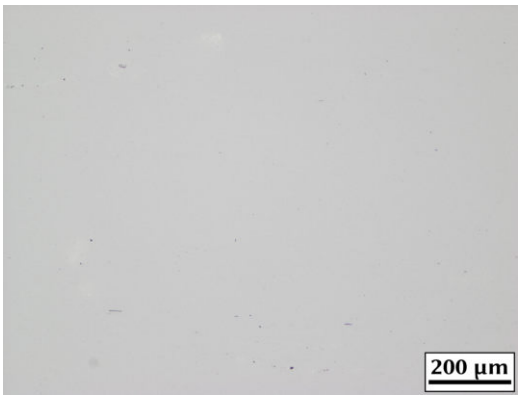

(a) LOM, 100x magnification.

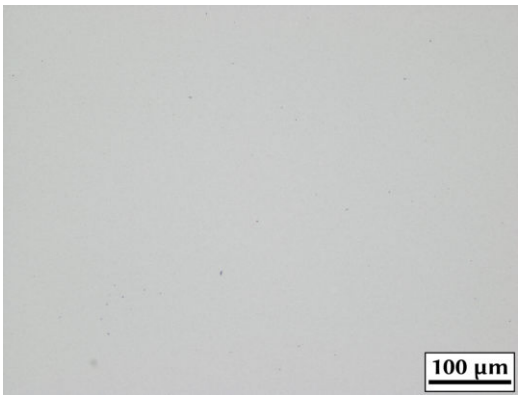

(b) LOM, 200x magnification.

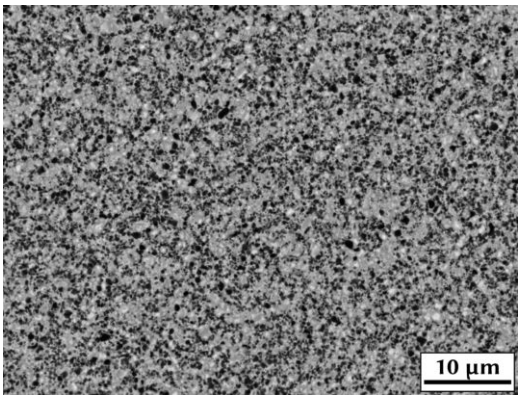

(c) BSE-SEM, 5000x magnification.

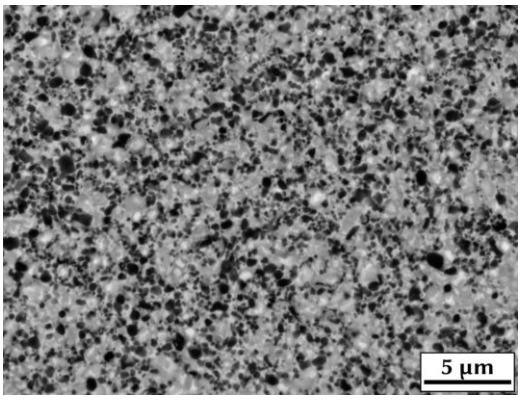

(d) BSE-SEM, 10,000x magnification.

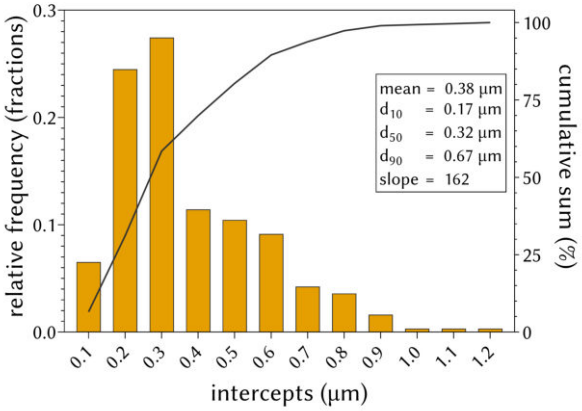

(e) GSD of cores.

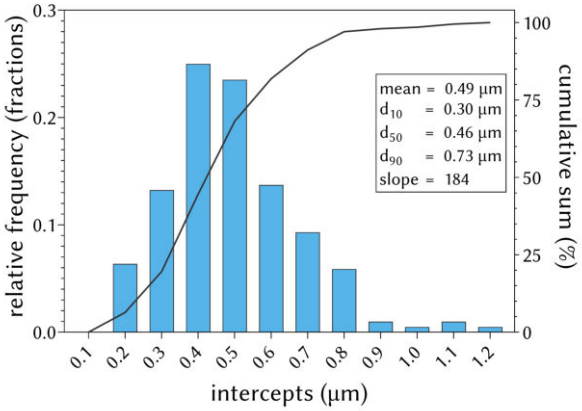

(f) GSD of grains.

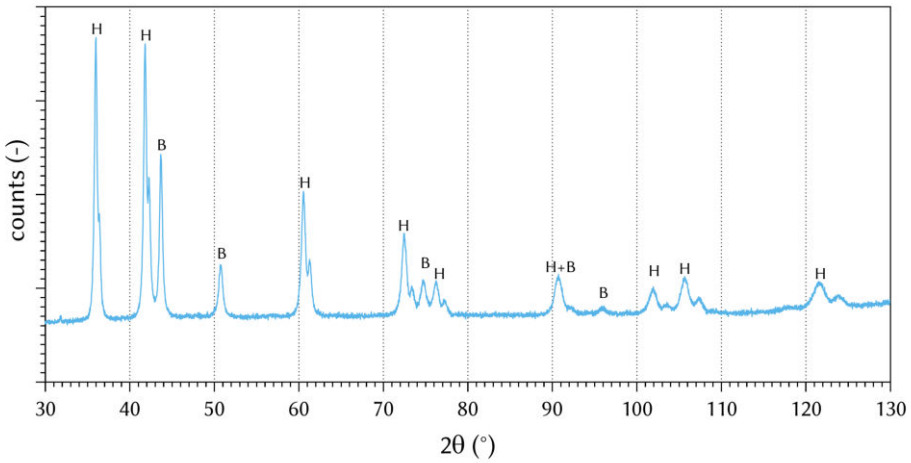

(g) XRD with hard phase (H) and binder (B) peaks identified.

Figure 67: LOM, BSE-SEM, GSD and XRD of I0-2_SAr.

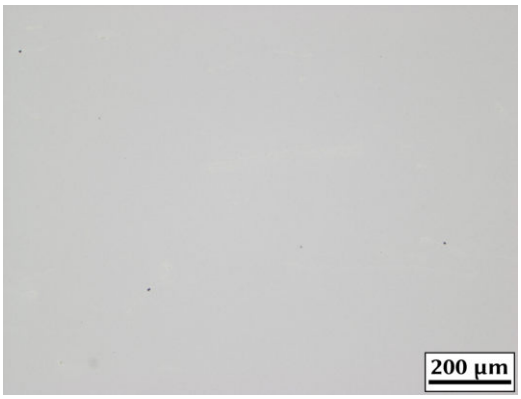

(a) LOM, 100x magnification.

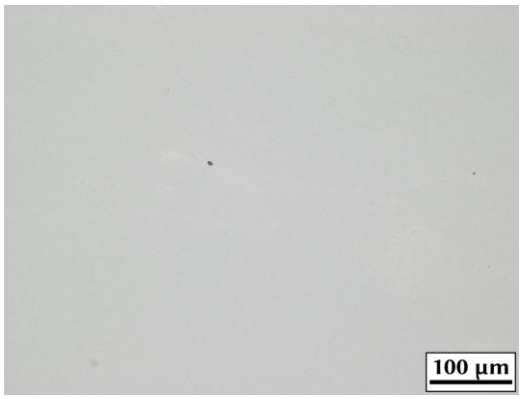

(b) LOM, 200x magnification.

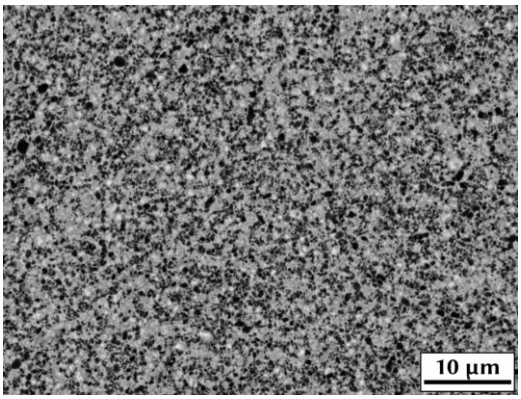

(c) BSE-SEM, 5000x magnification.

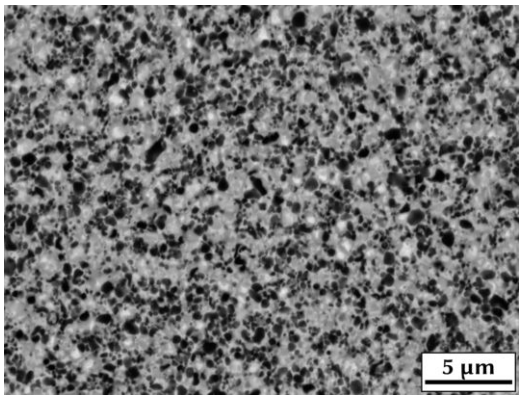

(d) BSE-SEM, 10,000x magnification.

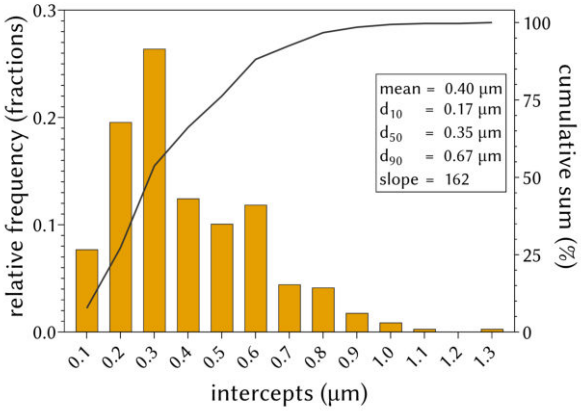

(e) GSD of cores.

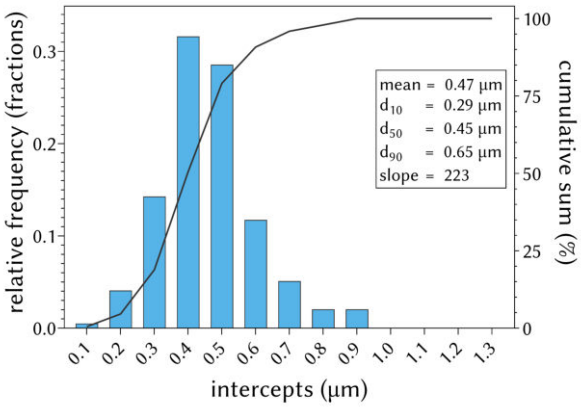

(f) GSD of grains.

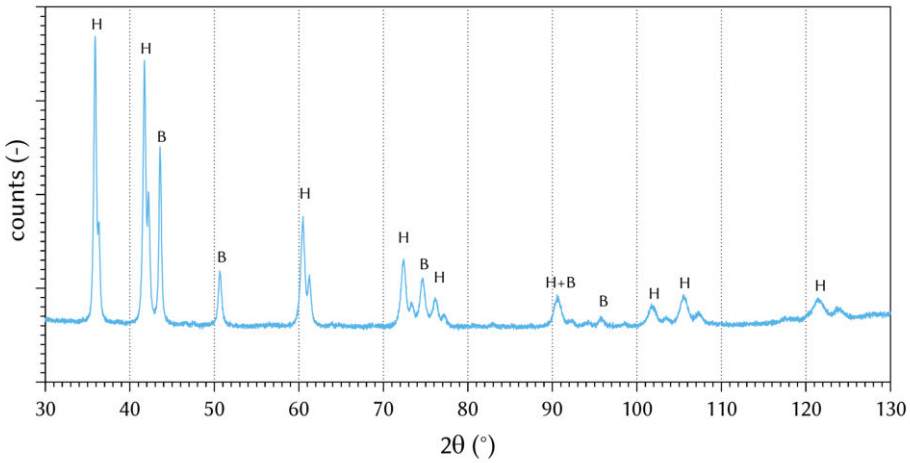

(g) XRD with hard phase (H) and binder (B) peaks identified.

Figure 68: LOM, BSE-SEM, GSD and XRD of I0-2_SN.

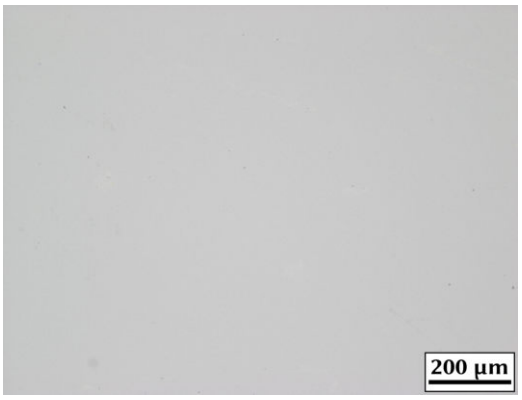

(a) LOM, 100x magnification.

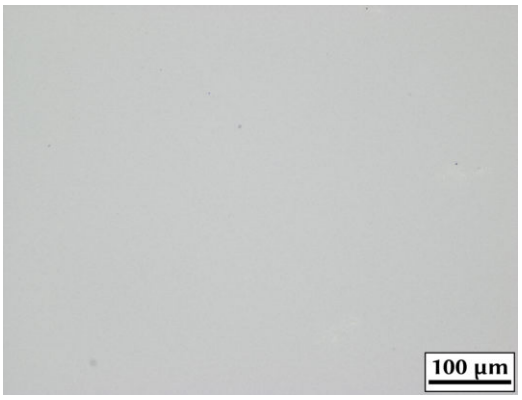

(b) LOM, 200x magnification.

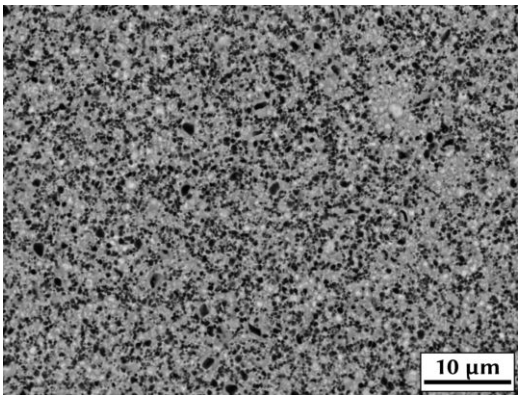

(c) BSE-SEM, 5000x magnification.

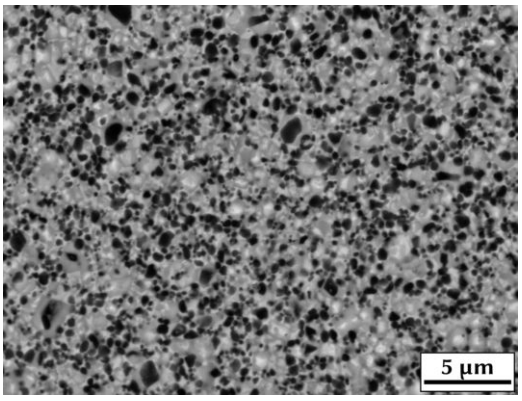

(d) BSE-SEM, 10,000x magnification.

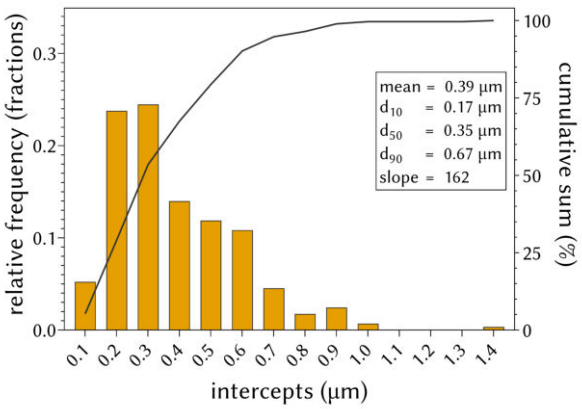

(e) GSD of cores.

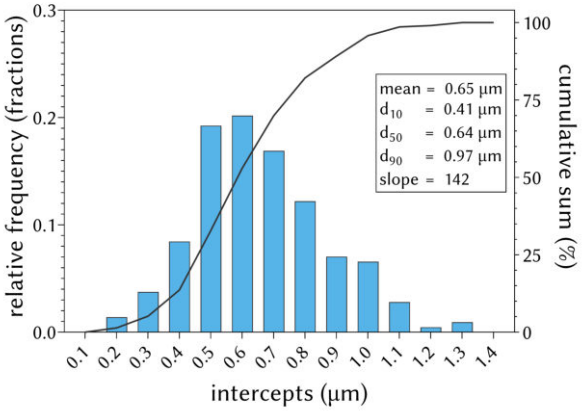

(f) GSD of grains.

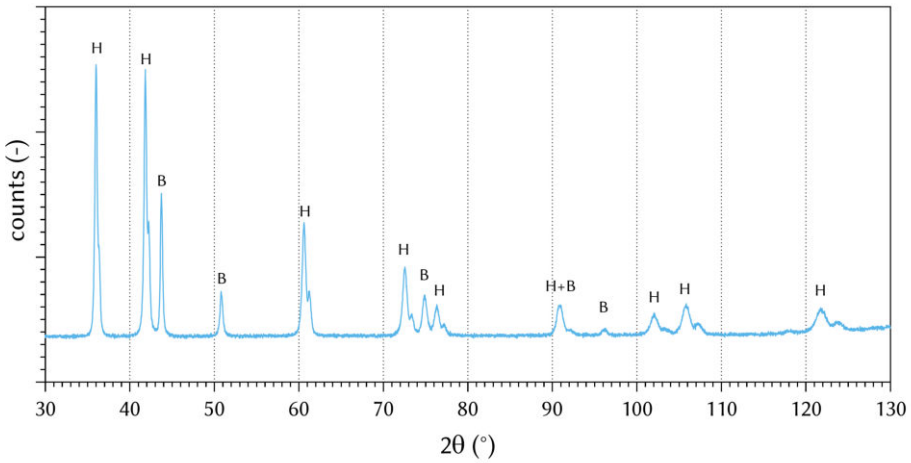

(g) XRD with hard phase (H) and binder (B) peaks identified.

Figure 69: LOM, BSE-SEM, GSD and XRD of I1-1_SAr.

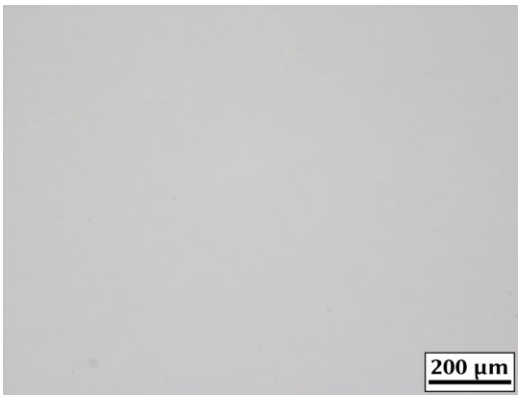

(a) LOM, 100x magnification.

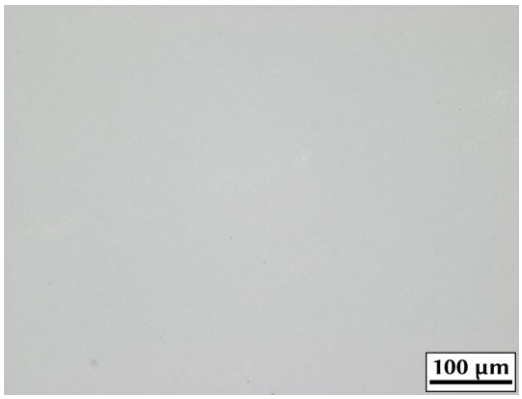

(b) LOM, 200x magnification.

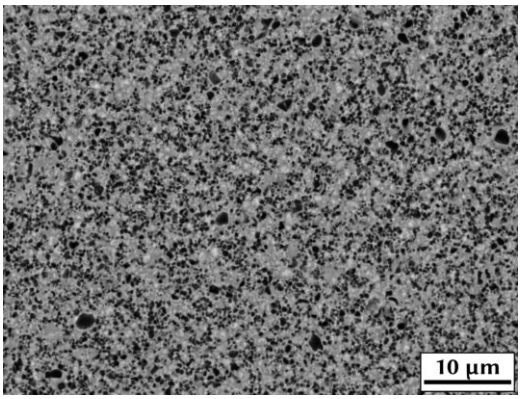

(c) BSE-SEM, 5000x magnification.

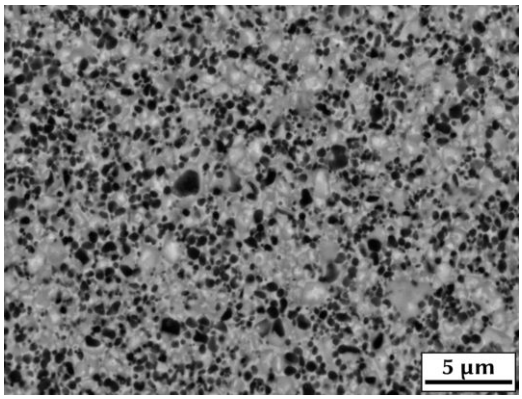

(d) BSE-SEM, 10,000x magnification.

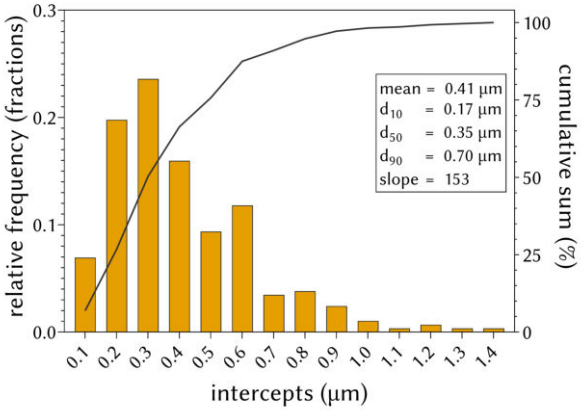

(e) GSD of cores.

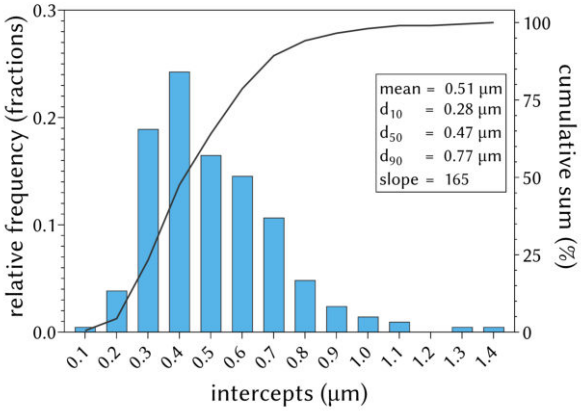

(f) GSD of grains.

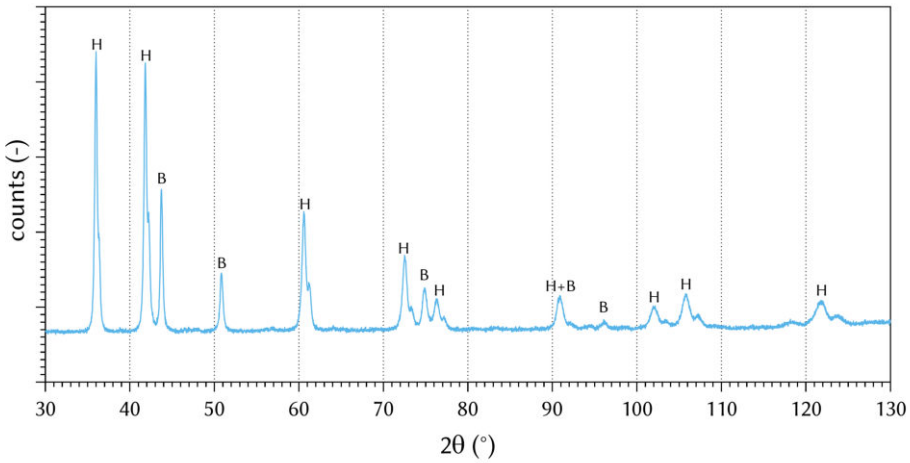

(g) XRD with hard phase (H) and binder (B) peaks identified.

Figure 70: LOM, BSE-SEM, GSD and XRD of I1-1_SN.

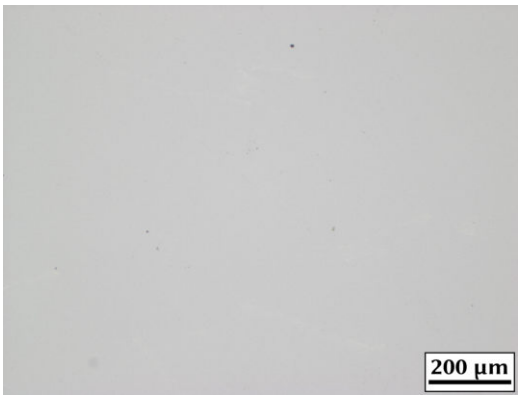

(a) LOM, 100x magnification.

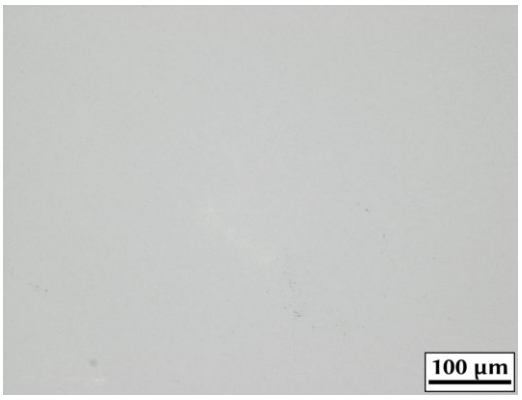

(b) LOM, 200x magnification.

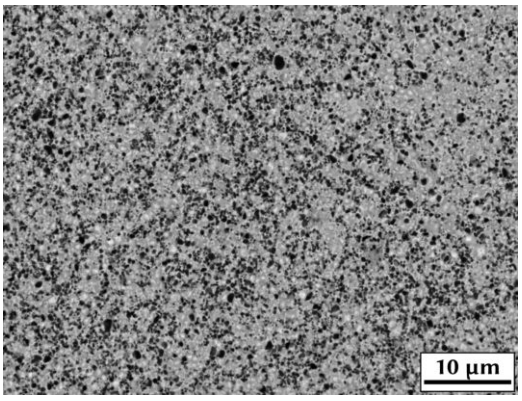

(c) BSE-SEM, 5000x magnification.

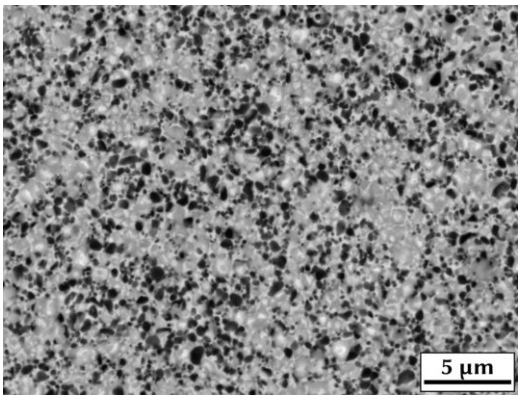

(d) BSE-SEM, 10,000x magnification.

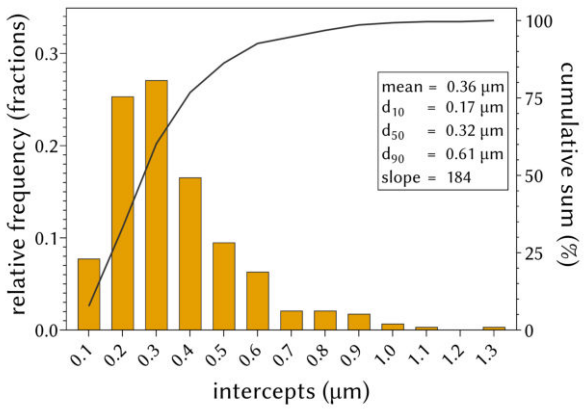

(e) GSD of cores.

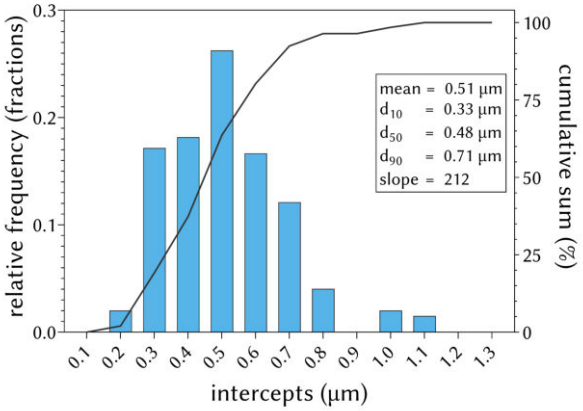

(f) GSD of grains.

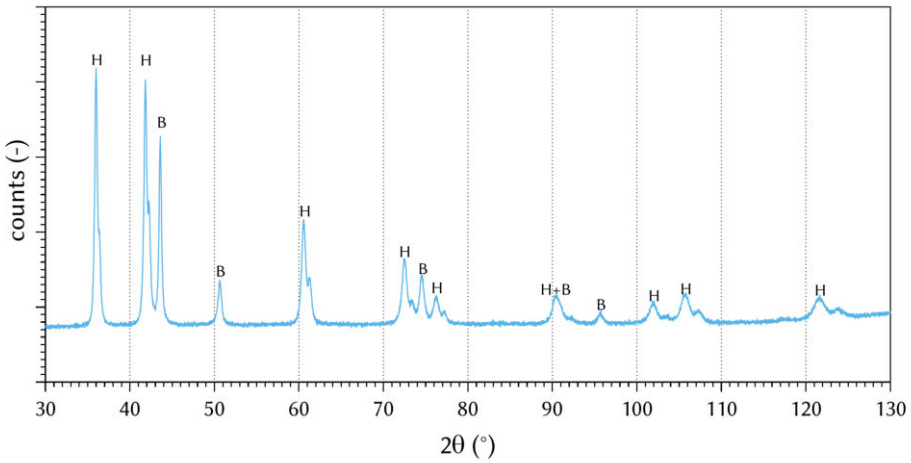

(g) XRD with hard phase (H) and binder (B) peaks identified.

Figure 71: LOM, BSE-SEM, GSD and XRD of I1-2_SAr.

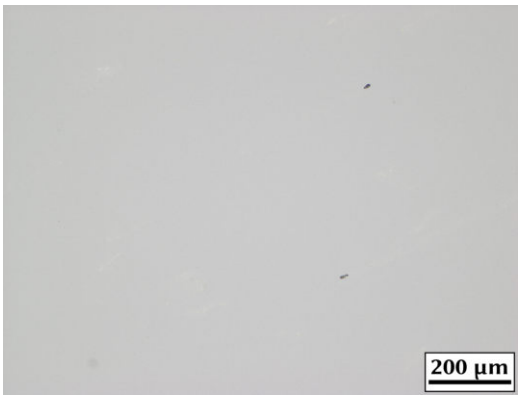

(a) LOM, 100x magnification.

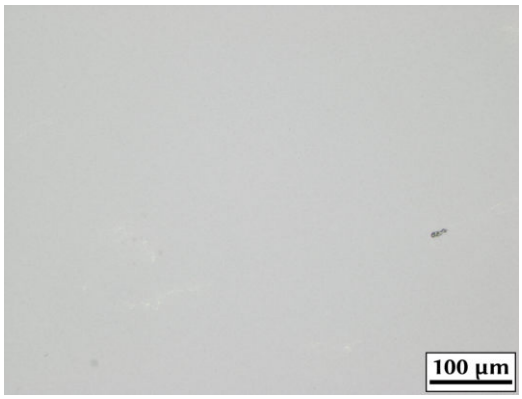

(b) LOM, 200x magnification.

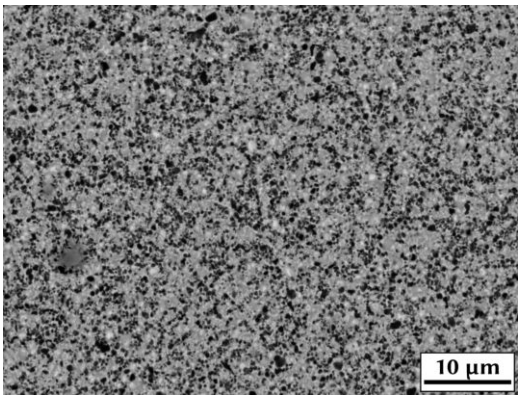

(c) BSE-SEM, 5000x magnification.

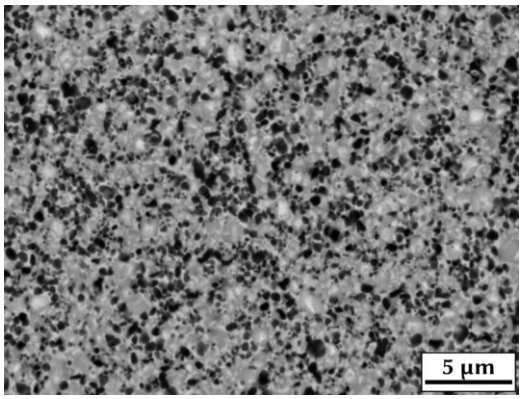

(d) BSE-SEM, 10,000x magnification.

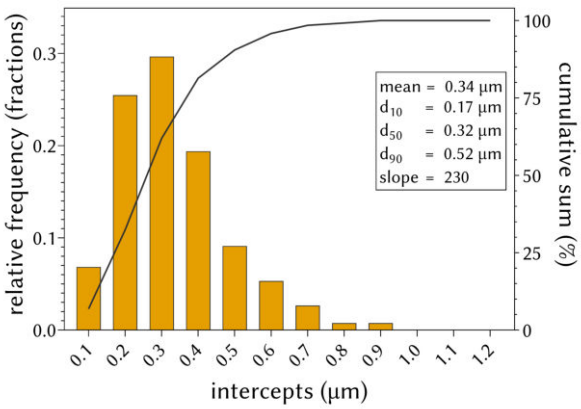

(e) GSD of cores.

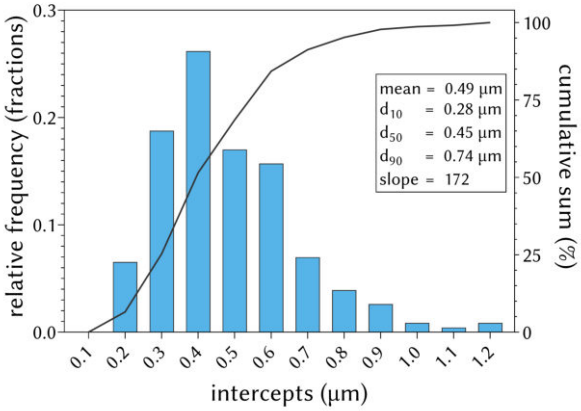

(f) GSD of grains.

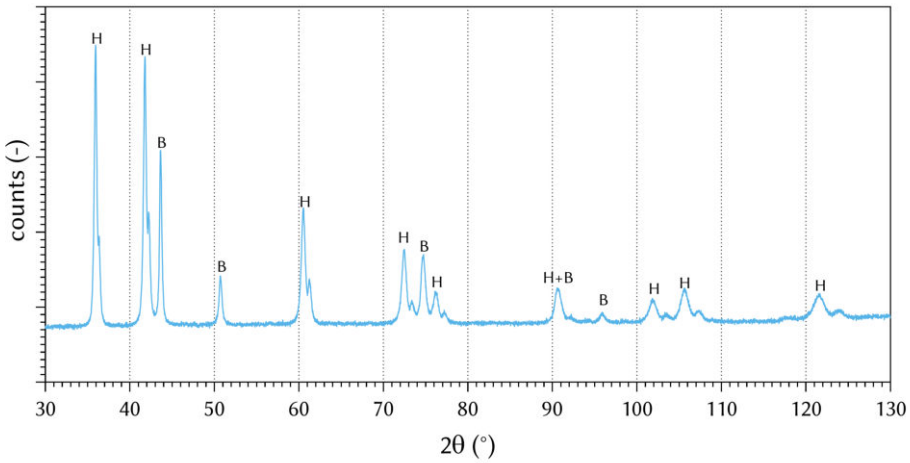

(g) XRD with hard phase (H) and binder (B) peaks identified.

Figure 72: LOM, BSE-SEM, GSD and XRD of I1-2_SN.

(a) LOM, 100x magnification.

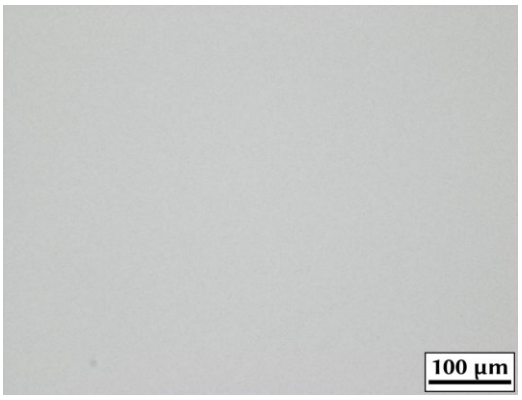

(b) LOM, 200x magnification.

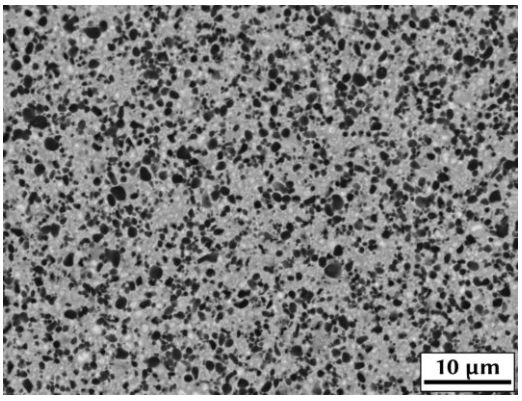

(c) BSE-SEM, 5000x magnification.

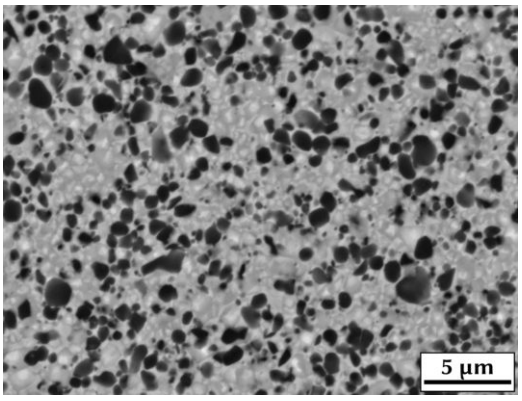

(d) BSE-SEM, 10,000x magnification.

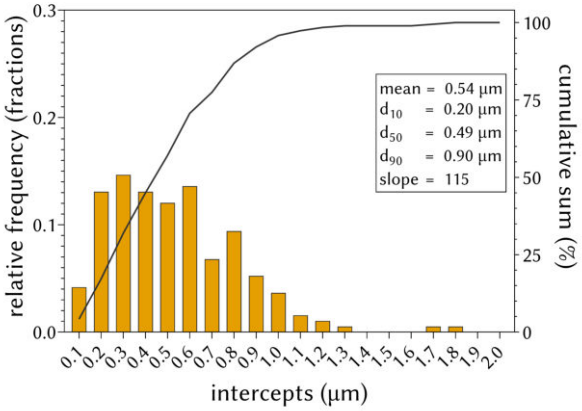

(e) GSD of cores.

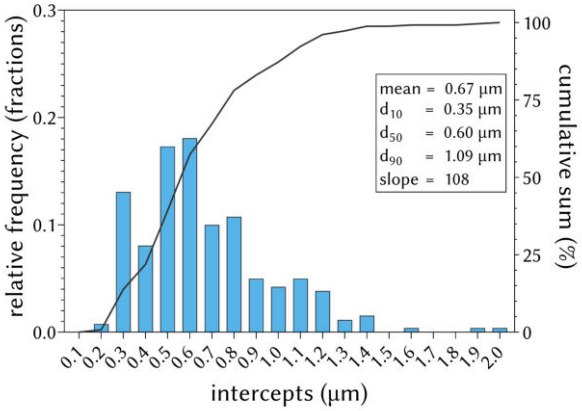

(f) GSD of grains.

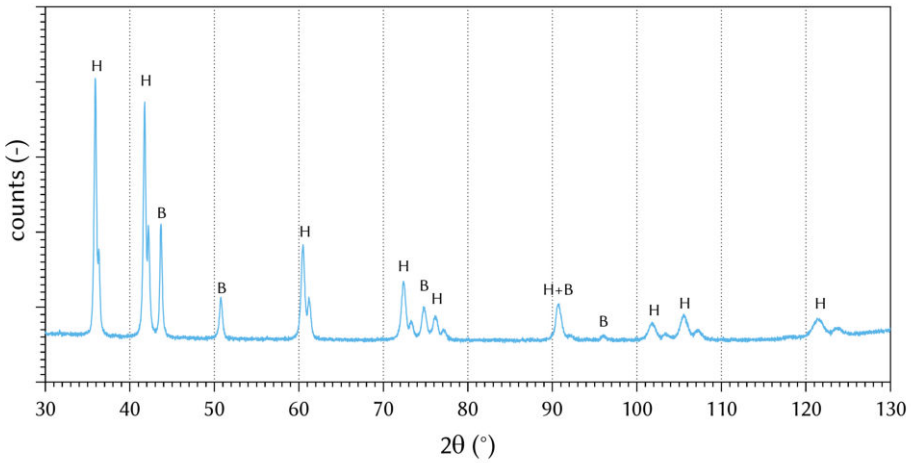

(g) XRD with hard phase (H) and binder (B) peaks identified.

Figure 73: LOM, BSE-SEM, GSD and XRD of I1-3_SAr.

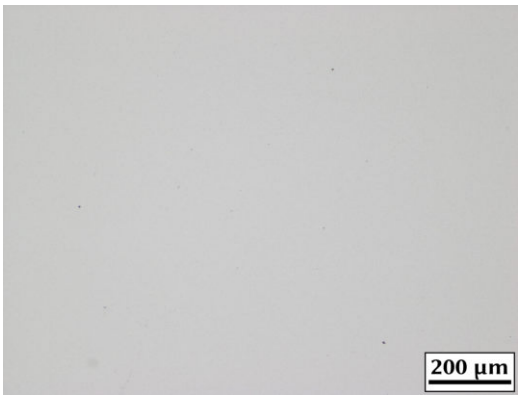

(a) LOM, 100x magnification.

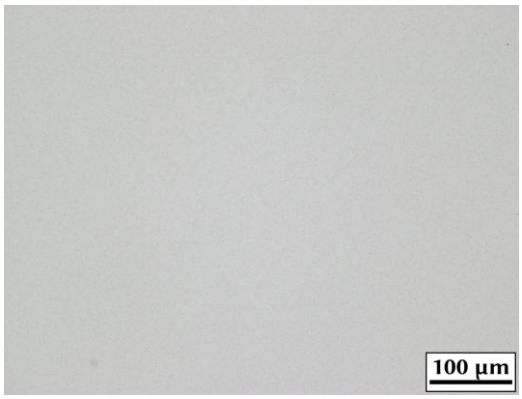

(b) LOM, 200x magnification.

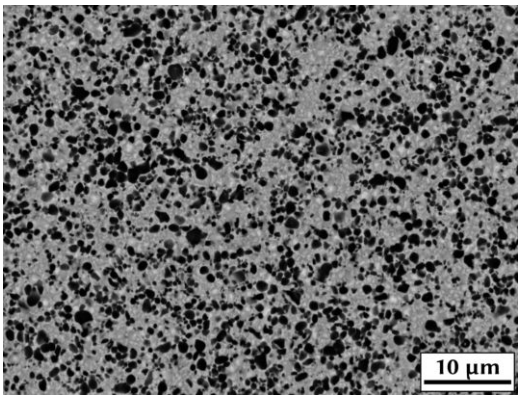

(c) BSE-SEM, 5000x magnification.

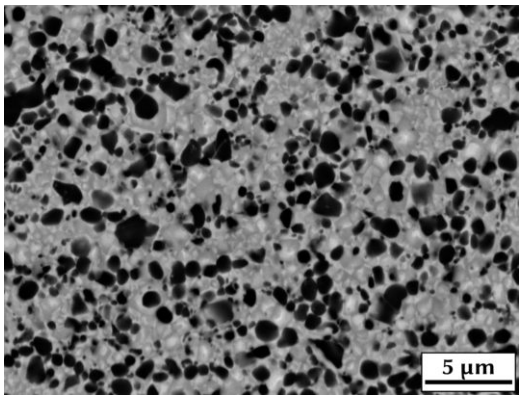

(d) BSE-SEM, 10,000x magnification.

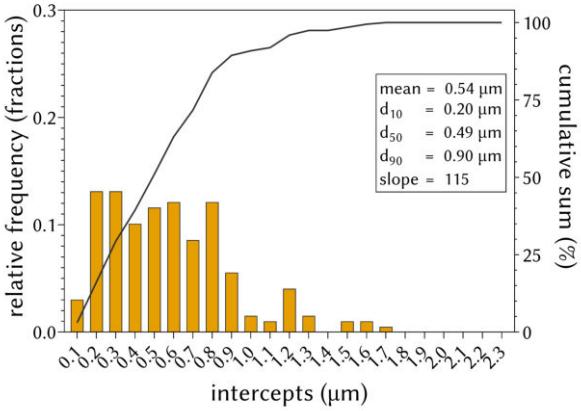

(e) GSD of cores.

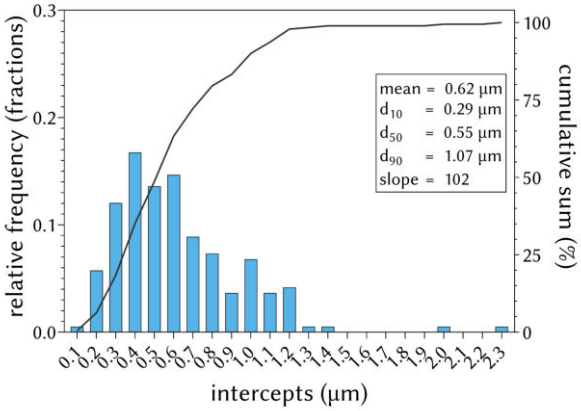

(f) GSD of grains.

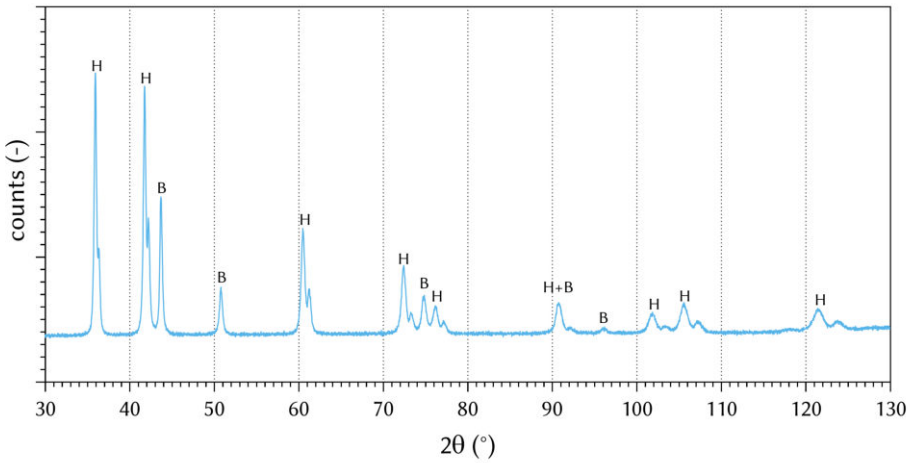

(g) XRD with hard phase (H) and binder (B) peaks identified.

Figure 74: LOM, BSE-SEM, GSD and XRD of I1-3_SN.

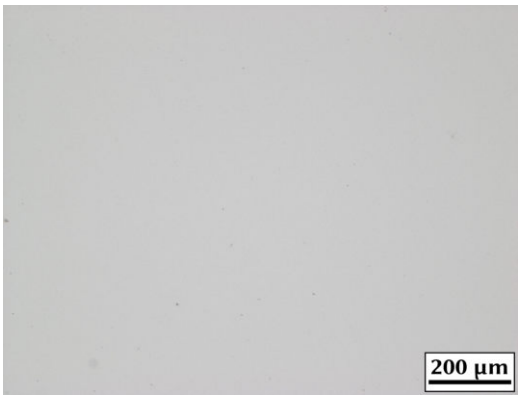

(a) LOM, 100x magnification.

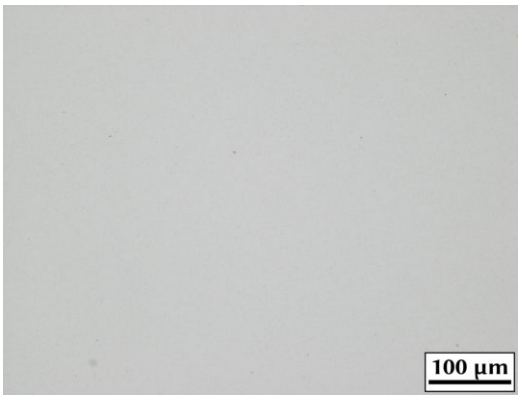

(b) LOM, 200x magnification.

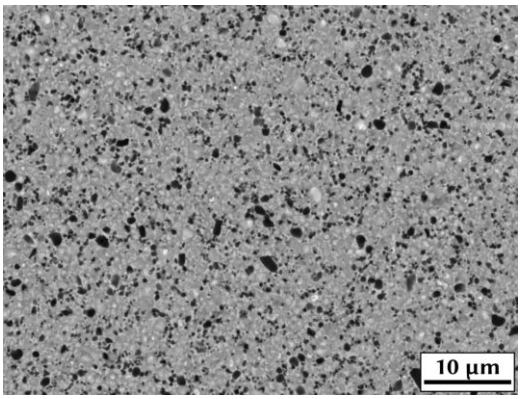

(c) BSE-SEM, 5000x magnification.

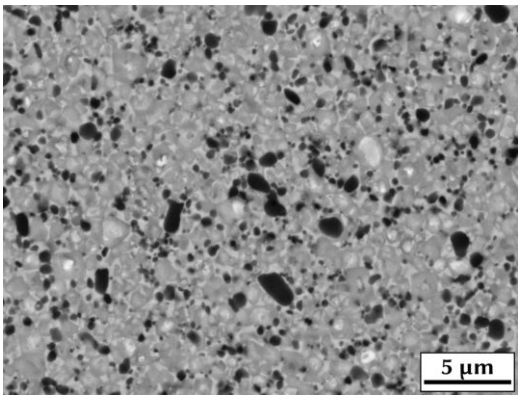

(d) BSE-SEM, 10,000x magnification.

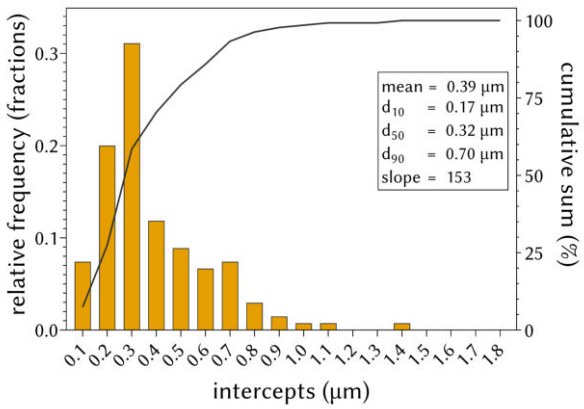

(e) GSD of cores.

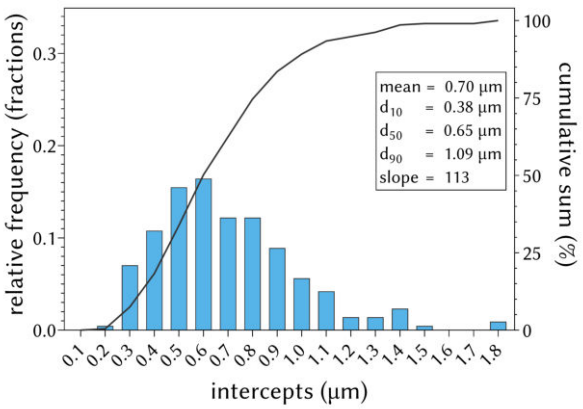

(f) GSD of grains.

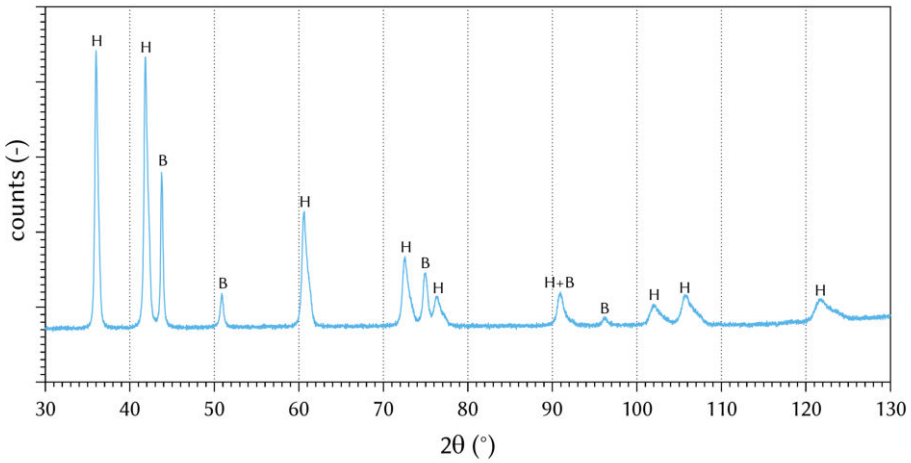

(g) XRD with hard phase (H) and binder (B) peaks identified.

Figure 75: LOM, BSE-SEM, GSD and XRD of I2-1_SAr.

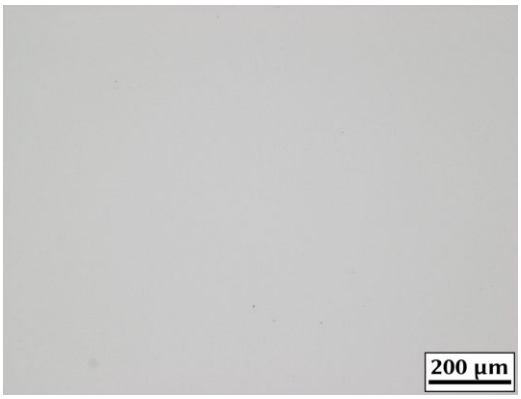

(a) LOM, 100x magnification.

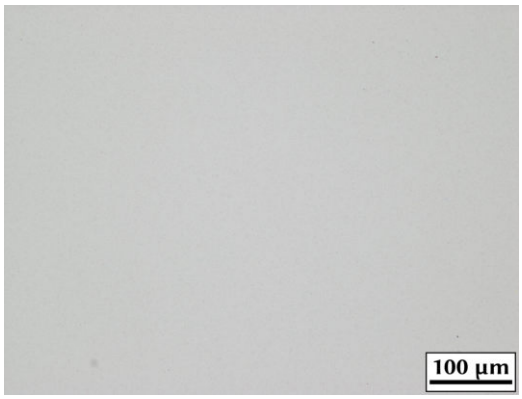

(b) LOM, 200x magnification.

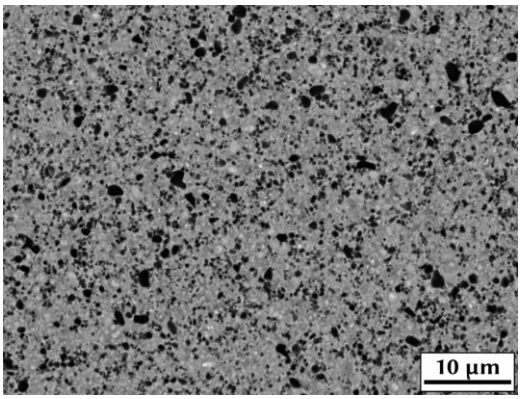

(c) BSE-SEM, 5000x magnification.

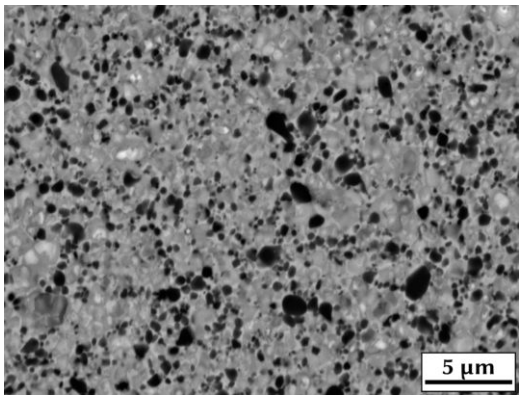

(d) BSE-SEM, 10,000x magnification.

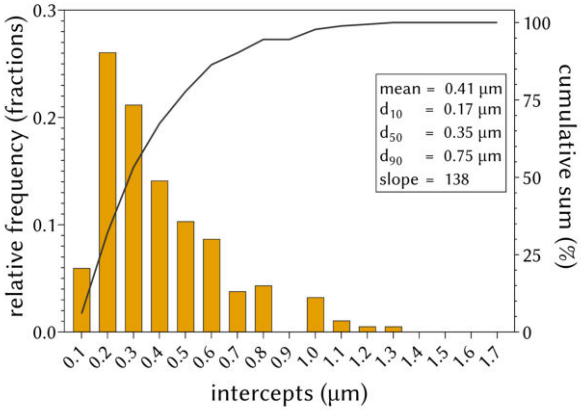

(e) GSD of cores.

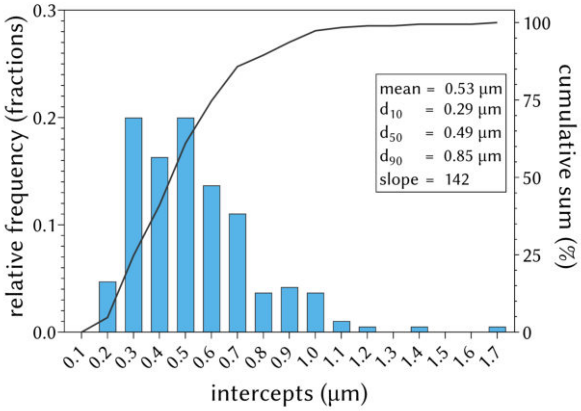

(f) GSD of grains.

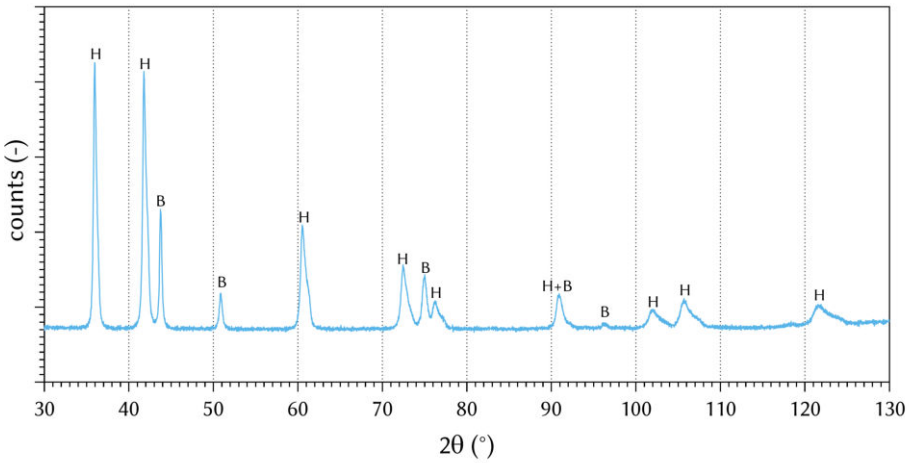

(g) XRD with hard phase (H) and binder (B) peaks identified.

Figure 76: LOM, BSE-SEM, GSD and XRD of I2-1_SN.

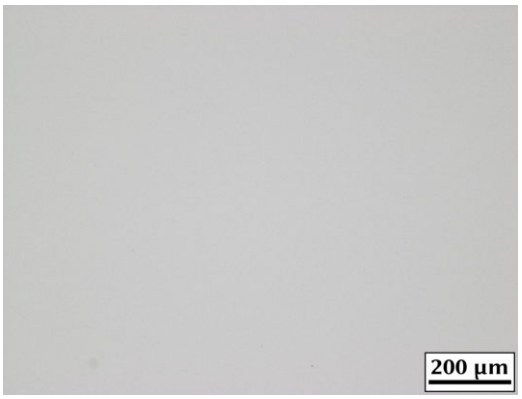

(a) LOM, 100x magnification.

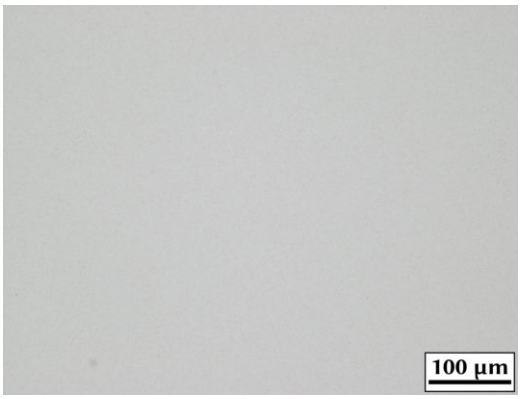

(b) LOM, 200x magnification.

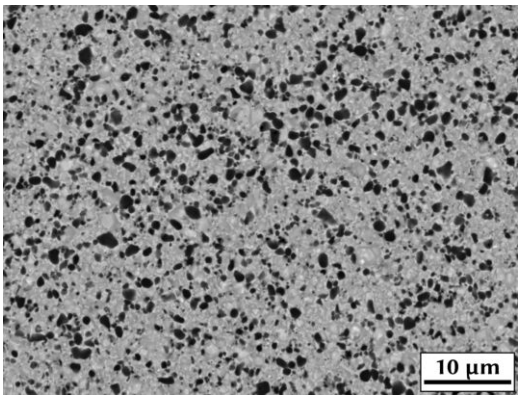

(c) BSE-SEM, 5000x magnification.

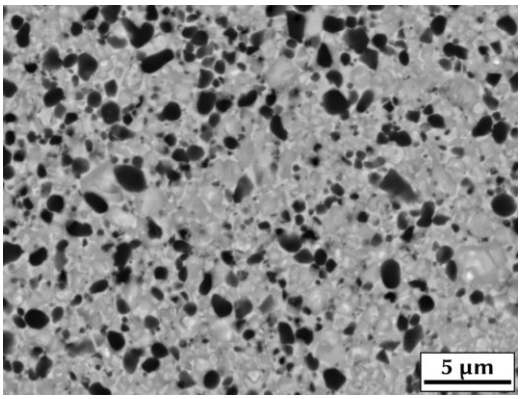

(d) BSE-SEM, 10,000x magnification.

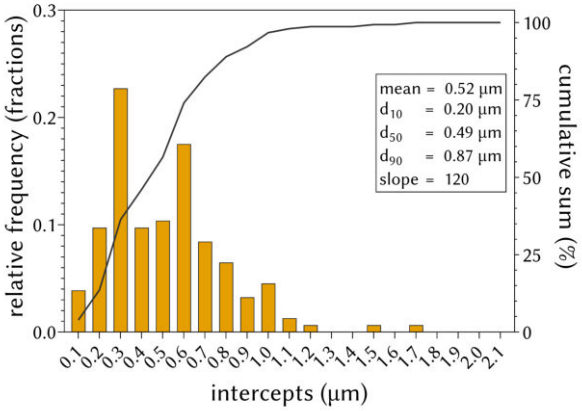

(e) GSD of cores.

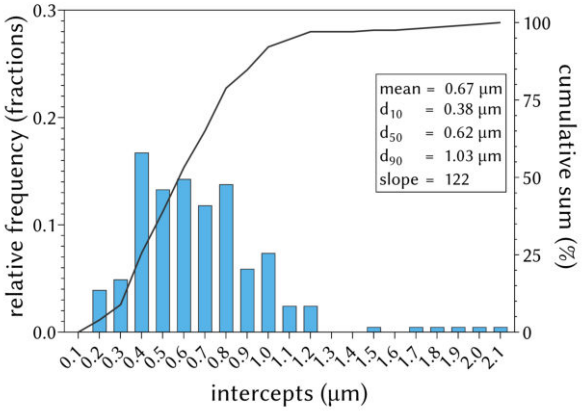

(f) GSD of grains.

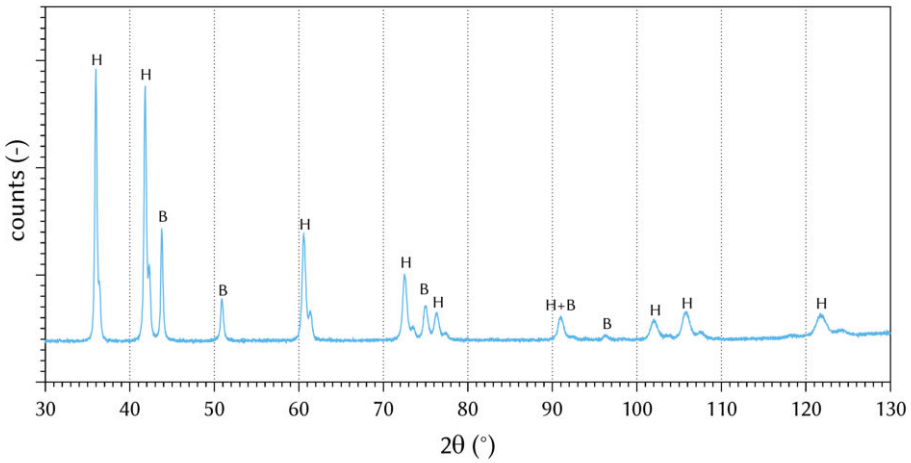

(g) XRD with hard phase (H) and binder (B) peaks identified.

Figure 77: LOM, BSE-SEM, GSD and XRD of I2-3_SAr.

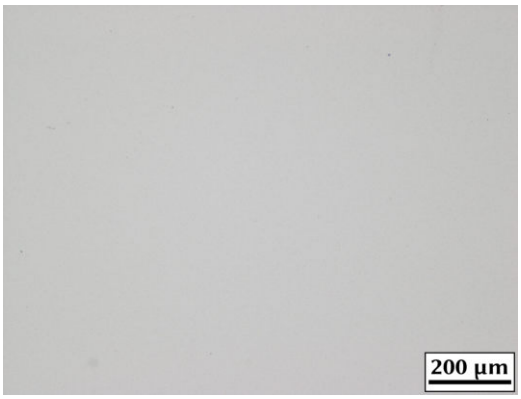

(a) LOM, 100x magnification.

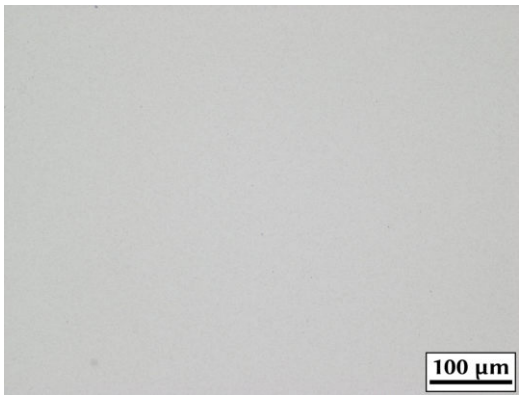

(b) LOM, 200x magnification.

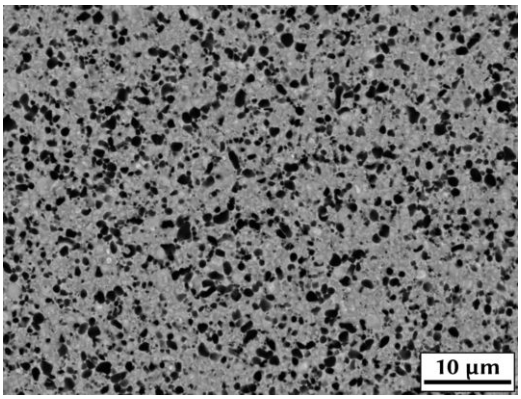

(c) BSE-SEM, 5000x magnification.

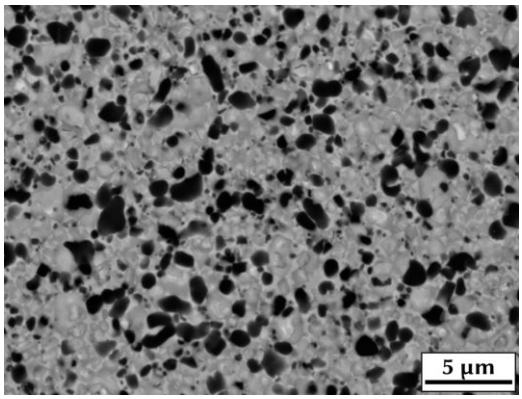

(d) BSE-SEM, 10,000x magnification.

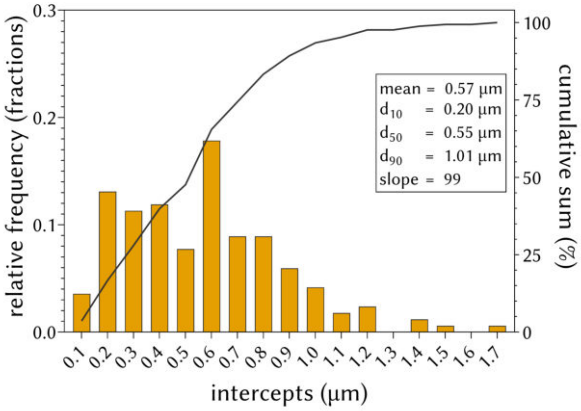

(e) GSD of cores.

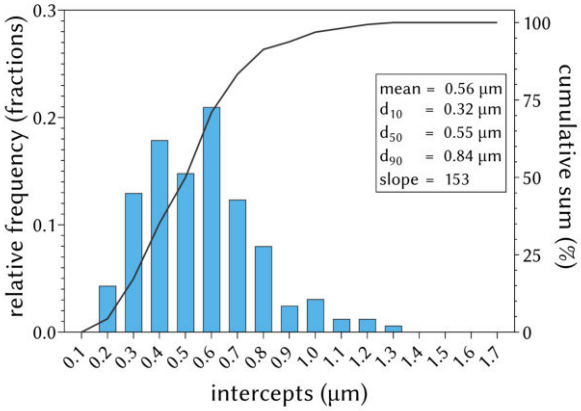

(f) GSD of grains.

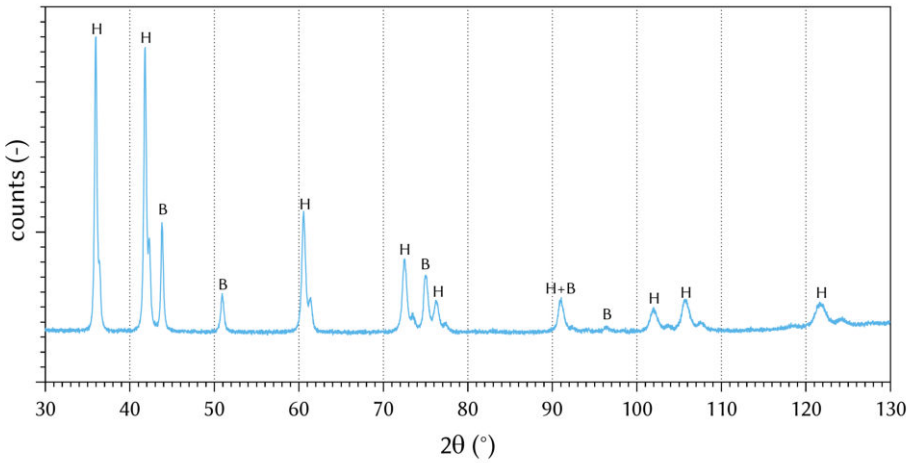

(g) XRD with hard phase (H) and binder (B) peaks identified.

Figure 78: LOM, BSE-SEM, GSD and XRD of I2-3_SN.

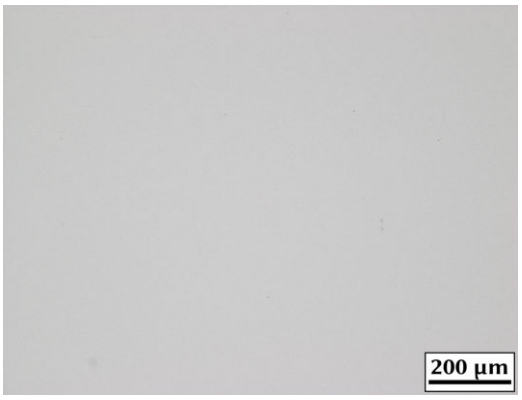

(a) LOM, 100x magnification.

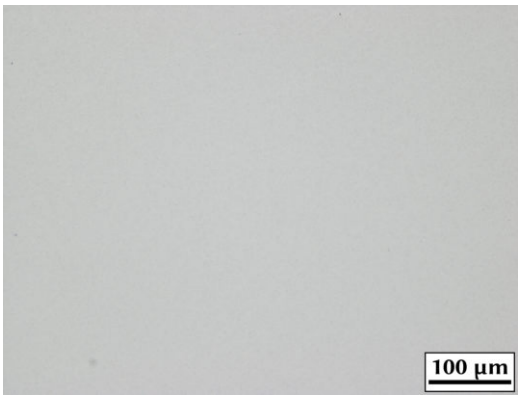

(b) LOM, 200x magnification.

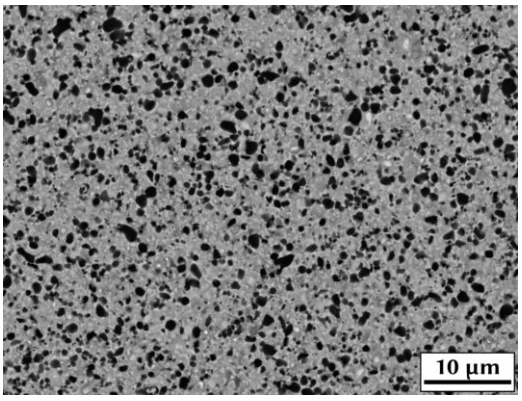

(c) BSE-SEM, 5000x magnification.

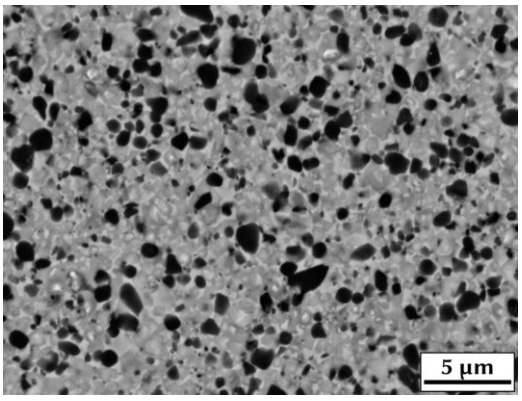

(d) BSE-SEM, 10,000x magnification.

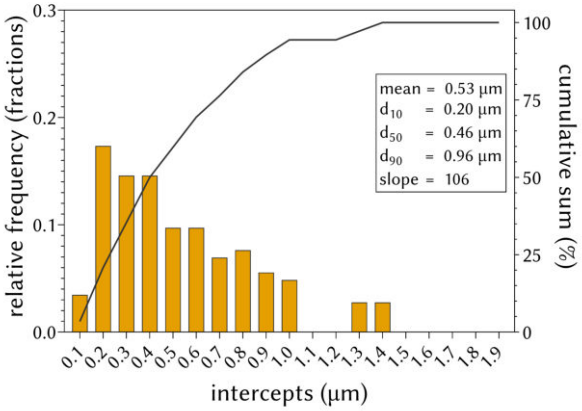

(e) GSD of cores.

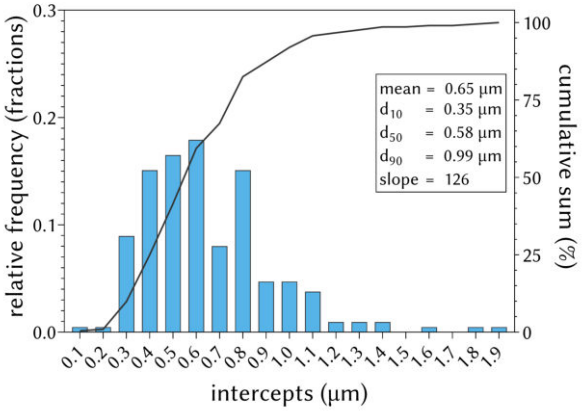

(f) GSD of grains.

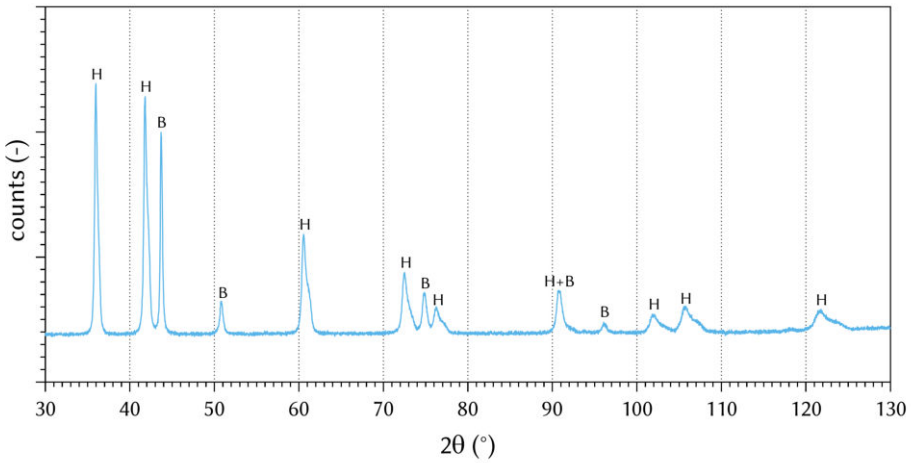

(g) XRD with hard phase (H) and binder (B) peaks identified.

Figure 79: LOM, BSE-SEM, GSD and XRD of I3-1_SAr.

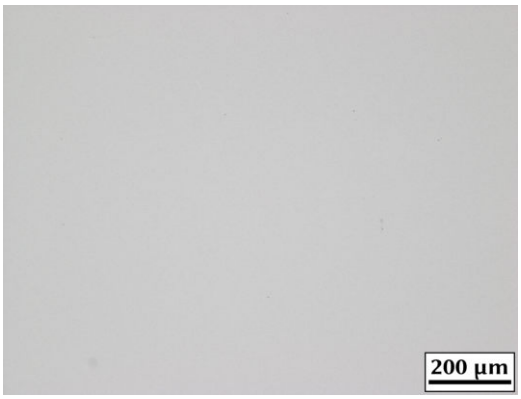

(a) LOM, 100x magnification.

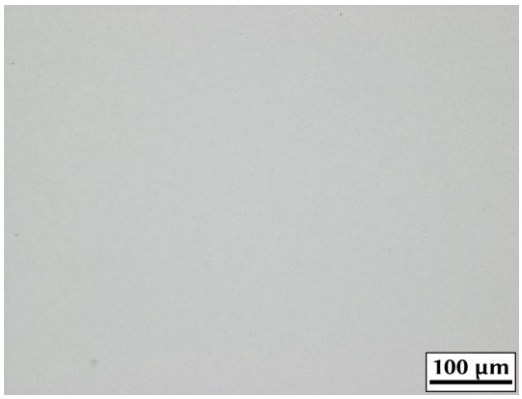

(b) LOM, 200x magnification.

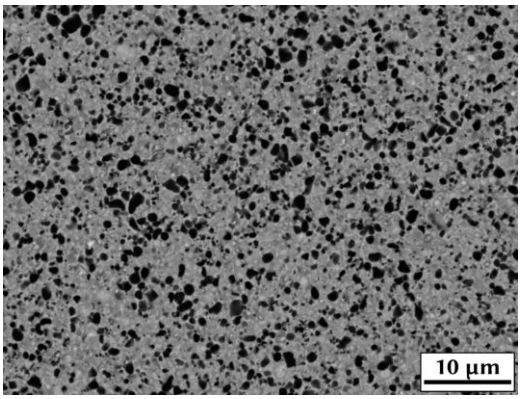

(c) BSE-SEM, 5000x magnification.

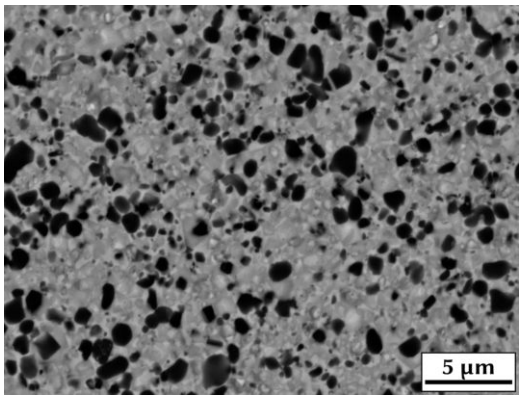

(d) BSE-SEM, 10,000x magnification.

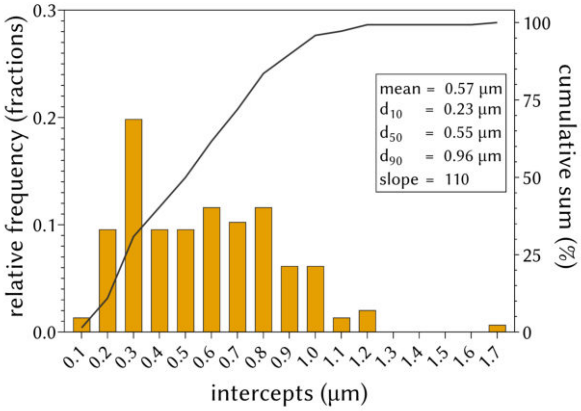

(e) GSD of cores.

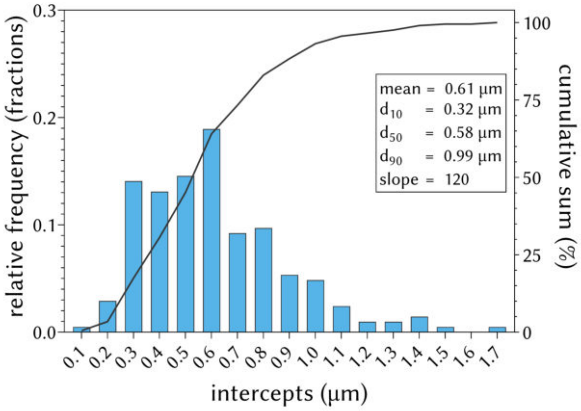

(f) GSD of grains.

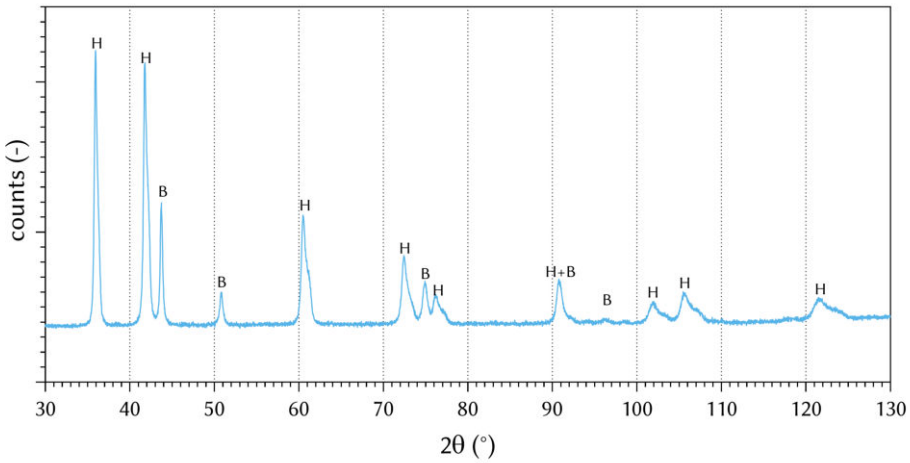

(g) XRD with hard phase (H) and binder (B) peaks identified.

Figure 80: LOM, BSE-SEM, GSD and XRD of I3-1_SN.

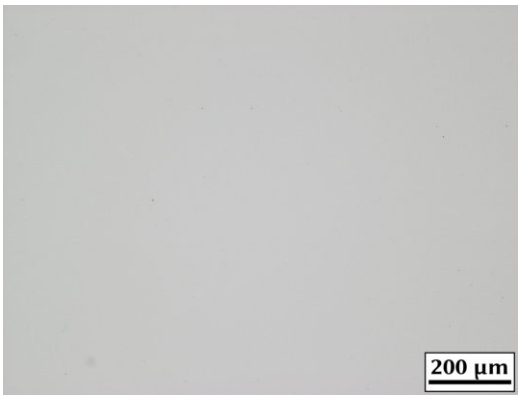

(a) LOM, 100x magnification.

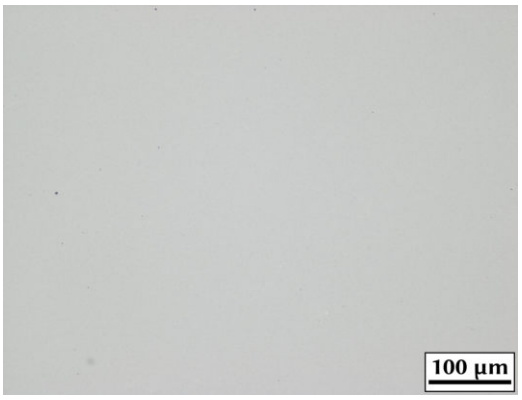

(b) LOM, 200x magnification.

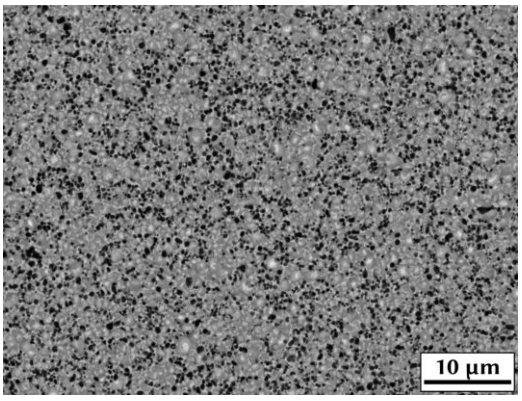

(c) BSE-SEM, 5000x magnification.

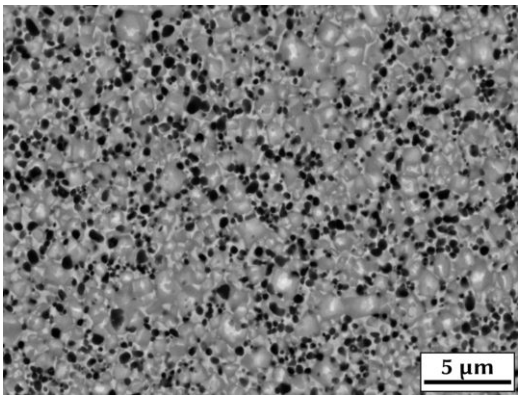

(d) BSE-SEM, 10,000x magnification.

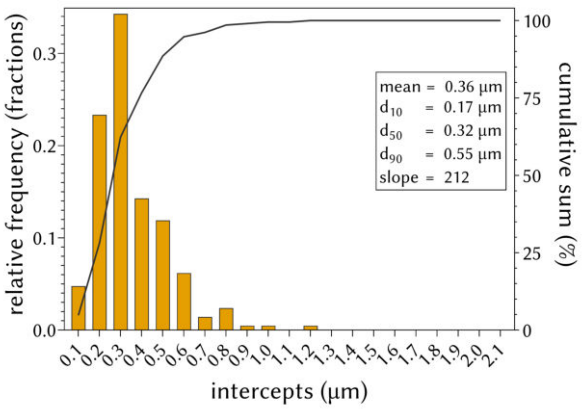

(e) GSD of cores.

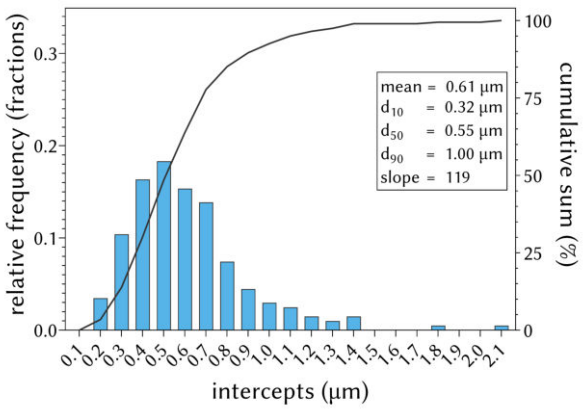

(f) GSD of grains.

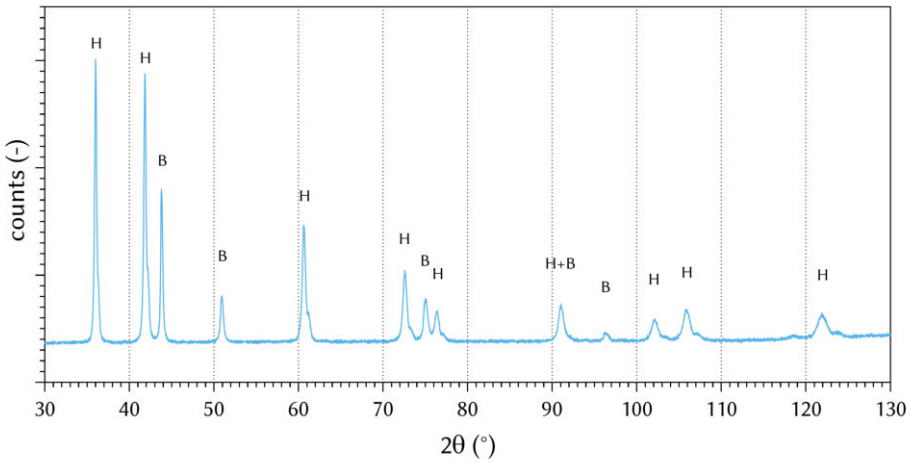

(g) XRD with hard phase (H) and binder (B) peaks identified.

Figure 81: LOM, BSE-SEM, GSD and XRD of I0-1+0.4%C_SAr.

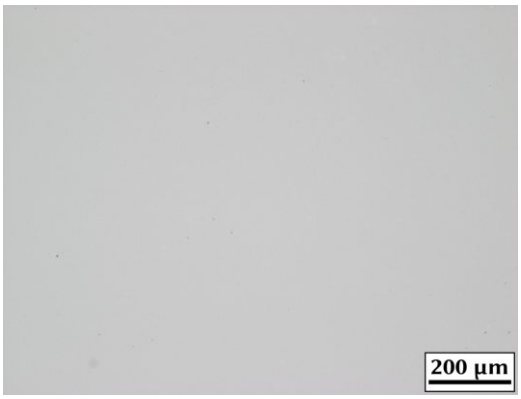

(a) LOM, 100x magnification.

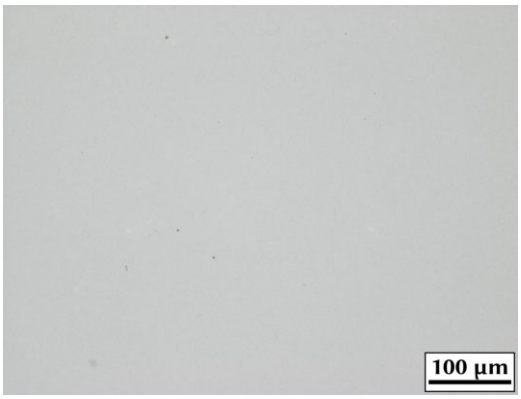

(b) LOM, 200x magnification.

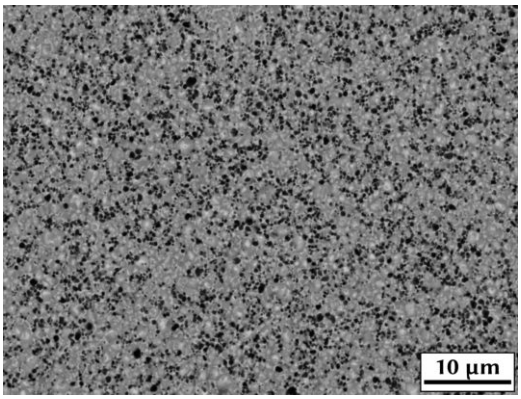

(c) BSE-SEM, 5000x magnification.

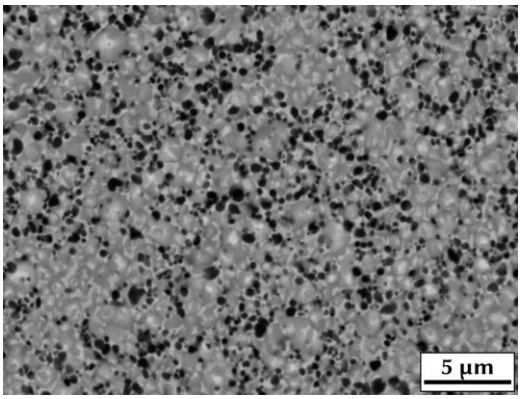

(d) BSE-SEM, 10,000x magnification.

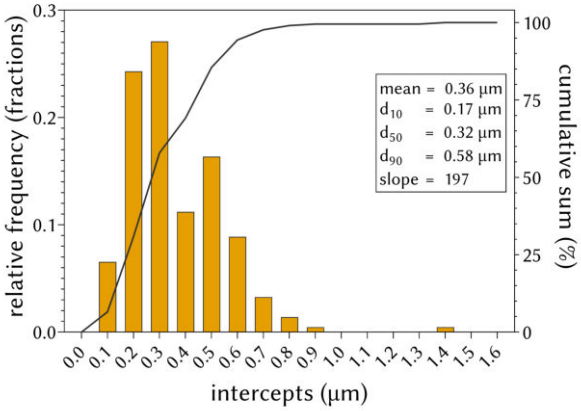

(e) GSD of cores.

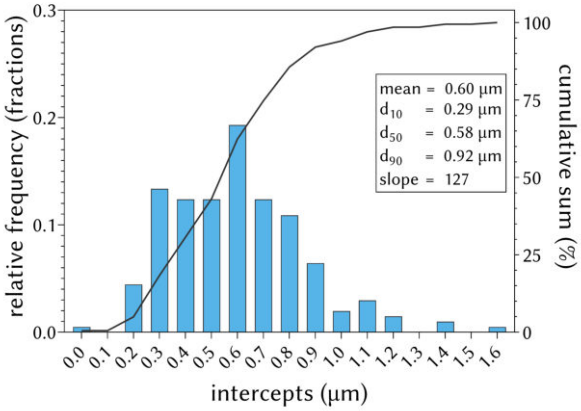

(f) GSD of grains.

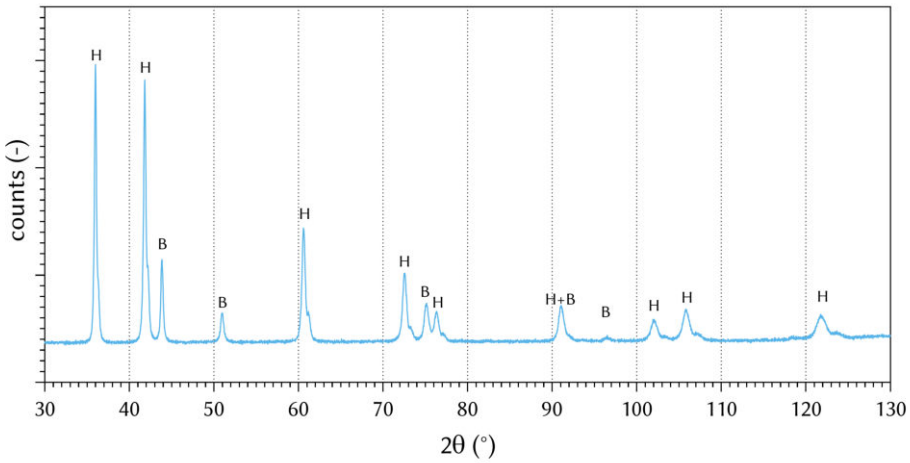

(g) XRD with hard phase (H) and binder (B) peaks identified.

Figure 82: LOM, BSE-SEM, GSD and XRD of I0-1+0.4%C_SN.

(a) LOM, 100x magnification.

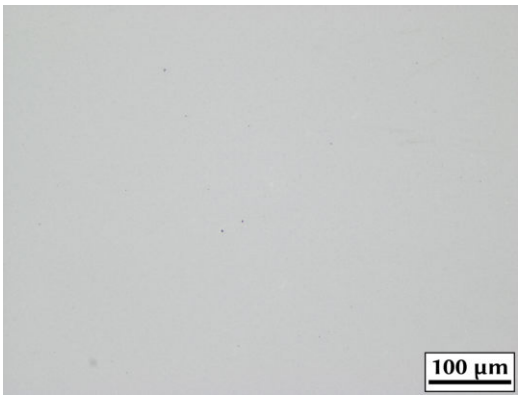

(b) LOM, 200x magnification.

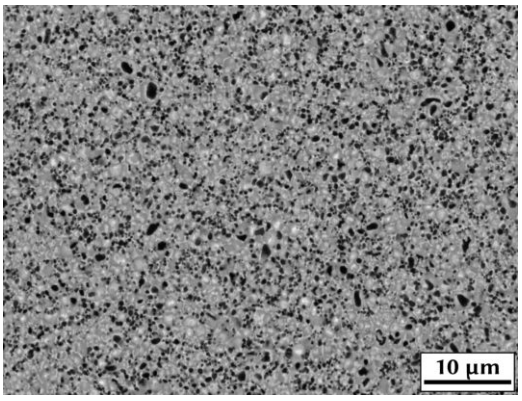

(c) BSE-SEM, 5000x magnification.

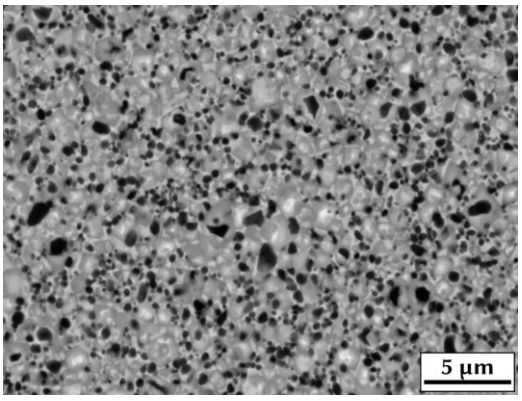

(d) BSE-SEM, 10,000x magnification.

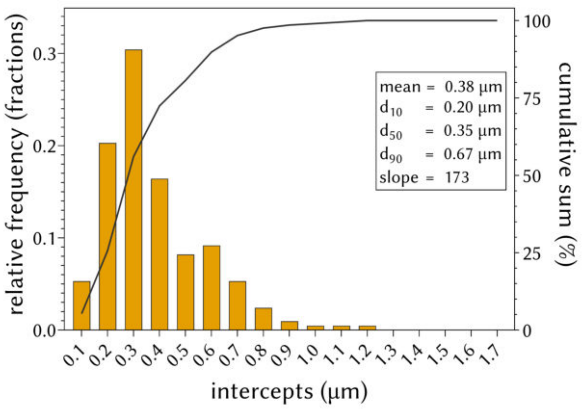

(e) GSD of cores.

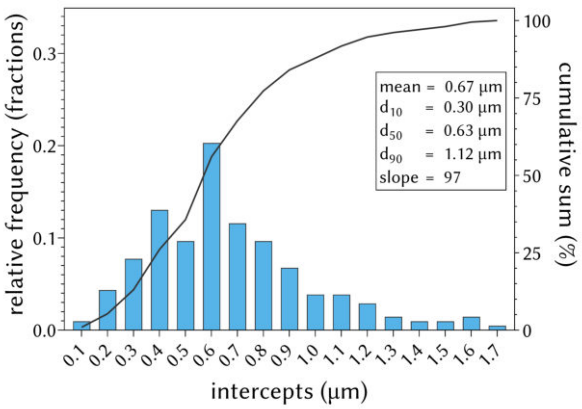

(f) GSD of grains.

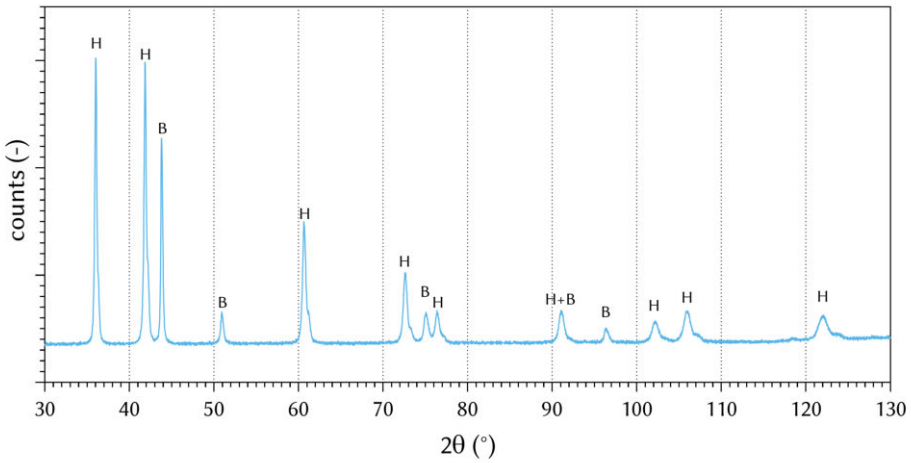

(g) XRD with hard phase (H) and binder (B) peaks identified.

Figure 83: LOM, BSE-SEM, GSD and XRD of I1-1+0.4%C_SAr.

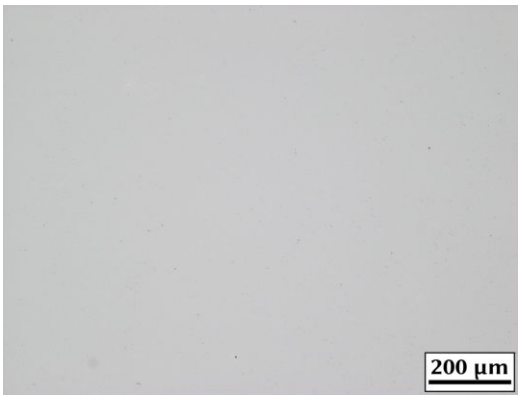

(a) LOM, 100x magnification.

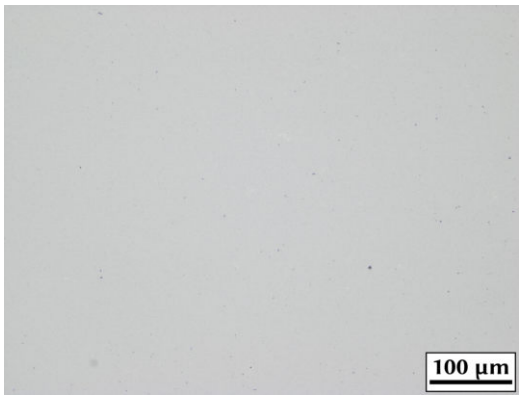

(b) LOM, 200x magnification.

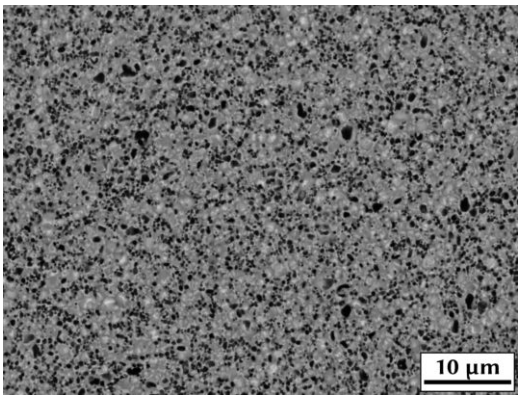

(c) BSE-SEM, 5000x magnification.

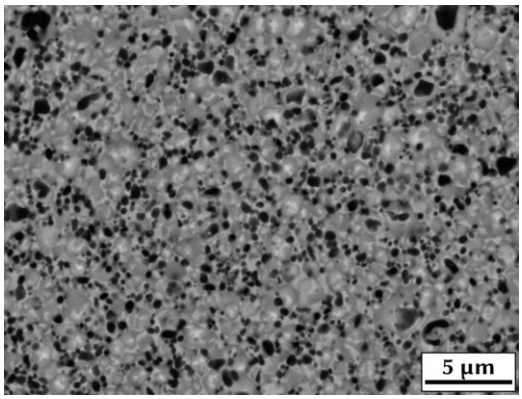

(d) BSE-SEM, 10,000x magnification.

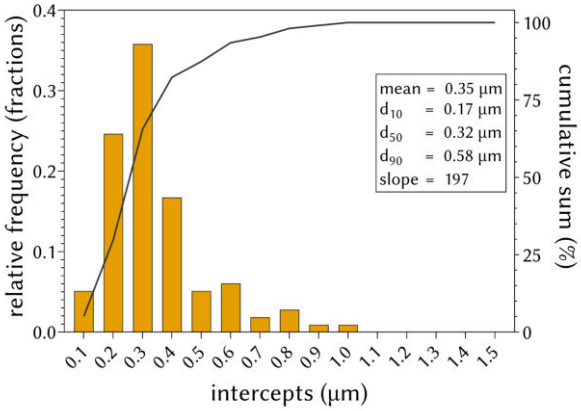

(e) GSD of cores.

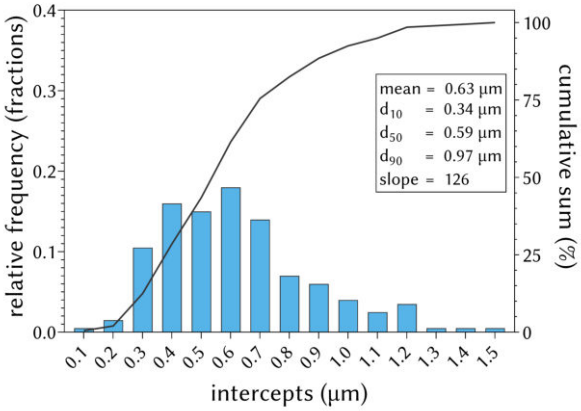

(f) GSD of grains.

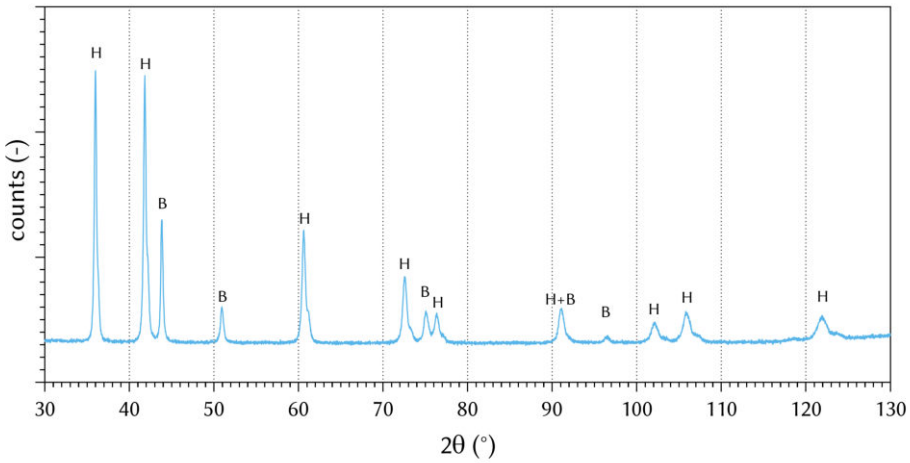

(g) XRD with hard phase (H) and binder (B) peaks identified.

Figure 84: LOM, BSE-SEM, GSD and XRD of I1-1+0.4%C_SN.

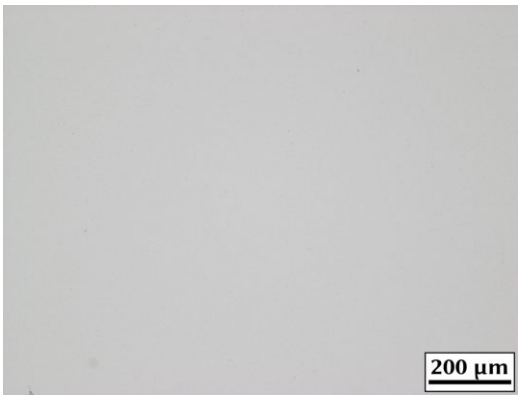

(a) LOM, 100x magnification.

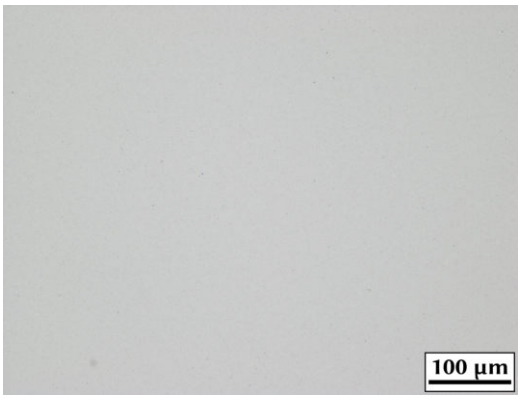

(b) LOM, 200x magnification.

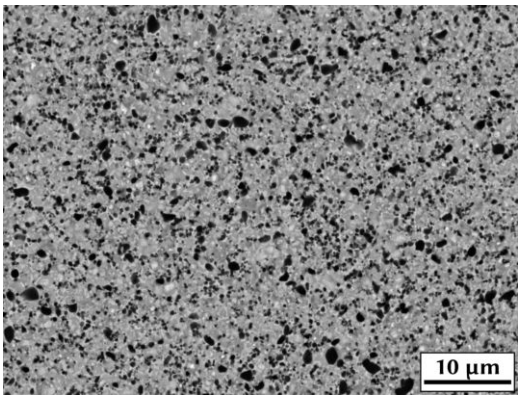

(c) BSE-SEM, 5000x magnification.

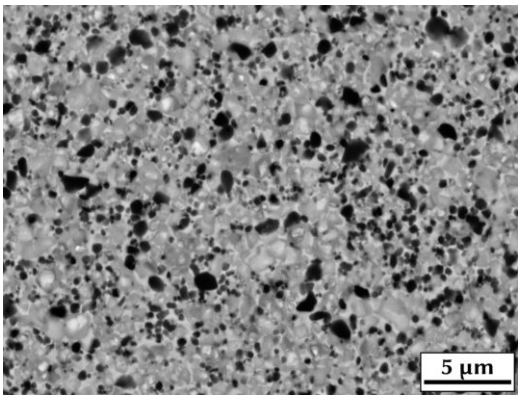

(d) BSE-SEM, 10,000x magnification.

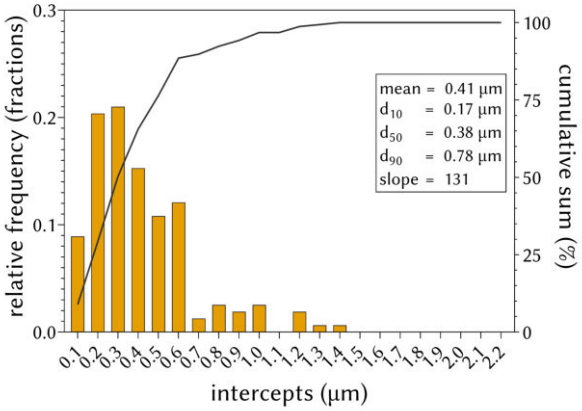

(e) GSD of cores.

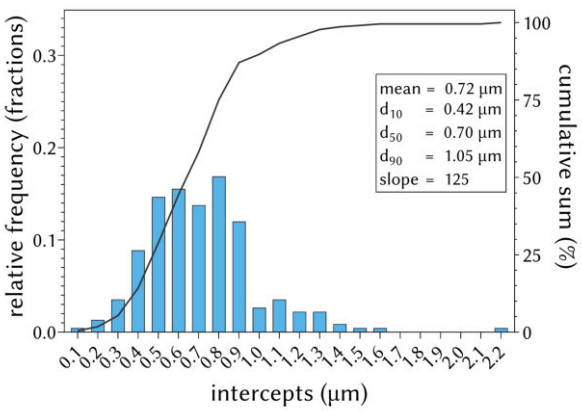

(f) GSD of grains.

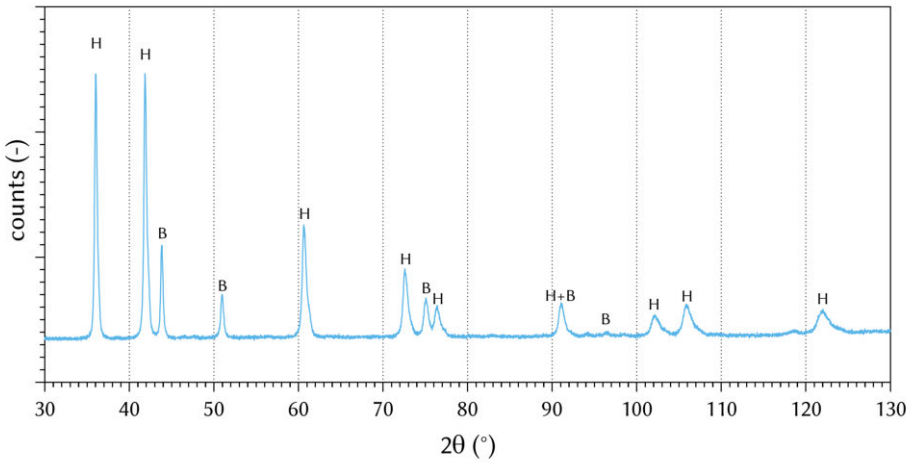

(g) XRD with hard phase (H) and binder (B) peaks identified.

Figure 85: LOM, BSE-SEM, GSD and XRD of I2-1+0.4%C_SAr.

(a) LOM, 100x magnification.

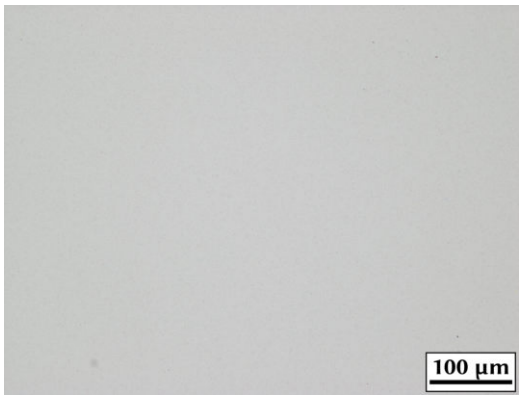

(b) LOM, 200x magnification.

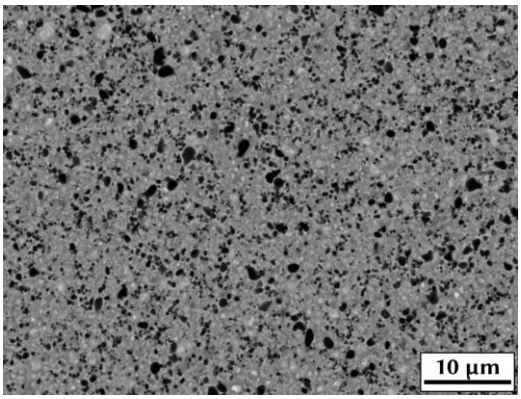

(c) BSE-SEM, 5000x magnification.

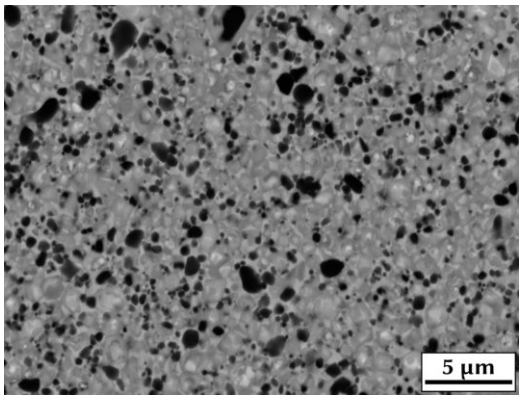

(d) BSE-SEM, 10,000x magnification.

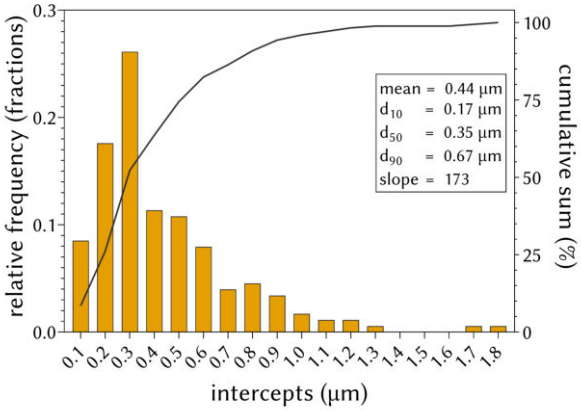

(e) GSD of cores.

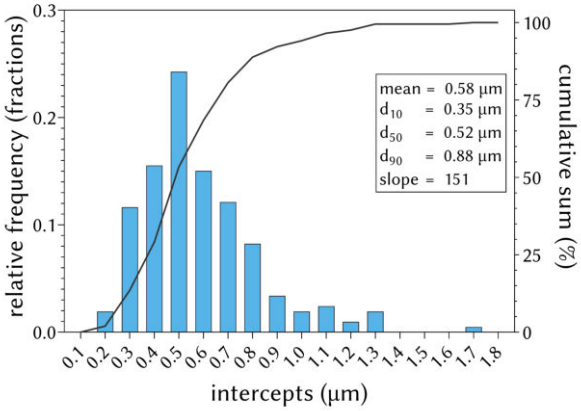

(f) GSD of grains.

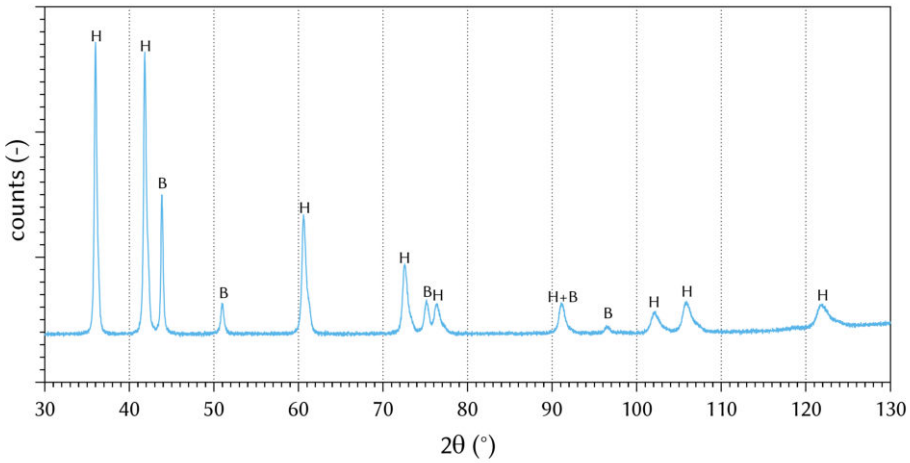

(g) XRD with hard phase (H) and binder (B) peaks identified.

Figure 86: LOM, BSE-SEM, GSD and XRD of I2-1+0.4%C_SN.

A.2. N series

Table 40: Powder weighing of N series mixtures.

	powder weighing (wt%)											
N Series	**N0-1**	**N0-2**	**N1-1**	**N1-2**	**N1-3**	**N1-4**	**N2-1**	**N2-2**	**N2-3**	**N3-1**	**N3-2**	**N3-3**
0.88µm TiC50N50	34.1006	-	24.1269	-	-	-	14.8811	-	-	29.9401	-	-
0.85µm TiC50N50	-	34.1160	-	23.1265	-	-	-	15.9279	-	-	28.7154	-
1.07µm TiC50N50	-	-	-	-	-	28.6544	-	-	-	-	-	-
1.76µm TiC50N50	-	-	-	-	27.1684	-	-	-	17.8857	-	-	25.0369
TiC70N30	-	-	10.0702	11.0904	7.0516	5.5358	3.8240	2.7823	-	0.7315	1.9727	-
TiC30N70	-	-	-	-	-	-	-	-	0.8119	-	-	5.6351
(Ti,W)(C,N)	-	-	-	-	-	-	28.1945	28.2013	28.2066	-	-	-
(Ti,W)C	-	-	-	-	-	-	-	-	-	7.0402	7.0393	7.0444
WC	13.0007	13.0069	12.9137	12.9079	12.9086	12.9201	-	-	-	9.3936	9.3909	9.3964
Mo2C	2.9706	2.9717	2.9481	2.9474	2.9464	2.9490	2.9414	2.9418	2.9427	2.9492	2.9479	2.9498
NbC	4.6224	4.6247	4.5726	4.5702	4.5710	4.5740	4.5620	4.5630	4.5641	4.5735	4.5730	4.5757
Co	10.2551	10.2389	10.2452	10.2385	10.2351	10.2446	10.3973	10.3888	10.3919	10.2481	10.2401	10.2413
Ni	5.0507	5.0419	5.1230	5.1189	5.1174	5.1220	5.1987	5.1942	5.1950	5.1244	5.1204	5.1202

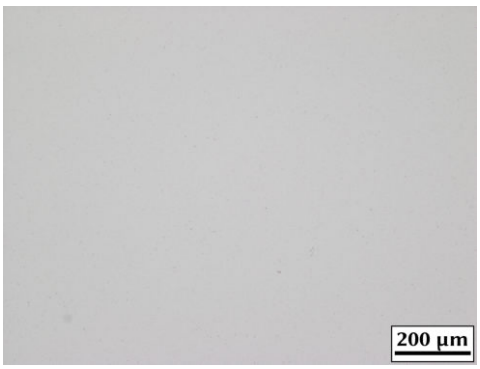

(a) LOM, 100x magnification.

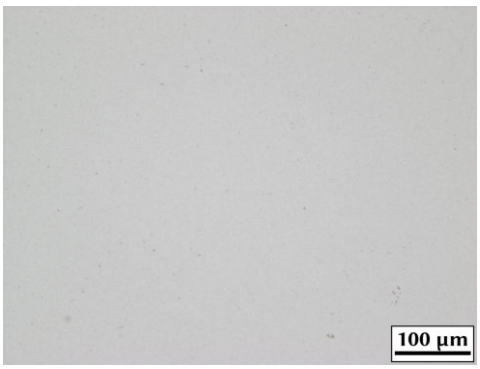

(b) LOM, 200x magnification.

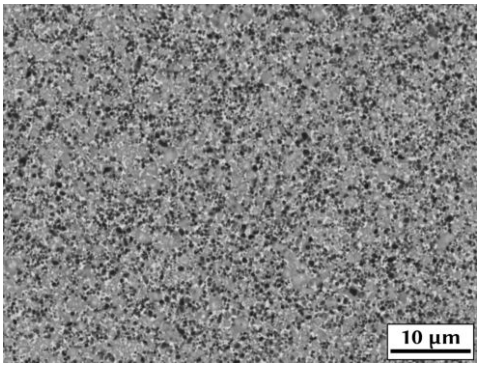

(c) BSE-SEM, 5000x magnification.

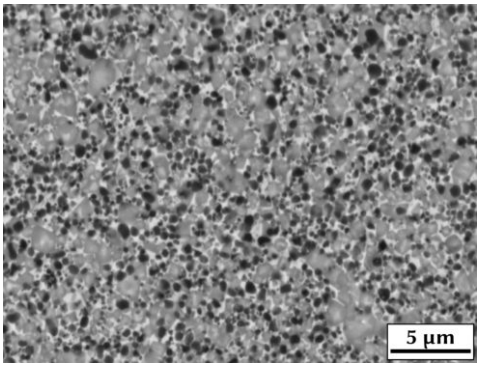

(d) BSE-SEM, 10,000x magnification.

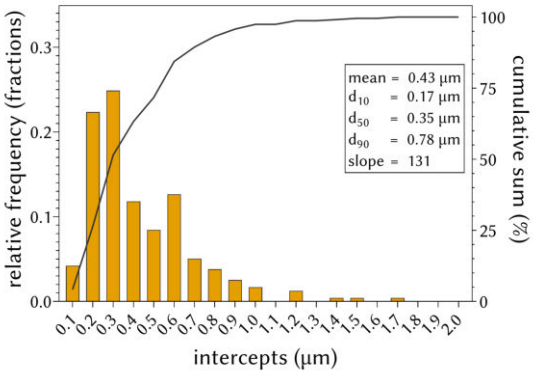

(e) GSD of cores.

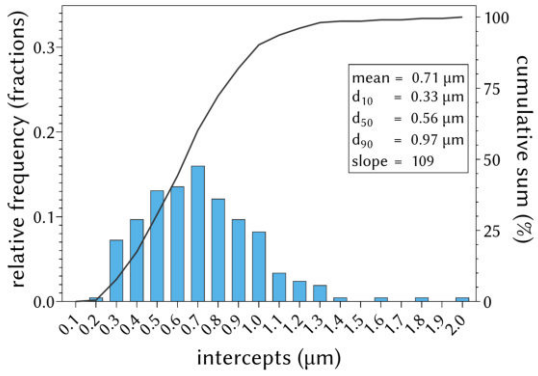

(f) GSD of grains.

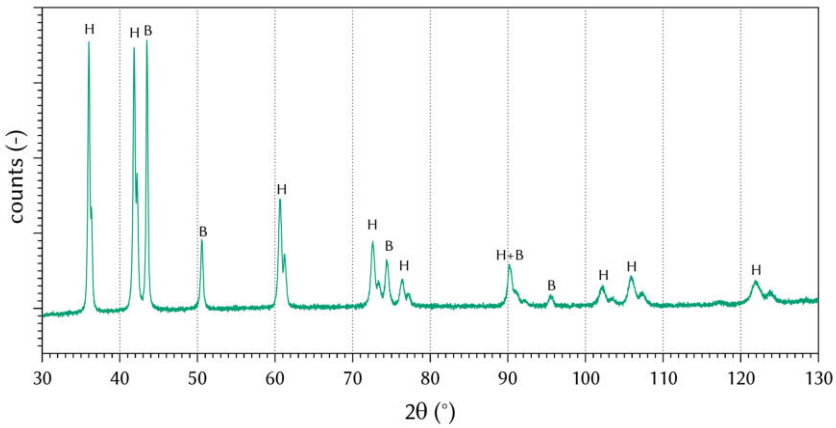

(g) XRD with hard phase (H) and binder (B) peaks identified.

Figure 87: LOM, BSE-SEM, GSD and XRD of N0-1_Ar.

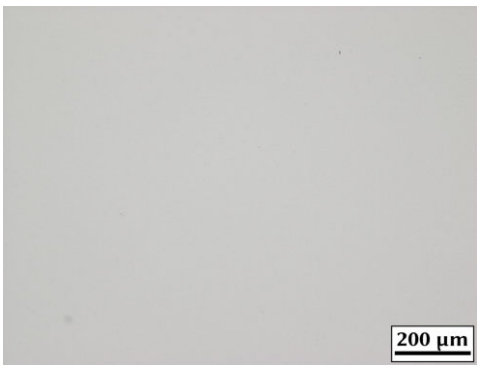

(a) LOM, 100x magnification.

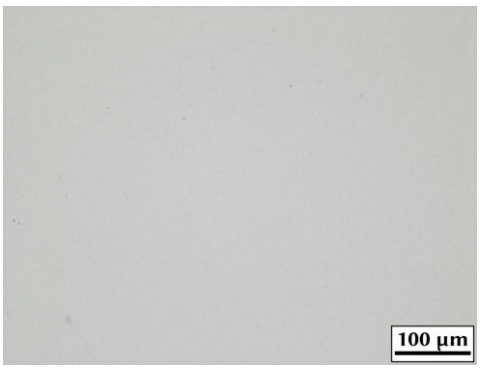

(b) LOM, 200x magnification.

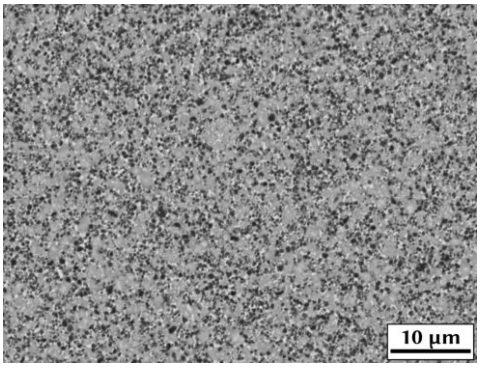

(c) BSE-SEM, 5000x magnification.

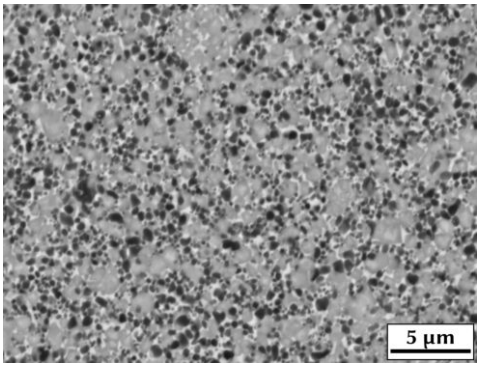

(d) BSE-SEM, 10,000x magnification.

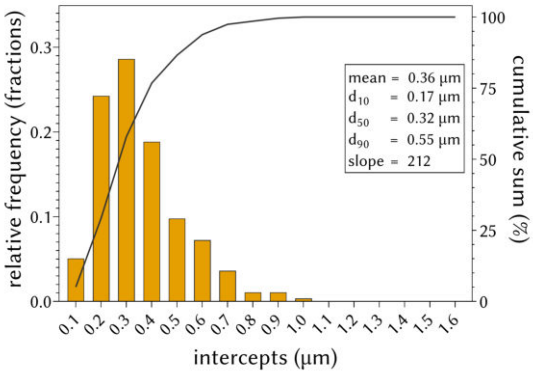

(e) GSD of cores.

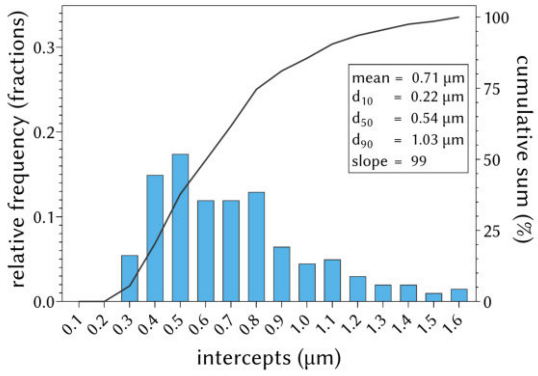

(f) GSD of grains.

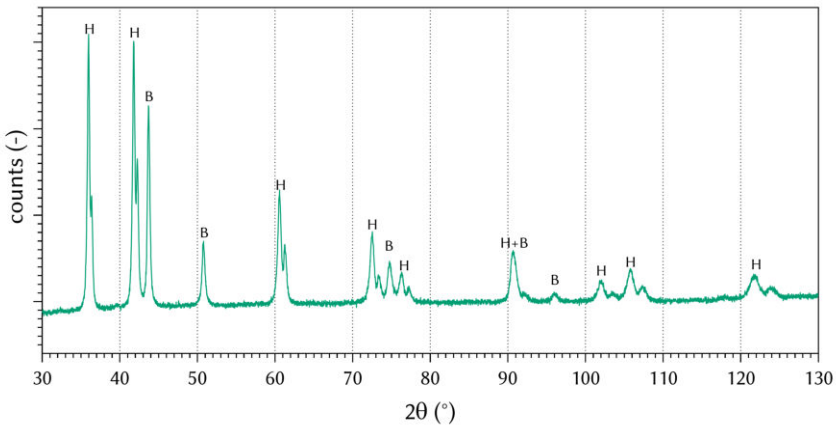

(g) XRD with hard phase (H) and binder (B) peaks identified.

Figure 88: LOM, BSE-SEM, GSD and XRD of N0-1_10N.

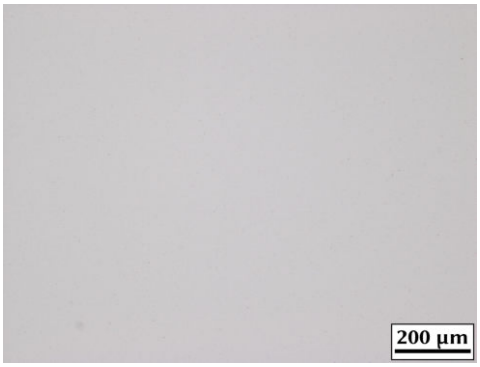

(a) LOM, 100x magnification.

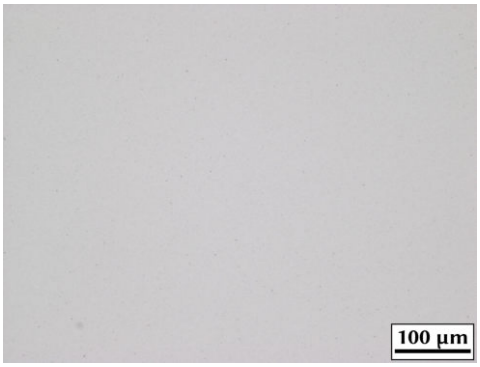

(b) LOM, 200x magnification.

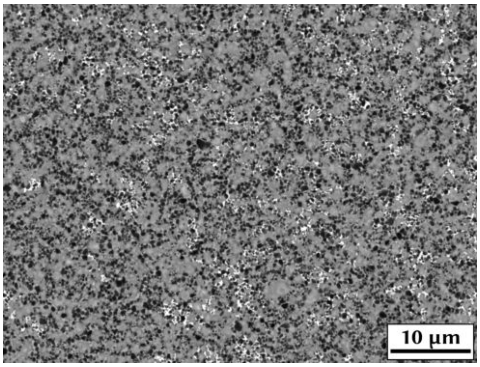

(c) BSE-SEM, 5000x magnification.

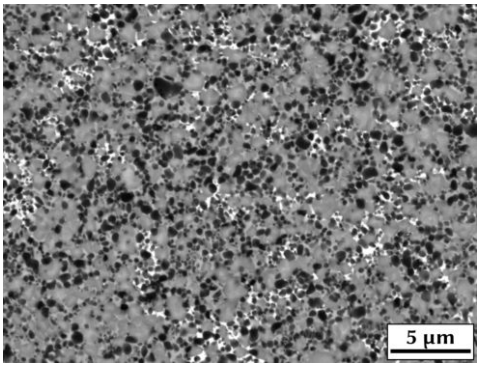

(d) BSE-SEM, 10,000x magnification.

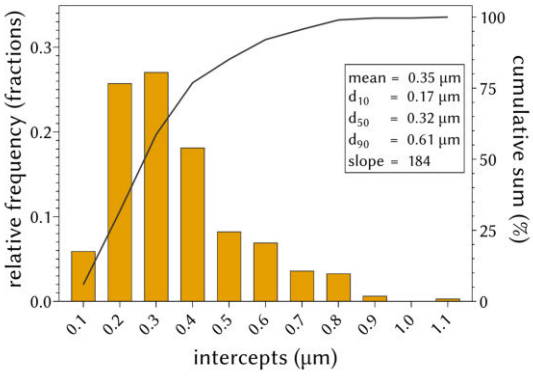

(e) GSD of cores.

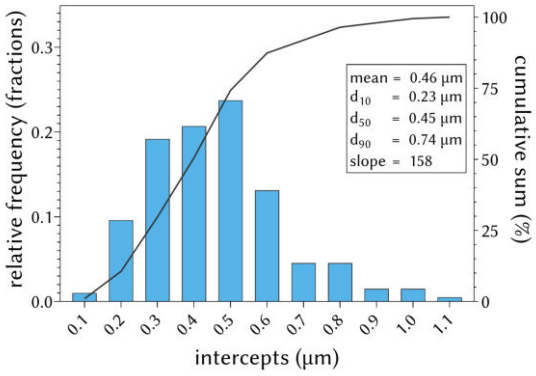

(f) GSD of grains.

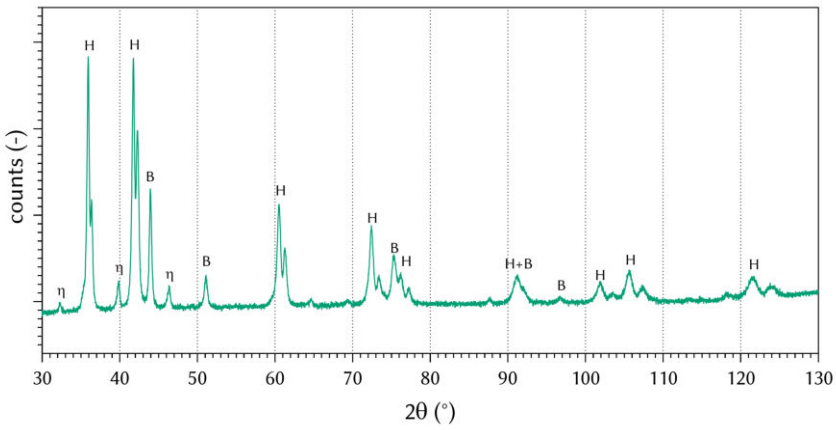

(g) XRD with hard phase (H) and binder (B) peaks identified.

Figure 89: LOM, BSE-SEM, GSD and XRD of N0-1_50N.

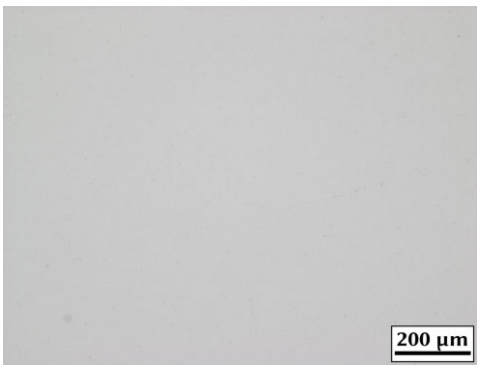

(a) LOM, 100x magnification.

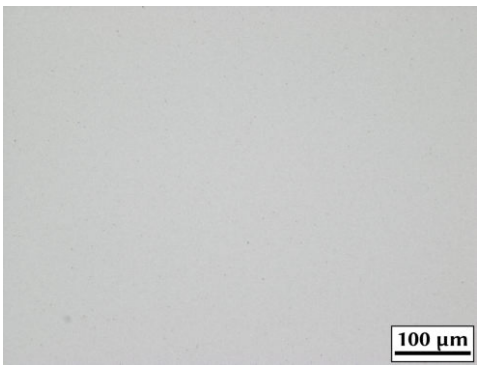

(b) LOM, 200x magnification.

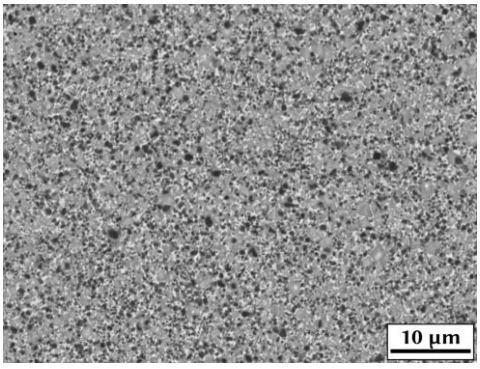

(c) BSE-SEM, 5000x magnification.

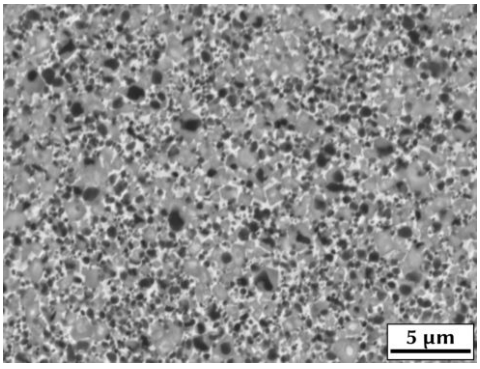

(d) BSE-SEM, 10,000x magnification.

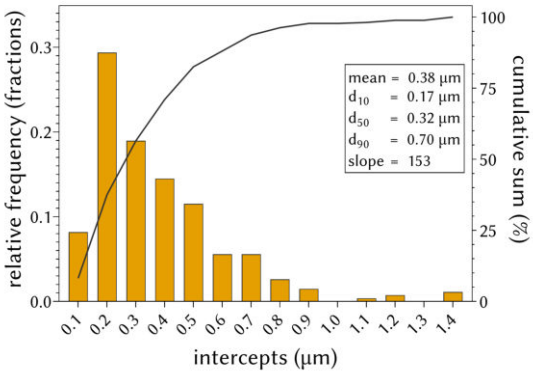

(e) GSD of cores.

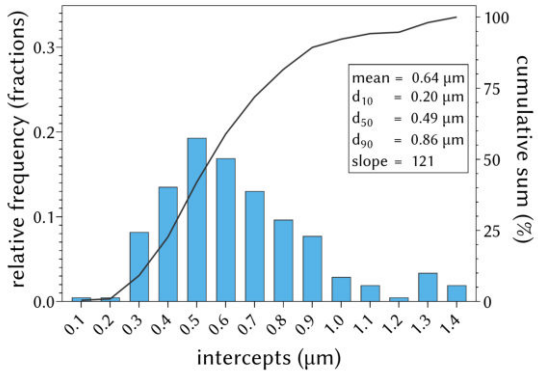

(f) GSD of grains.

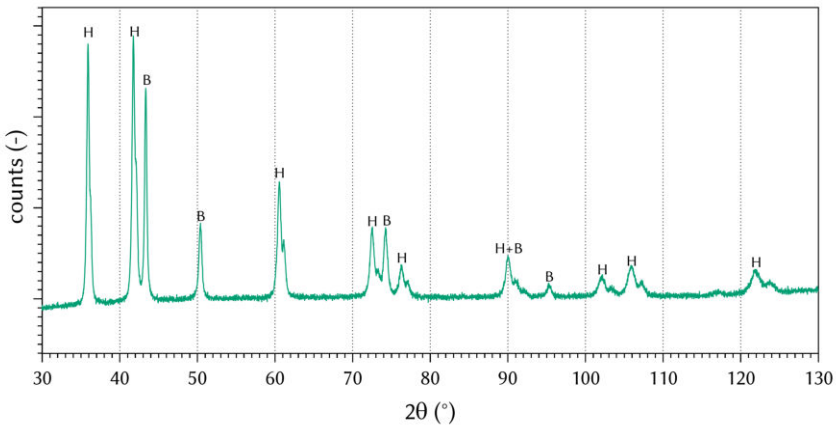

(g) XRD with hard phase (H) and binder (B) peaks identified.

Figure 90: LOM, BSE-SEM, GSD and XRD of N0-2_Ar.

(a) LOM, 100x magnification.

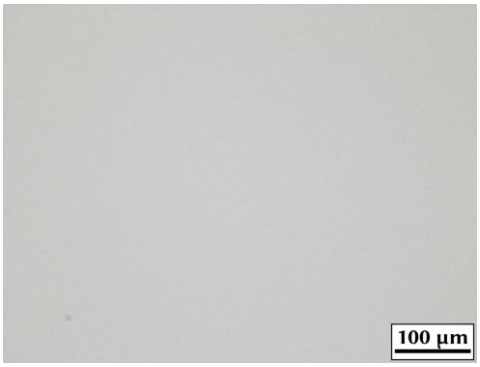

(b) LOM, 200x magnification.

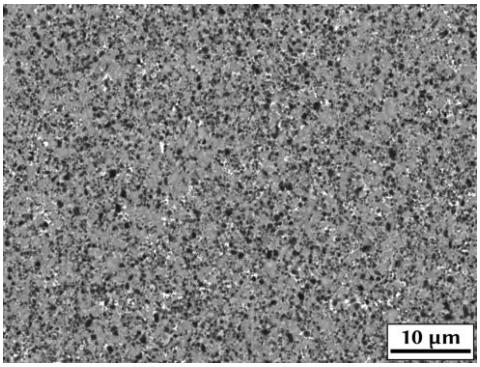

(c) BSE-SEM, 5000x magnification.

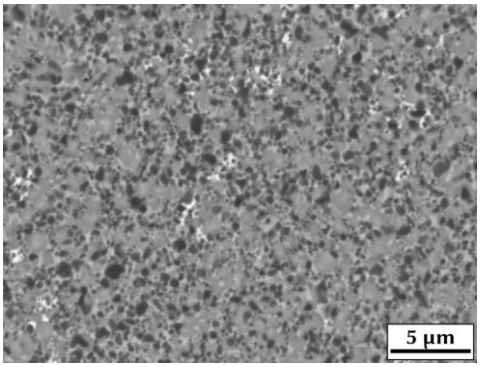

(d) BSE-SEM, 10,000x magnification.

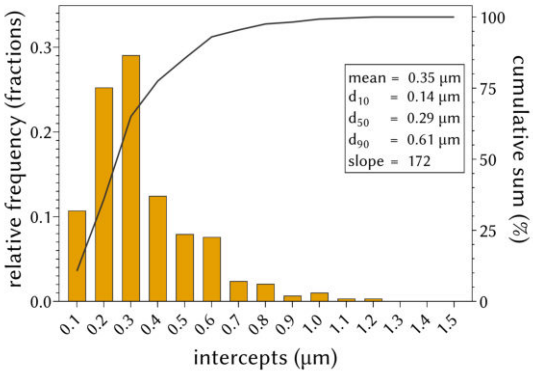

(e) GSD of cores.

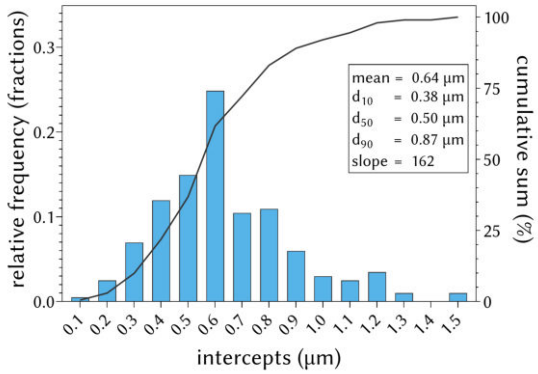

(f) GSD of grains.

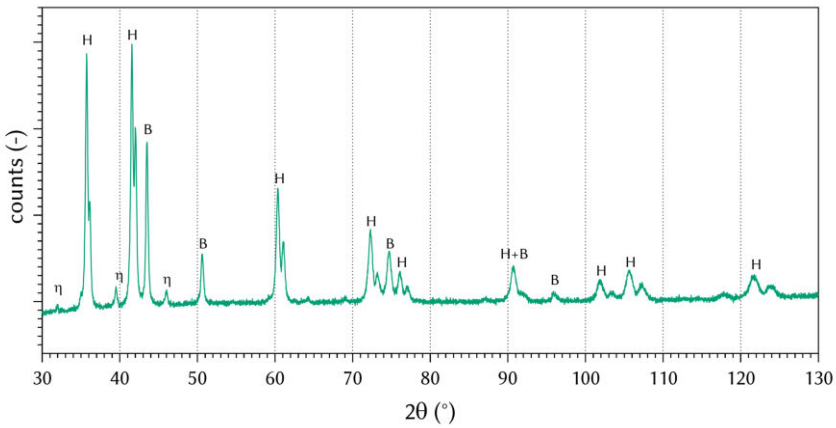

(g) XRD with hard phase (H) and binder (B) peaks identified.

Figure 91: LOM, BSE-SEM, GSD and XRD of N0-2_10N.

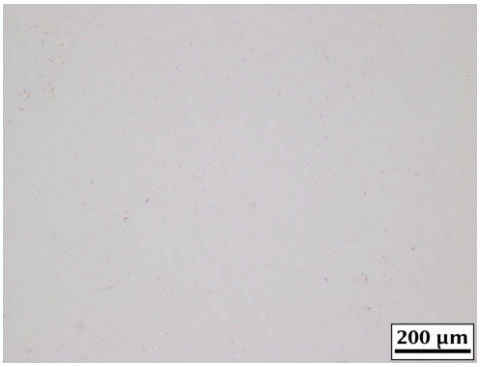

(a) LOM, 100x magnification.

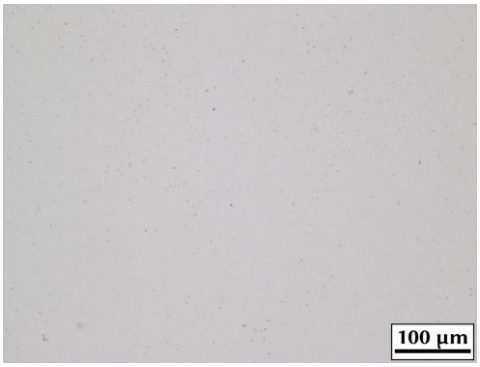

(b) LOM, 200x magnification.

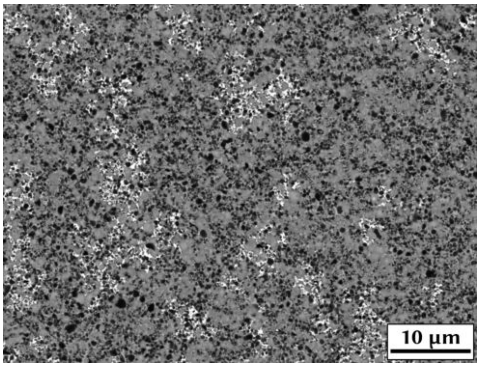

(c) BSE-SEM, 5000x magnification.

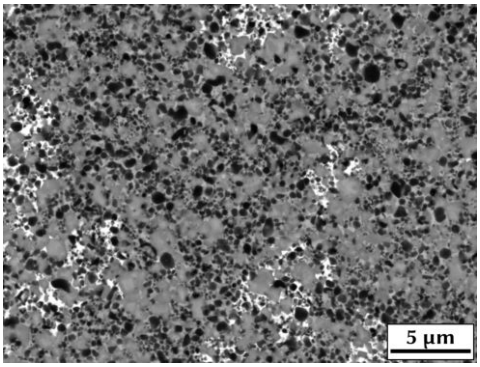

(d) BSE-SEM, 10,000x magnification.

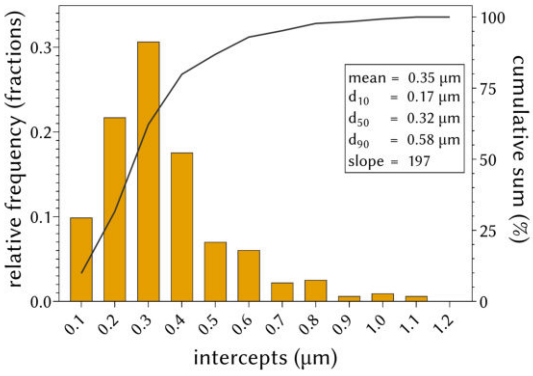

(e) GSD of cores.

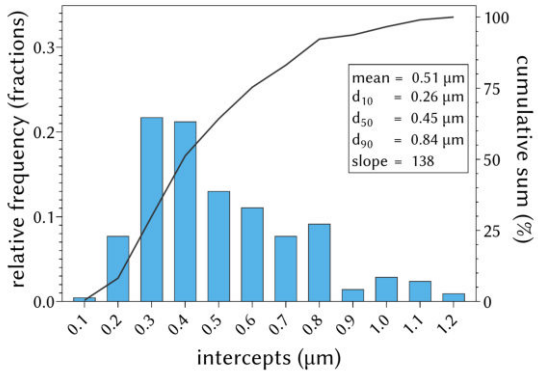

(f) GSD of grains.

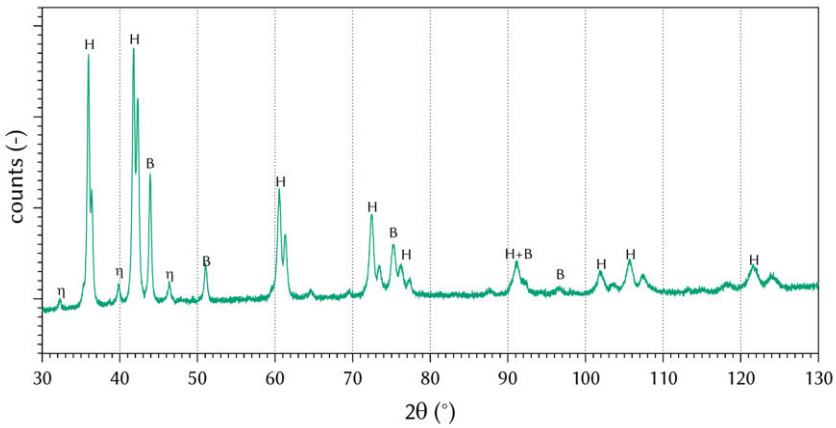

(g) XRD with hard phase (H) and binder (B) peaks identified.

Figure 92: LOM, BSE-SEM, GSD and XRD of N0-2_50N.

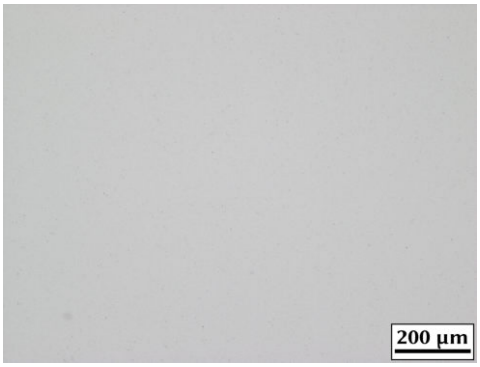

(a) LOM, 100x magnification.

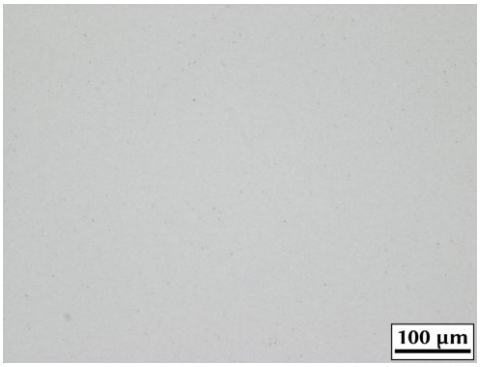

(b) LOM, 200x magnification.

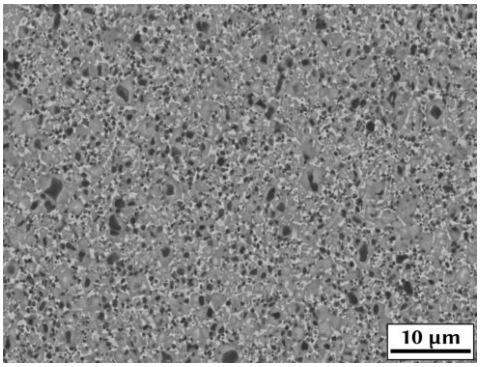

(c) BSE-SEM, 5000x magnification.

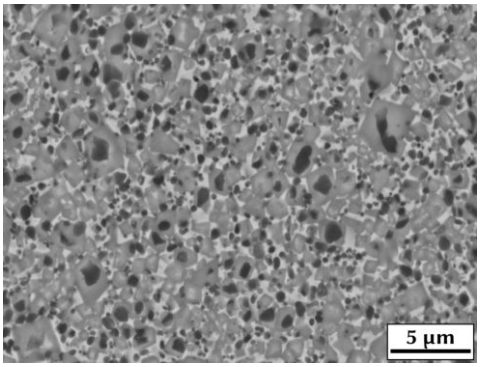

(d) BSE-SEM, 10,000x magnification.

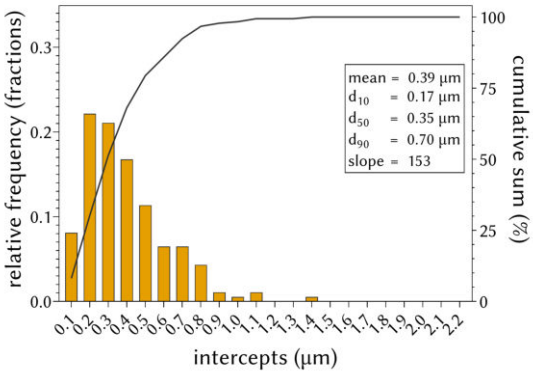

(e) GSD of cores.

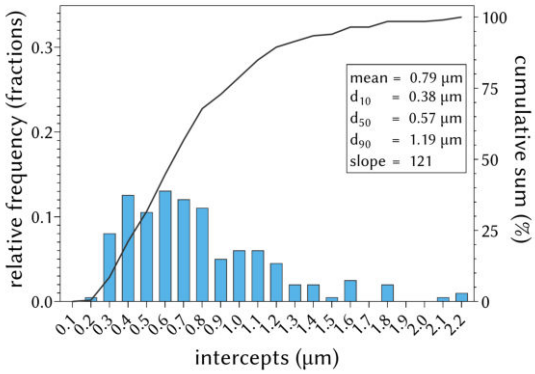

(f) GSD of grains.

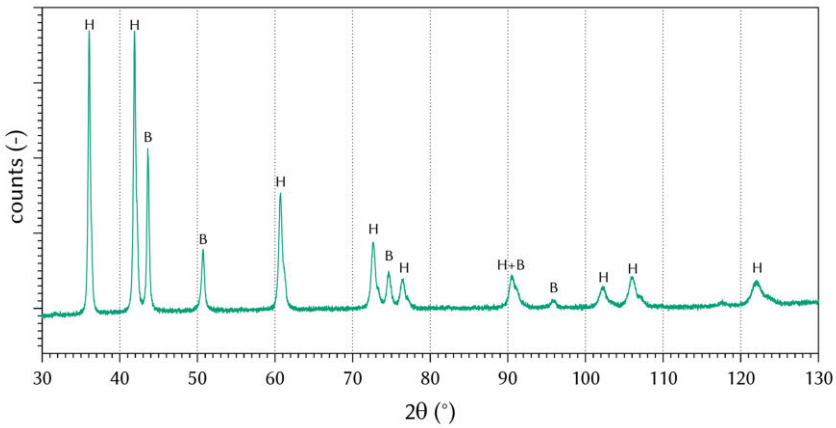

(g) XRD with hard phase (H) and binder (B) peaks identified.

Figure 93: LOM, BSE-SEM, GSD and XRD of N1-1_Ar.

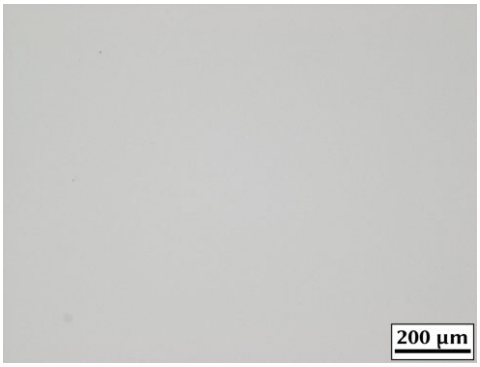

(a) LOM, 100x magnification.

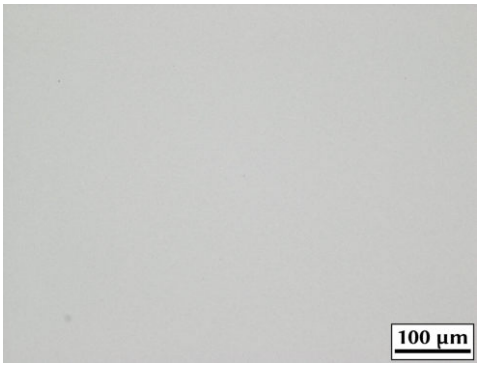

(b) LOM, 200x magnification.

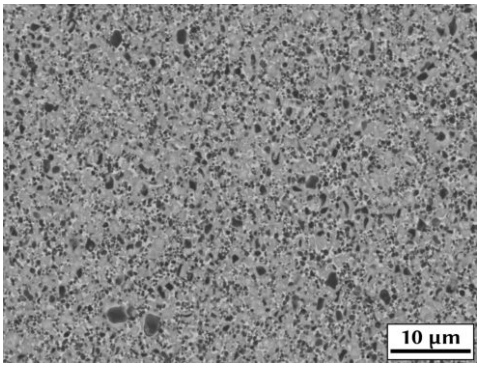

(c) BSE-SEM, 5000x magnification.

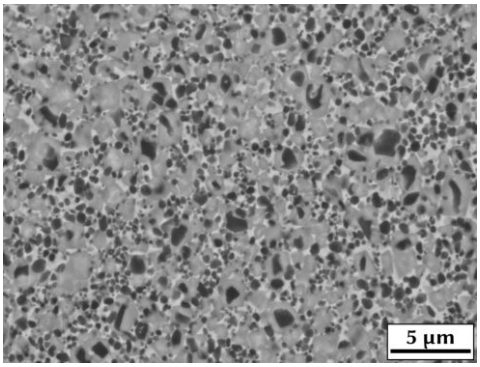

(d) BSE-SEM, 10,000x magnification.

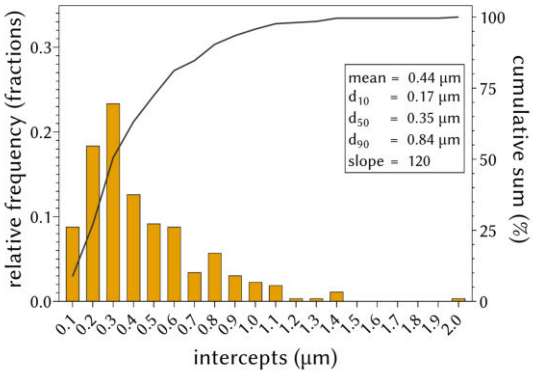

(e) GSD of cores.

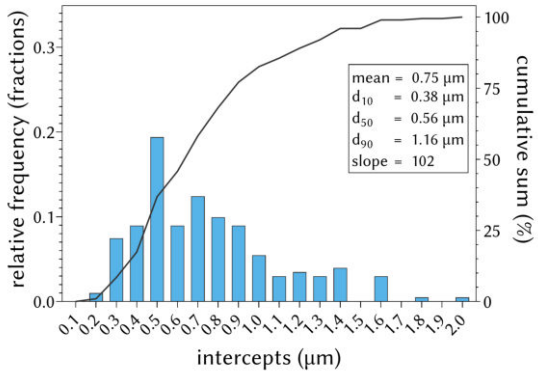

(f) GSD of grains.

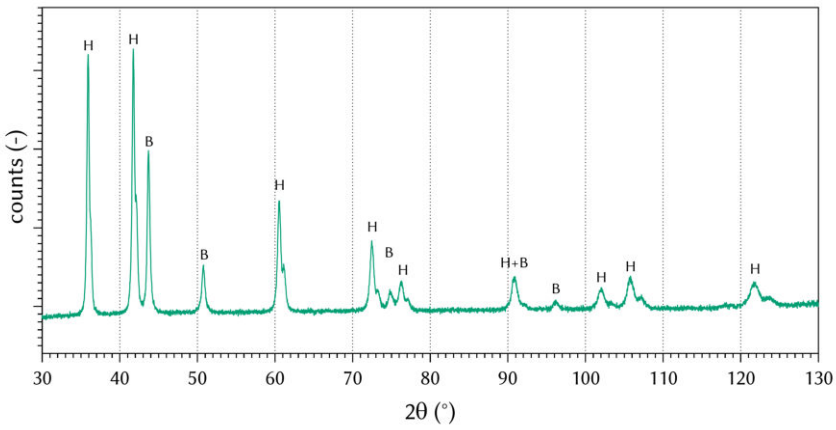

(g) XRD with hard phase (H) and binder (B) peaks identified.

Figure 94: LOM, BSE-SEM, GSD and XRD of N1-1_10N.

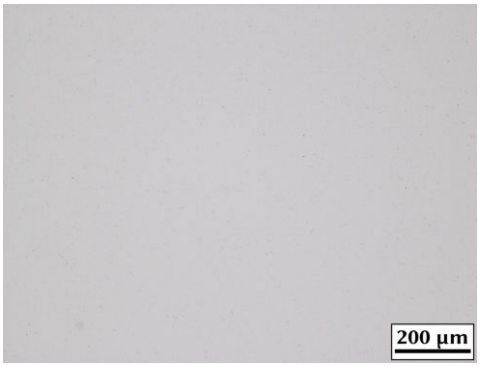

(a) LOM, 100x magnification.

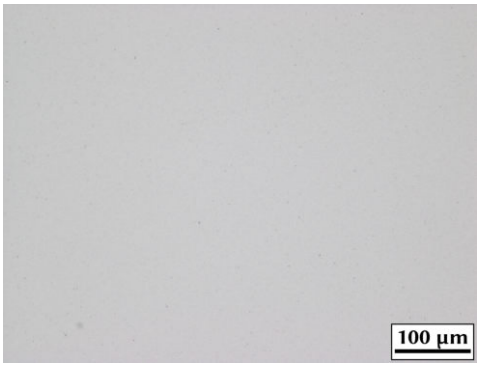

(b) LOM, 200x magnification.

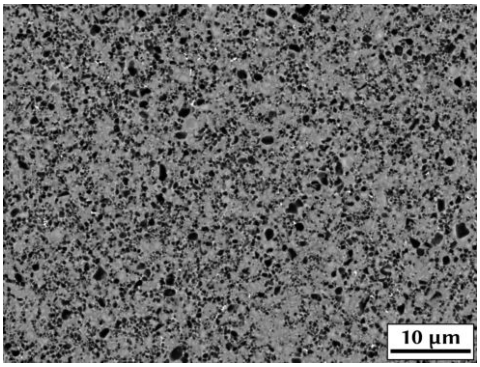

(c) BSE-SEM, 5000x magnification.

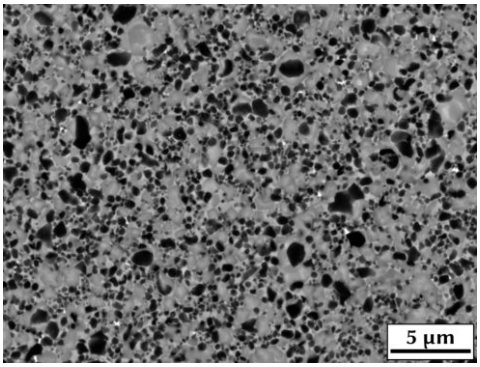

(d) BSE-SEM, 10,000x magnification.

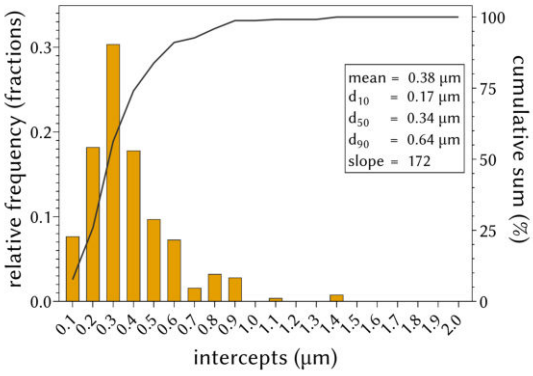

(e) GSD of cores.

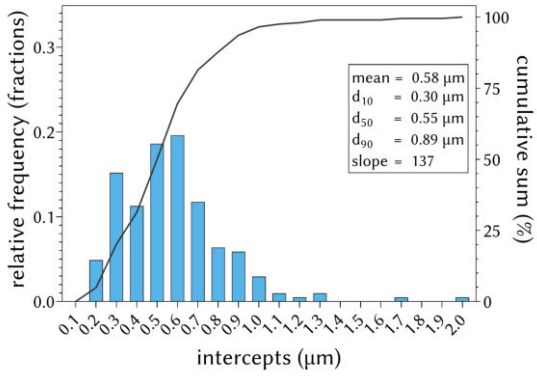

(f) GSD of grains.

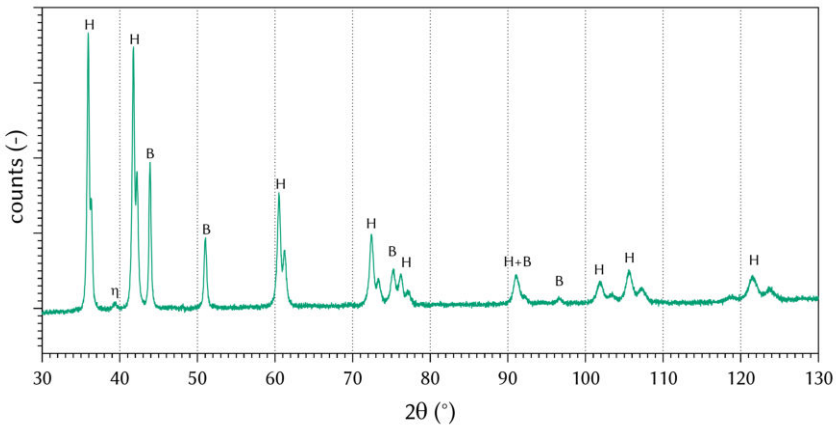

(g) XRD with hard phase (H) and binder (B) peaks identified.

Figure 95: LOM, BSE-SEM, GSD and XRD of N1-1_50N.

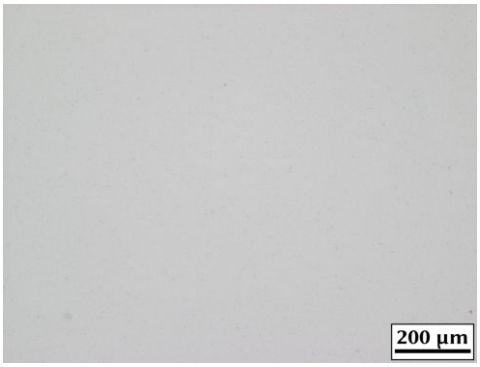

(a) LOM, 100x magnification.

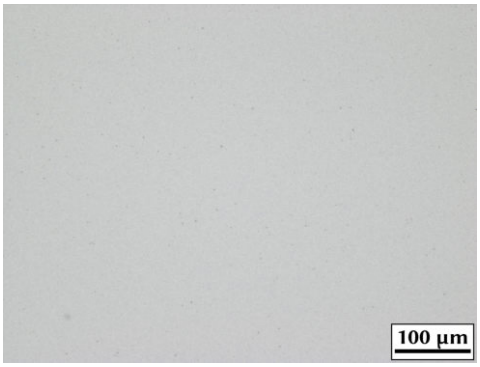

(b) LOM, 200x magnification.

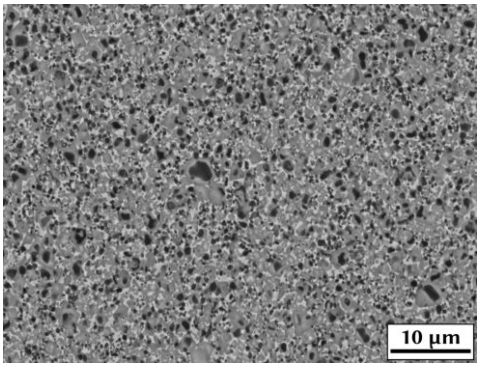

(c) BSE-SEM, 5000x magnification.

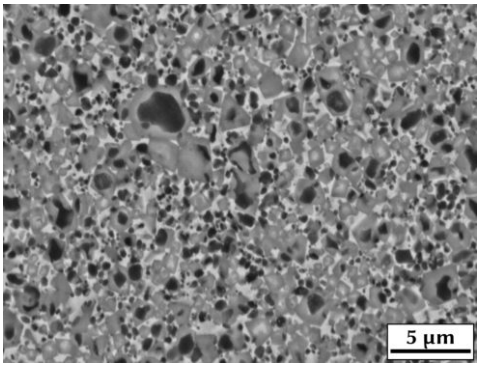

(d) BSE-SEM, 10,000x magnification.

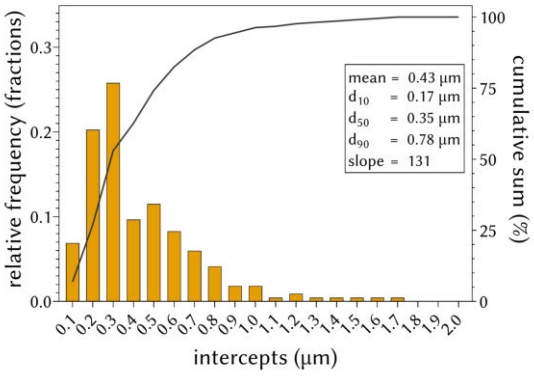

(e) GSD of cores.

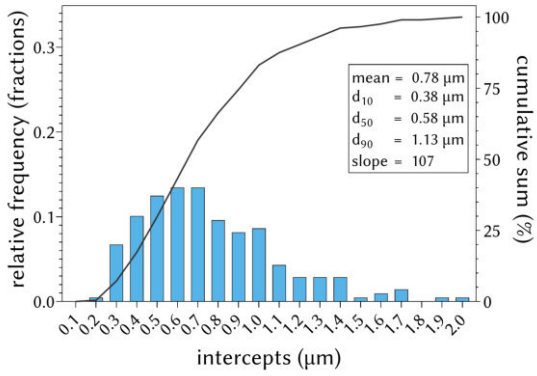

(f) GSD of grains.

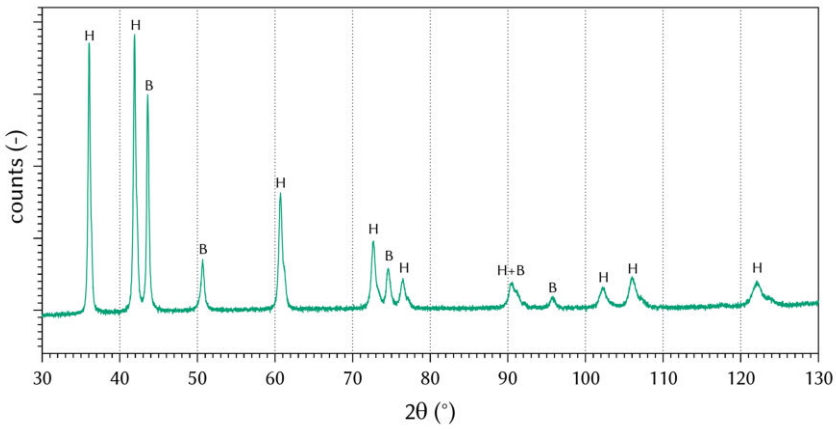

(g) XRD with hard phase (H) and binder (B) peaks identified.

Figure 96: LOM, BSE-SEM, GSD and XRD of N1-2_Ar.

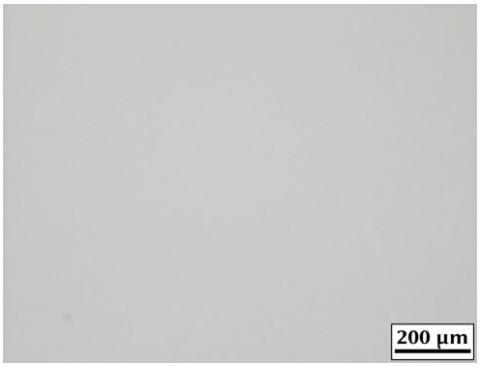

(a) LOM, 100x magnification.

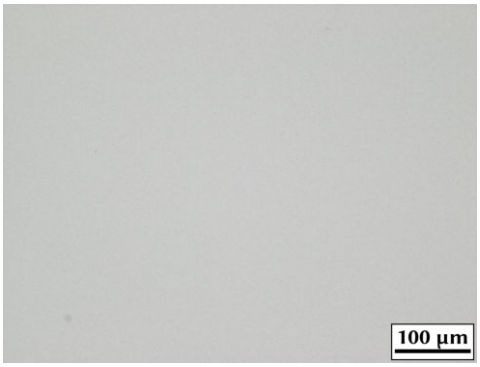

(b) LOM, 200x magnification.

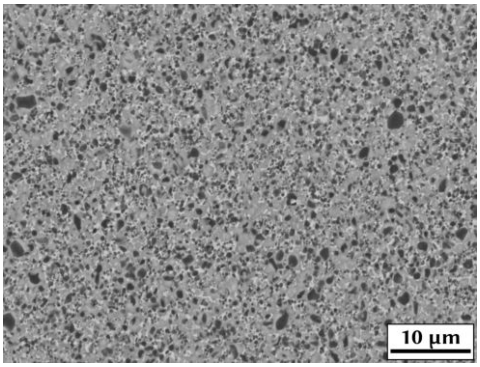

(c) BSE-SEM, 5000x magnification.

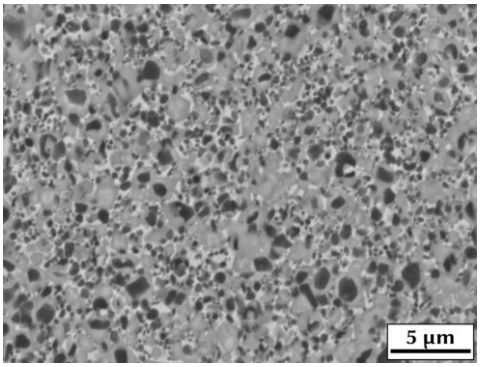

(d) BSE-SEM, 10,000x magnification.

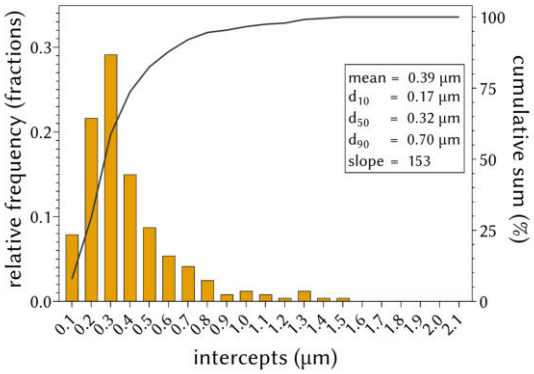

(e) GSD of cores.

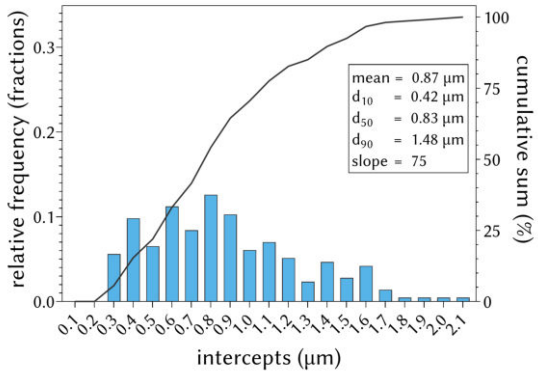

(f) GSD of grains.

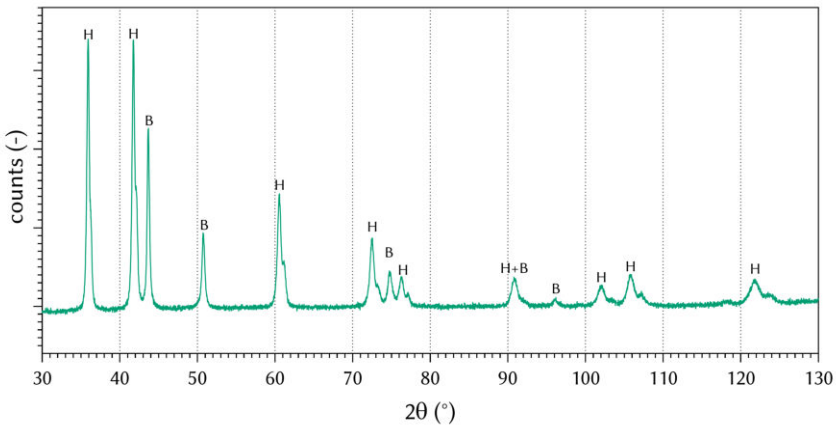

(g) XRD with hard phase (H) and binder (B) peaks identified.

Figure 97: LOM, BSE-SEM, GSD and XRD of N1-2_10N.

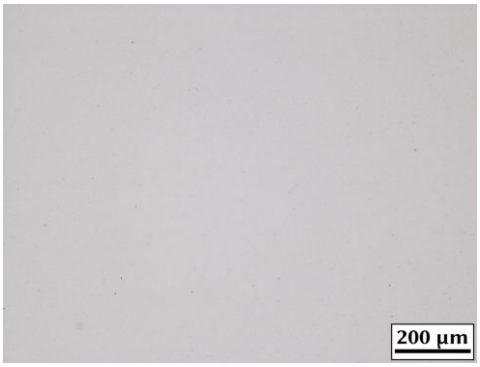

(a) LOM, 100x magnification.

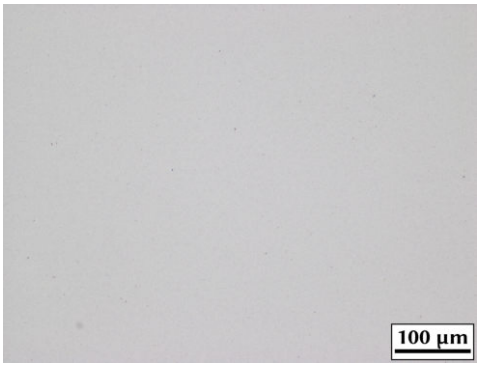

(b) LOM, 200x magnification.

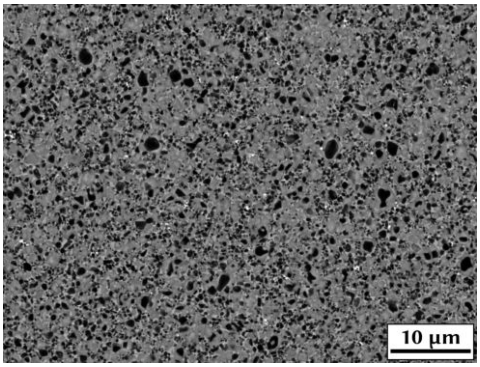

(c) BSE-SEM, 5000x magnification.

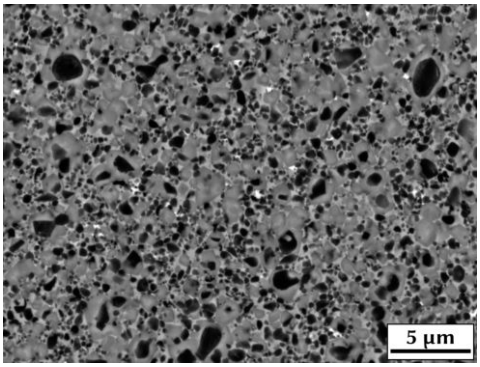

(d) BSE-SEM, 10,000x magnification.

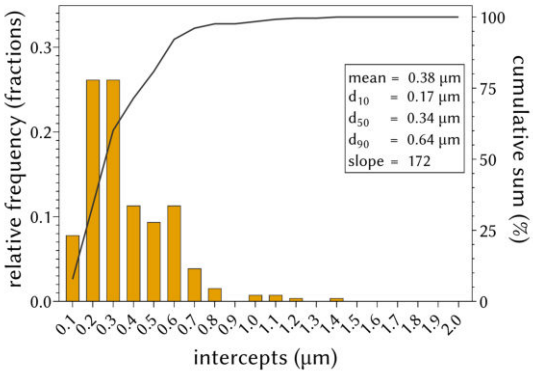

(e) GSD of cores.

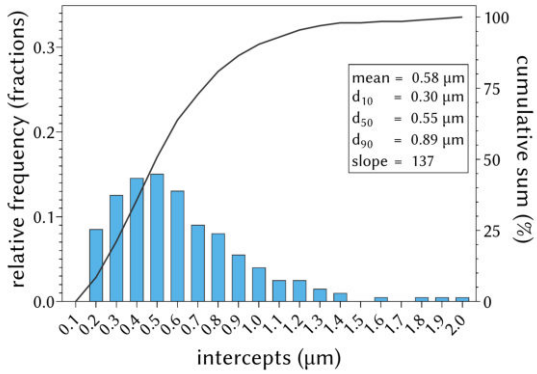

(f) GSD of grains.

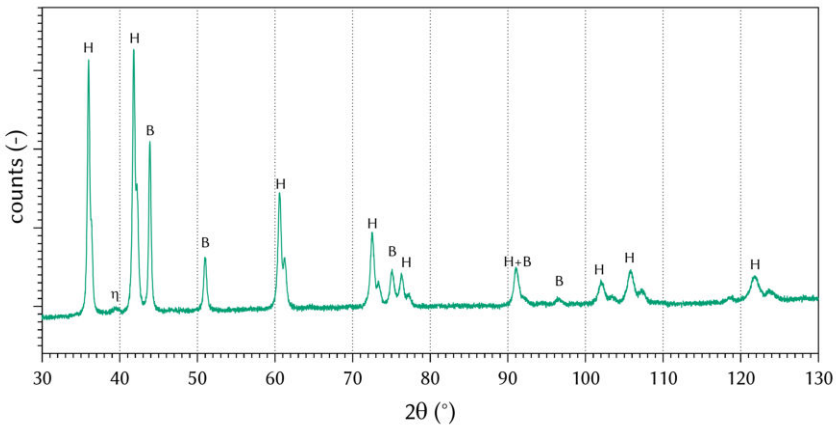

(g) XRD with hard phase (H) and binder (B) peaks identified.

Figure 98: LOM, BSE-SEM, GSD and XRD of N1-2_50N.

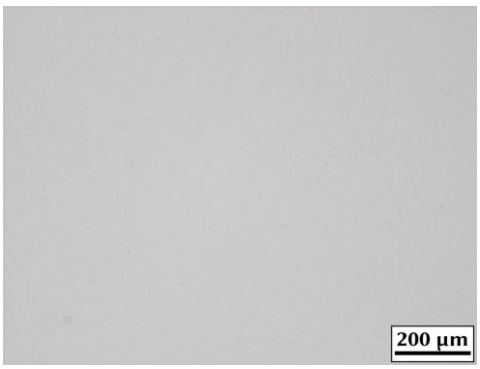

(a) LOM, 100x magnification.

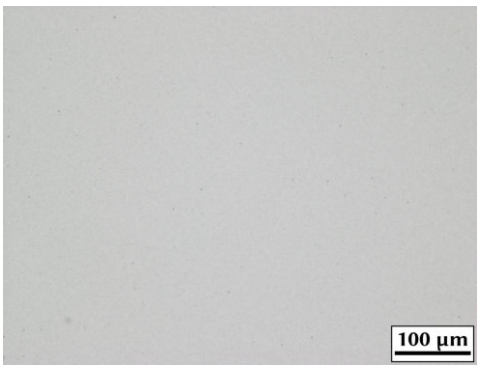

(b) LOM, 200x magnification.

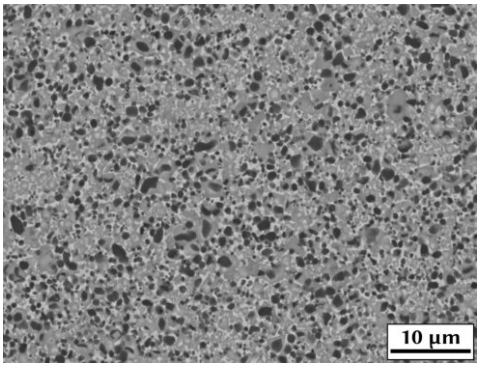

(c) BSE-SEM, 5000x magnification.

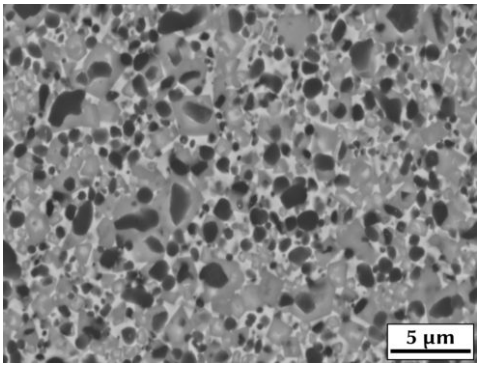

(d) BSE-SEM, 10,000x magnification.

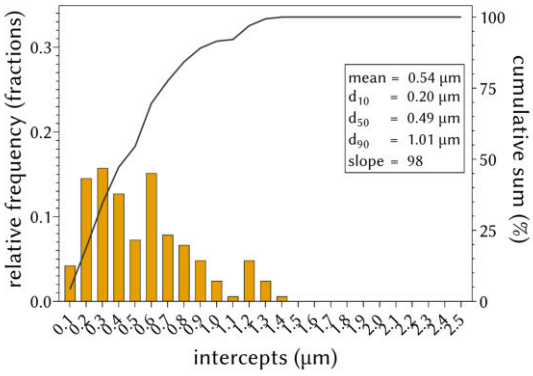

(e) GSD of cores.

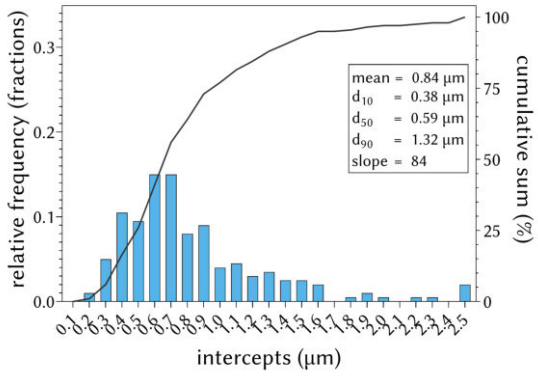

(f) GSD of grains.

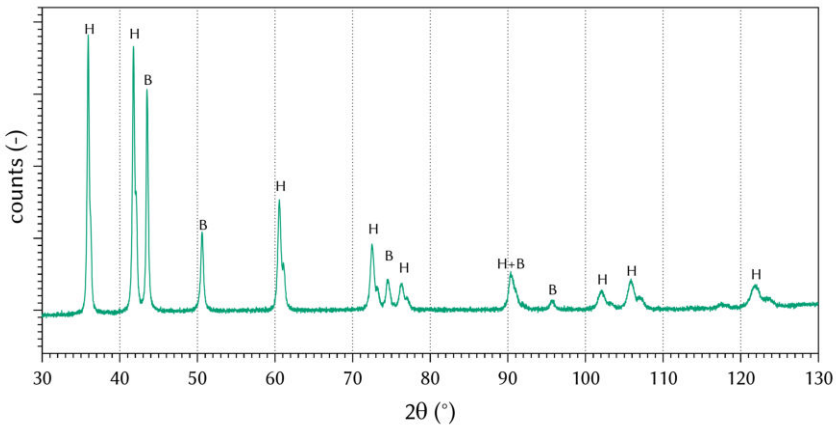

(g) XRD with hard phase (H) and binder (B) peaks identified.

Figure 99: LOM, BSE-SEM, GSD and XRD of N1-3_Ar.

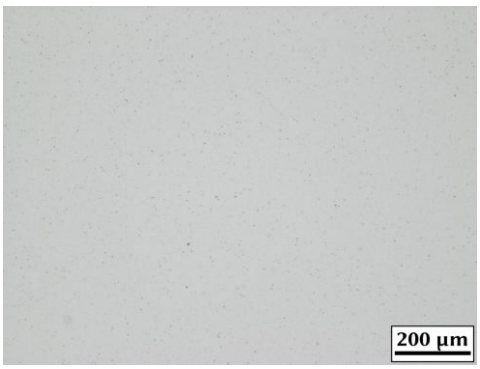

(a) LOM, 100x magnification.

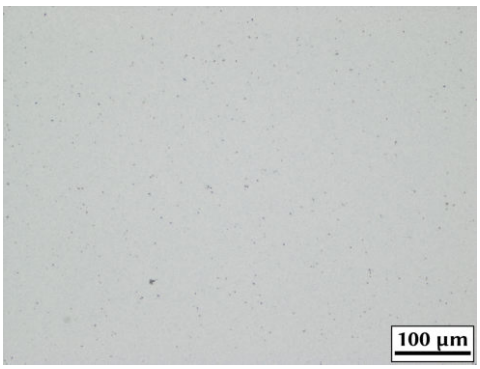

(b) LOM, 200x magnification.

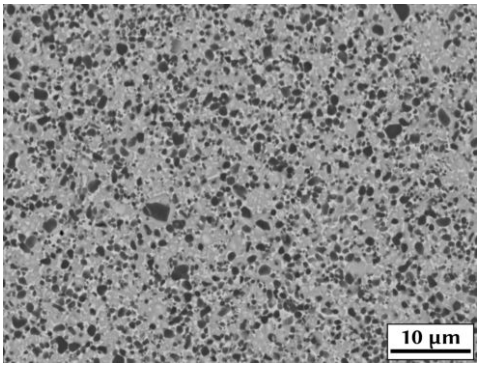

(c) BSE-SEM, 5000x magnification.

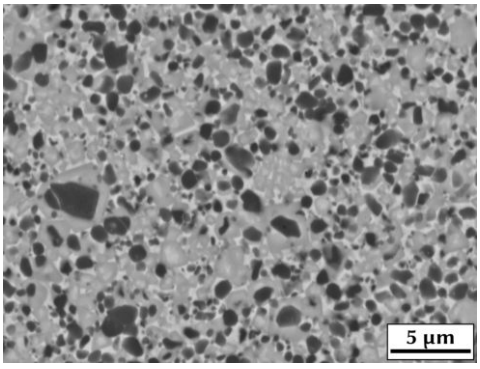

(d) BSE-SEM, 10,000x magnification.

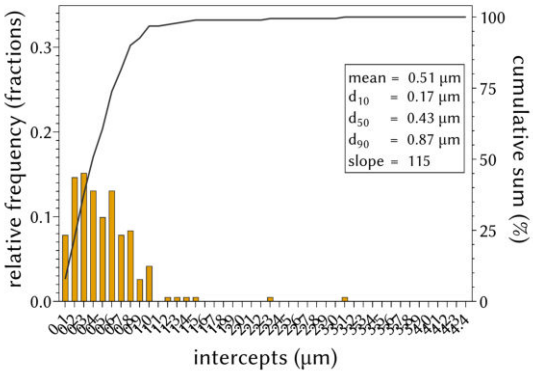

(e) GSD of cores.

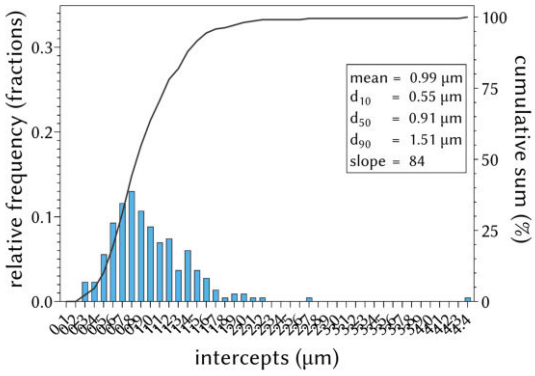

(f) GSD of grains.

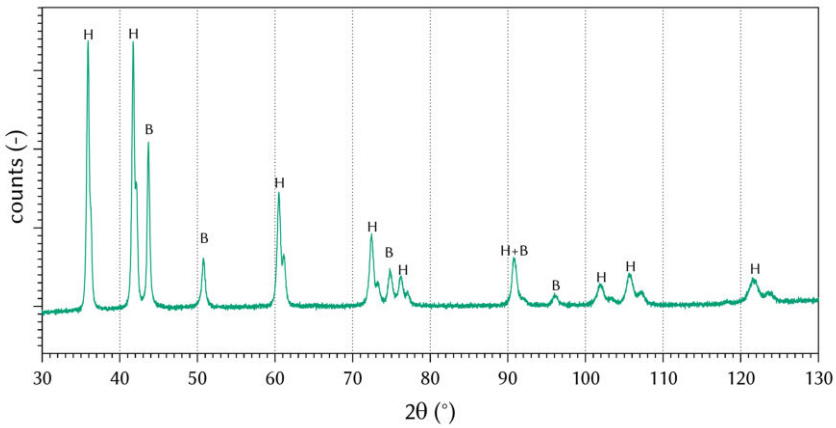

(g) XRD with hard phase (H) and binder (B) peaks identified.

Figure 100: LOM, BSE-SEM, GSD and XRD of N1-3_10N.

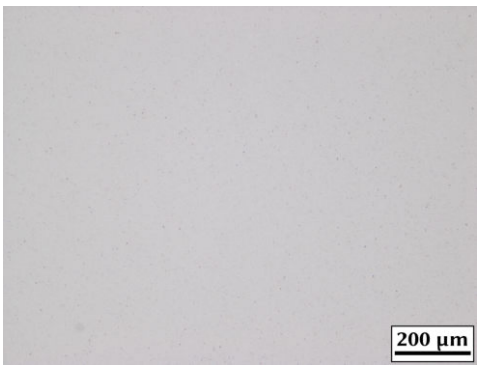

(a) LOM, 100x magnification.

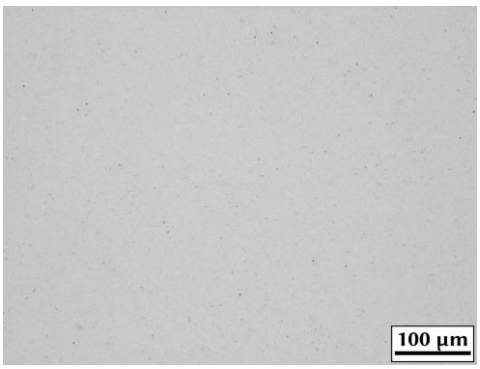

(b) LOM, 200x magnification.

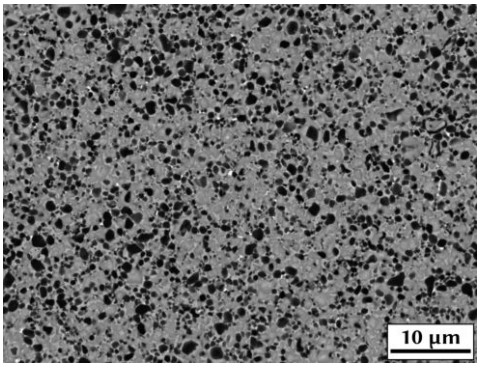

(c) BSE-SEM, 5000x magnification.

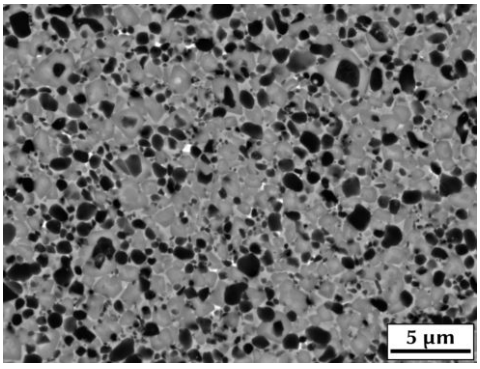

(d) BSE-SEM, 10,000x magnification.

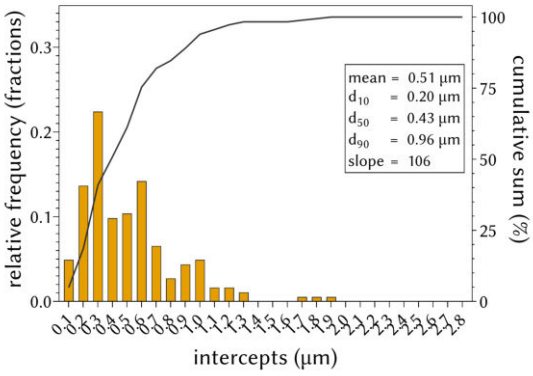

(e) GSD of cores.

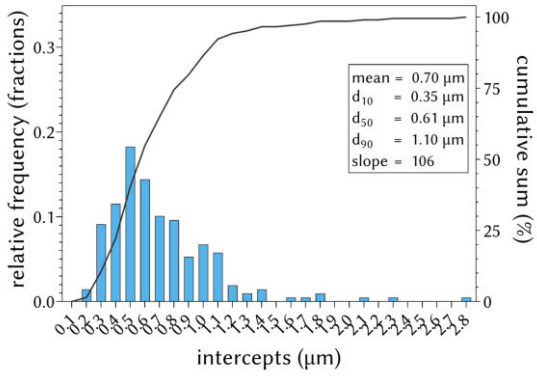

(f) GSD of grains.

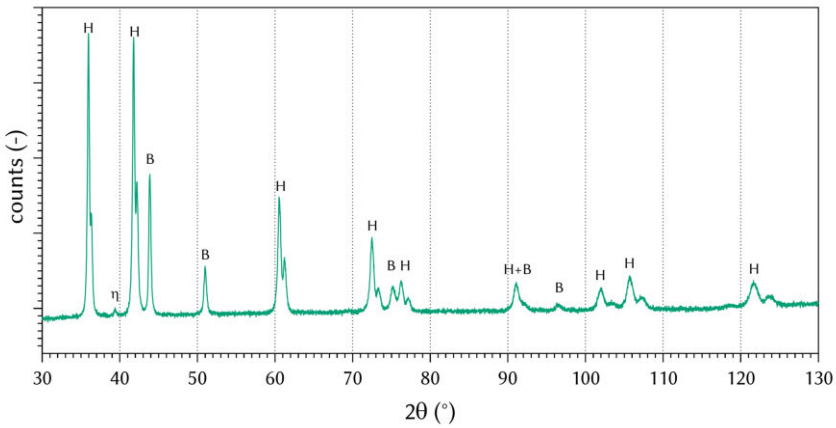

(g) XRD with hard phase (H) and binder (B) peaks identified.

Figure 101: LOM, BSE-SEM, GSD and XRD of N1-3_50N.

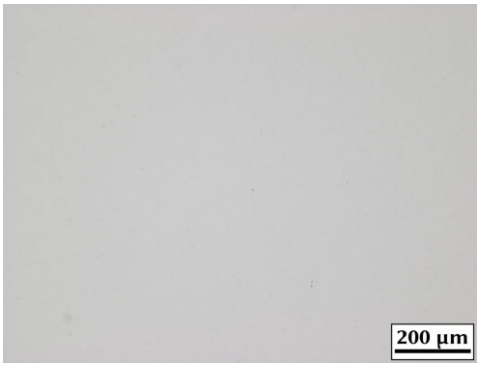

(a) LOM, 100x magnification.

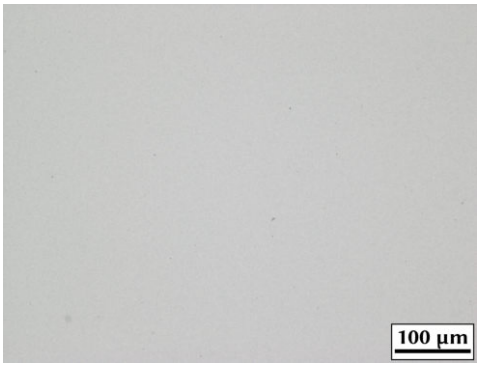

(b) LOM, 200x magnification.

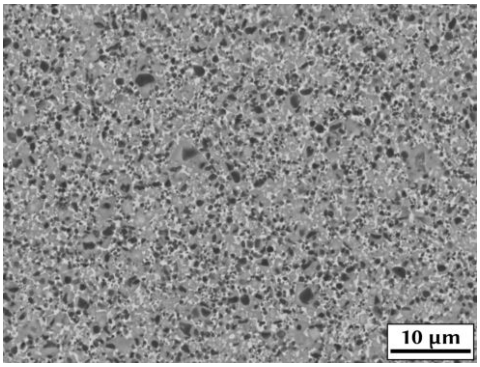

(c) BSE-SEM, 5000x magnification.

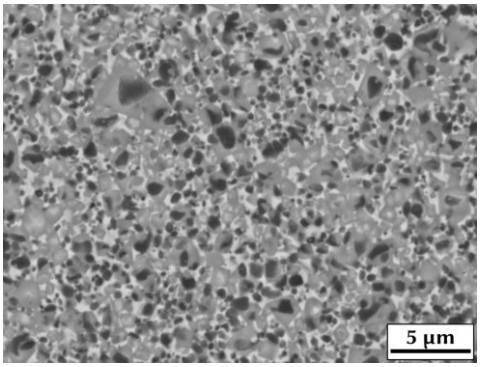

(d) BSE-SEM, 10,000x magnification.

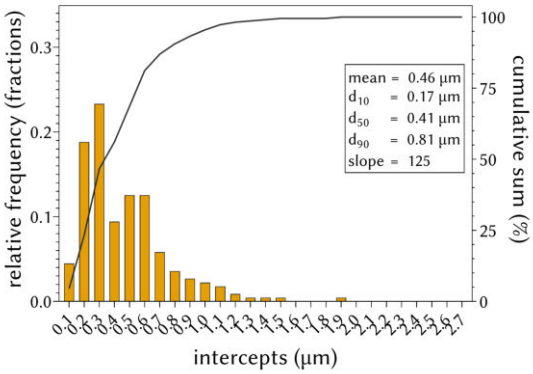

(e) GSD of cores.

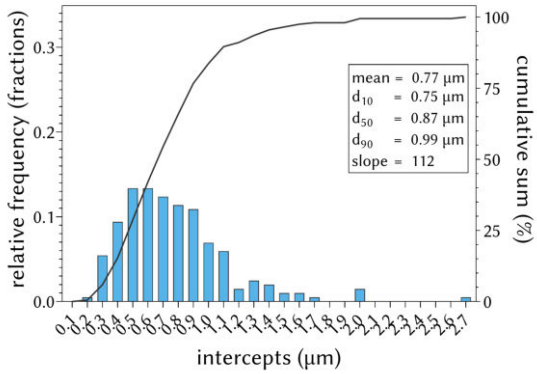

(f) GSD of grains.

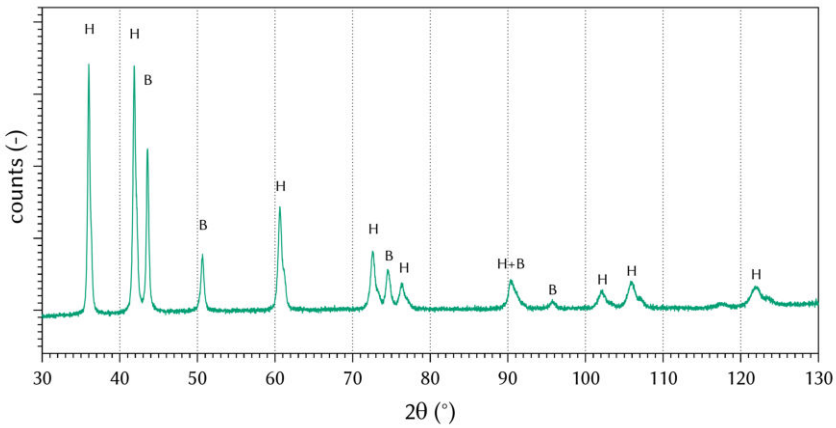

(g) XRD with hard phase (H) and binder (B) peaks identified.

Figure 102: LOM, BSE-SEM, GSD and XRD of N1-4_Ar.

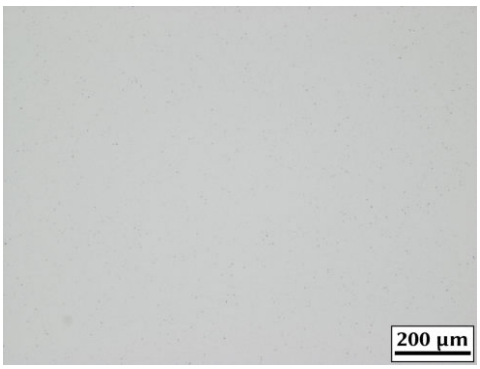

(a) LOM, 100x magnification.

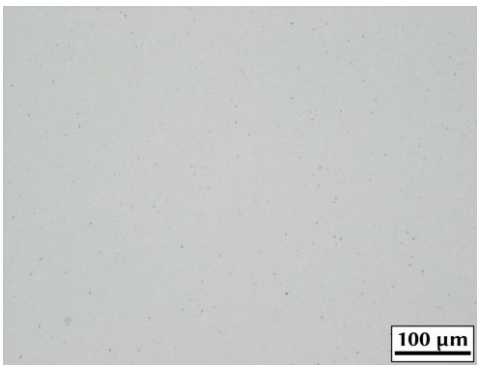

(b) LOM, 200x magnification.

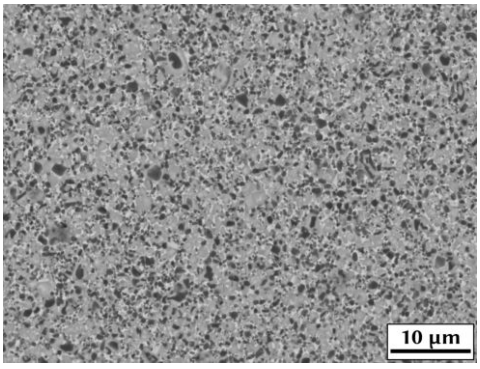

(c) BSE-SEM, 5000x magnification.

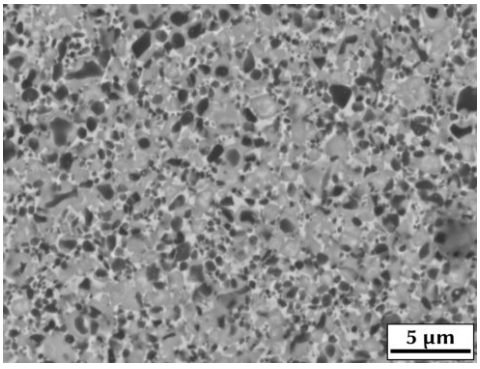

(d) BSE-SEM, 10,000x magnification.

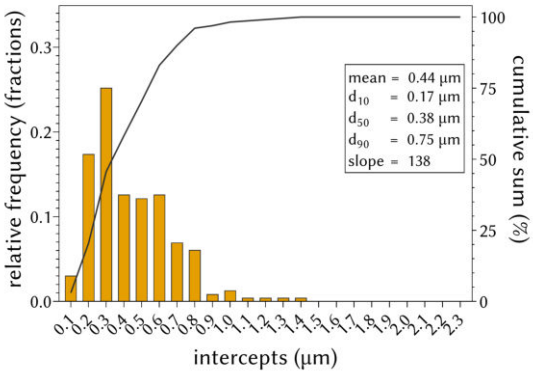

(e) GSD of cores.

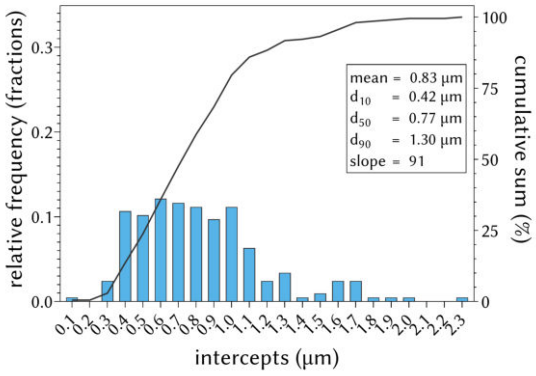

(f) GSD of grains.

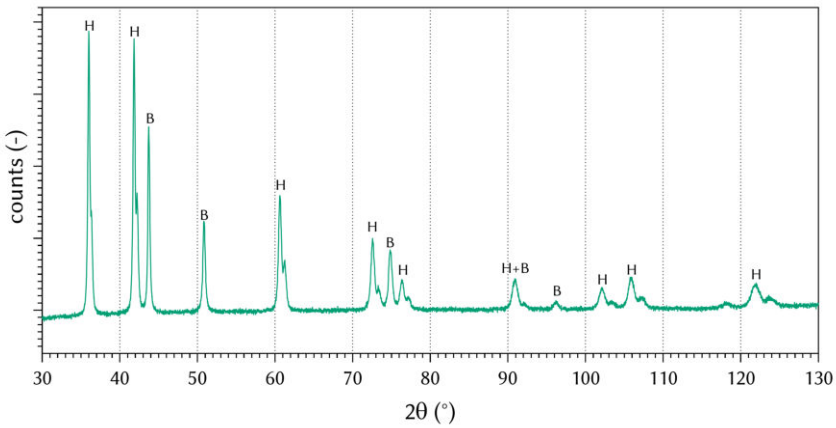

(g) XRD with hard phase (H) and binder (B) peaks identified.

Figure 103: LOM, BSE-SEM, GSD and XRD of N1-4_10N.

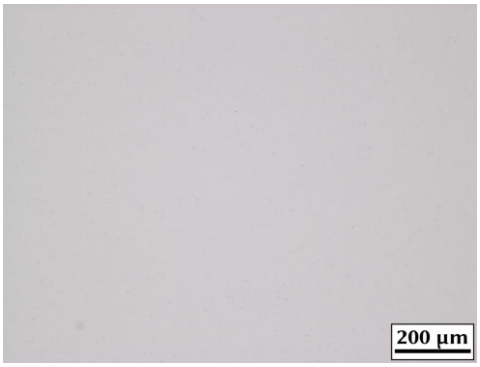

(a) LOM, 100x magnification.

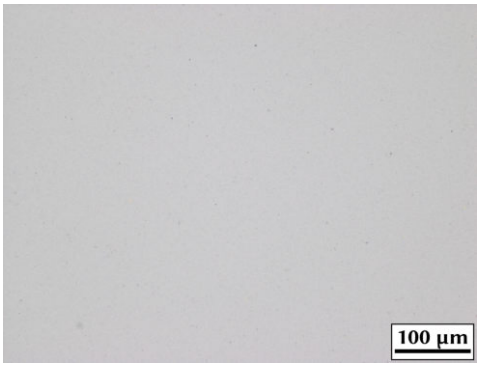

(b) LOM, 200x magnification.

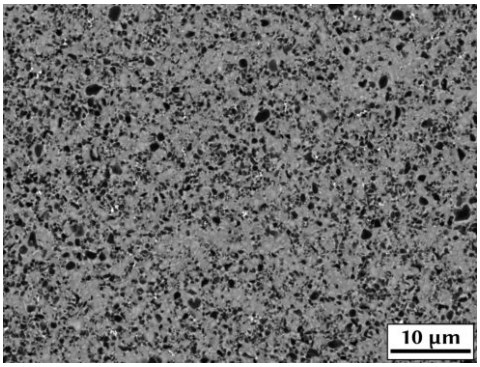

(c) BSE-SEM, 5000x magnification.

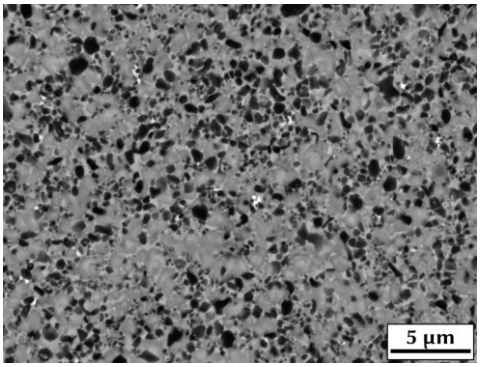

(d) BSE-SEM, 10,000x magnification.

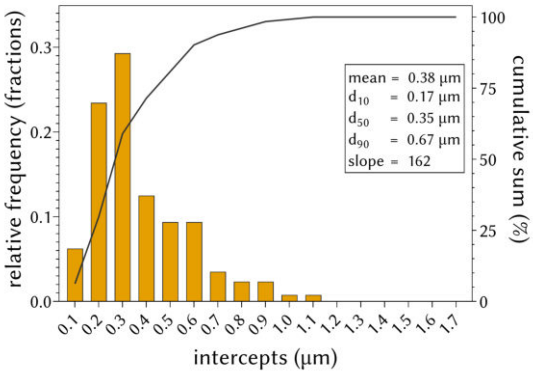

(e) GSD of cores.

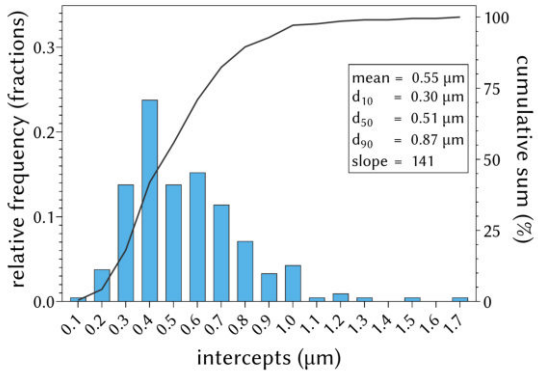

(f) GSD of grains.

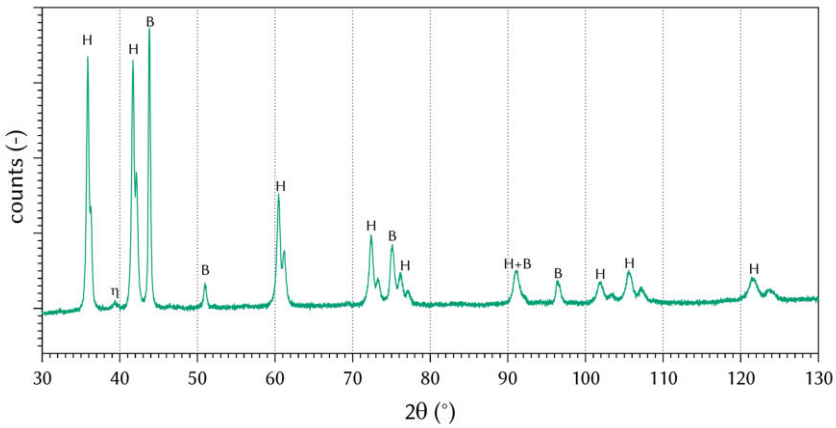

(g) XRD with hard phase (H) and binder (B) peaks identified.

Figure 104: LOM, BSE-SEM, GSD and XRD of N1-4_50N.

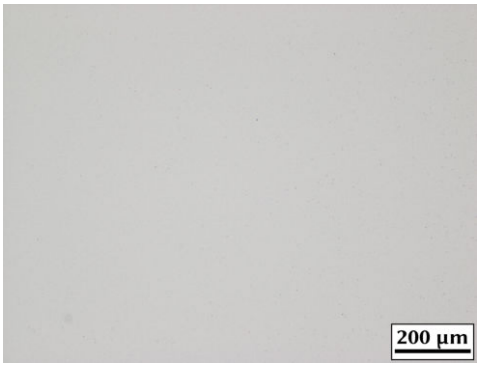

(a) LOM, 100x magnification.

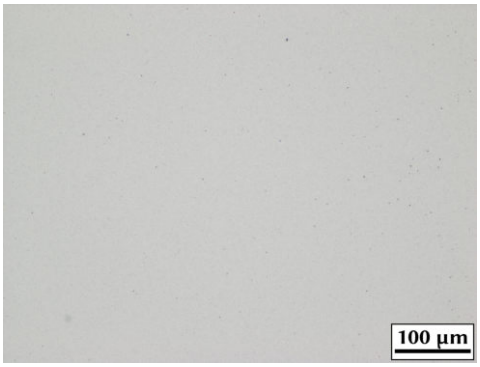

(b) LOM, 200x magnification.

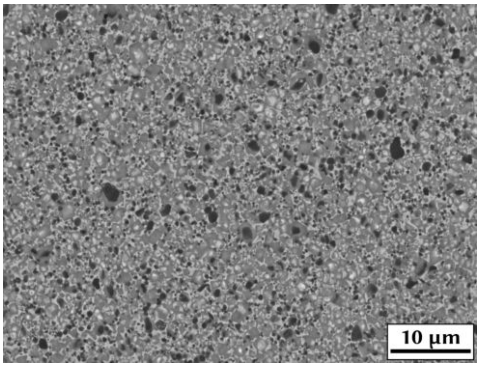

(c) BSE-SEM, 5000x magnification.

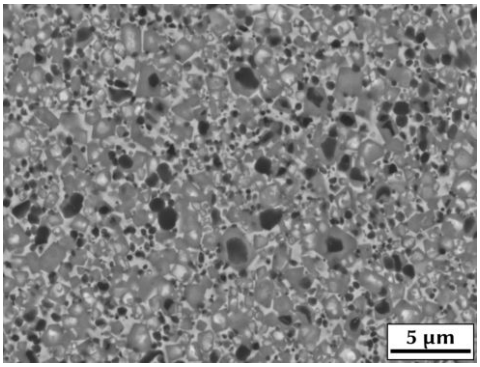

(d) BSE-SEM, 10,000x magnification.

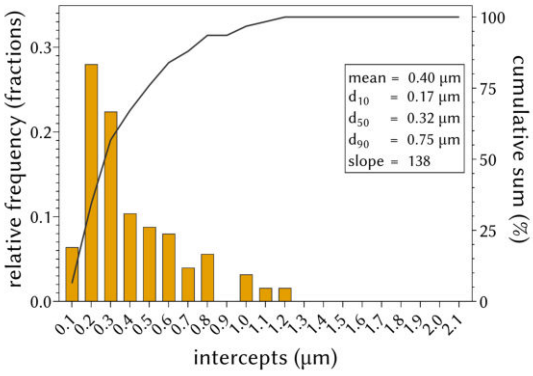

(e) GSD of cores.

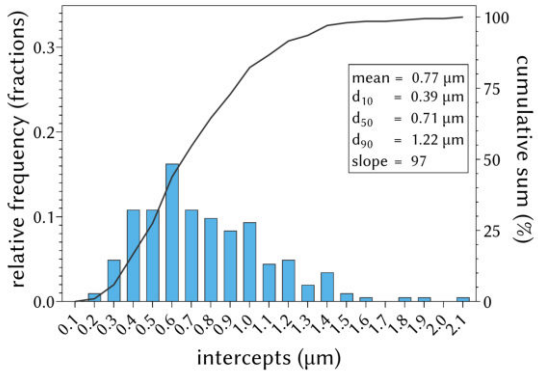

(f) GSD of grains.

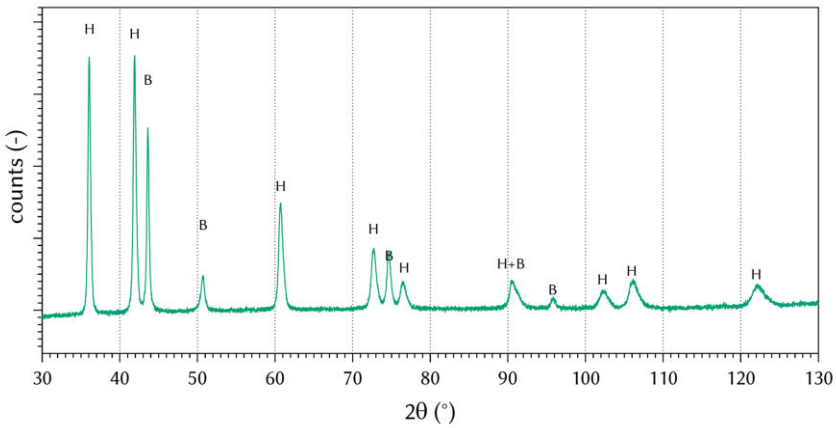

(g) XRD with hard phase (H) and binder (B) peaks identified.

Figure 105: LOM, BSE-SEM, GSD and XRD of N2-1_Ar.

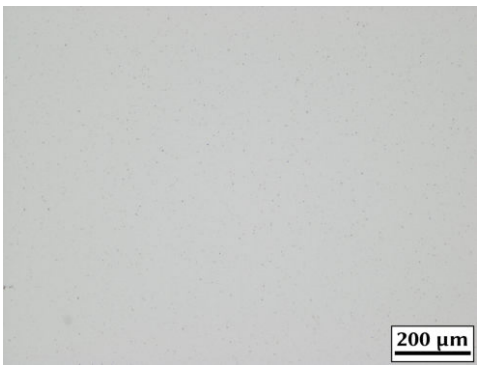

(a) LOM, 100x magnification.

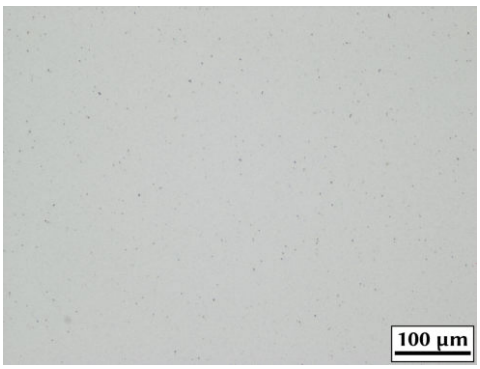

(b) LOM, 200x magnification.

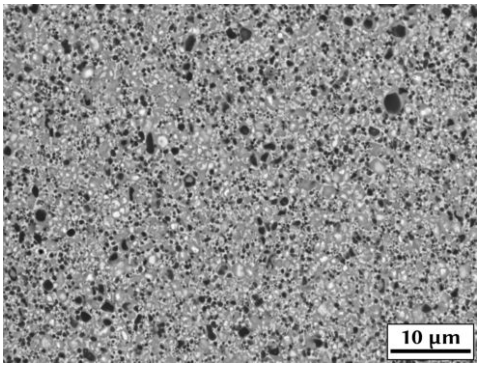

(c) BSE-SEM, 5000x magnification.

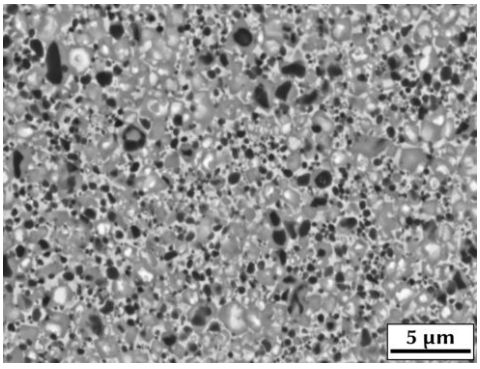

(d) BSE-SEM, 10,000x magnification.

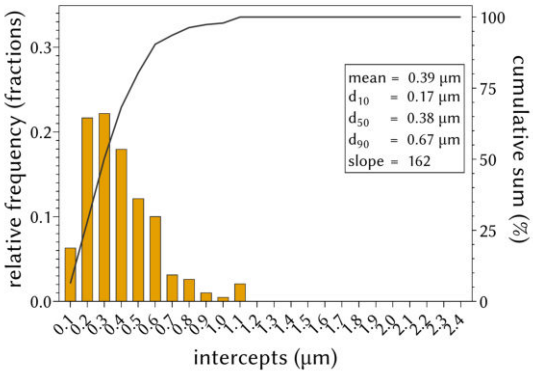

(e) GSD of cores.

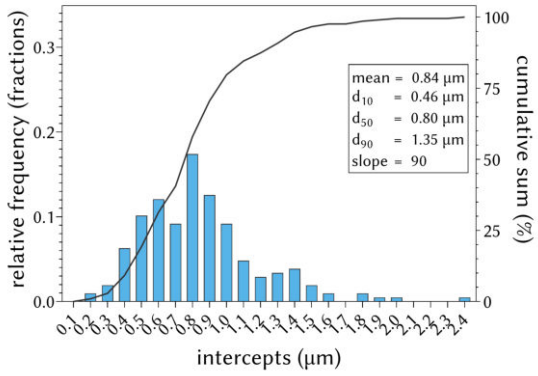

(f) GSD of grains.

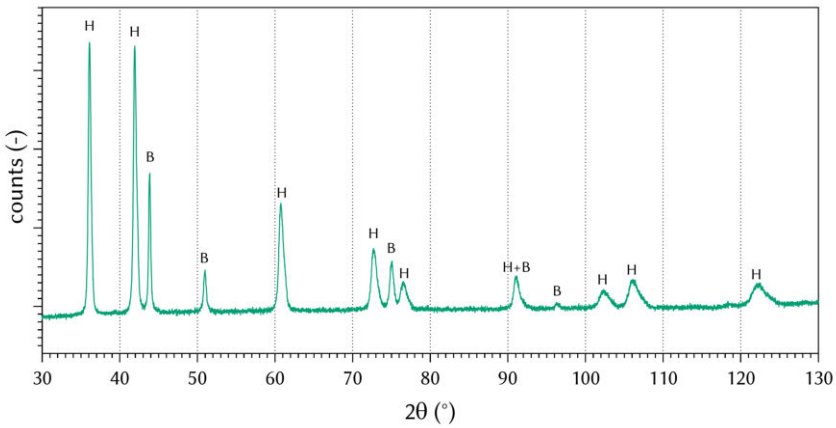

(g) XRD with hard phase (H) and binder (B) peaks identified.

Figure 106: LOM, BSE-SEM, GSD and XRD of N2-1_10N.

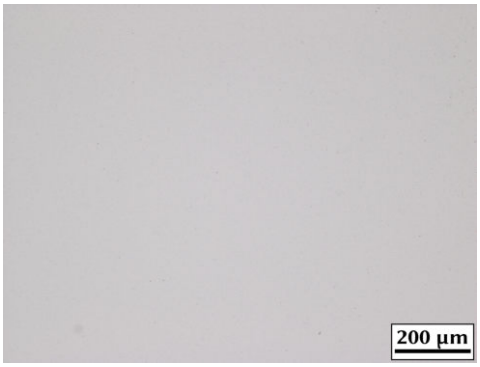

(a) LOM, 100x magnification.

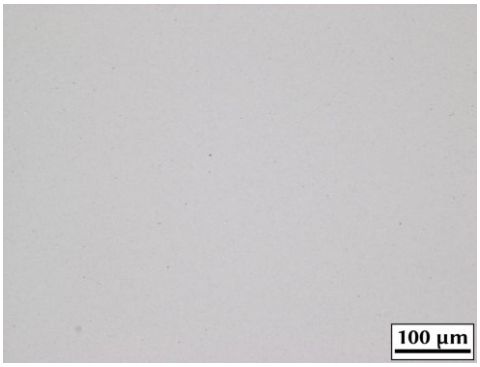

(b) LOM, 200x magnification.

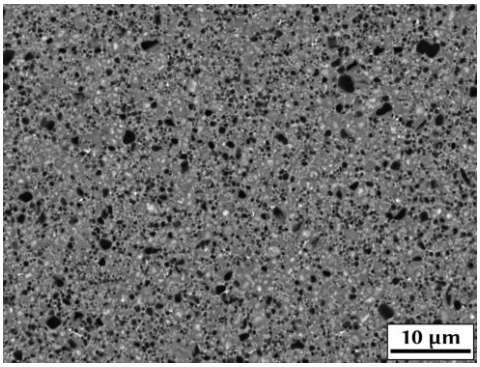

(c) BSE-SEM, 5000x magnification.

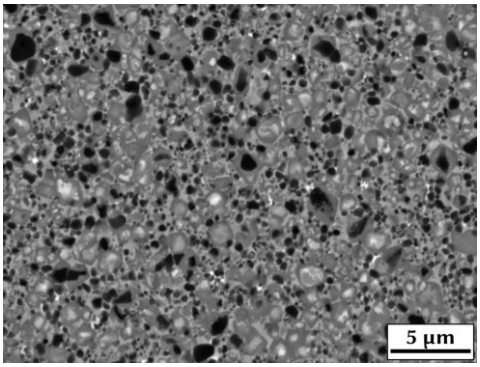

(d) BSE-SEM, 10,000x magnification.

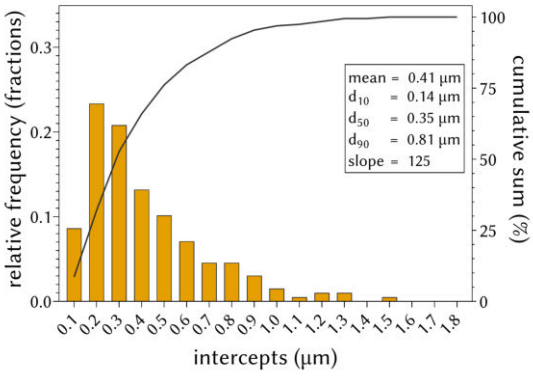

(e) GSD of cores.

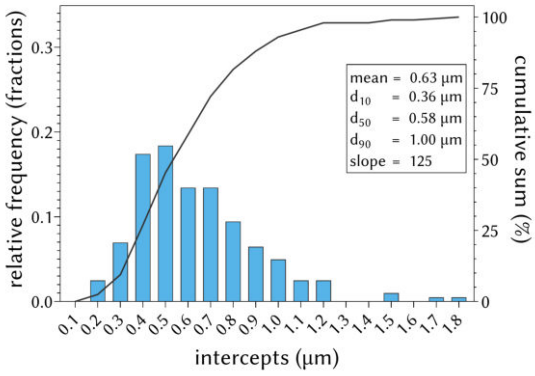

(f) GSD of grains.

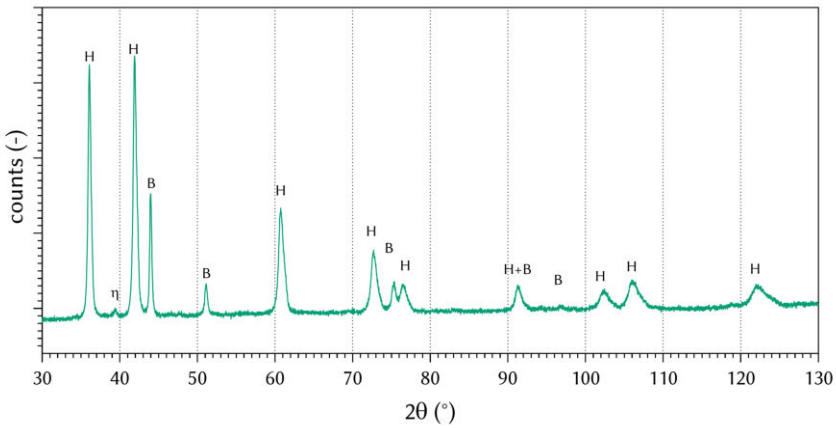

(g) XRD with hard phase (H) and binder (B) peaks identified.

Figure 107: LOM, BSE-SEM, GSD and XRD of N2-1_50N.

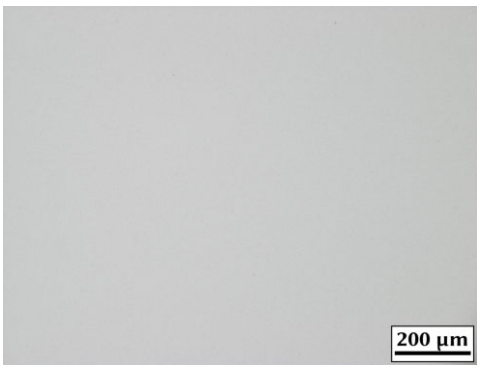

(a) LOM, 100x magnification.

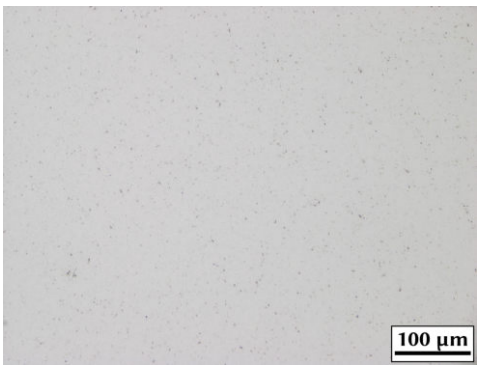

(b) LOM, 200x magnification.

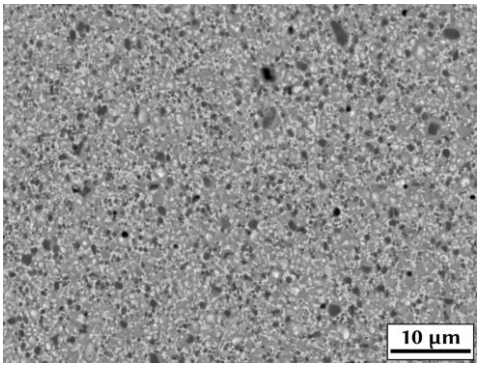

(c) BSE-SEM, 5000x magnification.

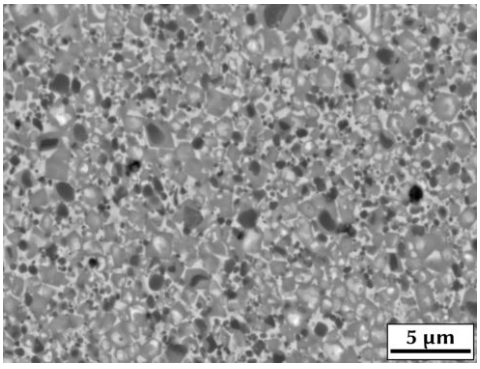

(d) BSE-SEM, 10,000x magnification.

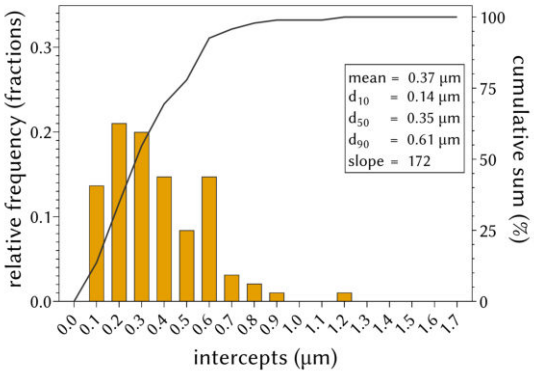

(e) GSD of cores.

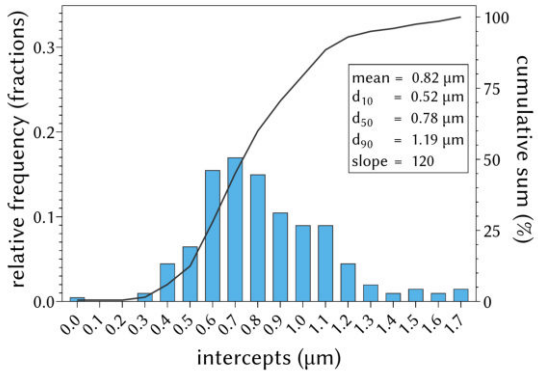

(f) GSD of grains.

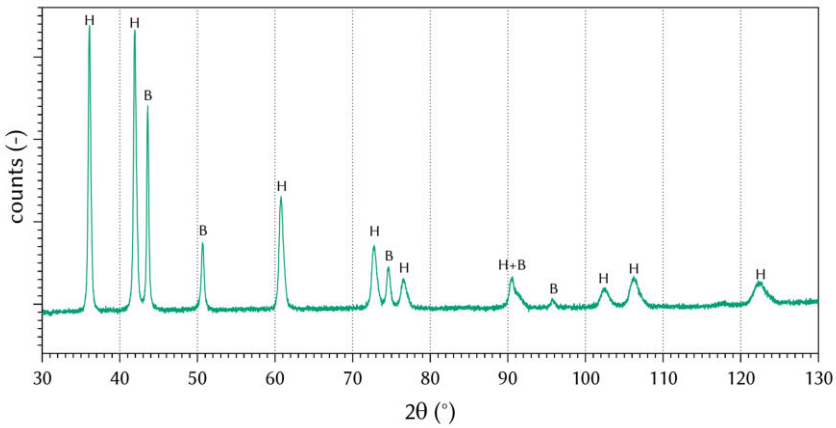

(g) XRD with hard phase (H) and binder (B) peaks identified.

Figure 108: LOM, BSE-SEM, GSD and XRD of N2-2_Ar.

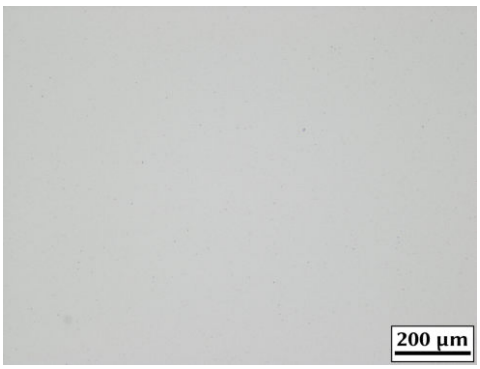

(a) LOM, 100x magnification.

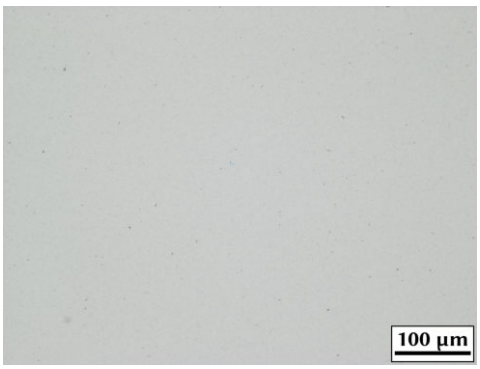

(b) LOM, 200x magnification.

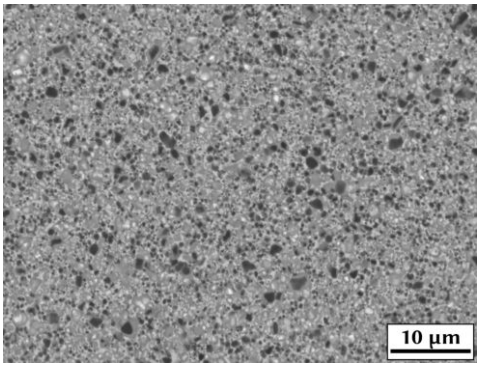

(c) BSE-SEM, 5000x magnification.

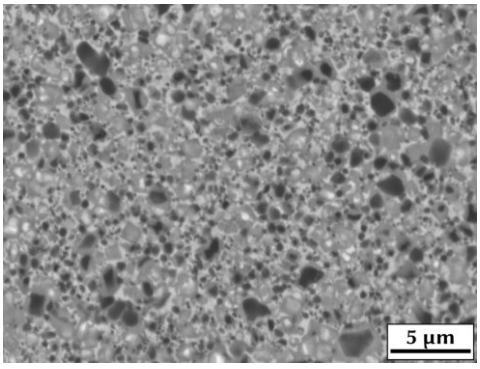

(d) BSE-SEM, 10,000x magnification.

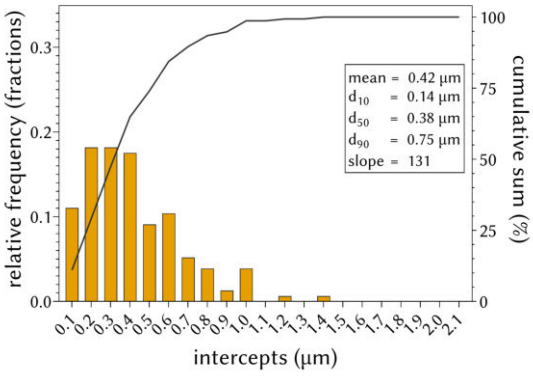

(e) GSD of cores.

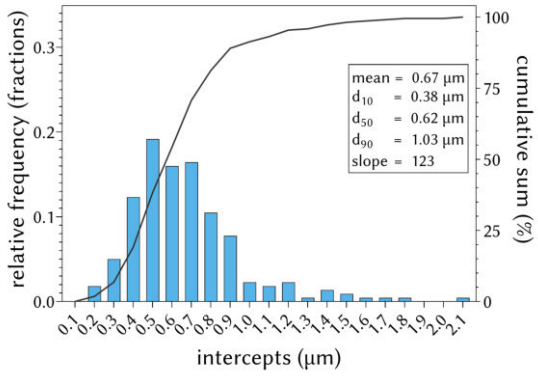

(f) GSD of grains.

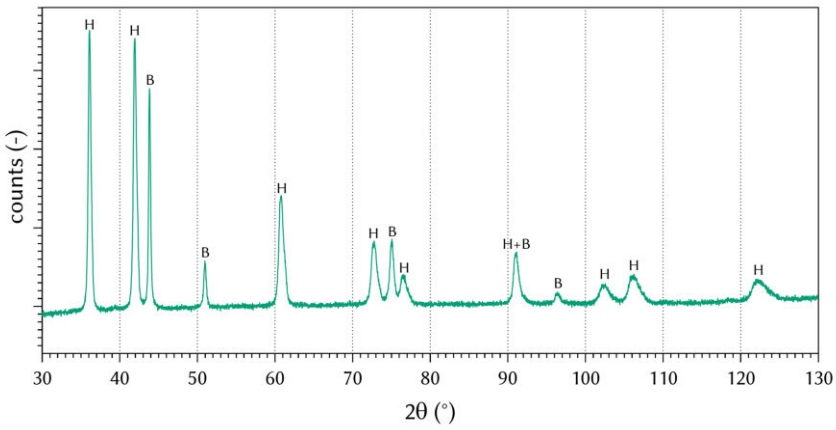

(g) XRD with hard phase (H) and binder (B) peaks identified.

Figure 109: LOM, BSE-SEM, GSD and XRD of N2-2_10N.

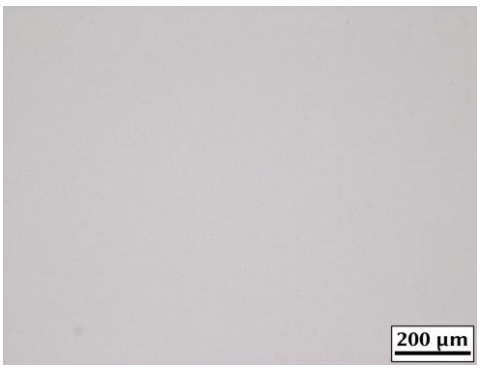

(a) LOM, 100x magnification.

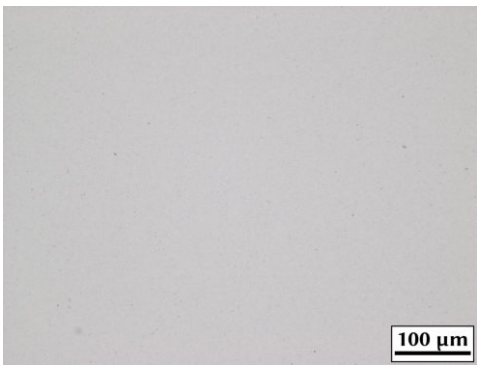

(b) LOM, 200x magnification.

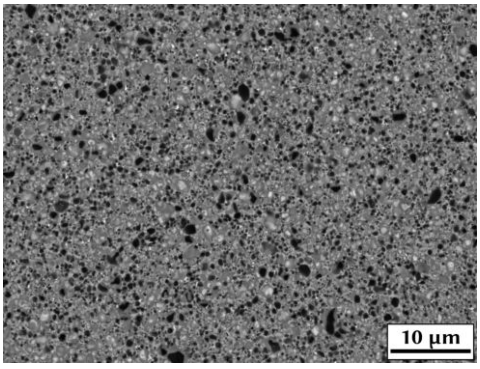

(c) BSE-SEM, 5000x magnification.

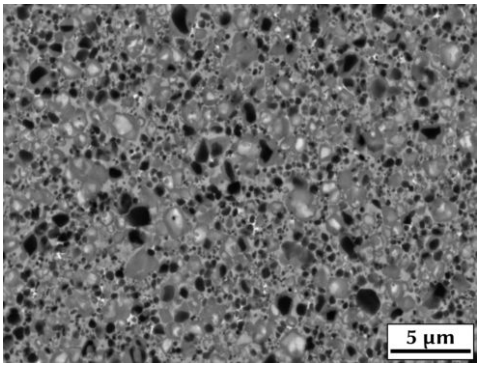

(d) BSE-SEM, 10,000x magnification.

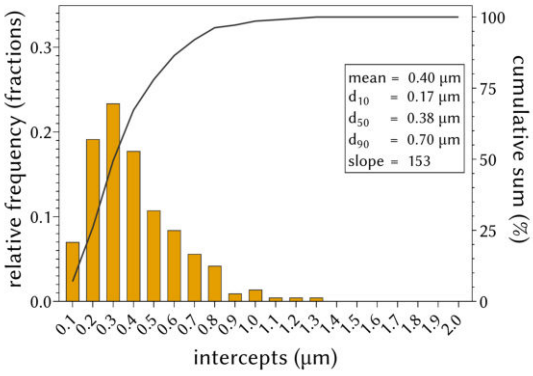

(e) GSD of cores.

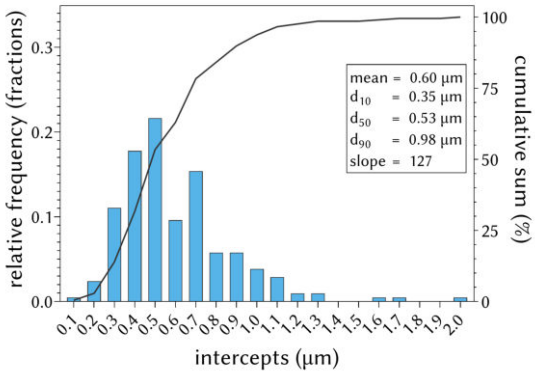

(f) GSD of grains.

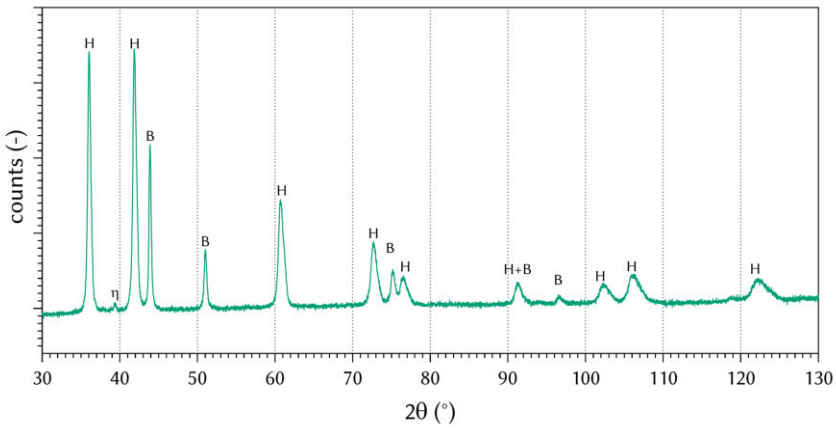

(g) XRD with hard phase (H) and binder (B) peaks identified.

Figure 110: LOM, BSE-SEM, GSD and XRD of N2-2_50N.

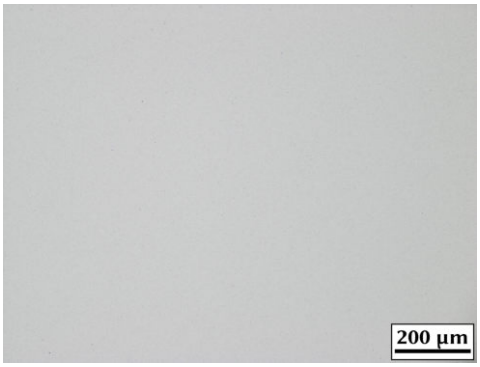

(a) LOM, 100x magnification.

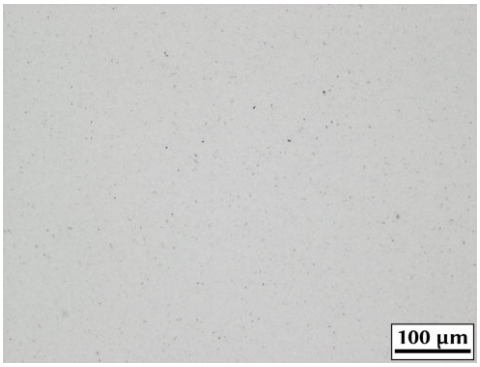

(b) LOM, 200x magnification.

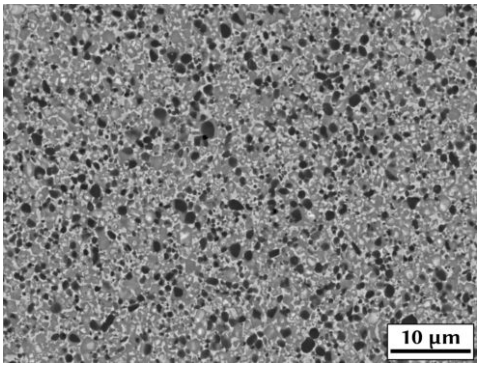

(c) BSE-SEM, 5000x magnification.

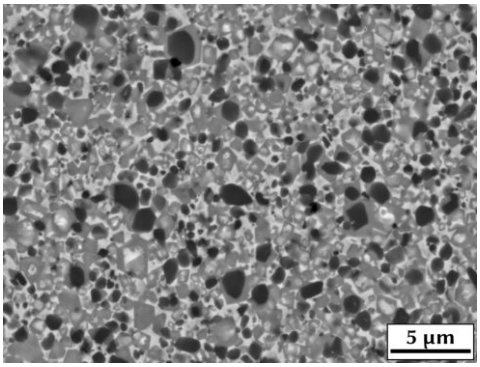

(d) BSE-SEM, 10,000x magnification.

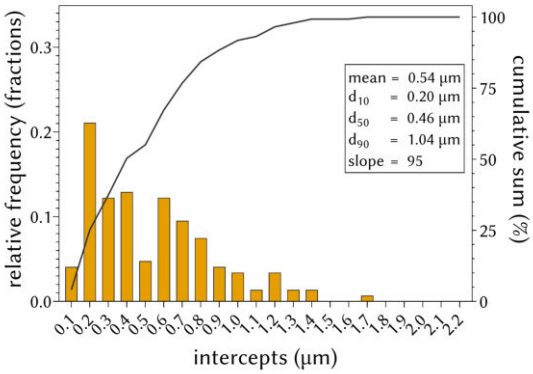

(e) GSD of cores.

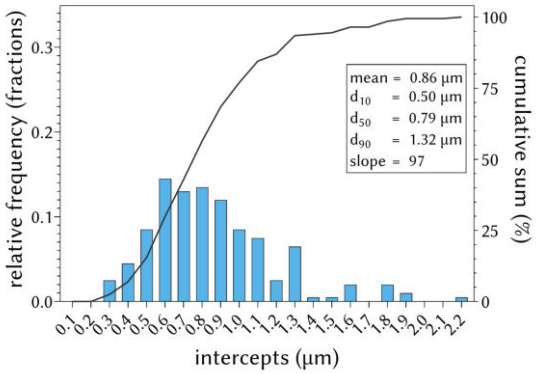

(f) GSD of grains.

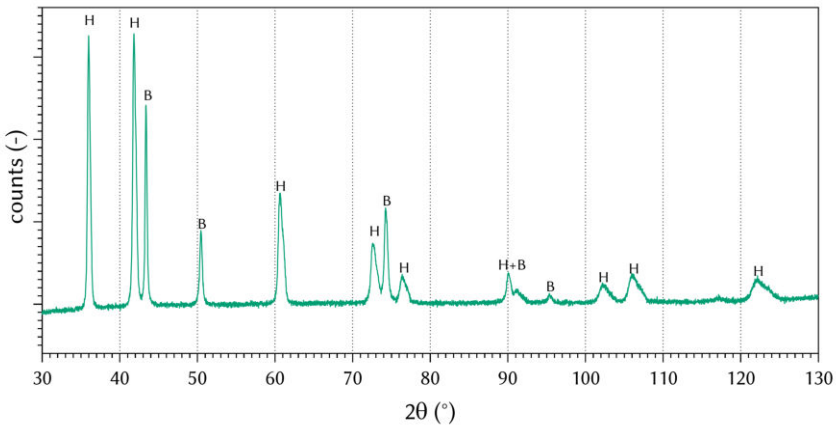

(g) XRD with hard phase (H) and binder (B) peaks identified.

Figure 111: LOM, BSE-SEM, GSD and XRD of N2-3_Ar.

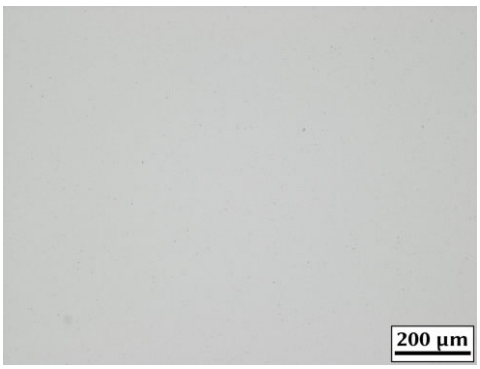

(a) LOM, 100x magnification.

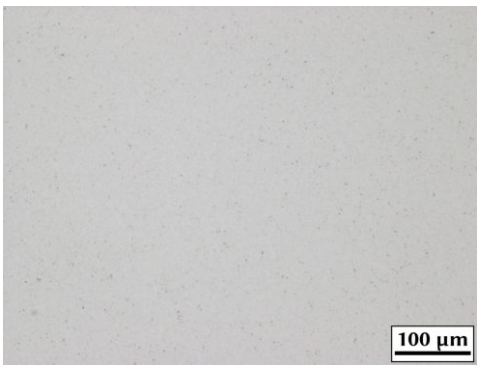

(b) LOM, 200x magnification.

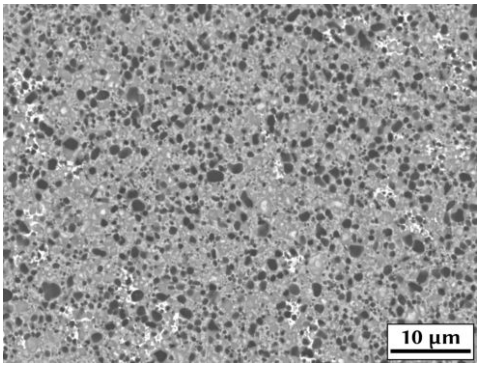

(c) BSE-SEM, 5000x magnification.

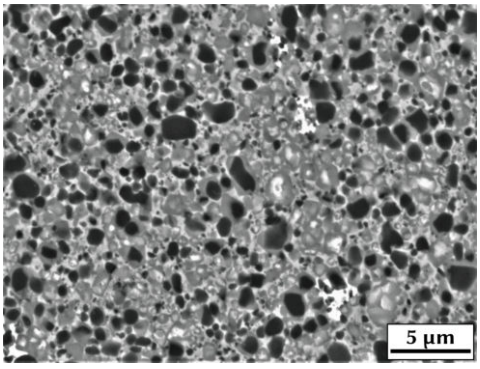

(d) BSE-SEM, 10,000x magnification.

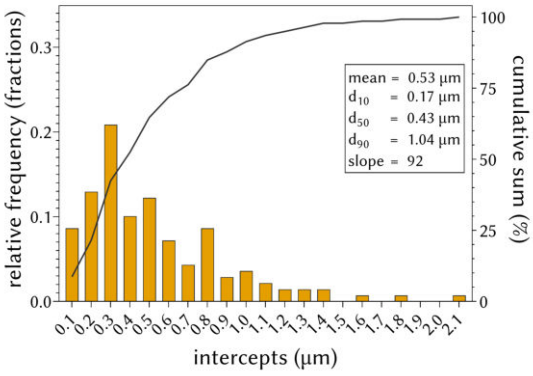

(e) GSD of cores.

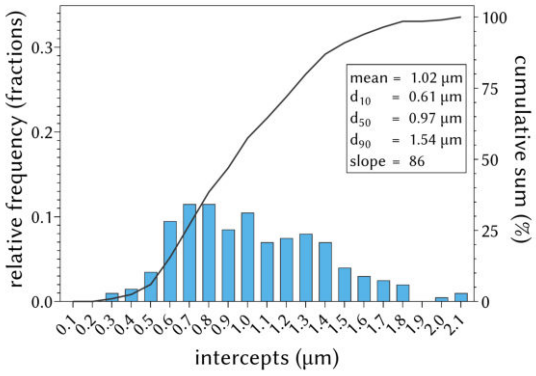

(f) GSD of grains.

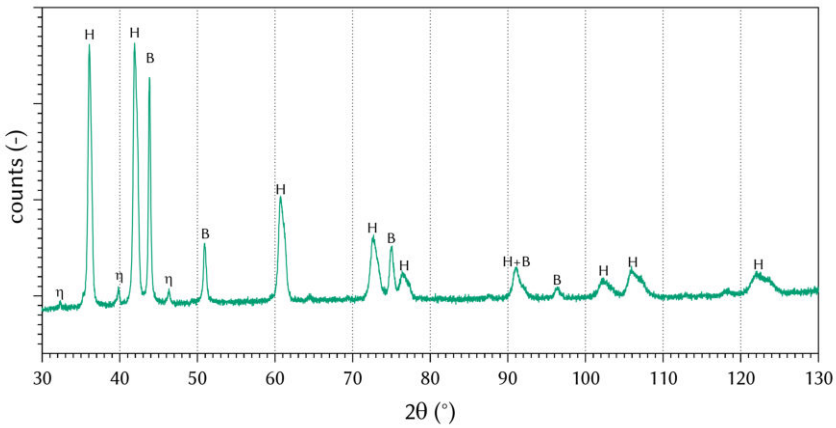

(g) XRD with hard phase (H) and binder (B) peaks identified.

Figure 112: LOM, BSE-SEM, GSD and XRD of N2-3_10N.

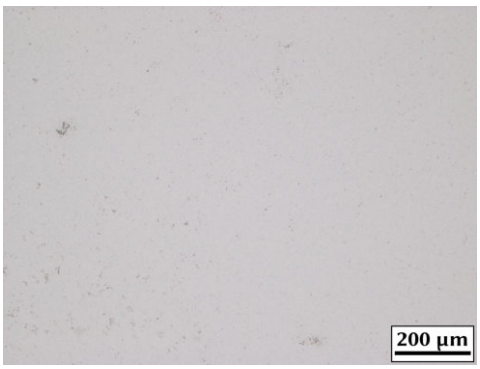

(a) LOM, 100x magnification.

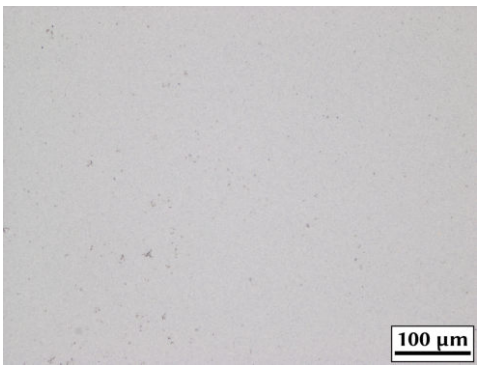

(b) LOM, 200x magnification.

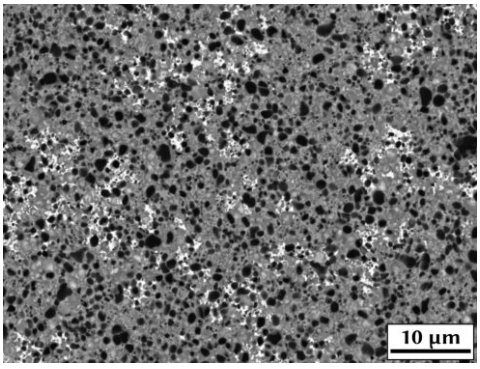

(c) BSE-SEM, 5000x magnification.

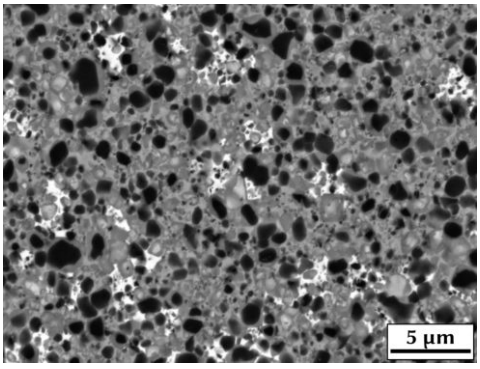

(d) BSE-SEM, 10,000x magnification.

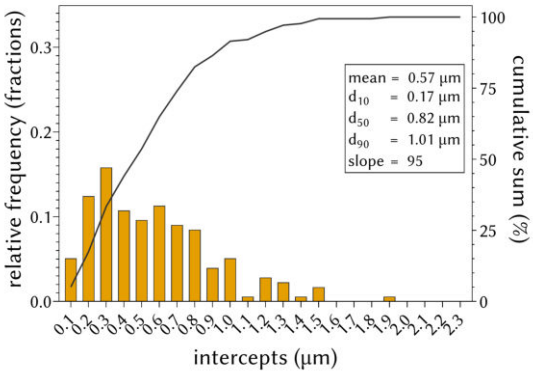

(e) GSD of cores.

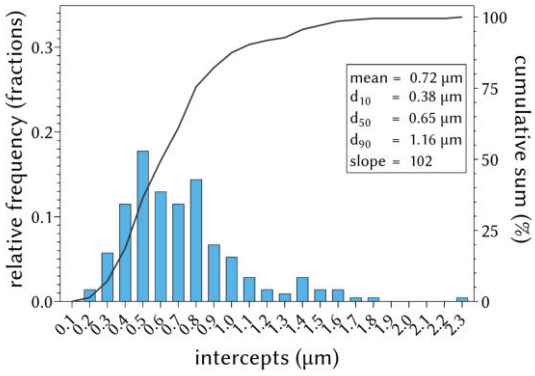

(f) GSD of grains.

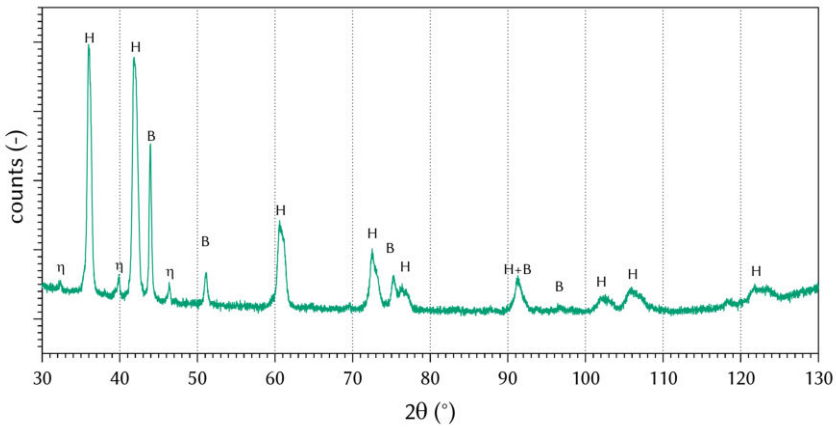

(g) XRD with hard phase (H) and binder (B) peaks identified.

Figure 113: LOM, BSE-SEM, GSD and XRD of N2-3_50N.

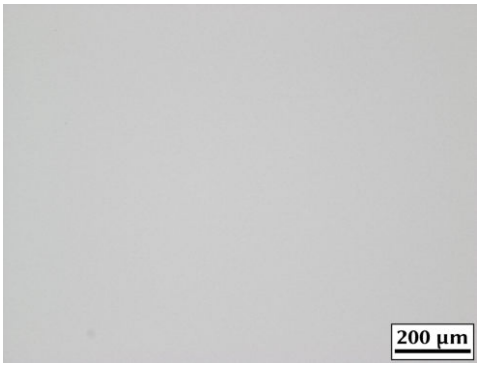

(a) LOM, 100x magnification.

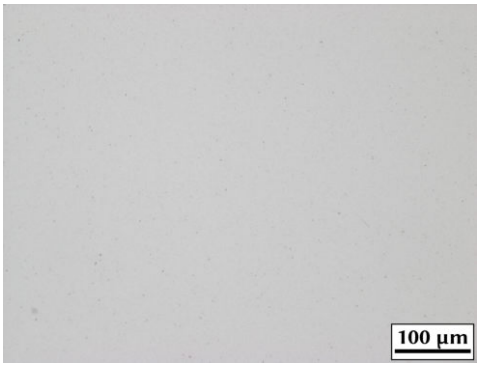

(b) LOM, 200x magnification.

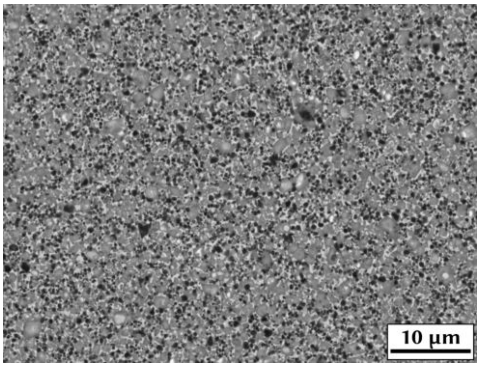

(c) BSE-SEM, 5000x magnification.

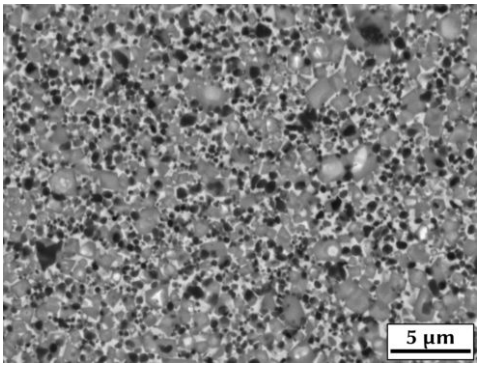

(d) BSE-SEM, 10,000x magnification.

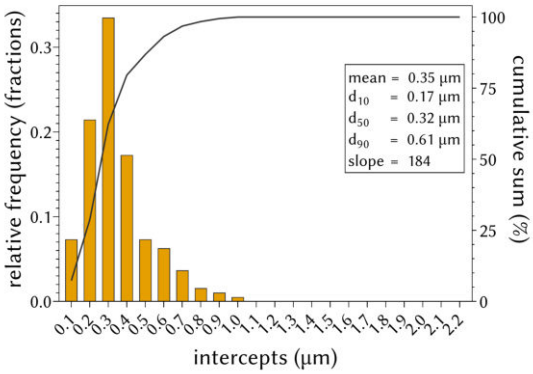

(e) GSD of cores.

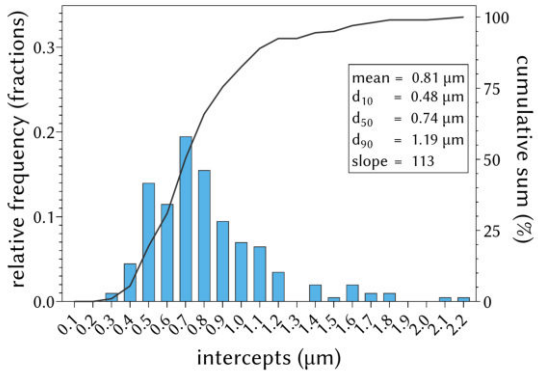

(f) GSD of grains.

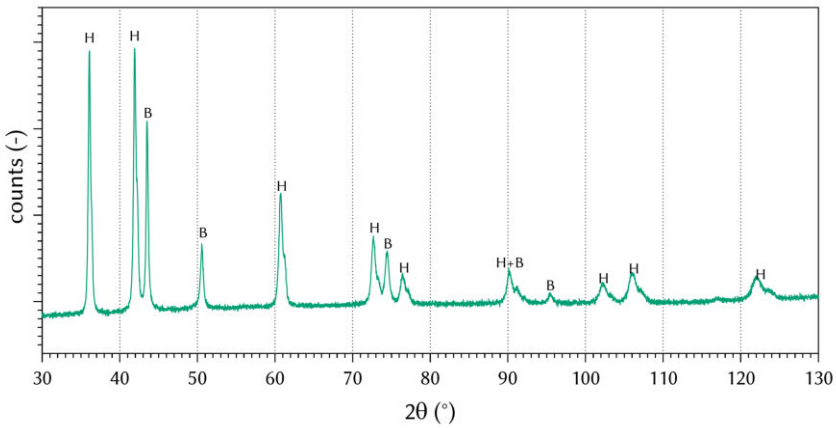

(g) XRD with hard phase (H) and binder (B) peaks identified.

Figure 114: LOM, BSE-SEM, GSD and XRD of N3-1_Ar.

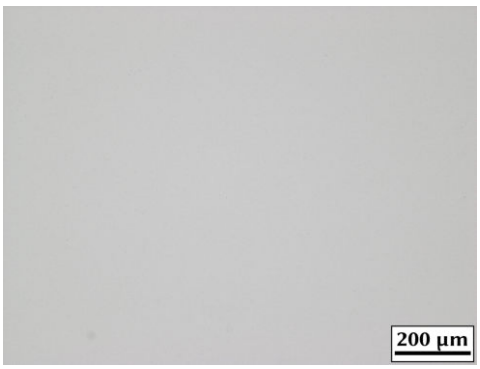

(a) LOM, 100x magnification.

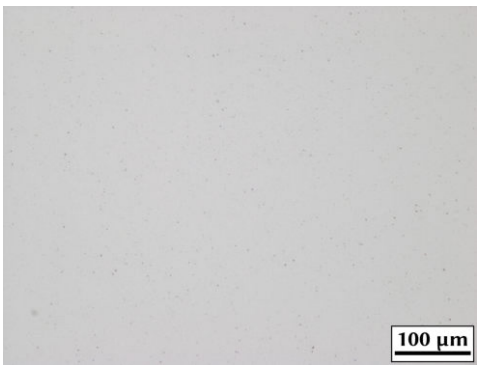

(b) LOM, 200x magnification.

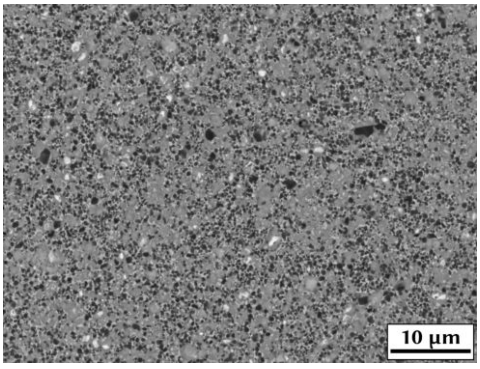

(c) BSE-SEM, 5000x magnification.

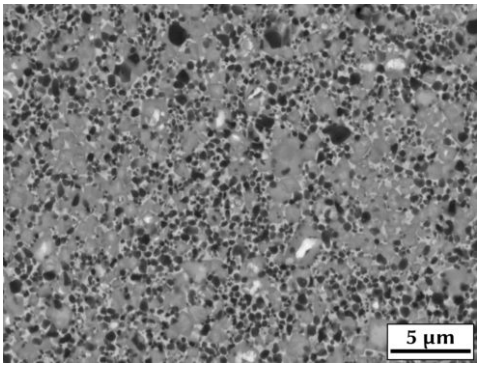

(d) BSE-SEM, 10,000x magnification.

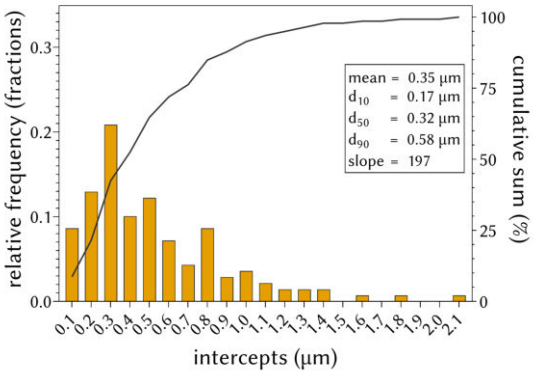

(e) GSD of cores.

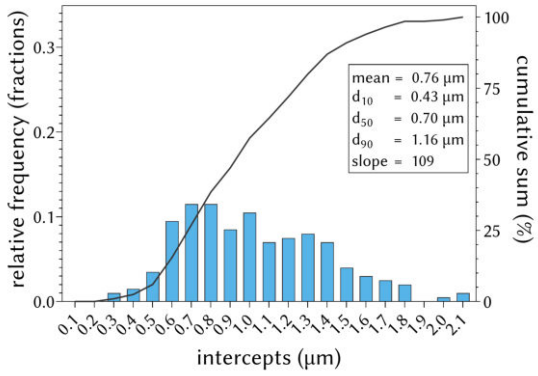

(f) GSD of grains.

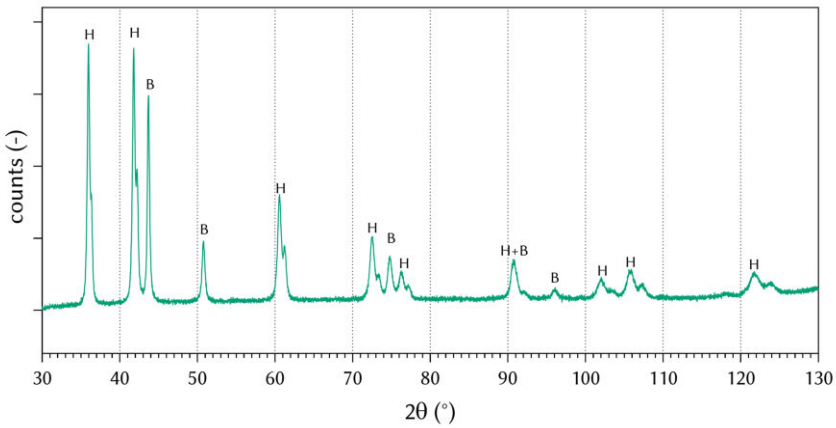

(g) XRD with hard phase (H) and binder (B) peaks identified.

Figure 115: LOM, BSE-SEM, GSD and XRD of N3-1_10N.

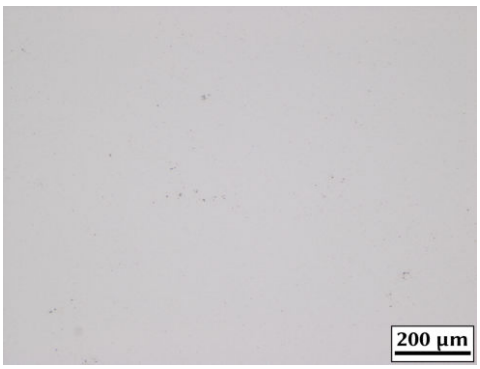

(a) LOM, 100x magnification.

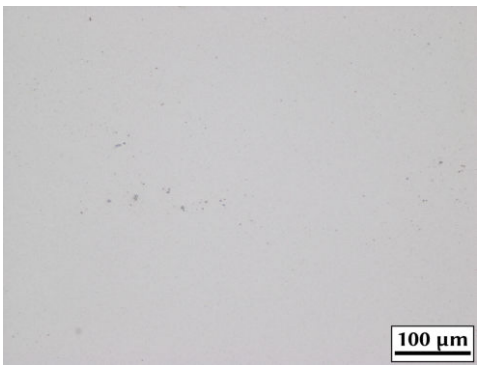

(b) LOM, 200x magnification.

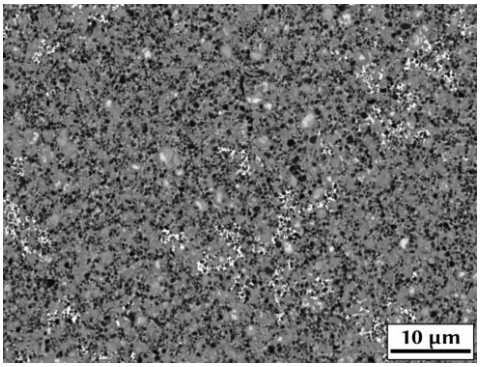

(c) BSE-SEM, 5000x magnification.

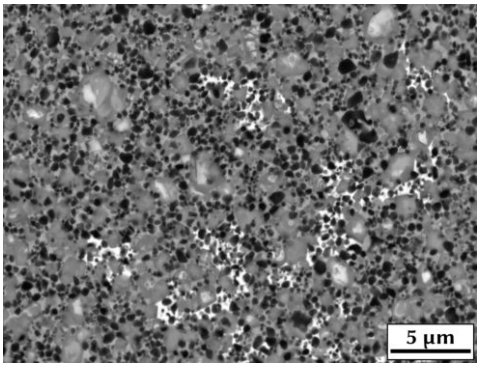

(d) BSE-SEM, 10,000x magnification.

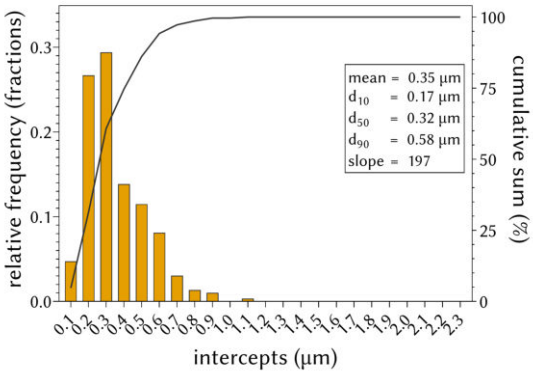

(e) GSD of cores.

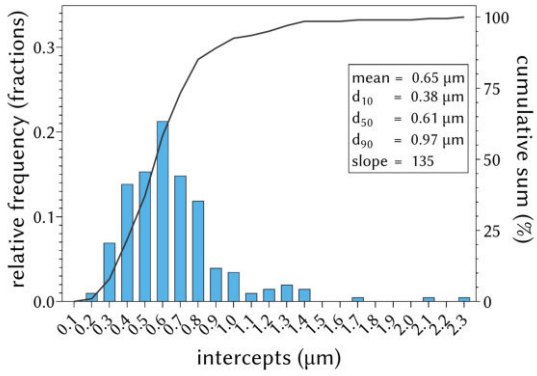

(f) GSD of grains.

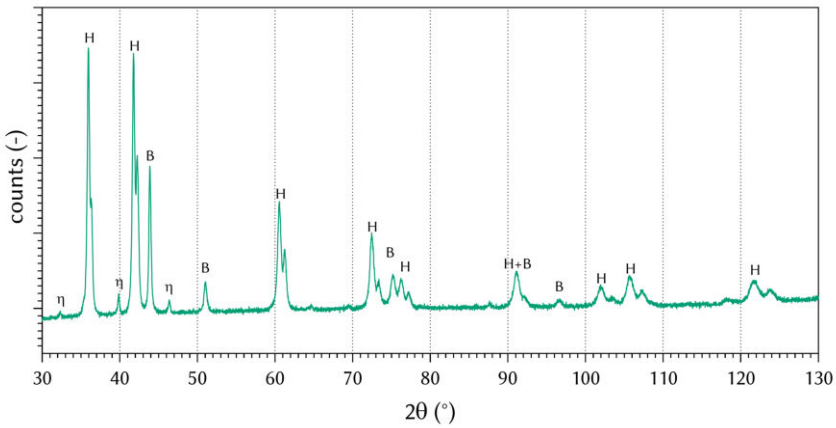

(g) XRD with hard phase (H) and binder (B) peaks identified.

Figure 116: LOM, BSE-SEM, GSD and XRD of N3-1_50N.

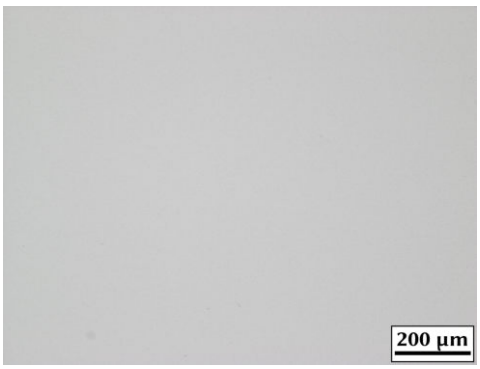

(a) LOM, 100x magnification.

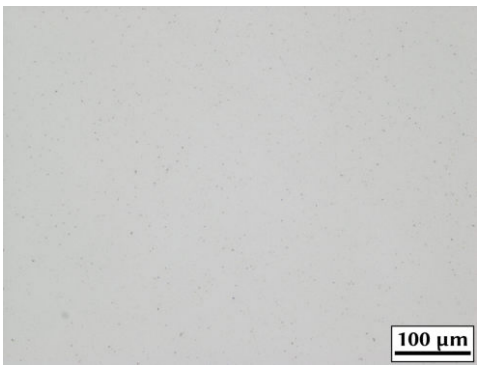

(b) LOM, 200x magnification.

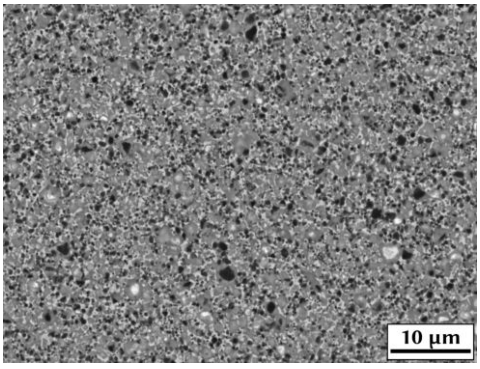

(c) BSE-SEM, 5000x magnification.

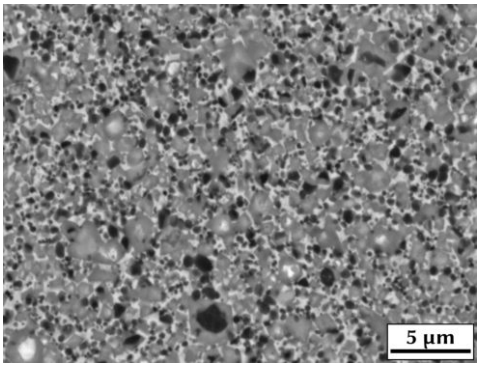

(d) BSE-SEM, 10,000x magnification.

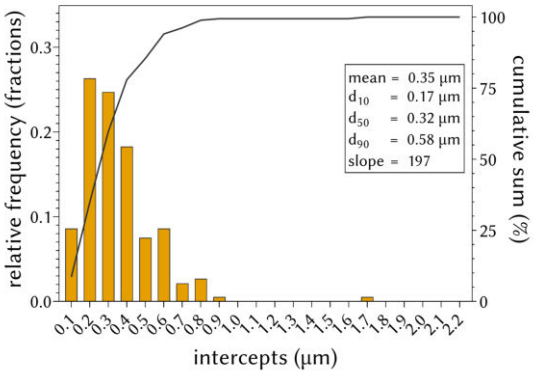

(e) GSD of cores.

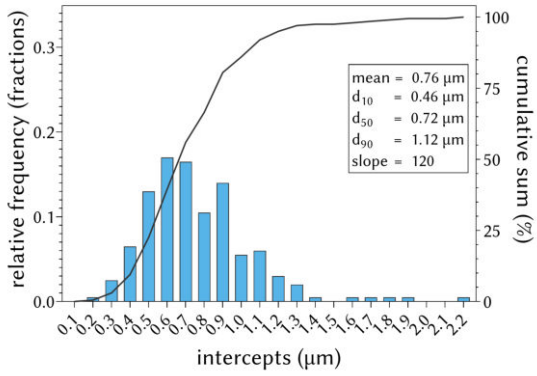

(f) GSD of grains.

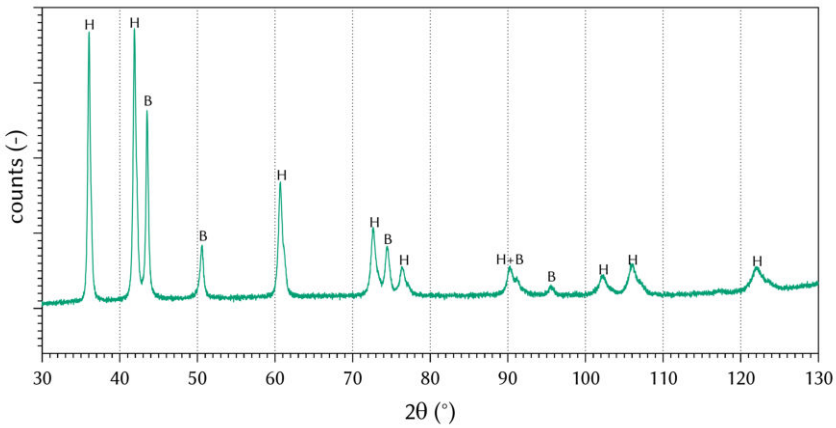

(g) XRD with hard phase (H) and binder (B) peaks identified.

Figure 117: LOM, BSE-SEM, GSD and XRD of N3-2_Ar.

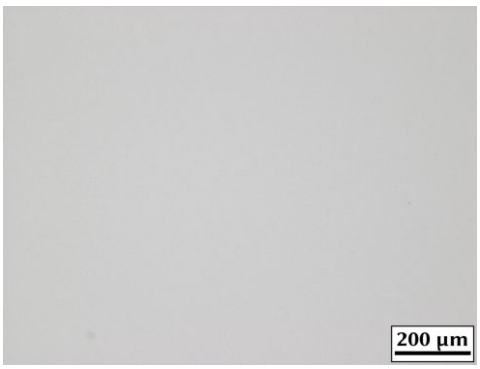

(a) LOM, 100x magnification.

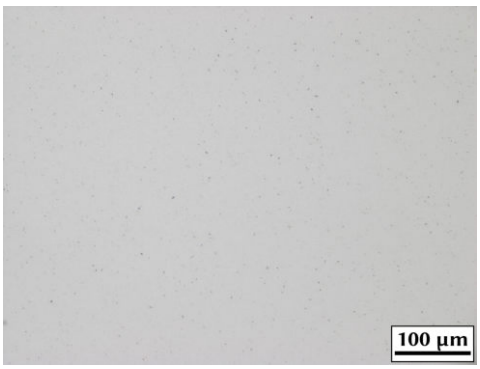

(b) LOM, 200x magnification.

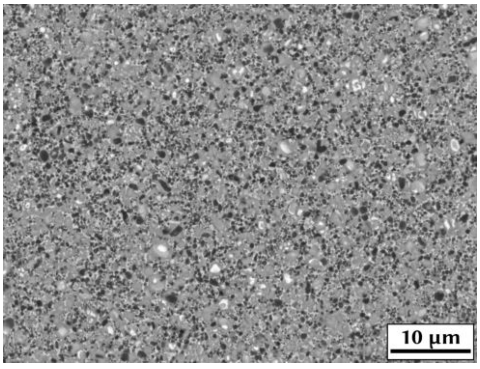

(c) BSE-SEM, 5000x magnification.

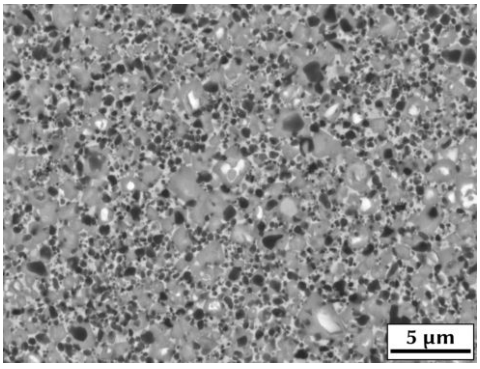

(d) BSE-SEM, 10,000x magnification.

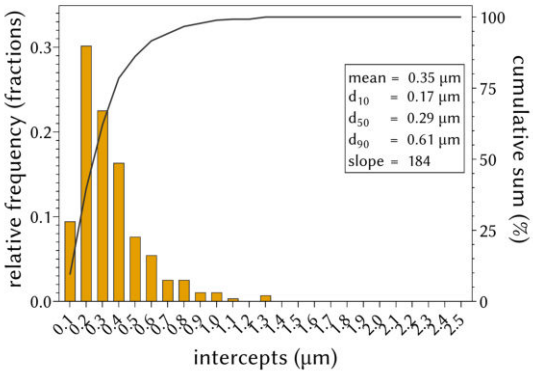

(e) GSD of cores.

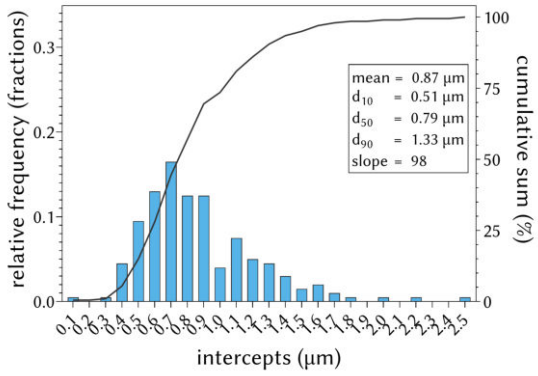

(f) GSD of grains.

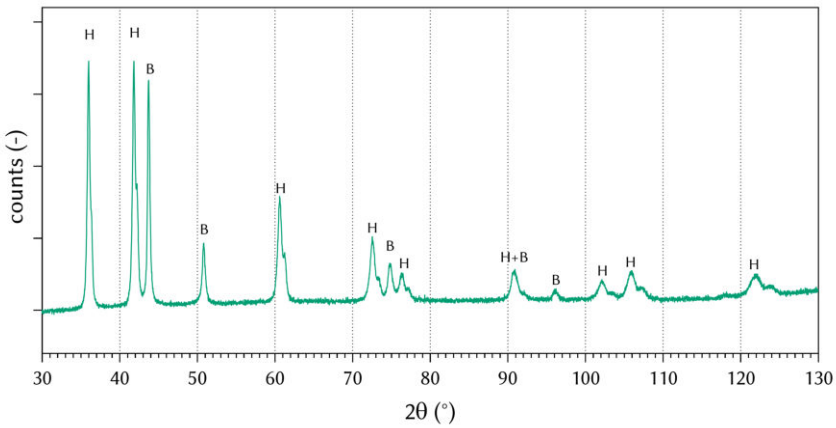

(g) XRD with hard phase (H) and binder (B) peaks identified.

Figure 118: LOM, BSE-SEM, GSD and XRD of N3-2_10N.

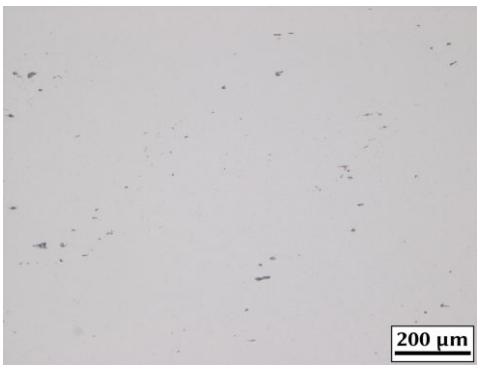

(a) LOM, 100x magnification.

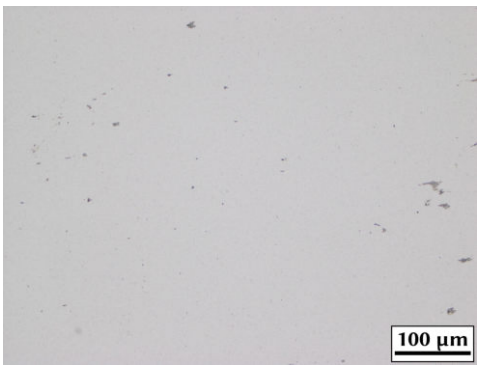

(b) LOM, 200x magnification.

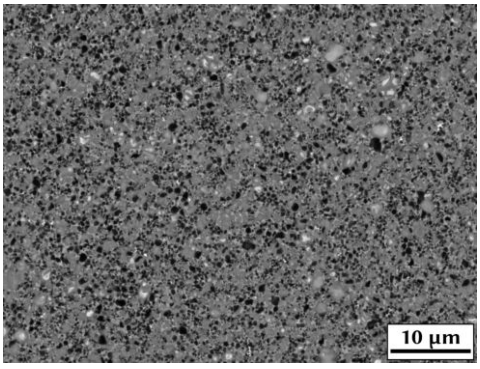

(c) BSE-SEM, 5000x magnification.

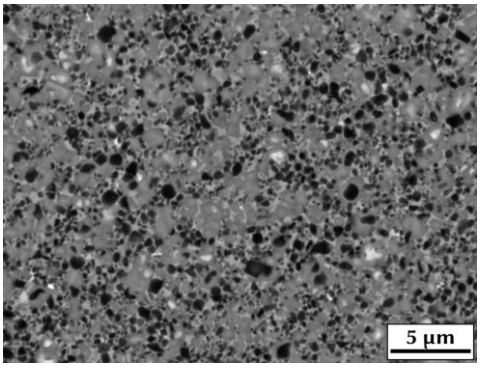

(d) BSE-SEM, 10,000x magnification.

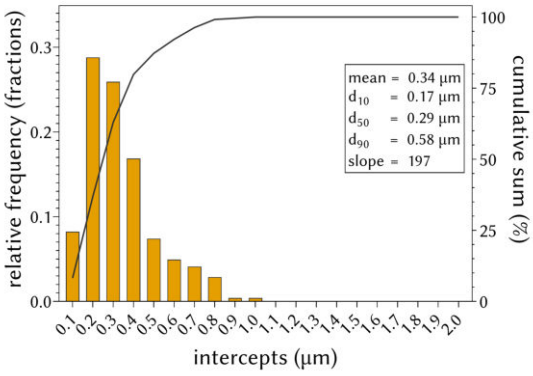

(e) GSD of cores.

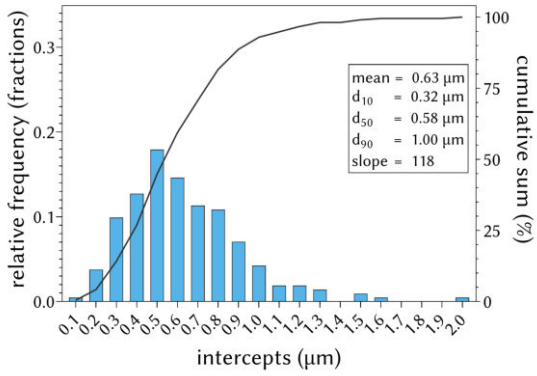

(f) GSD of grains.

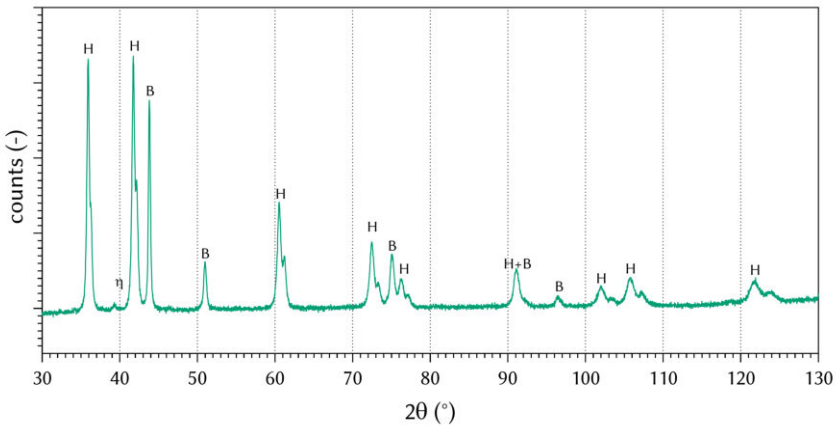

(g) XRD with hard phase (H) and binder (B) peaks identified.

Figure 119: LOM, BSE-SEM, GSD and XRD of N3-2_50N.

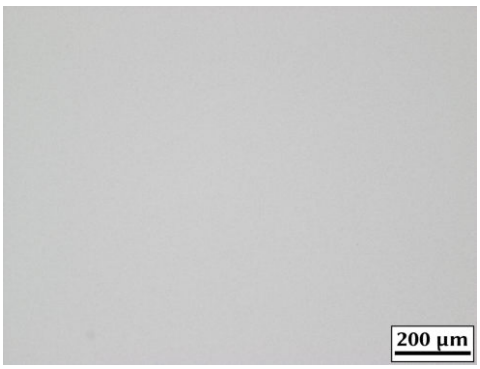

(a) LOM, 100x magnification.

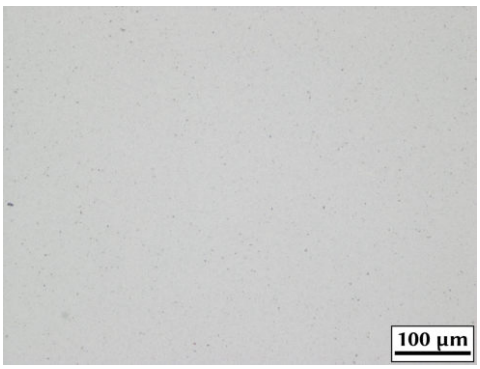

(b) LOM, 200x magnification.

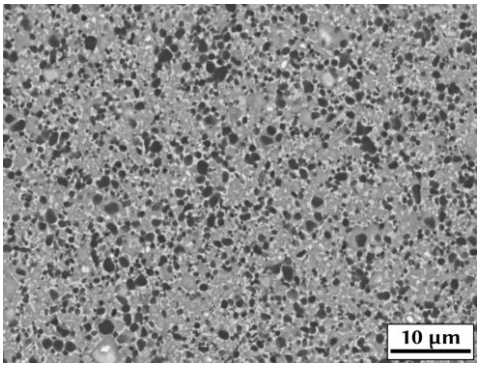

(c) BSE-SEM, 5000x magnification.

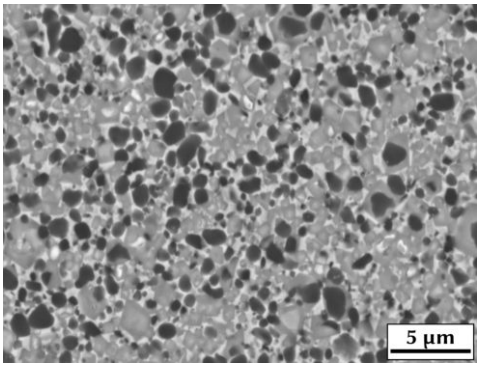

(d) BSE-SEM, 10,000x magnification.

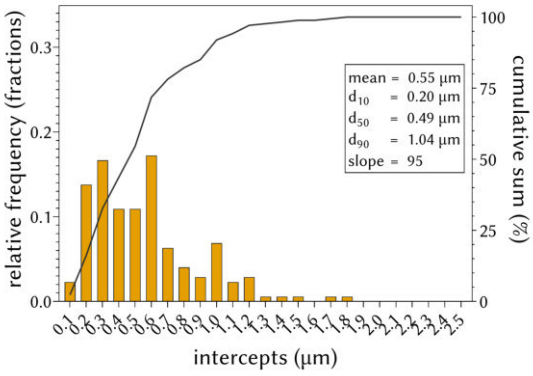

(e) GSD of cores.

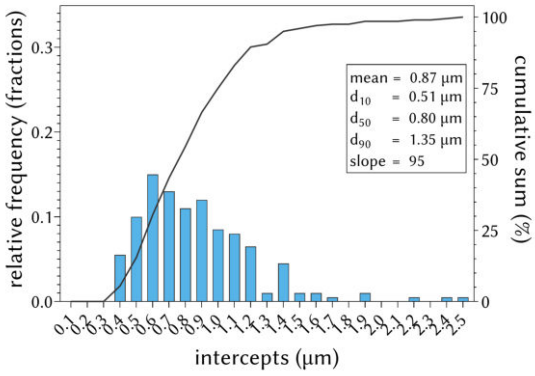

(f) GSD of grains.

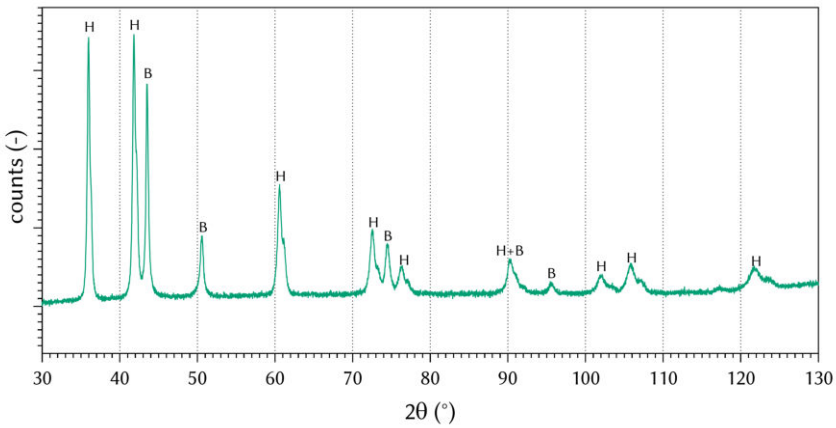

(g) XRD with hard phase (H) and binder (B) peaks identified.

Figure 120: LOM, BSE-SEM, GSD and XRD of N3-3_Ar.

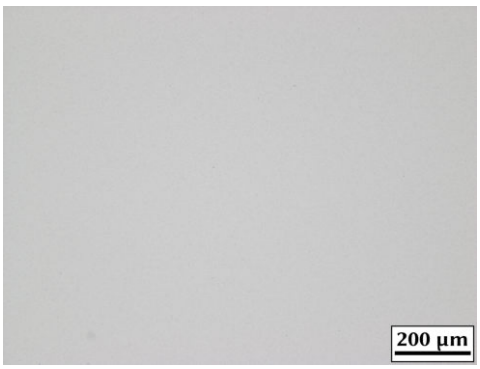

(a) LOM, 100x magnification.

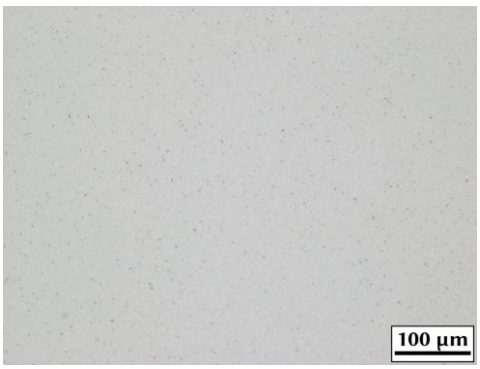

(b) LOM, 200x magnification.

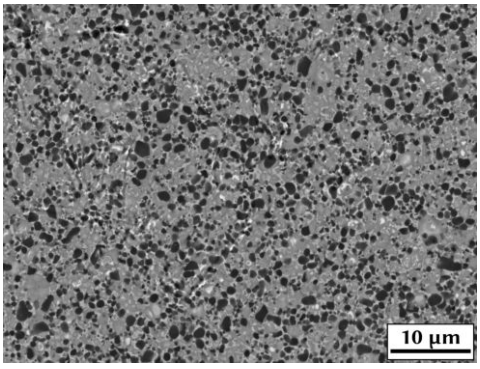

(c) BSE-SEM, 5000x magnification.

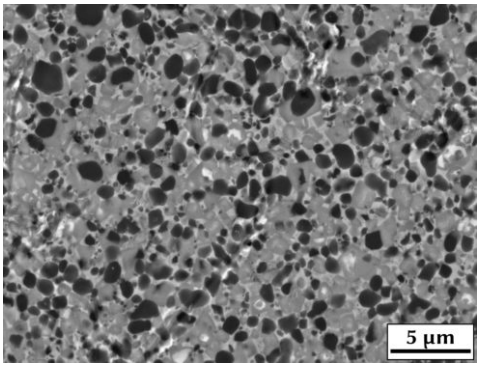

(d) BSE-SEM, 10,000x magnification.

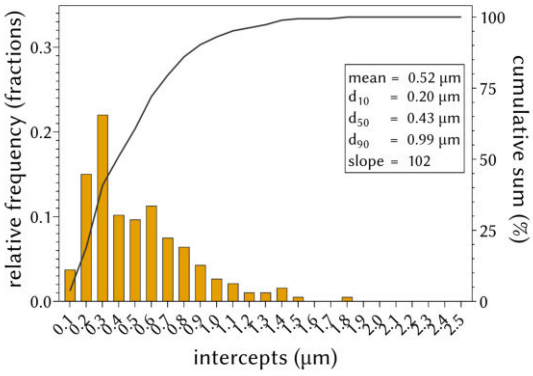

(e) GSD of cores.

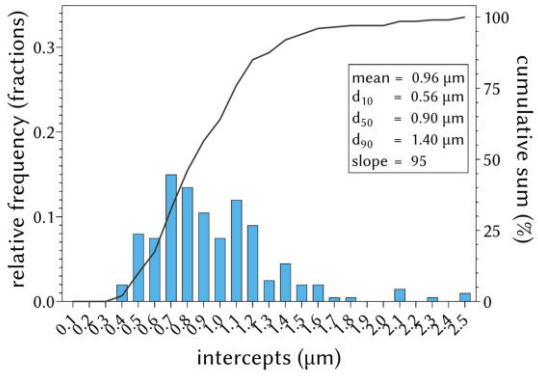

(f) GSD of grains.

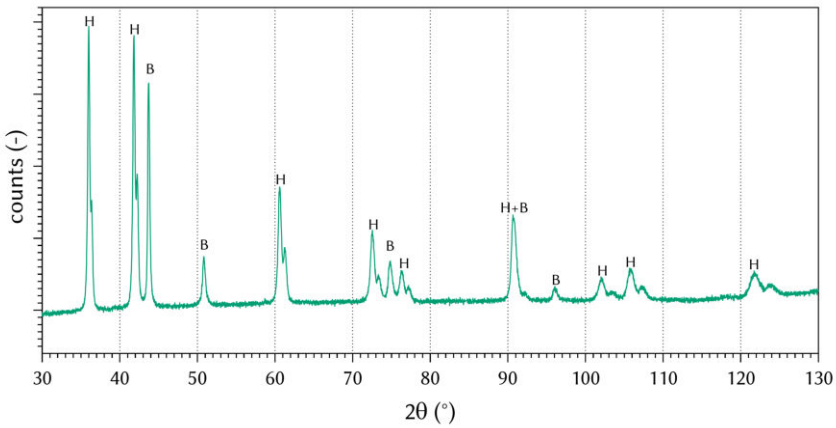

(g) XRD with hard phase (H) and binder (B) peaks identified.

Figure 121: LOM, BSE-SEM, GSD and XRD of N3-2_10N.

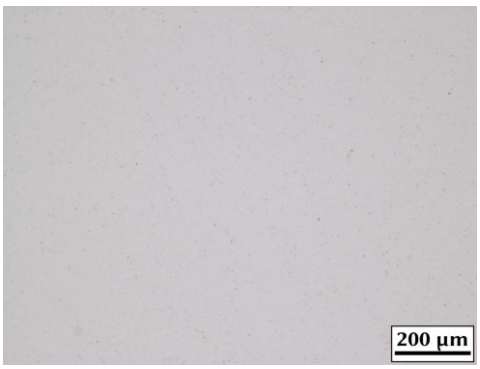

(a) LOM, 100x magnification.

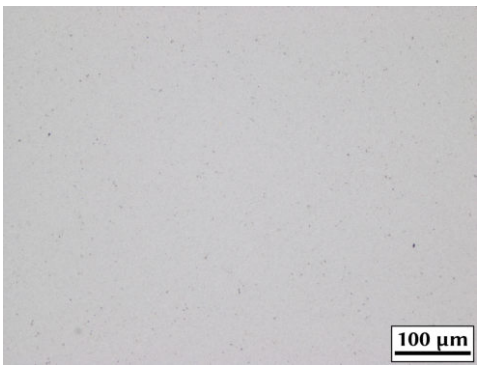

(b) LOM, 200x magnification.

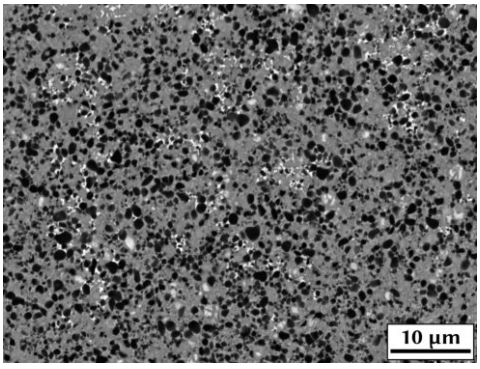

(c) BSE-SEM, 5000x magnification.

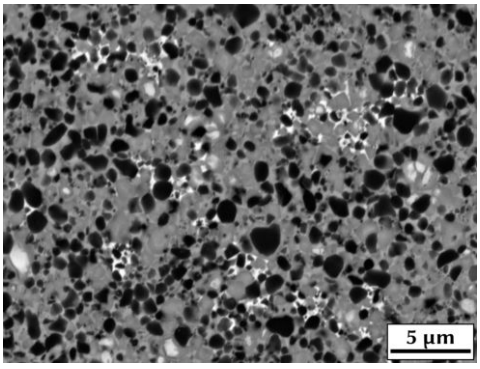

(d) BSE-SEM, 10,000x magnification.

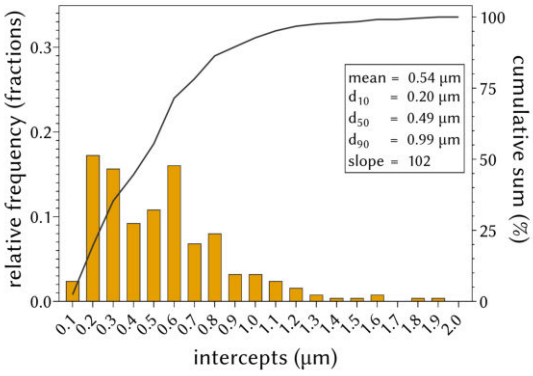

(e) GSD of cores.

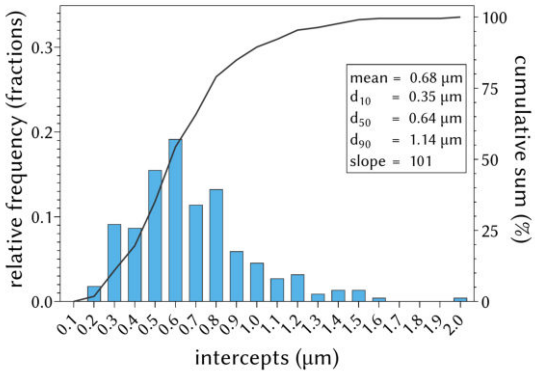

(f) GSD of grains.

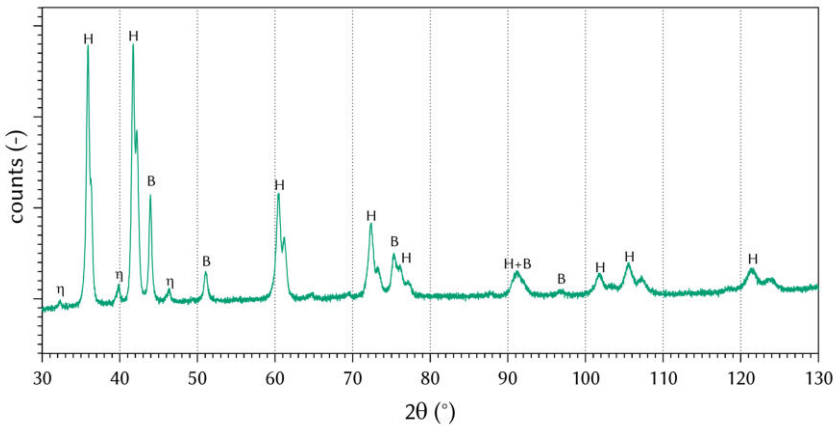

(g) XRD with hard phase (H) and binder (B) peaks identified.

Figure 122: LOM, BSE-SEM, GSD and XRD of N3-3_50N.

(a) LOM, 100x magnification.

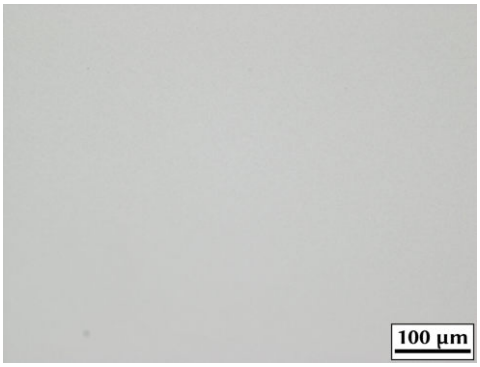

(b) LOM, 200x magnification.

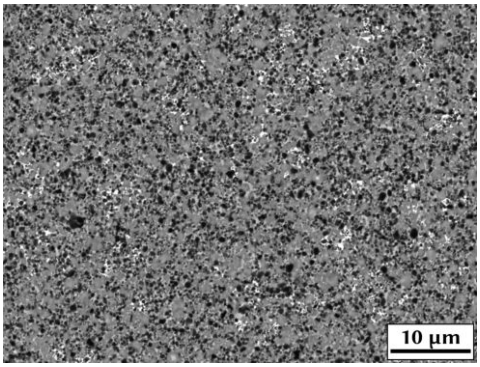

(c) BSE-SEM, 5000x magnification.

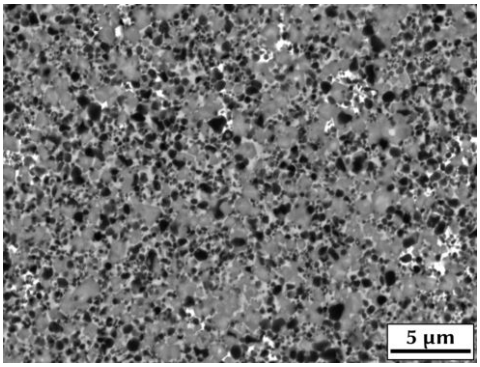

(d) BSE-SEM, 10,000x magnification.

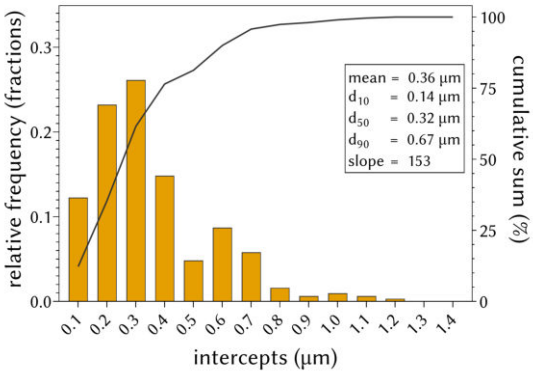

(e) GSD of cores.

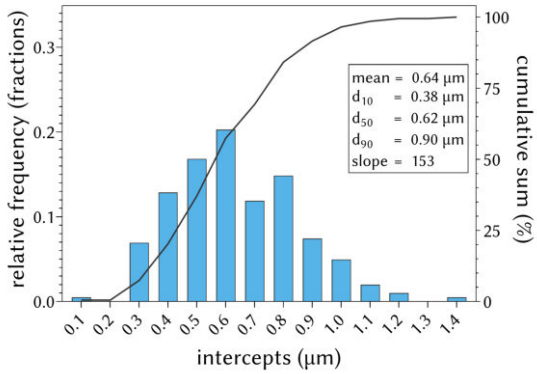

(f) GSD of grains.

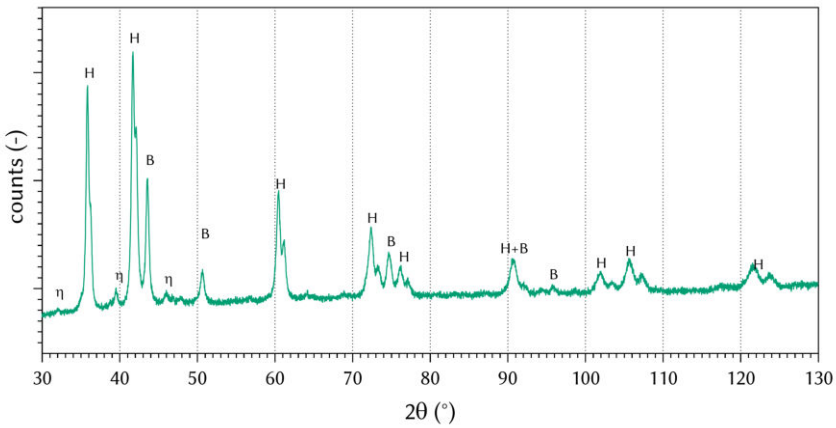

(g) XRD with hard phase (H) and binder (B) peaks identified.

Figure 123: LOM, BSE-SEM, GSD and XRD of N0-2_10Np.

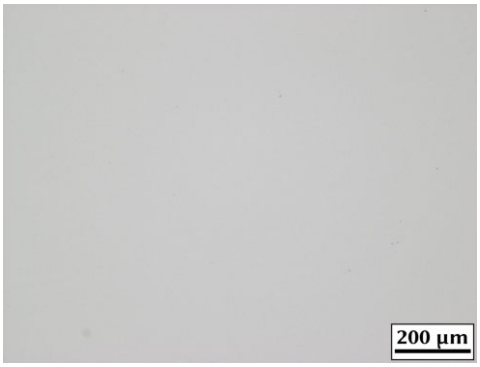

(a) LOM, 100x magnification.

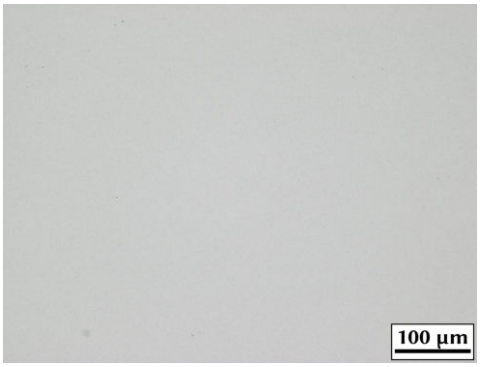

(b) LOM, 200x magnification.

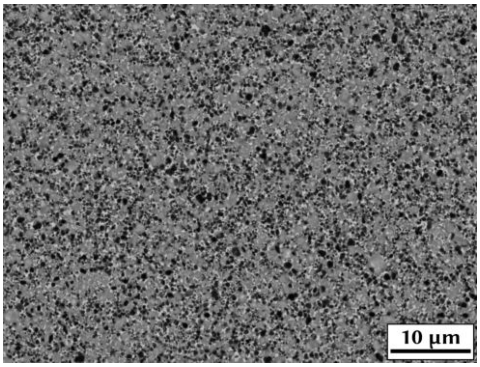

(c) BSE-SEM, 5000x magnification.

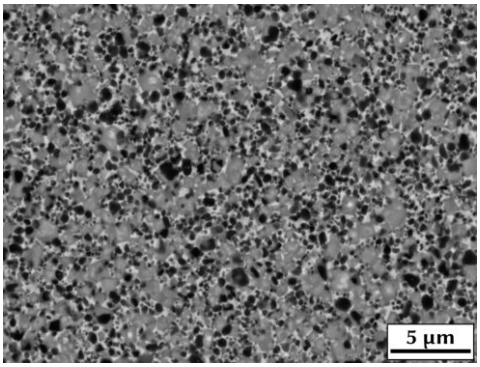

(d) BSE-SEM, 10,000x magnification.

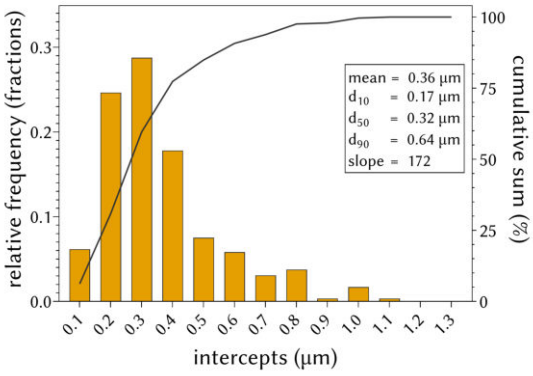

(e) GSD of cores.

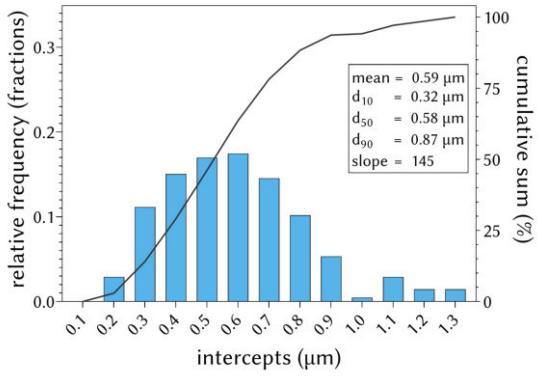

(f) GSD of grains.

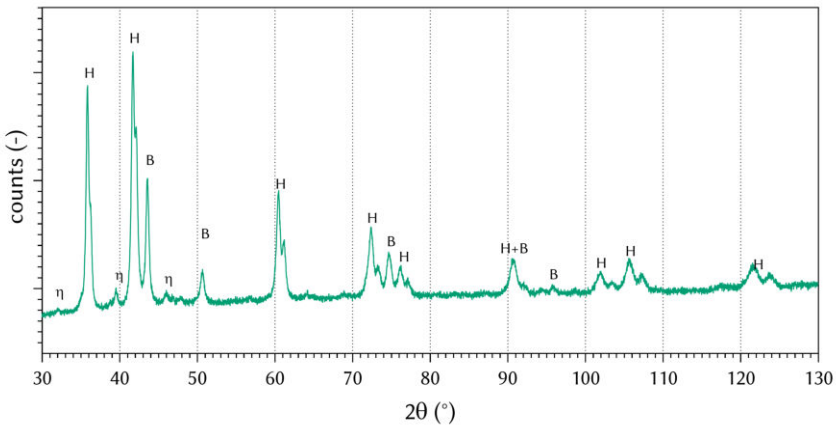

(g) XRD with hard phase (H) and binder (B) peaks identified.

Figure 124: LOM, BSE-SEM, GSD and XRD of N0-2+0.1%C_10Np.

(a) LOM, 100x magnification.

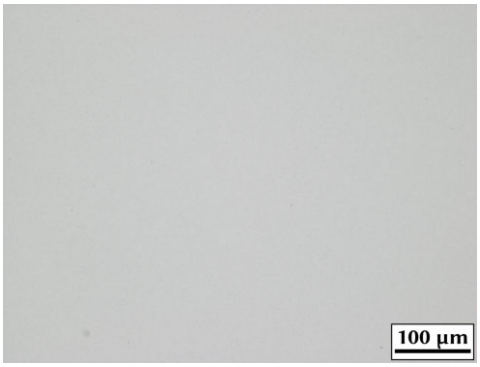

(b) LOM, 200x magnification.

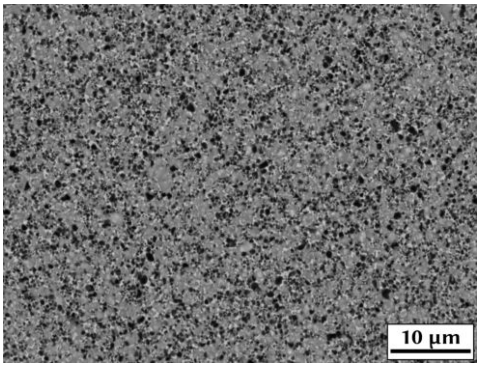

(c) BSE-SEM, 5000x magnification.

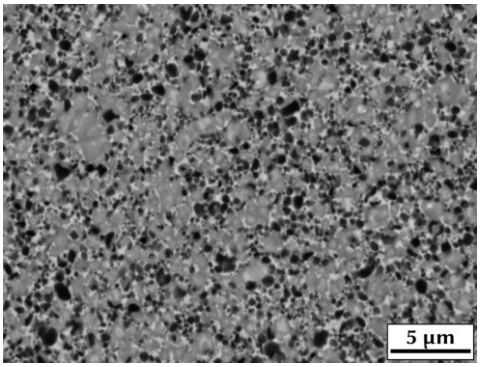

(d) BSE-SEM, 10,000x magnification.

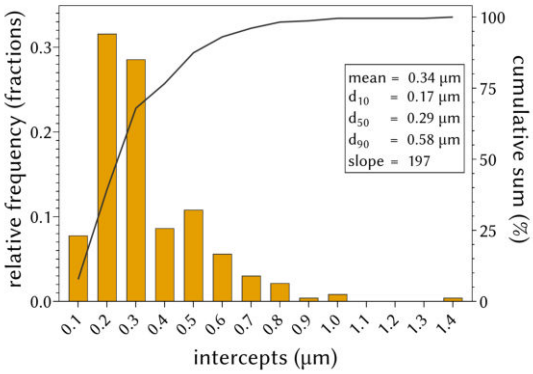

(e) GSD of cores.

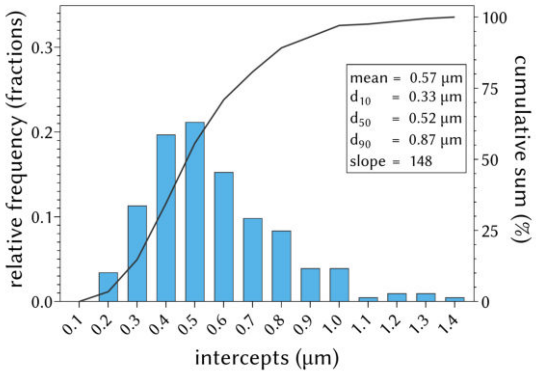

(f) GSD of grains.

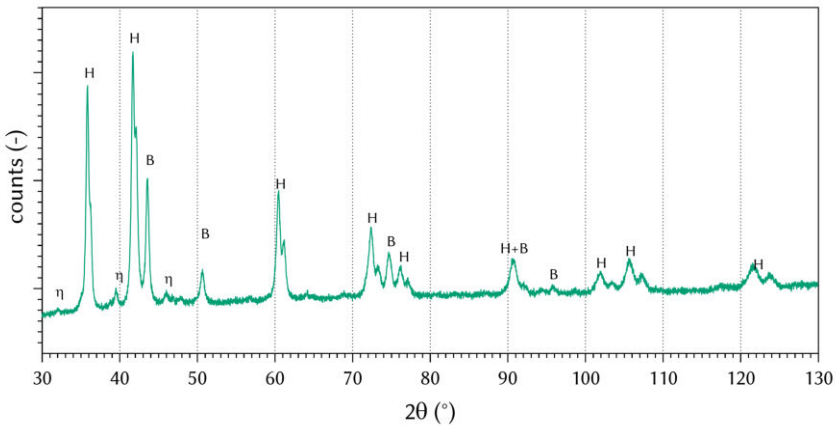

(g) XRD with hard phase (H) and binder (B) peaks identified.

Figure 125: LOM, BSE-SEM, GSD and XRD of N0-2+0.3%C_10Np.

(a) LOM, 100x magnification.

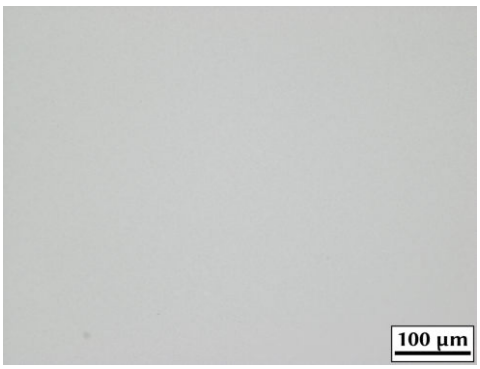

(b) LOM, 200x magnification.

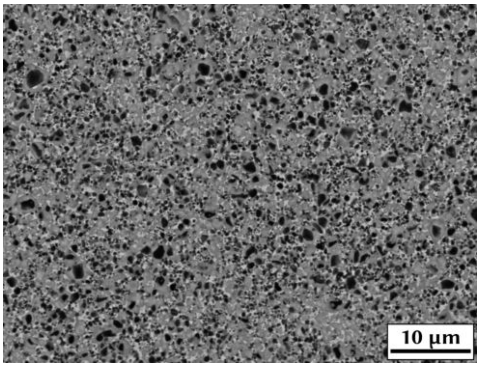

(c) BSE-SEM, 5000x magnification.

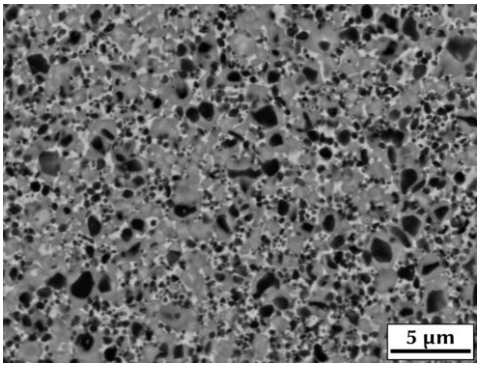

(d) BSE-SEM, 10,000x magnification.

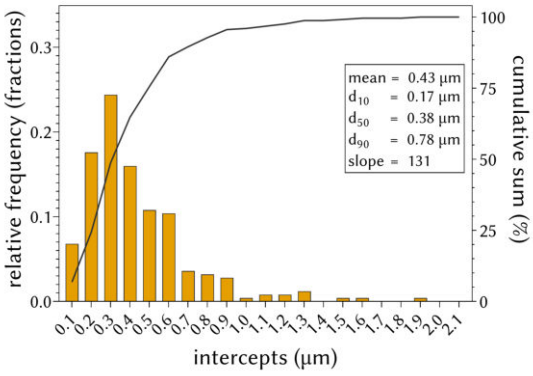

(e) GSD of cores.

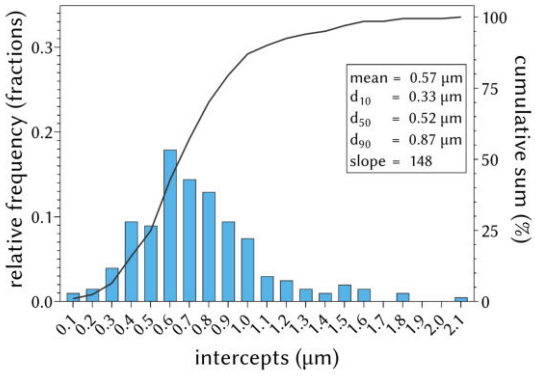

(f) GSD of grains.

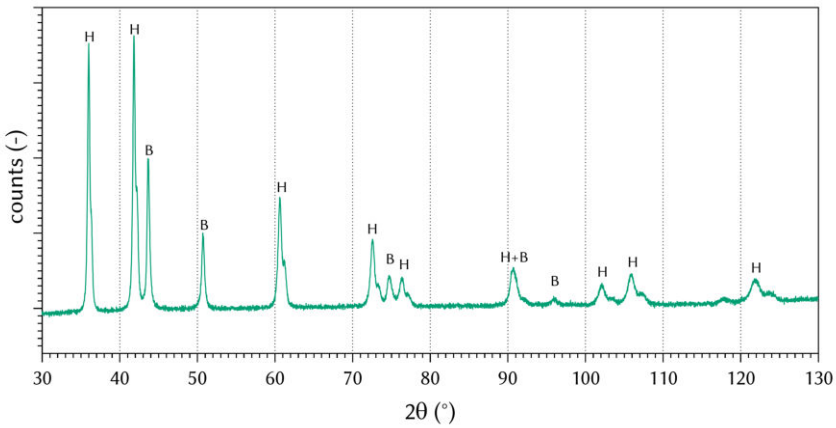

(g) XRD with hard phase (H) and binder (B) peaks identified.

Figure 126: LOM, BSE-SEM, GSD and XRD of N1-2_10Np.

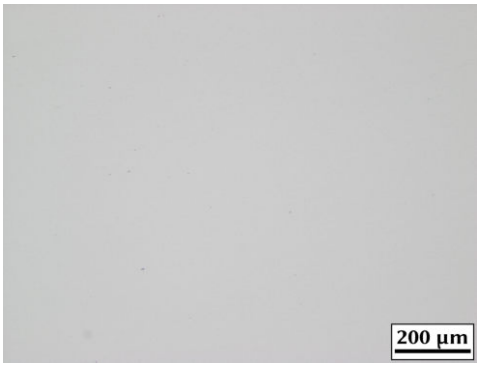

(a) LOM, 100x magnification.

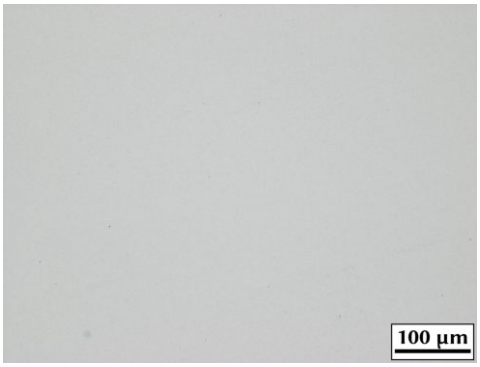

(b) LOM, 200x magnification.

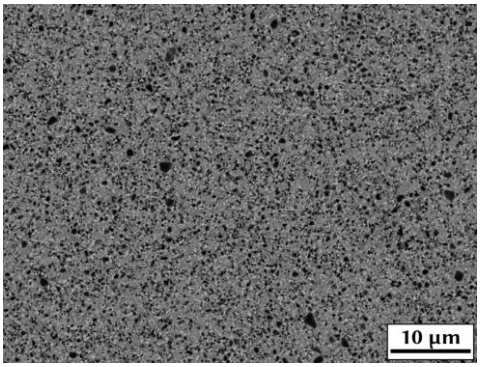

(c) BSE-SEM, 5000x magnification.

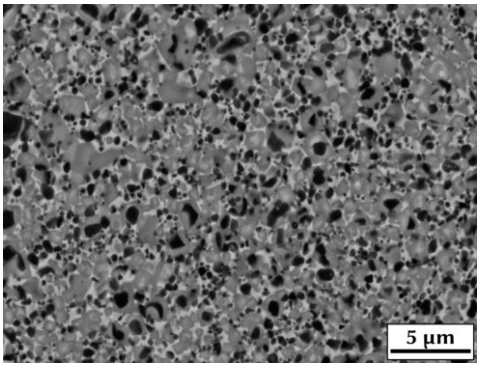

(d) BSE-SEM, 10,000x magnification.

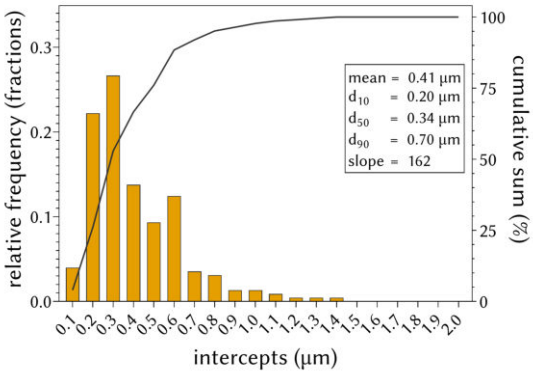

(e) GSD of cores.

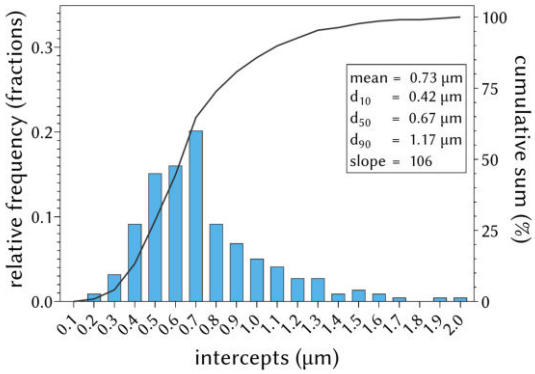

(f) GSD of grains.

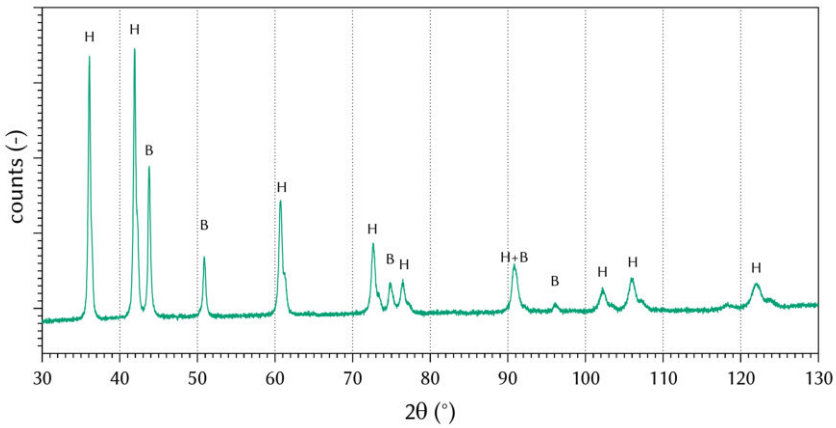

(g) XRD with hard phase (H) and binder (B) peaks identified.

Figure 127: LOM, BSE-SEM, GSD and XRD of N1-2+0.1%C_10Np.

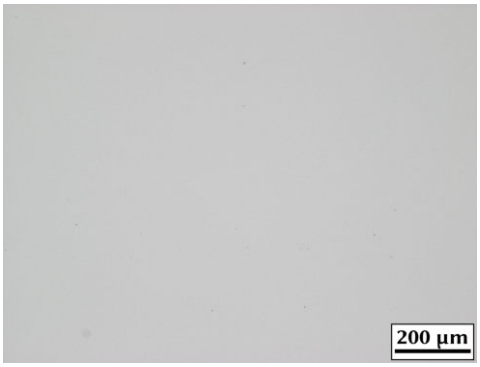

(a) LOM, 100x magnification.

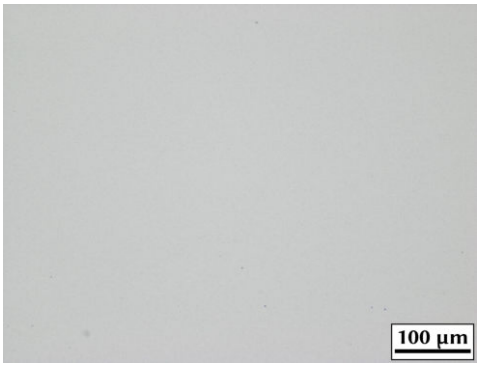

(b) LOM, 200x magnification.

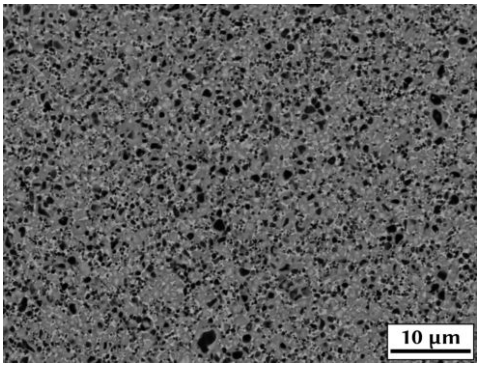

(c) BSE-SEM, 5000x magnification.

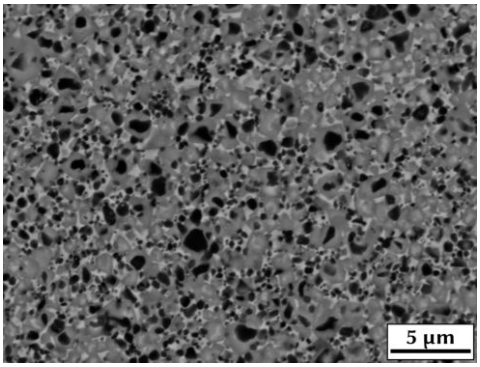

(d) BSE-SEM, 10,000x magnification.

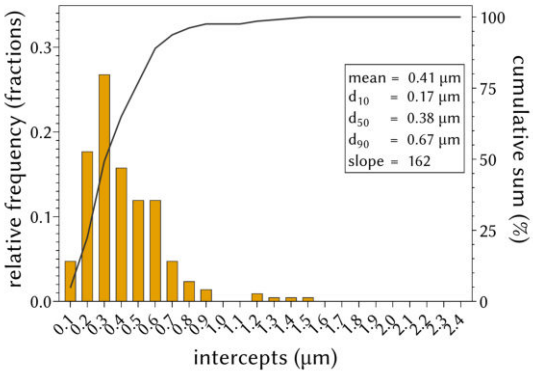

(e) GSD of cores.

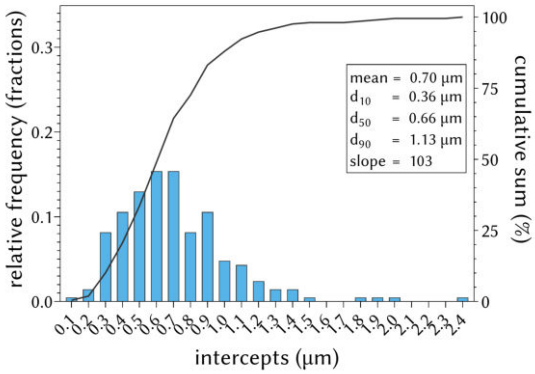

(f) GSD of grains.

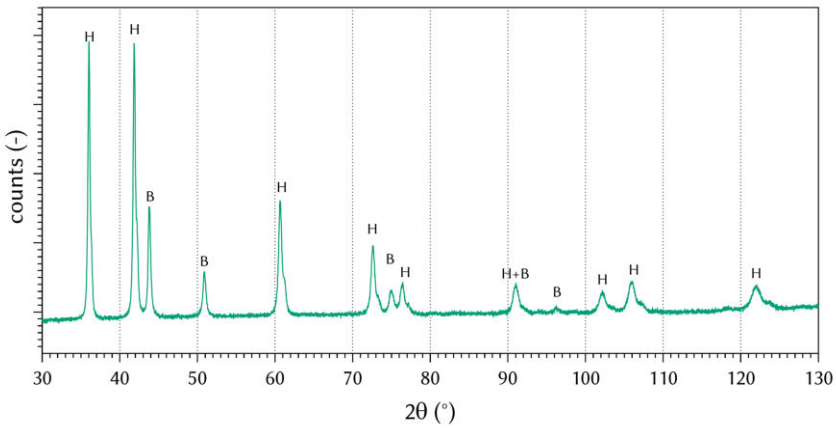

(g) XRD with hard phase (H) and binder (B) peaks identified.

Figure 128: LOM, BSE-SEM, GSD and XRD of N1-2+0.3%C_10Np.

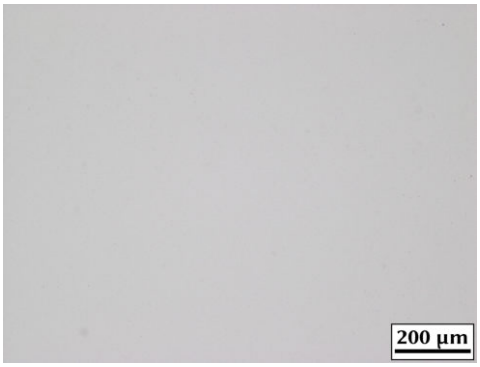

(a) LOM, 100x magnification.

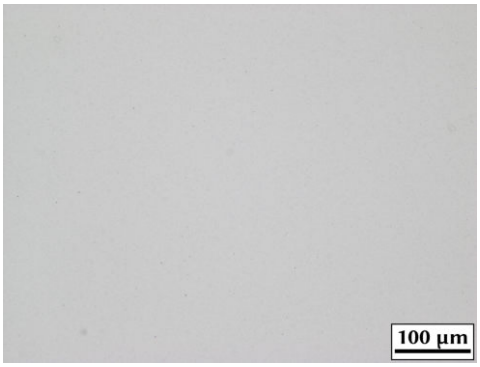

(b) LOM, 200x magnification.

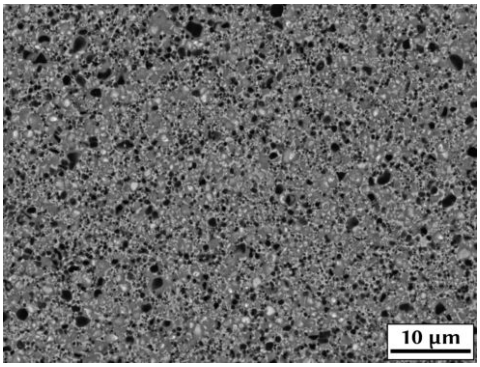

(c) BSE-SEM, 5000x magnification.

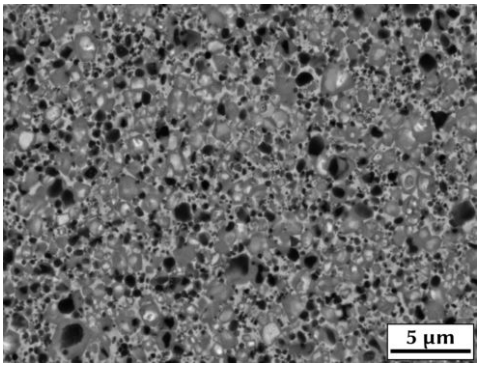

(d) BSE-SEM, 10,000x magnification.

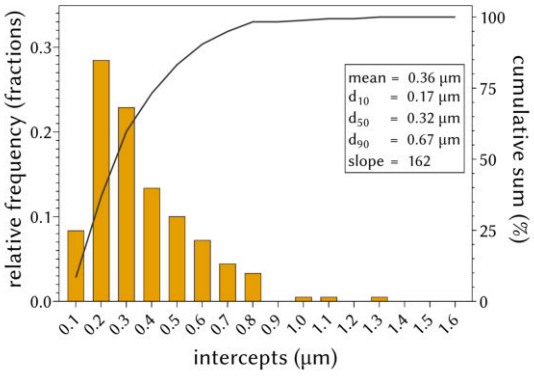

(e) GSD of cores.

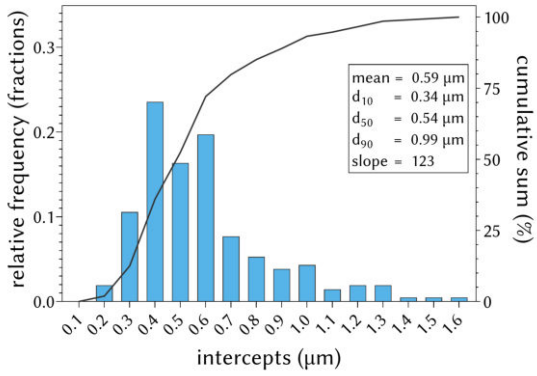

(f) GSD of grains.

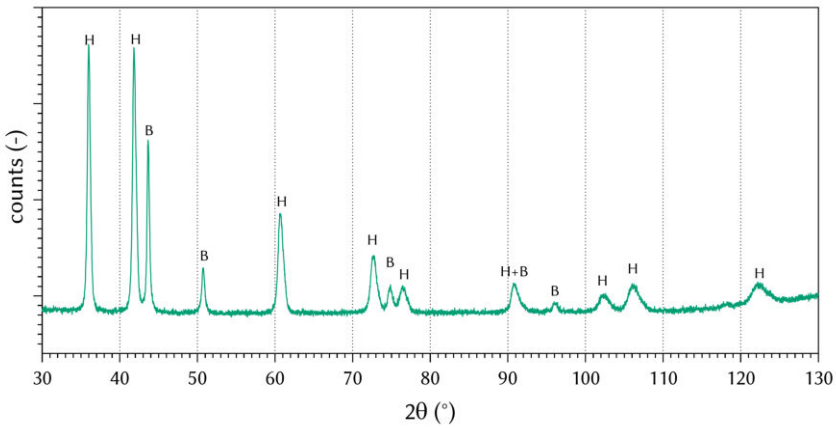

(g) XRD with hard phase (H) and binder (B) peaks identified.

Figure 129: LOM, BSE-SEM, GSD and XRD of N2-2_10Np.

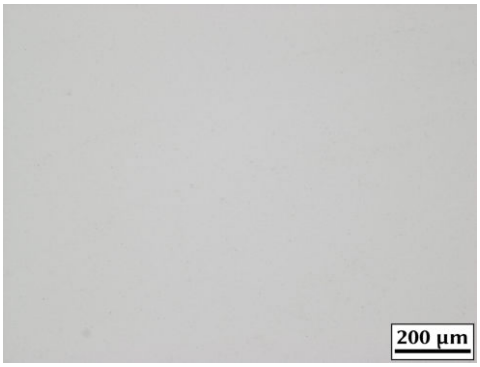

(a) LOM, 100x magnification.

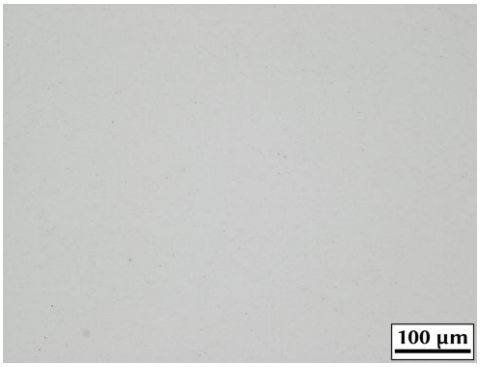

(b) LOM, 200x magnification.

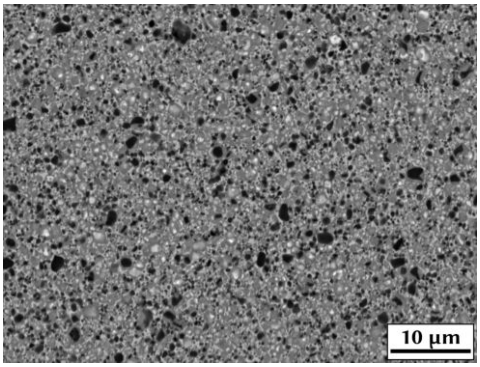

(c) BSE-SEM, 5000x magnification.

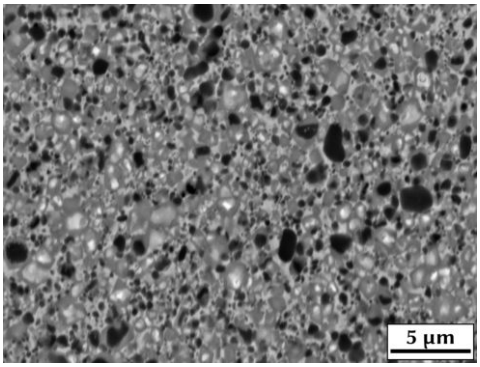

(d) BSE-SEM, 10,000x magnification.

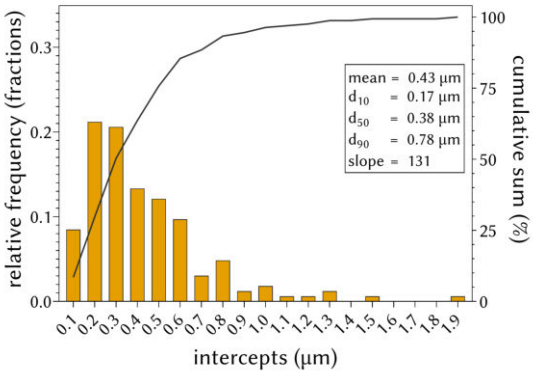

(e) GSD of cores.

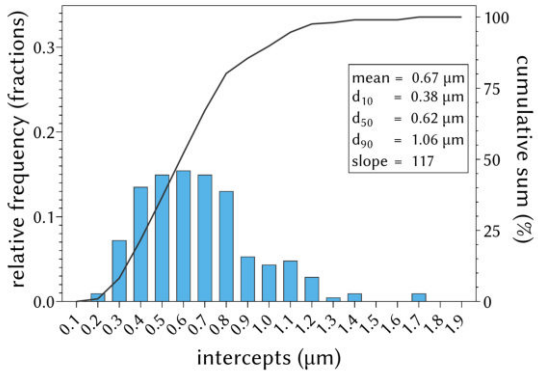

(f) GSD of grains.

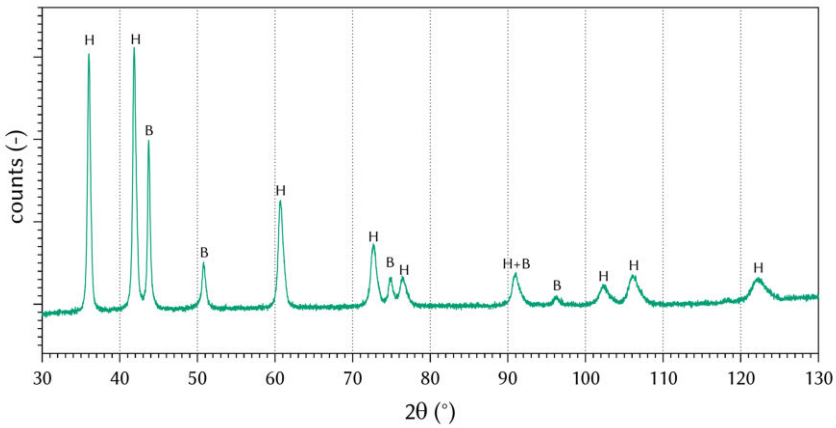

(g) XRD with hard phase (H) and binder (B) peaks identified.

Figure 130: LOM, BSE-SEM, GSD and XRD of N2-2+0.1%C_10Np.

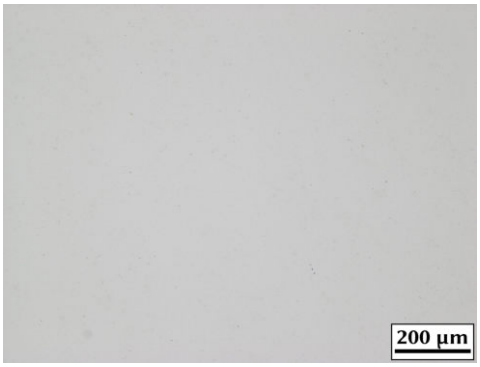

(a) LOM, 100x magnification.

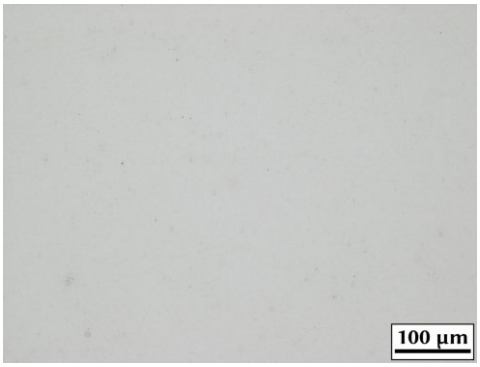

(b) LOM, 200x magnification.

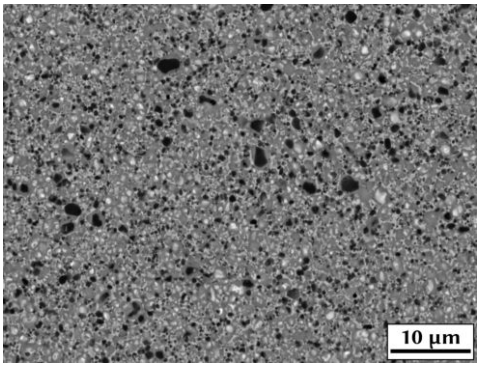

(c) BSE-SEM, 5000x magnification.

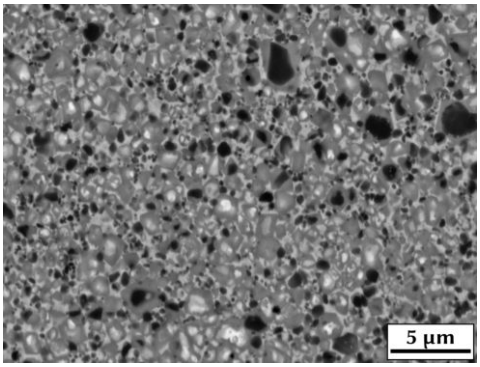

(d) BSE-SEM, 10,000x magnification.

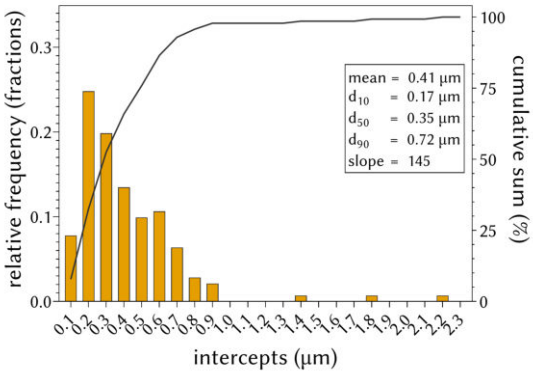

(e) GSD of cores.

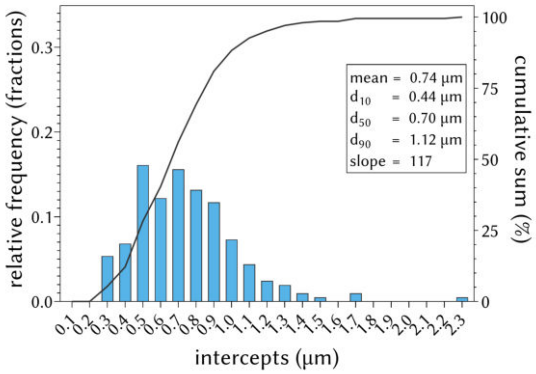

(f) GSD of grains.

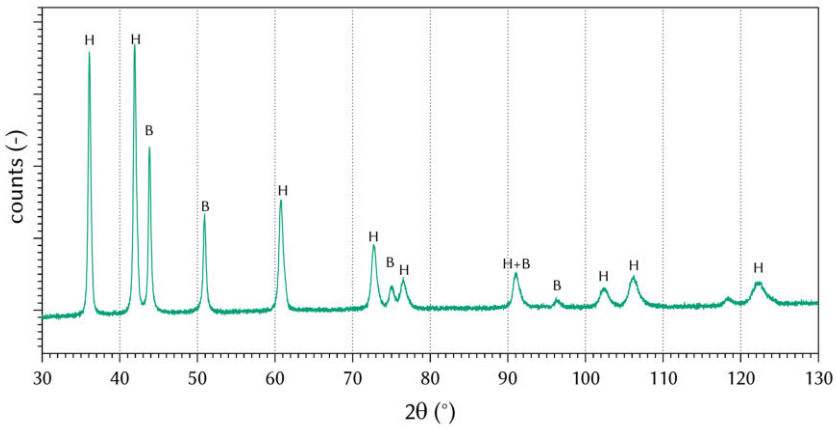

(g) XRD with hard phase (H) and binder (B) peaks identified.

Figure 131: LOM, BSE-SEM, GSD and XRD of N2-2+0.3%C_10Np.

(a) LOM, 100x magnification.

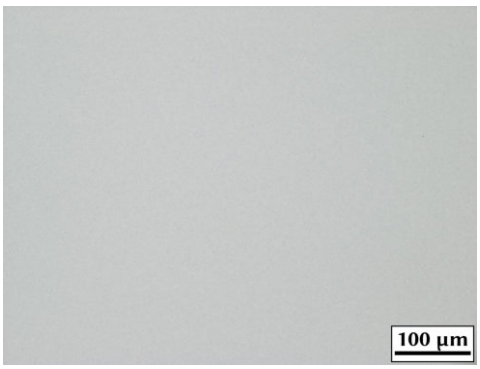

(b) LOM, 200x magnification.

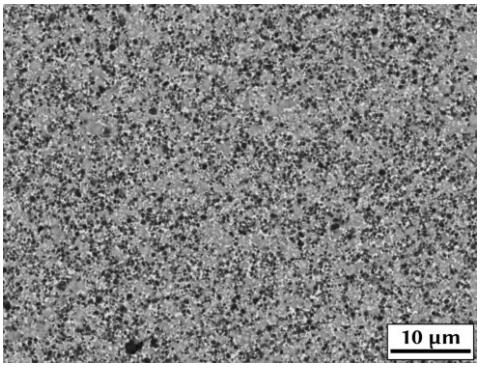

(c) BSE-SEM, 5000x magnification.

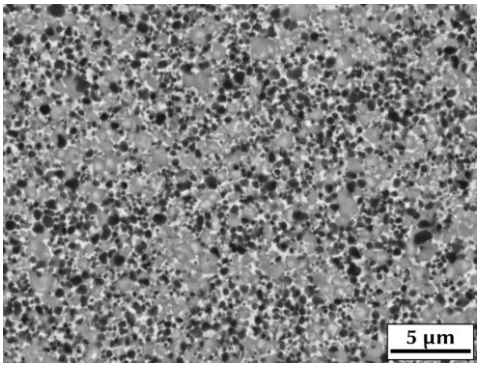

(d) BSE-SEM, 10,000x magnification.

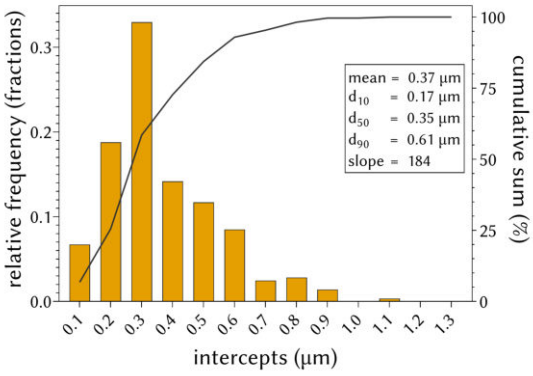

(e) GSD of cores.

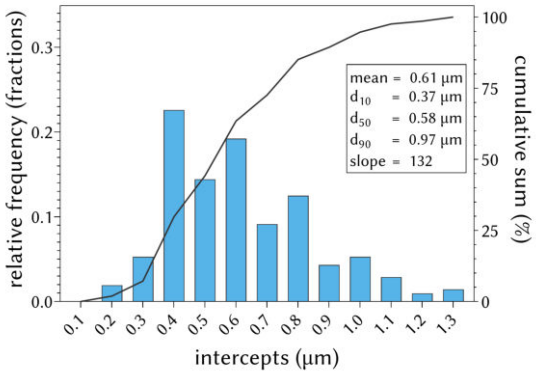

(f) GSD of grains.

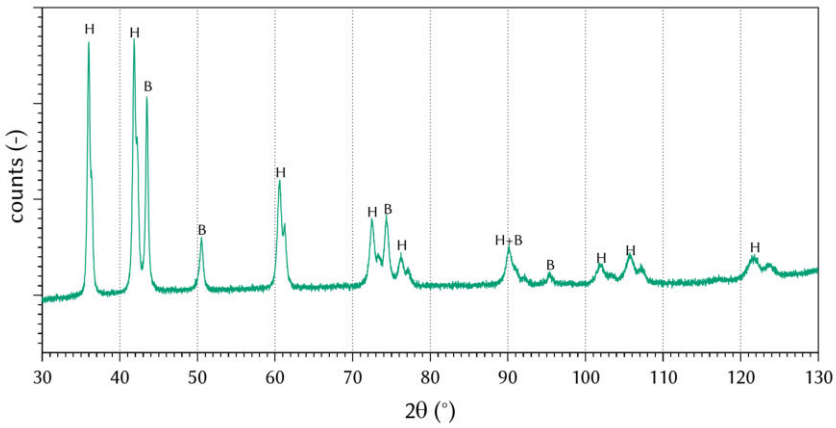

(g) XRD with hard phase (H) and binder (B) peaks identified.

Figure 132: LOM, BSE-SEM, GSD and XRD of N0-1_SAr.

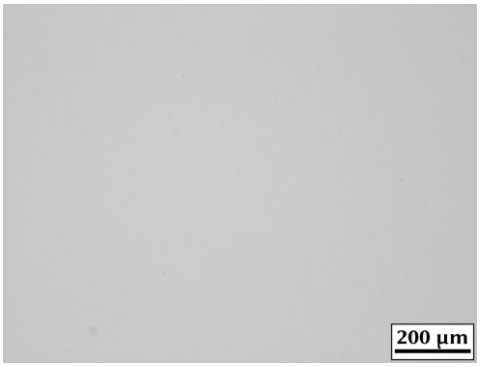

(a) LOM, 100x magnification.

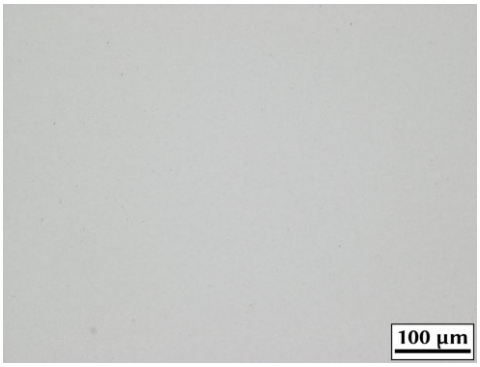

(b) LOM, 200x magnification.

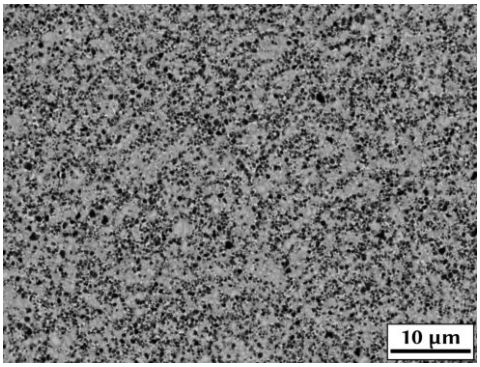

(c) BSE-SEM, 5000x magnification.

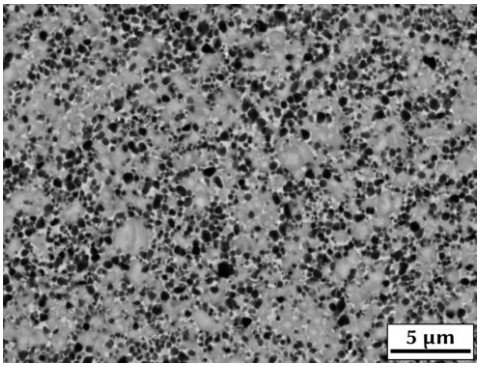

(d) BSE-SEM, 10,000x magnification.

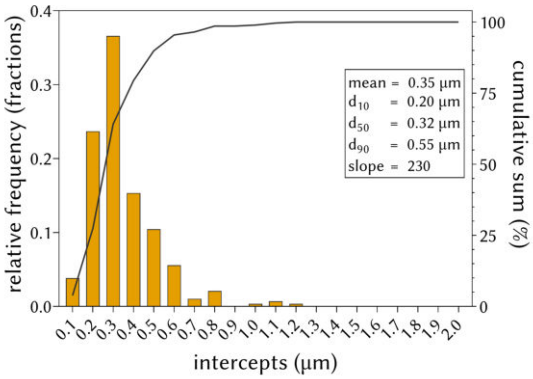

(e) GSD of cores.

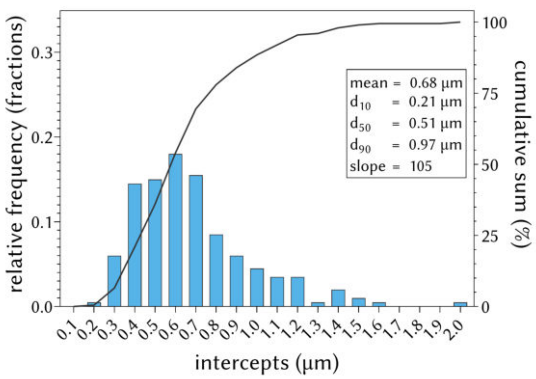

(f) GSD of grains.

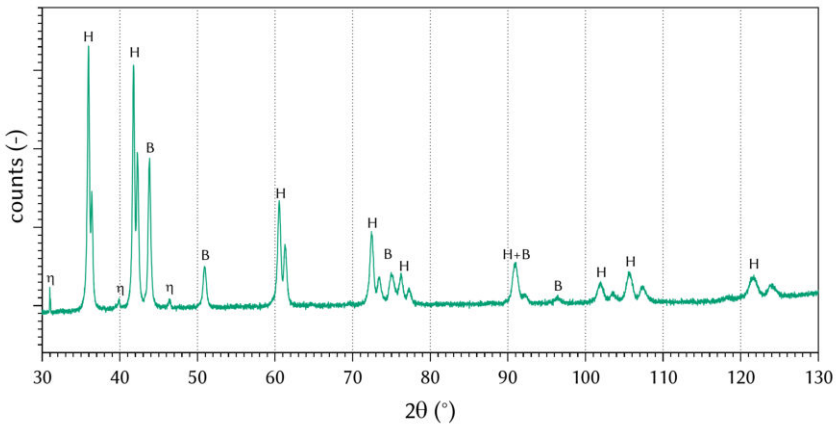

(g) XRD with hard phase (H) and binder (B) peaks identified.

Figure 133: LOM, BSE-SEM, GSD and XRD of N0-1_SN.

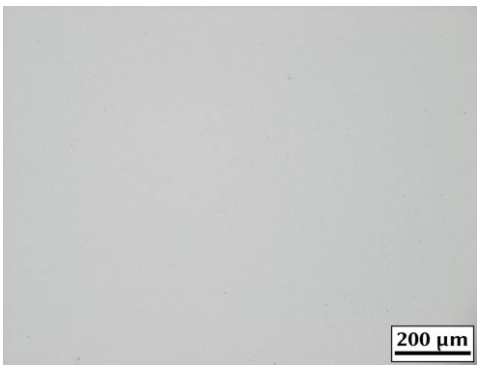

(a) LOM, 100x magnification.

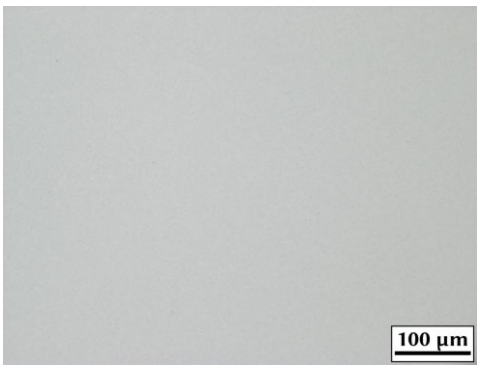

(b) LOM, 200x magnification.

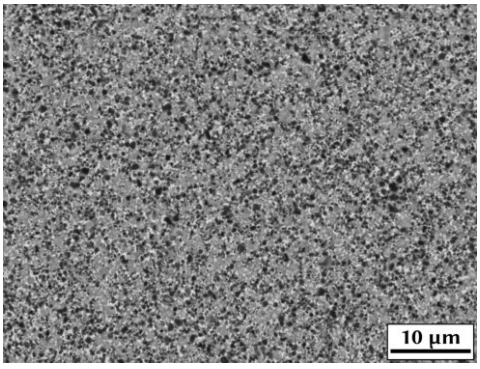

(c) BSE-SEM, 5000x magnification.

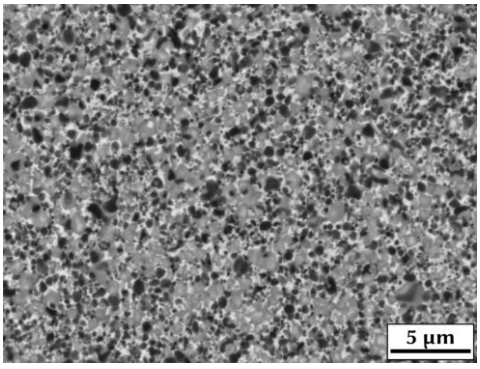

(d) BSE-SEM, 10,000x magnification.

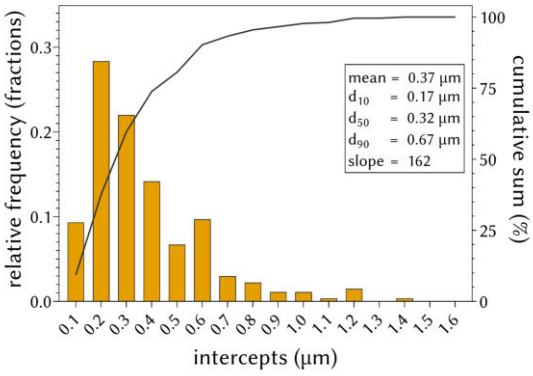

(e) GSD of cores.

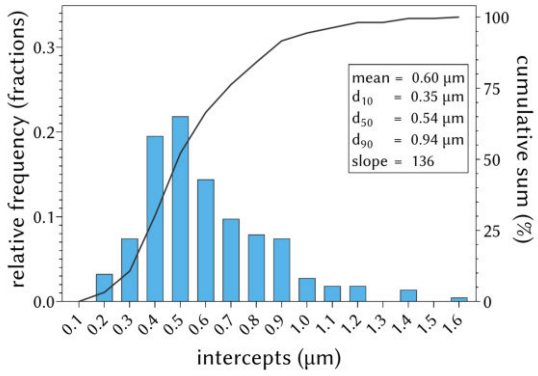

(f) GSD of grains.

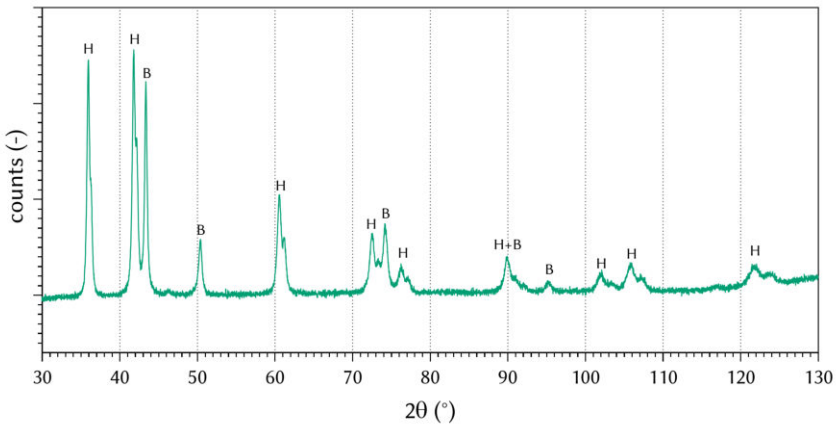

(g) XRD with hard phase (H) and binder (B) peaks identified.

Figure 134: LOM, BSE-SEM, GSD and XRD of N0-2_SAr.

(a) LOM, 100x magnification.

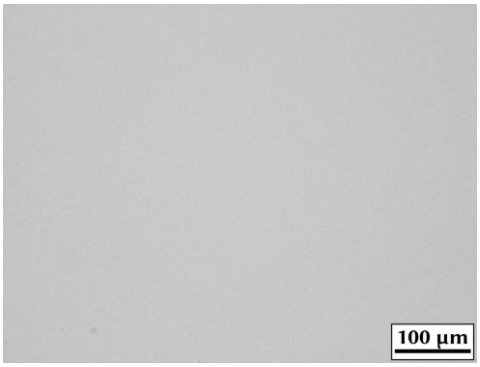

(b) LOM, 200x magnification.

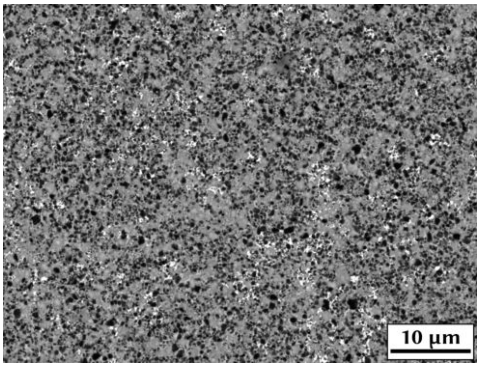

(c) BSE-SEM, 5000x magnification.

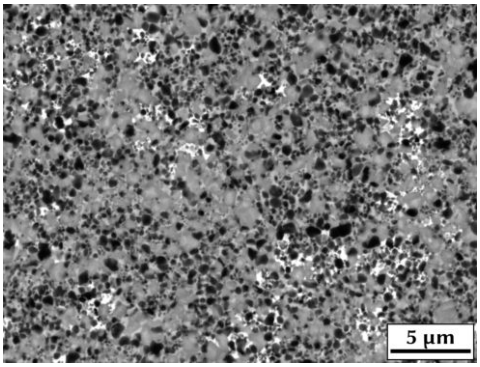

(d) BSE-SEM, 10,000x magnification.

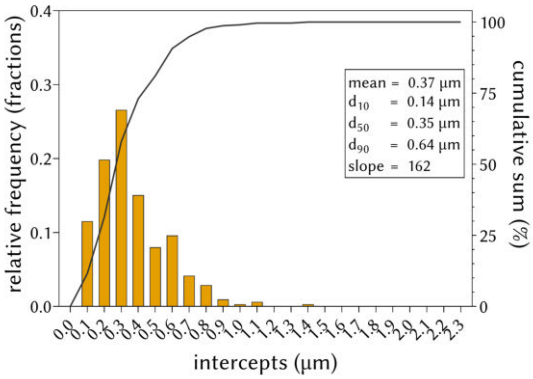

(e) GSD of cores.

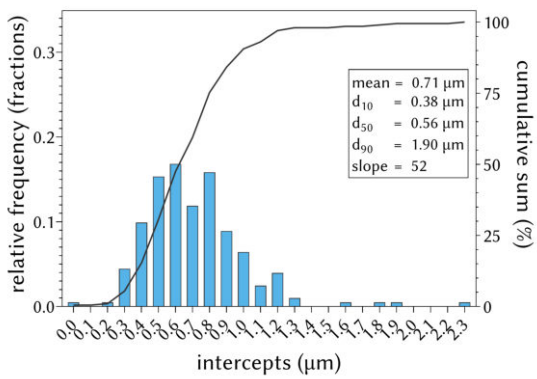

(f) GSD of grains.

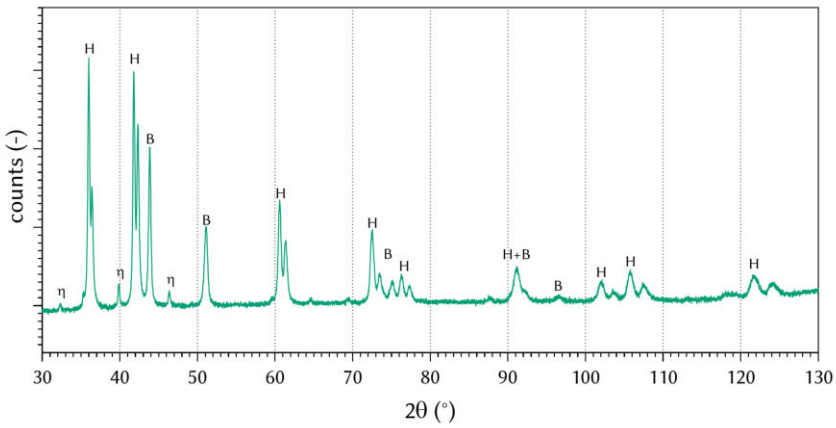

(g) XRD with hard phase (H) and binder (B) peaks identified.

Figure 135: LOM, BSE-SEM, GSD and XRD of N0-2_SN.

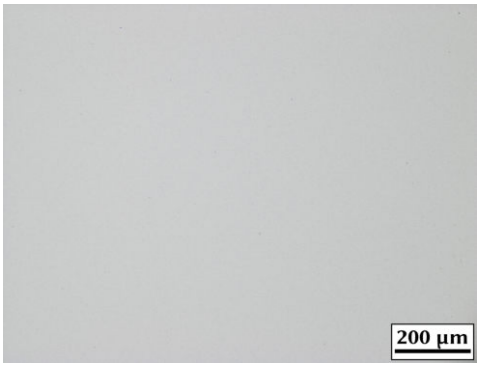

(a) LOM, 100x magnification.

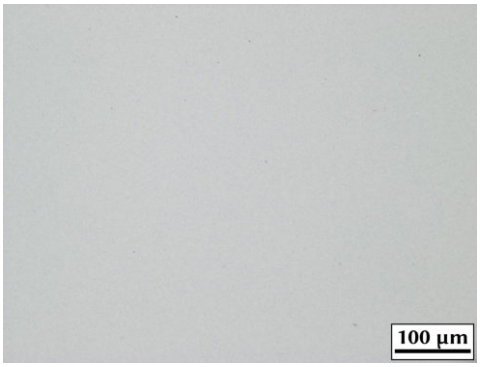

(b) LOM, 200x magnification.

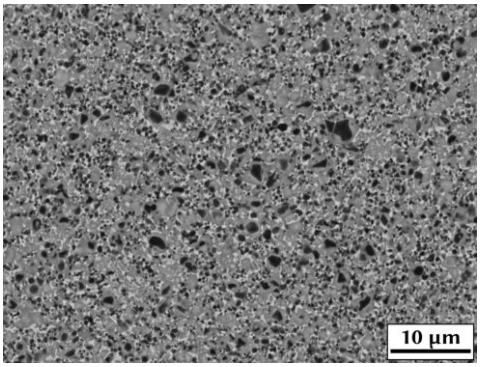

(c) BSE-SEM, 5000x magnification.

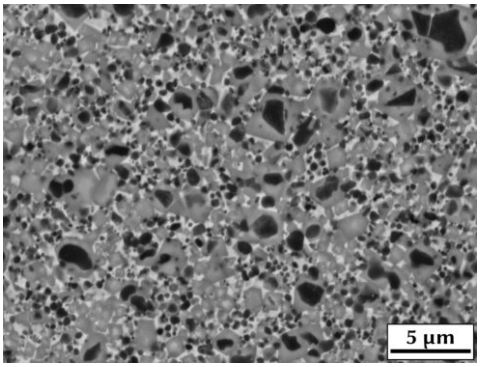

(d) BSE-SEM, 10,000x magnification.

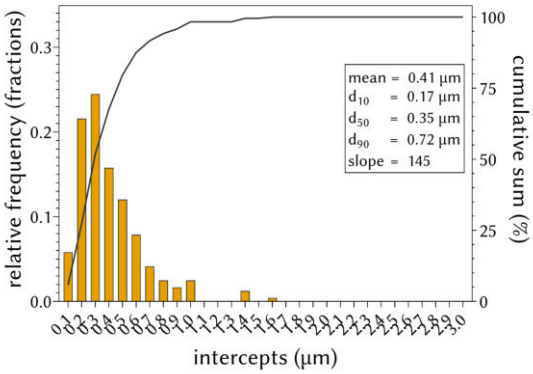

(e) GSD of cores.

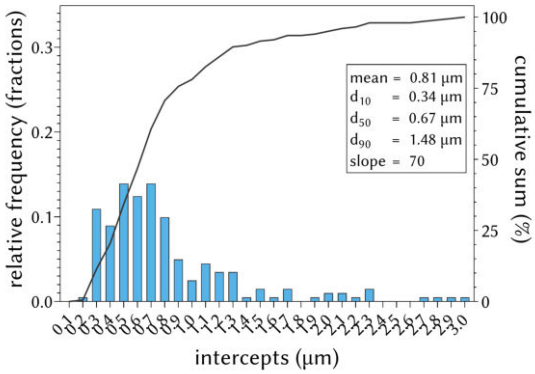

(f) GSD of grains.

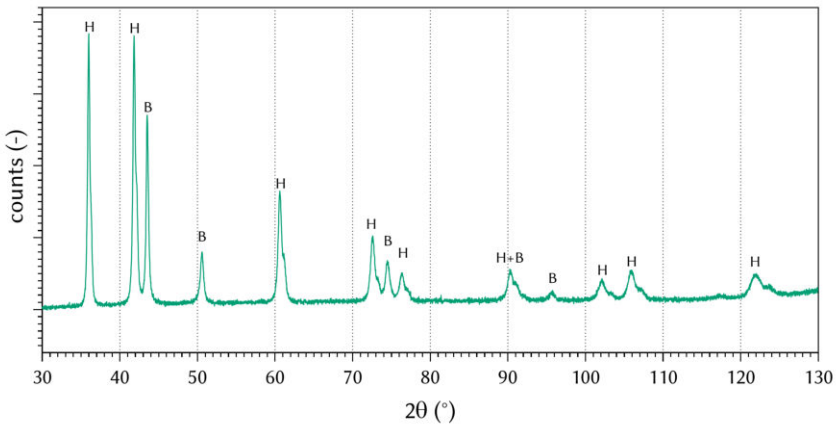

(g) XRD with hard phase (H) and binder (B) peaks identified.

Figure 136: LOM, BSE-SEM, GSD and XRD of N1-1_SAr.

(a) LOM, 100x magnification.

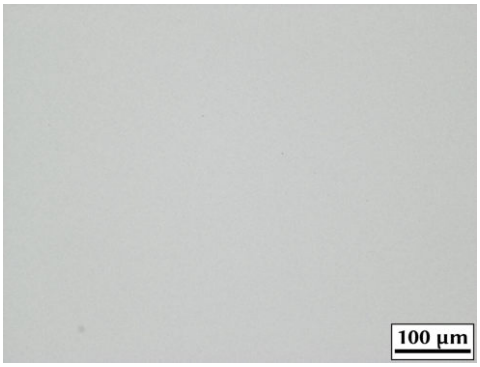

(b) LOM, 200x magnification.

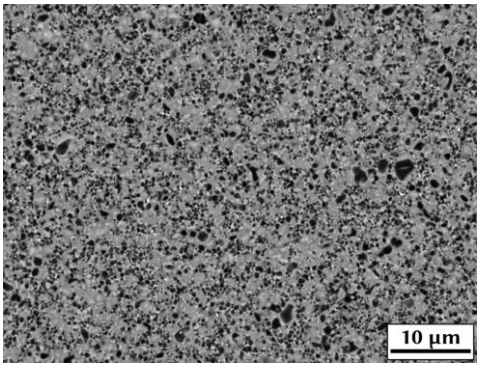

(c) BSE-SEM, 5000x magnification.

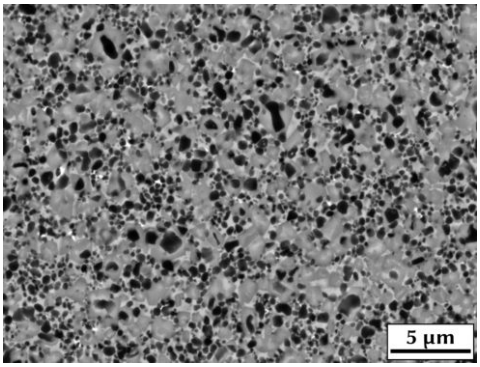

(d) BSE-SEM, 10,000x magnification.

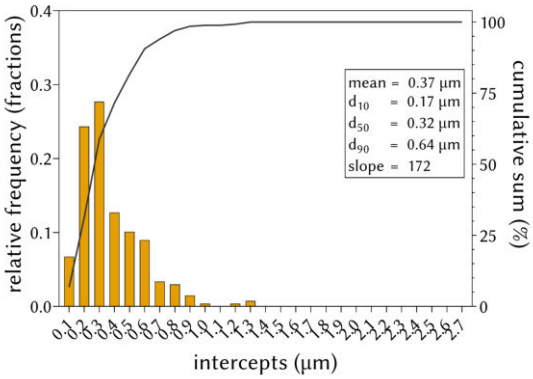

(e) GSD of cores.

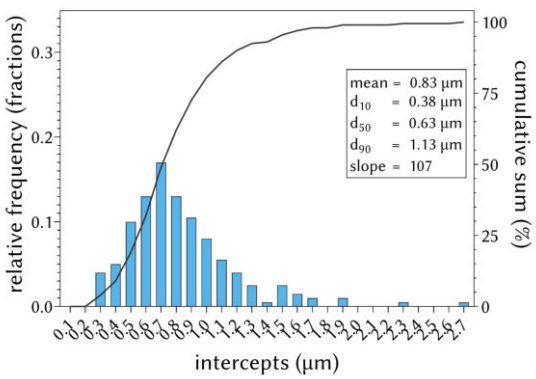

(f) GSD of grains.

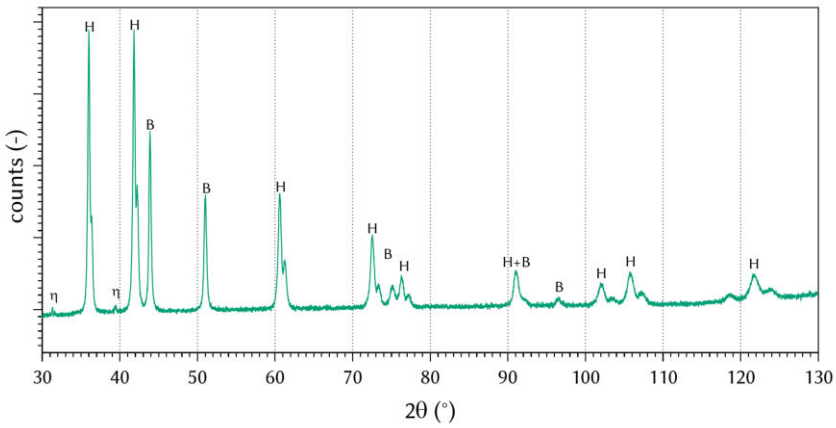

(g) XRD with hard phase (H) and binder (B) peaks identified.

Figure 137: LOM, BSE-SEM, GSD and XRD of N1-1_SN.

(a) LOM, 100x magnification.

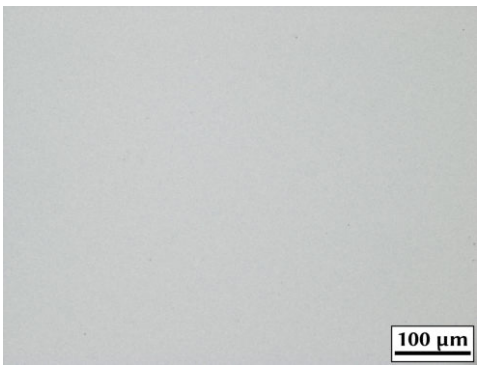

(b) LOM, 200x magnification.

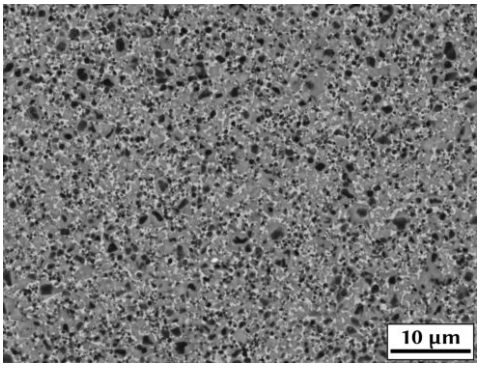

(c) BSE-SEM, 5000x magnification.

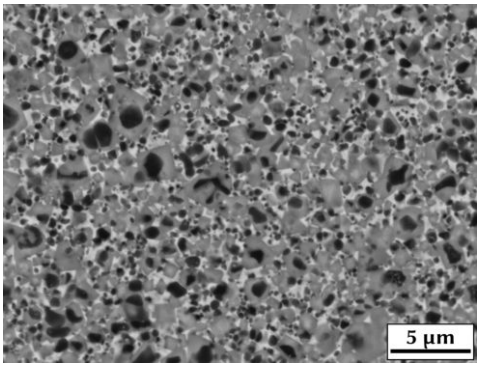

(d) BSE-SEM, 10,000x magnification.

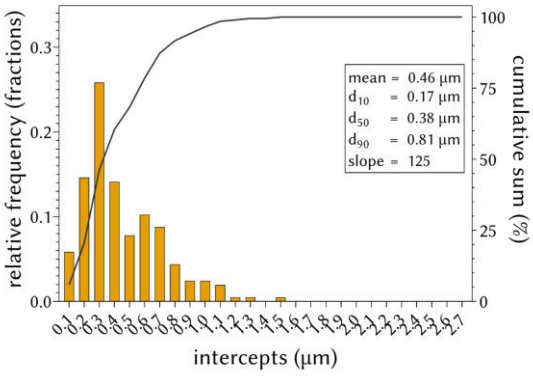

(e) GSD of cores.

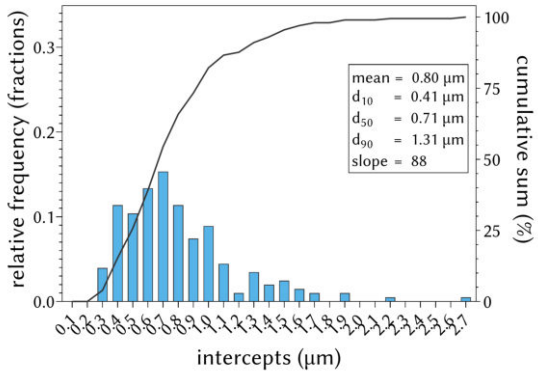

(f) GSD of grains.

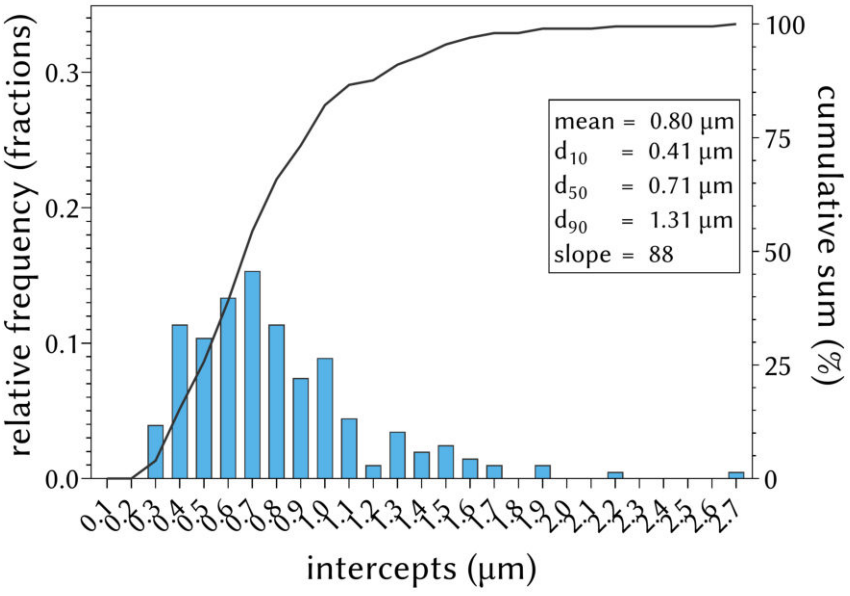

(g) XRD with hard phase (H) and binder (B) peaks identified.

Figure 138: LOM, BSE-SEM, GSD and XRD of N1-2_SAr.

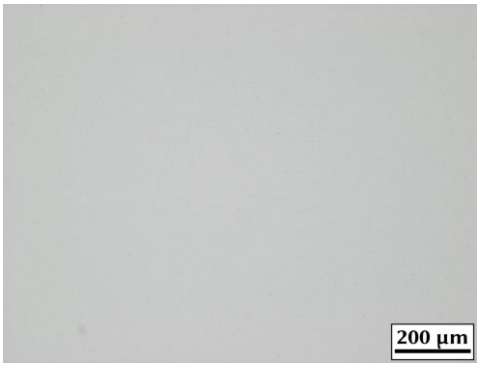

(a) LOM, 100x magnification.

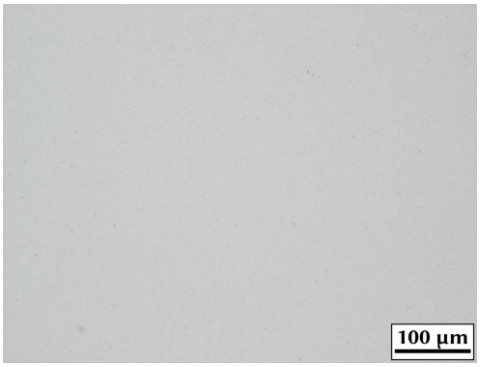

(b) LOM, 200x magnification.

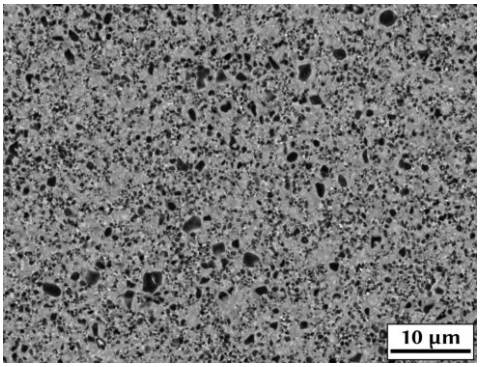

(c) BSE-SEM, 5000x magnification.

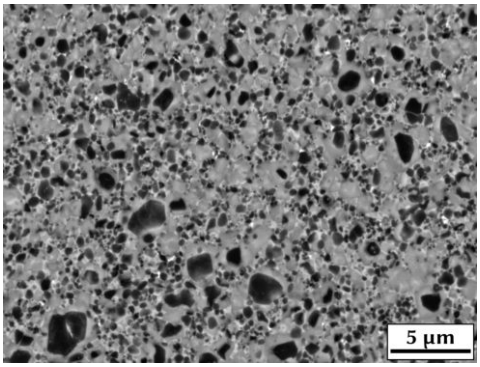

(d) BSE-SEM, 10,000x magnification.

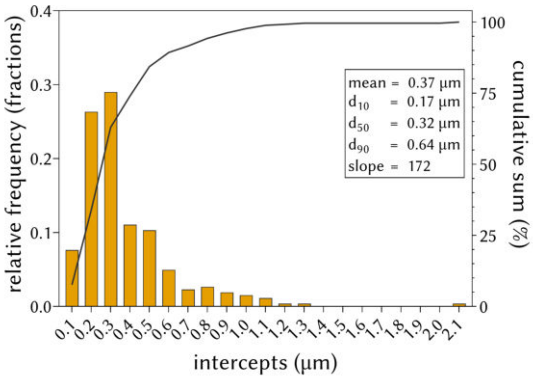

(e) GSD of cores.

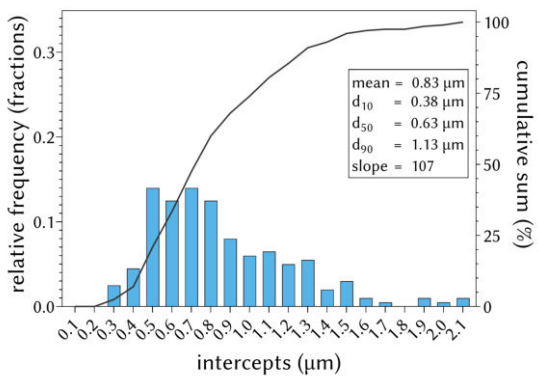

(f) GSD of grains.

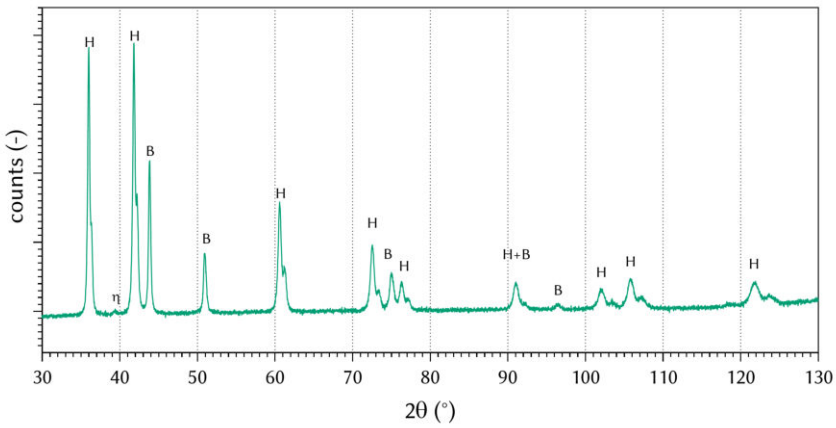

(g) XRD with hard phase (H) and binder (B) peaks identified.

Figure 139: LOM, BSE-SEM, GSD and XRD of N1-2_SN.

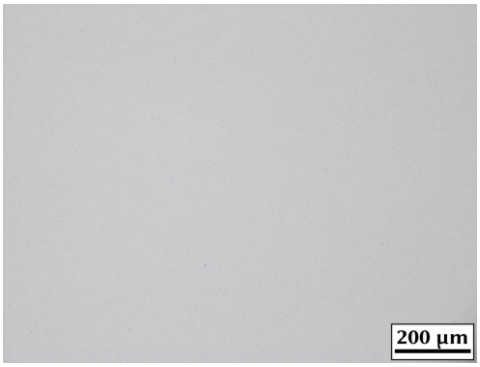

(a) LOM, 100x magnification.

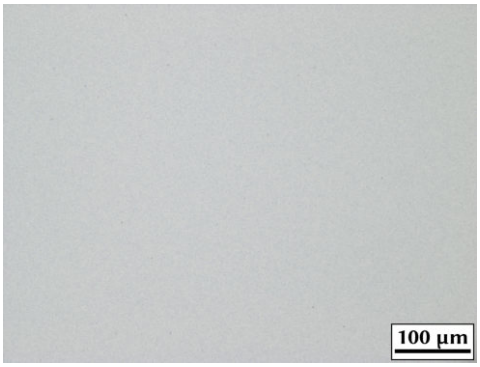

(b) LOM, 200x magnification.

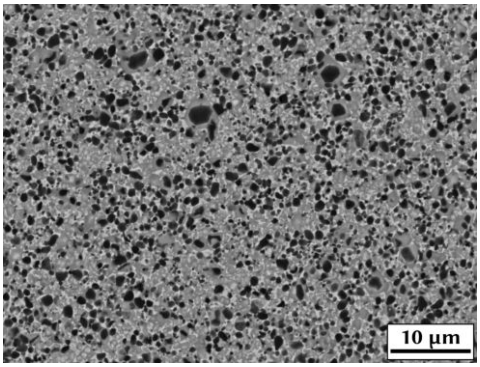

(c) BSE-SEM, 5000x magnification.

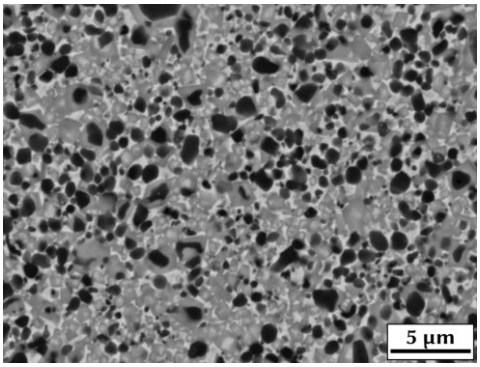

(d) BSE-SEM, 10,000x magnification.

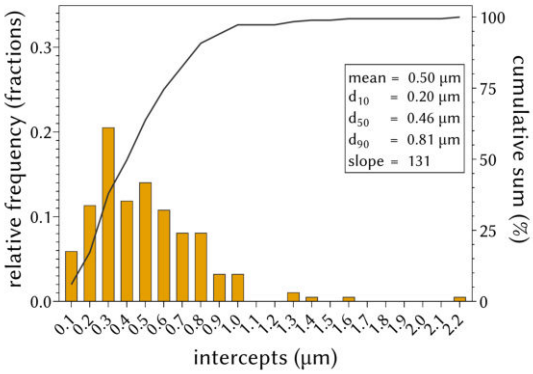

(e) GSD of cores.

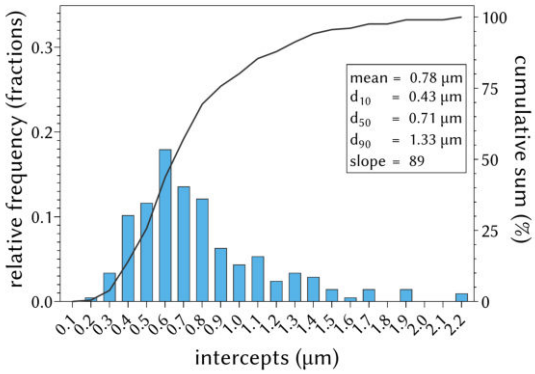

(f) GSD of grains.

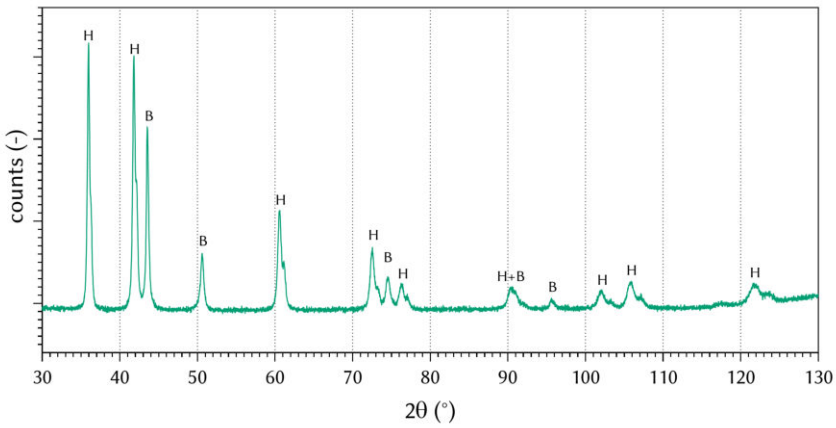

(g) XRD with hard phase (H) and binder (B) peaks identified.

Figure 140: LOM, BSE-SEM, GSD and XRD of N1-3_SAr.

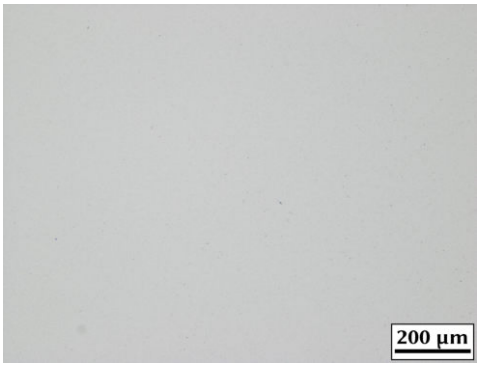

(a) LOM, 100x magnification.

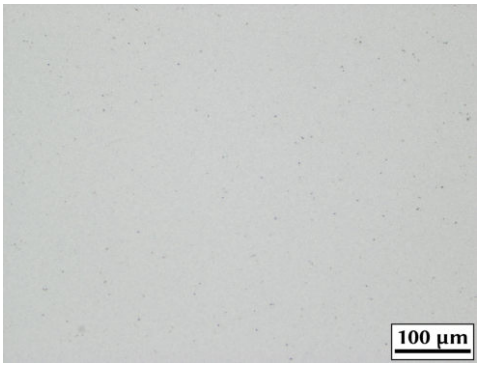

(b) LOM, 200x magnification.

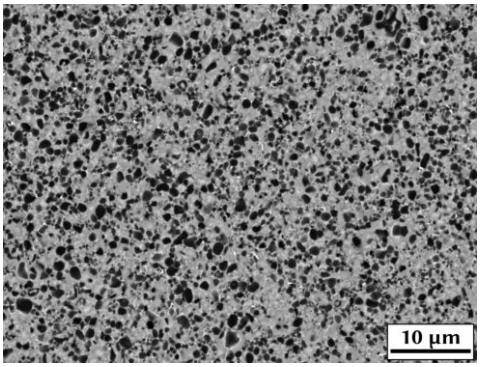

(c) BSE-SEM, 5000x magnification.

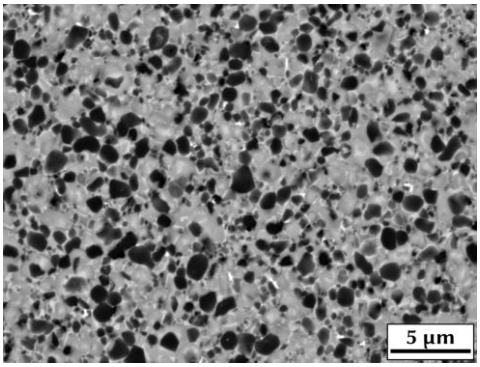

(d) BSE-SEM, 10,000x magnification.

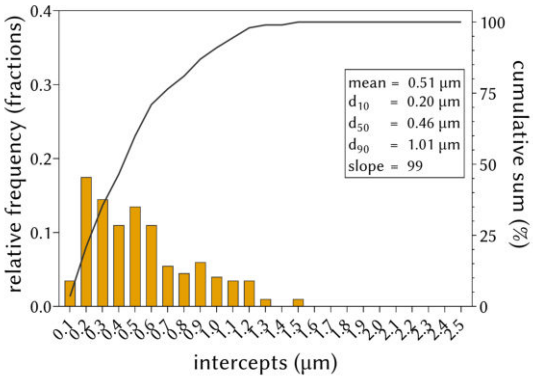

(e) GSD of cores.

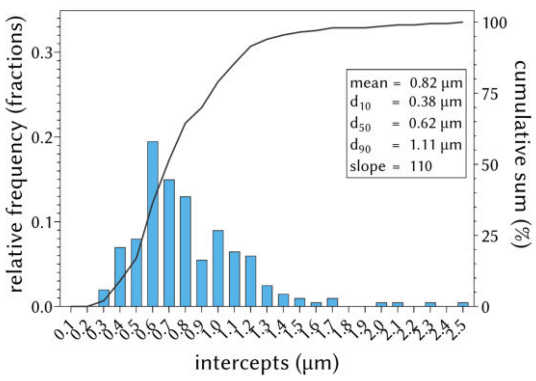

(f) GSD of grains.

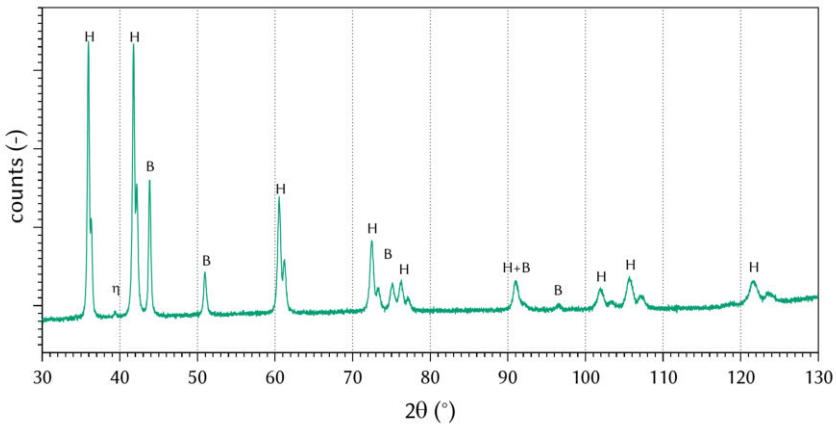

(g) XRD with hard phase (H) and binder (B) peaks identified.

Figure 141: LOM, BSE-SEM, GSD and XRD of N1-3_SN.

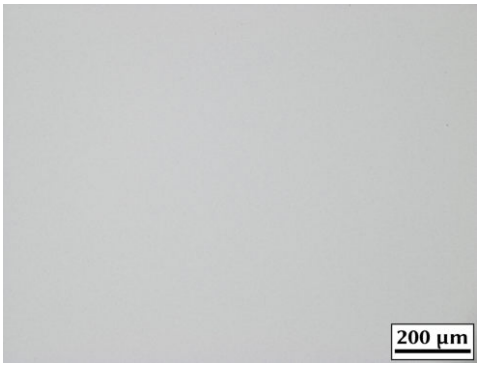

(a) LOM, 100x magnification.

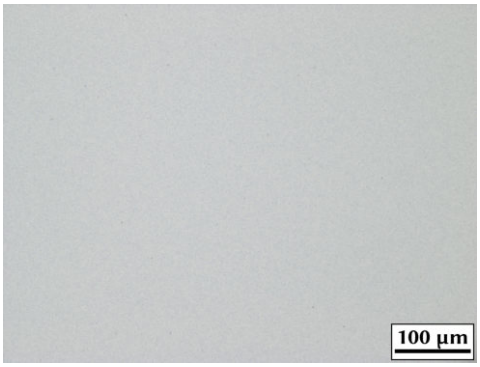

(b) LOM, 200x magnification.

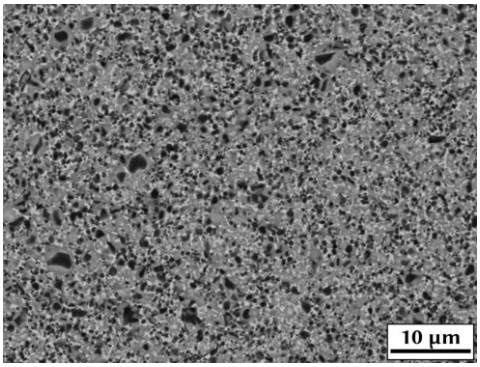

(c) BSE-SEM, 5000x magnification.

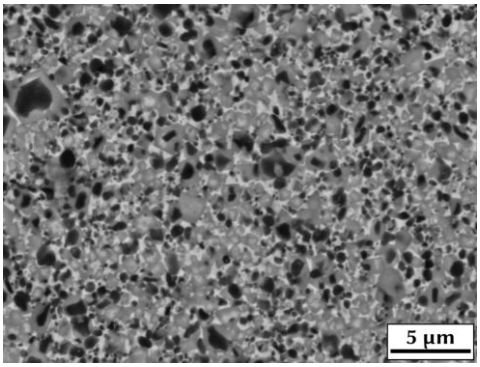

(d) BSE-SEM, 10,000x magnification.

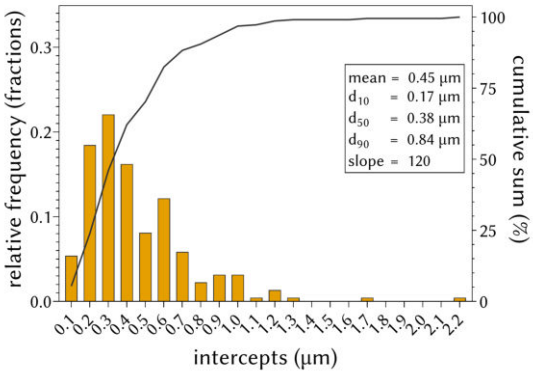

(e) GSD of cores.

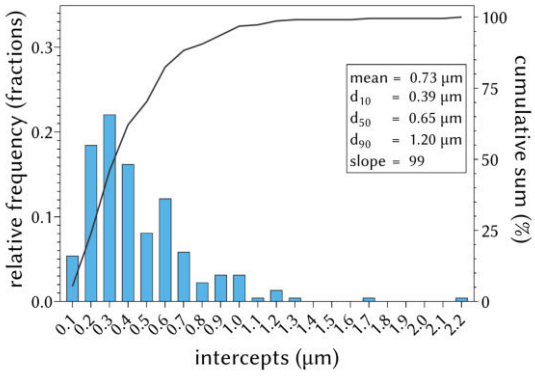

(f) GSD of grains.

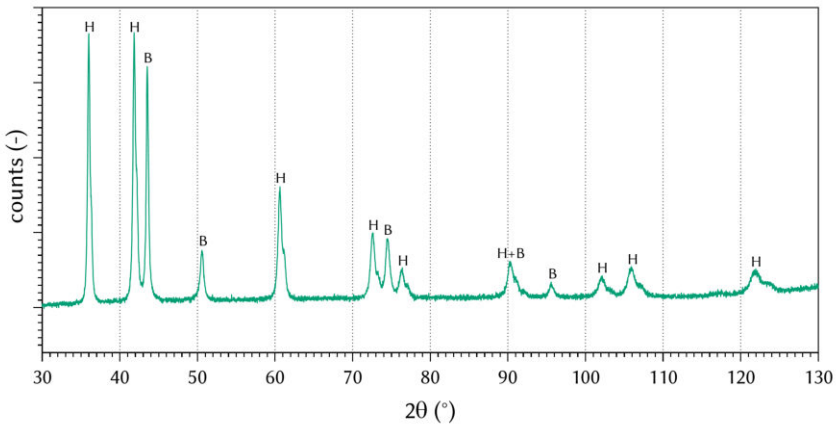

(g) XRD with hard phase (H) and binder (B) peaks identified.

Figure 142: LOM, BSE-SEM, GSD and XRD of N1-4_SAr.

(a) LOM, 100x magnification.

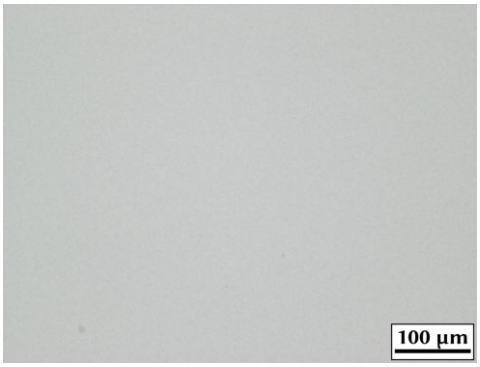

(b) LOM, 200x magnification.

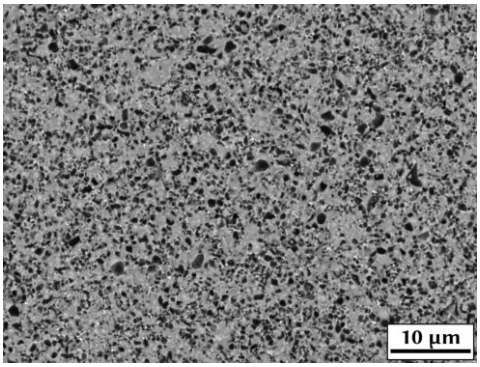

(c) BSE-SEM, 5000x magnification.

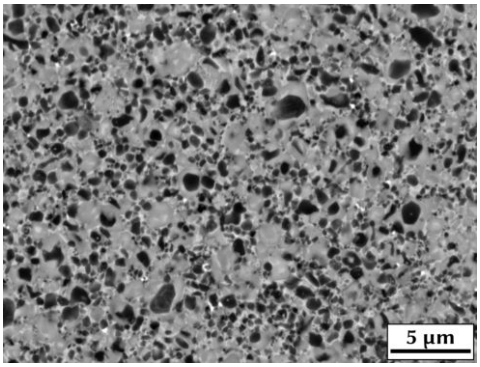

(d) BSE-SEM, 10,000x magnification.

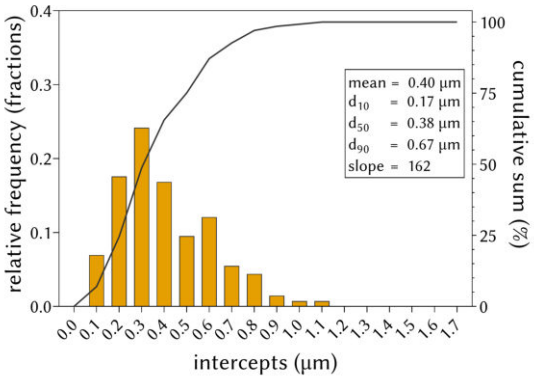

(e) GSD of cores.

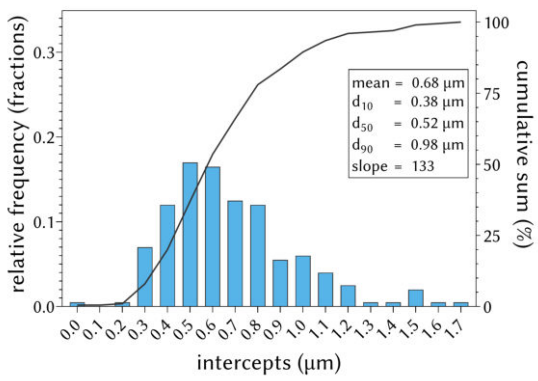

(f) GSD of grains.

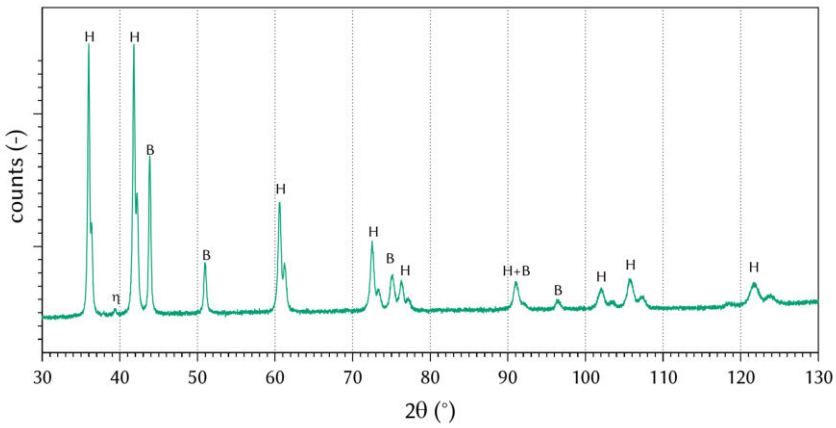

(g) XRD with hard phase (H) and binder (B) peaks identified.

Figure 143: LOM, BSE-SEM, GSD and XRD of N1-4_SN.

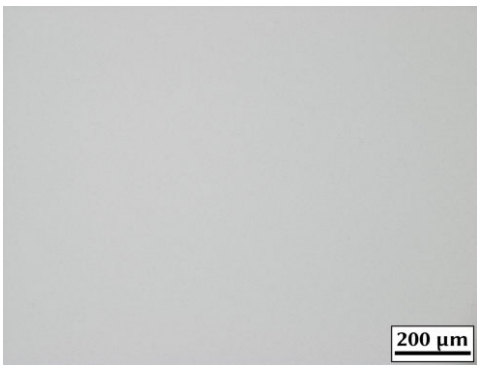

(a) LOM, 100x magnification.

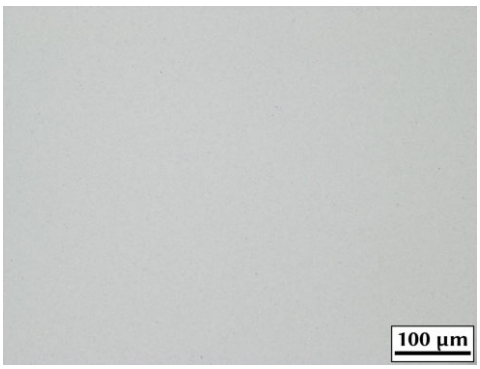

(b) LOM, 200x magnification.

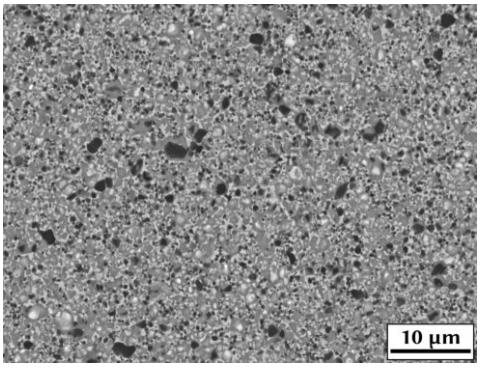

(c) BSE-SEM, 5000x magnification.

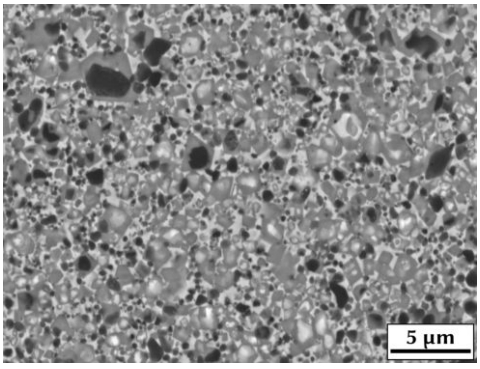

(d) BSE-SEM, 10,000x magnification.

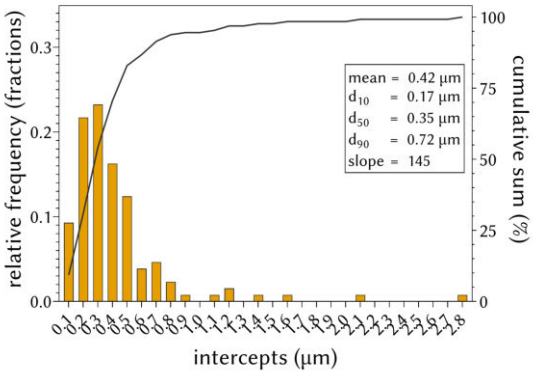

(e) GSD of cores.

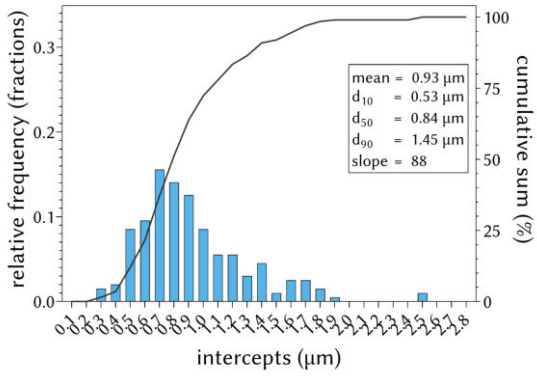

(f) GSD of grains.

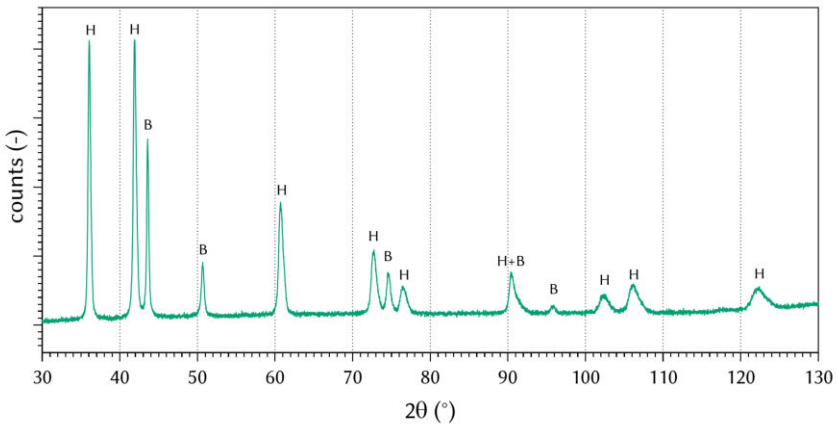

(g) XRD with hard phase (H) and binder (B) peaks identified.

Figure 144: LOM, BSE-SEM, GSD and XRD of N2-1_SAr.

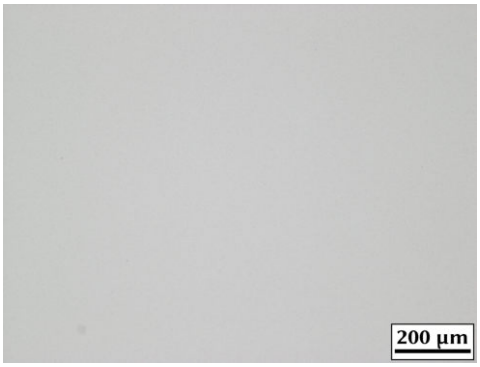

(a) LOM, 100x magnification.

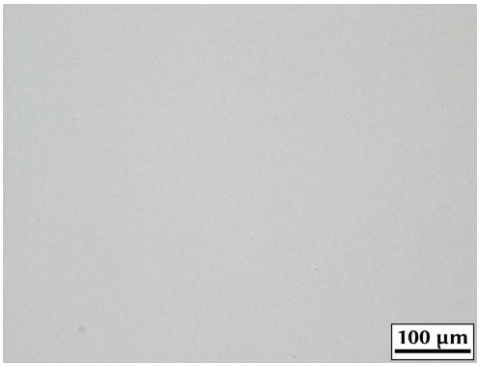

(b) LOM, 200x magnification.

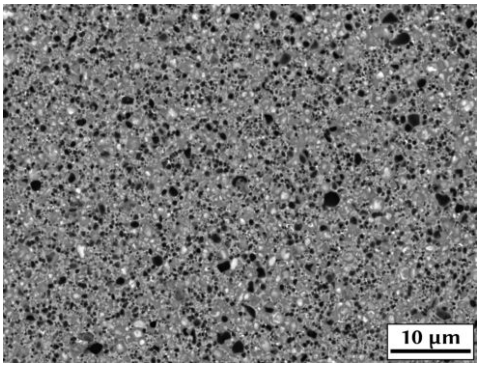

(c) BSE-SEM, 5000x magnification.

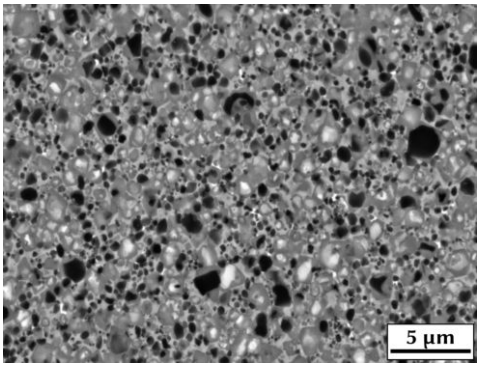

(d) BSE-SEM, 10,000x magnification.

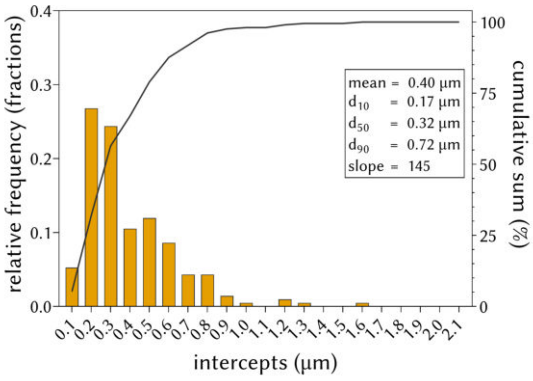

(e) GSD of cores.

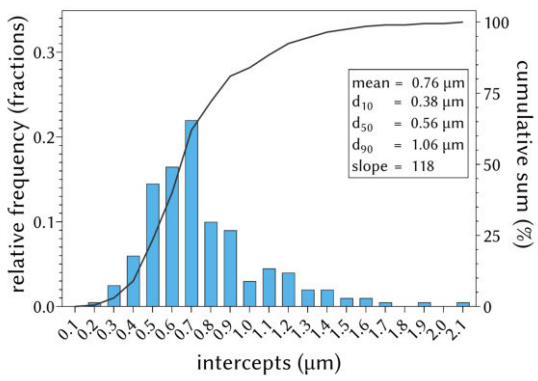

(f) GSD of grains.

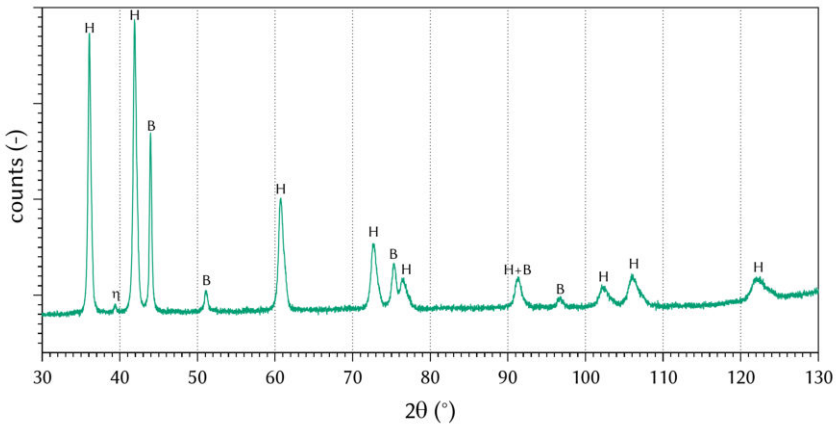

(g) XRD with hard phase (H) and binder (B) peaks identified.

Figure 145: LOM, BSE-SEM, GSD and XRD of N2-1_SN.

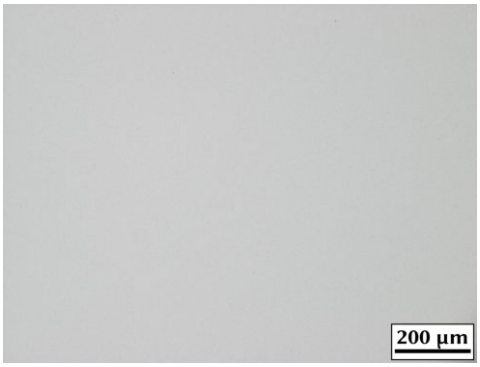

(a) LOM, 100x magnification.

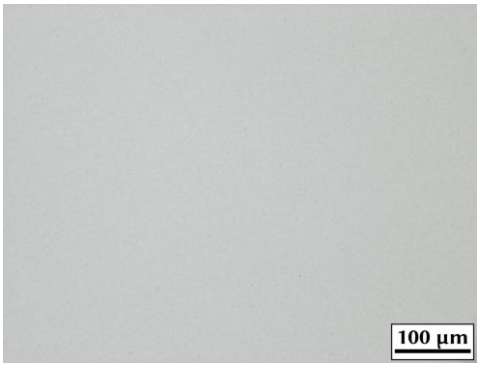

(b) LOM, 200x magnification.

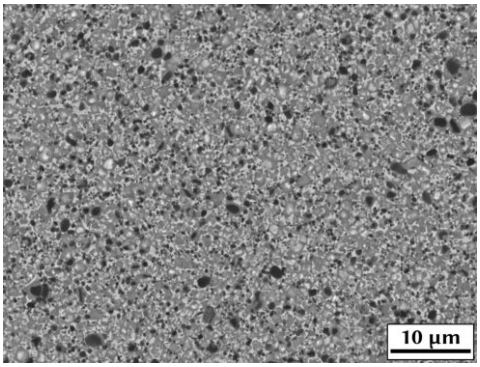

(c) BSE-SEM, 5000x magnification.

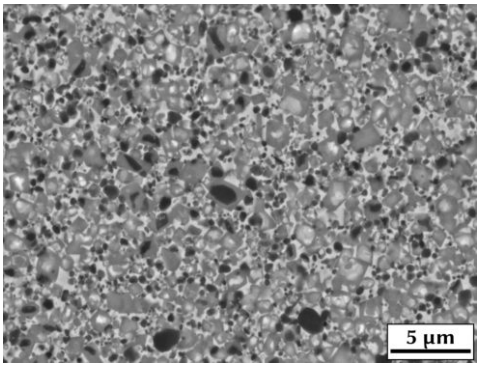

(d) BSE-SEM, 10,000x magnification.

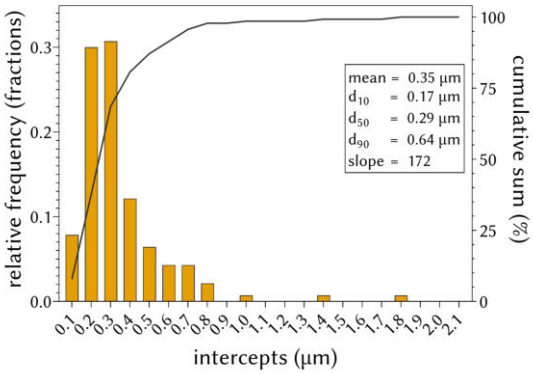

(e) GSD of cores.

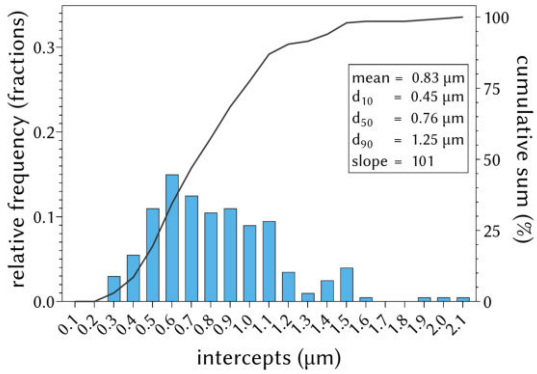

(f) GSD of grains.

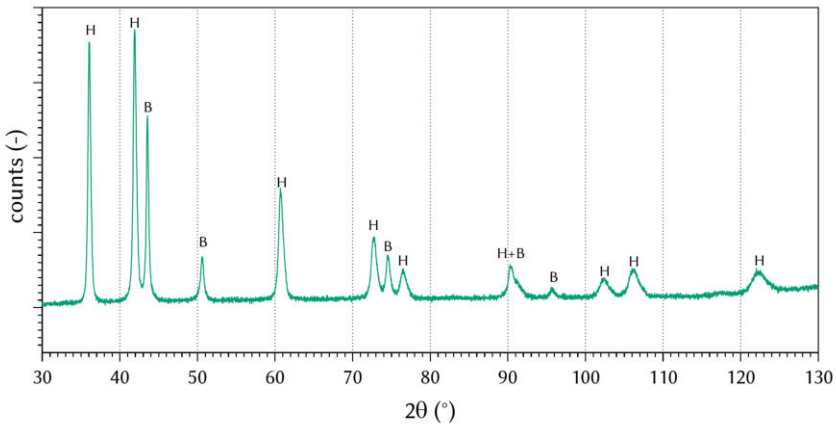

(g) XRD with hard phase (H) and binder (B) peaks identified.

Figure 146: LOM, BSE-SEM, GSD and XRD of N2-2_SAr.

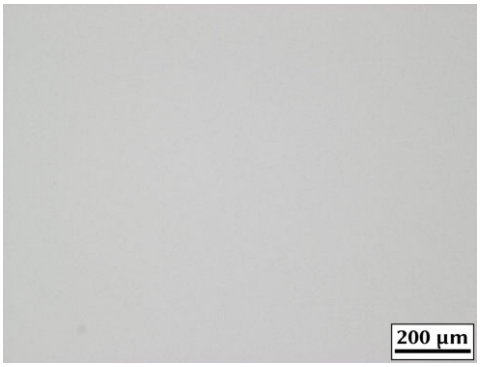

(a) LOM, 100x magnification.

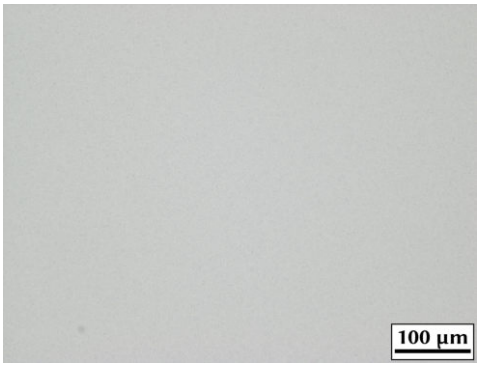

(b) LOM, 200x magnification.

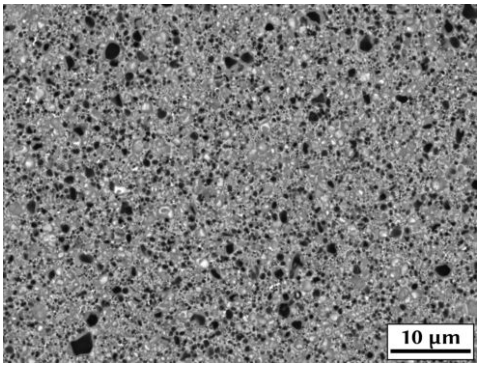

(c) BSE-SEM, 5000x magnification.

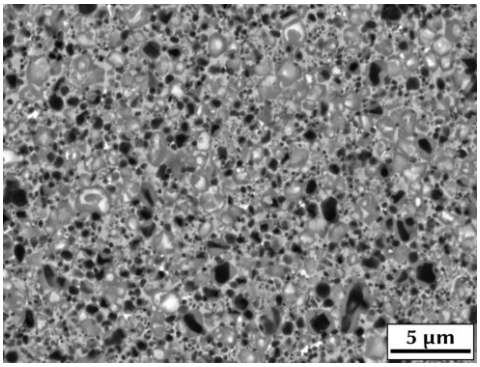

(d) BSE-SEM, 10,000x magnification.

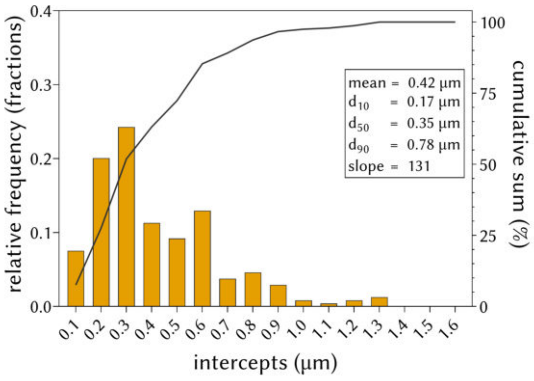

(e) GSD of cores.

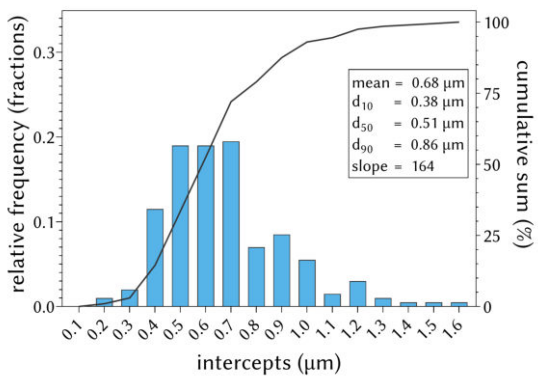

(f) GSD of grains.

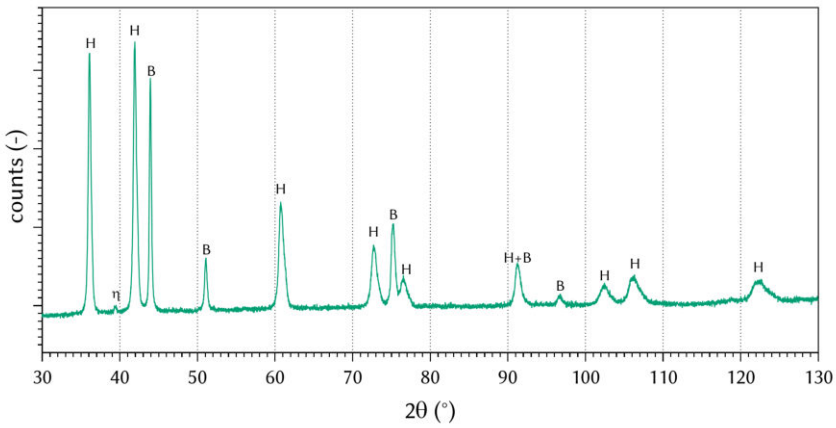

(g) XRD with hard phase (H) and binder (B) peaks identified.

Figure 147: LOM, BSE-SEM, GSD and XRD of N2-2_SN.

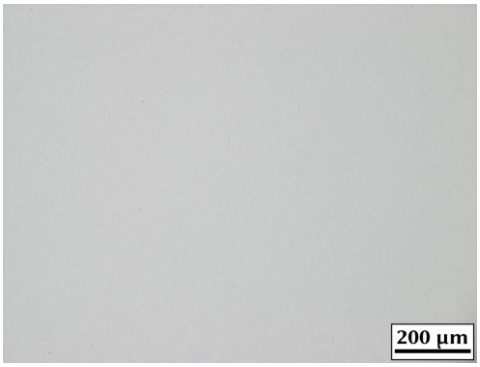

(a) LOM, 100x magnification.

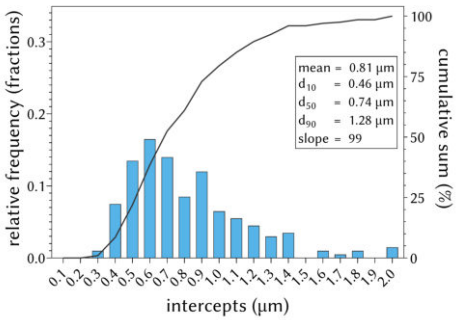

(b) LOM, 200x magnification.

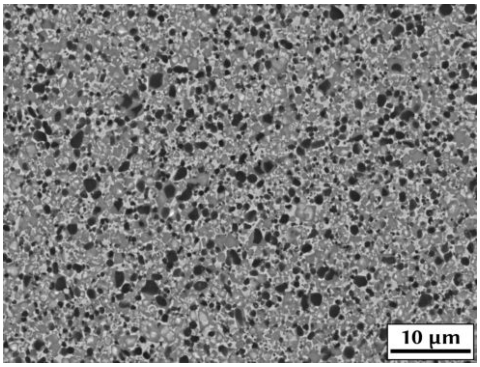

(c) BSE-SEM, 5000x magnification.

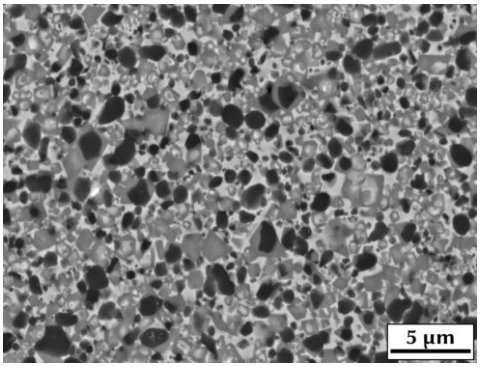

(d) BSE-SEM, 10,000x magnification.

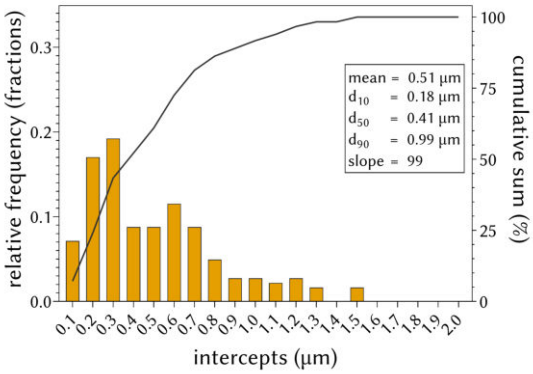

(e) GSD of cores.

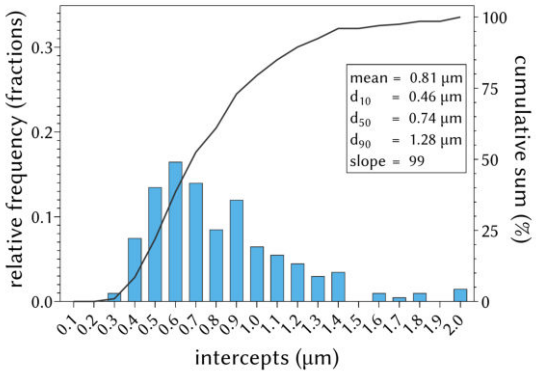

(f) GSD of grains.

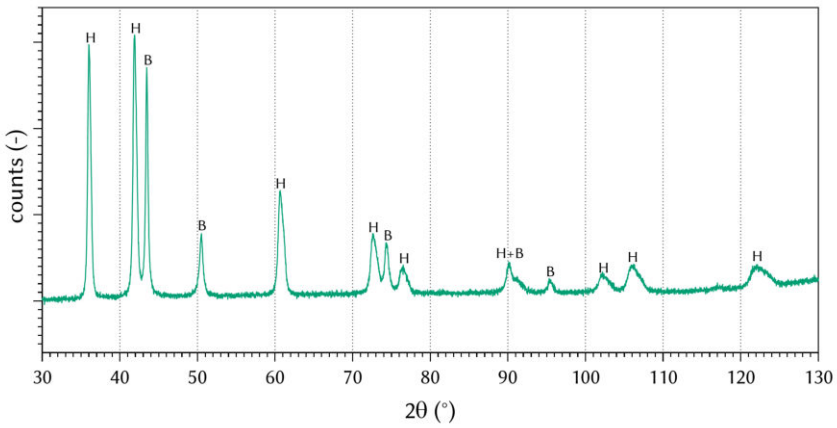

(g) XRD with hard phase (H) and binder (B) peaks identified.

Figure 148: LOM, BSE-SEM, GSD and XRD of N2-3_SAr.

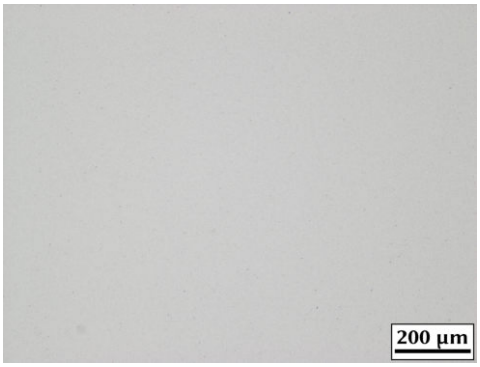

(a) LOM, 100x magnification.

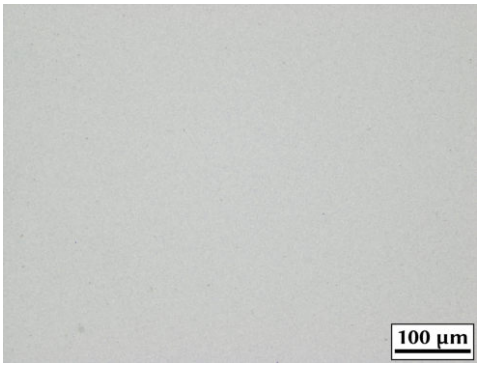

(b) LOM, 200x magnification.

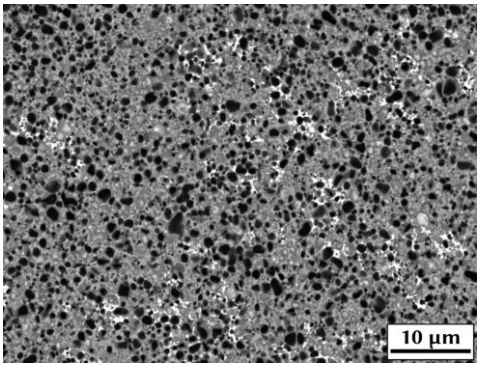

(c) BSE-SEM, 5000x magnification.

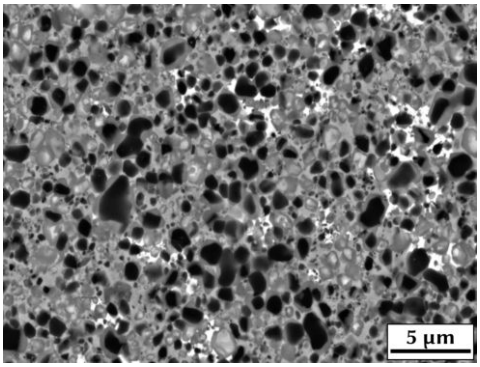

(d) BSE-SEM, 10,000x magnification.

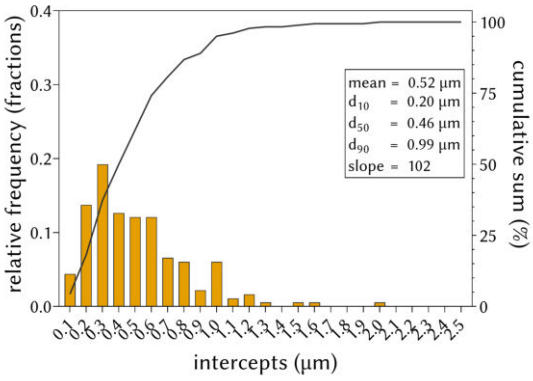

(e) GSD of cores.

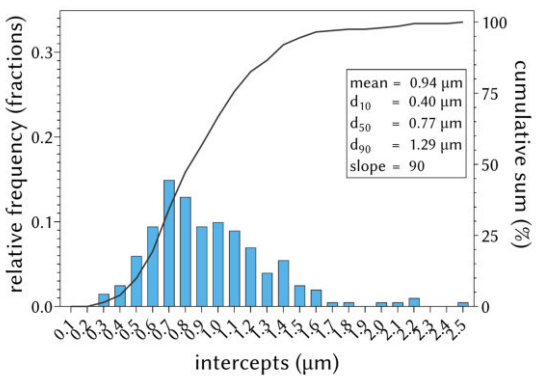

(f) GSD of grains.

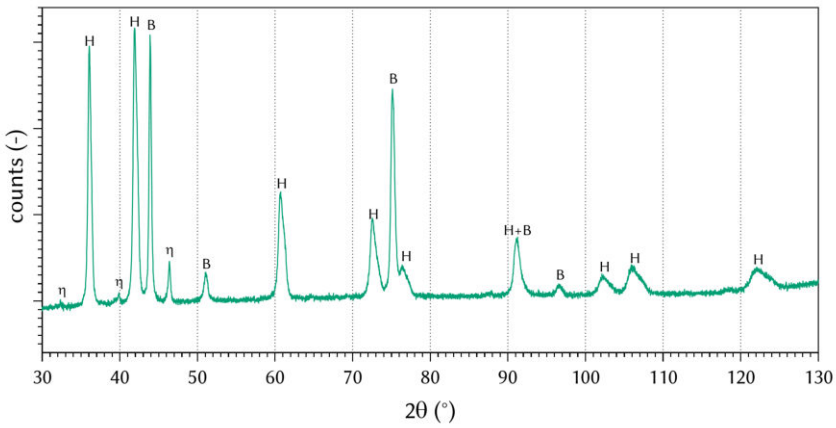

(g) XRD with hard phase (H) and binder (B) peaks identified.

Figure 149: LOM, BSE-SEM, GSD and XRD of N2-3_SN.

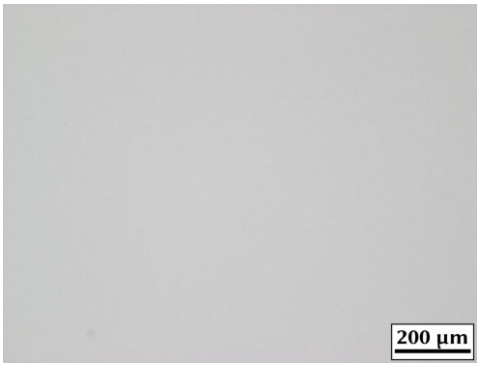

(a) LOM, 100x magnification.

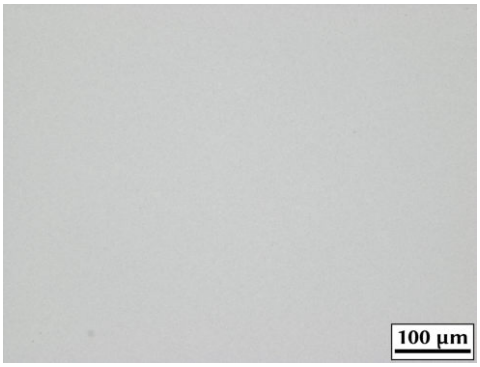

(b) LOM, 200x magnification.

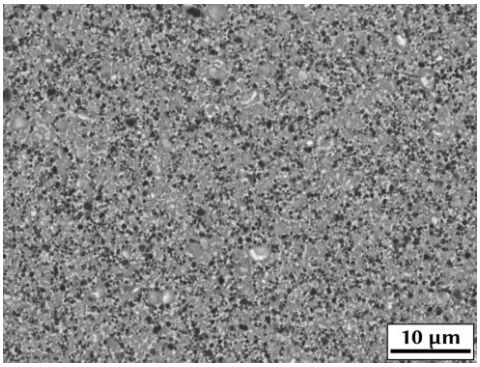

(c) BSE-SEM, 5000x magnification.

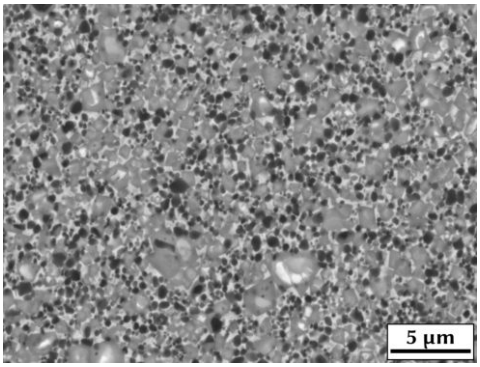

(d) BSE-SEM, 10,000x magnification.

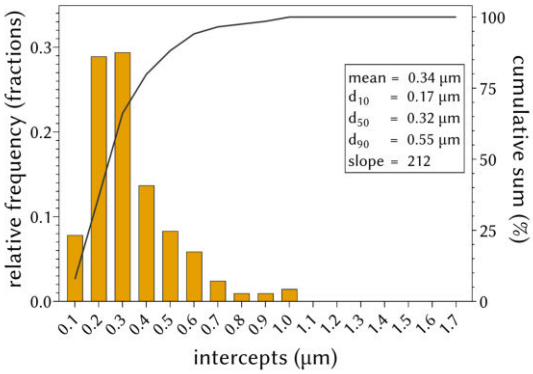

(e) GSD of cores.

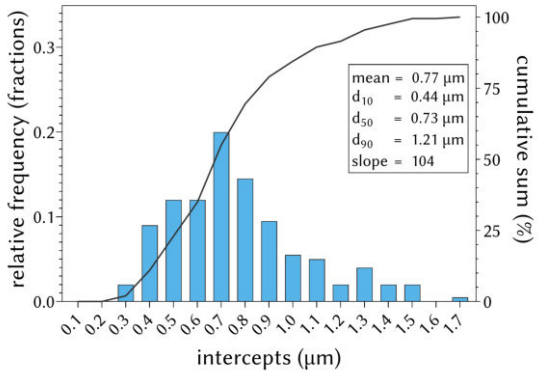

(f) GSD of grains.

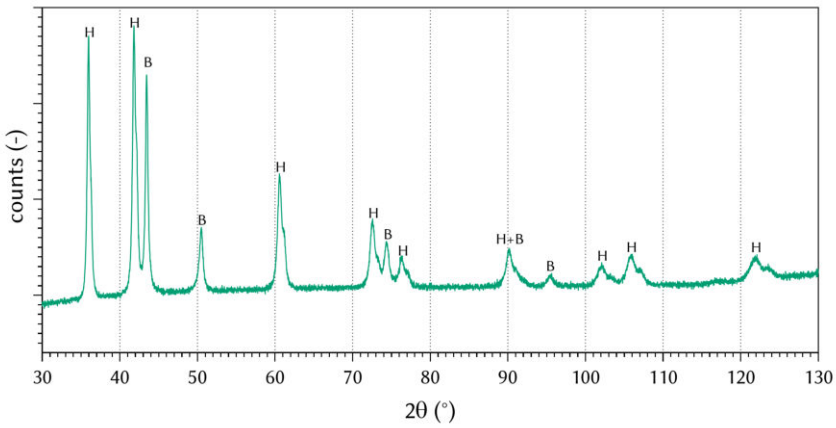

(g) XRD with hard phase (H) and binder (B) peaks identified.

Figure 150: LOM, BSE-SEM, GSD and XRD of N3-1_SAr.

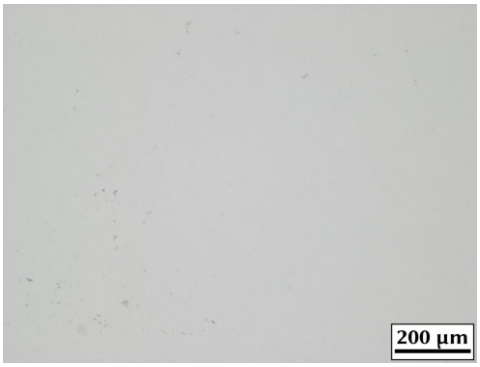

(a) LOM, 100x magnification.

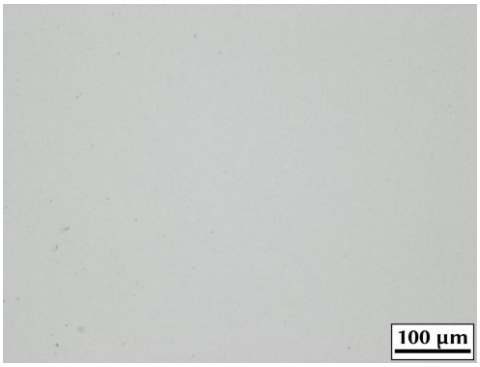

(b) LOM, 200x magnification.

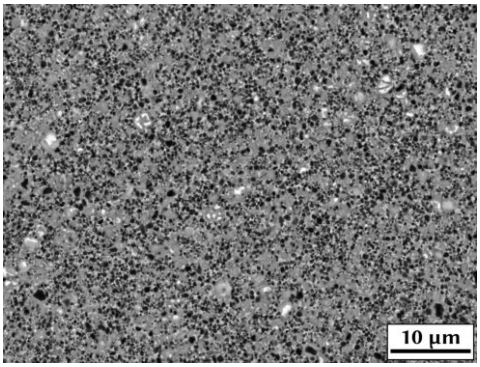

(c) BSE-SEM, 5000x magnification.

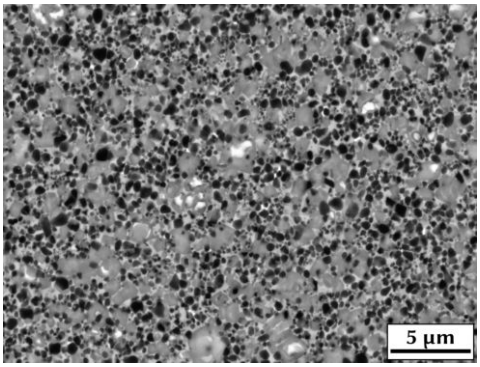

(d) BSE-SEM, 10,000x magnification.

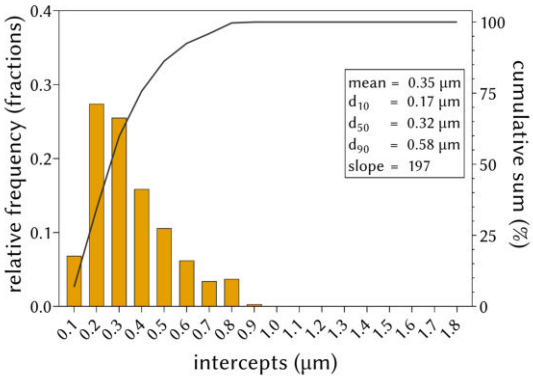

(e) GSD of cores.

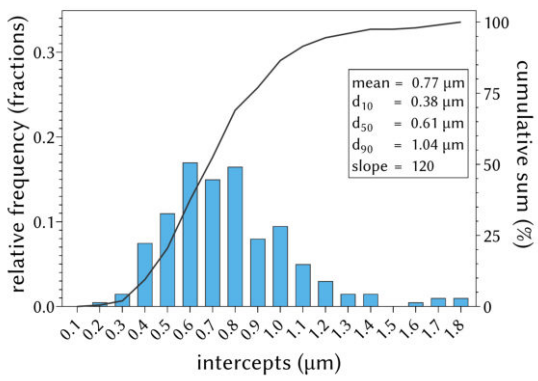

(f) GSD of grains.

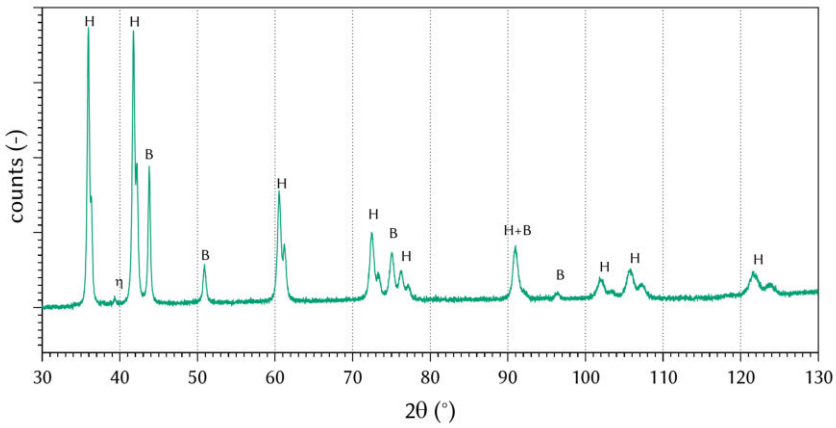

(g) XRD with hard phase (H) and binder (B) peaks identified.

Figure 151: LOM, BSE-SEM, GSD and XRD of N3-1_SN.

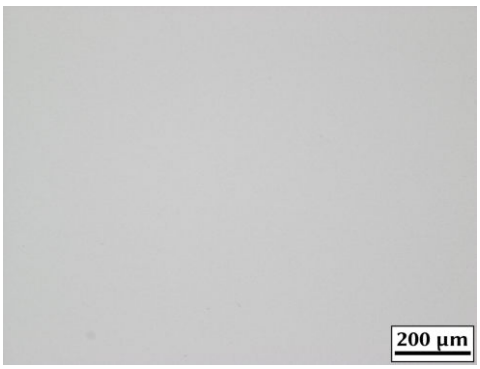

(a) LOM, 100x magnification.

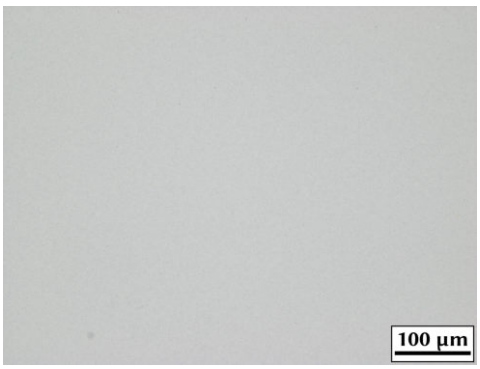

(b) LOM, 200x magnification.

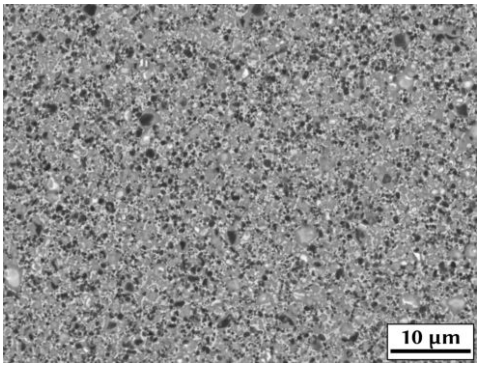

(c) BSE-SEM, 5000x magnification.

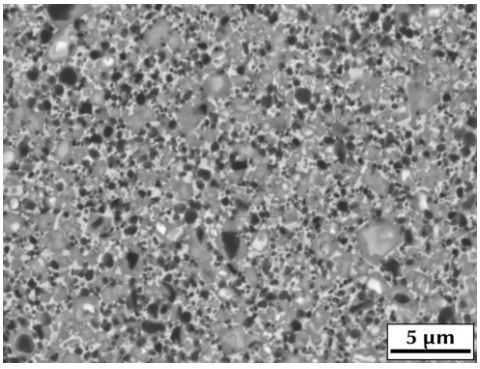

(d) BSE-SEM, 10,000x magnification.

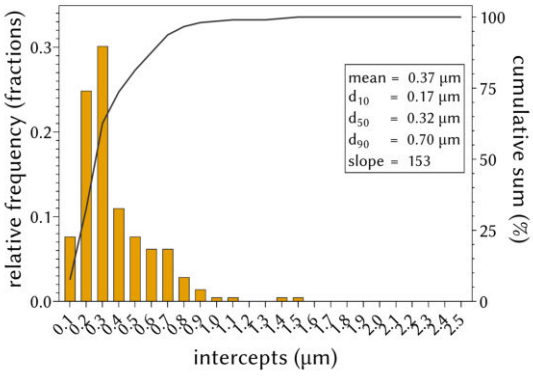

(e) GSD of cores.

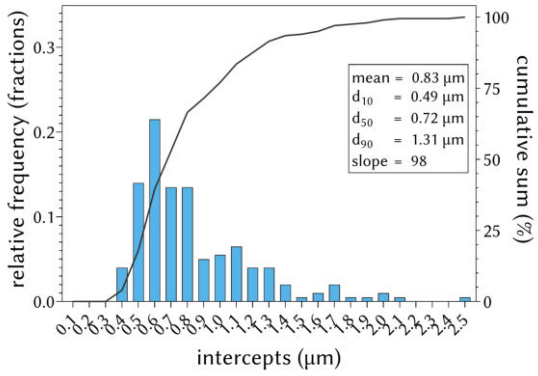

(f) GSD of grains.

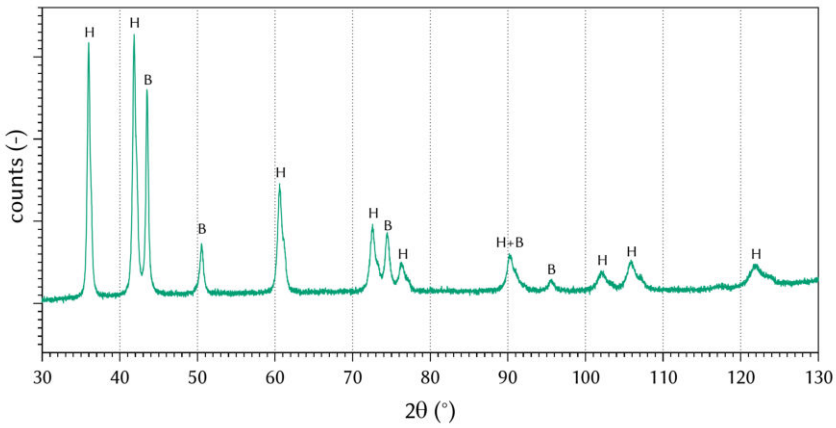

(g) XRD with hard phase (H) and binder (B) peaks identified.

Figure 152: LOM, BSE-SEM, GSD and XRD of N3-2_SAr.

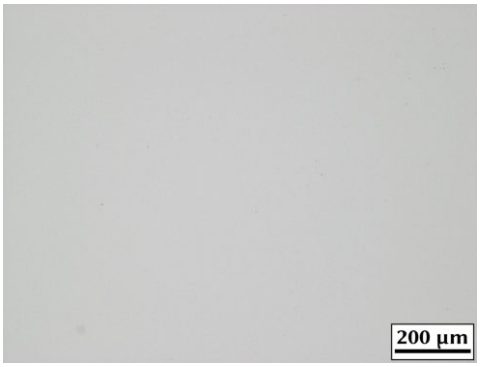

(a) LOM, 100x magnification.

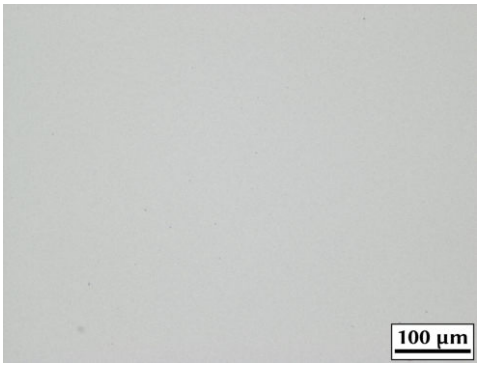

(b) LOM, 200x magnification.

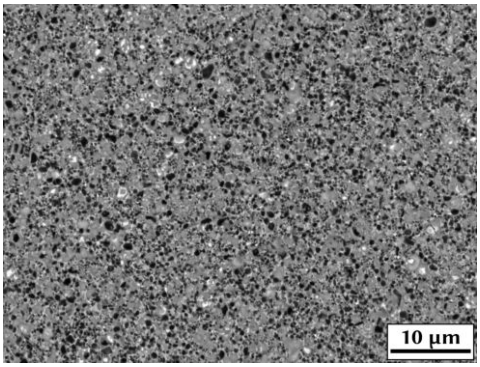

(c) BSE-SEM, 5000x magnification.

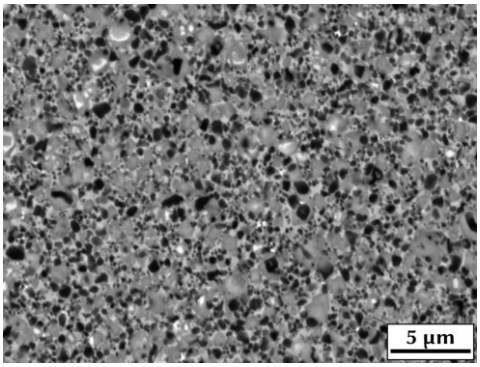

(d) BSE-SEM, 10,000x magnification.

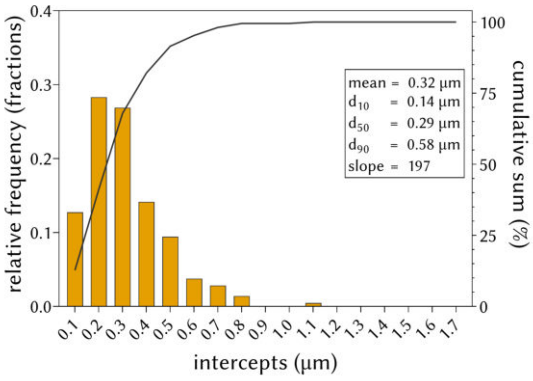

(e) GSD of cores.

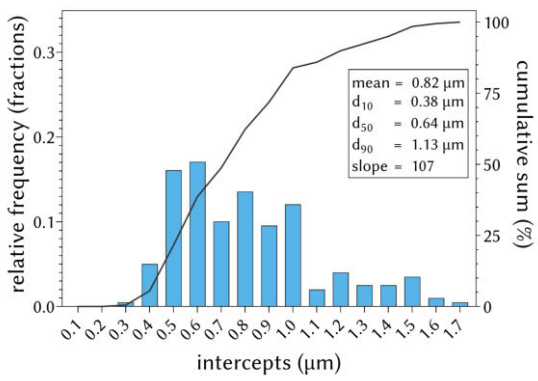

(f) GSD of grains.

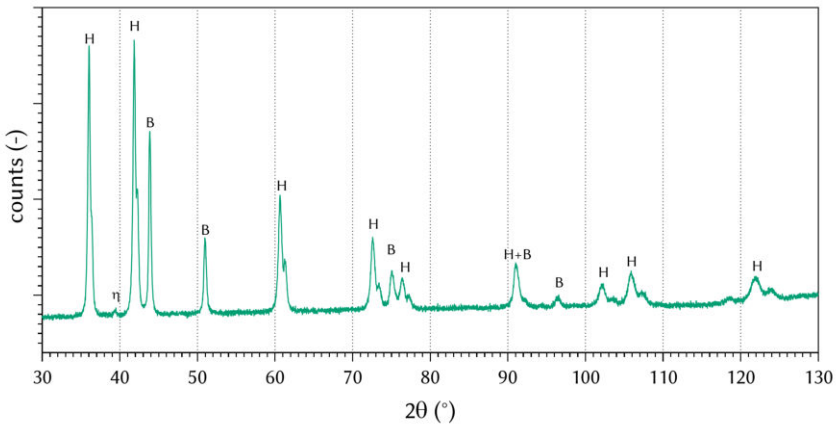

(g) XRD with hard phase (H) and binder (B) peaks identified.

Figure 153: LOM, BSE-SEM, GSD and XRD of N3-2_SN.

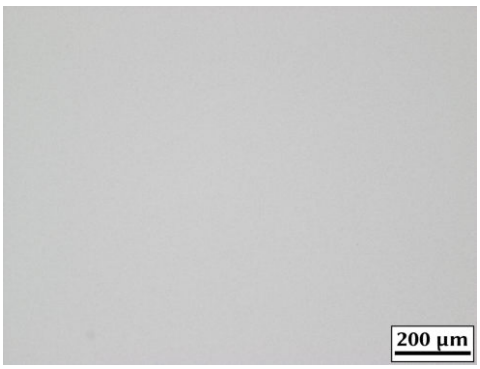

(a) LOM, 100x magnification.

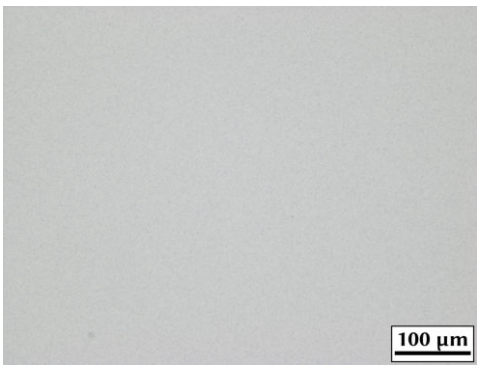

(b) LOM, 200x magnification.

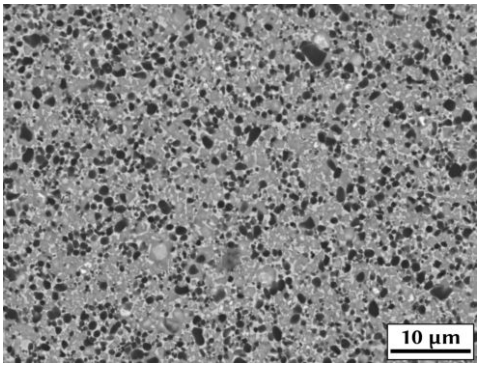

(c) BSE-SEM, 5000x magnification.

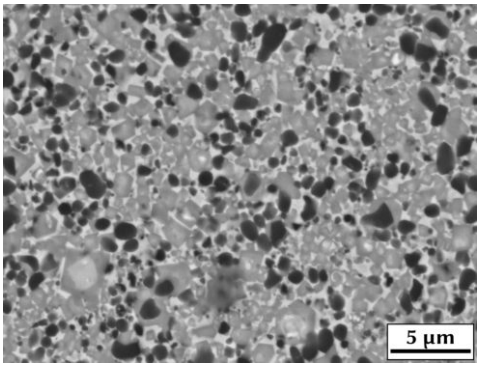

(d) BSE-SEM, 10,000x magnification.

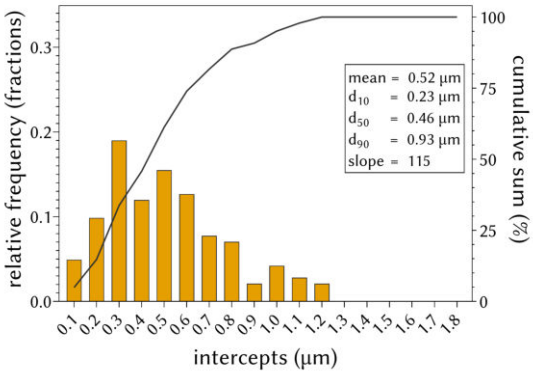

(e) GSD of cores.

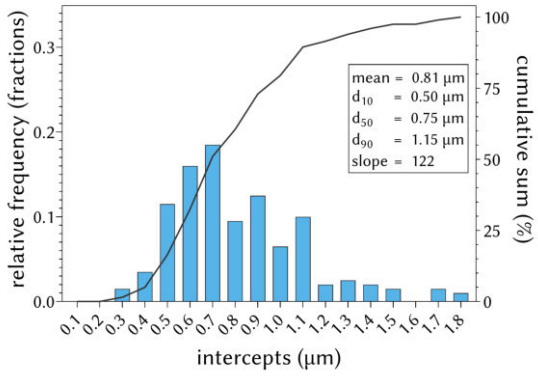

(f) GSD of grains.

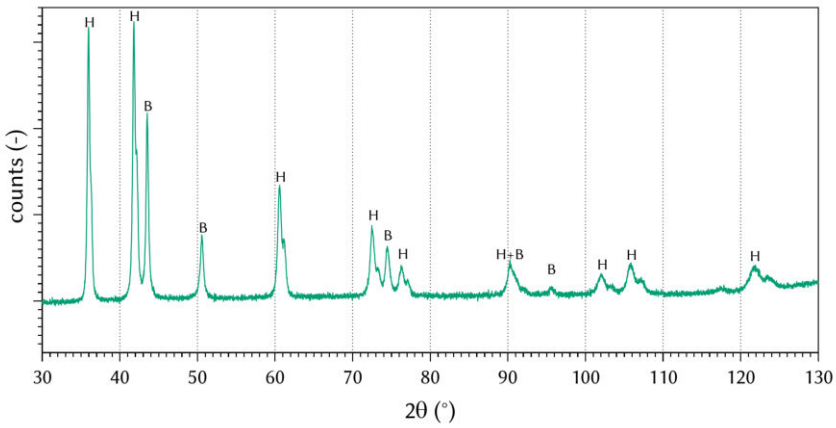

(g) XRD with hard phase (H) and binder (B) peaks identified.

Figure 154: LOM, BSE-SEM, GSD and XRD of N3-3_SAr.

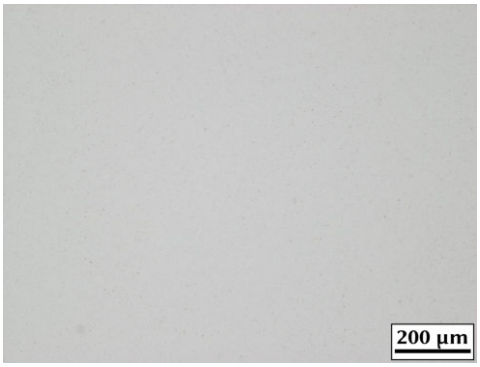

(a) LOM, 100x magnification.

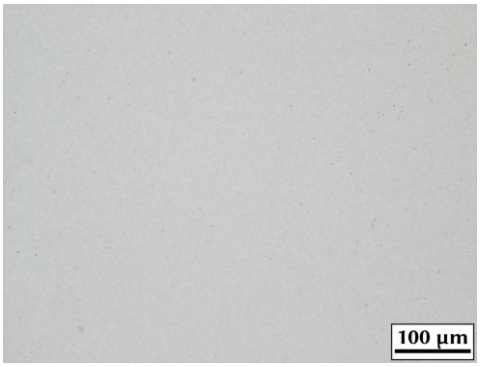

(b) LOM, 200x magnification.

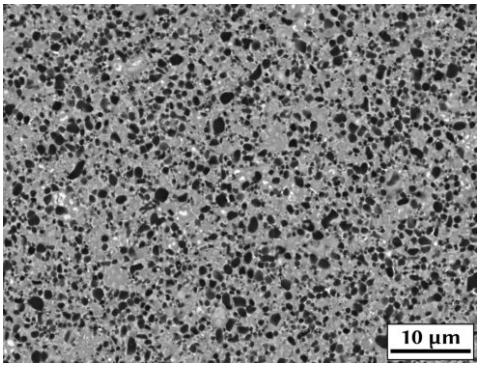

(c) BSE-SEM, 5000x magnification.

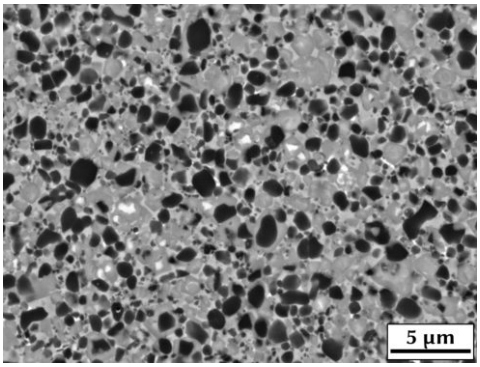

(d) BSE-SEM, 10,000x magnification.

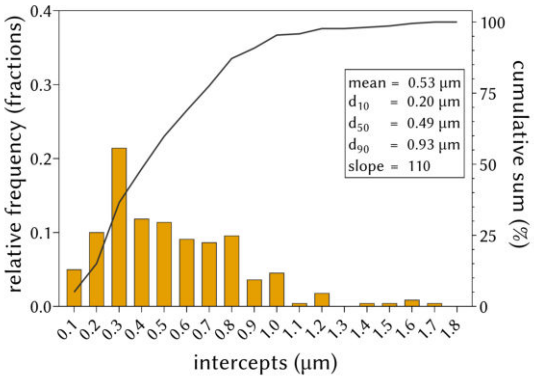

(e) GSD of cores.

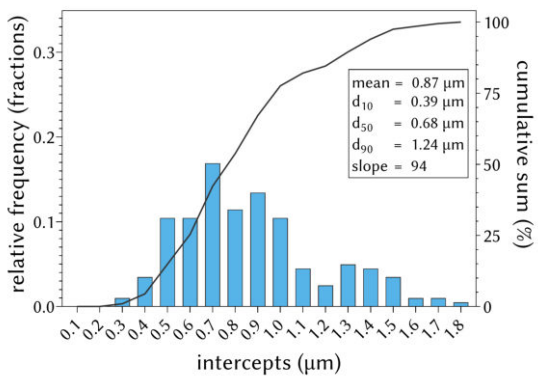

(f) GSD of grains.

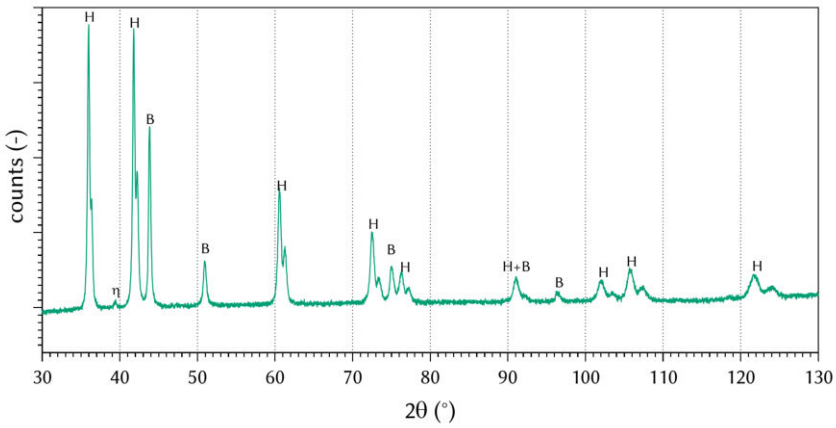

(g) XRD with hard phase (H) and binder (B) peaks identified.

Figure 155: LOM, BSE-SEM, GSD and XRD of N3-3_SN.

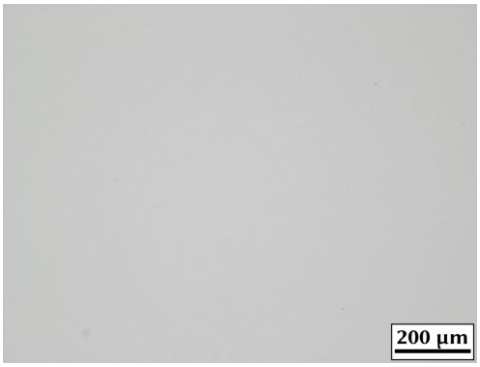

(a) LOM, 100x magnification.

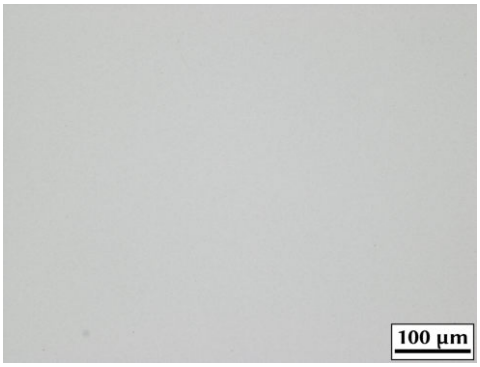

(b) LOM, 200x magnification.

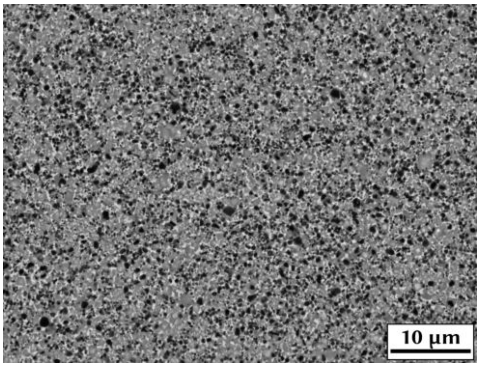

(c) BSE-SEM, 5000x magnification.

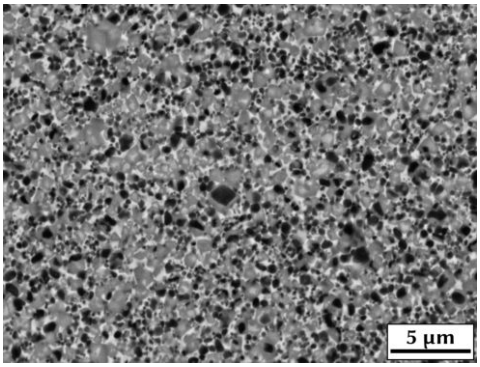

(d) BSE-SEM, 10,000x magnification.

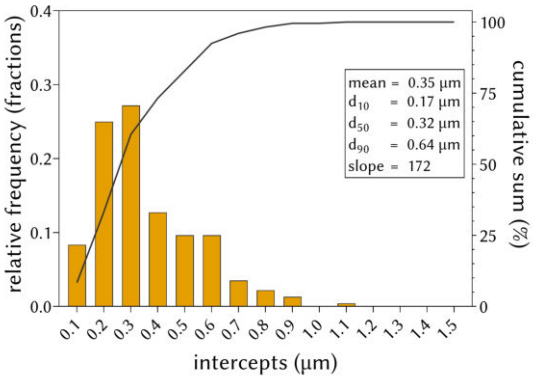

(e) GSD of cores.

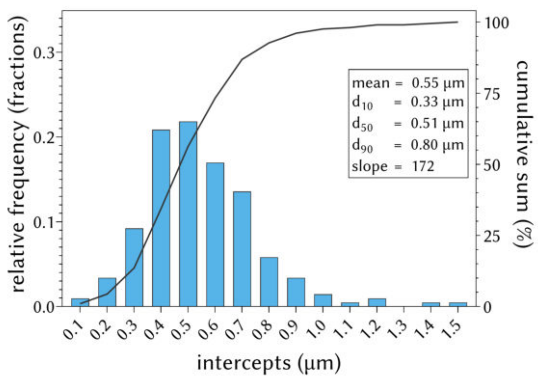

(f) GSD of grains.

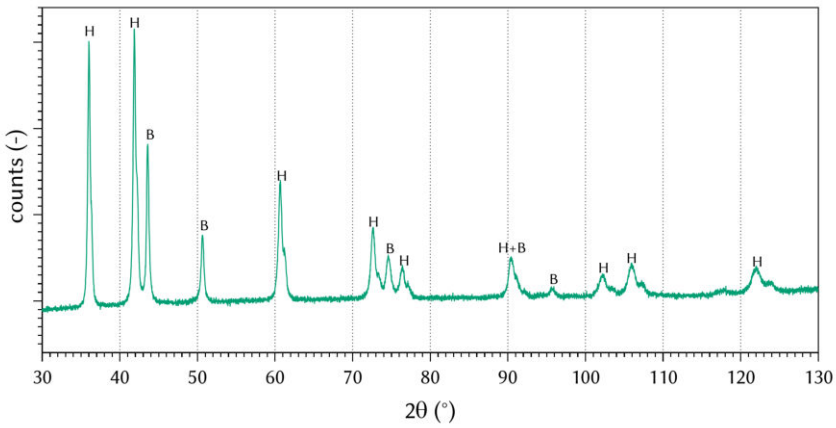

(g) XRD with hard phase (H) and binder (B) peaks identified.

Figure 156: LOM, BSE-SEM, GSD and XRD of N0-2+0.1%C_SAr.

(a) LOM, 100x magnification.

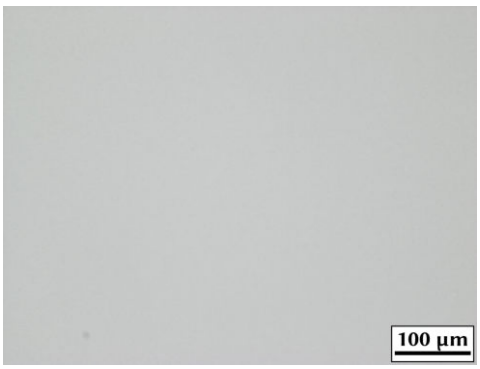

(b) LOM, 200x magnification.

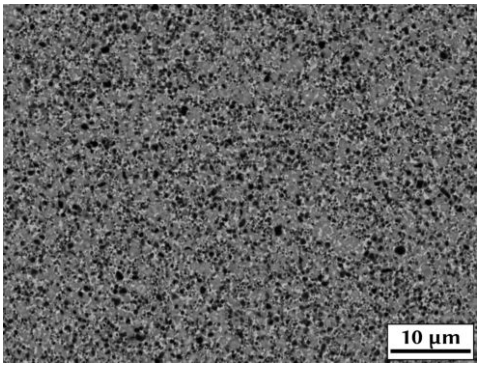

(c) BSE-SEM, 5000x magnification.

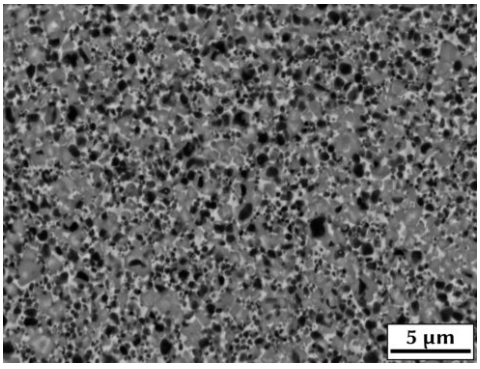

(d) BSE-SEM, 10,000x magnification.

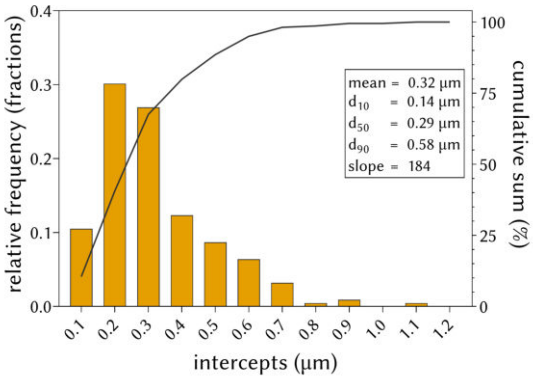

(e) GSD of cores.

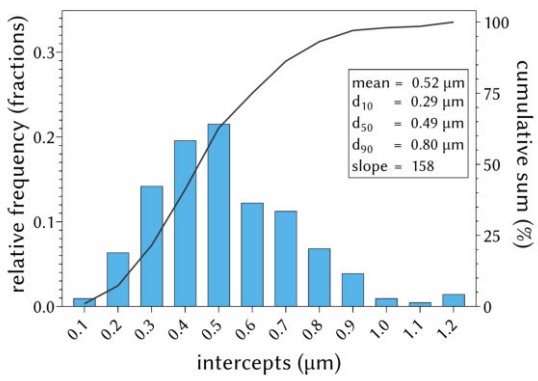

(f) GSD of grains.

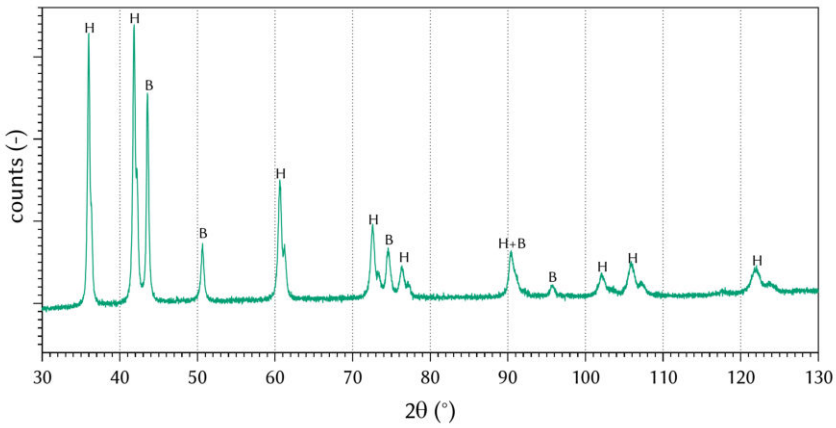

(g) XRD with hard phase (H) and binder (B) peaks identified.

Figure 157: LOM, BSE-SEM, GSD and XRD of N0-2+0.1%C_SN.

(a) LOM, 100x magnification.

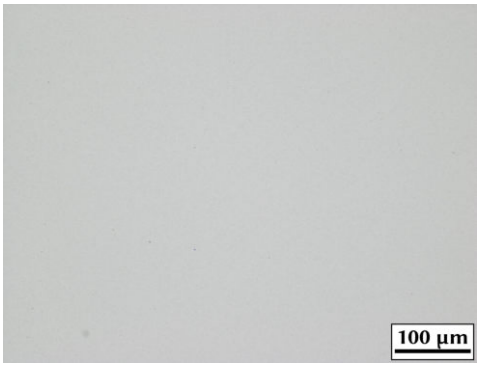

(b) LOM, 200x magnification.

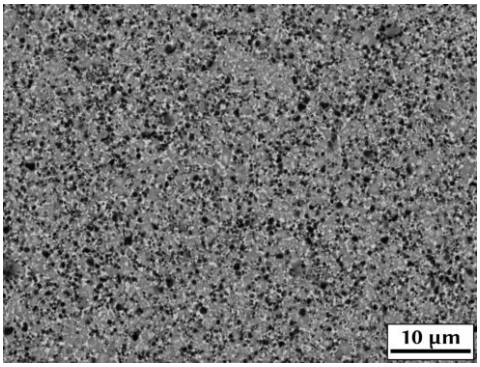

(c) BSE-SEM, 5000x magnification.

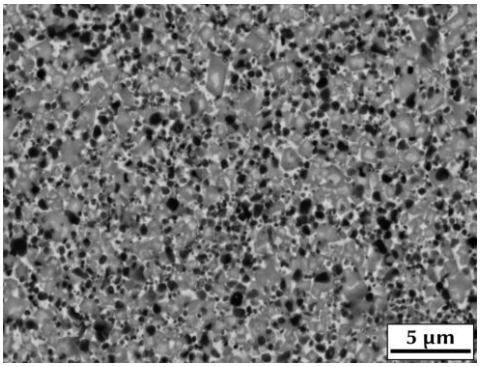

(d) BSE-SEM, 10,000x magnification.

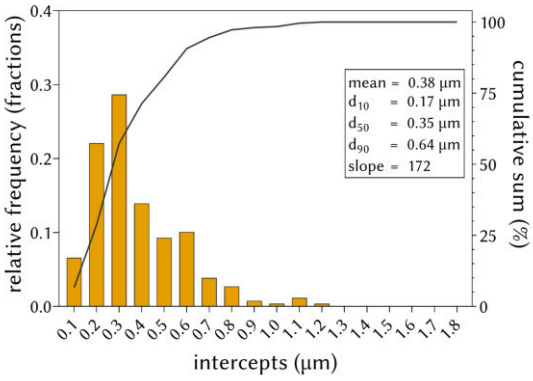

(e) GSD of cores.

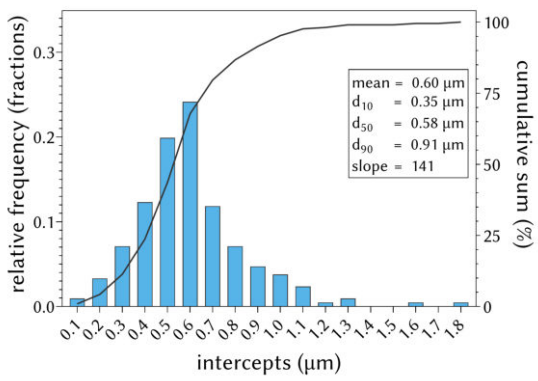

(f) GSD of grains.

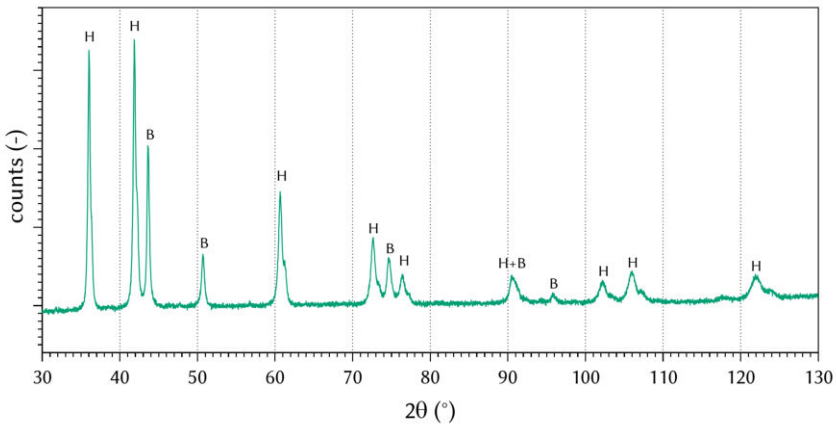

(g) XRD with hard phase (H) and binder (B) peaks identified.

Figure 158: LOM, BSE-SEM, GSD and XRD of N0-2+0.3%C_SAr.

(a) LOM, 100x magnification.

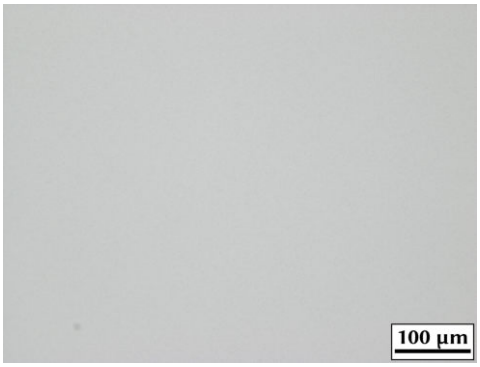

(b) LOM, 200x magnification.

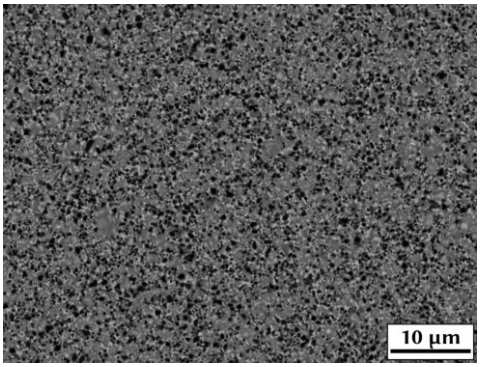

(c) BSE-SEM, 5000x magnification.

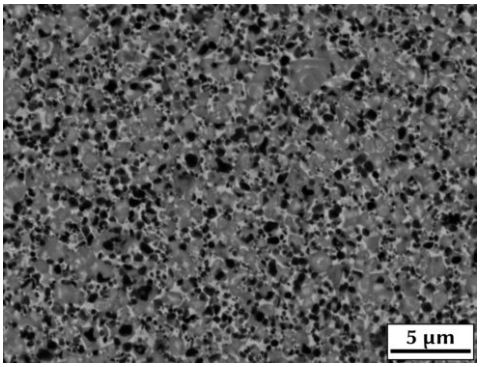

(d) BSE-SEM, 10,000x magnification.

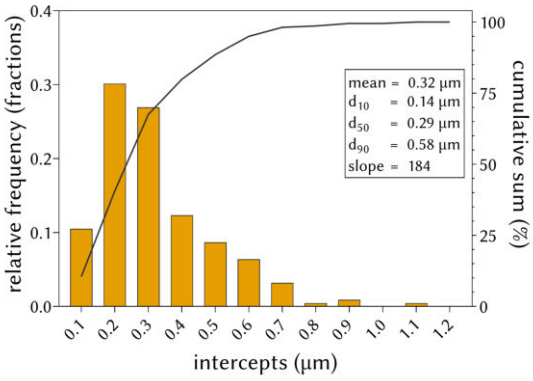

(e) GSD of cores.

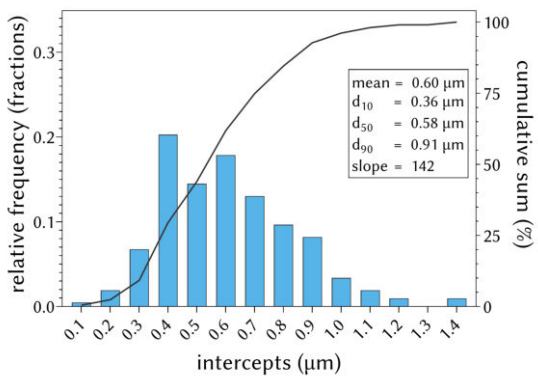

(f) GSD of grains.

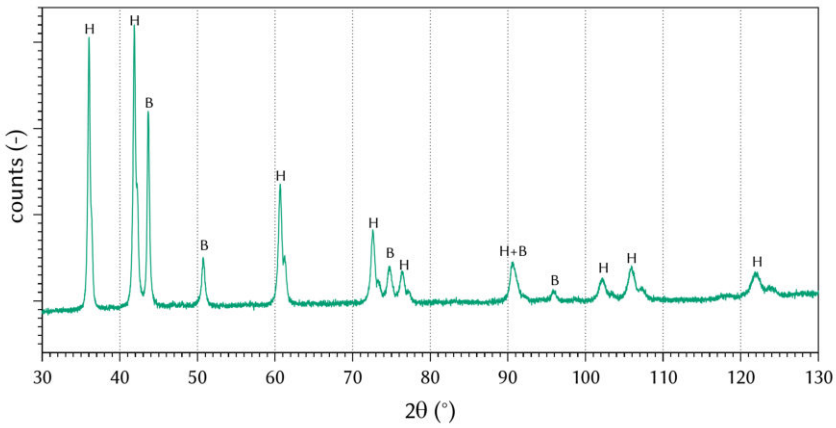

(g) XRD with hard phase (H) and binder (B) peaks identified.

Figure 159: LOM, BSE-SEM, GSD and XRD of N0-2+0.3%C_SN.

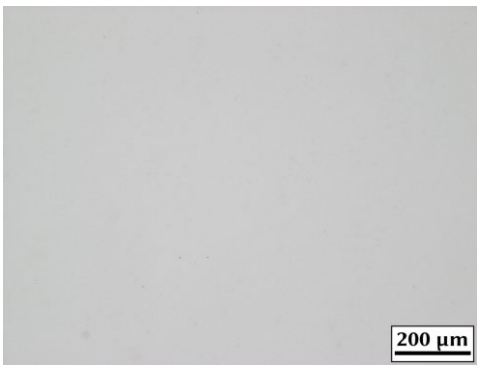

(a) LOM, 100x magnification.

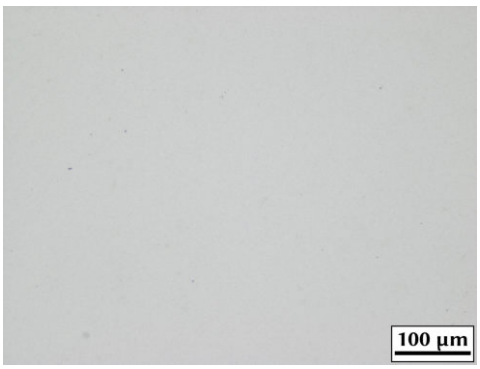

(b) LOM, 200x magnification.

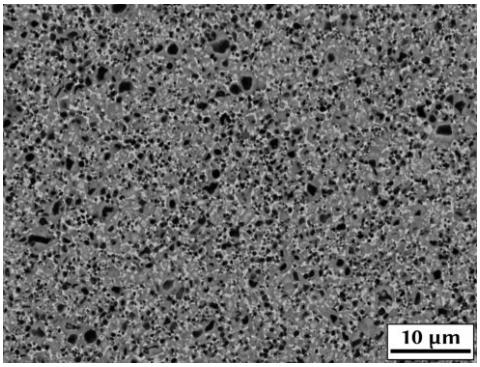

(c) BSE-SEM, 5000x magnification.

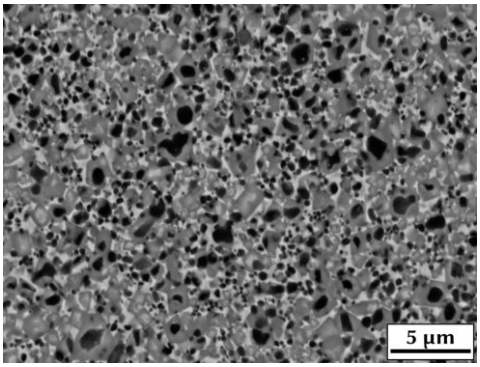

(d) BSE-SEM, 10,000x magnification.

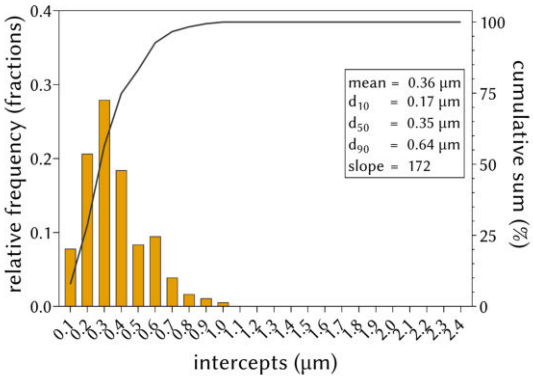

(e) GSD of cores.

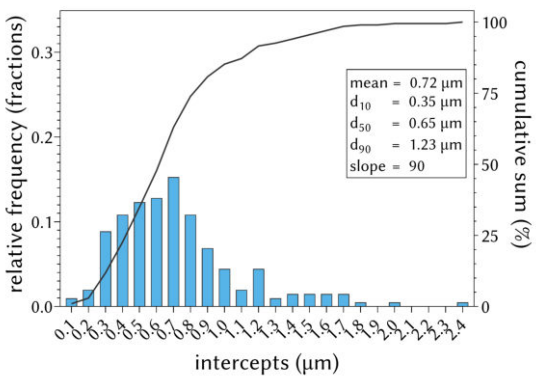

(f) GSD of grains.

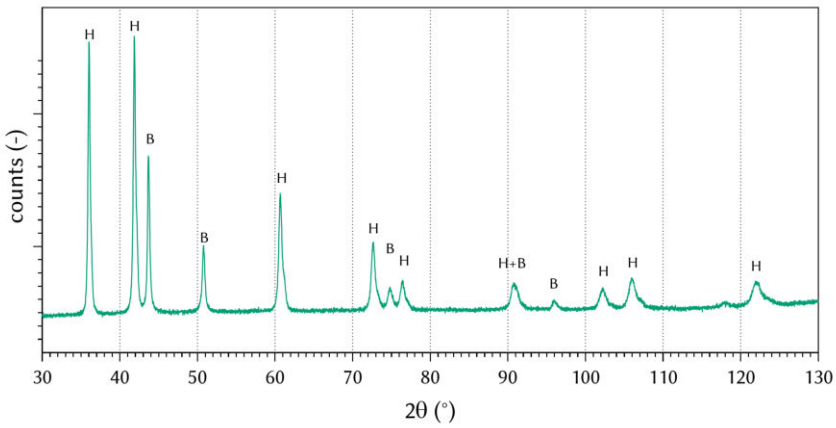

(g) XRD with hard phase (H) and binder (B) peaks identified.

Figure 160: LOM, BSE-SEM, GSD and XRD of N1-2+0.1%C_SAr.

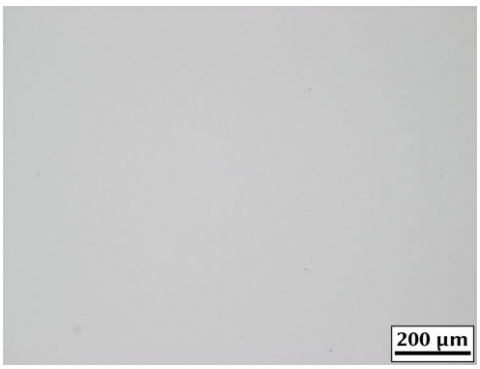

(a) LOM, 100x magnification.

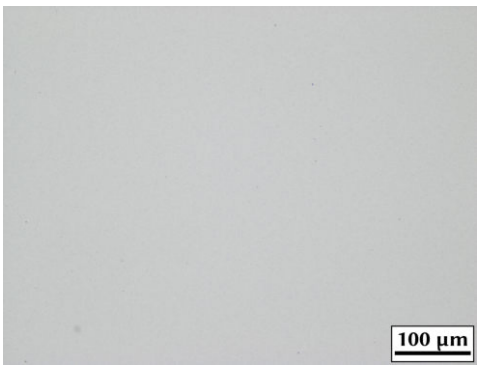

(b) LOM, 200x magnification.

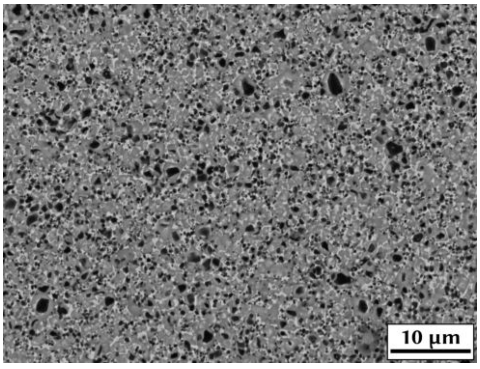

(c) BSE-SEM, 5000x magnification.

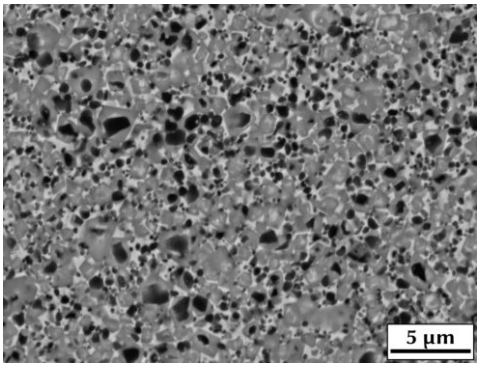

(d) BSE-SEM, 10,000x magnification.

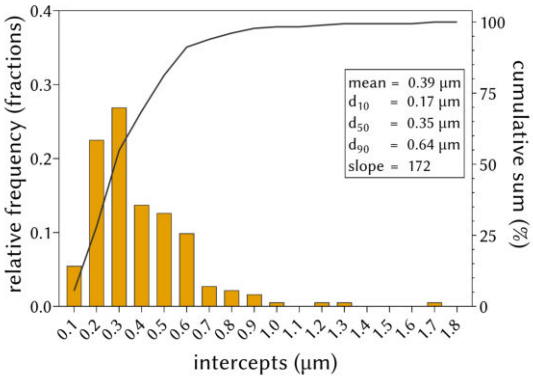

(e) GSD of cores.

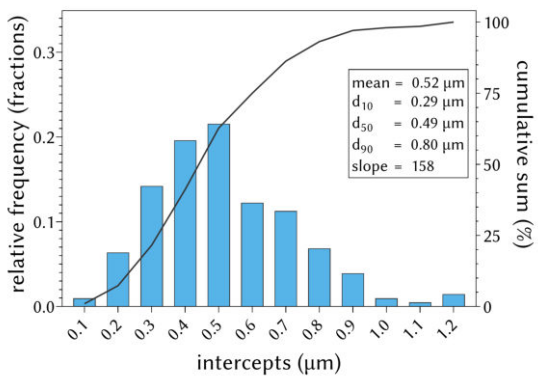

(f) GSD of grains.

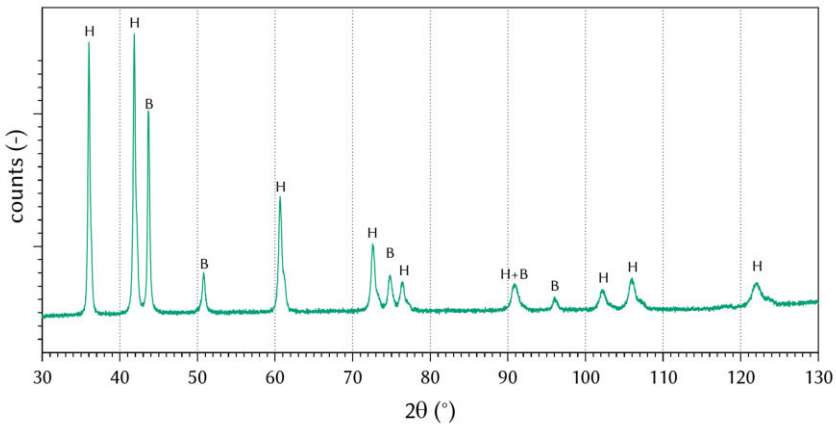

(g) XRD with hard phase (H) and binder (B) peaks identified.

Figure 161: LOM, BSE-SEM, GSD and XRD of N1-2+0.1%C_SN.

(a) LOM, 100x magnification.

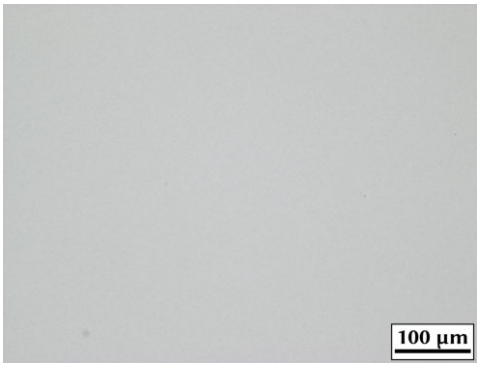

(b) LOM, 200x magnification.

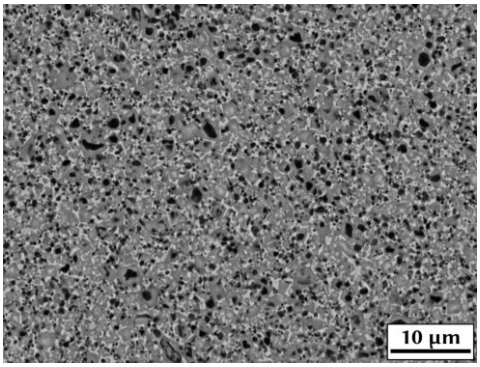

(c) BSE-SEM, 5000x magnification.

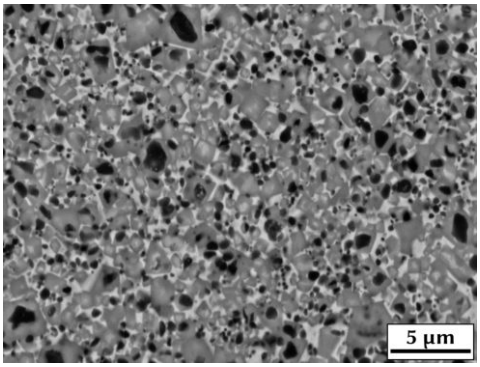

(d) BSE-SEM, 10,000x magnification.

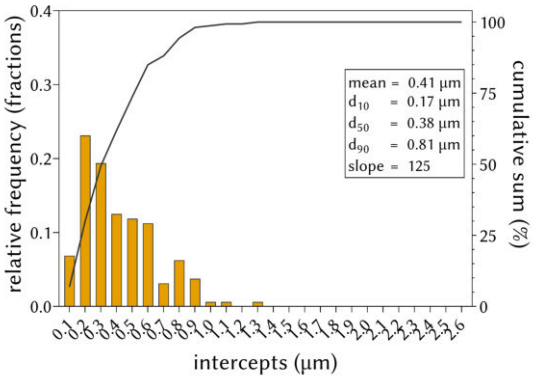

(e) GSD of cores.

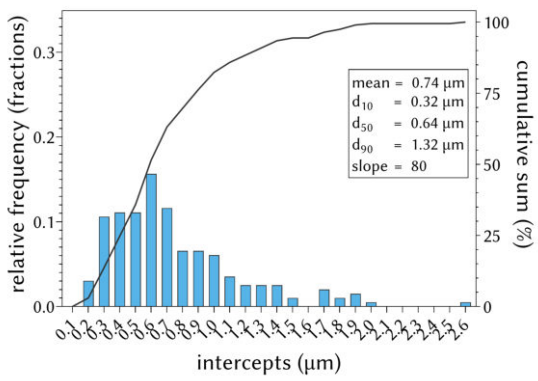

(f) GSD of grains.

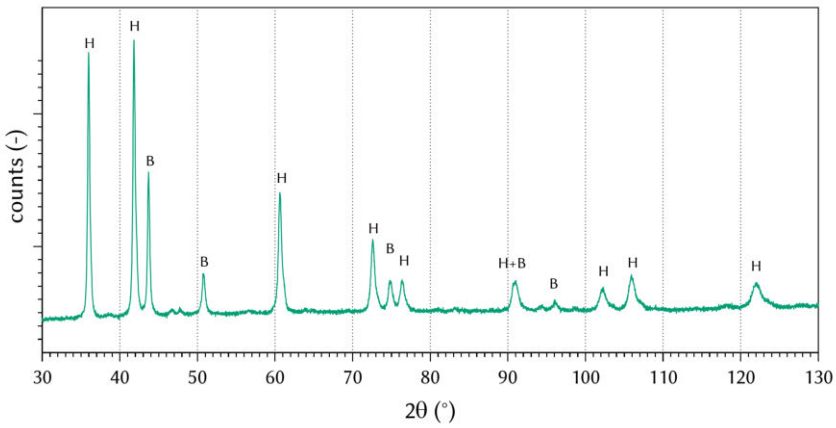

(g) XRD with hard phase (H) and binder (B) peaks identified.

Figure 162: LOM, BSE-SEM, GSD and XRD of N1-2+0.3%C_SAr.

(a) LOM, 100x magnification.

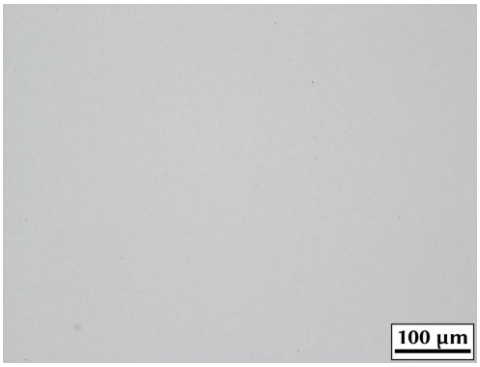

(b) LOM, 200x magnification.

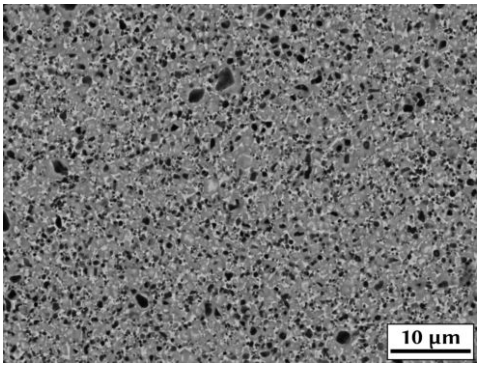

(c) BSE-SEM, 5000x magnification.

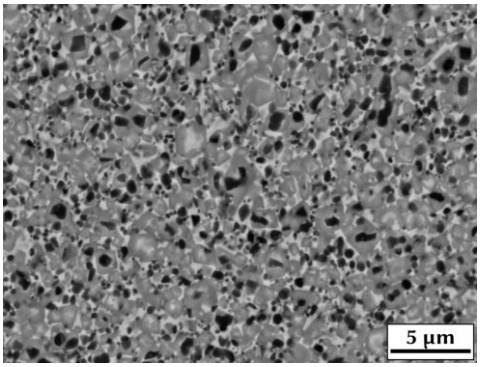

(d) BSE-SEM, 10,000x magnification.

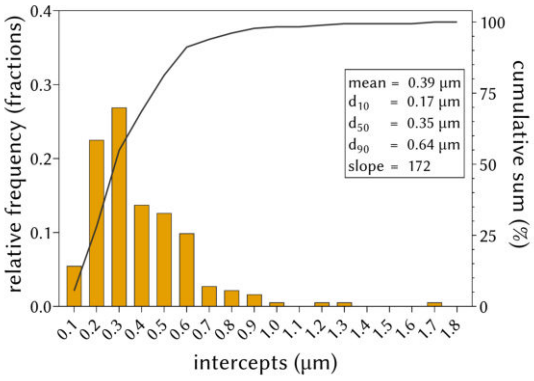

(e) GSD of cores.

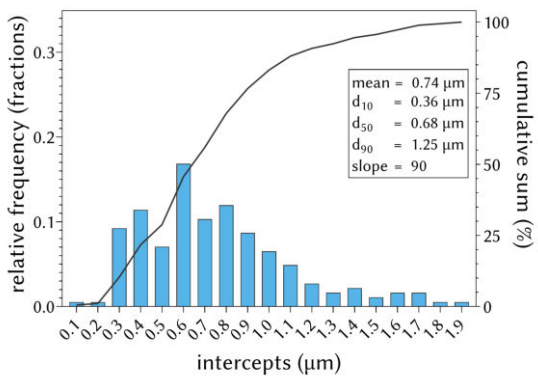

(f) GSD of grains.

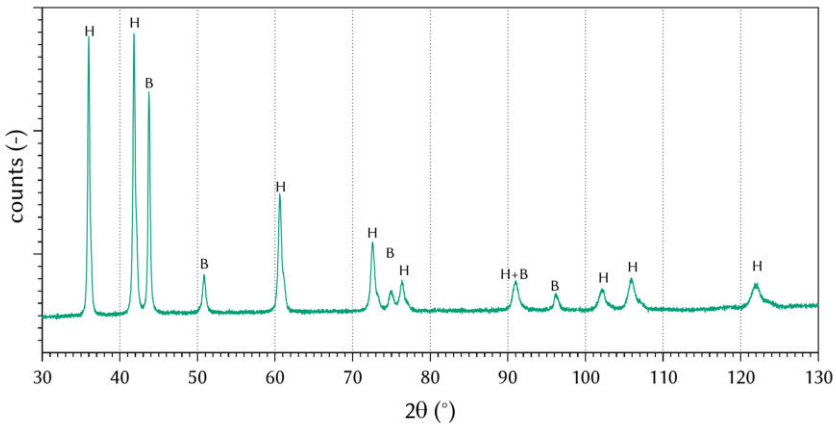

(g) XRD with hard phase (H) and binder (B) peaks identified.

Figure 163: LOM, BSE-SEM, GSD and XRD of N1-2+0.3%C_SN.

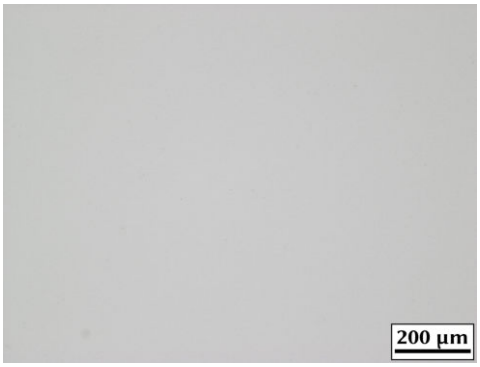

(a) LOM, 100x magnification.

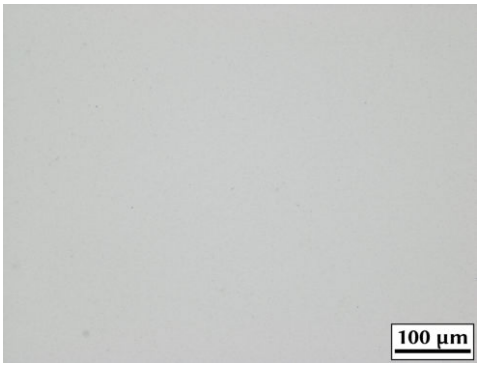

(b) LOM, 200x magnification.

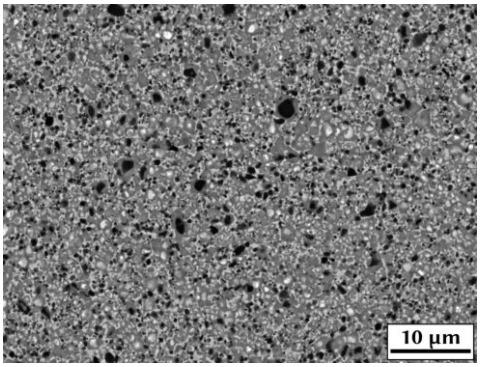

(c) BSE-SEM, 5000x magnification.

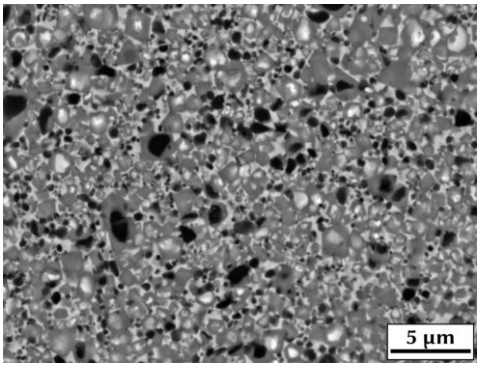

(d) BSE-SEM, 10,000x magnification.

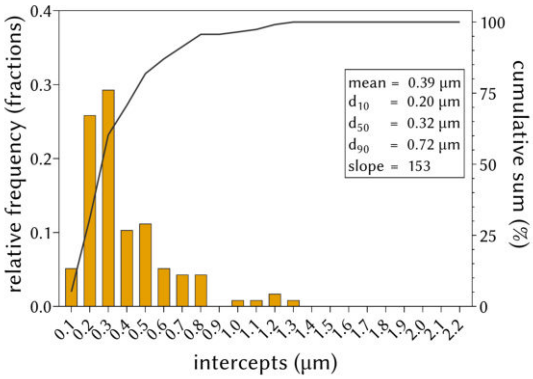

(e) GSD of cores.

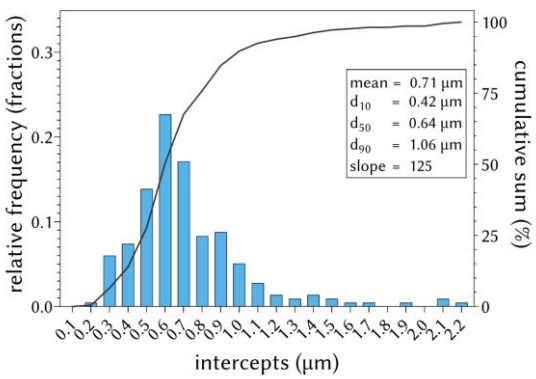

(f) GSD of grains.

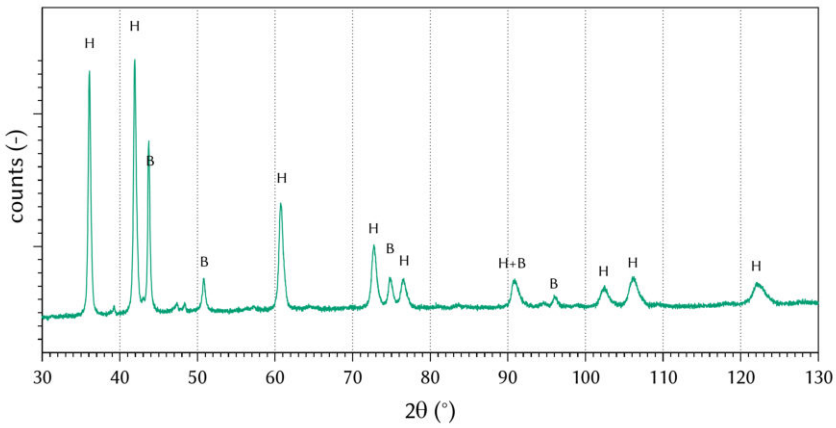

(g) XRD with hard phase (H) and binder (B) peaks identified.

Figure 164: LOM, BSE-SEM, GSD and XRD of N2-2+0.1%C_SAr.

(a) LOM, 100x magnification.

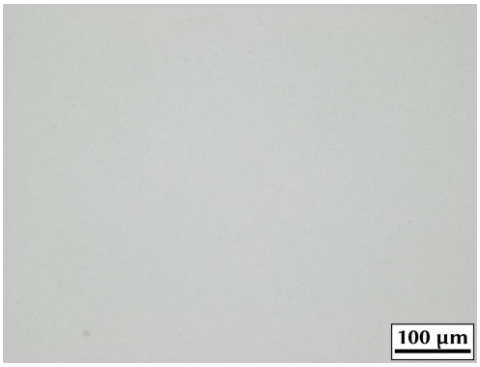

(b) LOM, 200x magnification.

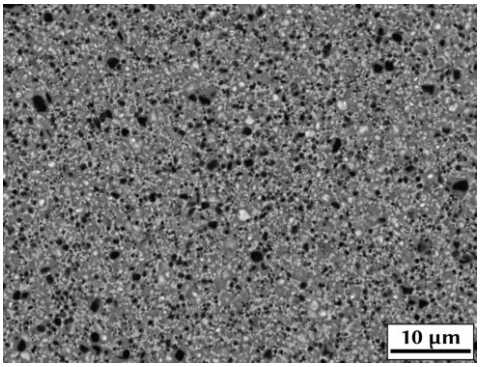

(c) BSE-SEM, 5000x magnification.

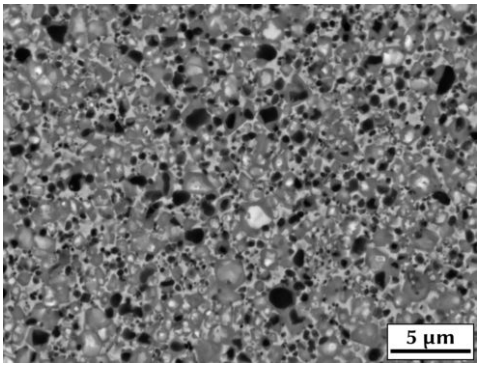

(d) BSE-SEM, 10,000x magnification.

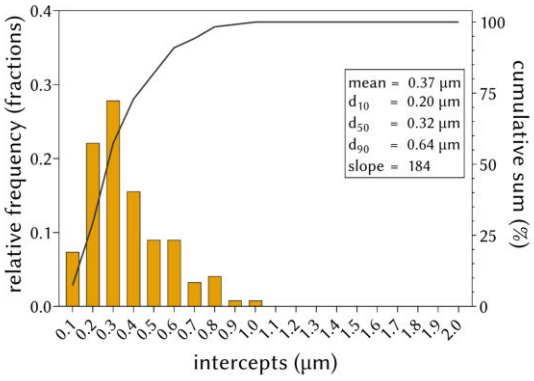

(e) GSD of cores.

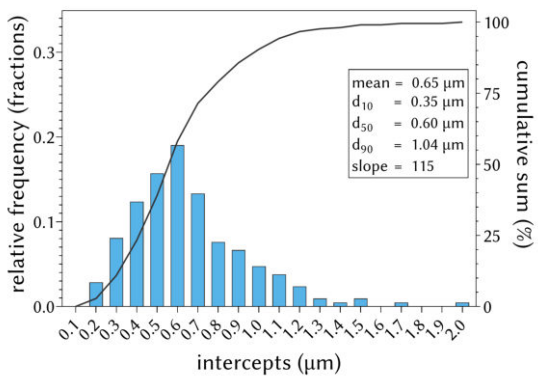

(f) GSD of grains.

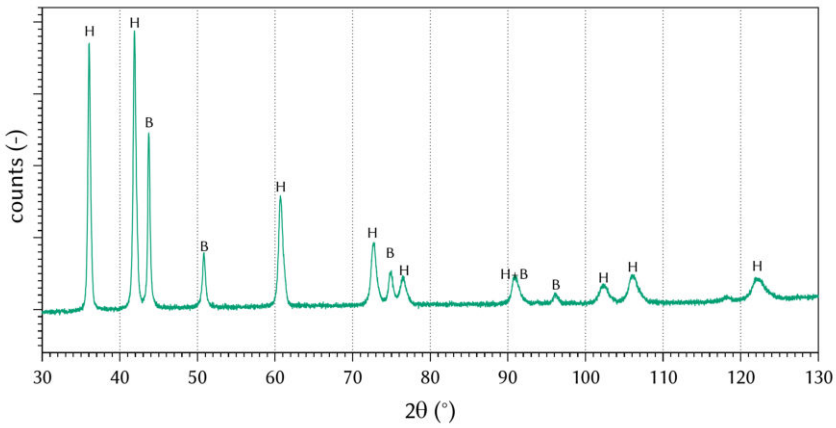

(g) XRD with hard phase (H) and binder (B) peaks identified.

Figure 165: LOM, BSE-SEM, GSD and XRD of N2-2+0.1%C_SN.

(a) LOM, 100x magnification.

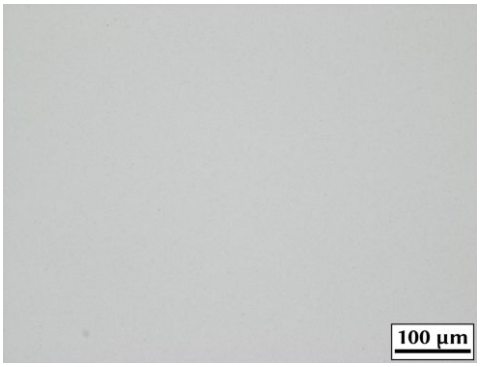

(b) LOM, 200x magnification.

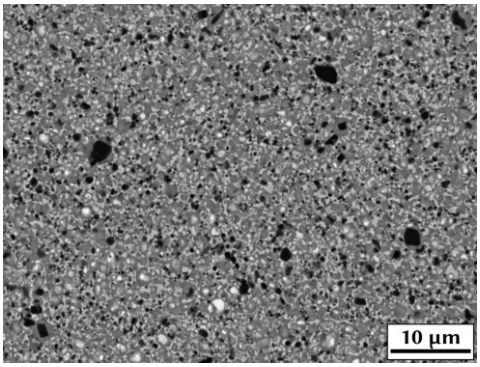

(c) BSE-SEM, 5000x magnification.

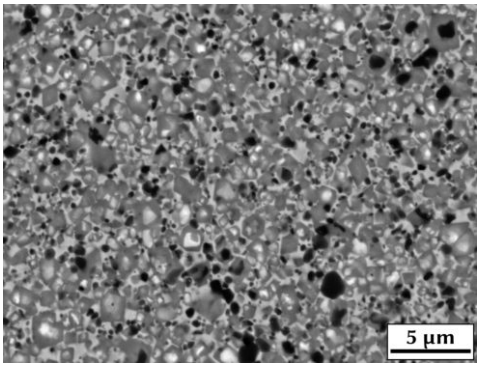

(d) BSE-SEM, 10,000x magnification.

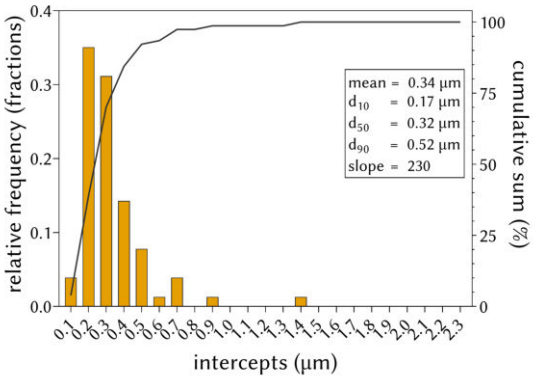

(e) GSD of cores.

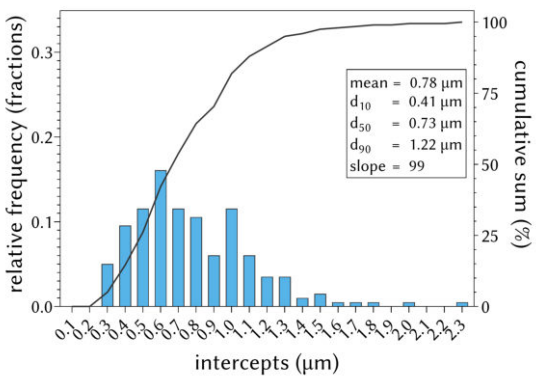

(f) GSD of grains.

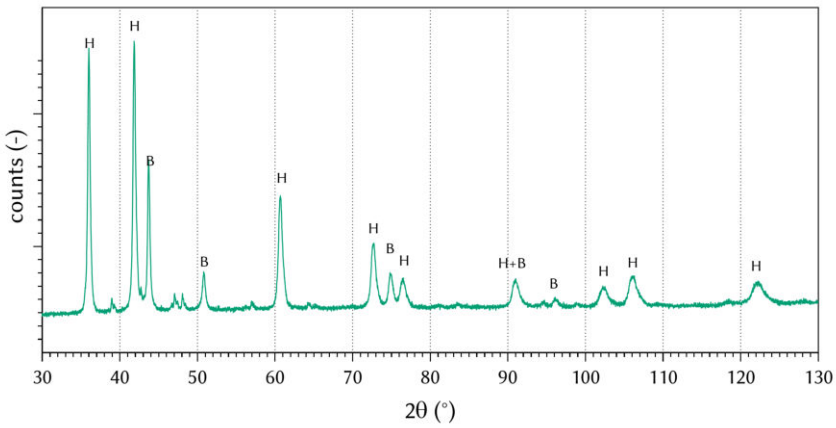

(g) XRD with hard phase (H) and binder (B) peaks identified.

Figure 166: LOM, BSE-SEM, GSD and XRD of N2-2+0.3%C_SAr.

(a) LOM, 100x magnification.

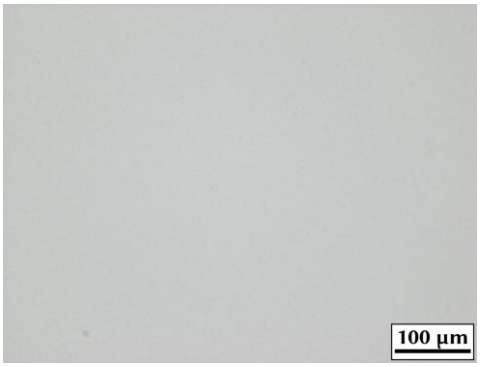

(b) LOM, 200x magnification.

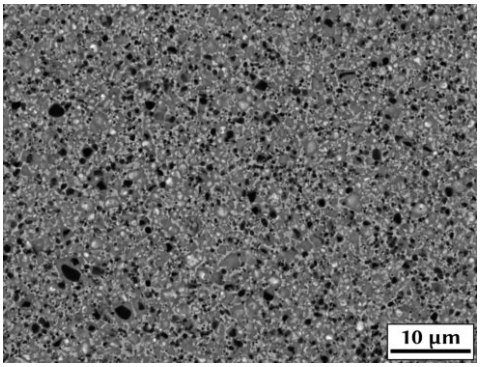

(c) BSE-SEM, 5000x magnification.

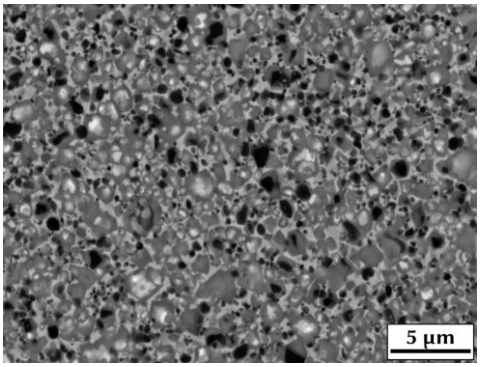

(d) BSE-SEM, 10,000x magnification.

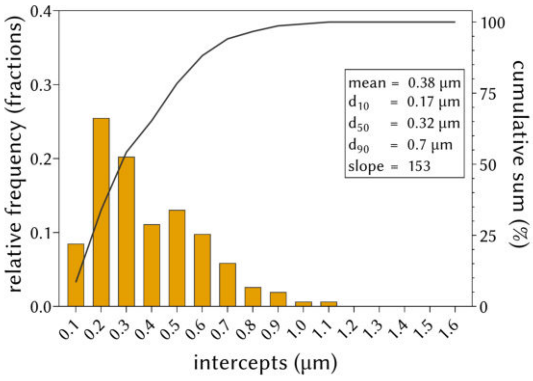

(e) GSD of cores.

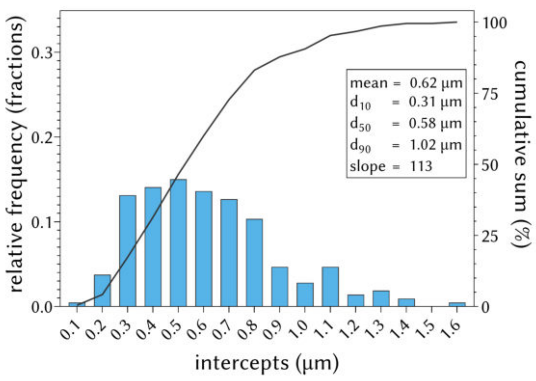

(f) GSD of grains.

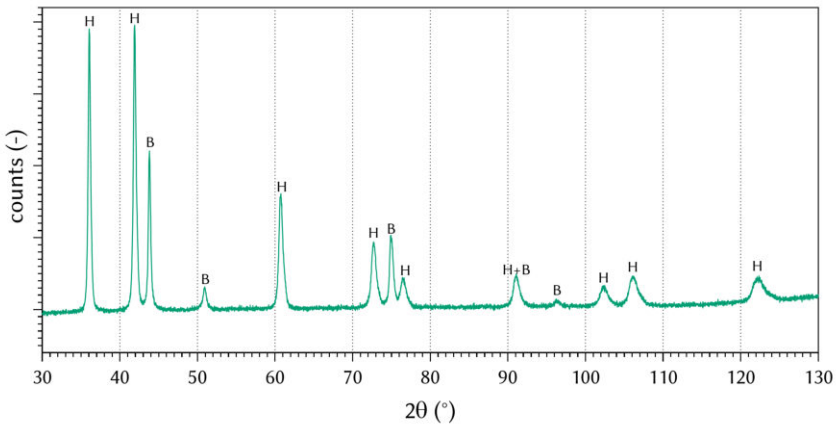

(g) XRD with hard phase (H) and binder (B) peaks identified.

Figure 167: LOM, BSE-SEM, GSD and XRD of N2-2+0.3%C_SN.